A NEW APPROACH TO VALIDATE SUBGRID MODELS IN COMPLEX HIGH REYNOLDS NUMBER FLOWS

Suresh Menon
School of Aerospace Engineering
Georgia Institute of Technology
Atlanta, Georgia 30332-0150

DISTRIBUTION STATEMENT A
Approved for public release;
Distribution Unlimited

submitted to

Office of Naval Research

March 1998

19980326 033

A NEW APPROACH TO VALIDATE SUBGRID MODELS IN COMPLEX HIGH REYNOLDS NUMBER FLOWS

Final Report
Grant Number: N00014-93-1-0342

Suresh Menon
School of Aerospace Engineering
Georgia Institute of Technology
Atlanta, Georgia 30332-0150

a. Description of the Scientific/Technical Goals

The overall objective was to develop new and advanced subgrid models that can be used for large-eddy simulations (LES) of high Reynolds number flows in complex geometries. This study was motivated by the fact that subgrid models for LES of high Reynolds number flows currently do not exist. Methods that use data from direct numerical simulations (DNS) to validate subgrid models cannot be used for high Reynolds number flows. In this research, techniques that do not require DNS results for evaluating the subgrid model capabilities were employed in physical space to evaluate subgrid models. A new local dynamic model was also developed in this study.

The overall technical objectives of this research were:

[1] To develop technique(s) to analyze the behavior of subgrid models in physical space
[2] To demonstrate the analysis technique(s) for high Reynolds number flows
[3] To use the analysis techniques to optimize and develop new subgrid models for high Reynolds number flows in complex domains.

All the above objectives have been successfully achieved in this research.

b. Significant Accomplishments

A new localized dynamic subgrid model was developed by using a method that employed the scale similarity concept for validating the behavior of the subgrid models and to determine the dynamically evolving model coefficients. This model is based on the transport solution of the subgrid kinetic energy. Since the scale similarity approach can be used directly in the physical space, there was no need to employ spectral space information for implementing the subgrid model. Also, this localized dynamic subgrid model does not require the Germano's identity since it employs the scale similarity between the Leonard's stress at the test filter level and the subgrid stress at the grid level. As a result, many of the problems encountered in the Germano's method (such as the numerical instability, ill-conditioning, etc.) are avoided completely. Fully local evaluation of the dynamic model coefficients are obtained in this model without any ad hoc fixes proposed in the past. Thus, the new dynamic approach has potential for application to more complex flows.

The flow fields where no averaging or ad hoc fixes were required are:

(i) Taylor-Green flow,
(ii) Decaying Isotropic turbulence,
(iii) Forced isotropic turbulence,
(iv) Rotating isotropic turbulence,
(v) Temporal mixing layers with and without chemical reactions,
(vi) Spatially evolving circular jet with axial entrainment,
(vi) Turbulent Couette flow,
(vii) Boundary layers with a separation bubble
(viii) Flow in a square duct
(ix) Supersonic Isotropic turbulence
(x) Supersonic Spatial Mixing Layers

These cases contain all element of complex turbulent flows and therefore, validation in these flows serves as the demonstration of the basic capability of this model. Test cases (i)-(iii) were studied in FY95 while the test cases (iv)-(vii) have been investigated during FY96. Validation in these flows was accomplished by direct comparison with high Reynolds number experimental data.

The results obtained this year are discussed in detail in the papers (Menon and Kim, 1996; Kim, 1996, Kim and Menon, 1996a, 1996b; Chakravarthy and Menon, 1996). The results presented in these papers clearly show that the proposed model is (i) superior to classical eddy viscosity based dynamic model, (ii) can predict the flow accurately using relatively coarse grids, and (iii) is computationally very efficient. In the following, we summarizes some of the highlights of the research.

Application of the New Local Dynamic Subgrid Model to Complex Flows:

The current model is based on the solution of the transport equation for the subgrid kinetic energy. The closure of the subgrid stresses is still carried out using an eddy viscosity representation; however, unlike the classical Germano's eddy viscosity model (which implicitly requires equilibrium between production and dissipation), the present model allows for local nonequilibrium between production and dissipation. Furthermore, in the Germano's approach, an exact mathematical identity between stresses in at the two filter levels is used to obtain the dynamic coefficient. However, since the terms in the mathematical identity are replaced by their respective models, the difference between the two modeled terms can become inaccurate or even go to zero resulting in numerical instability. This limitation has been overcome in the present formulation using an approach based on local scale similarity between stresses at the two filter levels (this assumption is supported by experimental data in jet flows).

Using the scale similarity concept, the coefficient in the eddy viscosity form and in the subgrid kinetic energy dissipation term are obtained locally and dynamically. No numerical instability has been observed in all the test flows studied so far and the localized model coefficients obtained from this model have been shown to be Galilean-invariant and very realizable. In addition, the computational cost for the new model is minimal compared to other localized techniques. It has been also shown that very high Re flows can be simulated relatively accurately using very

coarse grids provided scale-similarity is satisfied. Furthermore, it has been shown that this local model is capable of predicting results accurately using a relatively coarser grid (when compared to the Germano's eddy viscosity model).

A new non-staggered numerical scheme has also been developed to study complex flows with and without chemical reactions. This scheme has been validated for a variety of flows. LES of flows such as isotropic turbulence, temporal mixing layers with and without heat release, plane Couette flow and spatially evolving jets have been carried out successfully. Comparison with experimental data shows very good agreement for these flows.

Development of a new Compressible LES model

Along with the development of a localized dynamic subgrid model developed for low speed flows, a new version of this model for strongly compressible flows (i.e., for supersonic mixing) has also been developed. This model is developed not using Favre-filtering as done earlier by other researchers. Rather, this approach using non-density weighted filtering. As a result, additional terms appear in the Navier-Stokes equations that must be closed. The primary advantage of this approach is that direct comparison with experiments can be carried out. The new subgrid model still solves for the subgrid kinetic energy but also includes a compressible correction to the subgrid dissipation. The results of this study was recently compared with the spatial supersonic mixing studies of Sammimy. Comparison showed excellent agreement.

Publications/Presentations

Chakravarty, K. and Menon, S (1996), "Simulation of Unsteady Turbulent Jet Flow Using a Localized Dynamic Subgrid Model", presented at the 1996 International Mechanical Engineering Exposition (IMECE), Atlanta, Georgia, November 1996.

Chakravarty, K. and Menon, S. (1997), "On Large-Eddy Simulations of Non-Homogeneous Flows," AIAA 97-0652, 35th Aerospace Sciences Meeting, Reno, NV, January 6-9, 1997.

Kim, W.-W. and Menon, S. (1995), "A New Dynamic One-Equation Subgrid Model for Large-Eddy Simulations," AIAA Paper No. 95-0356, 33rd Aerospace Sciences Meeting, Reno, NV.

Kim, W.-W. and Menon, S. (1997) "Application of a Localized Dynamic Subgrid-Scale Model to Turbulent Wall-Bounded Flows," AIAA-97-0210, 35th Aerospace Sciences Meeting, Reno, NV, January 6-9, 1997.

Menon, S., and Yeung, P.-K. (1994) "Analysis of Subgrid Models using Direct and Large-Eddy Simulations of Isotropic Turbulence", 74th AGARD Fluid Dynamics Symposium on "Application of Direct and Large Eddy Simulation to Transition and Turbulence" AGARD CP-450.

Menon, S. and Kim, W.-W. (1994) "Analysis of Dynamic Subgrid Models Using Simulated Isotropic Turbulence Data," Meeting of the Division of Fluid Dynamics, American Physical Society, November 20-22, 1994, Atlanta, Georgia.

Menon, S., Yeung, P.-K. and Kim, W.-W. (1996) "The Effect of Subgrid Models on the Computed Interscale Energy Transfer in Isotropic Turbulence", Computer and Fluids, Vol. 25, pp. 165-186, 1996.

Menon, S., and Kim, W.-W. (1995) "Local Dynamic Subgrid Model for Large-Eddy Simulations of High Reynolds Number Turbulent Flows", presented at the American Physical Society, Forty-Eighth Annual Meeting of the Division of Fluid Dynamics, November 19-21, 1995.

Menon, S. and Kim, W.-W. (1996) "High Reynolds Number Flow Simulations using the Localized Dynamic Subgrid Model", AIAA Paper No. 96-0425, 34th Aerospace Sciences Meeting, January 15-18, 1996.

Menon, S. and Chakravarty, K. (1996) "Large-Eddy Simulations of Turbulent Premixed Flames in Couette Flow, "AIAA Paper No. 96-3077, 32nd AIAA/ASME/SAE/ASEE Joint Propulsion Meeting, Orlando, FL, July 1-3, 1996.

Nelson, C. and Menon, S. (1998) "Unsteady Simulations of Compressible Spatial Mixing Layers," AIAA Paper No. 98-0786, 36th Aerospace Sciences Meeting and Exhibit, Reno, NV, January 12-15, 1998.

Ph.D. Awarded

1. Won-Wook Kim, 1996 *"A New Dynamic Subgrid-Scale Model for Large-Eddy Simulation of Turbulent Flows"*

2. Christopher Nelson, 1997 *"Simulations of Spatially Evolving Compressible Turbulence using a Local Dynamic Subgrid Model"*

Submitted to Intn. J. of Numerical Methods

AN UNSTEADY INCOMPRESSIBLE NAVIER-STOKES SOLVER FOR LARGE-EDDY SIMULATION OF TURBULENT FLOWS

WON-WOOK KIM AND SURESH MENON

School of Aerospace Engineering

Georgia Institute of Technology

Atlanta, GA 30332, U.S.A.

SUMMARY

A dual time-stepping method combined with a spatially high-order-accurate, upwind-biased finite difference scheme has been developed for large-eddy simulation of incompressible turbulent flows. The artificial compressibility method is used with various convergence-acceleration techniques to obtain time-accurate solutions of turbulent flows. To evaluate the accuracy and the efficiency of the procedure, large-eddy simulation of various turbulent flows is carried out and the resulting turbulence statistics are compared with existing experimental and direct numerical simulation data.

KEY WORDS: incompressible Navier-Stokes; turbulent flow; numerical methods; large-eddy simulation

1 INTRODUCTION

Time-accurate simulation of turbulent incompressible flows is particularly time-consuming because of the elliptic nature of the governing equations. In principle, incompressible flows can be computed using compressible flow solvers by setting the Mach number very low. This procedure, however, becomes increasingly inefficient with decreasing Mach numbers because of the limitations of the permissible time-step (i.e., the compressible flow solvers have a singular behavior in the limit of truly incompressible flow). Therefore, alternate methods must be used to efficiently compute incompressible flows.

In addition to the difficulty of obtaining a solution of unsteady incompressible flow equations, turbulent flow simulation usually requires a very large number of grid points and extremely small grid spacing in order to obtain a grid-independent solution. This requirement further increases the computational cost. Furthermore, to accurately simulate turbulent flows, computational time step should be less than the smallest turbulent time scale resolved by the computational grid,[1] and spatial discretization should be carried out using high-order differencing schemes.[2,3]

Large-eddy simulations (LES) are carried out in this study using the localized dynamic subgrid-scale (SGS) model introduced by Kim and Menon.[4,5] This model was formulated based on the subgrid-scale kinetic-energy-equation model[6,7] (denoted here as LDKM). As in other dynamic models (e.g., Reference 8), two different filter levels are introduced to

dynamically determine the model coefficient. However, in the LDKM, similarity between the subgrid-scale stress tensor and the test-scale Leonard stress tensor is assumed to evaluate the model coefficient while in the classical dynamic models (e.g., Reference 8), the mathematical identity (so-called Germano's identity) is used to implicitly model the test-scale Leonard stress tensor in terms of the difference between model representations at two different filter levels. The scale similarity invoked in the LDKM is based on experimental observation[9] in high Reynolds number turbulent jets. This feature allows the LDKM to overcome some of the inherent shortcomings of the earlier dynamic models. For instance, unlike the Germano-type dynamic model, no mathematically inconsistent or *ad hoc* procedures are employed. The numerical instability caused by the ill-conditioning problem and the prolonged presence of negative model coefficient have also been prevented in the LDKM. As shown earlier,[10–13] the LDKM is simple to implement and efficient in comparison with the existing dynamic localization model (based on the subgrid-scale kinetic energy) by Ghosal *et al.*.[14] Moreover, the localized model coefficient obtained from the LDKM has been shown to be Galilean-invariant and very realizable.[4,5]

2 GOVERNING EQUATIONS

2.1 *Filtered Navier-Stokes equations*

In LES, the flow variables are decomposed into a large-scale component (denoted by an overbar) and a small subgrid-scale component by applying a filtering operation:

$$\overline{f}(x_i) = \int f(x_i')G(x_i, x_i')dx_i' \tag{1}$$

where G is the filter function and the integral is extended over the entire domain. Applying the filtering operation (in the present study, a low-pass filter of a computational mesh is used, hence, the characteristic size of this filter is the grid width $\overline{\Delta}$), the following incompressible Navier-Stokes equations for the evolution of the large-scale motions are obtained:

$$\frac{\partial \overline{u}_i}{\partial x_i} = 0 \tag{2}$$

$$\frac{\partial \overline{u}_i}{\partial t} + \overline{u}_j \frac{\partial \overline{u}_i}{\partial x_j} = -\frac{\partial}{\partial x_j}\left(\overline{p}\delta_{ij} + \tau_{ij}\right) + \nu \frac{\partial^2 \overline{u}_i}{\partial x_j \partial x_j} \tag{3}$$

where $\overline{u}_i(x_i, t)$ is the resolved velocity field. The effects of the unresolved small scales appear in the SGS stress tensor,

$$\tau_{ij} = \overline{u_i u_j} - \overline{u}_i \overline{u}_j \tag{4}$$

that must be modeled. In the present study, this term is parameterized using the localized dynamic SGS kinetic-energy-equation model (LDKM) as described in the following section.

2.2 *Localized dynamic subgrid-scale modeling*

The LDKM is based on the subgrid-scale kinetic energy

$$k_{sgs} = \frac{1}{2}\left(\overline{u_k u_k} - \overline{u}_k \overline{u}_k\right) \tag{5}$$

which is obtained by solving the following transport equation[7,8]

$$\frac{\partial k_{sgs}}{\partial t} + \overline{u}_i \frac{\partial k_{sgs}}{\partial x_i} = -\tau_{ij} \frac{\partial \overline{u}_i}{\partial x_j} - \varepsilon_{sgs} + \frac{\partial}{\partial x_i}\left(\nu_T \frac{\partial k_{sgs}}{\partial x_i}\right) \tag{6}$$

Here, the three terms on the right hand side represent, respectively, the production, the dissipation, and the diffusion of k_{sgs}. Using k_{sgs}, the SGS stress tensor τ_{ij} is usually modeled as follows,

$$\tau_{ij} = -2C_\tau \overline{\Delta} k_{sgs}^{1/2} \overline{S}_{ij} + \frac{2}{3}\delta_{ij} k_{sgs} \tag{7}$$

where $\overline{S}_{ij}$ is the resolved-scale strain-rate tensor,

$$\overline{S}_{ij} = \frac{1}{2}\left(\frac{\partial \overline{u}_i}{\partial x_j} + \frac{\partial \overline{u}_j}{\partial x_i}\right) \tag{8}$$

Implicit in equation (7) is the parameterization of the eddy viscosity ν_T,

$$\nu_T = C_\tau \overline{\Delta} k_{sgs}^{1/2} \tag{9}$$

Here, C_τ is an adjustable coefficient to be determined dynamically. Equation (6) is closed by providing a model for the SGS dissipation rate term, ε_{sgs}. Using simple scaling arguments, ε_{sgs} is usually modeled as

$$\varepsilon_{sgs} = C_\varepsilon \frac{k_{sgs}^{3/2}}{\overline{\Delta}} \tag{10}$$

where, C_ε is another coefficient also to be determined dynamically. In the following, the dynamic procedures for C_τ and C_ε are described.

The test-scale field is constructed from the grid-scale field by applying a test filter which is characterized by $\hat{\Delta}$ (typically, $\hat{\Delta} = 2\overline{\Delta}$). The test filter should be consistent with the grid filter. In the present study, the top-hat filter is employed for the test filtering. If the

application of the test filter on any variable ϕ is denoted by $\widehat{\phi}$, the test-scale Leonard stress tensor is defined as:

$$L_{ij} = \widehat{\overline{u}_i \overline{u}_j} - \widehat{\overline{u}}_i \widehat{\overline{u}}_j \tag{11}$$

Recently, Liu *et al.*[9] observed significant similarity between τ_{ij} and L_{ij} by analyzing experimental data obtained in the far field of a turbulent round jet at a reasonably high Reynolds number, $Re_\lambda \approx 310$. The experimental data showed that the correlation between these two stress tensors was quite high. Therefore, they suggested an appropriate SGS model based on this scale similarity: $\tau_{ij} = C_k L_{ij}$ where C_k is an adjustable constant (a value of 0.45 ± 0.15 was suggested by Liu *et al.*[9] based on experimental data). However, such a model does not have the requisite dissipation and, therefore, cannot be used for LES. In the LDKM, this similarity assumption is adopted to dynamically determine the model coefficient.

At the test-filter level, a resolved kinetic energy can be defined from the trace of equation (11):

$$k_{test} = \frac{1}{2}\left(\widehat{\overline{u}_k \overline{u}_k} - \widehat{\overline{u}}_k \widehat{\overline{u}}_k\right) \tag{12}$$

(note that $k_{test} = L_{kk}/2$). This energy is similar to k_{sgs}, however, it is produced at the large scales by $-L_{ij}(\partial \widehat{\overline{u}}_i / \partial x_j)$ and is dissipated by:

$$e = (\nu + \nu_T)\left(\widehat{\frac{\partial \overline{u}_i}{\partial x_j}\frac{\partial \overline{u}_i}{\partial x_j}} - \frac{\partial \widehat{\overline{u}}_i}{\partial x_j}\frac{\partial \widehat{\overline{u}}_i}{\partial x_j}\right) \tag{13}$$

at the small scales. Here, $(\nu+\nu_T)$ is used since k_{test} is fully resolved at the test-filter level and, thus, must be dissipated by both the eddy viscosity and the molecular viscosity. Experiments

suggest that τ_{ij} and L_{ij} are similar in variation. Thus, it is reasonable to assume that similar representations can be used to represent τ_{ij} and L_{ij} using appropriately defined parameters. Since τ_{ij} is modeled in terms of grid-resolved quantities, a similar representation is considered for L_{ij} as

$$L_{ij} = -2C_\tau \hat{\Delta} k_{test}^{1/2} \widehat{\overline{S}}_{ij} + \frac{1}{3}\delta_{ij} L_{kk} \tag{14}$$

where all quantities are defined at the test-filter level. (The applicability of the similarity assumption and the appropriateness of equation (14) has been verified in the past by carrying out LES of various flows.[10–13]) Now, equation (7) contains two unknowns τ_{ij} and C_τ while equation (14) contains only C_τ as the unknown. Thus, equation (14) can be viewed as an explicit model representation for C_τ in terms of quantities resolved at the test-filter level. Since equation (14) is an over-determined system, least-square method suggested by Lilly[15] is required to obtain C_τ:

$$C_\tau = \frac{1}{2}\frac{L_{ij}\sigma_{ij}}{\sigma_{ij}\sigma_{ij}} \tag{15}$$

where

$$\sigma_{ij} = -\hat{\Delta} k_{test}^{1/2} \widehat{\overline{S}}_{ij} \tag{16}$$

Here, σ_{ij} is determined completely from quantities at the test-filter level.

Similarity between the dissipation rates ε_{sgs} at the grid-filter level and e at the test-filter level is also invoked in the LDKM to obtain the dissipation model coefficient. Thus, we obtain

$$e = C_\varepsilon \frac{k_{test}^{3/2}}{\hat{\Delta}} \tag{17}$$

Note that the reasoning behind the model formulations, (14) and (17), has been discussed elsewhere (e.g., References 4 and 5) and, therefore, has been avoided here for brevity. Since equation (17) is a single equation with one unknown, C_ε can be determined easily from

$$C_\varepsilon = \frac{(\nu + \nu_T)\,\hat{\Delta}\left[\widehat{(\partial \overline{u}_i/\partial x_j)\,(\partial \overline{u}_i/\partial x_j)} - \left(\partial \widehat{\overline{u}}_i/\partial x_j\right)\left(\partial \widehat{\overline{u}}_i/\partial x_j\right)\right]}{k_{test}^{3/2}} \tag{18}$$

As shown above, by adopting the similarity assumption between τ_{ij} and L_{ij}, the LDKM can be formulated without employing any mathematically inconsistent or *ad hoc* procedure (the mathematical inconsistency of Germano *et al.*'s dynamic formulation[8] was pointed out by Cabot and Moin[16]). There are some more positive aspects to this approach. The denominators of equations (15) and (18) contain only well defined quantities and, therefore, the ill-conditioning problem (seen in Germano *et al.*'s dynamic formulation[8]) is significantly relieved (as demonstrated in the numerical studies[10–13]). The prolonged presence of negative model coefficient as discussed by Lund *et al.*[17] also has been avoided by adopting the SGS kinetic energy. Moreover, the dynamically determined C_ε from equation (18) does not have the unphysical property of vanishing at high Reynolds numbers (which was observed in the dynamic formulation of Wong[18]). From a computational standpoint, the cost of the dynamic procedure is not significant (about the same as that for the original dynamic model by Germano *et al.*[8]) due to its simplicity. The additional computational cost is primarily due to the inclusion of a transport equation for k_{sgs}. This model has been proved to be Galilean invariant and very realizable.

2.3 *Transformation of governing equations*

Following conventional methods, the Cartesian space (x, y, z) is mapped onto a generalized curvilinear space (ξ, η, ζ) and the governing equations, (2) and (3), are rewritten as

$$\frac{\partial}{\partial \xi}\left(\frac{U}{J}\right) + \frac{\partial}{\partial \eta}\left(\frac{V}{J}\right) + \frac{\partial}{\partial \zeta}\left(\frac{W}{J}\right) = 0 \tag{19}$$

$$\frac{1}{J}\frac{\partial q}{\partial t} + \left(\frac{U}{J}\right)\frac{\partial q}{\partial \xi} + \left(\frac{V}{J}\right)\frac{\partial q}{\partial \eta} + \left(\frac{W}{J}\right)\frac{\partial q}{\partial \zeta} = -\frac{\partial E}{\partial \xi} - \frac{\partial F}{\partial \eta} - \frac{\partial G}{\partial \zeta} \tag{20}$$

where J is the Jacobian of the transformation, and U, V, and W are, respectively, the contravariant velocities along the three spatial directions in computational domain,

$$\begin{aligned} U &= \xi_x \overline{u} + \xi_y \overline{v} + \xi_z \overline{w} \\ V &= \eta_x \overline{u} + \eta_y \overline{v} + \eta_z \overline{w} \\ W &= \zeta_x \overline{u} + \zeta_y \overline{v} + \zeta_z \overline{w} \end{aligned} \tag{21}$$

q is the velocity vector,

$$q = \left[\begin{array}{ccc} \overline{u}, & \overline{v}, & \overline{w} \end{array} \right]^T \tag{22}$$

and the vectors E, F, and G contain the pressure and viscous terms

$$\begin{aligned} E &= E_p - \frac{\xi_x}{J}E_v - \frac{\xi_y}{J}F_v - \frac{\xi_z}{J}G_v \\ F &= F_p - \frac{\eta_x}{J}E_v - \frac{\eta_y}{J}F_v - \frac{\eta_z}{J}G_v \\ G &= G_p - \frac{\zeta_x}{J}E_v - \frac{\zeta_y}{J}F_v - \frac{\zeta_z}{J}G_v \end{aligned} \tag{23}$$

$$
\begin{aligned}
E_p &= \frac{1}{J}\left[\, \xi_x\overline{p},\ \ \xi_y\overline{p},\ \ \xi_z\overline{p} \,\right]^T \\
F_p &= \frac{1}{J}\left[\, \eta_x\overline{p},\ \ \eta_y\overline{p},\ \ \eta_z\overline{p} \,\right]^T \\
G_p &= \frac{1}{J}\left[\, \zeta_x\overline{p},\ \ \zeta_y\overline{p},\ \ \zeta_z\overline{p} \,\right]^T
\end{aligned}
\tag{24}
$$

$$
E_v = (\nu+\nu_T)\begin{bmatrix}
2\left(\xi_x\overline{u}_\xi+\eta_x\overline{u}_\eta+\zeta_x\overline{u}_\zeta\right) \\
\xi_y\overline{u}_\xi+\eta_y\overline{u}_\eta+\zeta_y\overline{u}_\zeta+\xi_x\overline{v}_\xi+\eta_x\overline{v}_\eta+\zeta_x\overline{v}_\zeta \\
\xi_x\overline{w}_\xi+\eta_x\overline{w}_\eta+\zeta_x\overline{w}_\zeta+\xi_z\overline{u}_\xi+\eta_z\overline{u}_\eta+\zeta_z\overline{u}_\zeta
\end{bmatrix}
\tag{25}
$$

$$
F_v = (\nu+\nu_T)\begin{bmatrix}
\xi_y\overline{u}_\xi+\eta_y\overline{u}_\eta+\zeta_y\overline{u}_\zeta+\xi_x\overline{v}_\xi+\eta_x\overline{v}_\eta+\zeta_x\overline{v}_\zeta \\
2\left(\xi_y\overline{v}_\xi+\eta_y\overline{v}_\eta+\zeta_y\overline{v}_\zeta\right) \\
\xi_z\overline{v}_\xi+\eta_z\overline{v}_\eta+\zeta_z\overline{v}_\zeta+\xi_y\overline{w}_\xi+\eta_y\overline{w}_\eta+\zeta_y\overline{w}_\zeta
\end{bmatrix}
$$

$$
G_v = (\nu+\nu_T)\begin{bmatrix}
\xi_x\overline{w}_\xi+\eta_x\overline{w}_\eta+\zeta_x\overline{w}_\zeta+\xi_z\overline{u}_\xi+\eta_z\overline{u}_\eta+\zeta_z\overline{u}_\zeta \\
\xi_z\overline{v}_\xi+\eta_z\overline{v}_\eta+\zeta_z\overline{v}_\zeta+\xi_y\overline{w}_\xi+\eta_y\overline{w}_\eta+\zeta_y\overline{w}_\zeta \\
2\left(\xi_z\overline{w}_\xi+\eta_z\overline{w}_\eta+\zeta_z\overline{w}_\zeta\right)
\end{bmatrix}
$$

Here, the velocity gradients are written as $\overline{u}_\xi = \frac{\partial\overline{u}}{\partial\xi}$, *etc.*, and the metrics of the transformation are defined by $\xi_x = \frac{\partial\xi}{\partial x}$, *etc.*.

3 NUMERICAL METHODS

3.1 *Spatial discretization*

Spectral method is one of most reliable approaches for turbulent flow simulations, especially direct numerical simulations (DNS), because of their extremely high accuracy. However,

spectral method cannot be used for simulations of flows in complex geometry. For complex flows, numerical methods defined in the physical space like finite-difference method (FDM) and finite-volume method (FVM) are more appropriate. However, it is important to ensure that these physical space methods have high enough accuracy for turbulent simulations. In order to obtain an adequate accuracy for turbulent flow simulations without losing applicability to complex geometry and simplicity of the scheme, Rai and Moin[3] suggested a high-order accurate, upwind-biased finite-difference method. Their approach used a non-conservative form of the unsteady, incompressible Navier-Stokes equations, (2) and (3), and, hence, it is appropriate only for simulations of flow fields without discontinuity. The present study is limited to such flows and, therefore, a similar methodology is adopted here.

Similar to Rai and Moin[2], the convective terms are approximated using fifth-order accurate, upwind-biased finite-differences with a seven-point stencil. For example, the first term in the momentum equation, $(U/J)\, q_\xi$, is evaluated as;

$$\left(\frac{U}{J} q_\xi\right)_{i,j,k} = \frac{(U/J)_{i,j,k}}{120} \left(-6q_{i+2,j,k} + 60q_{i+1,j,k} + 40q_{i,j,k} - 120q_{i-1,j,k} + 30q_{i-2,j,k} - 4q_{i-3,j,k}\right) \tag{26}$$

if $U_{i,j,k} > 0$, and

$$\left(\frac{U}{J} q_\xi\right)_{i,j,k} = \frac{(U/J)_{i,j,k}}{120} \left(4q_{i+3,j,k} - 30q_{i+2,j,k} + 120q_{i+1,j,k} - 40q_{i,j,k} - 60q_{i-1,j,k} + 6q_{i-2,j,k}\right) \tag{27}$$

if $U_{i,j,k} < 0$. The remaining convective terms are evaluated in a similar manner.

The viscous terms are computed using central differences. By applying the fourth-order-

accurate, half-points differencing, the first viscous term in the u-momentum equation, $(c\overline{u}_\xi)_\xi$ where $c = 2(\nu + \nu_T)\xi_x/J$, is discretized as

$$[(c\overline{u}_\xi)_\xi]_{i,j,k} = \frac{1}{24}\left[-(c\overline{u}_\xi)_{i+3/2,j,k} + 27\,(c\overline{u}_\xi)_{i+1/2,j,k} - 27\,(c\overline{u}_\xi)_{i-1/2,j,k} + (c\overline{u}_\xi)_{i-3/2,j,k}\right] \quad (28)$$

Also, $\overline{u}_\xi$ which is defined at the half-points is computed using the same fourth-order-accurate finite-difference given as

$$(\overline{u}_\xi)_{i+1/2,j,k} = \frac{1}{24}\left(-\overline{u}_{i+2,j,k} + 27\overline{u}_{i+1,j,k} - 27\overline{u}_{i,j,k} + \overline{u}_{i-1,j,k}\right) \quad (29)$$

$c_{i+1/2,j,k}$ is interpolated using the information on same stencil which was used to evaluated $(\overline{u}_\xi)_{i+1/2,j,k}$, so as to retain high-order accuracy. Thus, the discretization of the viscous terms uses seven grid points and, therefore, the viscous terms are approximated to sixth-order accuracy on uniform grids.

Unlike central difference schemes, all the upwind and upwind-biased differences have leading truncation error terms that are dissipative in nature. In fact, some (low-order accurate) upwind (-biased) schemes are known to be highly dissipative numerically. This can overwhelm the true dissipation in the turbulent flow and, therefore, needs to be carefully evaluated.

Figure 1(a) shows the time variation of the turbulent kinetic energy in the decaying isotropic turbulence (the description of this flow field will be given in Section 4.1). Results obtained on a 48^3 grid resolution using fifth-order accurate upwind-biased finite-differences (implemented with and without employing the LDKM) are shown together with the experimental data. It can be clearly observed that the numerical dissipation of the finite-difference

scheme is lower than the turbulent dissipation. This is an essential requirement for a turbulent simulation code. As shown, the LES data agree with experimental data only when the SGS model is turned on. This demonstrates the need and the capability of the SGS model. For comparison, the results without the SGS model obtained using a well known pseudo-spectral code[19] with a "2/3 dealiasing rule" is also plotted (these data were obtained by scanning Figure 1 in Carati *et al.*[20]). Note that the simulation results which are obtained without employing any turbulence model from both FDM and spectral codes should not be considered as the DNS results since the 48^3 grid resolution is too coarse to resolve all the turbulence scales (as mentioned in Section 4.1, at least 384^3 grid resolution is required for the actual DNS of this particular case). The present finite-difference method appears to be less dissipative than the spectral method. This is somewhat surprising since the spectral method is known as one of the least dissipative methods available for turbulence simulation. Some small deviation in the initial energy distribution (in the spectral space) between the current implementation and Carati *et al.*'s initialization (even though they are supposed to be identical) may be responsible for the difference between the two cases. It can be observed from the comparison, however, that the dissipation in the current finite-different method is comparable to that of the spectral method.

Figure 1(b) shows unscaled energy spectra at the instant $t^* = 4.98$ and $t^* = 8.69$ obtained in the current calculation of the decaying isotropic turbulence implemented with and without employing the LDKM. At $t^* = 4.98$, without the model the spectrum shows that the energy builds up at the high wavenumber end. As time evolves, the prediction without the model worsens at all wavenumber.

Note that if a non-staggered grid (i.e., both velocity and pressure are defined at the grid

points) is used and the velocity derivatives in continuity equation and the pressure derivatives in the momentum equation are central-differenced, velocity and pressure are decoupled. That is, the pressure is computed by excluding the influence of velocity at that point, and vice versa (this kind of decoupling is not present in compressible flows due to the density-velocity coupling). This decoupling generates undesirable grid-scale (odd-even decoupling-type) oscillations in the pressure field. Some higher-order artificial dissipation terms are typically added to eliminate the pressure oscillations. However, the addition of artificial dissipation terms needs to be avoided in turbulent simulations since it may contaminate the turbulent behavior. Another common method to prevent the pressure oscillations is the usage of staggered grid scheme introduced by Harlow and Welch.[21] It avoids the pressure-velocity decoupling but requires more care when used with non-rectangular geometry and nonuniform grids. It also requires some special treatment at boundaries. When non-staggered grids are used, the pressure oscillations can be eliminated by using special interpolation techniques such as momentum interpolation[28] and elliptic-corrected linear interpolation.[29] Strikwerda[30] used the central difference scheme with the addition of regularizing terms for the pressure gradients and divergence operator (hence, it is called the regularized central difference). The regularizing terms ensure the coupling between pressure and velocities. In the scheme, the derivatives of pressure are approximated as

$$\frac{\partial p}{\partial x} \simeq \delta_x p - \alpha \Delta_x^2 \delta_{x-} \delta_{x+}^2 p \tag{30}$$

and the derivatives of the velocity in the divergence equation are approximated as

$$\frac{\partial u}{\partial x} \simeq \delta_x u - \alpha \Delta_x^2 \delta_{x+} \delta_{x-}^2 u \tag{31}$$

where α is a nonzero constant and δ_x, δ_{x+}, δ_{x-} are the central-, forward-, and backward-difference operators, respectively. For $\alpha = 1/6$, equations (30) and (31) are third-order accurate. In the present study, a similar scheme is adopted. However, to prevent the degradation of the overall order of accuracy, higher-order accurate differences, which are equivalent to the fifth-order accurate approximations used for the convective term calculations, are used. For instance,

$$\left[\left(\frac{\xi_x \overline{p}}{J}\right)_\xi\right]_{i,j,k} = \frac{1}{120}\left[\begin{array}{l} 4\left(\frac{\xi_x \overline{p}}{J}\right)_{i+3,j,k} - 30\left(\frac{\xi_x \overline{p}}{J}\right)_{i+2,j,k} + 120\left(\frac{\xi_x \overline{p}}{J}\right)_{i+1,j,k} \\ -40\left(\frac{\xi_x \overline{p}}{J}\right)_{i,j,k} - 60\left(\frac{\xi_x \overline{p}}{J}\right)_{i-1,j,k} + 6\left(\frac{\xi_x \overline{p}}{J}\right)_{i-2,j,k} \end{array}\right] \tag{32}$$

$$\left[\left(\frac{U}{J}\right)_\xi\right]_{i,j,k} = \frac{1}{120}\left[\begin{array}{l} -6\left(\frac{U}{J}\right)_{i+2,j,k} + 60\left(\frac{U}{J}\right)_{i+1,j,k} + 40\left(\frac{U}{J}\right)_{i,j,k} \\ -120\left(\frac{U}{J}\right)_{i-1,j,k} + 30\left(\frac{U}{J}\right)_{i-2,j,k} - 4\left(\frac{U}{J}\right)_{i-3,j,k} \end{array}\right] \tag{33}$$

Note that the regularized central difference scheme is a variant of the central difference scheme and, hence, the biasing of the scheme does not depend on the direction of the local contravariant velocity.

The accuracy and the effect of the non-symmetric regularizing terms on the turbulence statistics have been examined by simulating the decaying isotropic turbulence and comparing the results with those obtained using the following fourth-order-accurate (nonregular) central-differences

$$\left[\left(\frac{\xi_x \overline{p}}{J}\right)_\xi\right]_{i,j,k} = \frac{1}{12}\left[-\left(\frac{\xi_x \overline{p}}{J}\right)_{i+2,j,k} + 8\left(\frac{\xi_x \overline{p}}{J}\right)_{i+1,j,k} - 8\left(\frac{\xi_x \overline{p}}{J}\right)_{i-1,j,k} + \left(\frac{\xi_x \overline{p}}{J}\right)_{i-2,j,k}\right] \tag{34}$$

$$\left[\left(\frac{U}{J}\right)_{\xi}\right]_{i,j,k} = \frac{1}{12}\left[-\left(\frac{U}{J}\right)_{i+2,j,k} + 8\left(\frac{U}{J}\right)_{i+1,j,k} - 8\left(\frac{U}{J}\right)_{i-1,j,k} + \left(\frac{U}{J}\right)_{i-2,j,k}\right] \tag{35}$$

Figure 2 shows the comparison for the time evolution of the turbulent kinetic energy (a) and unscaled energy spectra (b). As shown, almost identical results have been obtained from the non-symmetric regularized central differences and the symmetric nonregular central differences. This observation demonstrates the accuracy of the regularized central differences and the negligible effect of the biasing of the scheme on the turbulence statistics.

3.2 *Dual time-stepping*

The major difference between the incompressible and the compressible Navier-Stokes formulation is the lack of a time derivative term in the continuity equation in the incompressible formulation. Therefore, satisfying the mass conservation equation is the primary issue in solving the incompressible equations. Physically, incompressible flow is characterized by the elliptic behavior of the (infinite speed) pressure waves. The pressure field is desired as a part of the solution. To achieve this, various primitive-variable formulations have been developed such as the marker-and-cell (MAC) method,[21] the fractional-step (or the projection) method,[22] and the artificial compressibility method[23] in the past, but at least to the authors' best knowledge no method has been proven superior.

In the present study, the artificial compressibility method (which was originally suggested by Chorin[23]) is adopted. The main advantage of this approach is that, by introducing artificial unsteady term into the continuity equation, efficient solution algorithms developed for time-dependent compressible flows can be utilized to compute incompressible flows. In

this formulation, the continuity equation is modified by adding a pseudo-time derivative of the pressure term which results in a hyperbolic-parabolic type of time-dependent equations together with the unsteady momentum equations,

$$\frac{\partial p}{\partial \tau} = -\beta^2 J \left[\frac{\partial}{\partial \xi}\left(\frac{U}{J}\right) + \frac{\partial}{\partial \eta}\left(\frac{V}{J}\right) + \frac{\partial}{\partial \zeta}\left(\frac{W}{J}\right) \right] \tag{36}$$

Here, β is a prescribed parameter which represents an artificial speed of sound and τ is the pseudo-time variable which is not related to the physical time t. The choice of β is crucial in determining convergence and stability properties of the numerical scheme. Since β has the dimensions of a speed, it cannot be a universal constant. For instance, if the nondimensionalized governing equations are employed, β is also nondimensionalized by a reference velocity. Therefore, the optimal β will depend on the choice of the reference velocity. Many researchers (e.g., Reference 24) chose β^2 to be slightly larger than $\overline{u}^2 + \overline{v}^2 + \overline{w}^2$ as an optimal choice. However, in general, the superiority of this choice of β over a constant β has not been verified. McHugh and Ramshaw[25] found that for large time step the fastest convergence is obtained by using conventional value of ($\beta^2 \sim \overline{u}^2 + \overline{v}^2 + \overline{w}^2$). However, in contrast, the fastest convergence for small time step is obtained by letting β be much larger than the conventional value. Based on this observation, they proposed a simple analytical expression for β as function of time step. In the present study, both a constant β and a variable β, i.e., $\beta^2 = C\,(\overline{u}^2 + \overline{v}^2 + \overline{w}^2)$ (where C is a constant of order unity) have been evaluated. It was determined that for most of the problems studied here, a constant β provided better convergence.

Figure 3 shows a typical example of the pseudo-time convergence for one physical time

step advance for various values of β. The decaying isotropic turbulence is solved on a 48^3 grid resolution using a 2-level multigrid, $CFL = 2$, and a physical time step equal to 0.05. For this test case, the choice of $\beta^2 \approx 20$ gives an optimum performance.

The time-accurate capability is obtained by adding pseudo-time velocity derivatives to the momentum equations (e.g., Reference 26),

$$\frac{\partial q}{\partial \tau} = -\frac{\partial q}{\partial t} - R^*(q) = -R(q) \tag{37}$$

where R^* represents the residual in the momentum equations which includes convective and viscous terms. In this unsteady formulation, the governing equations are marched in the pseudo-time (i.e., subiterated) until the divergence-free flow field is obtained. Therefore, the artificial compressibility does not corrupt the physical time solution as long as the pseudo-time solution converges to a steady state at each physical time level.

The integration in the pseudo-time is carried out by an explicit method based on a 5-stage Runge-Kutta time-stepping scheme. If m is the index associated with pseudo-time, it can be written in the form

$$\begin{aligned}
q^{(0)} &= q^m \qquad (38)\\
q^{(1)} &= q^{(0)} - \alpha_1 \Delta\tau R(q^{(0)})\\
q^{(2)} &= q^{(0)} - \alpha_2 \Delta\tau R(q^{(1)})\\
q^{(3)} &= q^{(0)} - \alpha_3 \Delta\tau R(q^{(2)})\\
q^{(4)} &= q^{(0)} - \alpha_4 \Delta\tau R(q^{(3)})\\
q^{(5)} &= q^{(0)} - \alpha_5 \Delta\tau R(q^{(4)})
\end{aligned}$$

$$q^{m+1} = q^{(5)}$$

Here, the coefficients are chosen as α_1 =0.059, α_2 =0.145, α_3 =0.273, α_4 =0.5, and α_5 =1.0 which are considered appropriate for the upwind scheme.[27]

The physical time derivatives in the momentum equations are computed using a second-order backward-difference that results in an implicit scheme,

$$\frac{\partial q}{\partial \tau} = -\frac{3q^{n+1} - 4q^n + q^{n-1}}{2\Delta t} - R^*(q^{n+1}) = -R(q^{n+1}) \tag{39}$$

where the superscript n denotes the physical time level.

3.3 *Convergence acceleration techniques*

To accelerate the convergence in pseudo-time-marching at each physical time step, efficient acceleration techniques developed for explicit steady-state solvers, such as local time-stepping, residual smoothing, and multigrid are employed. Local time-stepping involves using the locally maximum allowable time step. The local time step for viscous flow was computed as (e.g., Reference 31),

$$\Delta\tau = CFL \frac{1}{\lambda_\xi + \lambda_\eta + \lambda_\zeta + 2(\nu + \nu_T) J^2 \left(S_\xi^2 + S_\eta^2 + S_\zeta^2\right)} \tag{40}$$

where CFL is the Courant-Friedrichs-Lewy number. λ_ξ, λ_η, and λ_ζ are the spectral radii in the ξ, η, and ζ directions,

$$\lambda_\xi = |U| + \beta \left(\xi_x^2 + \xi_y^2 + \xi_z^2\right)^{1/2} \tag{41}$$

$$\lambda_\eta = |V| + \beta\left(\eta_x^2 + \eta_y^2 + \eta_z^2\right)^{1/2}$$

$$\lambda_\zeta = |W| + \beta\left(\zeta_x^2 + \zeta_y^2 + \zeta_z^2\right)^{1/2}$$

and

$$S_\xi^2 = x_\xi^2 + y_\xi^2 + z_\xi^2 \tag{42}$$

$$S_\eta^2 = x_\eta^2 + y_\eta^2 + z_\eta^2$$

$$S_\zeta^2 = x_\zeta^2 + y_\zeta^2 + z_\zeta^2$$

Note that the local time step $\Delta\tau$ is limited to be less than the physical time step Δt to make the scheme stable.

The stability limit of the basic scheme can be extended by employing residual smoothing as first demonstrated by Jameson[32]. In three dimensions, an implicit residual smoothing is carried out in the following form,

$$\left(1 - \epsilon_x\delta_x^2\right)\left(1 - \epsilon_y\delta_y^2\right)\left(1 - \epsilon_z\delta_z^2\right)\tilde{R} = R \tag{43}$$

where ϵ_x, ϵ_y, and ϵ_z are smoothing coefficients and δ_x^2, δ_y^2, and δ_z^2 are central difference operators in x, y, and z directions. R and $\tilde{R}$ are the residuals before and after smoothing. Thus, each residual is replaced by an average of itself and the neighboring residuals. In most cases, with residual smoothing CFL=5 was possible for the pseudo time iteration.

Convergence can be accelerated by also incorporating the full approximation storage (FAS) scheme based multigrid method as proposed by Brandt[33] and further developed by Jameson.[32] The basic idea is to solve the governing equations on a sequence of successively

coarser grids to speed up the propagation of the fine grid corrections. This has two advantages. First, the computational effort per time step is reduced on a coarser grid. Second, the use of coarser grids tracks the evolution on a larger scale, with the consequence that global equilibrium can be more rapidly attained (i.e., the system residuals can be more rapidly reduced). In the case of an explicit time stepping scheme, this manifests itself as successively larger time steps as the solution procedure moves to the coarser grids, without violating the stability limit. Auxiliary coarser grids are introduced by doubling the grid spacing. The FAS multigrid method is briefly illustrated here and further description of the method can be found in Brandt.[33]

The discretization of the governing equations on the hierarchy of the grids can be expressed as

$$L^k q^k = F^k \tag{44}$$

where $k = 1, \cdots, K$ and K denotes the finest grid. L^k can designate any explicit or implicit operator (in the present case, it represents explicit operator) and q^k is the solution of (44). F^k is the fine-to-coarse defect correction, so that $F^K = 0$. For brevity, the multigrid procedure is illustrated using only two grid levels, k and $k-1$. The multigrid cycle is started by first time-stepping the flow field on the finer grid, k. After one complete multi-stage time-step, the solution is transferred (or restricted) to the coarser grid $k-1$. The restriction of the solution can be expressed as

$$I_k^{k-1} q^k$$

where I_k^{k-1} denotes the restriction operator. Since the solution is not converged on the finer

grid, one can calculate the resulting residual as

$$R^k = F^k - L^k q^k \tag{45}$$

This residual is also restricted to the coarser grid as

$$I_k^{k-1} R^k = I_k^{k-1} F^k - I_k^{k-1} \left(L^k q^k \right) \tag{46}$$

If the truncation error of the finer grid is preserved on the coarser grid, the restricted residual should be same as the following residual obtained from the solution which has been restricted to the same grid,

$$F^{k-1} - L^{k-1} \left(I_k^{k-1} q^k \right)$$

From this, we can evaluate F^{k-1} as follows,

$$F^{k-1} = I_k^{k-1} F^k + L^{k-1} \left(I_k^{k-1} q^k \right) - I_k^{k-1} \left(L^k q^k \right) \tag{47}$$

Now, q^{k-1} is obtained by solving the following system of equations,

$$L^{k-1} q^{k-1} = I_k^{k-1} F^k + L^{k-1} \left(I_k^{k-1} q^k \right) - I_k^{k-1} \left(L^k q^k \right) \tag{48}$$

This procedure is repeated on a succession of coarser grids until the coarsest grid is reached. In most of the present work, a 4-level V-cycle is used for each time step. After corrections are calculated on the coarser grid, they are interpolated (or prolonged) back to the fine grid according to

$$\left(q^k\right)_{new} = q^k + I_{k-1}^k \left(q^{k-1} - I_k^{k-1} q^k\right) \tag{49}$$

where I_{k-1}^k denotes the prolongation operator.

It is worth noting that the success of the multigrid method is critically dependent upon the choice of the operators I_k^{k-1} and I_{k-1}^k. If the errors due to either the restriction or the prolongation procedure are significant, then the convergence will be seriously impaired. In general, the prolongation operator does not have to be the exact inverse of the restriction operator. Moreover, the restriction operator for the solution and for the residual need not be same. In the present study, point-to-point injection is used for restricting the solution while an volume-weighted average over the neighboring 27 points is used for residual restriction. The corrections are prolonged back to the finer grid by bilinear interpolation.

The treatment of the boundary conditions on the coarser grids also influences the multigrid convergence. In the present study, the boundary conditions are imposed in the same way on each grid and updated at every Runge-Kutta stage. The turbulent eddy viscosity on coarse grids is evaluated by injecting the subgrid-scale turbulent kinetic energy and the dynamically determined model coefficients from the fine grid instead of solving a transport equation on the coarse grids.

The pseudo-time convergence history during one physical time advance for the four different multigrid level cases is compared in Figure 4. Again, the decaying isotropic turbulence is solved on a 48^3 grid resolution using $\beta^2 = 10$, $CFL = 2$, and a physical time step equal to 0.05. As shown, increasing the number of multigrid levels from 1 to 3 shows an improvement in convergence. However, beyond three multigrid levels, the convergence saturates earlier.

The reason for the earlier convergence saturation in the higher level multigrid run seems to be related to the fact that 6^3 and 12^3 grid resolutions are too coarse to provide the accurate corrections for a very small velocity change.

In practice, a solution is considered converged if the root-mean-square of the pressure and velocity changes decrease less than 10^{-6} since, in most cases, further iterations to reduce these quantities do not noticeably change the solution. Both the eddy viscosity and the model coefficients are computed at each pseudo-time step. Usually, the model coefficients adjust themselves quickly and remain almost constant during pseudo-time iterations.

The efficiency of the present numerical method has been evaluated by simulating the lid-driven cavity (recirculating) flow (the detailed description of the flow field will be presented in Section 4.6) at the Reynolds number of 3200 and on $32 \times 32 \times 32$ grid, and comparing the CPU and memory usage with those of the existing numerical methods for the same test case. Existing schemes include two staggered-grid methods, one explicit and one fully implicit, and one non-staggered grid method by Zang et al.[34] which employs a semi-implicit, fractional-step method. The comparison is summarized in Table I for the CPU time (in μs) per grid point per time step and the number of three-dimensional variables defined per grid point. All three existing schemes' data have been adopted from Reference 34 and their CPU time has been measured on a Cray Y-MP 8/864 supercomputer. However, the present computation was carried out on a SGI workstation (MIPS 8000, 75MHz). Therefore, the CPU time can not be directly compared. For the present method, two subiterations have been performed at every time step. As shown in the table, the total number of the three-dimensional variables per grid point have been significantly reduced in the non-staggered-grid methods in comparison with the staggered-grid methods.

4 NUMERICAL RESULTS

To validate the incompressible Navier-Stokes solver developed in this study, we have implemented *a posteriori* tests of decaying (Section 4.1), forced (Section 4.2), and rotating (Section 4.3) isotropic turbulent flows, temporally evolving turbulent mixing layers (Section 4.4), turbulent plane Couette flows (Section 4.5), and turbulent recirculating flows (section 4.6). Comparisons with experimental data and DNS results are carried out to demonstrate the capability of the code.

4.1 *Decaying isotropic turbulence*

First, the experiment of decaying isotropic turbulence of Comte-Bellot and Corsin[35] is simulated. In the experiment, measurements of the energy spectra were carried out at three locations downstream of the grid (which generated the turbulence in the wind tunnel). At the first measuring station, the Reynolds number based on the Taylor microscale and the integral scale were, respectively, 71.6 and 187.9 (these values decreased to 60.7 and 135.7, respectively, at the last measuring station). By invoking Taylor's frozen turbulence hypothesis, the spatial evolution of turbulence can be converted to a temporally evolving state, more specifically, a decaying isotropic turbulence inside a cubical box which is moving with the mean flow velocity. The size of the box is chosen to be greater than the integral length scale of the measured real turbulence. The statistical properties of turbulence inside the box are believed to be realistic even after applying periodic boundary conditions for numerical implementation. All experimental data are nondimensionalized by the reference length scale $10M/2\pi$ (where $M = 5.08cm$ is the mesh size of the grid) and the reference time scale 0.1 *sec*

for computational convenience. By this nondimensionalization, the three measuring locations correspond to the three dimensionless time levels, t^* =2.13, 4.98 and 8.69, respectively.

The initial velocity field (primarily the amplitudes of the velocity Fourier modes) is chosen to match the three-dimensional energy spectrum at the first experimental station. The phases of Fourier modes are chosen to be random so that the initial velocity field satisfy Gaussian statistics. The initial pressure is assumed to be uniform throughout the flow field and the initial SGS kinetic energy is estimated by assuming the similarity between the SGS kinetic energy and the resolved-scale energy at the test filter level. Thus, at t^* =2.13,

$$k_{sgs} \approx \frac{C_k}{2}\left(\widehat{\overline{u}_k\overline{u}_k} - \widehat{\overline{u}}_k\widehat{\overline{u}}_k\right) \tag{50}$$

where the constant C_k is determined by matching the total amount of k_{sgs} to be the same as the exact amount of the energy remaining above the cut-off wavenumber at the first measuring station of the experiment.

Figure 5 shows the decay of the resolved turbulent kinetic energy computed using the LDKM at three grid resolutions, 48^3, 32^3, and 24^3. The results are compared with the experimental data of Comte-Bellot and Corsin[35]. The predictions of LES are in good agreement with the experiment. As is well known, the turbulent kinetic energy undergoes a power law decay, i.e., $E \sim (t^*)^r$, in the asymptotic self-similar regime.

Table II shows this decay exponent r which is obtained from a least-square fit to each data. These results confirm the agreement between the predictions of LES and the experiment. More importantly, the present results at all three grid resolutions used (even for the 24^3 grid resolution where about a half of the turbulent kinetic energy is not resolved) show

consistency in predicting the energy decay.

4.2 *Forced isotropic turbulence*

A statistically stationary isotropic turbulence is simulated using a 32^3 grid resolution. The results are compared with the existing high resolution DNS data by Vincent and Meneguzzi[36] and Jimenez *et al.*[37] obtained at $Re_\lambda \approx 150$ and $Re_\lambda \approx 170$, respectively. A statistically stationary turbulent field is obtained by forcing the large scales as was done by Kerr[38]. In this study, the initial value of all Fourier modes with wavenumber components equal to 1 is kept fixed. The initial condition is obtained by generating a random realization of the energy spectrum,[39]

$$E(k) = C\frac{k^4}{1+(k/k_0)^{5/3+4}} \tag{51}$$

where $k_0 = 1$ and C is a constant which normalizes the initial total energy to be 0.5.

In this study, LES are implemented under two different flow conditions. One is characterized by $Re_\lambda \approx 260$, $Re_\ell \approx 2400$, and $\tau \approx 3.7$; the other is characterized by $Re_\lambda \approx 80$, $Re_\ell \approx 220$, and $\tau \approx 4$ (where Re_λ, Re_ℓ, and τ, respectively, denote the Taylor microscale Reynolds number, the integral scale Reynolds number, and the large-eddy turnover time). The simulations have been run for 27 and 25 large-eddy turnover times, respectively. To ensure statistical independence, 20 fields are used for statistical analysis for both cases with the time interval between successive fields larger than (or at least same as) one large-eddy turnover time.

Figure 6(a) shows the probability distribution of velocity differences, $\delta u(r) = \overline{u}(x+r) -$

$\overline{u}(x)$, for various values of length scale r (note that all values of r used here are comparable with inertial range scales). Here, δu is normalized so that $\sigma^2 = \widetilde{\delta u^2} = 1$. The LES results (using the LDKM at $Re_\lambda \approx 260$) clearly show that the distribution changes from a non-Gaussian (which has tails) to a Gaussian, as r increases. The same behavior of the distribution was observed in the high resolution DNS of Vincent and Meneguzzi.[36] In addition to the basic agreement regarding the development of the non-Gaussian statistics, the LES accurately predicts the probability of each bin. Figure 6(b) shows good agreement between the distributions for $r = 0.39$ obtained from the LES and the DNS, except for deviations in the tail regions. However, as is well known, the tails of the non-Gaussian distribution develop mainly due to small-scale fluctuations. Therefore, the deviations between the LES and the DNS results in the tails are somewhat natural; since in LES, most small scales are not resolved and even the resolved portion of small scales lies under strong influence of the top-hat filter implicitly adopted in the FDM code.

The statistics of velocity (which are the property of the large scales and mostly resolved in LES) are also investigated. We computed the nth-order moments of u-velocity component distribution using

$$S_n = \frac{\widetilde{u^n}}{\widetilde{u^2}^{n/2}} \tag{52}$$

here, "$\sim$" denotes ensemble-averaging. The results of these calculations are summarized in Table III. The results of the 512^3 DNS ($Re_\lambda \approx 170$) are obtained from Reference 37. Two different Reynolds number cases were studied by the LES. As shown in the table, the velocity statistics predicted by the LES agree well with the DNS results.

4.3 *Rotating isotropic turbulence*

The principal effect of system rotation on isotropic turbulence is to alter the nonlinear interactions among turbulence scales. The system rotation inhibits energy transfer from large to small scales and, thus, leads to a reduction in turbulence dissipation and an associated decrease in the decay rate of turbulence energy. In this study, we simulate the experiment of rotating homogeneous turbulence of Jacquin *et al.*.[40] The effect of system rotation on the large-scale velocity field can be easily included by adding the following Coriolis term to the right hand side of (3),

$$2\epsilon_{ij3}\Omega\overline{u}_j$$

where ϵ_{ijk} is Levi-Civita's alternating tensor. The resulting equations represent the governing equations of large-scale motions in a reference frame rotating with constant angular velocity Ω about the z-axis. Four different cases, $\Omega = 0$, 15.7, 31.4, and 62.8 rad/sec, were simulated using the 32^3 grid resolution.

The same initial field, which was used for the simulation of decaying isotropic turbulence described in Section 4.1, is adopted. The total energy and the time scale of this initial state have been scaled to match those of Jacquin *et al.*'s[40] experiment at the imaginary origin of realistic turbulence where the grid wakes are believed to completely mix together. The imaginary origin is assumed to be $x/M = 2.6$ (M denotes the mesh size of the grid) as given by the authors for $\Omega = 0$ rad/sec and $M = 1.5$ cm.

In Figure 7, the decay of the resolved-scale turbulent kinetic energy for various rotation rates are compared to the experimental data of Jacquin *et al.*.[40] These results clearly demonstrate the principal effect of system rotation on isotropic turbulence, that is, increasing

rotation rate decreases the decay rate of turbulent kinetic energy. As shown, LES predictions of this phenomenon is in good agreement with the experimental data.

4.4 *Turbulent mixing layers*

Vreman *et al.*[41] simulated a temporal, weakly compressible (M=0.2) mixing layer in a cubic domain using 192^3 grid resolution. In their study, the length of the domain was $29.5\delta_\omega^0$ (where δ_ω^0 denotes the initial vorticity thickness) which corresponds to four times the wavelength of the most unstable mode as predicted by linear stability theory at M=0.2. Periodic boundary conditions are imposed in the streamwise (x-) and spanwise (z-) directions, while in the cross-stream (y-) direction the boundaries are assumed as slip walls. The initial velocity field is the hyperbolic-tangent profile, $u = \Delta U \tanh(2y/\delta_\omega^0)$, on which is superimposed a three-dimensional large-amplitude eigenfunction disturbance obtained from linear stability analysis.[42] For the present study of the temporally evolving incompressible mixing layer, the initial LES field is obtained by filtering the initial DNS field (generated using Vreman's code) for the length of the domain $50\delta_\omega^0$.

Figure 8 shows the time evolution of the momentum thickness scaled using:

$$\delta_m^*(t^*) = \frac{1}{\delta_m^S}\left[\delta_m\left(t^*\right) - \delta_m^S\right] \tag{53}$$

$$t^* = \frac{\Delta U}{\delta_m^S}\left(t - t^S\right) \tag{54}$$

where superscript $*$ denotes scaled variables and superscript S indicates scaling parameters at the self-similarity starting point. Subtractions by δ_m^S and t^S are implemented to assign

zero scaled time and scaled momentum thickness at the self-similarity starting point. In this study, the self-similarity starting point is estimated by the point where the mixing layer begins to grow linearly. 192^3 DNS results by Vreman *et al.*[43] are also plotted for comparison. As shown, DNS and LES results appear to collapse on each other reasonably well. The small difference between the LES and the DNS growth rate confirms the well-known fact that compressibility (the DNS data is for $M = 0.2$) reduces mixing layer growth rate.[42] Figure 8 also includes the asymptotic growth rate (slope) obtained from the experiment of Bell and Mehta[44] for a spatially evolving mixing layer begun from turbulent (tripped) splitter-plate boundary layers. The growth rates predicted by the LES agree very well with the experiment.

In Figure 9, mean (ensemble-averaged) velocity profiles U at five time levels (see figure) during the entire period after $t^* = 0$ are plotted with self-similar scaling using the time-dependent momentum thickness δ_m and the velocity difference ΔU. Also included are the experimental data of Bell and Mehta.[44] The collapse of the data at the five time-levels is excellent, and the mean profile agrees very well with the data of Bell and Mehta[44].

In Figure 10, Reynolds stress profiles $\widetilde{uv}$ scaled using self-similar parameters at $t^* = 110$ are shown together with the DNS data of Vreman *et al.*.[43] The overall agreement between the DNS and the LES is good.

4.5 *Turbulent plane Couette flows*

The experiments of Bech *et al.*[45] and Aydin and Leuthersser[46,47] were simulated. In the simulations, only the upper wall (at $y/h = 1$) was moving with a constant velocity U_w while the lower wall (at $y/h = -1$) was fixed. The chosen Reynolds number $\mathrm{Re} = U_w h/\nu$ (where

h is the channel half height) was 2600, while the Reynolds number $\mathrm{Re}_\tau = U_\tau h/\nu$ based on the wall-shear velocity $U_\tau = (\nu dU/dy|_{wall})^{1/2}$ was 81. The computational domain was $4\pi h \times 2h \times 2\pi h$ in the streamwise, normal, and spanwise directions, respectively. The grid resolution was $48 \times 48 \times 32$ with uniform spacing in the streamwise and spanwise directions, while in the normal direction, the grid was stretched using a 6% linear stretching in order to improve the resolution in the near-wall regions. Computational meshes are around $21.1\Delta y^+$ in the streamwise direction, $15.8\Delta y^+$ in spanwise direction, and the resolutions in the normal direction are $\Delta y^+ = 1.6$ next to the wall with stretching that reaches a maximum of $6.1\Delta y^+$. At the wall boundaries, no-slip conditions were used and in the homogeneous (streamwise and spanwise) directions, periodic conditions were imposed. The initial field was constructed of the laminar mean velocity profile with finite-amplitude velocity fluctuations superimposed. After about $150h/U_w$, the flow reaches a statistically steady state. Statistics were obtained by ensemble averaging for another $55h/U_w$.

Figure 11(a,b) shows the mean velocity distribution. For comparison, experimental data obtained by Aydin and Leutheusser[46] at Re =2600 and Bech *et al.*[45] at Re =2520, and DNS results by Bech *et al.*[45] at Re =2600 are also plotted in Figure 11(a). The DNS[45] was carried out using the $256 \times 70 \times 256$ grid resolution. The agreement between the LES and the experimental data is excellent both in the wall region and in the center of the channel. In Figure 11(b), the mean velocity is plotted in a semi-logarithm form, normalized with viscous scales. As shown, the velocity profile is clearly divided into a viscous sublayer, a buffer region, and a logarithm part. For comparison, the following universal velocity-distribution law for smooth-wall conditions is also plotted,

$$U^+ = A \ln y^+ + B \tag{55}$$

where $U^+ = U/U_\tau$, $y^+ = yU_\tau/\nu$ and A is the inverse of the von Kármán constant. The constants appearing in the equation have the universal values: A =2.5 and B =5.5. The LES results align well with the straight line with only small deviations. The logarithmic region extends to the center of the channel, a feature observed in the experiments and also captured here.

In Figure 12, turbulence intensities obtained from LES, DNS, and experiments are shown (only the moving wall part of the LES results are presented). The LES results show overall good agreement with the DNS and experimental data except for some deviations of the normal component in the region close to the wall. The highest intensity is observed in the streamwise component which has a maximum at $y^+ \approx 13$, whereas, (unlike the plane Poiseuille flow) the other components monotonically increase to a constant value in the center of the channel. In the present simulation, the ratio of the velocity fluctuations v_{rms}/u_{rms} ≈0.65 is obtained (this value lies in between the value of 0.6 obtained by Aydin and Leuthersser[47] and the value of 0.67 obtained by Bech *et al.*[45]).

4.6 *Turbulent recirculating flows*

The experiment of lid-driven three-dimensional cavity flows of Prasad and Koseff[48] is simulated. In the experiment, the three-dimensional cavity has square cross section (i.e., width (B) = depth (D)) and spanwise aspect ratio (i.e., L/B where L is the cavity span) of 0.5:1. The lid (the top wall) is moving at a velocity U_B and the other walls (i.e., the upstream and

downstream walls which are perpendicular to the streamwise (x-) direction, the bottom wall which is perpendicular to the vertical (y-) direction, and the end walls which are perpendicular to the spanwise (z-) direction), remain stationary. Hence, fluid motions are developed by the shear of the lid, resulting in a complicated three-dimensional flow field consisting of a stationary primary vortex and a number of complex secondary corner vortices. In these flows, the Reynolds number is usually defined to be $U_B B/\nu$. Koseff and Street[49] have shown that at Reynolds number higher than about 6000, instability occurs near the downstream corner vortex. As the Reynolds number increases, the flow becomes increasingly turbulent near walls, and at Reynolds numbers higher than 10000, the flow near the downstream corner vortex becomes fully turbulent. In the present study, the Reynolds number of 10000 is considered. Therefore, the present case belongs to the locally turbulent regime.

The simulation has been carried out using a $64 \times 64 \times 32$ grid, which is stretched in the streamwise and vertical directions using 6.5% and 13.4% linear stretchings, respectively, but is uniform in the spanwise direction (i.e., grids are not clustered near the side walls). Small random velocity perturbations are initially prescribed to prevent the initial k_{sgs} field from becoming zero. The computation was first conducted with a 32^3 grid. After the flow was fully developed, the coarser-resolution field was interpolated onto the finer-resolution field. Simulation was then continued and statistics were collected after a sufficient relaxation time.

The three-dimensional flow in a cubic cavity has a very complex structure. The main structure of the flow is similar to that in a two-dimensional square cavity but is significantly more complicated due to the end walls. In planes perpendicular to the z-direction, the flow field consists of a primary vortex with two corner vortices at the bottom wall and a vortex at the top upstream corner. The strengths of these vortices vary with the distance from the

end walls. In the mid-plane, the strengths of the vortices are strongest due to the viscous damping at the end walls. In planes perpendicular to the x-direction, the flow field also consists of various vortices. The complete details of the observed three-dimensional flow field are not presented here for brevity.

Figure 13 shows the computed mean streamwise ($U-$) and vertical ($V-$) velocity profiles on the center-lines in the mid-plane. Measurements by Prasad and Koseff[48] are given for comparison. As shown in the figure, the predicted profiles by the LES agree very well with the experimental data except that the calculation overpredicts the maximum vertical velocity and the thickness of the boundary layers on the upstream wall ($x/B = 0$).

The root-mean-square (rms) of fluctuating velocities on the center-lines in the mid-plane are shown in Figure 14. Note that this is multiplied by a factor of 10 for a better presentation. The calculation shows a good overall agreement with the experiment although it underpredicts the magnitude of the peaks. Note that the LDKM computation captures the two humps in the experimental profile on the upstream wall (at $x/B \approx 0$) with reasonable accuracy.

Figure 15 displays the center-line Reynolds stress profiles on the mid-plane. This quantity is also magnified by a factor of 500 for a presentation purpose. LES predicts the profiles fairly accurately.

5 CONCLUSIONS

In this paper, we have presented a high-order-accurate, upwind-biased finite-difference method for solving the unsteady incompressible Navier-Stokes equations. Time accuracy has been

achieved by using the dual time-stepping based on the artificial compressibility method. Various efficient (pseudo-time) convergence-acceleration techniques have been adopted in conjunction with an implicit (physical) time discretization. Validation of the method for various turbulent flows using the localized dynamic subgrid-scale model has been carried out and results indicate that the present solver is accurate and efficient. The efficiency of the solver is believed to be considerably improved by employing incompressible preconditioning methods which have received much attention during recent years. This issue is under consideration.

ACKNOWLEDGMENT

We wish to thank Professor B. Vreman for providing the initial disturbance field generator of turbulent mixing layer and the data presented in Figs. 7 and 9. This work was supported by the Fluid Dynamics Division of the Office of Naval Research under grant N00014-93-1-0342, monitored by Dr. L. P. Purtell. Computing time was provided by the DoD High Performance Computing (HPC) Centers: Army Research Laboratory (ARL), Naval Oceanographic Office (NAVOCEANO), and Army Engineer Waterways Experiment Station (CEWES).

References

[1] H. Choi and P. Moin, 'Effects of the computational time step on numerical solutions of turbulent flows', *J. Comput. Phys.*, **113**, 1 (1994).

[2] M. M. Rai and P. Moin, 'Direct simulations of turbulent flow using finite-difference schemes', *J. Comput. Phys.*, **96**, 15 (1991).

[3] S. K. Lele, 'Compact finite difference schemes with spectral-like resolution', *J. Comput. Phys.*, **103**, 16 (1992).

[4] W.-W. Kim and S. Menon, 'On the properties of a localized dynamic subgrid-scale model for large-eddy simulations', submitted to *J. Fluid Mech.*, (1996).

[5] W.-W. Kim, 'A new dynamic subgrid-scale model for large-eddy simulation of turbulent flows', Ph. D. Thesis, School of Aerospace Engineering, Georgia Institute of Technology, Atlanta, Georgia, 1996.

[6] U. Schumann, 'Subgrid scale model for finite difference simulations of turbulent flows in plane channels and annuli', *J. Comput. Phys.*, **18**, 376 (1975).

[7] S. Menon, P.-K. Yeung and W.-W. Kim, 'Effect of subgrid models on the computed interscale energy transfer in isotropic turbulence', *Comput. Fluids*, **25**, 165 (1996).

[8] M. Germano, U. Piomelli, P. Moin and W. H. Cabot, 'A dynamic subgrid-scale eddy viscosity model', *Phys. Fluids* A, **3**, 1760 (1991).

[9] S. Liu, C. Meneveau and J. Katz, 'On the properties of similarity subgrid-scale models as deduced from measurements in a turbulent jet', *J. Fluid Mech.*, **275**, 83 (1994).

[10] W.-W. Kim and S. Menon, 'A New Dynamic One-Equation Subgrid-Scale Model for Large-Eddy Simulations', AIAA Paper 95-0356, 1995.

[11] S. Menon and W.-W. Kim 'High Reynolds number flow simulations using the localized dynamic subgrid-scale model', AIAA Paper 96-0425, 1996.

[12] W.-W. Kim and S. Menon, 'On the time-accurate numerical simulations of temporally evolving turbulent mixing layers', submitted to *AIAA J.*, (1996).

[13] W.-W. Kim and S. Menon, 'Application of the localized dynamic subgrid-scale model to turbulent wall-bounded flows', AIAA Paper 97-0210, 1997.

[14] S. Ghosal, T. S. Lund, P. Moin and K. Akselvoll, 'A dynamic localization model for large-eddy simulation of turbulent flows', *J. Fluid Mech.*, **286**, 229 (1995).

[15] D. K. Lilly, 'A proposed modification of the Germano subgrid-scale closure method', *Phys. Fluids*, **4**, 633 (1992).

[16] W. H. Cabot and P. Moin, 'Large eddy simulation of scalar transport with the dynamic subgrid-scale model', in B. Galperin and S. A. Orszag (eds), *Large Eddy Simulation of Complex Engineering and Geophysical Flows*, Cambridge University Press, 1993, p. 411.

[17] T. S. Lund, S. Ghosal and P. Moin, 'Numerical experiments with highly-variable eddy viscosity models', in U. Piomelli and S. Ragab (eds), *Engineering Applications of Large Eddy Simulations*, ASME-FED, **162**, 1993, p. 7.

[18] V. C. Wong, 'A proposed statistical-dynamic closure method for the linear or nonlinear subgrid-scale stresses', *Phys. Fluids* A, **4**, 1080 (1992).

[19] R. S. Rogallo, 'Numerical experiments in homogeneous turbulence', NASA Tech. Memo. 81315, 1981.

[20] D. Carati, S. Ghosal and P. Moin, 'On the representation of backscatter in dynamic localization models', *Phys. Fluids*, **7**, 606 (1995).

[21] F. H. Harlow and J. E. Welch, 'Numerical calculation of time-dependent viscous incompressible flow with free surfaces', *Phys. Fluids,* **8**, 2182 (1965).

[22] A. J. Chorin, 'Numerical solution of Navier-Stokes equations', *Math. Comput.,* **22**, 745 (1968).

[23] A. J. Chorin, 'A numerical method for solving incompressible viscous flow problems', *J. Comput. Phys.*, **2**, 12 (1967).

[24] E. Turkel, 'Preconditioned methods for solving the incompressible and low speed compressible equations', *J. Comput. Phys.,* **72**, 277 (1987).

[25] P. R. McHugh and J. D. Ramshaw, 'Damped artificial compressibility iteration scheme for implicit calculations of unsteady incompressible flow', *Int. J. numer. methods fluids*, **21**, 141 (1995).

[26] S. E. Rogers and D. Kwak, 'Numerical solution of the incompressible Navier-Stokes equations for steady and time-dependent problems', AIAA Paper 89-0463, 1989.

[27] M. Breuer and D. Hänel, 'A dual time-stepping method for 3-D, viscous, incompressible vortex flows', *Comput. Fluids,* **22**, 467 (1993).

[28] C. M. Rhie and W. L. Chow, 'Numerical study of the turbulent flow past an airfoil with trailing edge separation', *AIEE J.*, **21**, 1525 (1983).

[29] S. W. Armfield, 'Finite difference solution of the Navier-Stokes equations on staggered and non-staggered grids', *Comput. Fluids*, **20**, 1 (1991).

[30] J. C. Strikwerda, 'Finite difference methods for the Stokes and Navier-Stokes equations', *SIAM J. Sci. Stat. Comput.*, **5**, 56 (1984).

[31] R. W. MacCormack, 'An efficient numerical method for solving the time-dependent compressible Navier-Stokes equations at high Reynolds number', NASA Tech. Memo. x-73, 1976.

[32] A. Jameson, 'Solution of the Euler equations for two dimensional transonic flow by a multigrid method', *Appl. Math. Comp.,* **13**, 327 (1983).

[33] A. Brandt, 'Guide to Multigrid Development', in *Lecture Notes in Mathematics*, **960**, Springer-Verlag, 1981, p. 220.

[34] Y. Zang, R. L. Street and J. R. Koseff, 'A non-staggered grid, fractional step method for time-dependent incompressible Navier-Stokes equations in curvilinear coordinates', *J. Comput. Phys.*, **114**, 18 (1994).

[35] G. Comte-Bellot and S. Corsin, 'Simple Eulerian time correlation of full- and narrow-band velocity signals in grid-generated, 'isotropic' turbulence', *J. Fluid Mech.*, **48**, 273 (1971).

[36] A. Vincent and M. Meneguzzi, 'The spatial structure and statistical properties of homogeneous turbulence', *J. Fluid Mech.* **225**, 1 (1991).

[37] J. Jimenez, A. A. Wray, P. S. Saffman and R. S. Rogallo, 'The structure of intense vorticity in isotropic turbulence', *J. Fluid Mech.*, **255**, 65 (1993).

[38] R. M. Kerr, 'Higher order derivative correlations and the alignment of small-scale structures in isotropic numerical turbulence',*J. Fluid Mech.*, **153**, 31 (1985).

[39] M. Briscolini and P. Santangelo, 'The non-Gaussian statistics of the velocity field in low-resolution large-eddy simulations of homogeneous turbulence', *J. Fluid Mech.*, **270**, 199 (1994).

[40] L. Jacquin, O. Leuchter, C. Cambon and J. Mathieu, 'Homogeneous turbulence in the presence of rotation', *J. Fluid Mech.*, **220**, 1 (1990).

[41] B. Vreman, B. Geurts and H. Kuerten, 'Comparison of numerical schemes in large-eddy simulation of the temporal mixing layer', *Int. j. numer. methods fluids*, **22**, 297 (1996).

[42] N. D. Sandham and W. C. Reynolds, 'Three-dimensional simulations of large eddies in the compressible mixing layer', *J. Fluid Mech.*, **224**, 133 (1991).

[43] B. Vreman, B. Geurts and H. Kuerten, 'On the formulation of the dynamic mixed subgrid-scale model', *Phys. Fluids*, **6**, 4057 (1994).

[44] J. H. Bell and R. D. Mehta, 'Development of a two-stream mixing layer from tripped and untripped boundary layers', *AIAA J.*, **28**, 2034 (1990).

[45] K. H. Bech, N. Tillmark, P. H. Alfredsson and H. I. Andersson, 'An investigation of turbulent plane Couette flow at low Reynolds numbers', *J. Fluid Mech.*, **286**, 291 (1995).

[46] E. M. Aydin and H. J. Leutheusser, 'Experimental investigation of turbulent plane Couette flow', in *ASME Forum on Turbulent Flows, FED,* **51**, 1987, p. 51.

[47] E. M. Aydin and H. J. Leutheusser, 'Plane-Couette flow between smooth and rough walls', *Exps Fluids,* **11**, 302 (1991).

[48] A. K. Prasad and J. R. Koseff, 'Reynolds number and end-wall effects on a lid-driven cavity flow', *Phys. Fluids* A, **1**, 208 (1989).

[49] J. R. Koseff and R. L. Street, 'Visualization studies of a shear driven three-dimensional recirculating flow', *J. Fluids Eng.*, **106**, 21 (1984).

Table I. Comparison of CPU time per grid point per time step and number of 3-dimensional variables per grid point between the present method and previous incompressible methods.

	CPU time (μs)	Number of variables
Explicit staggered-grid[34]	60 (Y-MP 8/864)	103
Implicit staggered-grid[34]	110 (Y-MP 8/864)	94
Fractional step (Zang *et al.*[34])	28 (Y-MP 8/864)	51
Artificial comp. (present)	100 (SGI MIPS 8000)	36

Table II. Decay exponent r of the power law decay $E \sim (t^*)^r$ in isotropic turbulence. Experimental data are computed from the energy spectra given by Comte-Bellot and Corsin[35].

Grid resolution	48^3	32^3	24^3
Experiment	-1.20	-1.16	-1.12
LDKM	-1.17	-1.13	-1.09

Table III. Higher-order moments of u-velocity component in forced isotropic turbulence. The nth-order moments are denoted by S_n. Results of 512^3 DNS are adopted from Reference 37.

	S_4	S_6
512^3 DNS ($\mathrm{Re}_\lambda \approx 170$)	2.80	12.5
32^3 LDKM ($\mathrm{Re}_\lambda \approx 260$)	2.78	11.9
32^3 LDKM ($\mathrm{Re}_\lambda \approx 80$)	2.80	12.1
Gaussian	3.0	15.0

Captions

Figure 1. (a) Decay of resolved turbulent kinetic energy and (b) energy spectra in decaying isotropic turbulence. Spectral code results of Carati *et al.*[20] (no model case) and experimental data of Comte-Bellot and Corsin[35] are also plotted in (a).

Figure 2. Comparison between the regularized central differences and the nonregular central differences using the decaying isotropic turbulence results, (a) decay of resolved turbulent kinetic energy and (b) energy spectra. Experimental data of Comte-Bellot and Corsin[35] are also plotted in (a).

Figure 3. Pseudo-time convergence history for variation of β during one physical time step advance in the simulation of decaying isotropic turbulence.

Figure 4. Pseudo-time convergence history for variation of multigrid levels during one physical time step advance in the simulation of decaying isotropic turbulence.

Figure 5. Decay of turbulent kinetic energy in isotropic turbulence, resolved by LES with three different grid resolutions. Experimental data of Comte-Bellot and Corsin[35] are also plotted.

Figure 6. Probability distribution of normalized velocity difference for (a) five different scales (r) and (b) $r = 0.39$ predicted by LES of forced isotropic turbulence. High resolution DNS results of Vincent and Meneguzzi[36] are also plotted in (b).

Figure 7. Decay of resolved turbulent kinetic energy predicted by LES of rotating isotropic turbulence for various rotation rates. Experimental data of Jacquin *et al.*[40] are also plotted.

Figure 8.Time variation of the momentum thickness of temporally evolving turbulent mixing layer in scaled coordinates using self-similarity starting point parameters. Results of 192^3 DNS by Vreman *et al.*[43] and experimental data of Bell and Mehta[44] are also plotted.

Figure 9. Mean streamwise velocity profiles in self-similar scaled coordinates obtained from LES of temporally evolving turbulent mixing layer. Experimental data of Bell and Mehta[44] at three downstream locations are also plotted.

Figure 10.Comparison of time-accurate simulation results obtained from LES of temporally evolving turbulent mixing layer. Reynolds stresses $\widetilde{uv}$ at $t^* = 110$ are plotted in self-similar scaled coordinates. Results of 192^3 DNS by Vreman *et al.*[43] are also plotted.

Figure 11. (a) Mean velocity distribution and (b) mean velocity distribution in a semi-logarithm form normalized with viscous scales obtained from turbulent plane Couette flow simulation. Experimental data of Aydin and Leutheusser[46] and Bech *et al.*,[45] and DNS results of Bech *et al.*[45] are also plotted in (a). In (b), universal velocity-distribution law for smooth wall conditions is plotted for comparison.

Figure 12. Turbulence intensities obtained from turbulent plane Couette flow simulation. Experimental data of Aydin and Leutheusser[47] and Bech *et al.*,[45] and DNS results of Bech *et al.*[45] are also plotted.

Figure 13. Mean velocity distributions on the center-lines in the mid-plane obtained from turbulent recirculating flow simulation. Experimental data of Prasad and Koseff[48] are also plotted.

Figure 14. Turbulence intensities on the center-lines in the mid-plane obtained from turbulent recirculating flow simulation. Experimental data of Prasad and Koseff[48] are also plotted.

Figure 15. Reynolds stress profiles on the center-lines in the mid-plane obtained from turbulent recirculating flow simulation. Experimental data of Prasad and Koseff[48] are also plotted.

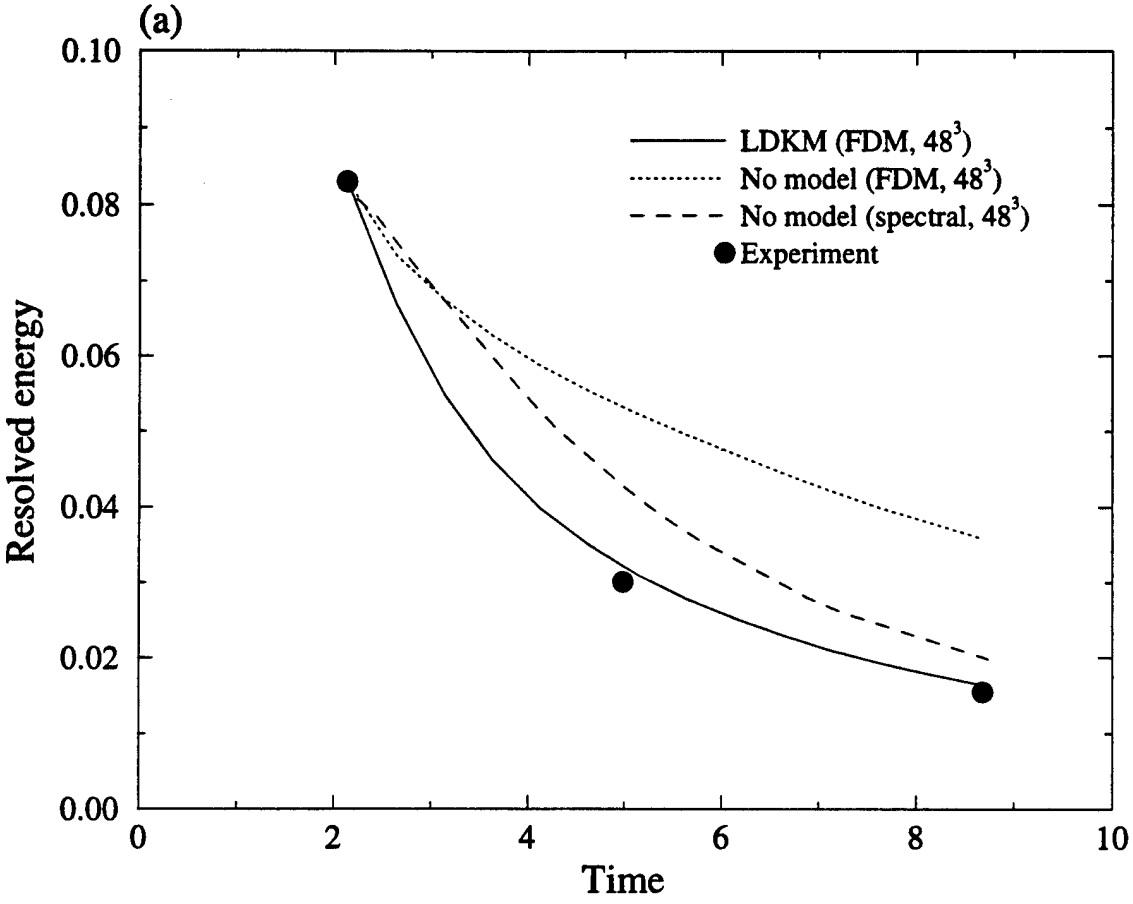

(a)
0.10
0.08
0.06
0.04
0.02
0.00
Resolved energy
0
2
4
6
8
10
Time
LDKM (FDM, 48³)
No model (FDM, 48³)
No model (spectral, 48³)
Experiment

Figure 1(a)

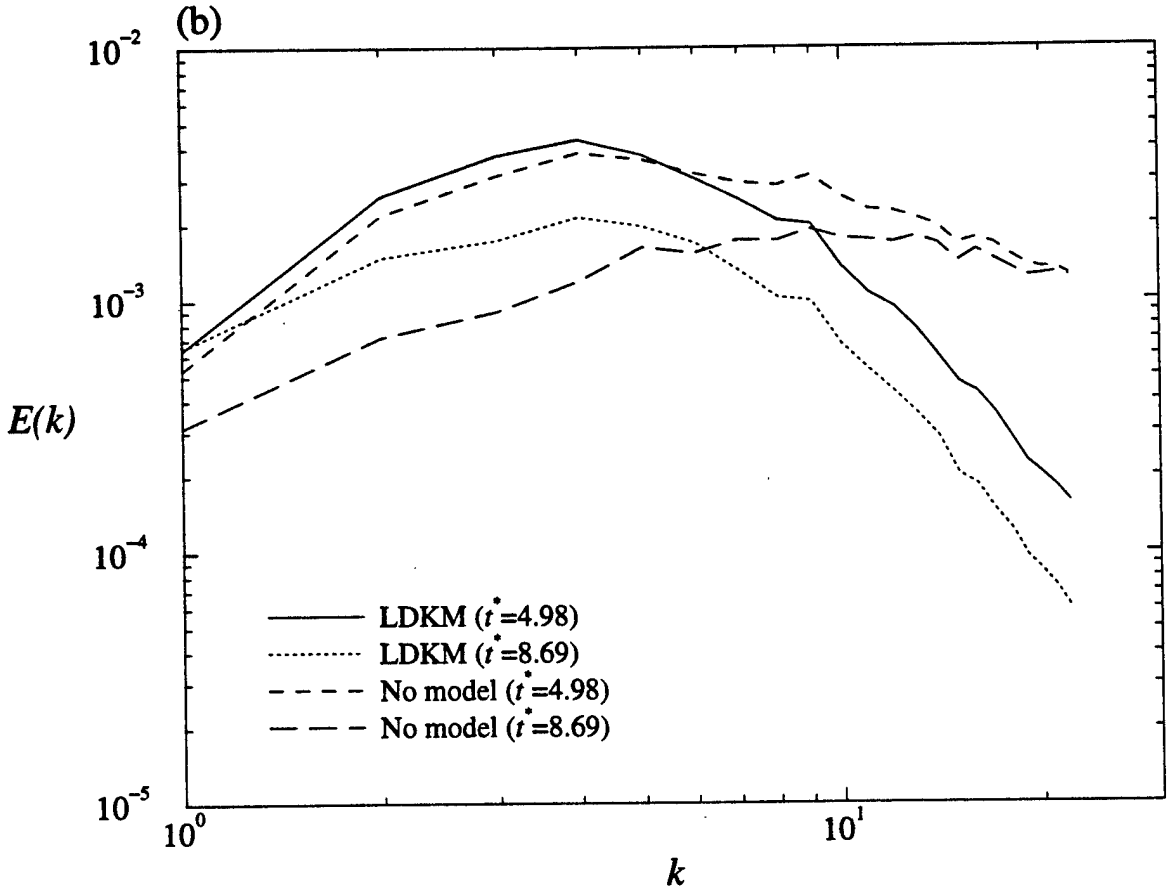

(b)
10^{-2}
10^{-3}
10^{-4}
10^{-5}
$E(k)$
10^{0}
10^{1}
k
LDKM (t^*=4.98)
LDKM (t^*=8.69)
No model (t^*=4.98)
No model (t^*=8.69)

Figure 1(b)

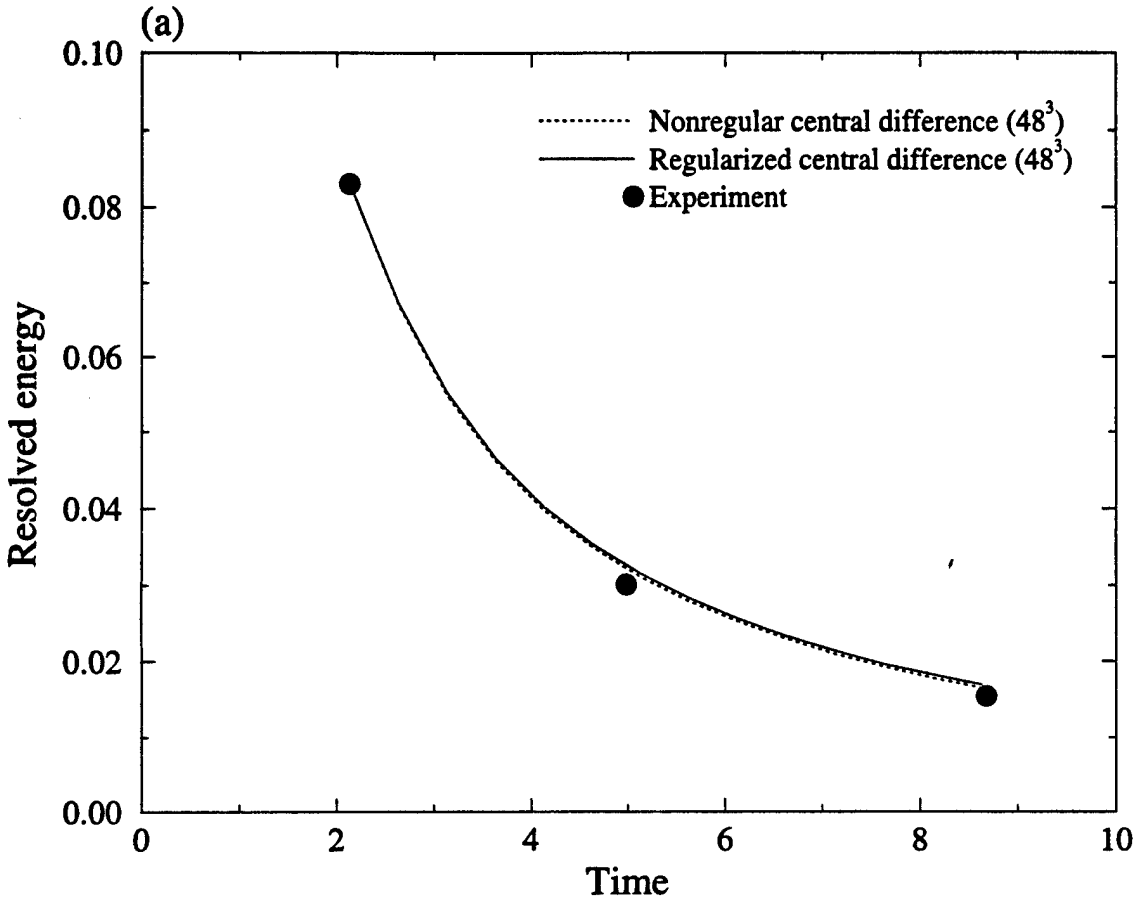

(a)
0.10
0.08
0.06
0.04
0.02
0.00
Resolved energy
0
2
4
6
8
10
Time
Nonregular central difference (48^3)
Regularized central difference (48^3)
Experiment

Figure 2(a)

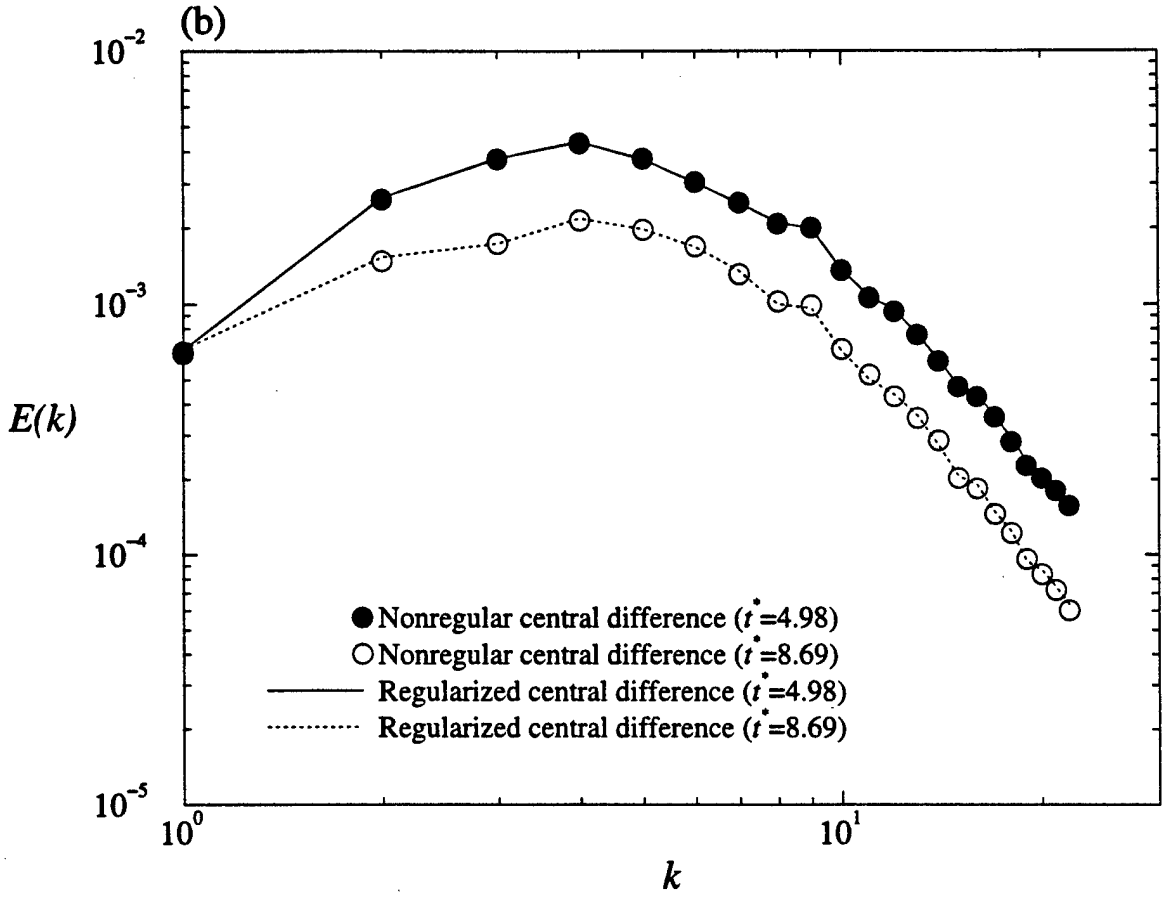

(b)
10^{-2}
10^{-3}
10^{-4}
10^{-5}
E(k)
10^{0}
10^{1}
k
Nonregular central difference (t^*=4.98)
Nonregular central difference (t^*=8.69)
Regularized central difference (t^*=4.98)
Regularized central difference (t^*=8.69)

Figure 2(b)

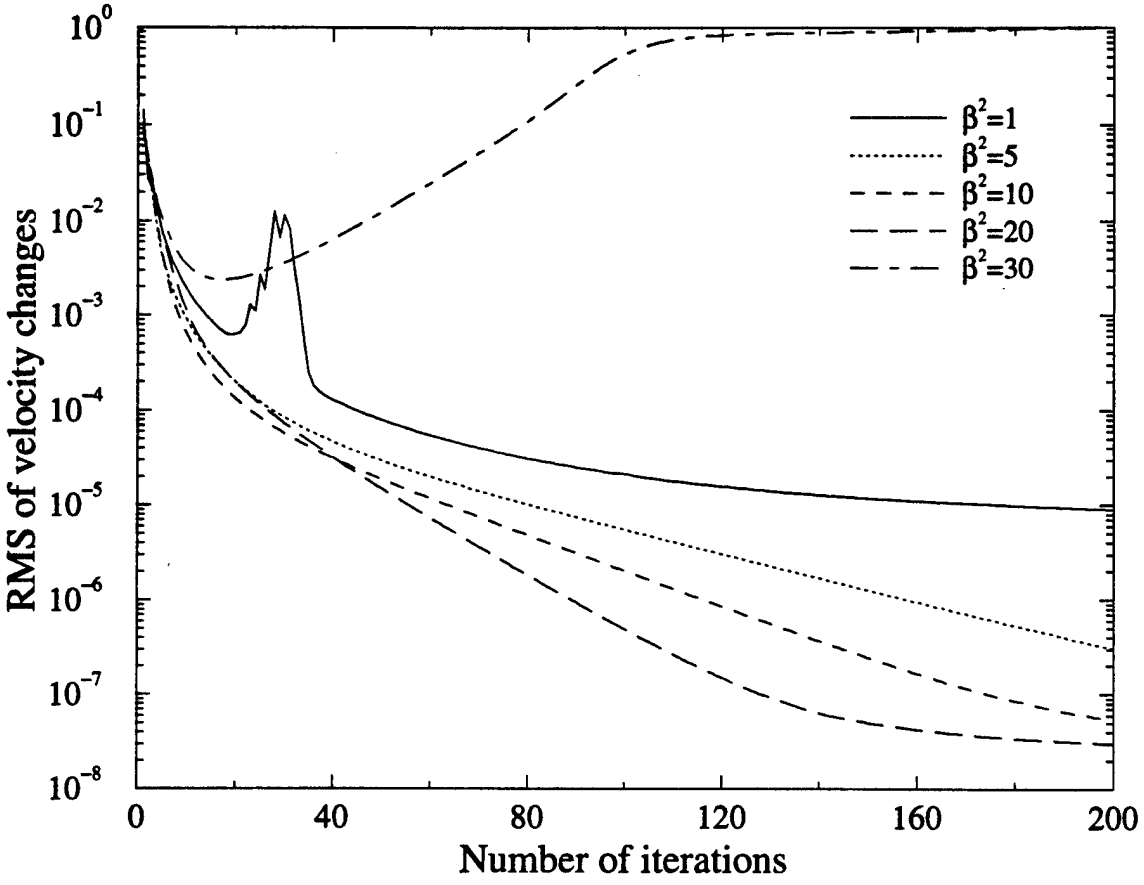

RMS of velocity changes
Number of iterations
10^{0}
10^{-1}
10^{-2}
10^{-3}
10^{-4}
10^{-5}
10^{-6}
10^{-7}
10^{-8}
0
40
80
120
160
200
β^2=1
β^2=5
β^2=10
β^2=20
β^2=30

Figure 3

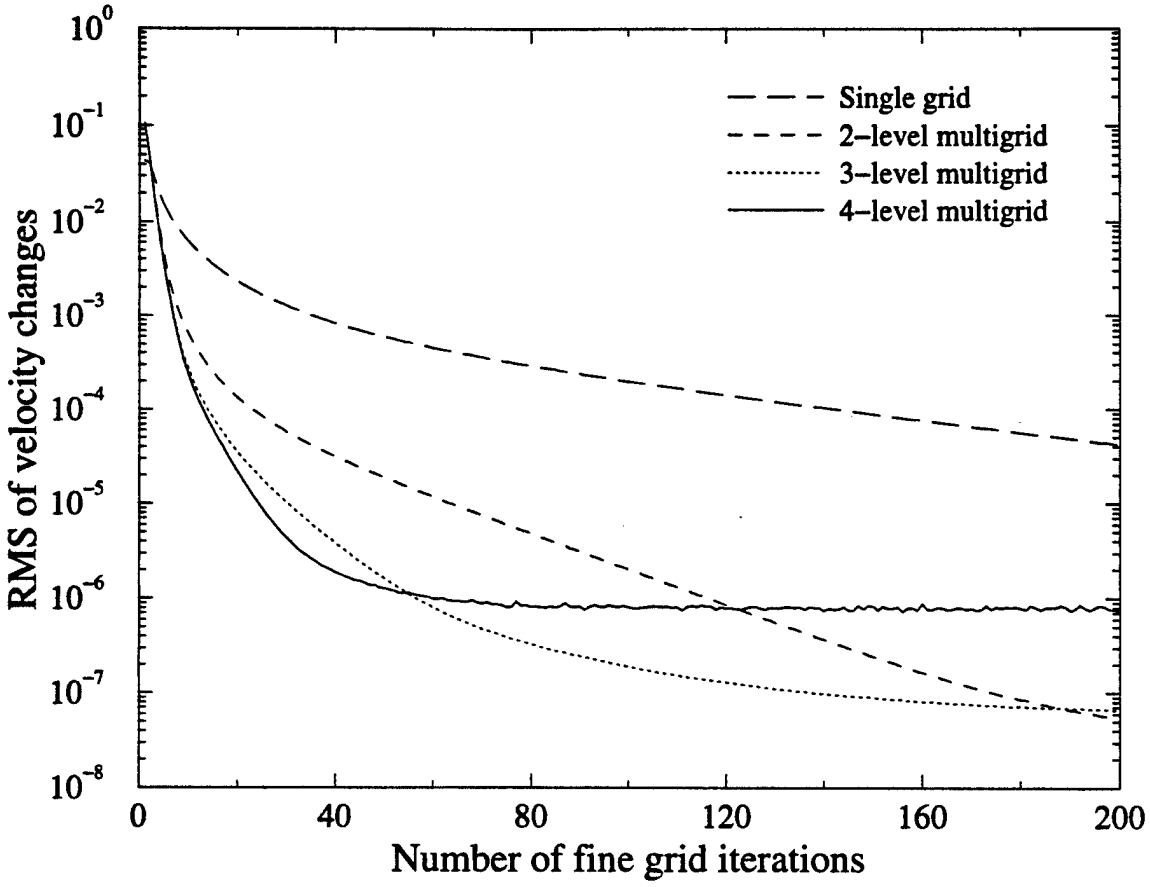

RMS of velocity changes
10^{0}
10^{-1}
10^{-2}
10^{-3}
10^{-4}
10^{-5}
10^{-6}
10^{-7}
10^{-8}
0
40
80
120
160
200
Number of fine grid iterations
Single grid
2–level multigrid
3–level multigrid
4–level multigrid

Figure 4

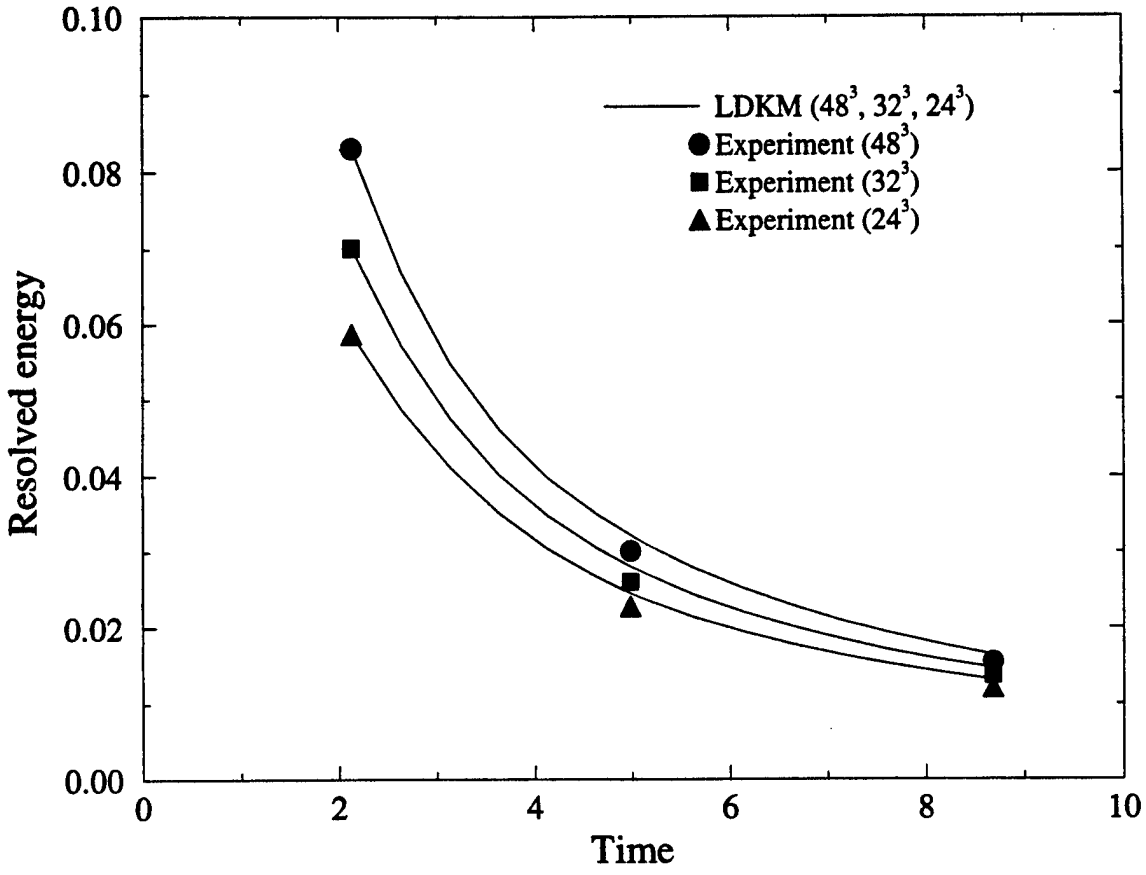

0.10
0.08
0.06
0.04
0.02
0.00
Resolved energy
0
2
4
6
8
10
Time
LDKM (48³, 32³, 24³)
Experiment (48³)
Experiment (32³)
Experiment (24³)

Figure 5

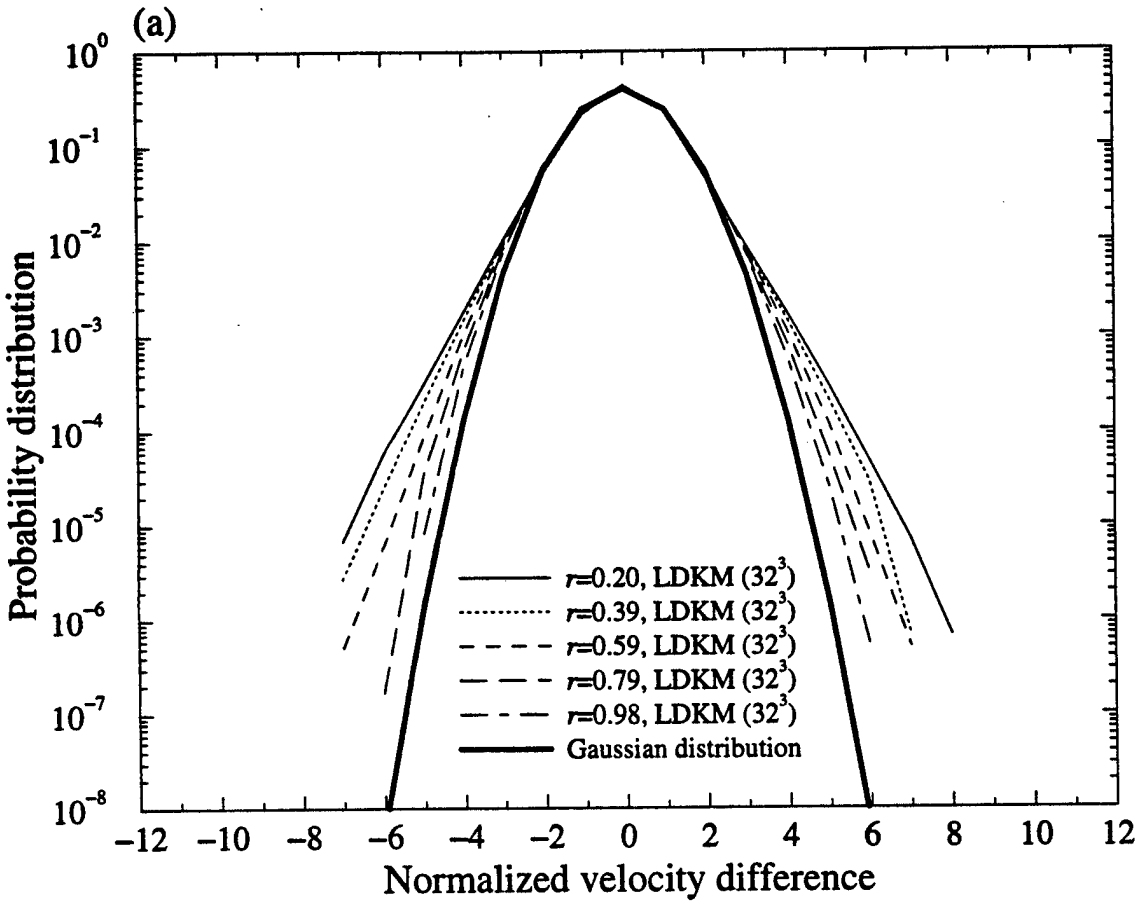

(a)
Probability distribution
Normalized velocity difference
r=0.20, LDKM (32^3)
r=0.39, LDKM (32^3)
r=0.59, LDKM (32^3)
r=0.79, LDKM (32^3)
r=0.98, LDKM (32^3)
Gaussian distribution

Figure 6(a)

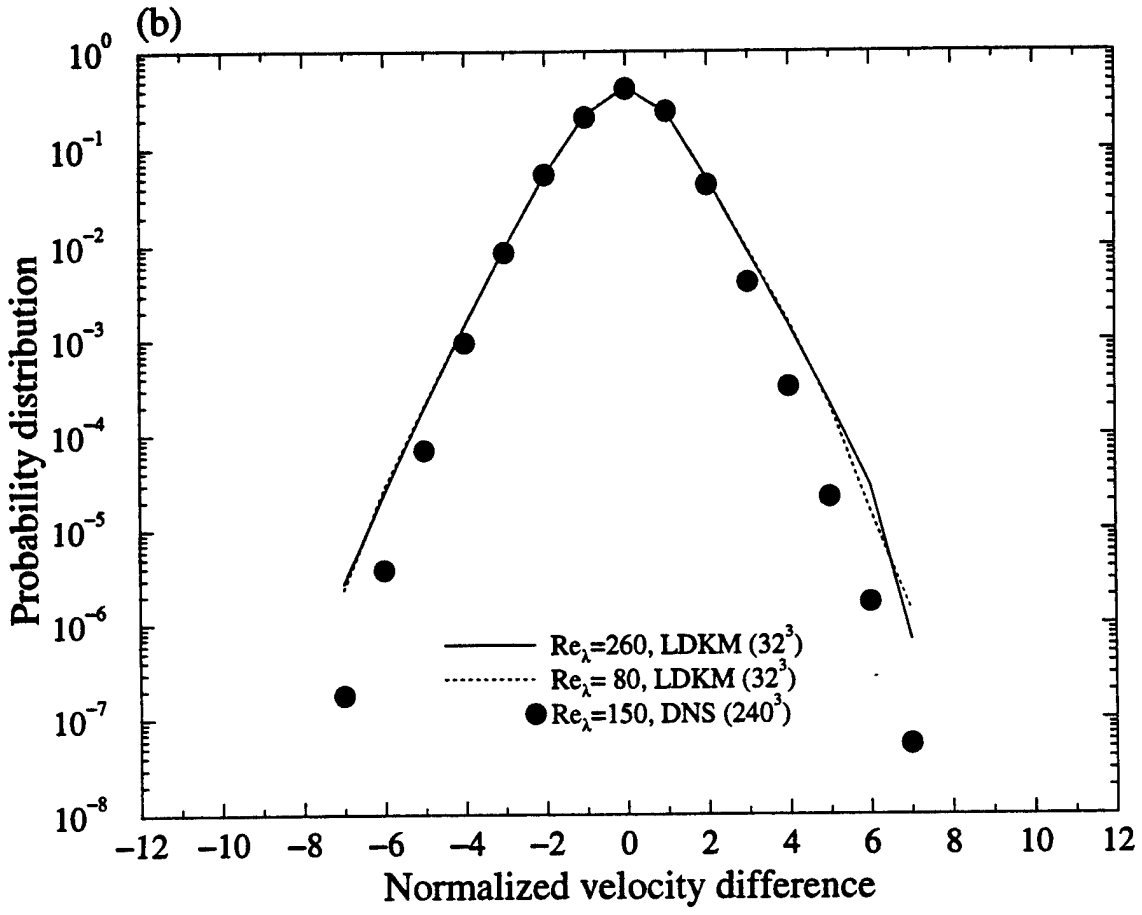

(b)
Probability distribution
Normalized velocity difference
Re$_\lambda$=260, LDKM (32^3)
Re$_\lambda$= 80, LDKM (32^3)
Re$_\lambda$=150, DNS (240^3)

Figure 6(b)

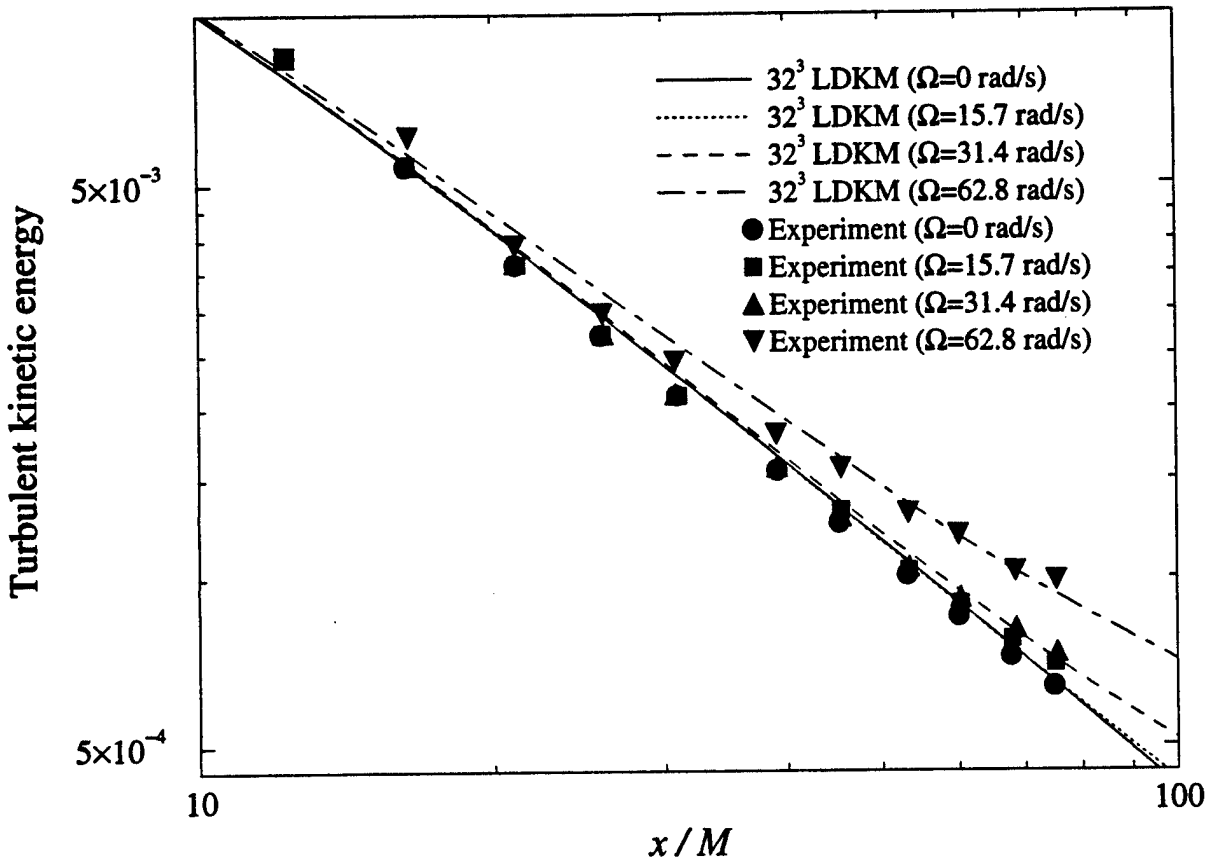

Turbulent kinetic energy
5×10^-3
5×10^-4
10
100
x / M
32^3 LDKM (Ω=0 rad/s)
32^3 LDKM (Ω=15.7 rad/s)
32^3 LDKM (Ω=31.4 rad/s)
32^3 LDKM (Ω=62.8 rad/s)
Experiment (Ω=0 rad/s)
Experiment (Ω=15.7 rad/s)
Experiment (Ω=31.4 rad/s)
Experiment (Ω=62.8 rad/s)

Figure 7

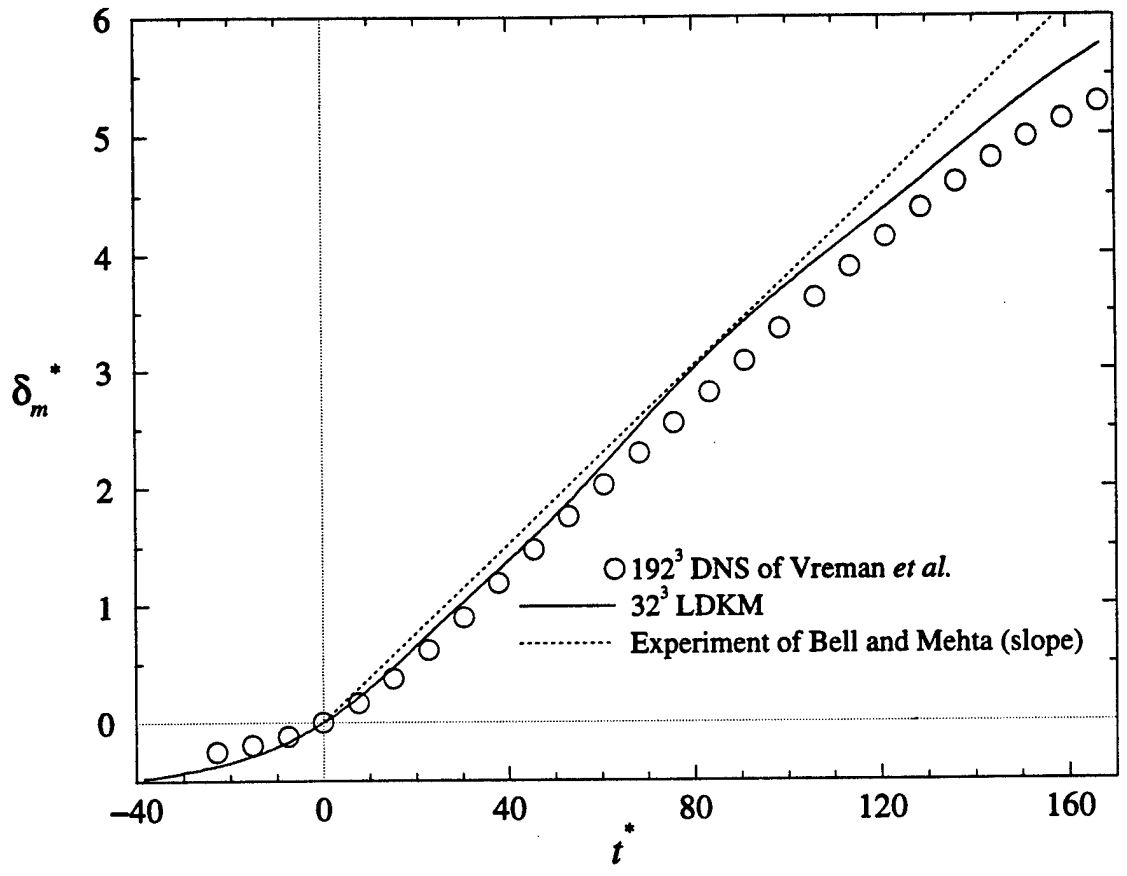

6
5
4
3
2
1
0
δ_m^*
–40
0
40
80
120
160
t^*
192^3 DNS of Vreman *et al.*
32^3 LDKM
Experiment of Bell and Mehta (slope)

Figure 8

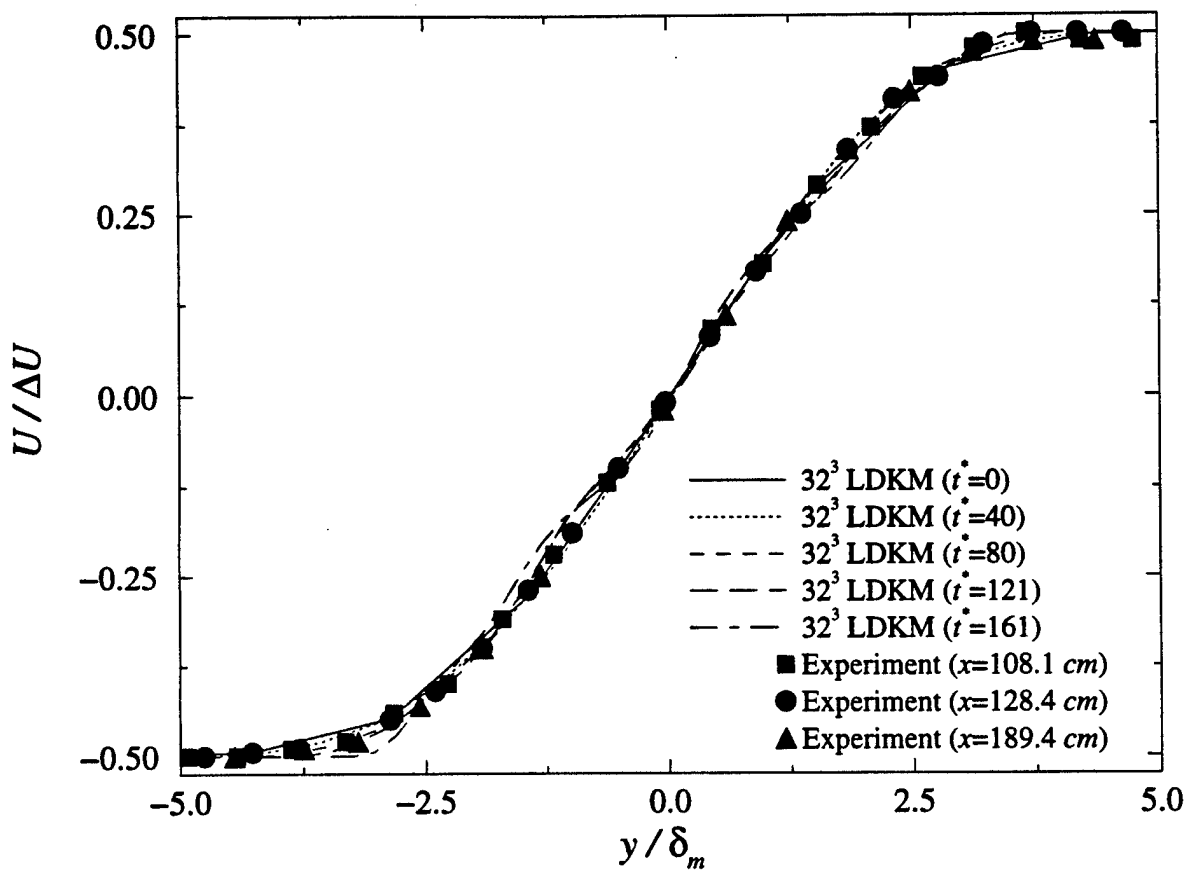

0.50
0.25
0.00
−0.25
−0.50
U / ΔU
−5.0
−2.5
0.0
2.5
5.0
y / δ_m
32³ LDKM (t*=0)
32³ LDKM (t*=40)
32³ LDKM (t*=80)
32³ LDKM (t*=121)
32³ LDKM (t*=161)
Experiment (x=108.1 cm)
Experiment (x=128.4 cm)
Experiment (x=189.4 cm)

Figure 9

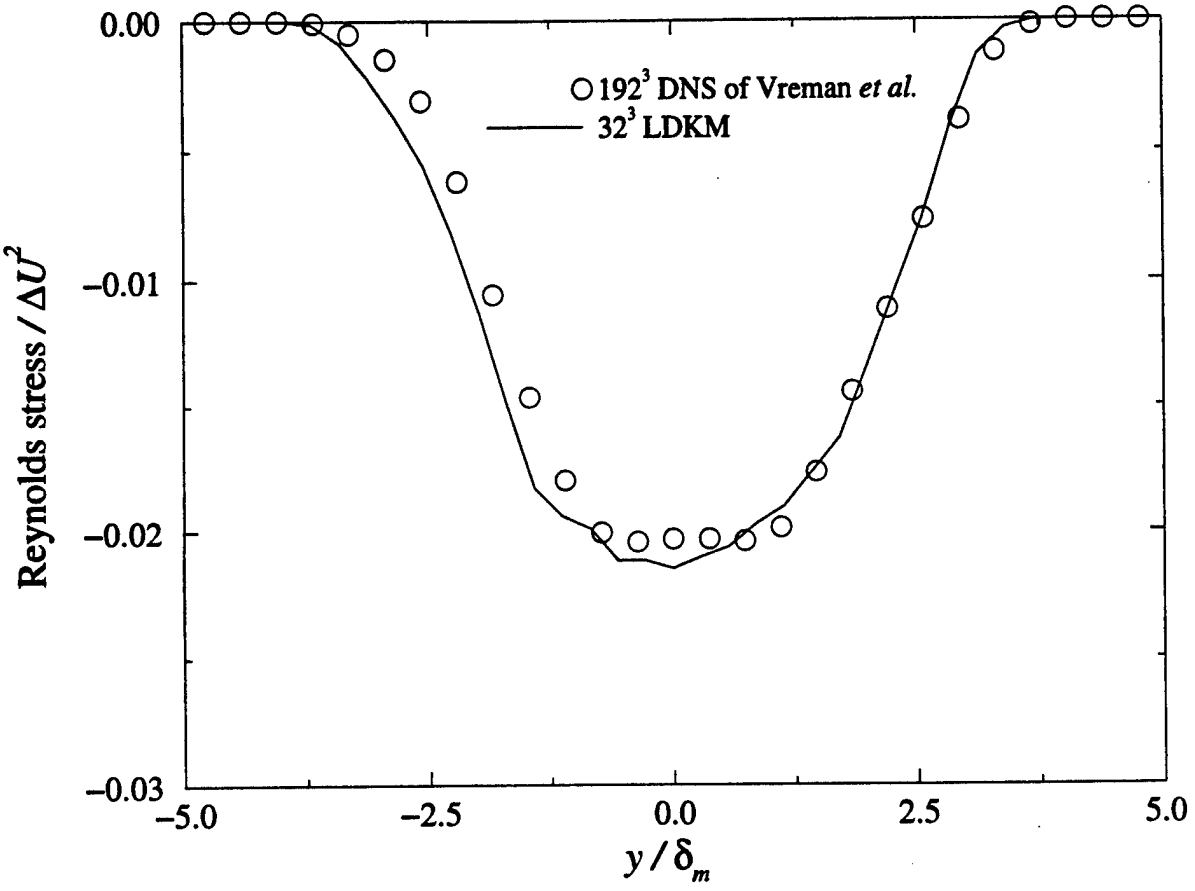

0.00
−0.01
−0.02
−0.03
−5.0
−2.5
0.0
2.5
5.0
Reynolds stress / ΔU^2
y / δ_m
192^3 DNS of Vreman *et al.*
32^3 LDKM

Figure 10

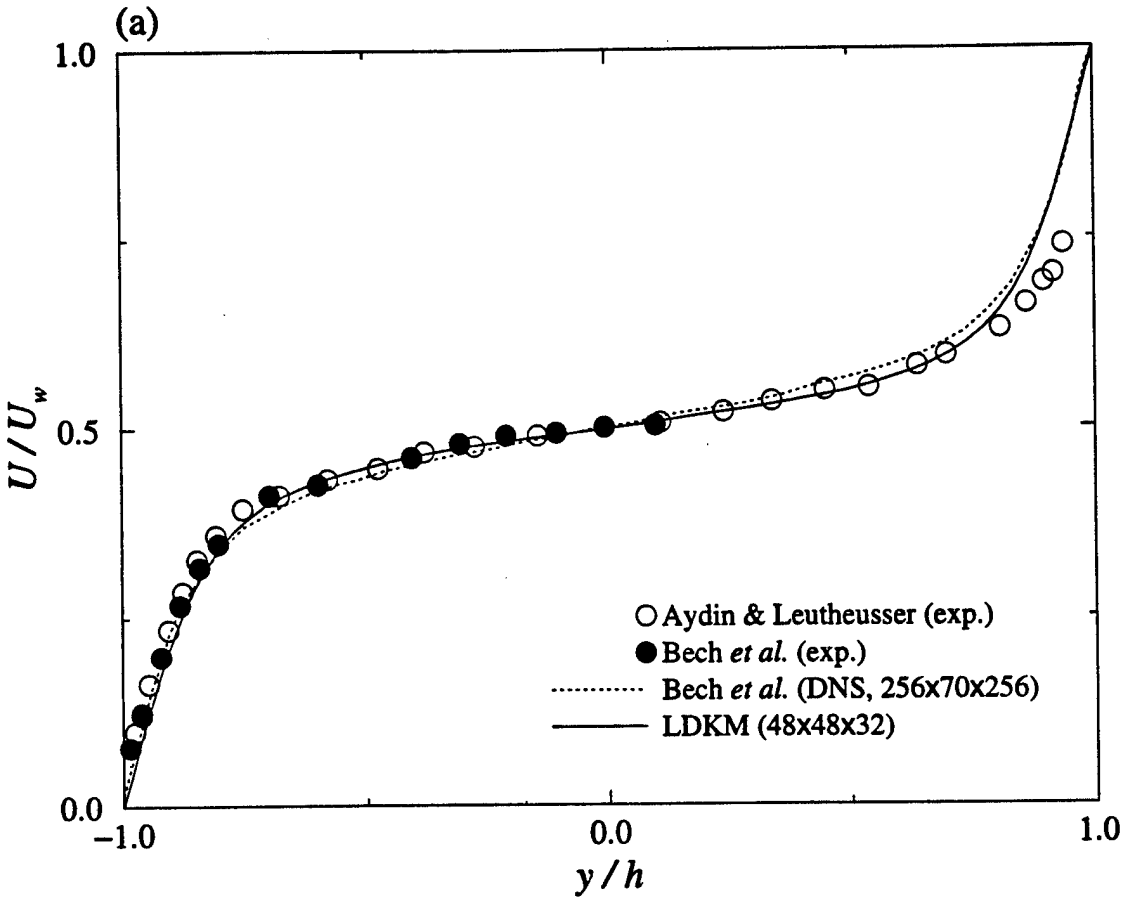

(a)
1.0
0.5
0.0
U/U_w
−1.0
0.0
1.0
y/h
Aydin & Leutheusser (exp.)
Bech *et al.* (exp.)
Bech *et al.* (DNS, 256x70x256)
LDKM (48x48x32)

Figure 11(a)

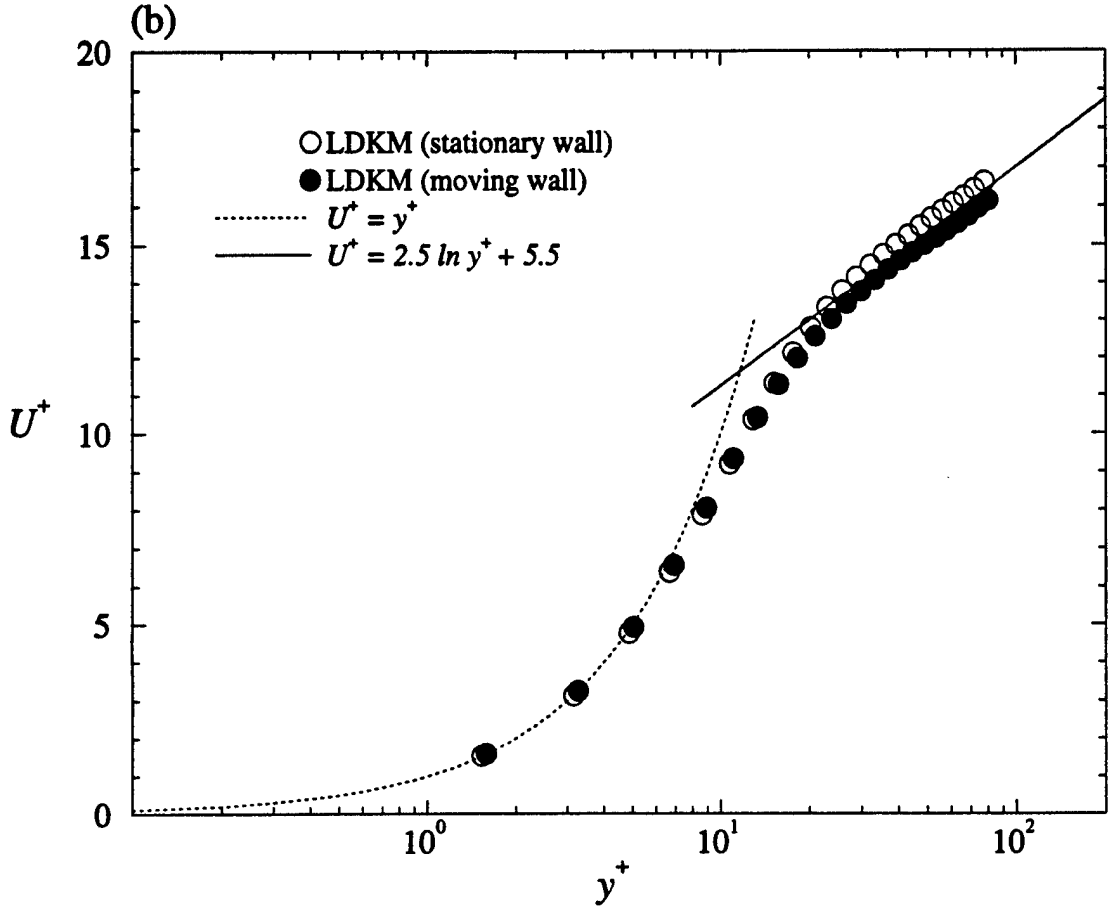

(b)
20
15
10
5
0
U^+
LDKM (stationary wall)
LDKM (moving wall)
$U^+ = y^+$
$U^+ = 2.5 \ln y^+ + 5.5$
10^0
10^1
10^2
y^+

Figure 11(b)

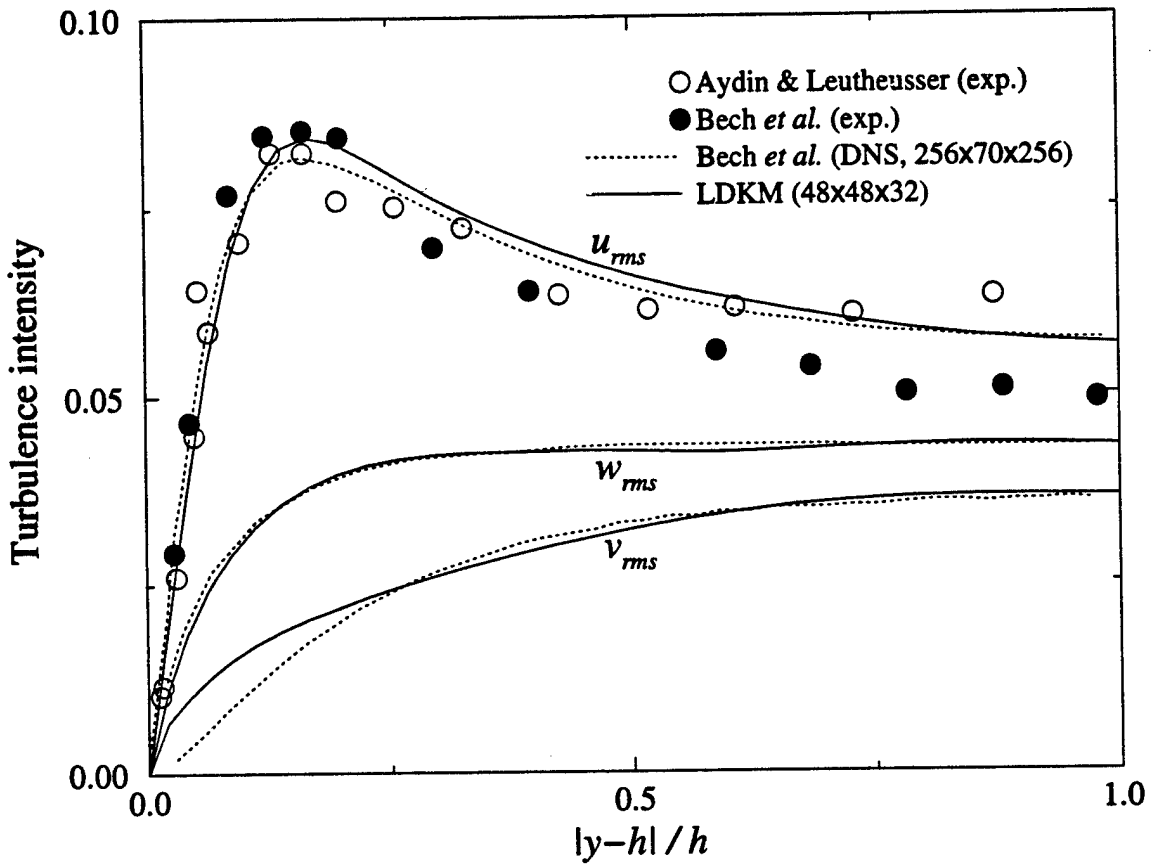

0.10
0.05
0.00
0.0
0.5
1.0
Turbulence intensity
|y−h| / h
Aydin & Leutheusser (exp.)
Bech et al. (exp.)
Bech et al. (DNS, 256x70x256)
LDKM (48x48x32)
u_{rms}
w_{rms}
v_{rms}

Figure 12

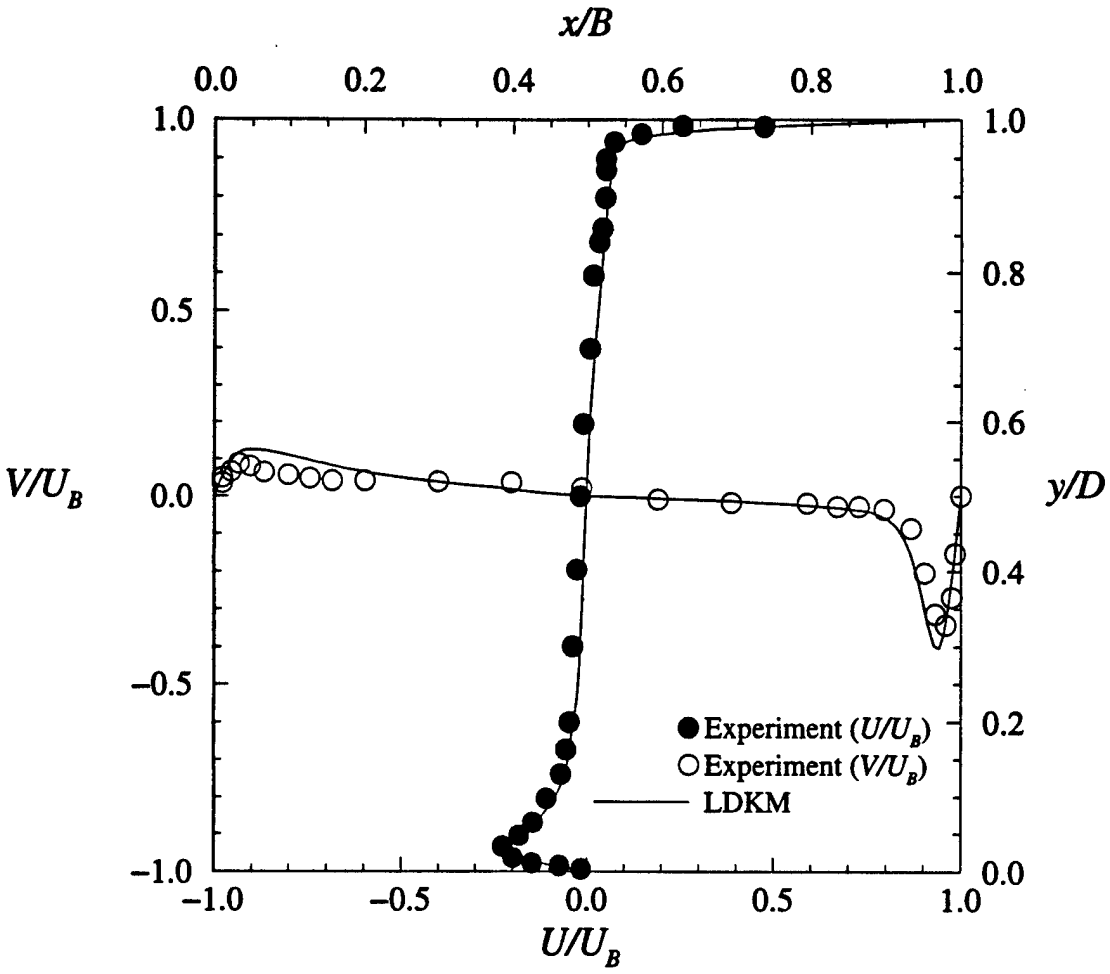

x/B
0.0
0.2
0.4
0.6
0.8
1.0
1.0
0.5
0.0
−0.5
−1.0
V/U_B
y/D
0.8
0.6
0.4
0.2
0.0
−1.0
−0.5
0.0
0.5
1.0
U/U_B
Experiment (U/U_B)
Experiment (V/U_B)
LDKM

Figure 13

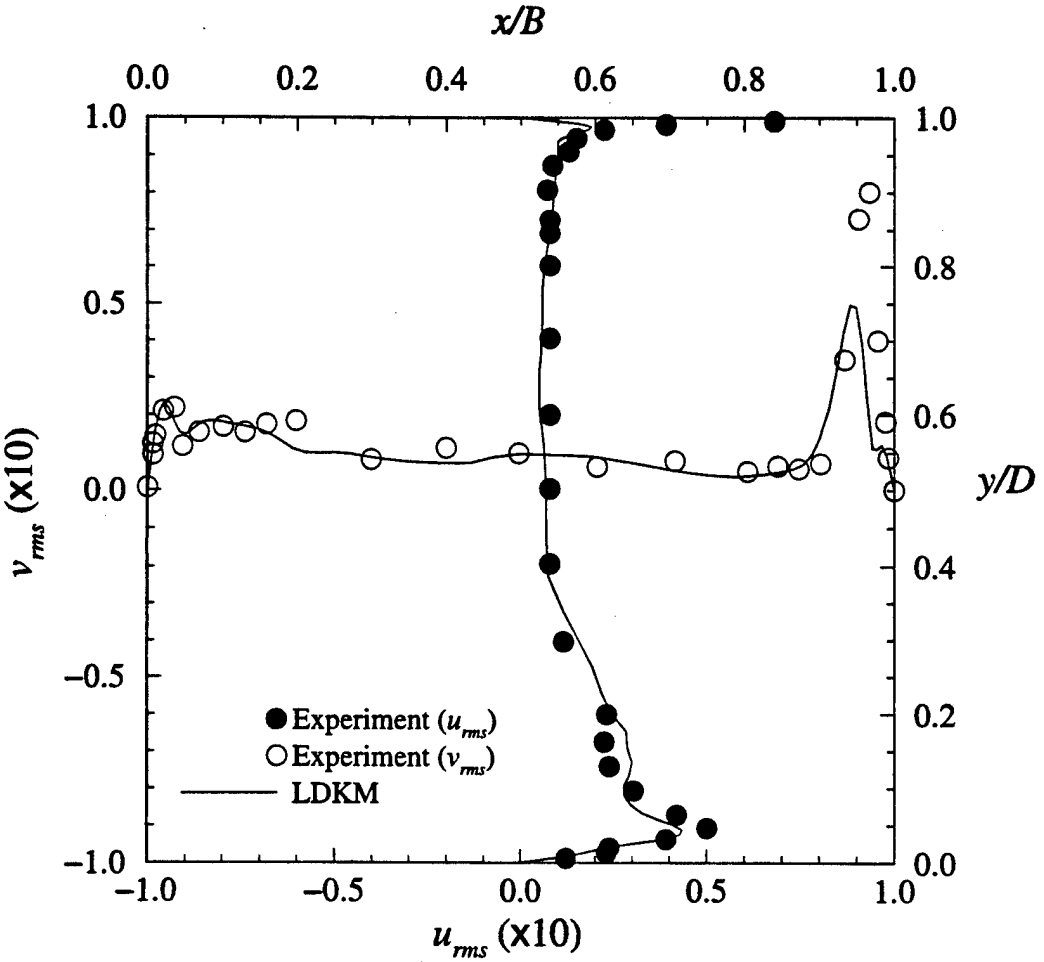

x/B
0.0
0.2
0.4
0.6
0.8
1.0
1.0
0.5
0.0
−0.5
−1.0
v_rms (x10)
y/D
0.8
0.6
0.4
0.2
0.0
Experiment (u_rms)
Experiment (v_rms)
LDKM
−1.0
−0.5
0.0
0.5
1.0
u_rms (x10)

Figure 14

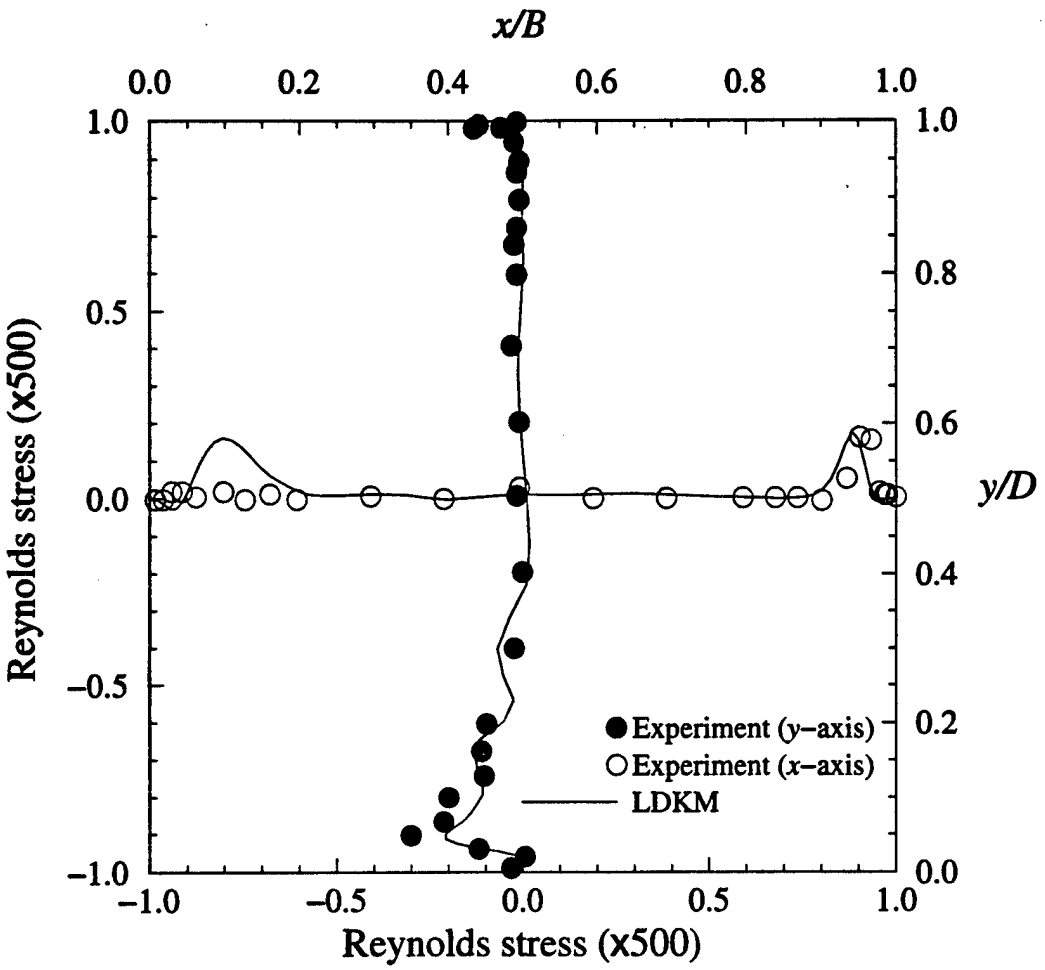

x/B
0.0
0.2
0.4
0.6
0.8
1.0
1.0
0.5
0.0
−0.5
−1.0
Reynolds stress (x500)
y/D
0.8
0.6
0.4
0.2
0.0
Experiment (y−axis)
Experiment (x−axis)
LDKM
−1.0
−0.5
0.0
0.5
1.0
Reynolds stress (x500)

Figure 15



AIAA-98-0786

Unsteady Simulations of Compressible Spatial Mixing Layers

C. Nelson
Sverdrup Technology, Inc.
AEDC Group
Arnold Air Force Base, TN 37389-6001

S. Menon
School of Aerospace Engineering
Georgia Institute of Technology
Atlanta, GA 30332-0150

36th Aerospace Sciences Meeting & Exhibit
January 12–15, 1998 / Reno, NV

For permission to copy or republish, contact the American Institute of Aeronautics and Astronautics
1801 Alexander Bell Drive, Suite 500, Reston, Virginia 20191-4344

AIAA-98-0786
Unsteady Simulations of Compressible Spatial Mixing Layers

C. Nelson*
Sverdrup Technology, Inc.
AEDC Group
Arnold Air Force Base, TN 37389-6001

S. Menon†
School of Aerospace Engineering
Georgia Institute of Technology
Atlanta, GA 30332-0150

1 Abstract

A local dynamic one-equation subgrid model has been used to carry out large-eddy simulations of unsteady spatially developing compressible mixing layers. Simulations of the supersonic mixing layers studied by Samimy and Elliott[1,2] have been carried out. Despite the very high Reynolds numbers of these flows and the comparatively coarse grids employed, good qualitative and reasonable quantitative results are obtained.

2 Introduction

It has long been noted that turbulent compressible mixing layers grow slower than equivalent incompressible layers. Birch and Eggars[3] believed that it was due to the mean density gradient. Later work[4–6] showed that the primary cause of the reduced growth rate was linked to compressibility.

Several ideas have been presented to account for this decrease in growth rate. Papamoschou[7] suggested that this was due to eddy shocklets: regions of strong compression caused by the turbulent motion which would increase energy dissipation. This increased energy dissipation has been associated with the dilatation dissipation term in the Reynolds averaged turbulent kinetic energy equation. Zeman[8] and Sarkar *et al.*[9] developed models for the dilatation dissipation term which were added to standard k-ε models. These models were able to better predict the reduction in mixing layer growth rate associated with increased compressibility.

A similar term exists in the LES subgrid kinetic energy equation. For LES, however, very little work on dilatation dissipation has been conducted. Spyropoulos and Blaisdell[10] claimed no such modifications were needed for their dynamic algebraic model, since it apparently adjusted automatically to account for compressibility effects. Their work, however, did not investigate strongly compressible flows. Therefore, the limitations of the dynamic model, if any, were not thoroughly tested.

The importance of eddy shocklets was called into question by Sandham and Reynolds[11] who were unable to find any such structures in 3-D DNS of temporal mixing layers. They suggested, rather, that linear stability theory accounted for most of the observed decrease in mixing layer growth rates.[12] Linear theory predicted the increase in three dimensionality of mixing layers as convective Mach number increases. This was found to be due to oblique instability modes becoming dominant at high compressibility, whereas purely two dimensional modes dominate at lower convective Mach numbers. This is in keeping with experimental observations.[13–16]

Sarkar *et al.*[9] also attributed some of the kinetic energy growth rate reduction to the action of pressure-dilatation, and derived a model for this term for Reynolds averaged Navier-Stokes (RANS) solvers. A related term occurs in the subgrid kinetic energy equation. The work by Koutmos *et al.*[17] used a model proposed by Schumann to address this issue in an LES context. For compressible decaying isotropic turbulence, however, pressure-dilatation's contribution to dissipation was found to be insignificant.[18]

A third mechanism proposed for the observed reduction in kinetic energy growth rates is the reduction in Reynolds shear stress anisotropy. This reduction results in decreased turbulent energy production.[19] Sarkar has found in direct simulations of homogeneous shear flow that the reduction in kinetic energy growth is primarily due to this reduced level of energy production, not any explicitly dilatational effects.[20,21] While pressure-dilatation and dilatation-dissipation were found to increase with compressibility, they did not add appreciably to the overall dissipation.

The inability of conventional RANS based codes to capture the decrease in growth rate led to the development of the models for dilatation dissipation. The inherent weaknesses in the RANS approach, however, make general development and application difficult. In this paper, the LES technique is applied to study spatially evolving

*Senior Engineer, Member AIAA
†Professor, Senior Member AIAA

Copyright © 1998 by C. Nelson and S. Menon- Published by the American Institute of Aeronautics and Astronautics, Inc. with permission.

mixing layers. In LES, all scales larger than the grid scale are captured using a time- and space-accurate numerical scheme, and only the small scales are modeled. The present approach uses a localized dynamic model for the subgrid kinetic energy. It is the purpose of this paper to demonstrate that the LES technique can be used to capture the effects of compressibility without any model adjustments.

3 Governing Equations

The equations of motion for LES are obtained by filtering the Navier-Stokes equations. For compressible flow, the standard technique is to use a Favre (or density weighted) filter. This avoids some complexity, but gives rise to difficulties when comparing to experimental data, which is not Favre filtered. Thus, here we explicitly include the compressibility effects into the model by using standard (not mass weighted) spatial filtering. Written this way, the governing equations may be written as:

$$\frac{\partial \bar{\rho}}{\partial t} = -\frac{\partial \bar{\rho}\bar{u}_i}{\partial x_i} - \frac{\partial}{\partial x_i}\left(\overline{\rho u_i} - \bar{\rho}\bar{u}_i\right) \tag{1}$$

$$\begin{aligned}\frac{\partial \bar{\rho}\bar{u}_i}{\partial t} = &-\frac{\partial}{\partial x_j}\left(\overline{\rho u_i}\overline{u}_j\right) - \frac{\partial \bar{p}}{\partial x_i} + \frac{\partial \bar{t}_{ij}}{\partial x_j} \\ &- \frac{\partial}{\partial x_j}\left(\overline{\rho u_i u_j} - \bar{\rho}\bar{u}_i\bar{u}_j\right) + \frac{\partial}{\partial x_j}\left(\overline{\tau}_{ij} - \bar{t}_{ij}\right) \\ &- \frac{\partial}{\partial t}\left(\overline{\rho u_i} - \bar{\rho}\bar{u}_i\right)\end{aligned} \tag{2}$$

$$\begin{aligned}\frac{\partial \bar{\rho}\bar{E}}{\partial t} = &-\frac{\partial}{\partial x_i}\left(\bar{\rho}\bar{E} + \bar{p}\right)\bar{u}_i - \frac{\partial}{\partial x_i}\left(\overline{\rho E u_i} - \bar{\rho}\bar{E}\bar{u}_i\right) \\ &- \frac{\partial}{\partial x_i}\left(\overline{pu_i} - \bar{p}\bar{u}_i\right) \\ &+ \frac{\partial}{\partial x_i}\left(\bar{u}_j\bar{t}_{ij}\right) + \frac{\partial}{\partial x_i}\left(\overline{u_j\tau_{ij}} - \bar{u}_j\bar{t}_{ij}\right) \\ &+ \frac{\partial}{\partial x_i}\left(\bar{\kappa}\frac{\partial \bar{T}}{\partial x_i}\right) + \frac{\partial}{\partial x_i}\left(\overline{\kappa\frac{\partial T}{\partial x_i}} - \bar{\kappa}\frac{\partial \bar{T}}{\partial x_i}\right) \\ &- \frac{R}{\gamma - 1}\frac{\partial}{\partial t}\left(\overline{\rho T} - \bar{\rho}\bar{T}\right) - \frac{1}{2}\frac{\partial}{\partial t}\left(\overline{\rho u_i u_i} - \bar{\rho}\bar{u}_i\bar{u}_i\right) \\ &+ \frac{\partial}{\partial t}\left(\bar{\rho}k^{sgs}\right)\end{aligned} \tag{3}$$

The resolved viscous stress tensor in the above equation takes the following form:

$$\bar{t}_{ij} = 2\bar{\mu}\left[\frac{1}{2}\left(\frac{\partial \bar{u}_i}{\partial x_j} + \frac{\partial \bar{u}_j}{\partial x_i}\right) - \frac{1}{3}\frac{\partial \bar{u}_k}{\partial x_k}\delta_{ij}\right] \tag{4}$$

Viscosity is assumed to follow Sutherland's Law (using the filtered temperature as the argument). The other viscous term in the above equation, $\overline{\tau}_{ij}$, is the filter of the exact viscous stress tensor. The total energy is defined here as:

$$\bar{E} = \bar{e} + \frac{1}{2}\bar{u}_i\bar{u}_i + k^{sgs} \tag{5}$$

The subgrid kinetic energy (k^{sgs}) is defined as:

$$k^{sgs} = \frac{1}{2}\left(\overline{u_i u_i} - \bar{u}_i\bar{u}_i\right) \tag{6}$$

The subgrid kinetic energy is allowed to evolve according to its own transport equation, as described in the following section The LES thermal conductivity ($\bar{\kappa}$) and internal energy ($\bar{e}$) are, like viscosity, assumed to be functions of the filtered temperature. Finally, the LES equation of state is written as:

$$\overline{p} = \overline{\rho}R\bar{T} + R\left(\overline{\rho T} - \bar{\rho}\bar{T}\right) \tag{7}$$

4 Closure of Subgrid Terms

Many of the subgrid terms in the above equations have been found to be generally small (in compressible homogeneous isotropic flow[22]), and therefore they have been neglected. These include the viscous subgrid terms ($(\overline{\tau}_{ij} - \bar{t}_{ij})$ and $(\overline{u_j\tau_{ij}} - \bar{u}_j\bar{t}_{ij})$), the state equation subgrid term ($R\left(\overline{\rho T} - \bar{\rho}\bar{T}\right)$), and the subgrid heat convection term $\left(\overline{\kappa\frac{\partial T}{\partial x_i}} - \bar{\kappa}\frac{\partial \bar{T}}{\partial x_i}\right)$.

The density-velocity correlation term which appears in the LES continuity equation (1) is a purely compressible term which has no direct analog in constant density flows. Some properties, however, can be deduced *a priori*. First, this subgrid term may be rewritten as the difference between the Favre filtered and "straight filtered" velocity:

$$c_i^{sgs} = \overline{\rho u_i} - \bar{\rho}\bar{u}_i = \bar{\rho}\left(\tilde{u} - \bar{u}\right) \tag{8}$$

Obviously, since this term appears only in the compressible equations, any model for it should vanish for a constant density flow. Also, this term is expected to be significant only in regions of strong compression, such as a shock. This is in keeping with the findings of Chen *et al.*,[23] who investigated the differences between Favre filtering and conventional filtering in the context of RANS simulations of combustion. They found that the differences between $\tilde{u}$ and $\bar{u}$ were virtually undetectable in regions with mild density gradients. When density is varying more abruptly, it can be argued, in a fashion similar to that used for the mixing length model of turbulent heat flux,[24] that the contribution of this term should be proportional to the mean density gradient.

In light of this, a gradient diffusion model is adopted for this term:

$$c_i^{sgs} = \overline{\rho u_i} - \bar{\rho}\bar{u}_i \approx -\nu_c\frac{\partial \bar{\rho}}{\partial x_i} \tag{9}$$

The scaling factor in the above equation (ν_c- designated the "compressibility viscosity") is formulated in the following manner. Since this term is expected to be significant only near strong density (pressure) gradients, a switch is used to prevent excessive dissipation from being added to regions where the mean flow is smooth. It is

defined in a discrete sense in a manner similar to that developed by MacCormack and Baldwin.[25] On the i-faces, for example, it may be written:

$$S_{p_{i+\frac{1}{2},j,k}} = \max\left(S_{p_{i,j,k}}, S_{p_{i+1,j,k}}\right) \tag{10a}$$

$$\text{where } S_{p_{i,j,k}} = \frac{|p_{i+1,j,k} - 2p_{i,j,k} + p_{i-1,j,k}|}{p_{i+1,j,k} + 2p_{i,j,k} + p_{i-1,j,k}} \tag{10b}$$

A characteristic length and velocity can be used to obtain the correct dimensions for this term. The grid spacing, Δ, is chosen as the length scale. The characteristic velocity is defined as the magnitude of the velocity normal to the cell face. Thus the expression for the "compressibility viscosity" may be written as:

$$\nu_c = a_c S_p \left|\bar{u}_k n_k\right| \Delta \tag{11}$$

where a_c is a scaling parameter chosen as:

$$a_c = \begin{cases} a_0 \exp\left[\frac{-1}{K_1\left(R_{e_\Delta} - R_{e_{\min}}\right)}\right] & R_{e_\Delta} > R_{e_{\min}} \\ 0 & R_{e_\Delta} \le R_{e_{\min}} \end{cases} \tag{12}$$

$$R_{e_\Delta} = \frac{\left|\bar{u}_k n_k\right| \Delta}{\nu + \nu_t}$$

Numerical experiments on the one-dimensional nonlinear Burger's equation have been used to obtain the above form for the scaling factor. The Burger's equation was used as a model problem to test the behavior of the numerical scheme (with an added dissipation term similar to the proposed model) in the presence of sharp gradients, such as those found at shocks. The exact solution (a hyperbolic tangent) is compared to the numerically obtained solution to find an optimal value for the scaling factor for different cell "Reynolds" numbers. A curve fit is applied to the resulting data to obtain an analytic expression for the scaling factor (at a cell face): The value used for K_1 is 0.257, and the minimum cell Reynolds number is 1.67. A value of 0.60 was used for the scaling coefficient, a_c, in this work. The denominator of the above expression for cell Reynolds number includes an eddy viscosity (ν_t), which is defined as:

$$\nu_t = c_\nu \sqrt{k^{sgs}} \Delta \tag{13}$$

The eddy viscosity is used in modeling the "incompressible" portions of the subgrid terms for the momentum, energy, and subgrid kinetic energy equations. In the momentum equation, the "incompressible" portion of the subgrid stress tensor is modeled as:

$$\begin{aligned} \tau_{ij}^{sgs^{(i)}} &= \bar{\rho}\left(\overline{u_i u_j} - \bar{u}_i \bar{u}_j\right) \\ &\approx -2\bar{\rho}\nu_t \left(\bar{S}_{ij} - \frac{1}{3}\bar{S}_{kk}\delta_{ij}\right) + \frac{2}{3}\bar{\rho}k^{sgs}\delta_{ij} \end{aligned} \tag{14}$$

In the energy equation, the pressure-velocity correlation and convective subgrid terms are combined by rewriting them in terms of total enthalpy and modeled as:

$$\bar{\rho}\left(\overline{Hu_i} - \bar{H}\bar{u}_i\right) \approx -c_e \bar{\rho}\sqrt{k^{sgs}}\Delta \frac{\partial \bar{H}}{\partial x_i} \tag{15}$$

Finally, in the subgrid kinetic energy equation, the transport of k^{sgs} by subgrid processes is modeled as:

$$\text{Subgrid Transport} \approx \frac{\partial}{\partial x_i}\left(\overline{\rho}\nu_t \frac{\partial k^{sgs}}{\partial x_i}\right) \tag{16}$$

The "compressibility" viscosity ν_c is used to model additional effects of compressibility in the momentum, energy, and subgrid kinetic energy equations (using simple gradient diffusion models). Incorporating the above models and assumptions into the governing equations results in the following model LES equations:

$$\frac{\partial \bar{\rho}}{\partial t} = -\frac{\partial \overline{\rho}\bar{u}_i}{\partial x_i} + \frac{\partial}{\partial x_i}\left(\nu_c \frac{\partial \overline{\rho}}{\partial x_i}\right) \tag{17}$$

$$\begin{aligned} \frac{\partial \overline{\rho}\bar{u}_i}{\partial t} &= -\frac{\partial}{\partial x_j}\left(\bar{\rho}\bar{u}_i\bar{u}_j\right) - \frac{\partial \bar{p}}{\partial x_i} + \frac{\partial \bar{t}_{ij}}{\partial x_j} - \frac{\partial \tau_{ij}^{sgs^{(i)}}}{\partial x_j} \\ &\quad - \frac{\partial M_{ij}^{sgs^{(c)}}}{\partial x_j} \end{aligned} \tag{18}$$

$$\begin{aligned} \frac{\partial \overline{\rho}\bar{E}}{\partial t} &= -\frac{\partial}{\partial x_i}\left(\bar{\rho}\bar{E} + \bar{p}\right)\bar{u}_i + \frac{\partial}{\partial x_i}\left(c_e\bar{\rho}\sqrt{k^{sgs}}\Delta\frac{\partial \bar{H}}{\partial x_i}\right) \\ &\quad + \frac{\partial}{\partial x_i}\left(\bar{u}_j \bar{t}_{ij}\right) + \frac{\partial}{\partial x_i}\left(\left[\bar{\kappa} + \frac{\gamma c_v \bar{\rho}\nu_c}{\Pr}\right]\frac{\partial \bar{T}}{\partial x_i}\right) \end{aligned} \tag{19}$$

$$\begin{aligned} \frac{\partial \overline{\rho}k^{sgs}}{\partial t} &= -\frac{\partial}{\partial x_i}\left(\bar{\rho}k^{sgs}\bar{u}_i\right) + \frac{\partial}{\partial x_i}\left(\overline{\rho}\left(\nu_t + \nu_c\right)\frac{\partial k^{sgs}}{\partial x_i}\right) \\ &\quad - \tau_{ij}^{sgs^{(i)}}\frac{\partial \bar{u}_j}{\partial x_i} - \overline{\rho}c_\varepsilon \frac{\left(k^{sgs}\right)^{\frac{3}{2}}}{\Delta} \end{aligned} \tag{20}$$

$$\bar{p} = \bar{\rho}R\bar{T} \tag{21}$$

where

$$M_{ij}^{sgs^{(c)}} = -2\bar{\rho}\nu_c\left(\bar{S}_{ij} - \frac{1}{3}\bar{S}_{kk}\delta_{ij}\right) \tag{22}$$

The above equations contain three model coefficients (c_ν, c_ε, and c_e). These coefficients are computed dynamically for this study. In order to do this, it is assumed that the subgrid scales behave very much like the smallest resolved scales. This proposition has been experimentally shown to be reasonable for the subgrid stress tensor by Liu, *et al.*[26] for the case of free jets. A "test" filter is used to isolate the smallest resolved scales. This filter (denoted by a circumflex- *e.g.* $\widehat{\phi}$) must have a characteristic length, $\widehat{\Delta}$, larger than the grid resolution. Usually $\widehat{\Delta}$ is taken to be twice the size of the local grid spacing (Δ), but this is somewhat arbitrary. Coefficients may then be computed by comparing quantities that are resolved in the LES flow field but not by a corresponding "test" filtered field.

Because only positive filters are used in this work, the incompressible portion of the subgrid stress tensor

($\tau_{ij}^{sgs^{(i)}}$) must be positive semidefinite. Therefore, the model coefficient, c_ν, is constrained such that the resulting modelled tensor has this property. The conditions which enforce this are known as the "realizability" conditions.[27] These may be stated as follows:

$$\tau_{\alpha\alpha}^{sgs^{(i)}} \geq 0 \text{ for } \alpha \in \{1,2,3\} \tag{23a}$$

$$\left|\tau_{\alpha\beta}^{sgs^{(i)}}\right|^2 \leq \tau_{\alpha\alpha}^{sgs^{(i)}} \tau_{\beta\beta}^{sgs^{(i)}} \text{ for } \alpha,\beta \in \{1,2,3\} \tag{23b}$$

$$\det\left(\tau_{ij}^{sgs^{(i)}}\right) \geq 0 \tag{23c}$$

Note that, unlike conventional tensor notation, repeated indices in the above expressions do not indicate summation. In addition, c_ν is also constrained such that the resulting effective viscosity $(\nu + \nu_t)$ is positive. The other two constants (c_ϵ and c_e) are also constrained to be positive.

The subgrid stress tensor model coefficient is found using the following equation:

$$c_\nu = \frac{-L_{ij} D_{ij}}{2 D_{ij} D_{ij}} \tag{24}$$

where:

$$L_{ij} = \widehat{\overline{\rho}}\left(\widehat{\overline{u}_i \overline{u}_j} - \widehat{\overline{u}}_i \widehat{\overline{u}}_j\right) - \frac{1}{3}\widehat{\overline{\rho}}\left(\widehat{\overline{u}_k \overline{u}_k} - \widehat{\overline{u}}_k \widehat{\overline{u}}_k\right)\delta_{ij} \tag{25}$$

$$D_{ij} = \widehat{\Delta}\widehat{\overline{\rho}}\left(\frac{\widehat{\overline{u}_k \overline{u}_k}}{2} - \frac{\widehat{\overline{u}}_k \widehat{\overline{u}}_k}{2}\right)^{\frac{1}{2}}\left(\widehat{\overline{S}}_{ij} - \frac{\widehat{\overline{S}}_{kk}}{3}\delta_{ij}\right) \tag{26}$$

$$\widehat{\overline{S}}_{ij} = \frac{1}{2}\left[\frac{\partial \widehat{\overline{u}}_i}{\partial x_j} + \frac{\partial \widehat{\overline{u}}_j}{\partial x_i}\right] \tag{27}$$

The dissipation model coefficient is computed as:

$$c_\epsilon = \frac{\widehat{\Delta}\left(\widehat{\overline{t}_{ij}\frac{\partial \overline{u}_i}{\partial x_i}} - \widehat{T}_{ij}\frac{\partial \widehat{\overline{u}}_i}{\partial x_i}\right)}{\widehat{\overline{\rho}}\left(\frac{\widehat{\overline{u}_k \overline{u}_k}}{2} - \frac{\widehat{\overline{u}}_k \widehat{\overline{u}}_k}{2}\right)^{\frac{3}{2}}} \tag{28}$$

where the viscous stresses resolved on the test filtered field are defined as:

$$\widehat{T}_{ij} = \widehat{\overline{\mu}}\left(\frac{\partial \widehat{\overline{u}}_i}{\partial x_j} + \frac{\partial \widehat{\overline{u}}_j}{\partial x_i} - \frac{2}{3}\frac{\partial \widehat{\overline{u}}_k}{\partial x_k}\delta_{ij}\right) \tag{29}$$

The energy equation model coefficient is computed as follows:

$$c_e = \frac{n_i d_i}{d_i d_i} \tag{30}$$

$$\text{where } n_i = \widehat{\overline{\rho}}\left(\widehat{\overline{H}\overline{u}_i} - \widehat{\overline{H}}\widehat{\overline{u}}_i\right) \tag{31}$$

$$d_i = \widehat{\overline{\rho}}\left(\frac{\widehat{\overline{u}_k \overline{u}_k}}{2} - \frac{\widehat{\overline{u}}_k \widehat{\overline{u}}_k}{2}\right)^{\frac{1}{2}} \widehat{\Delta}\frac{\partial \widehat{\overline{H}}}{\partial x_i} \tag{32}$$

The above model differs from the original compressible extension[28] of Germano's dynamic model[29] in that, rather than being completely algebraic, the current work uses the subgrid kinetic energy, which develops with the rest of the flow field, as the basis for deriving the velocity scale used to compute the eddy viscosity. The subgrid kinetic energy acts as a limiter on the eddy viscosity, eliminating much of the instability which, in previous dynamic models, necessitated *ad hoc* averaging in one or more homogeneous directions. Any remaining instability is controlled through the enforcement of the conditions (*e.g.* realizability) discussed above.

5 Numerical Algorithm

The choice of numerical algorithm is extremely important when attempting to perform time-accurate simulations of turbulent flows. Schemes which give excellent results for other applications, are often unacceptable due to excessive numerical dissipation. An example of this is shown in figure 1. In this plot, three different schemes are employed to simulate the same homogeneous isotropic turbulent flow on a coarse grid, but without any subgrid model. The three schemes are the Gottleib-Turkel[30] extension of the MacCormack scheme (GT 2-4), a fifth order upwind-biased, Advection Upstream Splitting Method (AUSM) scheme,[31] and a new scheme (New 2-4) which, like GT 2-4, is a higher order extension to MacCormack's scheme. The experimental results are from Comte-Bellot and Corrsin's grid turbulence tests.[32] Without a model, the 2-4 schemes show significantly less energy decay than the experiment predicted, but the AUSM scheme, because of its much higher level of numerical dissipation, obtains results which mimic the experiment.

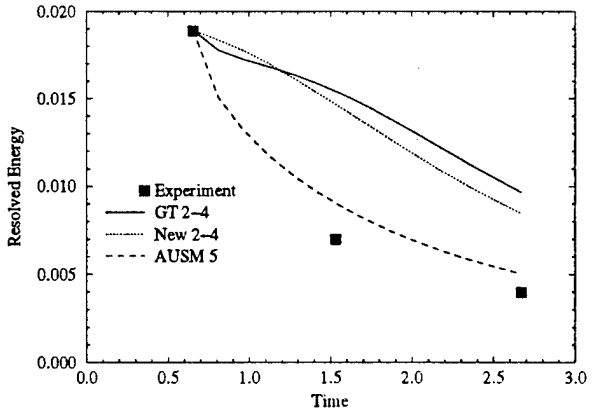


Figure 1: Comparison of predicted kinetic energy decay for various numerical schemes

If one could rely on the numerical scheme's dissipation to damp the resolved energy at the correct rate, then subgrid models would be unnecessary. Unfortunately, there

are no guarantees that this will take place. In this case, for example, while the resolved energy is being dissipated as the solution progresses, AUSM's results do not match the experiment. Thus a subgrid model is still necessary. If the cell Reynolds number can be kept low enough, the effects of numerical dissipation will remain sufficiently small that the subgrid model can still function. The Reynolds number for this case, for instance, while high enough to make DNS difficult, is still comparatively low, and the numerical dissipation has not exceeded the actual dissipation observed in the experiment. For a truly high Reynolds number flow, however, it is easy to see that the dissipation in the AUSM scheme would overwhelm the viscous and turbulent forces to the extent that no subgrid model could compensate enough to obtain the correct results.

The numerical scheme used for this work is a MacCormack-type method similar to the Gottlieb-Turkel method.[30] In contrast to that method, the current scheme is truly fourth order in space (on a uniform grid) and (like Gottlieb-Turkel) it is second order in time. The algorithm is implemented in a finite volume sense. On stretched grids, the algorithm uses an interpolant which attempts to preserve some of the properties that the scheme has on uniform grids, but the scheme does not remain strictly fourth order.

6 Model Validation

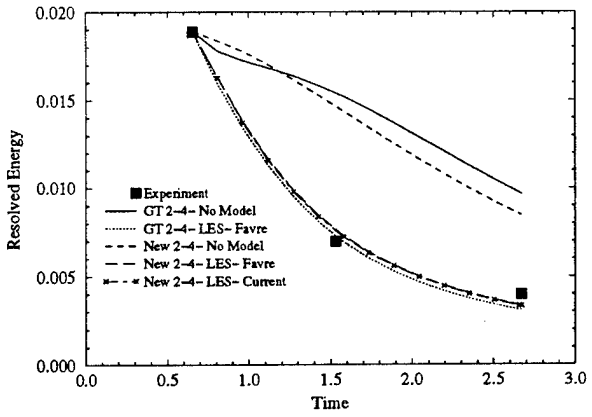


Figure 2: Resolved kinetic energy of isotropic LES compared with grid turbulence experimental data

Several decaying isotropic cases have been run to validate the numerical scheme and the model. The first case to be considered here attempts to duplicate the grid-turbulence experiments of Comte-Bellot and Corrsin.[32] Figure 2 shows the results (on the same 32^3 grid) from two different schemes (Gottlieb-Turkel's 2-4 and the current 2-4) and different modelling strategies (no model, the conventional Favre filtering approach, and the current approach). As can be seen, the two numerical schemes give very similar results. Also, without a model, the energy decay is not properly captured. Finally, in the near-incompressible regime, it is seen that the Favre filtering approach and the current approach to subgrid modelling yield the same results. This is to be expected, since the difference between a Favre filter and a 'straight' filter is solely dependant on density variations.

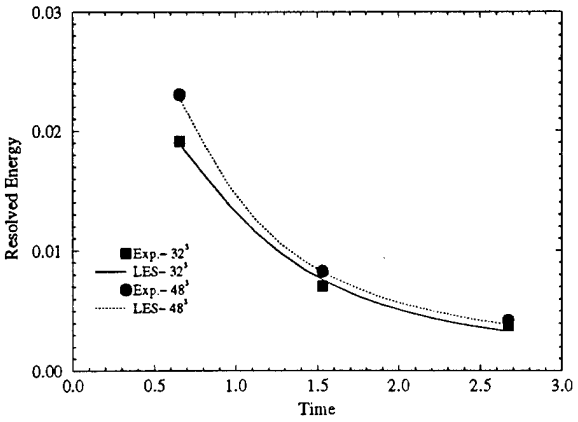


Figure 3: Comparison of the resolved kinetic energy from LES with the filtered experimental data

Two grid resolutions were run (32^3 and 48^3). The decay of the mean resolved kinetic energy is plotted in figure 3. It should be noted that, for a direct simulation, a grid of on the order of 384^3 points would be needed. Even with the fairly coarse 32^3 grid, the model predicts reasonable agreement with the experimental data. Naturally, the 48^3 case is in even better agreement. These results are consistent with those of other researchers[10,33,34] and demonstrate the validity of the model in the near-incompressible regime.

To examine the behavior of the model in a more compressible regime, LES results (on a 16^3 grid) from a decaying isotropic case are compared with filtered DNS results (on a 64^3 grid) for the same case. The initial turbulent Mach number for the DNS was 0.826, and the initial Taylor Reynolds number was 34.9. Again, the code obtains good results, as shown in figures 4 (mean Mach number), 5 (resolved kinetic energy normalized by the experimentally measured initial kinetic energy), and 6 (RMS of density fluctuations normalized by the mean density).

7 The Mixing Layer Simulations

Isotropic turbulence cases, such as those discussed above, can be useful in model development, but the real challenge for LES lies in applying it to problems of a more practical nature. As a step in that direction, spatially evolving mixing layers were studied. The simulated mixing layers were designed to duplicate the experimental

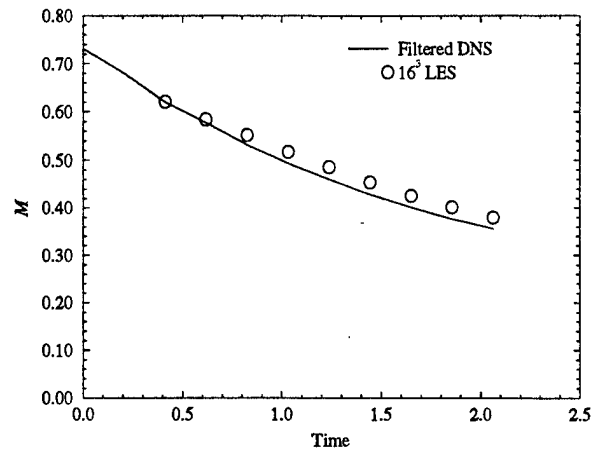


Figure 4: Evolution of the mean Mach number in compressible decaying isotropic turbulence

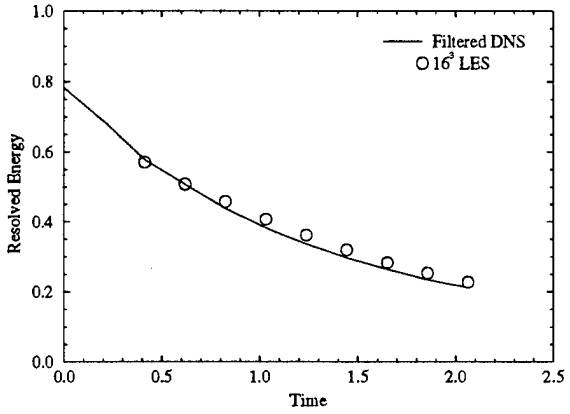


Figure 5: Decay of mean resolved kinetic energy in compressible decaying isotropic turbulence

work of Samimy and Elliott. The incoming flow parameters for these two cases are summarized in Table 1. Here, M_c is the convective Mach number.[5] The Reynolds number for both of these cases is on the order of one million per meter.

7.1 Computational Domain

The domain used for the simulations of both cases (shown schematically in figure 7) starts just upstream of the splitter plate lip, and ends 0.4 meters downstream of the lip. Since experimental data is only available for the first $250\,mm$, this allows a sufficient buffer to prevent corruption of the solution from the outflow boundary. As in the experiments, the splitter plate is $0.5\,mm$ thick at the lip. In the experimental rig, the subsonic side of the splitter plate was machined at approximately a 1° angle. This

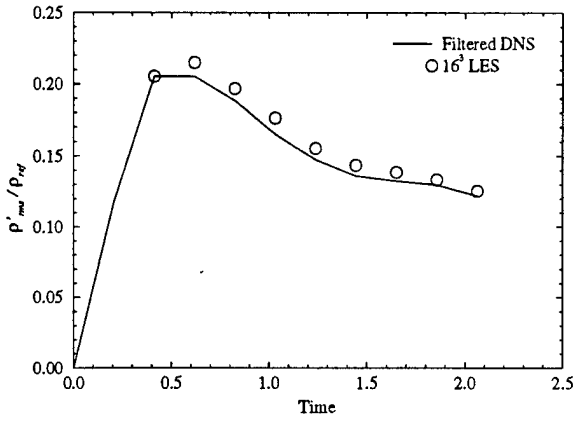


Figure 6: Normalized RMS of density fluctuations in compressible decaying isotropic turbulence

Case	T_0 (K)	P_{0_1} (kPa)	M_1	M_2	M_c
1	291.0	314.0	1.80	0.51	0.53
2	276.0	722.0	3.01	0.45	0.88

Case	U_1 (m/s)	$\frac{U_2}{U_1}$	$\frac{\rho_2}{\rho_1}$	$\delta\ (mm)$
1	479.5	0.355	0.638	8.0
2	597.7	0.246	0.370	9.2

Table 1: Flow parameters for spatial mixing layer cases

is ignored, however, for the LES, and the subsonic side of the splitter plate is assumed to be aligned horizontally. The full height of the experimental rig ($152.4\ mm$) is simulated, but only the middle $76\ mm$ (out of $152\ mm$) are computed in the spanwise direction.

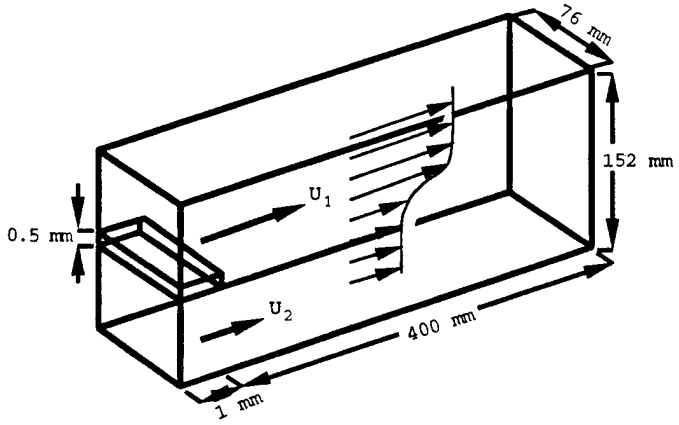


Figure 7: Spatial mixing layer computational domain schematic

The grids employed for this case had a curvilinear H-H topology. Three different grids were used in order to investigate the effects of resolution: $61 \times 41 \times 18$, $91 \times 61 \times 34$, and $121 \times 91 \times 50$ (including ghost points). Of these, the two higher resolution grids gave essentially the same

solution (although, by definition, true grid independence will never be obtained in an LES).[22] Only the results from the highest resolution grid are presented here.

7.2 Boundary Conditions

The upper and lower boundaries are treated as slip-walls, since the grid does not have adequate resolution to resolve the boundary layers. Periodic boundary conditions were used in the spanwise direction. This was done for convenience rather than any requirement of the code or the subgrid models. The flow at the outflow boundary was computed after the manner of Thompson[35] and Poinsot and Lele.[36] The inflow on the supersonic side is fully specified, while on the subsonic side, a characteristic boundary condition was employed. In order to better match the experimental predictions, pseudo-turbulent velocity fluctuations were added at the inflow boundaries.

Conceptually, the present approach to inflow turbulence may be described as computing a "box" of frozen turbulence which is convected by the mean flow into the computational domain This field is computed initially in a cubic domain that is assumed periodic in all directions. For the sake of economy, it is computed on a 48^3 uniform Cartesian grid. Given the assumed spectrum (similar to Lee, Lele, and Moin[37]), this level of resolution is sufficient to capture the majority of the energy containing wavenumbers, but it does mean that near the splitter plate, where grid points are highly concentrated, the computational domain is able to resolve much higher wavenumbers than are calculated in the inflow turbulence. For curvilinear grids, the velocity field must now be interpolated to a grid whose j-k planes (which are also y-z planes in the current spatial mixing layer case) match the actual inflow boundary grid and are uniformly spaced in the i direction (which is aligned with the x coordinate axis- the direction of mean flow). Here, the inflow boundary is vertical and is uniformly spaced in the k direction, so that a simple cubic spline along vertical grid lines is sufficient, but in other, more general, cases a two- or three-dimensional interpolating technique would be necessary.

One now has a solenoidal isotropic velocity field which has been computed on a grid which can be allowed to "convect" into the computational domain. This field, however, does not take into account the experimentally determined distribution of turbulence, nor does it take into account the varying distribution of resolved and unresolved turbulence due to differences in grid cell sizes. Thus, the velocity field must be modified, and a subgrid kinetic energy field computed such that the following relationship is satisfied:

$$\left\langle \overline{u'^2} \right\rangle_{ik} + \frac{2}{3} \left\langle k^{sgs} \right\rangle_{ik} = \sigma_u^2(y) \tag{33}$$

In the above equation, the angle brackets, $\langle\rangle_{ik}$, represent averaging in an i-k plane. Note that in a more general configuration, averaging would be performed only in the i direction, since the grid might vary in the k direction. The other terms in the above equation are defined as follows: $\overline{u'}$ is the resolved inflow turbulence u-velocity field; k^{sgs} is the (yet to be determined) subgrid kinetic energy relative to the grid at the inflow boundary; and σ_u is the experimentally determined streamwise turbulent intensity (from Elliott[2] for the current work). In the absence of more complete information, the v and w components of velocity are assumed to behave in the same manner as u.

Given the assumed form of the energy spectrum and the grid resolution, an estimate can be made for the fraction of the turbulent energy which is resolved and how much energy is in the subgrid. Once the subgrid portion of the energy is known, the resolved turbulent velocity field which is entering the computational domain through the location in question can be scaled as follows:

$$\left(\overline{u_i'}\right)_{final} = \overline{u_i'} \sqrt{\frac{3\left(1 - E_{sgs}\right)\sigma_u^2}{\left\langle \overline{u_j' u_j'} \right\rangle_{xz}}} \tag{34}$$

In the above expression, $\left\langle \overline{u_j' u_j'} \right\rangle_{xz}$ is the average (in the $x-z$ plane) of the unscaled inflow velocity perturbation field and E_{sgs} is the fraction of energy in the subgrid. One can also compute the average value of k_{sgs} which will enter the computational domain at this point:

$$k_{avg}^{sgs} = \frac{3 E_{sgs} \sigma_u^2}{2} \tag{35}$$

This provides an estimate for the average amount of subgrid kinetic energy entering at any given point, but it does not provide any information about its specific spatial distribution. Several researchers (such as Liu *et al.*[26] and Meneveau[38]) have found that the actual subgrid terms are similar to the highest wavenumber components of the resolved field. In keeping with this idea (and similar to the dynamic model coefficient calculations), the subgrid kinetic energy field is computed using the resolved field and a test field. This is then scaled to match the predicted value of the average subgrid kinetic energy from equation 36:

$$k^{sgs} = \left(\widehat{\overline{u_i' u_i'}} - \widehat{\overline{u_i'}}\,\widehat{\overline{u_i'}} \right) \frac{k_{avg}^{sgs}}{\left\langle \widehat{\overline{u_j' u_j'}} - \widehat{\overline{u_j'}}\,\widehat{\overline{u_j'}} \right\rangle_{xz}} \tag{36}$$

For the supersonic side of the mixing layer, the perturbation velocities are added to the mean quantities and the sum is directly specified at the inflow boundary. For the subsonic side, however, while the v and w components of velocity can be specified directly, the velocity perturbation in the streamwise direction is input as a perturbation in the total pressure and total temperature.. This is found to work reasonably well, although this case is not really a

fair test, because the high speed side's perturbations are so much larger than the low speed side's that the latter are comparatively insignificant. Indeed, Samimy and Elliott have presented no data on the boundary layers or levels of turbulence for the low speed side inflow.

7.3 Results

The general procedure used for both the cases presented here was to run the solver until the initial conditions had been washed out of the domain. At this point (designated as a single flowthrough time), time averaging was begun. The simulations were then run for four ($M_c = 0.86$) or five ($M_c = 0.51$) more flowthrough times. By this time, the time-averaged statistics were essentially stationary. Despite the relative coarseness of even the finest grid used in this study ($121 \times 91 \times 50$), the results are surprisingly good when compared to experiment. The momentum thickness as a function of position downstream of the splitter plate, shown in figure 8, is reasonably well captured by the LES. The effect of compressibility is shown in the decrease in thickness (both in the simulation and experiment) for the higher convective Mach number case.

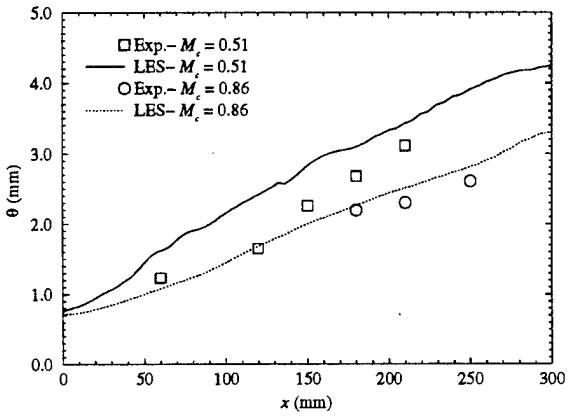


Figure 8: Comparison of LES predicted momentum thickness with the experimental data of Samimy and Elliott

In general, the simulation results for the $M_c = 0.51$ agree very well with experiment. Normalized velocity profiles for this case at various streamwise stations are plotted in figure 9. The agreement with the experimental data is excellent. As the figure shows, the self-similar character of the mean flow is well resolved by the current scheme.

Turbulent quantities are also in good agreement with experiment. Figure 10 shows streamwise turbulent intensity profiles at the same locations as for the previous figure. Both the peak magnitude and the overall distribution of turbulence are well predicted compared to the experiment. The width is correct, as is the shape and the self-similar nature of the profiles. Note, however, that the freestream values are underpredicted (probably due to lack of resolution in these areas). As with the experiment, the U^* profiles showed self-similarity earlier than the turbulent quantities, which are not fully similar until $150mm$ downstream of the splitter plate. For the succeeding plots of turbulent quantities, data is shown only for those measuring stations which are downstream of the onset of self-similar behavior.

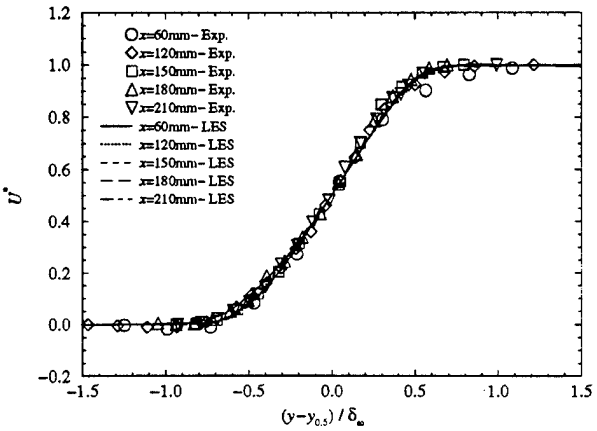


Figure 9: Normalized mean velocity profiles in the $M_c = 0.51$ mixing layer

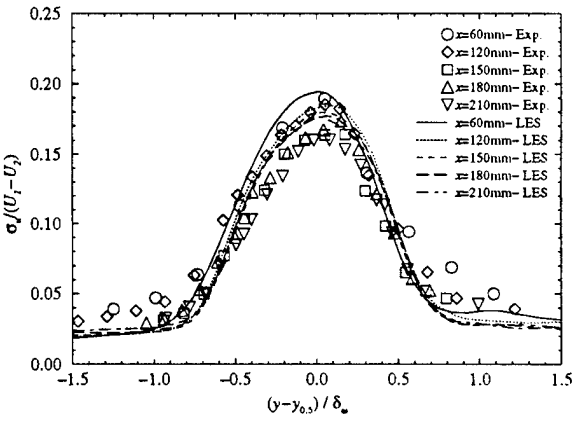


Figure 10: Profiles of streamwise turbulence intensity in the $M_c = 0.51$ mixing layer

The lateral turbulence intensity, shown in figure 11, is also in excellent agreement with experiment. Not only are the shape and the width of the profiles in the self-similar region correct, but the magnitude is also correct. The Reynolds stress profiles ($\overline{u'v'}$) shown in figure 12, are not as well resolved. Although the width of the profiles is correct and self-similar behavior is predicted, the magnitudes are significantly higher in the simulation. There are several possible sources for this error. It may be a result

of deficiencies in formulation of the current model. Errors in the numerical scheme (either dispersion or weaknesses in the scheme's ability to handle sharp curvature) might also play a part. Another possibility is a deficiency in the incoming pseudo-turbulence.

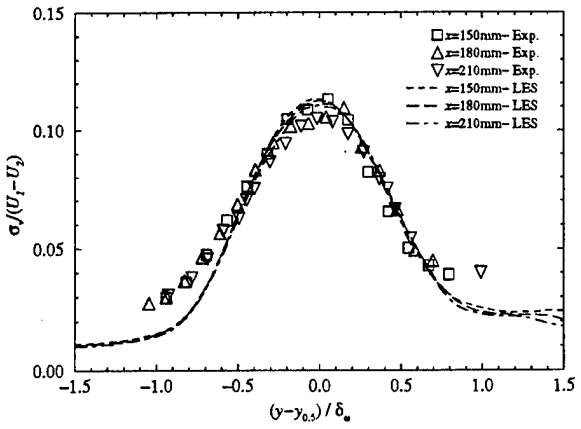


Figure 11: Profiles of lateral turbulence intensity in the $M_c = 0.51$ mixing layer

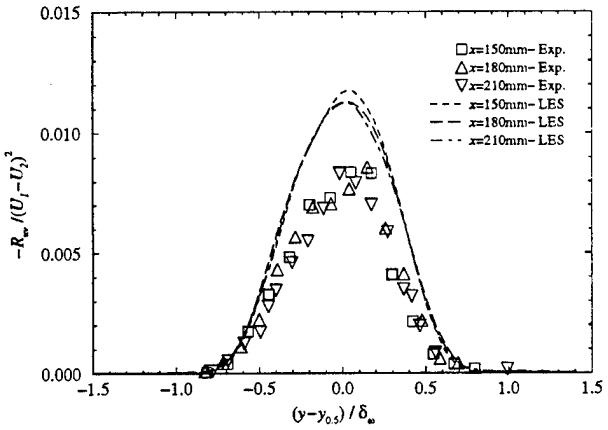


Figure 12: Reynolds stress profiles in the $M_c = 0.51$ mixing layer

The ability of the LES to capture the higher moments was also evaluated. Figures 13 and 14 show respectively, the streamwise and lateral turbulent transport of turbulent kinetic energy. It can be seen that these third order velocity fluctuation correlations are in excellent agreement with the measured data. Similarly, the streamwise and transverse velocity skewness are also well resolved for this case (see figures 15 and 16). Self-similarity is achieved, and the profiles show the correct shape and magnitude within the core region. The peak values, however, are slightly overpredicted. This is due to the previously discussed drop-off in the predicted turbulence intensities away from the core region.

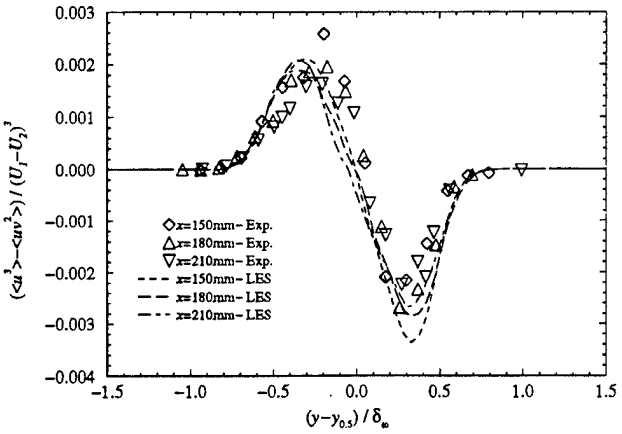


Figure 13: Streamwise turbulent energy transport in the $M_c = 0.51$ mixing layer

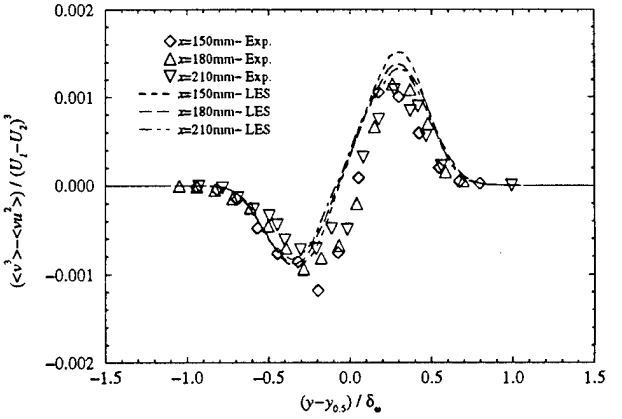


Figure 14: Lateral turbulent energy transport in the $M_c = 0.51$ mixing layer

The velocity flatness profiles (figure 17 and 18) also show very good agreement with experiment in the majority of the mixing layer. On the high speed side, however, the results become unstable above a non-dimensional coordinate of 0.5. Similar, though not as dramatic, instability is observed on the low-speed side for $(y-y_{0.5})/\delta_\omega$ less than 1.0. The reasons for this behavior are the same as those cited above for the skewness: the underprediction of the turbulence intensity at the fringes of the mixing region.

The current model, therefore, has been quite successful in predicting the major features of a low to moderate compressibility mixing layer. Self-similarity is achieved in the core region of the mixing layer for all of the turbulent moments that were examined. Quantitative and qualitative agreement was obtained with experiment on all of

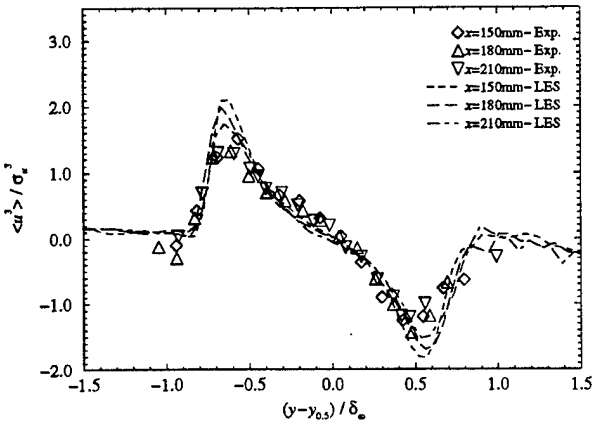


Figure 15: Streamwise velocity skewness profiles in the $M_c = 0.51$ mixing layer

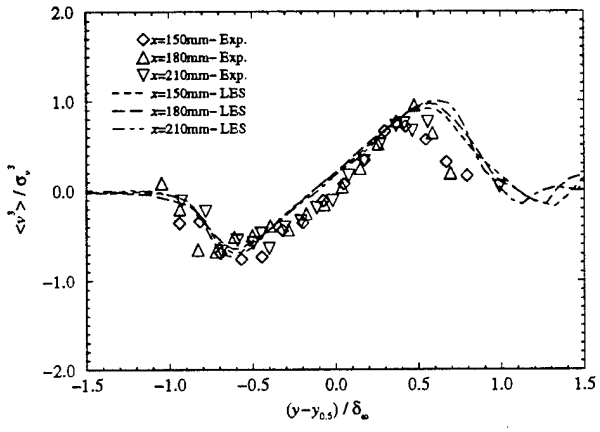


Figure 16: Lateral velocity skewness profiles in the $M_c = 0.51$ mixing layer

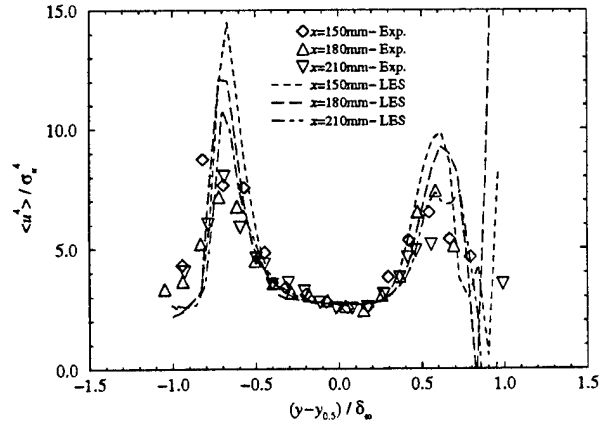


Figure 17: Streamwise velocity flatness profiles in the $M_c = 0.51$ mixing layer

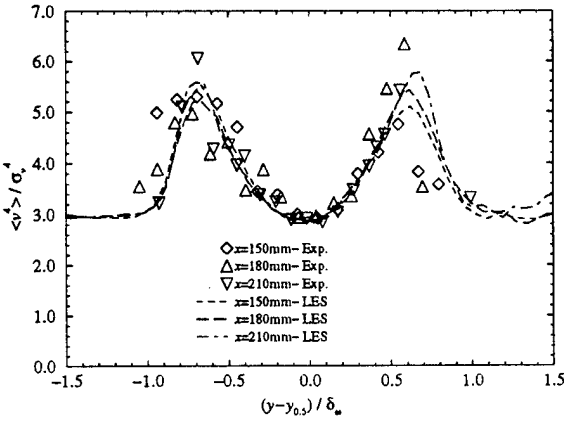


Figure 18: Lateral velocity flatness profiles in the $M_c = 0.51$ mixing layer

the quantities examined except the off-diagonal Reynolds stresses (R_{uv}), which were somewhat overpredicted.

In general, the results from simulations of the $M_c = 0.86$ mixing layer show more divergence from the experimental results than for the previous case. As mentioned above, these results are from flow fields which have been averaged (in time) over four flowthrough times. The normalized streamwise velocity profiles are shown in figure 19. Good agreement is obtained both in the shape and self-similar nature of the curves. Note that the horizontal axis coordinate for this case has been non-dimensionalized using the shear thickness rather than the vorticity thickness. This is because the vorticity thickness growth is predicted as being somewhat irregular for this case (unlike the $M_c = 0.51$ case). Thus, when this quantity is used as the normalizing factor, an artificial scattering is introduced. The shear thickness does not, in general, exhibit the same problem. In other respects, the results for this case were analyzed in the same manner as the $M_c = 0.51$ case.

Discrepancies between experiment and simulation become more apparent when turbulent quantities are examined. While the low-speed side of the curve is reasonably well predicted, the streamwise turbulence intensity profiles (shown in figure 20) are significantly overpredicted on the high-speed side. In general, the magnitude is also somewhat overpredicted. In addition, the width of the profile appears to be greater than in the experiments. The results are, however, self-similar. The self-similarity indicates that the problem is not growing spatially, but the dynamic model coefficients and ν_c may be similarly in error everywhere in the domain. One possible factor causing this is the use of a pressure switch in the computation of ν_c. A density switch might be more appropriate in this case, since the terms which are being modeled are directly related to density, and only indirectly to pressure. Unfortunately, the experimental data did not contain error

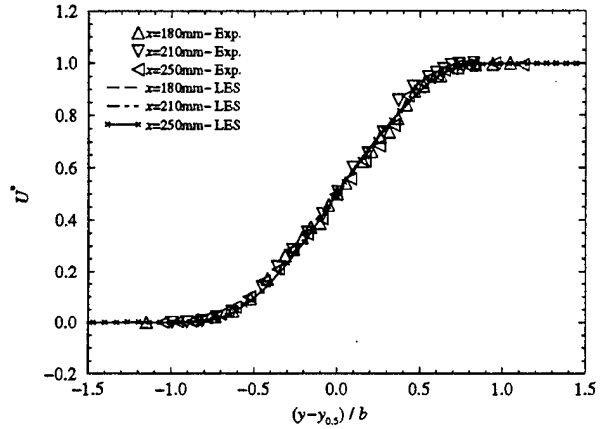


Figure 19: Normalized mean velocity profiles in the $M_c = 0.86$ mixing layer

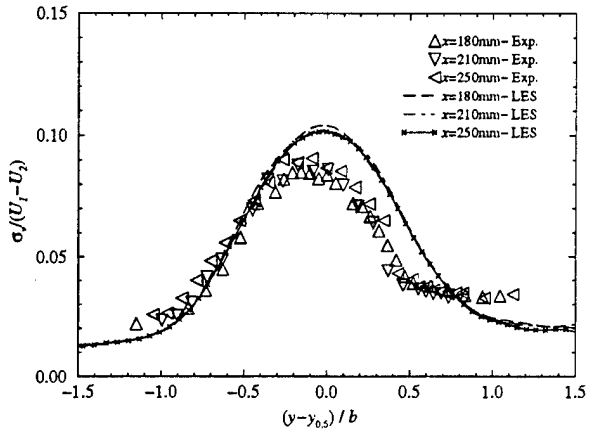


Figure 21: Profiles of lateral turbulence intensity in the $M_c = 0.86$ mixing layer

estimates, so it is impossible to say whether any part of the observed discrepancies might be due to experimental error.

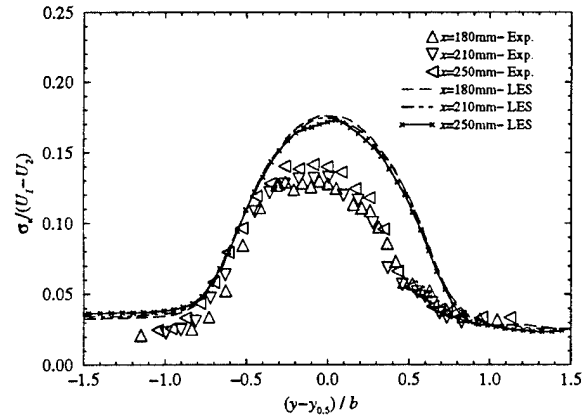


Figure 20: Profiles of streamwise turbulence intensity in the $M_c = 0.86$ mixing layer

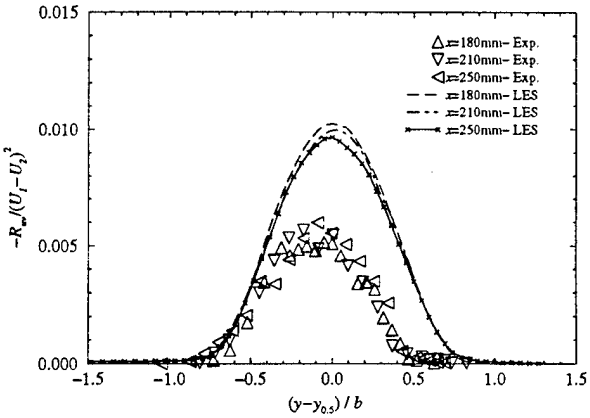


Figure 22: Reynolds stress profiles in the $M_c = 0.86$ mixing layer

This trend of reasonable predictions on the low-speed side and overprediction on the high speed side is seen on almost all of the turbulent quantities. The lateral turbulence intensity profiles, for example, are shown in figure 21. As before, they are somewhat skewed toward the high speed side of the flow, and the peak magnitude is overpredicted, though not as much as is the streamwise intensity. Again, the profiles are strongly self-similar.

The Reynolds stress profiles, shown in figure 22, are similarly skewed, but the magnitude is overpredicted to a greater degree than in the previous two plots. This is similar to the behavior that is observed in the $M_c = 0.51$ simulations, as shown above.

Third order correlations (figures 23 and 24) show a sim-

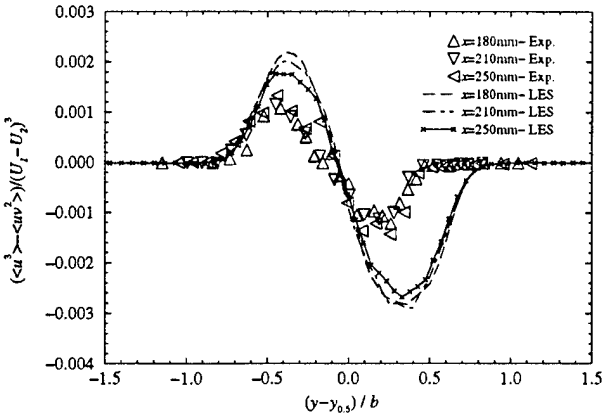


Figure 23: Profiles of streamwise turbulent transport of turbulent energy in the $M_c = 0.86$ mixing layer

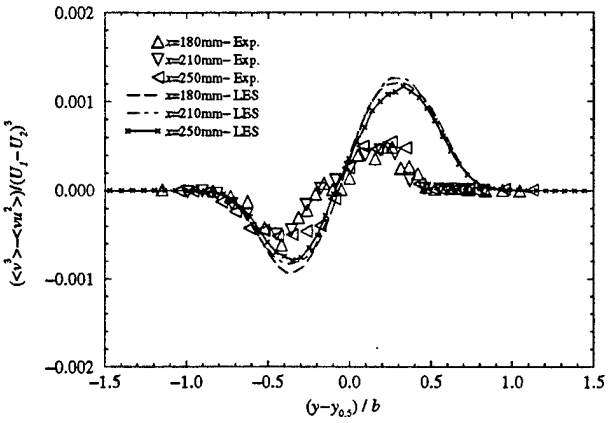


Figure 24: Profiles of lateral turbulent transport of turbulent energy in the $M_c = 0.86$ mixing layer

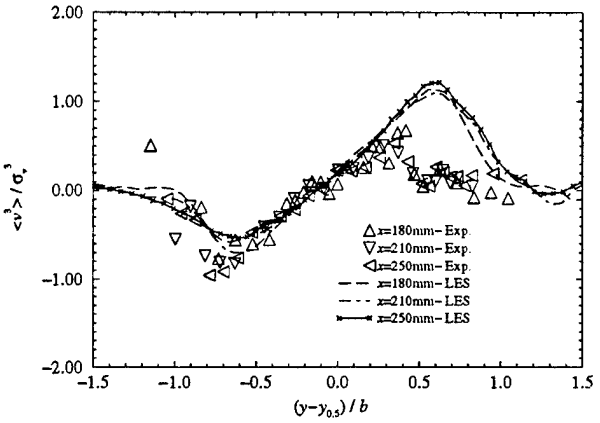


Figure 26: Profiles of lateral velocity skewness in the $M_c = 0.86$ mixing layer

ilar trend of overpredicting the high-speed side and better agreement on the low-speed side. These are plots of the transport of turbulent kinetic energy by streamwise and lateral velocity fluctuations, respectively. Streamwise velocity skewness (figure 25) shows excellent agreement on the low-speed side of the mixing layer. Again, however, the high speed side of the mixing layer is not correctly predicted. Instead of the flattened character found in this region in the experiment, the profiles take the same general shape as was observed in the $M_c = 0.51$ mixing layer. The same basic trend is visible in the lateral velocity skewness, shown in figure 26. This quantity, however, is underpredicted on the low-speed side, in contrast to the previously mentioned quantities.

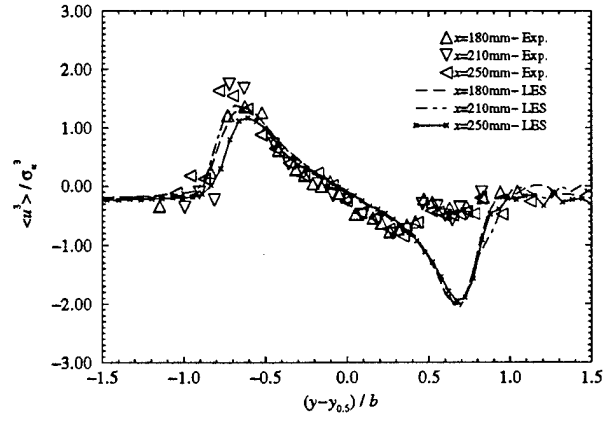


Figure 25: Streamwise velocity skewness profiles in the $M_c = 0.86$ mixing layer

The behavior of the velocity flatness (figures 27 and 28) is similar to the above skewness profiles. Again, the high-speed side is incorrectly predicted in much the same shape as for $M_c = 0.51$, while the low-speed side is in reasonably good agreement with experiment. As with the lower Mach number case, the profiles become extremely unstable on the high-speed side beyond the edge of the mixing layer (non-dimensional coordinates greater than about 0.6) due to the drop-off in predicted turbulence intensity in that region.

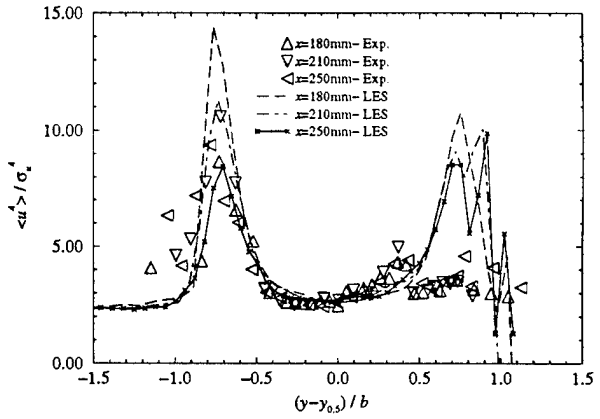


Figure 27: Profiles of streamwise velocity flatness in the $M_c = 0.86$ mixing layer

8 Conclusions

The current scheme, in combination with the compressible local dynamic subgrid model, has been shown to work reasonably well for turbulent flows with low to moderate compressibility- even when relatively coarse grids are used. In the decaying isotropic turbulence cases, the scheme closely matched experimental and DNS results. In the spatial mixing layer cases, the simulations compared extremely well with experiment for the lower convective

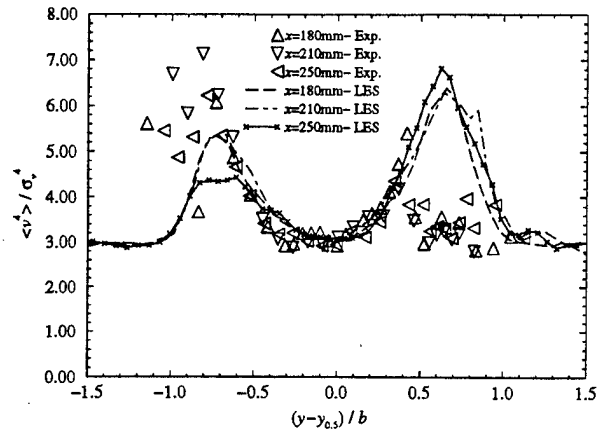


Figure 28: Lateral velocity flatness profiles in the $M_c = 0.86$ mixing layer

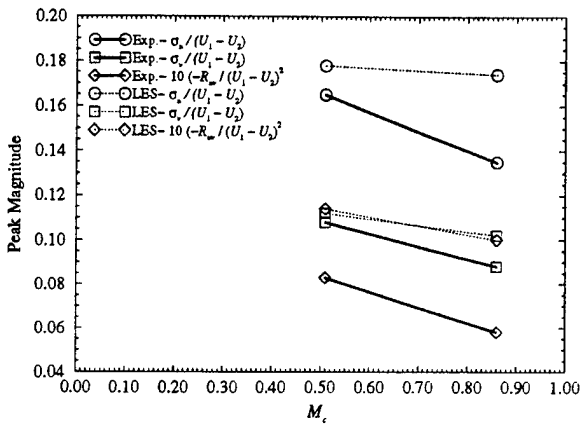


Figure 29: Maximum turbulence intensities and Reynolds stress versus convective Mach number

Mach number case. The higher convective Mach number case also captured the growth of the shear layer, as well as the expected self-similarity. Many of the expected qualitative features of the flow were also resolved.

It appears, however, that the model is not properly predicting a fundamental feature of highly compressible turbulence. Specifically, it is not capturing the full extent of the suppression of turbulence in the high speed region with increasing compressibility. This is illustrated in figure 29 which shows that the peak magnitudes of the streamwise and lateral turbulent intensities, as well as the Reynolds stress. While Elliott observed decreases in all three quantities, the current work predicts only a slight decrease in the streamwise intensity. Goebel and Dutton[39] (also see Gruber *et al.*[40]) observed a trend similar to that of the present work: streamwise intensity remained roughly constant as Mach number increased. The behavior of the lateral intensity and Reynolds stress, however, does not agree with either set of experiments. While these values do decrease with increasing convective Mach number, they do not do so to the extent predicted by experiment.

Based on the above plots, it would seem that the majority of the error is from the high speed side of the mixing layer, rather than uniformly distributed throughout. From the experimental results, it appears that strong compressibility effects are felt strongly on the high speed side of the mixing layer, and these effects are not being correctly captured by the model. Thus, while the method appears to be adequate for low to moderate compressibility, the present results suggest that more research is needed to enhance the accuracy for highly compressible, high Reynolds number flows.

9 Acknowledgments

The authors would like to acknowledge the financial support of the Fluid Dynamics Division of the Office of Naval Research. Additional funding was also provided by the Air Force Office of Scientific Research under the Focused Research Initiative. Computer time was provided by the Aeronautical Systems Center at Wright-Patterson Air Force Base under the Department of Defense Major Shared Resource Center program. The authors would like to thank Prof. M. Samimy for providing the raw data from Dr. Elliott's experimental work.

References

[1] M. Samimy, M. F. Reeder, and G. S. Elliott. Compressibility effects on large structures in free shear flows. *Physics of Fluids A*, 4(6):1251–1258, 1992.

[2] G. Elliott. *A Study of Compressible Mixing Layers Using Laser Based Diagnostic Techniques.* PhD thesis, The Ohio State University, 1993.

[3] S. F. Birch and J. M. Eggers. A critical review of the experimental data for developed free turbulent shear layers. In *Free Turbulent Shear Flows*, pages 11–37. NASA SP-321, 1972.

[4] G. L. Brown and A. Roshko. On density effects and large structure in turbulent mixing layers. *Journal of Fluid Mechanics*, 64(4):775–816, 1974.

[5] D. Papamoschou and A. Roshko. The compressible turbulent shear layer: an experimental study. *Journal of Fluid Mechanics*, 197:453–477, 1988.

[6] D. W. Bogdanoff. Compressibility effects in turbulent shear layers. *AIAA Journal*, 21(6):926–927, 1983.

[7] D. Papamoschou. Structure of the compressible turbulent shear layer. *AIAA Journal*, 29(5):680–681, 1991.

[8] O. Zeman. Dilatation dissipation: The concept and application in modeling compressible mixing layers. *Physics of Fluids A*, 2(2):178–188, 1990.

[9] S. Sarkar, G. Erlebacher, M. Y. Hussaini, and H. O. Kreiss. The analysis and modelling of dilatational terms in compressible turbulence. *Journal of Fluid Mechanics*, 227:473–493, 1991.

[10] E. T. Spyropoulos and G. A. Blaisdell. Evaluation of the dynamic subgrid-scale model for large eddy simulations of compressible turbulence flows. *AIAA-95-0355*, 1995.

[11] N. D. Sandham and W. C. Reynolds. Three-dimensional simulations of large eddies in the compressible mixing layer. *Journal of Fluid Mechanics*, 224:133–158, 1991.

[12] N. D. Sandham and W. C. Reynolds. Compressible mixing layer: Linear theory and direct simulations. *AIAA Journal*, 28(4):618–624, 1990.

[13] D. Papamoschou and A. Roshko. Observations of supersonic free shear layers. *AIAA-86-0162*, 1986.

[14] N. T. Clemens and M. G. Mungal. Two- and three-dimensional effects in the supersonic mixing layer. *AIAA Journal*, 30(4):973–981, 1992.

[15] N. L. Messersmith, S. G. Goebel, J. P. Renie, J. C. Dutton, and H. Krier. Investigation of supersonic mixing layers. *Journal of Propulsion and Power*, 6(4):353–354, 1990.

[16] G. S Elliott, M. Samimy, and S. A. Arnette. Study of compressible mixing layers using filtered Rayleigh scattering based visualizations. *AIAA Journal*, 30(10):2567–2569, 1992.

[17] P. Koutmos, C. Mavridis, and D. Papailiou. A study of turbulent diffusion flames formed by planar fuel injection into the wake formation region of a slender square cylinder. In *Submitted to 26th International Symposium on Combustion*, 1996.

[18] S. Lee, S. K. Lele, and P. Moin. Eddy shocklets in decaying compressible turbulence. *Physics of Fluids A*, 3(4):657–664, 1991.

[19] S. Sarkar, G. Erlebacher, and M. Y. Hussaini. Compressible homogeneous shear: Simulation and modeling. Technical Report ICASE 92-6, Institute for Computer Applications in Science and Engineering, 1992.

[20] S. Sarkar. The stabilizing influence of compressibility on turbulence in high-speed shear flows. *AIAA-94-2243*, 1994.

[21] S. Sarkar. The stabilizing effect of compressibility in turbulent shear flow. *Journal of Fluid Mechanics*, 282:163–186, 1995.

[22] C. C. Nelson. *Simulations of Spatially Evolving Compressible Turbulence Using a Local Dynamic Subgrid Model.* PhD thesis, Georgia Institute of Technology, 1997.

[23] C. Chen, J. J. Riley, and P. A. McMurtry. A study of favre averaging in turbulent flows with chemical reaction. *Combustion and Flame*, 87:257–277, 1991.

[24] H. Tennekes and J. L. Lumley. *A First Course in Turbulence.* The MIT Press, 1972.

[25] R. W. MacCormack and B. S. Baldwin. A numerical method for solving the navier-stokes equations with application to shock-boundary layer interactions. *AIAA-75-1*, 1975.

[26] S. Liu, C. Meneveau, and J. Katz. On the properties of similarity subgrid-scale models as deduced from measurements in a turbulent jet. *Journal of Fuid Mechanics*, 275:85–, 1994.

[27] B. Vreman, B. Geurts, and H. Kuerten. Realizibility conditions for the tubulent stress tensor in large-eddy simulation. *Journal of Fluid Mechanics*, 276:351–362, 1994.

[28] P. Moin, K. Squires, W. Cabot, and S. Lee. A dynamic subgrid-scale model for compressible turbulence and scalar transport. *Physics of Fluids A*, 3(11):2746–2757, 1991.

[29] M. Germano, U. Piomelli, P. Moin, and W. H. Cabot. A dynamic subgrid-scale eddy viscosity model. In *Center for Turbulence Research- Proceedings of the Summer Program 1990*, pages 5–17, 1990.

[30] D. Gottlieb and E. Turkel. Dissipative two-four methods for time-dependant problems. *Mathematics of Computation*, 30(136):703–723, 1976.

[31] M.-S. Liou and Jr. Steffen, C. J. A new flux splitting scheme. *Journal of Computational Physics*, 107:23–39, 1993.

[32] G. Comte-Bellot and S. Corrsin. Simple Eulerian time correlation of full- and narrow-band velocity signals in grid-generated, 'isotropic' turbulence. *Journal of Fluid Mechanics*, 48(2):273–337, 1971.

[33] W.-W. Kim. *A New Dynamic Subgrid-Scale Model for Large-Eddy Simulation of Turbulent Flows.* PhD thesis, Georgia Institute of Technology, 1996.

[34] S. Ghosal, T. S. Lund, P. Moin, and K. Akselvoll. A dynamic localization model for large-eddy simulation of turbulent flows. *Journal of Fluid Mechanics*, 286:229–255, 1995.

[35] K. W. Thompson. Time-dependant boundary conditions for hyperbolic systems, II. *Journal of Computational Physics*, 89:439–461, 1990.

[36] T. J. Poinsot and S. K. Lele. Boundary conditions for direct simulations of compressible viscous flows. *Journal of Computational Fluids*, 101:104–129, 1992.

[37] S. Lee, S. K. Lele, and P. Moin. Simulation of spatially evolving turbulence and the applicability of Taylor's hypothesis in compressible flow. *Physics of Fluids A*, 4(7):1521–1530, 1992.

[38] C. Meneveau. Statistics of turbulence subgrid-scale stresses: Necessary conditions and experimental tests. *Physics of Fluids*, 6(2):815–833, 1994.

[39] S. G. Goebel and J. C. Dutton. Experimental study of compressible turbulent mixing layers. *AIAA Journal*, 29(4):538–546, 1991.

[40] M. R. Gruber, N. L. Messersmith, and J. C. Dutton. Three-dimensional velocity field in a compressible mixing layer. *AIAA Journal*, 31(11):2061–2067, 1993.



AIAA 97-0652
On Large Eddy Simulation of non-homogeneous flows

V. K. Chakravarthy and S. Menon
School of Aerospace Engineering
Georgia Institute of Technology
Atlanta, GA 30332-0150.

35th Aerospace Sciences Meeting & Exhibit
January 6-10, 1997 / Reno, NV

For permission to copy or republish, contact the American Institute of Aeronautics and Astronautics
1801 Alexander Bell Drive, Suite 500, Reston, VA 22091

On large eddy simulation of non-homogeneous flows*

V. K. Chakravarthy ‡ & S. Menon†
School of Aerospace Engineering
Georgia Institute of Technology
Atlanta, GA 30332-0150

ABSTRACT

The performance of the subgrid kinetic energy equation model for a wall bounded inhomogeneous flow is evaluated and reported in this paper. Near wall behavior has eluded any kind of modeling in turbulence simulations. Most Large eddy simulations have a near DNS (direct numerical simulation) resolution in the near wall region. As a consequence, the finite difference computation of the derivatives need special attention because of the rapid stretching encountered in the near wall region. This increases the computational expense and is perhaps one of the major factors preventing LES as an affordable tool in engineering. The effect of inadequate grid resolution and unresolved viscous sublayer phenomena on the core region turbulence is studied. Such a study could provide valuable information for developing LES models that could predict turbulence away from the wall despite the errors in the near wall region or for development of simple empiricisms to account for near wall effects in a LES. It is shown in this study that the subgrid kinetic energy model shows a tendency of capturing, at least qualitatively, the near wall turbulence and could be used as a starting point for development of near wall models that could be used in conjunction with large eddy simulations.

1 Introduction

In the recent years, the dynamic evaluation procedure has greatly enhanced the performance of the large eddy simulation models (see Germano et al. [1]). This procedure is used to determine the model coefficients in large eddy simulation (LES) models by assuming that the model is valid at the grid scale and a larger resolved scale (corresponding to the test filter width). Given the fact that the spectrum at the test filter scale corresponds to the form assumed in deriving the LES model, this technique can greatly extend the use of LES in modeling of complex flows. In this study, we focus on the issues concerning LES of wall bounded turbulent flows. Temporally evolving pressure driven flow in a square duct at two different Reynolds numbers is considered. Each of these flows have secondary flow patterns that present a great difficulty in terms of subgrid modeling. The performance of the dynamic LES model is evaluated in these complex flows.

The flow in a square duct is an ideal choice for the present study because it has two inhomogeneous directions and two mutually perpendicular boundary layers. The interaction between these two layers gives rise to secondary flow patterns in the cross plane. The flow normal to the streamwise direction is directed away from the center towards the corners of the duct where it gets turned around creating recirculatory patterns. These patterns have been the root cause of the difficulty in terms of turbulence modeling. Speziale [2] has shown that these patterns are related to the fact the normal Reynolds stresses are unequal and hence the much used $K-\epsilon$ model in Reynolds averaged approach fails. There have been attempts to model this flow field using non-linear $K-\epsilon$ model [3], but the results are not fully satisfactory. A large eddy simulations, given that it has in it, less empiricisms in terms of modeling may be a better tool for this purpose. The secondary flow patterns in this flow have been studied in detail by Gavrilakis [4] and Reichert et al.[5] using high resolution DNS. Their results provide a basis

† Associate Professor, Senior Member, AIAA.
‡ Graduate Research Assistant.
* Copyright ©by V. K. Chakravarthy & S. Menon. Published by the American Institute of Aeronautics and Astronautics, Inc., with permission.

against which the results of the present LES could be compared.

The LES models are usually derived with an assumption that the subgrid scales are isotropic. This is very unlikely in case of many inhomogeneous flows (at Reynolds numbers encountered in engineering applications) resolved at a grid size limited by the present day computational resources. In using LES to model such flows, it is assumed that the weak homogeneity that exists in the subgrid scales does not significantly affect the evolution of the large scales in the flow. Furthermore, the flow near a solid wall does not follow the phenomenology applied in modeling fully developed turbulence. The accurate prediction of near-wall behavior without resolving all the relevant scales is beyond the present stage of modeling in turbulence. Very fine grids are still needed to resolve the near wall phenomena, thus, requiring very high grid stretching. Special finite difference approximations need to be constructed in these regions and usually these are lower in order and increase the computational cost enormously. This may not be affordable or practical for use in LES. In the present study, the impact of using coarse grids near walls on LES is studied. The eventual goal is to ensure that the errors in near wall region do not diffuse into the interior of the flow field and destroy the overall accuracy of the prediction. The near wall behavior, however, cannot be accurate but in this study, LES is mostly targeted towards modeling combustion and mixing which seldom occur in the vicinity of the walls. If one were to use LES for predictions that depend heavily on near wall behavior like the fluid dynamic drag, there is no choice but to cluster the grid in the wall region.

The governing equations and numerical methods used are explained in the next section. Section 3 details the model used in the simulation along with the dynamic evaluation procedure. The results from the simulations, conclusions and suggestions for future research can be found in the last section.

2 Governing equations

The Navier-Stokes equations, on convolution with a spatial filter, reduce to the following set of LES equations.

$$\frac{\partial \overline{U}_i}{\partial x_i} = 0 \tag{1}$$

$$\frac{\mathrm{d}\overline{U}_i}{\mathrm{dt}} = -\frac{\partial \overline{p}}{\partial x_i} + \nu \frac{\partial^2 \overline{U}_i}{\partial x_k \partial x_k} + \frac{\partial \tau_{ij}}{\partial x_j} \tag{2}$$

where the overbar indicates a filtered variable, $\tau_{ij} = (\overline{U_i\ U_j} - \overline{U_i U_j})$ is the subgrid stress. For a closed set of equations , one needs to approximate the subgrid stresses using a model. The velocity variations in the scales below the characteristic filter width Δ are unresolved in a LES. Due to the nonlinear nature of the Navier-Stokes equations, these small scale fluctuations effect the large scale motions. This effect comes from the subgrid stress, which in the present study is approximated as $\tau_{ij} = -\frac{2}{3}K\delta_{ij} + 2\nu_t\overline{S_{ij}}$, where $\overline{S_{ij}} = \frac{1}{2}\left[\frac{\partial \overline{U_i}}{\partial x_j} + \frac{\partial \overline{U_j}}{\partial x_i}\right]$ is the resolved strain tensor, ν_t is subgrid eddy viscosity (to be defined later) and $K = -\frac{1}{2}(\overline{U_i\ U_i} - \overline{U_i U_i})$ is the subgrid kinetic energy. Filtered variables are also called supergrid variables because they carry information about a variables at all length scales above the filter width (set equal to the grid spacing here, although not necessary). The model equations for the subgrid kinetic energy and the eddy viscosity are presented in the next section.

The equations are discretized on a non-staggered grid (with spacing corresponding to the characteristic filter width Δ) and numerically integrated using a two step semi-implicit fractional step method. In this method, all of the primitive variables are defined at the grid points. The well known checker board type oscillations occur in velocity field due to velocity-pressure decoupling when one uses central finite difference schemes for approximating the spatial derivatives. Use of QUICK scheme for calculation of velocity gradients that arise in the source term of the elliptic equation for pressure is found to effectively couple the velocity and pressure fields, thus, removing these oscillations [6]. The convective terms are computed using a upwind biased finite difference approximations (third-order in wall normal and fifth-order in streamwise directions) while the viscous terms are computed using a fourth-order central difference approximation. The Poisson equation is solved numerically using a second-order accurate elliptic solver that uses a four-level multigrid scheme to converge the solution. The

finite difference equations are integrated in time using a second-order scheme.

3 LES Model

A K-equation model with dynamic evaluation of the model coefficients based on the Germano's filtering approach is used as a LES model. First proposed by Schumann, the K-equation model been shown to be very useful especially in LES of reacting flows (see Weeratunga and Menon [7]). The advantage of this model is that it solves a single scalar equation for the subgrid kinetic energy which characterizes the velocity scale of subgrid turbulence. This velocity scale along with the length scale (grid spacing or the filter width) provides a subgrid timescale representing the non-equilibrium relaxation of the subgrid scales. This is one step forward (in the direction of developing non-equilibrium models) than the equilibrium models(algebraic or the zero equation models), wherein the production and dissipation of the subgrid kinetic energy are assumed to balance instantaneously.

Menon and Kim [8] suggested a dynamic modeling approach using the K-equation model. The amount of subgrid kinetic energy in the subgrid scales gives the extent of unresolved scales (energy content as well as the range). Given the fact that the modeling of resolved scales is yet far from accurate, the subgrid kinetic energy can be looked upon as an error estimator in a LES. On the other hand, LES using algebraic models can give no information in this regard. It is imperative while using algebraic models that the grid scale cut off lie in the dissipative end of the inertial range of scales (because of the assumption that subgrid production equals dissipation). One has to rely on experimental results or grid independence tests (sometimes involving usage of near DNS resolution grids for the purpose) for validation. On the other hand, in the one equation model the grid scale cut-off could be at a larger scale (in the inertial range), allowing coarse grid large eddy simulations.

Only an outline of the present model is provided here, since a more comprehensive description, including the implementation issues, can be found in Ref.8. The eddy viscosity and subgrid dissipation in physical space, for a characteristic filter width Δ, are given as follows.

$$\nu_t = C_\nu K^{\frac{1}{2}} \Delta, \tag{3}$$

$$\epsilon^{sgs} = C_\epsilon \frac{K^{\frac{3}{2}}}{\Delta} \tag{4}$$

These expressions are same as the expressions obtained if one uses dimensional arguments considering the subgrid kinetic energy and filter width as the relevant parameters for determining the subgrid eddy viscosity. The assumptions made in arriving at these expressions from analytical arguments in turbulence and their validity are discussed to some extent in ref.9.

For the transport term, a gradient diffusion model based on eddy diffusivity model (with unit eddy Prandtl number) has been proposed and studied by Menon and Kim. This approximation was found to adequately model the transport terms. Hence this is used in a similar form in this study. The dynamic equation for K can now be written as:

$$\frac{\partial K}{\partial t} + \overline{U_j}\frac{\partial K}{\partial x_j} = \tau_{ij}\frac{\partial \overline{U_i}}{\partial x_j} - \epsilon^{sgs} + \frac{\partial}{\partial x_j}\left[\nu_t \frac{\partial K}{\partial x_j}\right] \tag{5}$$

C_ν and C_ϵ are the model constants that need to be specified. These constants, however, are not universal and differ with flow fields in general. This suggests that these constants also depend on the local (supergrid) structure of the flow field. It is, then appropriate to refer to them as coefficients rather than constants. A dynamic approach is applied here to evaluate these coefficients. This procedure acts as an online calibration method thus removing the arbitrariness in prescribing these coefficients. The approach is based on the concept of subgrid stress similarity supported by experiments in jets (Liu et al. [10]). In this approach, a test filter(similar to the LES filter) of characteristic width 2Δ is defined and the corresponding filtered velocity field is denoted by $\widetilde{U_i}$. This new velocity field is obtained by convolution of the LES filtered velocity with the test filter. The subgrid stress corresponding to the scales in between the grid filter width and the test filter width can be written as [8]:

$$t_{ij} = \widetilde{\overline{U_i}}\ \widetilde{\overline{U_j}} - \widetilde{\overline{U_i}}\ \widetilde{\overline{U_j}} \tag{6}$$

and the corresponding dissipation is defined as

$$e = (\nu + \nu_t)\left[\frac{\partial\widetilde{\overline{U_i}}}{\partial x_j}\frac{\partial\overline{U_i}}{\partial x_j} - \frac{\partial\widetilde{\overline{U_i}}}{\partial x_j}\frac{\partial\widetilde{\overline{U_i}}}{\partial x_j}\right] \quad (7)$$

Assuming stress similarity and the present model to be valid for length scales between Δ and 2Δ (which imposes a further restriction that the test filter width is also in the inertial range of length scales), t_{ij} and e can be written as follows.

$$t_{ij} = -\frac{2}{3}\widetilde{K}\delta_{ij} + 2\widetilde{\nu_t}\widetilde{\overline{S_{ij}}} \quad (8)$$

and

$$e = C_\epsilon \frac{\widetilde{K}^{\frac{3}{2}}}{2\Delta}, \quad (9)$$

where $\widetilde{K} = -\frac{1}{2}t_{ii}$ and $\widetilde{\nu_t}$ is the eddy viscosity corresponding to the test filter of width 2Δ and is given by $C_\nu \widetilde{K}^{\frac{1}{2}}(2\Delta)$. From eq.(14), the value of C_ϵ can be evaluated. There are, however, six equations represented by eq.(8) using which C_ν could be evaluated. This is a over-determined system of equations and in the present formulation, is solved using least-squares technique. These coefficients are then used for evaluation of eddy viscosity and to advance the dynamic equation for K in time, thus achieving complete closure.

In the past studies, the spatial variation of the model coefficients evaluated using many of the dynamic approaches in the past, was found to be oscillatory and susceptible to numerical instabilities. Various methods like filtering, spatial averaging were used to remove this oscillatory behavior. The present dynamic evaluation procedure is, however, completely localized and does not lead to any instabilities in integration. The present model, hence, is a considerable improvement over the existing LES models, as shown by Menon and Kim [8].

4 Results and discussion

The turbulent flow in a square duct is simulated at two different Reynolds numbers. The flow in this geometry is strongly dependent on the interaction (discussed earlier) between the primary and the secondary flows (strain rates). This interaction was found to cause fairly strong dependence of turbulence on the Reynolds number as compared to flows with unidirectional mean shear (channel flow, Couette flow etc.). Most modeling approaches using Reynolds averaged Navier-Stokes equations rely on phenemenology of high Reynolds number asymptotics and have only a weak incorporation of Reynolds number effects. LES may be better suited for these type of flows.

Flow at a Reynolds number of 10000 (corresponding to a Reynolds number of 600 based on friction velocity and duct width) was simulated as a test case on a 65x49x49 grid with hyperbolic tangent stretching rate in the wall normal directions. The clustering of the grid at the walls is found to resolve the wall layer adequately. Owing to rapid stretching, finite difference approximations are computed using stretching dependent stencils in these directions. It is acknowledged that the effects of very non-uniform filter on LES have been ignored in this simulation. This case was chosen because of the availability of reliable DNS data at this Reynolds number (Huser and Biringen [11]).

The near wall variation of the turbulence intensities at the mid-section, normalized by local skin friction velocity is shown in fig.1(a-c) along with data from channel flow DNS (Kim and Moin[12]) and square duct DNS (Huser and Biringen [11]). The viscous sublayer turbulence is found to fairly similar in all three cases indicating a universal (but Reynolds number dependent) nature. It is well known that turbulence intensity near the wall grows with Reynolds number and this fact is reflected in the figures. The data from channel flow DNS is found to be higher because of a slightly higher Reynolds number (13200). The stream-wise turbulence intensity is overpredicted by the present LES as compared to DNS because of the coarse resolution in the stream-wise direction. Rai and Moin[13] infer that use of upwind biased scheme in an under resolved simulation tends to overpredict turbulence intensity in the direction of inadequate resolution. This fact is further confirmed by Huser and Biringen [11]. Yet it is still better to use a higher order upwind biased scheme as opposed to central or spectral schemes (though less dissipative) in order to minimize aliasing errors (see Rai and Moin[13]).

An LES is conducted with same conditions as in the previous case but with a 65x33x33 grid which is algebraically stretched out in the wall normal directions. The grid spacing in the wall normal direction near the

wall is close to 10 nondimensional wall units. Considerable amount of the kinetic energy is produced in the close vicinity of the wall and it is very unlikely that this could be captured using this grid. The intent here, is to study the effect of this inadequacy on the core region turbulence. Shown in fig.2(a,b) are respectively, the variation of u'^2 and subgrid kinetic energy along the wall bisector along with corresponding values from DNS. As can be seen u'^2 is largely underpredicted (despite low axial resolution) especially in the wall region. The peak in u'^2 is shifted away from the wall. This was noticed earlier by Menon and Chakravarthy [14] in turbulent Couette flow simulated on a very coarse grid. In the present flow, it was noticed however, that the kinetic energy (resolved and subgrid) seems to be predicted with fair amount of accuracy. This perhaps may be due to the fact that the Couette flow is a wall driven flow as against the square duct (which is pressure driven) thus making the wall layer phenomena more important.

Figure 2b shows the variation of normalized kinetic energy (both resolved and the subgrid) in comparison to DNS. The total kinetic energy prediction seems satisfactory with small differences in the core region. While this may be an error in the simulation, it could also be due to the difference in axial length between the two simulations. However, the point to be noted here is that the subgrid kinetic energy is very high in this simulation. In the near wall region, the subgrid kinetic energy peaks close to where the peak in DNS is observed. While this is encouraging, as stated earlier, high subgrid kinetic energy indicates high uncertainity in the validity of the results.

It can be concluded from this study that in a LES with coarse wall layer resolution, the near wall turbulence cannot be captured with in the range of resolved scales. The phenomenology on which the subgrid kinetic energy is based, fails in this region. However, the kinetic energy does tend to peak in the near wall region as if to capture the unresolved turbulence, but, this could also be an indication of high modeling uncertainity.

A Re = 5000 simulation was then conducted on a 65x49x49 grid with algebraic stretching in the wall normal directions. The stretching was kept under 4% in all regions. Shown in fig.3(a-d) are the resolved scaled normalized variances in the velocities with corresponding values from a 33x65x65 LES using a Smagorinsky model (Madabhushi and Vanka [15]). The latter LES used very low resolution in the axial direction. A spectral method was used to compute the derivatives in this direction which could lead to significant aliasing errors. The net effect would be an overprediction of u'^2.

As can be seen, u'^2 compares favorably in the core region but the present simulation predicts a shifted peak with a lower value. The difference is also magnified by the fact the u'^2 could be highly overpredicted in the LES using algebraic model. Similar is the trend in case of v'^2 and w'^2. Shown in fig.3d is the variation of kinetic energy (resolved and subgrid combined) along with LES conducted by Madabhushia and Vanka [15]. As seen, there seems to be significant differences in the wall region. Further, unlike in the case of 10000 Reynolds number simulation, the subgrid kinetic energy does not even have a large peak in the near wall region.

Two point correlations along the axial direction was computed at three different locations. The first location is at the center line, the second location is at the midpoint of the center and one of the corners and the third location is the midpoint of the center and the wall along the wall bisector. The one dimensional velocity spectrum at these locations is plotted in Fig 4. The inertial spectrum that is expected is also shown. $G[K_x]$ is the Fourier transform of the filter function. The inertial range form of the energy spectrum would be the actual spectrum times the square of this function. The core region seems to have a range of wavenumbers in the Kolmogorov inertial range.

At a glance, it seems that the subgrid kinetic energy equation tries to account for unresolved turbulence in the near wall region better at a higher Reynolds number. This is puzzling, but could be explained on the grounds that the secondary flow patterns that are the prime cause of difficulty in modeling this flow have reduced amplitudes at higher Reynolds numbers. The instantaneous velocity vectors of the secondary flow pattern in the cross plane are shown in Fig 5.

The effects of secondary flow wane with increasing Reynolds number. It is further likely that the region of fully developed turbulence extends much closer to the

wall in the higher Reynolds number case thus making the phenemenology of LES modeling more accurate.

In conclusion, it is seen that, at higher Reynolds number, the subgrid kinetic energy does have a tendency to capture significant amount of unresolved turbulence. While the quantitative agreement is fairly acceptable in the core region, this model also shows promise in the viscous sublayer and might need some near wall modifications for a better performance. At lower Reynolds numbers, the cross plane has secondary velocities which are recirculatory and cause significant problems. Further research into recirculatory flows at right angled corners using LES is required to modify the present model.

Acknowledgements

The authors are grateful for the financial support from the Fluid Dynamics Division of the Office of Naval Research under Grant N00014-93-1-0342 (monitored by Dr. P. Purtell). The computer time was provided by the DoD on the SGI Power Challenge Array at the HPC Center, Army Research Laboratories, Maryland.

References

1. M. Germano, U. Piomelli, P. Moin, and W.H. Cabot., 1991, "A dynamic subgrid-scale eddy viscosity model." Phys. Fluids A 3, 1760.

2. C.G. Speziale, Computation of internal flows: Methods and Applications (ASME, New York, 1984), FED 14.

3. C.G. Speziale, "On Nonlinear K-l and K- epsilon Models of Turbulence," J. Fluid Mech. 178, 459.

4. S. Gavrilakis., 1994, "Large-scale structures in the turbulent flow near a right angled corner," First ERCOFTAC Workshop on Direct and Large-eddy simulation.

5. R. S. Reichert, F. F. Hatay, S. Biringen, and A. Huser, 1994, "Proper orthogonal decomposition applied to turbulent flow in a square duct," Phys. Fluids 6(9).

6. Yan Zang, R. L. Street, and J. R. Koseff, 1994, "A non-staggered grid, fractional step method for the time-dependent incompressible Navier-Stokes equations in curvilinear coordinates," J. Comp. Phys. 114, 18-33.

7. S. Weeratunga and S. Menon., 1993, "Parallel computations of unsteady combustion in a Ramjet Engine," AIAA Paper 93-1914, AIAA/SAE/ASME/ASEE 29^{th} Joint Propulsion Conference and Exhibit, Monterey, CA.

8. S. Menon and W.-W. Kim, 1996, "High Reynolds number flow simulations using the localized dynamic subgrid scale model," AIAA Paper 96-0425, 34^{th} Aerospace Sciences Meeting and Exhibit, Reno, NV.

9. V. K. Chakravarthy and S. Menon, 1996, "Simulation of unsteady turbulent jet flow using a localized dynamic subgrid model,", to be presented at the 1996 International Mechanical Engineering Congress & Exposition, Atlanta, Nov 1996.

10. S. Liu, C. Meneveau, and J. Katz, 1994, "On the properties of similarity subgrid scale models as deduced from measurements in a turbulent jet," J. Fluid Mech. 275, 83.

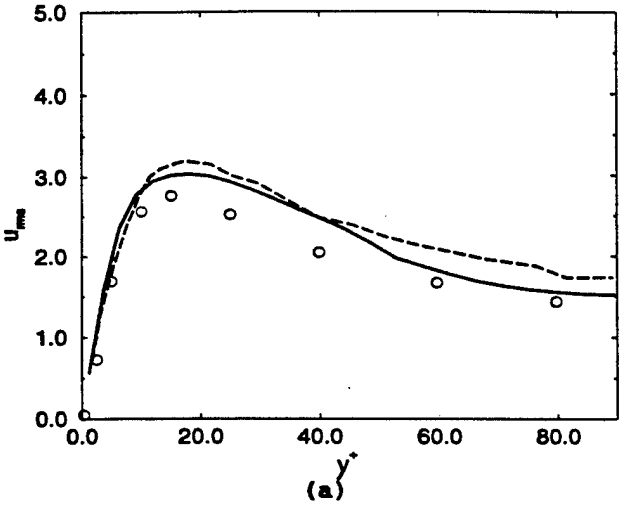
11. A. Huser and S. Biringen, 1993,"Direct Numerical Simulation of turbulent flow in a square duct," J. Fluid Mech. 257, 67-95.

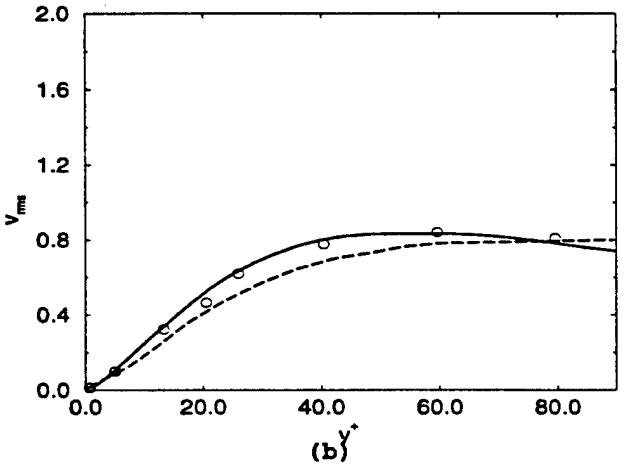
12. J. Kim, P. Moin and R. Moser, 1987, "Turbulence statistics in fully developed channel flow at low Reynolds number," J. Fluid. Mech., 177, 133.

13. M.M. Rai and P. Moin, 1991, "Direct simulation of turbulent flow using finite difference schemes." J. Comp. Phys. 96, 15.

14. S. Menon and V.K. Chakravarthy, 1996, "Large eddy simulation of premixed flames in Couette flow," AIAA paper 96-3077, 32nd AIAA/ASME/SAE/ASEE Joint Propulsion Conference, July 1-3,1996.

15. R.K. Madabhushi and S.P.Vanka, 1991, "Large eddy simulation of turbulence driven secondary flow in a square duct", Phys. Fluids A 3(11), 2734.





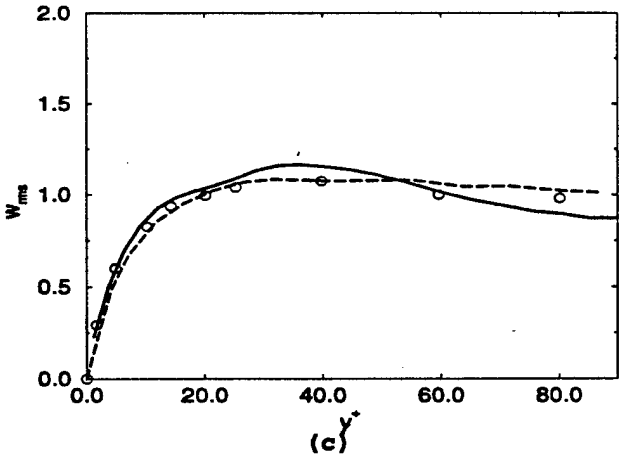


Figure 1: Comparison of rms velocity fluctuations at the mid-section of the duct.
Solid line:LES, dashed line:DNS(Huser and Biringen [11])
O: DNS (Kim and Moin [12])

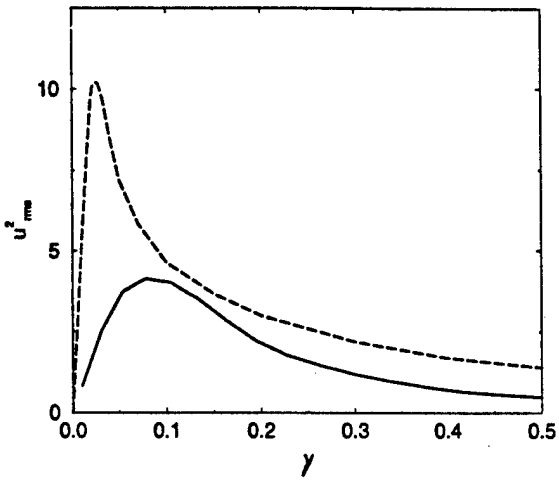


Figure.2a : Variation of axial velocity variance of along the wall bisector
——— LES, - - - - DNS (Huser et al.)

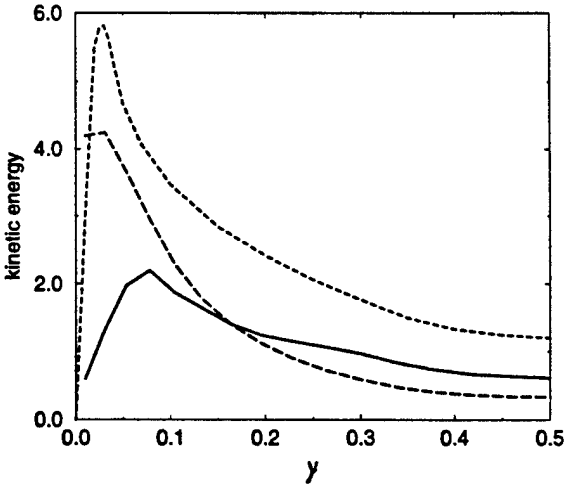


Figure.2b: Variation of turbulent kinetic energy along the wall bisector
——— LES(resolved),— — · LES(subgrid)
- - - - - DNS(Huser and Biringen [11])

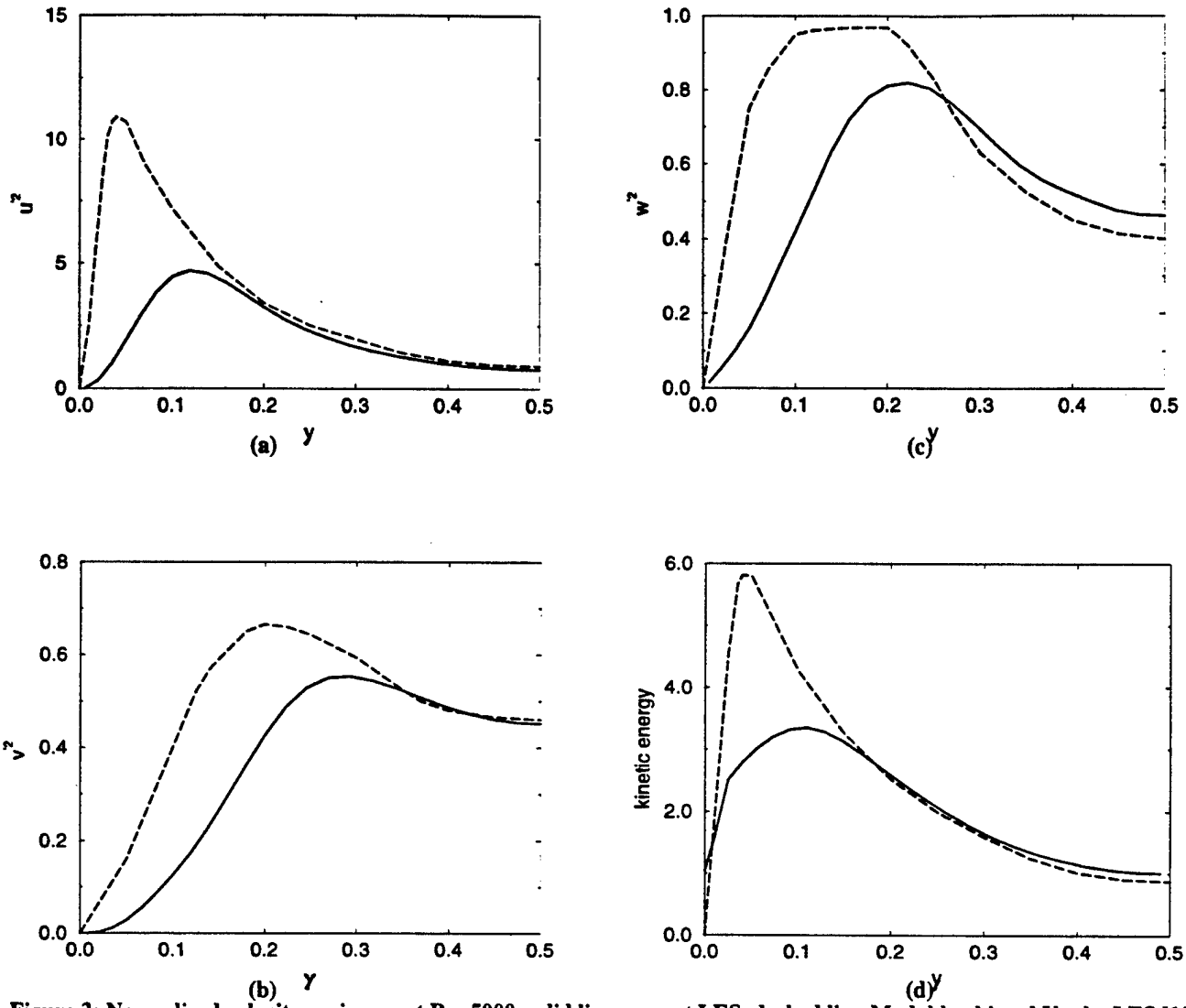


Figure 3: Normalized velocity variances at Re=5000, solid line:present LES, dashed line:Madabhushi and Vanka LES [15]

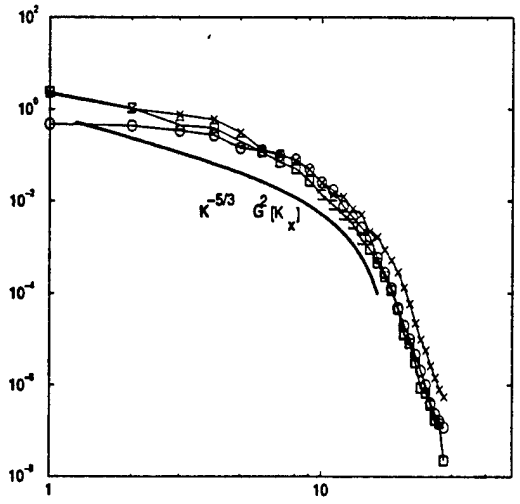


Figure 4: 1-D spectrum along the stream
○ point 1, □ point2, x point 3

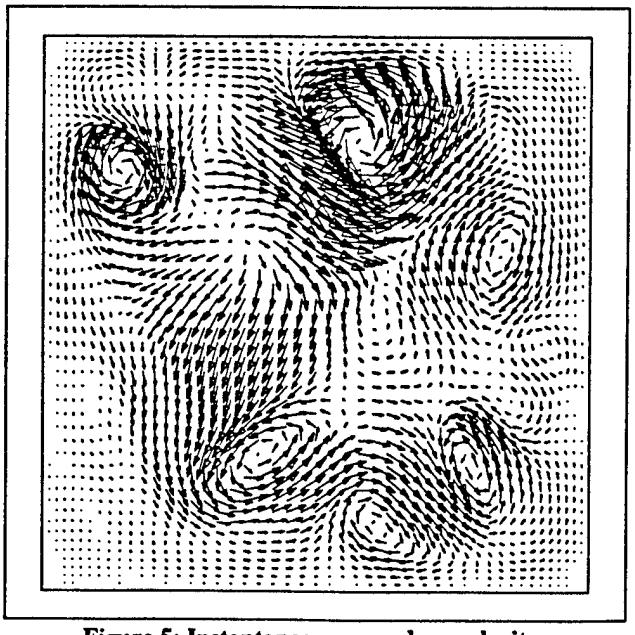


Figure 5: Instantaneous secondary velocity field in the cross-plane



AIAA 97-0210
Application of the Localized Dynamic Subgrid-Scale Model to Turbulent Wall-Bounded Flows

W.-W. Kim and S. Menon
School of Aerospace Engineering
Georgia Institute of Technology
Atlanta, GA 30332-0150

35th Aerospace Sciences Meeting & Exhibit
January 6-10, 1997 / Reno, NV

For permission to copy or republish, contact the American Institute of Aeronautics and Astronautics
1801 Alexander Bell Drive, Suite 500, Reston, VA 22091

APPLICATION OF THE LOCALIZED DYNAMIC SUBGRID-SCALE MODEL TO TURBULENT WALL-BOUNDED FLOWS

Won-Wook Kim*and Suresh Menon†
School of Aerospace Engineering
Georgia Institute of Technology
Atlanta, Georgia 30332

ABSTRACT

Large-eddy simulation of various turbulent wall-bounded flows such as turbulent plane Couette flows, recirculating flows, and separated flows has been carried out using the localized dynamic subgrid-scale model. The applicability and the capability of the model in predicting the complicated features of turbulent wall-bounded flows have been tested. The results show good agreement with existing computational and experimental data.

1 INTRODUCTION

In previous papers (Kim & Menon, 1995a & b, 1996; Menon & Kim, 1996), the basic formulation of the localized dynamic k_{sgs}-equation model (LDKM) for large-eddy simulation (LES), its properties, and capability were presented. The model has been successfully applied to Taylor-Green vortex flow (Kim & Menon, 1995a), decaying, forced, and rotating isotropic turbulence (Kim & Menon, 1995b), temporally evolving turbulent mixing layer (Kim & Menon, 1996), and some high Reynolds number turbulent flows (Menon & Kim, 1996). In the present study, the model is applied to the simulation of turbulent wall-bounded flows.

The main objective of these consecutive studies is to develop and validate a new dynamic subgrid-scale (SGS) model which is generally applicable to various turbulent flows. We set some requirements which the new model must satisfy: (i) the modeling procedure should be relatively easy to implement in finite-difference codes, (ii) the model should not depend on *ad hoc* procedures, (iii) the computational cost required for actual implementation of the model should not be significant compared to other existing models, and, finally, (iv) the model should be applicable to various kind of flow fields without any adjustment of the model. The LDKM seems to fulfill all of these requirements. Moreover, the localized (both in time and space) model coefficients obtained from this model is proved to be Galilean-invariant and very realizable. In the present study, the properties of the model is further evaluated for turbulent wall-bounded flows.

In section 2, the LDKM is summarized along with a discussion of its salient features. The numerical method employed in this study is briefly described in section 3. In section 4, the LDKM is applied to various turbulent wall-bounded flows, such as turbulent plane Couette flows (section 4.1), recirculating flows (section 4.2), and separated flows (section 4.3). Conclusions are finally presented in section 5.

2 LOCALIZED DYNAMIC k_{sgs}-EQUATION MODEL (LDKM)

In LES, the flow variables are decomposed into a large-scale component (denoted by an overbar) and a small subgrid-scale component by applying a filtering operation:

$$\overline{f}(x_i) = \int f(x_i')G(x_i, x_i')dx_i' \tag{1}$$

where G is the filter function and the integral is extended over the entire domain. Applying the filtering operation (in the present study, a low-pass filter of a computational mesh is used, hence, the characteristic size of this filter is the grid width $\overline{\Delta}$), the incompressible Navier-Stokes equations for the evolution of the large-scale motions are obtained. The resulting governing equations are:

$$\frac{\partial \overline{u}_i}{\partial x_i} = 0 \tag{2}$$

$$\frac{\partial \overline{u}_i}{\partial t} + \overline{u}_j \frac{\partial \overline{u}_i}{\partial x_j} = -\frac{\partial}{\partial x_j}(\overline{p}\delta_{ij} + \tau_{ij}) + \nu \frac{\partial^2 \overline{u}_i}{\partial x_j \partial x_j} \tag{3}$$

where $\overline{u}_i(x_i, t)$ is the resolved velocity field. The effects

*Post-Doctoral Fellow, Member AIAA.
†Associate Professor, Senior Member AIAA.

Copyright © 1997 by W.-W. Kim and S. Menon. Published by the American Institute of Aeronautics and Astronautics, Inc. with permission.

of the unresolved small scales appear in the SGS stress tensor,

$$\tau_{ij} = \overline{u_i u_j} - \overline{u}_i \overline{u}_j \tag{4}$$

that must be modeled.

The LDKM is based on the subgrid-scale kinetic energy

$$k_{sgs} = \frac{1}{2}\left(\overline{u_k u_k} - \overline{u}_k \overline{u}_k\right) \tag{5}$$

which is obtained by solving the following transport equation (Schumann, 1975; Menon *et al.*, 1996)

$$\frac{\partial k_{sgs}}{\partial t} + \overline{u}_i \frac{\partial k_{sgs}}{\partial x_i} = -\tau_{ij}\frac{\partial \overline{u}_i}{\partial x_j} - \varepsilon_{sgs} + \frac{\partial}{\partial x_i}\left(\nu_T \frac{\partial k_{sgs}}{\partial x_i}\right) \tag{6}$$

Here, the three terms on the right hand side represent, respectively, the production, the dissipation, and the diffusion of k_{sgs}. Using k_{sgs}, the SGS stress tensor τ_{ij} is usually modeled as follows,

$$\tau_{ij} = -2C_\tau \overline{\Delta} k_{sgs}^{1/2} \overline{S}_{ij} + \frac{2}{3}\delta_{ij} k_{sgs} \tag{7}$$

where $\overline{S}_{ij}$ is the resolved-scale strain-rate tensor,

$$\overline{S}_{ij} = \frac{1}{2}\left(\frac{\partial \overline{u}_i}{\partial x_j} + \frac{\partial \overline{u}_j}{\partial x_i}\right) \tag{8}$$

Implicit in Eq. (7) is the parameterization of the eddy viscosity ν_T,

$$\nu_T = C_\tau \overline{\Delta} k_{sgs}^{1/2} \tag{9}$$

Here, C_τ is an adjustable coefficient to be determined dynamically. Equation (6) is closed by providing a model for the SGS dissipation rate term, ε_{sgs}. Using simple scaling arguments, ε_{sgs} is usually modeled as

$$\varepsilon_{sgs} = C_\varepsilon \frac{k_{sgs}^{3/2}}{\overline{\Delta}} \tag{10}$$

where, C_ε is another coefficient also to be determined dynamically. In the following, the dynamic procedures for C_τ and C_ε are described.

The test-scale field is constructed from the grid-scale field by applying a test filter which is characterized by $\widehat{\Delta}$ (typically, $\widehat{\Delta} = 2\overline{\Delta}$). The test filter should be consistent with the grid filter. In the present study, the top-hat filter is employed for the test filtering. If the application of the test filter on any variable ϕ is denoted by $\widehat{\phi}$, the test-scale Leonard stress tensor is defined as:

$$L_{ij} = \widehat{\overline{u}_i \overline{u}_j} - \widehat{\overline{u}}_i \widehat{\overline{u}}_j \tag{11}$$

Recently, Liu *et al.* (1994) observed significant similarity between τ_{ij} and L_{ij} by analyzing experimental data obtained in the far field of a turbulent round jet at a reasonably high Reynolds number, $Re_\lambda \approx 310$. The experimental data showed that the correlation between these two stress tensors was quite high. Therefore, they suggested an appropriate SGS model based on this scale similarity: $\tau_{ij} = C_k L_{ij}$ where C_k is an adjustable constant (a value of 0.45 ± 0.15 was suggested by Liu *et al.* (1994) based on experimental data). In the LDKM, this similarity is adopted to dynamically determine the model coefficient.

At the test-filter level, a (numerically) resolved kinetic energy can be defined from the trace of Eq. (11):

$$k_{test} = \frac{1}{2}\left(\widehat{\overline{u}_k \overline{u}_k} - \widehat{\overline{u}}_k \widehat{\overline{u}}_k\right) \tag{12}$$

(note that $k_{test} = L_{kk}/2$). This energy is similar to k_{sgs}, however, it is produced at the large scales by $-L_{ij}(\partial \widehat{\overline{u}}_i/\partial x_j)$ and is dissipated by:

$$e = (\nu + \nu_T)\left(\widehat{\frac{\partial \overline{u}_i}{\partial x_j}\frac{\partial \overline{u}_i}{\partial x_j}} - \frac{\partial \widehat{\overline{u}}_i}{\partial x_j}\frac{\partial \widehat{\overline{u}}_i}{\partial x_j}\right) \tag{13}$$

at the small scales. Here, $(\nu + \nu_T)$ is used in the above expression since k_{test} is fully resolved at the test-filter level and, thus, must be dissipated by both the eddy viscosity and the molecular viscosity (see Kim & Menon (1995b) and Kim (1996) for a detailed discussion on this issue). Obviously, $k_{test}^{1/2}$ is the characteristic velocity scale for both the large- and small-scale energy transfer processes (i.e., the production and the dissipation of k_{test}) and the characteristic length scale of the large-scale energy transfer is $\widehat{\Delta}$ (since this energy transfer occurs at the energy level $\widehat{\overline{u}}_k \widehat{\overline{u}}_k$ and is fully resolved at the test-filter level). However, the characteristic length scale for the dissipation process at the small scales is unknown even though the kinetic energy k_{test} is dissipated at the energy level $\widehat{\overline{u}_k \overline{u}_k}$ (which is located in the resolved-scale range between $\overline{\Delta}$ and $\widehat{\Delta}$). Hence, a closure assumption is needed to model e.

Consider first the closure for τ_{ij}. As noted above, experiments suggest that τ_{ij} and L_{ij} are similar in variation. Furthermore, the above arguments show that $-L_{ij}(\partial \widehat{\overline{u}}_i/\partial x_j)$ is the production term for k_{test} (just as $-\tau_{ij}(\partial \overline{u}_i/\partial x_j)$ is the production term for k_{sgs}). Thus, it is reasonable to assume that similar parameterization can be used to represent τ_{ij} and L_{ij} using appropriately defined parameters. Since τ_{ij} is modeled in terms of grid-resolved quantities, a similar parameterization is considered for L_{ij} as

$$L_{ij} = -2C_\tau \widehat{\Delta} k_{test}^{1/2} \widehat{\overline{S}}_{ij} + \frac{1}{3}\delta_{ij} L_{kk} \tag{14}$$

where all quantities are defined at the test-filter level. (The applicability of the similarity assumption and

the appropriateness of Eq. (14) has been verified in the past by carrying out LES of various flows (Kim & Menon, 1995a & b, 1996; Menon & Kim, 1996).) Now, Eq. (7) contains two unknowns τ_{ij} and C_τ while Eq. (14) contains only C_τ as the unknown. Thus, Eq. (14) can be viewed as an explicit model representation for C_τ in terms of quantities resolved at the test-filter level. Since Eq. (14) is an over-determined system, least-square method suggested by Lilly (1992) is required to obtain C_τ:

$$C_\tau = \frac{1}{2}\frac{L_{ij}\sigma_{ij}}{\sigma_{ij}\sigma_{ij}} \tag{15}$$

where

$$\sigma_{ij} = -\widehat{\Delta}k_{test}^{1/2}\widehat{\overline{S}}_{ij} \tag{16}$$

Here, σ_{ij} is determined completely from quantities at the test-filter level. In actual simulations, the local value of negative C_τ computed from Eq. (15) is limited by $-\nu/(\overline{\Delta}k_{sgs}^{1/2})$ to prevent the total viscosity $(\nu+\nu_T)$ from becoming negative (although this happened very rarely).

Similarity between the dissipation rates ε_{sgs} at the grid-filter level and e at the test-filter level is also invoked in the LDKM to obtain the dissipation model coefficient. Thus, we obtain

$$e = C_\varepsilon \frac{k_{test}^{3/2}}{\widehat{\Delta}} \tag{17}$$

Since Eq. (17) is a single equation with one unknown, C_ε can be determined by combining Eqs. (13) and (17):

$$C_\varepsilon = \frac{\left[\widehat{(\partial\overline{u}_i/\partial x_j)(\partial\overline{u}_i/\partial x_j)} - \left(\partial\widehat{\overline{u}}_i/\partial x_j\right)\left(\partial\widehat{\overline{u}}_i/\partial x_j\right)\right]}{\left[(\nu+\nu_T)\widehat{\Delta}\right]^{-1}k_{test}^{3/2}} \tag{18}$$

As shown above, by adopting the similarity assumption between τ_{ij} and L_{ij}, the LDKM can be formulated without employing any mathematically inconsistent or *ad hoc* procedure (the mathematical inconsistency of Germano *et al.*'s dynamic formulation (1991) and some of its variants (Moin *et al.*, 1991; Wong, 1992; Zang *et al.*, 1993) was pointed out earlier by Cabot & Moin (1993)). There are some more positive aspects to the present approach. The denominators of Eqs. (15) and (18) contain only well defined quantities and, therefore, the ill-conditioning problem (seen in the earlier dynamic models) is significantly relieved (as demonstrated in the numerical studies (Kim & Menon, 1995a & b, 1996; Menon & Kim, 1996)). The prolonged presence of negative model coefficient (Lund *et al.*, 1993) also has been avoided by adopting the SGS kinetic energy. Moreover, the dynamically determined C_ε from Eq. (18) does not have the unphysical property of vanishing at high Reynolds numbers (which was observed in the dynamic formulation of Wong (1992)). From computational standpoint, the cost of the dynamic procedure is not significant (about the same as that for the original dynamic model by Germano *et al.* (1991)) due to its simplicity. The additional computational cost is primarily due to the inclusion of a transport equation for k_{sgs}.

Analysis (Kim & Menon, 1995b; Kim 1996) has shown that this model is Galilean invariant and satisfies the realizability conditions given by (Schumann, 1977; Vreman *et al.*, 1994)

$$\tau_{\alpha\alpha} \geq 0 \tag{19}$$

$$\tau_{\alpha\beta}^2 \leq \tau_{\alpha\alpha}\tau_{\beta\beta} \tag{20}$$

Following inequalities have been derived (Kim & Menon, 1995b; Kim 1996) from Eqs. (19) and (20), respectively,

$$\frac{k_{sgs}^{1/2}}{3\overline{\Delta}\,\overline{S}_{33}} \leq C_\tau \leq \frac{k_{sgs}^{1/2}}{3\overline{\Delta}\,\overline{S}_{11}} \tag{21}$$

$$-\frac{2}{\sqrt{3}}\frac{k_{sgs}^{1/2}}{\overline{\Delta}\,|\overline{S}|} \leq C_\tau \leq \frac{2}{\sqrt{3}}\frac{k_{sgs}^{1/2}}{\overline{\Delta}\,|\overline{S}|} \tag{22}$$

where $|\overline{S}| = \left(2\overline{S}_{ij}\overline{S}_{ij}\right)^{1/2}$ and $\overline{S}_{\alpha\alpha}$ (the summation convention is not applied to Greek subscripts) denote the eigenvalues of the strain-rate tensor which are assumed to be ordered as $\overline{S}_{11} \geq \overline{S}_{22} \geq \overline{S}_{33}$, for convenience. The signs of the eigenvalues of the strain-rate tensor are determined from the incompressibility condition $(\overline{S}_{11}+\overline{S}_{22}+\overline{S}_{33}=0)$ so that the largest eigenvalue $\overline{S}_{11} \geq 0$, the smallest eigenvalue $\overline{S}_{33} \leq 0$, and, $\overline{S}_{22}$ can have either sign. The two conditions, Eqs. (21) and (22), give the realizable range for the dynamically determined model coefficient C_τ. The model coefficient C_τ should, therefore, fall inside this range for the LDKM to become a realizable model of the SGS stress tensor. This was verified by simulating the experiment of decaying isotropic turbulence of Comte-Bellot & Corsin (1971) (the detailed description of this flow field is omitted here for brevity). It was observed that more than 99.9% (for a 48^3 grid resolution), 99.8% (for a 32^3 grid resolution), and 99.6% (for a 24^3 grid resolution) of the grid points satisfy both realizability conditions, Eqs. (21) and (22), at the same time during the entire simulation. Therefore, it appears that the LDKM satisfies the realizability conditions even in a strict sense. In comparison, Ghosal *et al.* (1995) reported that their dynamic localization model (based on the subgrid-scale kinetic energy) satisfied the first

realizability condition, Eq. (21), at about 95% of the grid points in the simulation of this experiment using a 48^3 grid resolution.

The LDKM has not required any adjustment of the model parameters in its application to various turbulent flows including various (decaying, forced, and rotating) isotropic turbulent flows (Kim & Menon, 1995a & b), turbulent mixing-layer (Kim & Menon, 1996), and high Reynolds number flows (Menon & Kim, 1996). Hence, the original formulation of the LDKM is used in the present turbulent wall-bounded flow simulation without any adjustment of the model.

3 Numerical Method

Rai & Moin (1991) suggested a high-order accurate, upwind-biased finite-difference method in order to obtain an adequate accuracy for turbulent flow simulations without losing applicability to complex geometry and simplicity of the scheme. Their approach used a non-conservative form of the unsteady, incompressible Navier-Stokes equations and, hence, it is appropriate only for simulations of flow fields without discontinuity. The present study is limited to such flows and, therefore, a similar methodology is adopted here. For instance, the convective terms are approximated using fifth-order accurate, upwind-biased finite-differences with a seven-point stencil. The viscous terms are computed using central differences by applying the fourth-order accurate, half-points differencing. The velocity derivative terms which are defined at the half-points, are also computed using the same fourth-order accurate finite differences. Thus, the discretization of the viscous terms uses seven grid points and, therefore, the viscous terms are approximated to sixth-order accuracy on uniform grids.

The velocity derivative terms in the continuity equation and the pressure derivative terms in the momentum equations are computed using the regularized central difference scheme originally suggested by Strikwerda (1984) to prevent the pressure-velocity decoupling. In the present study, the scheme is extended to a seven-point stencil, fifth-order accurate approximation (Kim & Menon, in preparation).

In the present study, the pressure field which is required as a part of the solution of the incompressible Navier-Stokes equations, has been obtained using the artificial compressibility method, originally proposed by Chorin (1967). The main advantage of this approach is that by introducing artificial unsteady term into the continuity equation, efficient solution algorithms developed for time-dependent compressible flows can be utilized to compute incompressible flows. In this formulation, the continuity equation is modified by adding a pseudo-time derivative of the pressure term which results in a hyperbolic-parabolic type of time-dependent equations together with the unsteady momentum equations. The time-accurate capability is obtained by adding pseudo-time velocity derivatives to the momentum equations (e.g., Rogers & Kwak, 1989). In this unsteady formulation, the governing equations are marched in the pseudo time (i.e., subiterated) until the divergence-free flow field is obtained. Therefore, the artificial compressibility does not corrupt the physical-time solution as long as the pseudo-time solution converges to a steady state at each physical-time level. The integration in the pseudo time is carried out by an explicit 5-stage Runge-Kutta time-stepping scheme. The physical-time derivatives in the momentum equations are computed using a second-order, backward difference that results in an implicit scheme.

To accelerate the convergence in pseudo-time, efficient acceleration techniques for explicit steady-state solvers, such as local time-stepping, residual smoothing, and multigrid method (based on the full approximation storage (FAS) scheme as proposed by Brandt (1981)) are employed. In practice, a solution is considered converged if the root-mean-square of the pressure and velocity changes decrease less than 10^{-6}, since, in most cases, further iterations to reduce these quantities do not change the solution. Both the eddy viscosity and the model coefficients are computed at each pseudo-time step. Usually, the model coefficients adjust themselves quickly and remain almost constant during pseudo-time iterations.

4 Results and Discussion

The LDKM has been applied to turbulent plane Couette flows (section 4.1), turbulent recirculating flows (section 4.2), and turbulent separated flows (section 4.3). In the following, the results from these simulations are discussed.

4.1 Turbulent plane Couette flows

Turbulent plane Couette flows are driven by shear generated at two infinite flat walls which are in rectilinear, parallel movement relative to each other. A distinguished feature of the flows is that they have a constant shear stress across the entire channel (all other turbulent shear flows near walls have a thin constant shear stress layer very close to the wall). In plane Couette flows, (since most of turbulent energy production occurs in the constant shear stress layer) turbulence production is finite across the channel (even though it still has a maximum close to the wall), whereas in channel flows maximum turbulence production occurs close to the wall and then rapidly decreases towards zero at the channel centerline. This feature of these flows is a direct consequence of zero mean pressure

gradient throughout the flows and makes them significantly different from pressure-driven shear flows.

The experiments of Bech *et al.* (1995) and Aydin & Leuthersser (1987, 1991) were simulated. In the simulations, only the upper wall (at $y/h = 1$) was moving with a constant velocity U_w while the lower wall (at $y/h = -1$) was fixed. The chosen Reynolds numbers $\mathrm{Re} = U_w h/\nu$ (where h is the channel half-height) were 2600 and 4762, while the Reynolds number $\mathrm{Re}_\tau = U_\tau h/\nu$ based on the wall-shear velocity $U_\tau = (\nu dU/dy|_{wall})^{1/2}$ were 81 and 133, respectively. The computational domain was $4\pi h \times 2h \times 2\pi h$ in the streamwise, normal, and spanwise directions, respectively. The grid resolution was $48 \times 48 \times 32$ with uniform spacing in the streamwise and spanwise directions, while in the normal direction, the grid was stretched using a 6% (Re =2600) and 9% (Re =4762) linear stretching in order to improve the resolution in the near-wall regions. Computational meshes are around $21.1\Delta y^+$ (Re =2600) and $34.2\Delta y^+$ (Re =4762) in the streamwise direction, $15.8\Delta y^+$ (Re =2600) and $25.7\Delta y^+$ (Re =4762) in spanwise direction, and the resolutions in the normal direction are $\Delta y^+ = 1.6$ (Re =2600) and $\Delta y^+ = 1.7$ (Re =4762) next to the wall with stretching that reaches a maximum of $6.1\Delta y^+$ (Re =2600) and $12.4\Delta y^+$ (Re =4762). At the wall-boundaries, no-slip conditions were used and in the homogeneous (streamwise and spanwise) directions, periodic conditions were imposed. The initial field was constructed of the laminar mean velocity profile with finite-amplitude velocity fluctuations superimposed. After about $150h/U_w$, the flow reaches a statistically steady state. Statistics were obtained by ensemble-averaging for another $55h/U_w$ (Re =2600) and $42h/U_w$ (Re =4762).

Before time-averaged statistics obtained from the LES are presented, it is worthwhile to describe how the (time-averaged) Reynolds stresses are calculated from the LES field. By ensemble-averaging the LES governing equations (3), the Reynolds stresses are defined as follows,

$$R_{ij} = \widetilde{\overline{u_i}\overline{u_j}} - \widetilde{\overline{u}}_i\widetilde{\overline{u}}_j \qquad (23)$$

where "$\sim$" denotes ensemble-averaging. In the above expression, $\overline{u_i u_j}$ is an unknown quantity but it can be estimated using the SGS model, i.e., $\overline{u_i u_j} = \tau_{ij}^{\mathrm{model}} + \overline{u}_i\overline{u}_j$. A common mistake in calculating the turbulence intensities is the usage of $u_{rms} = (\widetilde{\overline{u}\,\overline{u}} - \widetilde{\overline{u}}\,\widetilde{\overline{u}})^{0.5}$ instead of $u_{rms} = (\widetilde{\overline{u}\,\overline{u}} - \widetilde{\overline{u}}\,\widetilde{\overline{u}})^{0.5}$. In this case, the SGS contribution to the turbulence intensities will be totally neglected.

Figure 1(a) and (b) shows the mean velocity distribution from the simulation at Re =2600. For comparison, experimental data obtained by Aydin & Leutheusser (1987) at Re =2600 and Bech *et al.* (1995) at Re =2520, and direct numerical simulation (DNS) results by Bech *et al.* (1995) at Re =2600 are also plotted in figure 1(a). The DNS (Bech *et al.*, 1995) was carried out using the $256 \times 70 \times 256$ grid resolution. The agreement between the LES and the experimental data is excellent both in the wall region and in the center of the channel. In figure 1(b), the mean velocity is plotted in a semi-logarithm form, normalized by the viscous scales. As shown, the velocity profile is clearly divided into a viscous sublayer, a buffer region, and a logarithm part. For comparison, the following universal velocity-distribution law for smooth wall conditions is also plotted,

$$U^+ = A \ln y^+ + B \qquad (24)$$

where $U^+ = U/U_\tau$, $y^+ = yU_\tau/\nu$ and A is the inverse of the von Kármán constant. The constants appearing in the equation have the universal values: A =2.5 and B =5.5. The LES results align well with the straight line with only small deviations. The logarithmic region extends to the center of the channel, a feature observed in the experiments and also captured here.

In figure 2, turbulence intensities obtained from LES, DNS, and experiments are shown (only the moving wall part of the LES results are presented). The LES results show overall good agreement with the DNS and experimental data except for some deviations of the normal component in the region close to the wall. The highest intensity is observed in the streamwise component which has a maximum at $y^+ \approx 13$ whereas (unlike the plane Poiseuille flow) the other components monotonically increase to a constant value in the center of the channel. In the present simulation, the ratio of the velocity fluctuations $v_{rms}/u_{rms} \approx 0.65$ is obtained (this value lies in between the value of 0.6 obtained by Aydin & Leuthersser (1991) and the value of 0.67 obtained by Bech *et al.* (1995)).

Figures 3 and 4 show the profiles of the mean velocity and the turbulence intensities, respectively, for Re =4762 together with the experimental data of Aydin & Leuthersser (1987, 1991). LES predicts quite well the mean velocity distribution, while the predicted level of the streamwise intensity shows some deviations from the experimental data.

Figure 5 shows the time-averaged profile of the subgrid-scale kinetic energy across the channel. For Re =2600, the peak of the SGS kinetic energy is located at $y^+ \approx 21$, that is, the peak of the SGS fluctuation is somewhat shifted towards the center of the channel than the resolved-scale fluctuation. This is because the small-scale fluctuations are more easily dissipated by the wall-damping than the large-scale fluctuations. As expected, the Re =4762 case has a higher level of the SGS kinetic energy than the Re =2600 case.

In figure 6(a), the time-averaged distribution of

the model coefficient is plotted. Without employing the exponential damping of Van Driest (1956), the smooth variation of the model coefficient is obtained close to the wall. When approaching the core region, the model coefficient monotonically increase to a constant level (≈ 0.055) which matches well with the value predicted by the forced isotropic turbulence simulation at high Reynolds number (Kim & Menon, 1995b; Kim, 1996). Figure 6(b) shows the time-averaged distribution of the dissipation model coefficient. Close to the wall, the dissipation model coefficient rapidly increases indicating the pronounced effects of the small-scale dissipation, however, it approaches a constant level in the core region.

In figure 7, the model coefficient distribution is redrawn in a logarithm form to closely examine the model behavior in the wall region. This figure confirms the exponential decay in the wall region. The constant model coefficient (here, 0.055 is used to match with the present calculation at the core region) distributions are also plotted combined with the exponential damping function as proposed by Moin & Kim (1982),

$$C_\tau = 0.055[1 - \exp(-y^+/A^+)] \qquad (25)$$

and by Piomelli *et al.* (1987),

$$C_\tau = 0.055[1 - \exp(-(y^+)^3/(A^+)^3)]^{1/2} \qquad (26)$$

with wall damping constant $A^+ = 25$. These damping functions were determined from *a priori* test (where the exact SGS quantities are calculated from exact DNS data and then the modeled quantities are evaluated by comparing with the exact ones). In most cases, however, the results obtained from the *a priori* test can not be confirmed by *a posteriori* test (where the SGS models are actually implemented in an LES code and then the results of the simulation are evaluated) since, in *a priori* test, the results are obtained by completely ignoring the dynamics at the cut-off. The present results also show some discrepancies with the damping functions based on *a priori* test. According to the results based on *a posteriori* test using the LDKM, the following damping function seems to represent more accurately the distribution of model coefficient in the wall region,

$$C_\tau = 0.055[1 - \exp(-(y^+)^2/(A^+)^2)] \qquad (27)$$

4.2 TURBULENT RECIRCULATING FLOWS

The experiment of lid-driven three-dimensional cavity flows of Prasad & Koseff (1989) is simulated. In the experiment, the three-dimensional cavity has square cross section (i.e., width (B) = depth (D)) and spanwise aspect ratio (i.e., L/B where L is the cavity span) of 0.5:1. The lid (the top wall) is moving at a velocity U_B and the other walls (i.e., the upstream and downstream walls which are perpendicular to the streamwise (x-) direction, the bottom wall which is perpendicular to the vertical (y-) direction, and the end walls which are perpendicular to the spanwise (z-) direction), remain stationary. Hence, fluid motions are developed by the shear of the lid, resulting in a complicated three-dimensional flow field consisting of a stationary primary vortex and a number of complex secondary corner vortices. In these flows, the Reynolds number is usually defined to be $U_B B/\nu$. Koseff & Street (1984) have shown that at Reynolds number higher than about 6000, instability occurs near the downstream corner vortex. As the Reynolds number increases, the flow becomes increasingly turbulent near walls, and at Reynolds numbers higher than 10000, the flow near the downstream corner vortex becomes fully turbulent. In the present study, the Reynolds number of 10000 is considered. Therefore, the present case belongs to the locally turbulent regime.

Using conventional 'constant-coefficient' SGS models or even using most of the existing dynamic models which require spatial averaging for numerical stability, successful simulation of these flows is difficult since these flows are highly inhomogeneous. Only the SGS model which is capable of adjusting itself in a localized manner to the local flow dynamics, can successfully parameterize these flows. Therefore, this problem is considered a good test case for the validation of localized dynamic models. Zang *et al.* (1993) have tested their local-averaging technique in which the model coefficient field is test-filtered, by applying it to this problem. However, their approach neither can be physically justified nor can guarantee the numerical stability for the general problems.

The simulation has been carried out using a $64 \times 64 \times 32$ grid, which is stretched in the streamwise and vertical directions using 6.5% and 13.4% linear stretchings, respectively, but is uniform in the spanwise direction (i.e., grids are not clustered near the side walls). Small random velocity perturbations are initially prescribed to prevent the initial k_{sgs} field from becoming zero. The computation was first conducted with a 32^3 grid. After the flow was fully developed, the coarser-resolution field was interpolated onto the finer-resolution field. Simulation was then continued and statistics were collected after a sufficient relaxation time.

The three-dimensional flow in a cubic cavity has a very complex structure. The main structure of the flow is similar to that in a two-dimensional square cavity but is significantly more complicated due to the end walls. In planes perpendicular to the z-direction, the flow field consists of a primary vortex with two corner vortices at the bottom wall and a vortex at the top

upstream corner. The strengths of these vortices vary with the distance from the end walls. In the mid-plane, the strengths of the vortices are strongest due to the viscous damping at the end walls. In planes perpendicular to the x-direction, the flow field also consists of various vortices. The complete details of the observed three-dimensional flow field are not presented here for brevity. Only a figure of the time-averaged velocity vector field in the mid-plane is given in figure 8. This figure shows the typical flow pattern of lid-driven cavity flows.

Figure 9 shows the computed mean streamwise ($U-$) and vertical ($V-$) velocity profiles on the center-lines in the mid-plane. Measurements by Prasad & Koseff (1989) are given for comparison. LES results from Zang *et al.* (1993), which were obtained using the dynamic mixed model (DMM) on the same grid resolution ($64 \times 64 \times 32$), are also shown. The DMM was formulated by employing the mixed model (where the eddy-viscosity model is combined with the scale-similarity term to parameterize the SGS stress) as the base model and, therefore, does not require alignment of the SGS stress tensor and the strain rate tensor. As mentioned earlier, in this dynamic procedure, the model coefficient was calculated locally by test-filtering the model coefficient field. Zang *et al.* (1993) have demonstrated the superiority of the DMM over the conventional dynamic Smagorinsky model of Germano *et al.* (1991) by showing a better agreement of fluctuating velocity statistics with experiments in the simulation of the recirculating flows at $Re = 7500$. As shown in the figure, the predicted profiles by the LDKM and the DMM are very close to each other and agree very well with the experimental data except that both calculations overpredict the maximum vertical velocity and the thickness of the boundary layers on the upstream wall ($x/B = 0$).

The root-mean-square (rms) of fluctuating velocities on the center-lines in the mid-plane are shown in figure 10. Note that this is multiplied by a factor of 10 for a better presentation. Both calculations show a good overall agreement with the experiment although they both underpredicted the magnitude of the peaks. It is interesting to note that the LDKM computation captures the two humps in the experimental profile on the upstream wall (at $x/B \approx 0$) with reasonable accuracy while the DMM prediction shows only one hump.

Figure 11 displays the center-line Reynolds stress profiles on the mid-plane. This quantity is also magnified by a factor of 500 for a presentation purpose. Both LES's predict the profiles fairly accurately. The LDKM gives a better agreement with the experiment than the DMM in the profiles along the bottom half of the vertical center-line and near the downstream wall ($x/B = 1$) but it overpredicts the Reynolds stress near the upstream wall.

The time-averaged SGS kinetic energy on the center-line in the mid-plane is shown in figure 12. It is observed that the SGS kinetic energy is relatively large near the bottom of the vertical center-line indicating that turbulence is generated near the downstream corner vortex (i.e., near the corner of the downstream and the bottom walls).

In figure 13, the center-line distributions on the mid-plane of the time-averaged model coefficients C_τ (a) and C_ϵ (b) are plotted. As is shown, negative C_τ appears in extended regions (especially, along the vertical center-line) indicating the occurrence of energy backscatter in those regions. C_ϵ is distributed similarly as in the turbulent plane Couette flow case. It has peaks near walls.

4.3 Turbulent separated flows

In the present study, the applicability of the LDKM to separated flows was tested by simulating a weakly separated turbulent boundary layer which was also studied by Coleman & Spalart (1993) using DNS. However, it was difficult to exactly duplicate the (streamwise) boundary conditions employed for the DNS (these boundary conditions were originally introduced by Spalart & Watmuff (1993) for the study of turbulent boundary layers in the presence of pressure gradients). In their approach, periodic conditions were applied along the streamwise direction combined with some extra terms added to the equations (hence, the governing equations are no longer the Navier Stokes equations) in a so-called 'fringe region'. These extra terms were defined in spectral space and, therefore, it is difficult to duplicate them in a physical space code.

Here, periodic conditions were applied with an extended computational domain along the streamwise direction (the present computational domain along the streamwise direction was almost twice as large as the DNS domain of Coleman & Spalart (1993)) to recover the upstream turbulence. The required grid resolution for this extended domain was minimized by using a linearly stretched grid. However, it was found that the effects of the separation bubble could not be fully removed from the reentry flow even with this fairly extended recovery region. And, it was also found that the domain could not be further extended since the boundary layer thickness increased sufficiently to invalidate the periodic boundary conditions. Therefore, the present simulation is not fully compatible with Coleman & Spalart's (1993) DNS as the separation bubble effects are fed back upstream of separation. Moreover, a reasonable statistically-steady-state could not be obtained in the present approach. Therefore, the results of this simulation are not presented here (see Kim (1996) for a qualitative discussion on the re-

sults). Figure 14 shows the instantaneous vorticity magnitude isosurfaces (only the region near the separation bubble is shown). Highly three-dimensional structures are seen even though the mean flow may have a predominantly two-dimensional nature.

The LDKM still needs to be tested in the simulation of separated flows using a well-defined test case. Turbulent flow over a backward-facing step seems to be an excellent choice for further validation of the model since, in this flow, the isolated phenomena of separation can be studied using well-defined boundary conditions. This is an issue under consideration

5 CONCLUSIONS

In the simulation of the turbulent Couette flows, the LDKM has demonstrated its capability by capturing correctly the behavior near solid walls without any adjustments of the model. The mean velocity distribution and turbulent intensities were very accurately predicted and compared well with the existing experimental and DNS data. It was also shown that the prediction of the mean velocity profile confirmed the universal velocity-distribution law for smooth wall conditions clearly showing the division into a viscous sublayer, a buffer region, and a logarithm part. Furthermore, the (time-averaged) dynamically determined model coefficients showed correct asymptotic behaviors near solid walls by confirming the exponential decay suggested by Van Driest (1956). However, the damping function determined from the present LES data was different with the damping functions estimated based on *a priori* test using DNS data.

The simulation of the (locally-) turbulent recirculating flows compares well with the experiment and the existing computation using the dynamic mixed model. The LDKM shows overall good agreement with the experimental data and in some aspects, better than the dynamic mixed model (which was proved to work better than the conventional dynamic Smagorinsky model in the similar recirculating flow simulation). Since these flows above the critical Reynolds number ($Re \approx 6000$) are known to be highly inhomogeneous, these fairly accurate results demonstrate that the LDKM is capable of adjusting itself to the local flow dynamics.

In the simulation of the turbulent separated flows, no difficulty has been found in the application of the LDKM to the chosen separated flow. The prediction of separation by the LDKM seems to be qualitatively correct. However, due to the ambiguity of the imposed boundary conditions, it was difficult to evaluate the present results against the existing DNS data, hence, no conclusions on the model performance have been drawn.

While more study may still need to be done to fully validate the general applicability of the LDKM to the simulation of complex, high-Reynolds number turbulent flows, the LDKM has demonstrated great success in predicting various turbulent flows. At this point, it appears that the LDKM has the potential to be a generally applicable SGS model without any adjustment of the model parameters.

ACKNOWLEDGMENT

This work was supported by the Fluid Dynamics Division of the Office of Naval Research under grant N00014-93-1-0342, monitored by Dr. L. P. Purtell. Computing time was provided by the DoD High Performance Computing (HPC) Centers: Army Research Laboratory (ARL), Naval Oceanographic Office (NAVOCEANO), and Army Engineer Waterways Experiment Station (CEWES).

REFERENCES

Aydin, E. M. & Leutheusser, H. J. 1987 Experimental investigation of turbulent plane Couette flow. *ASME Forum on Turbulent Flows, FED* v. 51, p. 51.

Aydin, E. M. & Leutheusser, H. J. 1991 Plane-Couette flow between smooth and rough walls. *Exps Fluids* **11**, 302.

Bech, K. H., Tillmark, N., Alfredsson, P. H. & Andersson, H. I. 1995 An investigation of turbulent plane Couette flow at low Reynolds numbers. *J. Fluid Mech.* **286**, 291.

Brandt, A. 1981 Guide to multigrid development. In *Lecture Notes in Mathematics* v. 960. Springer-Verlag, p. 220.

Cabot, W. H.. & Moin, P. 1993 Large eddy simulation of scalar transport with the dynamic subgrid-scale model. In *Large Eddy Simulation of Complex Engineering and Geophysical Flows* (ed. B. Galperin & S. A. Orszag). Cambridge University Press, p. 411.

Chorin, A. J. 1967 A numerical method for solving incompressible viscous flow problems. *J. Comput. Phys.* **2**,12.

Coleman, G. N. & Spalart, P. R. 1993 Direct numerical simulation of a small separation bubble. In *Near-Wall Turbulent Flows* (ed. R. M. C. So, C. G. Speziale & B. E. Launder). Elsevier Science Publishers B. V., p. 277.

Comte-Bellot, G. & Corsin, S. 1971 Simple Eulerian time correlation of full- and narrow-band velocity signals in grid-generated, 'isotropic' turbulence. *J. Fluid Mech.* **48**, 273.

Germano, M., Piomelli, U., Moin, P. & Cabot, W. H. 1991 A dynamic subgrid-scale eddy viscosity model. *Phys. Fluids* A **3**, 1760.

Ghosal, S., Lund, T. S., Moin, P. & Akselvoll, K. 1995 A dynamic localization model for large-eddy simulation of turbulent flows. *J. Fluid Mech.* **286**, 229.

Kim, W.-W. 1996 A New Dynamic Subgrid-Scale Model for Large-Eddy Simulation of Turbulent Flows. Ph. D. Thesis, School of Aerospace Engineering, Georgia Institute of Technology, Atlanta, Georgia.

Kim, W.-W. & Menon S. 1995a A new dynamic one-equation subgrid-scale model for large-eddy simulations. *AIAA Paper 95-0356, AIAA 33rd Aerospace Sciences Mtg, Reno, NV.*

Kim, W.-W. & Menon S. 1995b On the properties of a localized dynamic subgrid-scale model for large-eddy simulations. Submitted to *J. Fluid Mech.*.

Kim, W.-W. & Menon S. 1996 On the time-accurate numerical simulations of temporally evolving turbulent mixing layers. Submitted to *AIAA J.*.

Koseff, J. R. & Street, R. L. 1984 Visualization studies of a shear driven three-dimensional recirculating flow. *J. Fluids Eng.* **106**, 21.

Lilly, D. K. 1992 A proposed modification of the Germano subgrid-scale closure method. *Phys. Fluids* **4**, 633.

Liu, S., Meneveau, C. & Katz, J. 1994 On the properties of similarity subgrid-scale models as deduced from measurements in a turbulent jet. *J. Fluid Mech.* **275**, 83.

Lund, T. S., Ghosal, S. & Moin, P. 1993 Numerical experiments with highly-variable eddy viscosity models. In *Engineering Applications of Large Eddy Simulations* (ed. U. Piomelli & S. Ragab). ASME-FED v. 162, p. 7.

Menon, S., Yeung, P.-K. & Kim, W.-W. 1996 Effect of subgrid models on the computed interscale energy transfer in isotropic turbulence. *Comput. Fluids*, **25**, 165.

Menon, S., & Kim, W.-W., "High Reynolds Number Flow Simulations Using the Localized Dynamic Subgrid-Scale Model," AIAA Paper 96-0425, Jan. 1996.

Moin, P. & Kim, J. 1982 Numerical investigation of turbulent channel flow. *J. Fluid Mech.* **118**, 341.

Moin, P., Squires, K., Cabot, W. & Lee, S. 1991 A dynamic subgrid-scale model for compressible turbulence and scalar transport. *Phys. Fluids* A **3**, 2746.

Piomelli, U., Ferziger, J. H. & Moin, P. 1987 Models for large eddy simulations of turbulent channel flows including transpiration. Report TF-32, Stanford University, Dept. of Mechanical Engineering.

Prasad, A. K. & Koseff, J. R. 1989 Reynolds number and end-wall effects on a lid-driven cavity flow. *Phys. Fluids* A **1**, 208.

Rai, M. M. & Moin, P. 1991 Direct simulations of turbulent flow using finite-difference schemes. *J. Comput. Phys.* **96**, 15.

Rogers, S. E. & Kwak, D. 1989 Numerical solution of the incompressible Navier-Stokes equations for steady and time-dependent problems. *AIAA Paper 89-0463.*

Schumann, U. 1975 Subgrid scale model for finite difference simulations of turbulent flows in plane channels and annuli. *J. Comput. Phys.* **18**, 376.

Schumann, U. 1977 Realizability of Reynolds-stress turbulence models. *Phys. Fluids* **20**, 721.

Spalart, P. R. & Watmuff, J. H. 1993 Experimental and numerical study of a turbulent boundary layer with pressure gradients. *J. Fluid Mech.* **249**, 337.

Strikwerda, J. C. 1984 Finite difference methods for the Stokes and Navier-Stokes equations. *SIAM J. Sci. Stat. Comput.*, **5**, 56.

Van Driest, E. R. 1956 On the turbulent flow near a wall. *J. Aerospace Sci.* **23**, 1007.

Vreman, B., Geurts, B. & Kuerten, H. 1994 Realizability conditions for the turbulent stress tensor in large-eddy simulation. *J. Fluid Mech.* **278**, 351.

Wong, V. C. 1992 A proposed statistical-dynamic closure method for the linear or nonlinear subgrid-scale stresses. *Phys. Fluids* A **4**, 1080.

Zang, Y., Street, R. L. & Koseff, J. R. 1993 A dynamic mixed subgrid-scale model and its application to turbulent recirculating flows. *Phys. Fluids* A **5**, 3186.

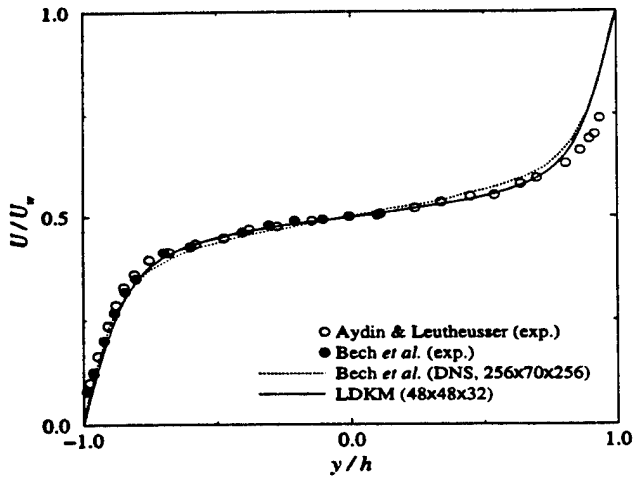


Fig. 1(a) Mean velocity distribution obtained from turbulent plane Couette flow simulation at Re=2600.

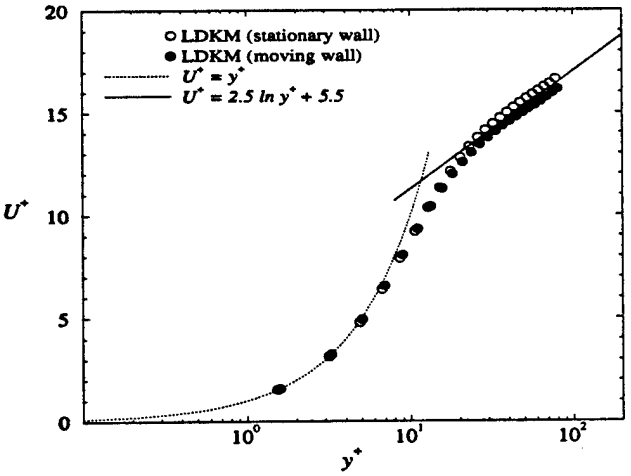


Fig. 1(b) Mean velocity distribution in a semi-logarithm form normalized with viscous scales obtained from turbulent plane Couette flow simulation at Re=2600.

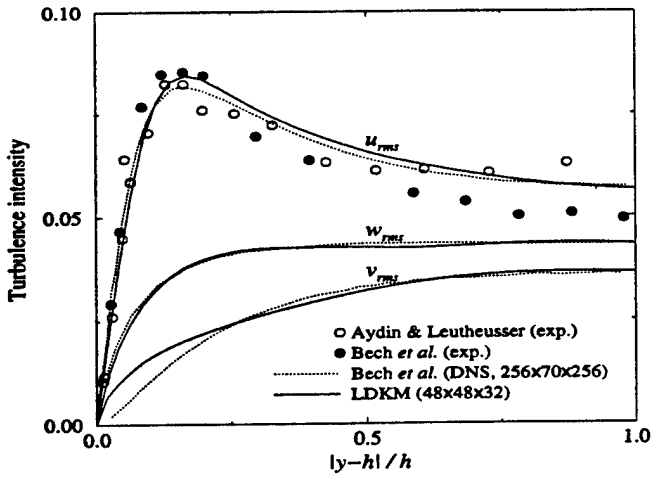


Fig. 2 Turbulence intensities obtained from turbulent plane Couette flow simulation at Re=2600.

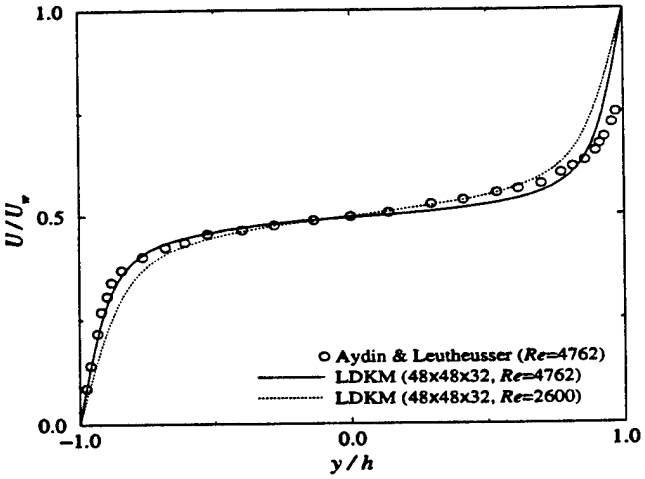


Fig. 3 Mean velocity distribution obtained from turbulent plane Couette flow simulation at Re=4762.

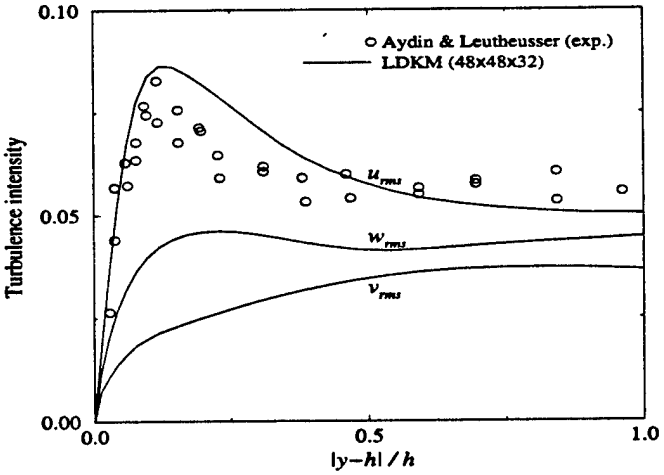


Fig. 4 Turbulence intensities obtained from turbulent plane Couette flow simulation at Re=4762.

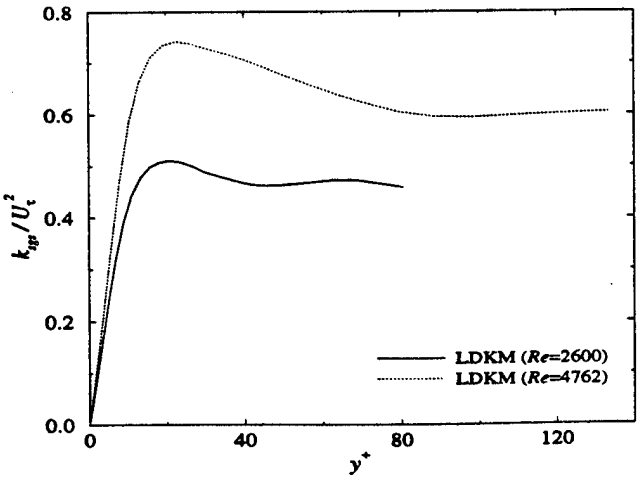


Fig. 5 Time-averaged profile (across the channel) of SGS kinetic energy (normalized with viscous scales) obtained from turbulent plane Couette flow simulation.

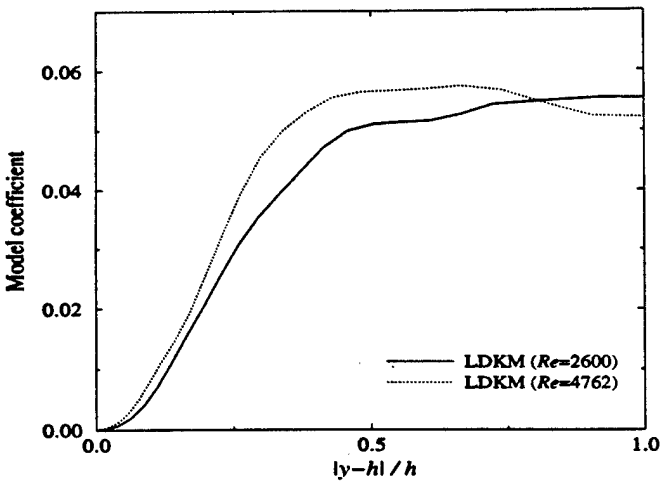


Fig. 6(a) Time-averaged distribution (across the channel) of the model coefficient (normalized with viscous scales) obtained from turbulent plane Couette flow simulation.

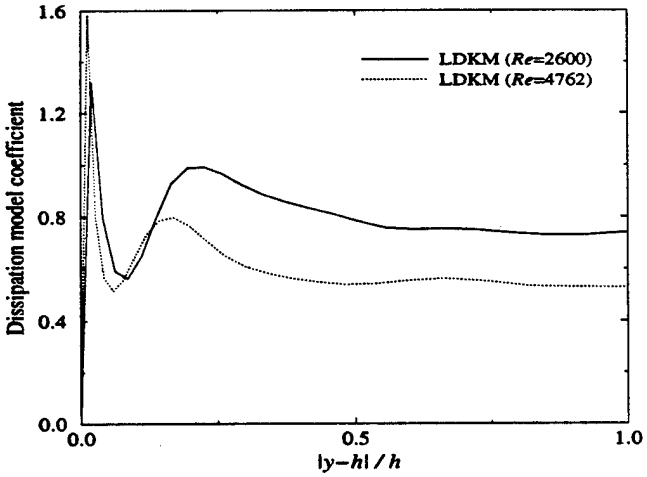


Fig. 6(b) Time-averaged distribution (across the channel) of the dissipation model coefficient (normalized with viscous scales) obtained from turbulent plane Couette flow simulation.

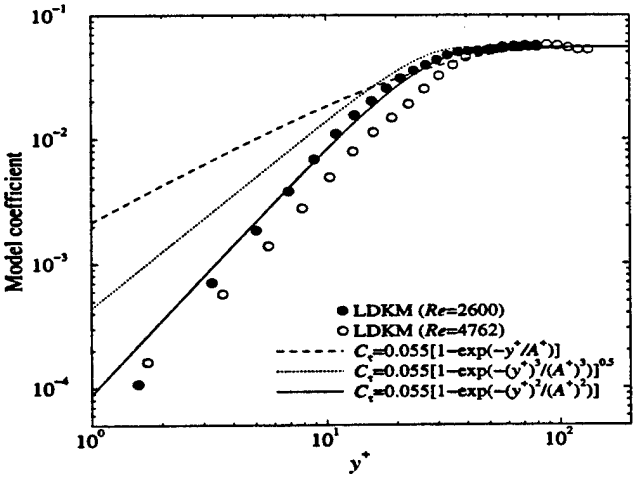


Fig. 7 Time-averaged distribution (across the channel) of the model coefficient in a logarithm form (normalized with viscous scales) from turbulent plane Couette flow simulation.

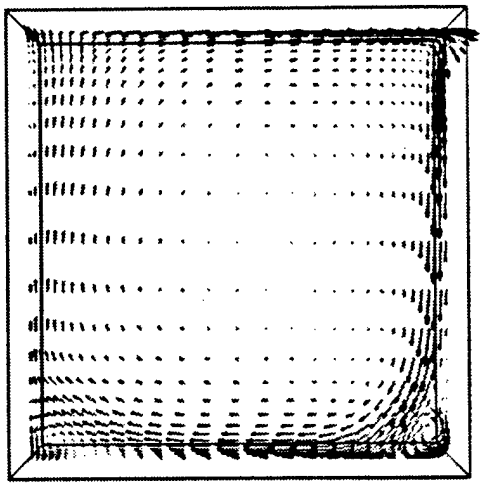


Fig.8 Time-averaged velocity vector field in the mid-plane obtained from turbulent recirculating flow simulation at Re=10000.

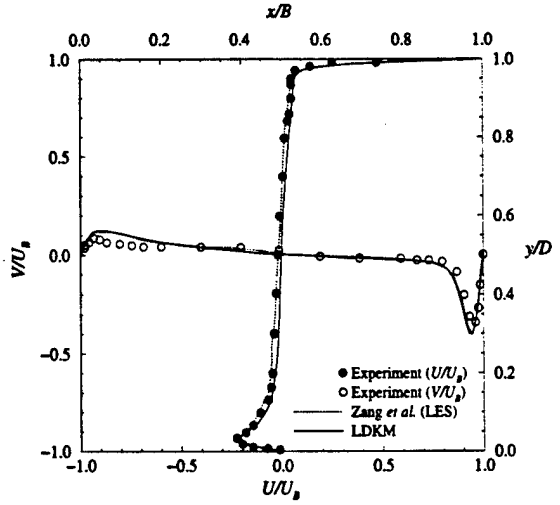


Fig. 9 Mean velocity distributions on the center-lines in the mid-plane obtained from turbulent recirculating flow simulation at Re=10000.

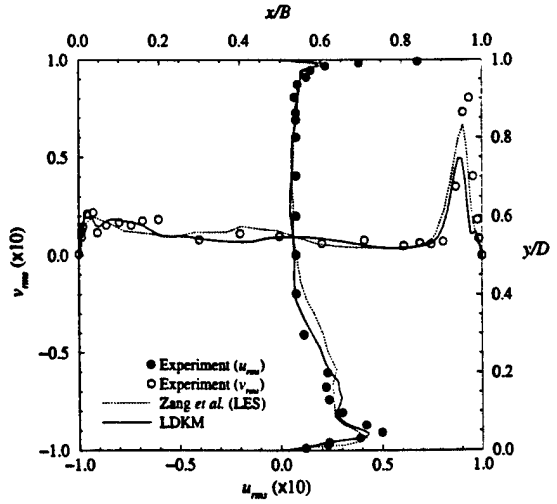


Fig. 10 Turbulence intensities on the center-lines in the mid-plane obtained from turbulent recirculating flow simulation at Re=10000.

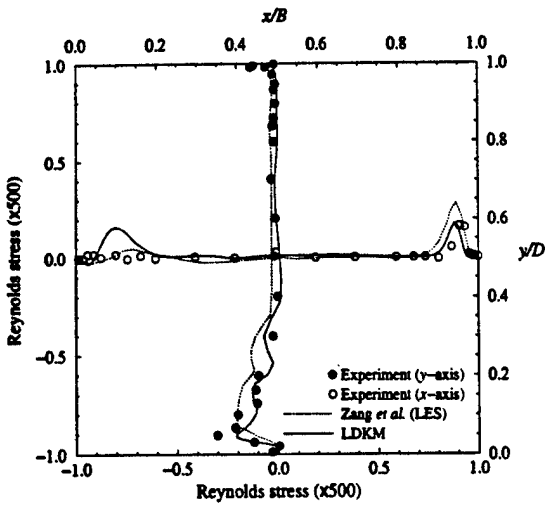


Fig. 11 Reynolds stress profiles on the center-lines in the mid-plane obtained from turbulent recirculating flow simulation at Re=10000.

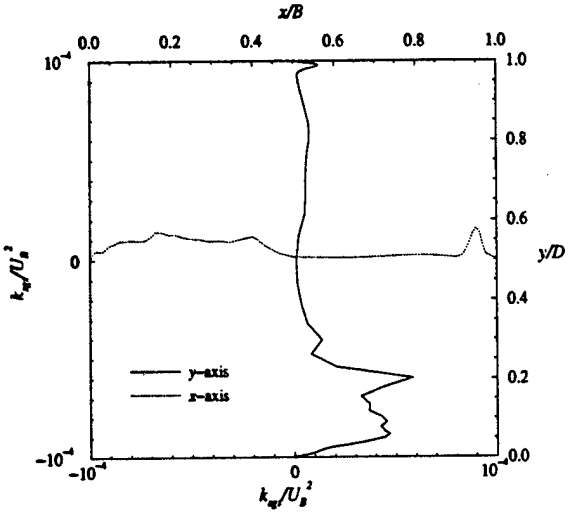


Fig. 12 Time averaged profiles of SGS kinetic energy on the center-lines in the mid-plane obtained from turbulent recirculating flow simulation at Re=10000.

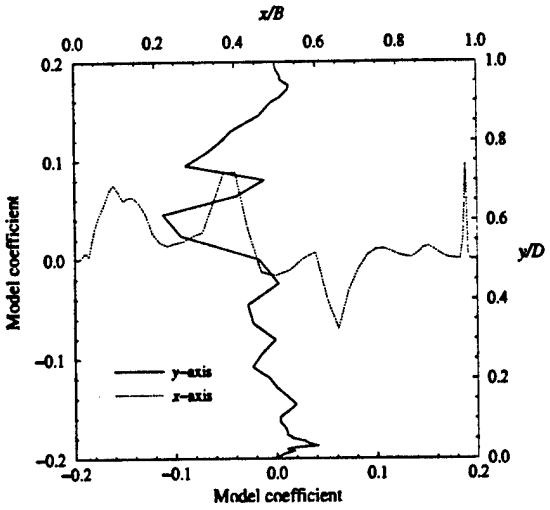


Fig. 13(a) Time averaged distributions of the model coefficient on the center-lines in the mid-plane obtained from turbulent recirculating flow simulation at Re=10000.

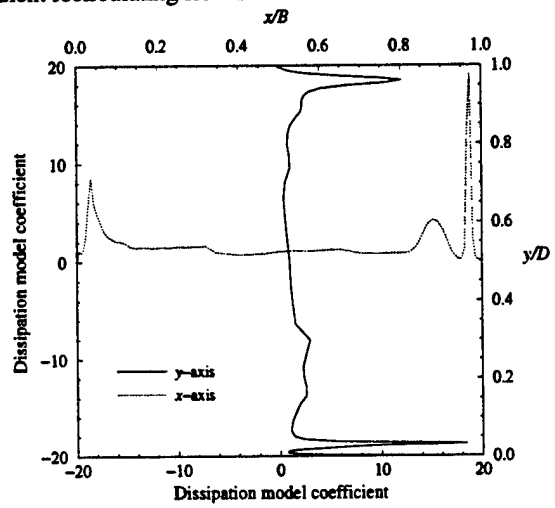


Fig. 13(b) Time averaged distributions of the dissipation model coefficient on the center-lines in the mid-plane from turbulent recirculating flow simulation at Re=10000.

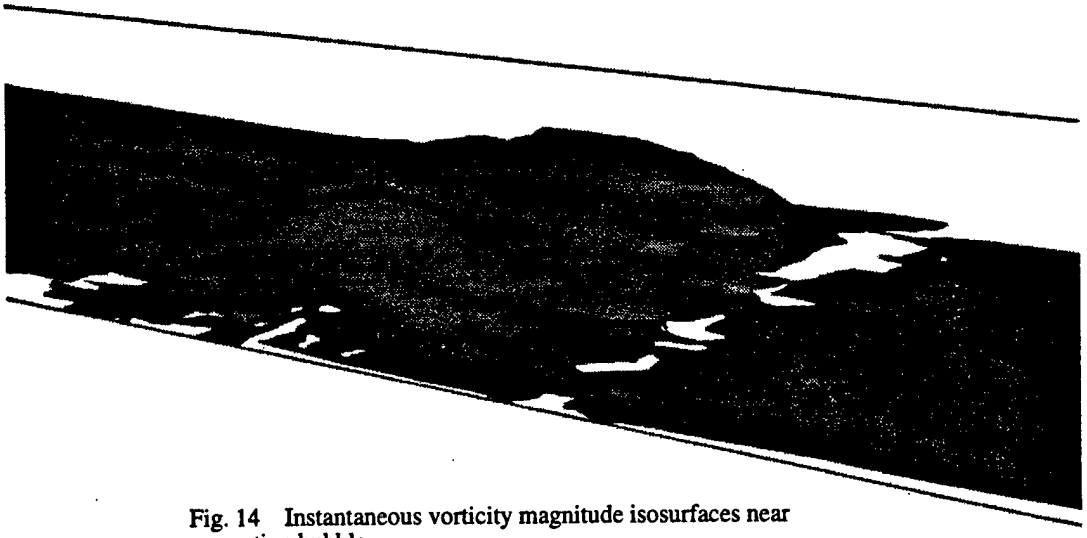


Fig. 14 Instantaneous vorticity magnitude isosurfaces near separation bubble.

To be presented at the 1996 International Mechanical Engineering Congress & Exposition, Atlanta, Nov 1996.

Simulation of unsteady turbulent jet flow using a localized dynamic subgrid model

V. K. Chakravarthy & Suresh Menon
School of Aerospace Engineering
Georgia Institute of Technology
Atlanta, GA 30332-0150

ABSTRACT

Large eddy simulations of spatially evolving turbulent jets are conducted using a dynamic one equation model. The study focuses on the aspects of the simulations specific to spatially evolving flows. Spatially evolving shear layers, in the near field, are not fully turbulent. The performance of LES models, derived from the phenomenology of fully developed turbulence, is then in question. The effect of the model under such circumstances is studied. The one equation model while capable of representing the non-equilibrium of the subgrid scales, suffers from the inadequacy that an extra inflow condition for the scalar needs to be specified. This specification could be one of the most significant factors in the simulation. Hence, LES, using realistic turbulent inflow conditions are compared to simulations without a model to study the effect of the model. It is seen that the model significantly alters the evolution of the flow field. However, it is also seen that the backscatter of energy from subgrid scales to the resolved scales, which is ignored in the present simulations, plays a significant role in evolving flows. The role of backscatter in such flows and the implications of neglecting it in a LES is discussed as a pointer towards future LES research.

1 Introduction

Circular jet with coflow is an important component of many engineering systems that involve combustion , aeroacoustics and exhaust emissions. The near field of a jet while relatively unimportant in constant density far field fluid dynamic studies, plays a significant role in the study of mixing (combustion) and aeroacoustics. This is mainly due to the presence of the strong vortical structures that effect the near field entrainment rate, unmixedness (in case of scalar mixing investigations) and turbulent noise production. These structures grow by extracting kinetic energy from the mean motion and the inflow turbulence. Hence, there is a backscatter of energy from small scale turbulence into the large scale coherent structures. In the downstream region, these structures break down and the kinetic energy is transported back to the small scales. This scale interaction poses a problem in terms of turbulence modeling since the present knowledge of the behavior of turbulence in the presence of coherent structures is limited. Most of the research on jet flows in the past concentrated on prediction of self-similar (far field) characteristics like the entrainment, momentum profiles and spreading rate,etc. These studies relied on models developed for the Reynolds averaged Naver-Stokes equations which are inherently inadequate for representation of rapidly evolving unsteady turbulent flows. Direct numerical simulation (DNS) is perhaps the best computational tool for this purpose, but is limited to low Reynolds number flows. Jets, in most physical applications, are high Reynolds number flows and the near field characteristics like entrainment and length of the potential core region are found to depend strongly on Reynolds number [1]. Because of this, most near field studies have relied on experiments [1,2,3]. Simulation model based on turbulence theory that can handle evolving turbulent flows adequately and efficiently, is still needed. Large eddy simulation (LES) is one such tool and it involves simulating large scales while accounting for the effect of small scales using a model based on the phenemenology of small scale turbulence.

Here, a LES model based on turbulence theory is developed and used to model the near field of a circular jet. The model is similar to Schumann's model [4] but the model coefficients are evaluated dynamically based on the local large scale characteristics of the flow field. The details regarding the governing equations and the numerical method can be found in section 2 and the model derivation is described in section 3.

Numerical simulation of turbulent flows have been restricted mostly to temporally evolving flows and relatively less research has been conducted on spatially evolving flows.

This research was supported by the Office of Naval Research under Grant N00014-93-1-0342.

This is because of the requirement in the spatially evolving flows, that the unsteady inflow conditions, corresponding to realistic turbulence, need to be specified. Pourquie et al. [5] have conducted a study on the effect of three different inflow conditions including the concept of re-scaled feed-back (introduced by Spalart [6] for DNS of a boundary layer). This study asks for further research into the problem. One way of circumventing this problem would be to let the turbulent flow evolve naturally from a laminar inflow with superposed disturbances (essentially a spatial transition). Melander et al. [7] and Verzicco [8] et al. have conducted DNS studies using such inflow conditions. Their simulations are essentially in the transitional regime and emphasis is on the topology of the vortex structures and related instabilities. A spatial transition to fully developed turbulence requires modeling over very long distances and is not always possible at the present day.

Also, the assumption of fully developed turbulence becomes invalid in case of many free shear layers. As mentioned before, free shear layers have coherent structures and turbulent/non-turbulent interface regions which do not admit the same scaling laws as fully developed turbulence (on which the models are based). In this study, the effectiveness of the LES model in modeling such flows is investigated. Disturbances in the form of coherent modes (at various Strouhal numbers) along with some white noise superposed over a axial mean velocity profile are prescribed as inflow conditions to the simulations. Some simulations are also conducted by prescribing the inflow turbulence based on LES of temporally evolving pipe flow. The simulations are conducted with and without the model, to test the effects of the model at various scales. Since the same inflow conditions are used for each of the simulations, the effect of the inflow can be considered minimal thus providing a self consistent way of evaluating the LES model. The details of the simulations, results and their implications for the future research are discussed in the concluding section.

2 Governing equations

The Navier-Stokes equations, on convolution with a spatial filter, reduce to the following set of LES equations.

$$\frac{\partial \overline{U}_i}{\partial x_i} = 0 \tag{1}$$

$$\frac{\mathrm{d}\overline{U}_i}{\mathrm{d}t} = -\frac{\partial \overline{p}}{\partial x_i} + \nu \frac{\partial^2 \overline{U}_i}{\partial x_k \partial x_k} + \frac{\partial \tau_{ij}}{\partial x_j} \tag{2}$$

where the overbar indicates a filtered variable, $\tau_{ij} = (\overline{U_i}\ \overline{U_j} - \overline{U_i U_j})$ is the subgrid stress. For a closed set of equations , one needs to approximate the subgrid stresses using a model. The velocity variations in the scales below the characteristic filter width Δ cannot be accounted for in an LES. Owing to the nonlinear nature of the Navier-Stokes equations, these small scale fluctuations effect the large scale motions. This effect comes from the subgrid stress, which in the present study is approximated as $\tau_{ij} = -\frac{2}{3}K\delta_{ij} + 2\nu_t \overline{S_{ij}}$, where $\overline{S_{ij}} = \frac{1}{2}\left[\frac{\partial \overline{U_i}}{x_j} + \frac{\partial \overline{U_j}}{x_i}\right]$ is the resolved strain tensor, ν_t is subgrid eddy viscosity (to be defined later) and $K = -\frac{1}{2}(\overline{U_i}\ \overline{U_i} - \overline{U_i U_i})$ is the subgrid kinetic energy. Filtered variables are also called supergrid variables because they carry information about a variables at all length scales above the filter width (grid spacing). The derivation of the model equation for the subgrid kinetic energy and the eddy viscosity is presented in the next section. The equations are discretized on a non-staggered grid (with spacing corresponding to the characteristic filter width Δ) and numerically integrated using a two step semi-implicit fractional step method. In this method, all of the primitive variables are defined at the grid points. The well known checker board type oscillations occur in velocity field due velocity-pressure decoupling when one uses central finite difference schemes for approximating spatial derivatives. Use of QUICK scheme for calculation of velocity gradients that arise in the source term of the elliptic equation for pressure is found to effectively couple the velocity and pressure fields thus removing these oscillations [9]. The convective terms are computed using a third-order upwind biased finite difference approximation while the viscous terms are computed using a fourth-order central difference approximation. The Poisson equation is solved numerically using a second order accurate elliptic solver that uses a four-level multigrid scheme to converge the solution. The finite difference equations are integrated in time using a second order scheme.

3 LES Model

A K-equation model with dynamic evaluation of the model coefficients based on the Germano's filtering approach is used as a LES model. First proposed by Schumann, the K-equation model been shown to be very useful especially in LES of reacting flows (see Weeratunga et al. [10]). The advantage of this model is that it solves a single scalar equation for the subgrid kinetic energy which characterizes the velocity scale of subgrid turbulence. This velocity scale along with the length scale (grid spacing or the filter width) provides a subgrid timescale representing the non-equilibrium relaxation of the subgrid scales. This is one level higher (in the direction of developing non-equilibrium models) than the equilibrium models(algebraic or the zero equation models), wherein the production and dissipation of the subgrid kinetic energy are assumed to balance instantaneously.

A brief derivation of the model is presented here. A more comprehensive description can be found in Menon et al. [11]. Consider the dynamic equation for the subgrid kinetic energy.

$$\frac{dK}{dt} = \tau_{ij}\frac{\partial \overline{U}_i}{\partial x_j} - \epsilon^{sgs} + \text{other transport terms} \qquad (3)$$

The first term on the right side represents the production of subgrid kinetic energy and the second term, the dissipation. The rest of the terms represent the transport of turbulent kinetic energy due to supergrid-subgrid and subgrid-subgrid interactions (both inertial and viscous). The specific form of these terms is unimportant from the modeling point of view, as only a few of these terms have a significant contribution to the above equation and these can be modeled adequately using a single term. The representation of a physical velocity field by primitive supergrid variables and subgrid kinetic energy is only statistical, since only a single scalar characterizes all of the subgrid field. There are several physical velocity fields corresponding to a single set of variables chosen for representation here. So the subgrid kinetic energy and the terms in it's dynamic equation are all statistical quantities. This allows for the use of the eddy viscosity model derived from statistical theories [12].

There have been attempts to view LES as completely deterministic and develop models based on single time correlations using apriori analysis of DNS or experimental data. A brief overview of this technique is as follows. The DNS data at a given time in the evolution is first filtered on to a coarse grid (say a grid that one can perform a LES on). The subgrid stresses corresponding to this coarse grid is also computed form the DNS data. It is usually at this stage that a model for the subgrid stress is proposed in terms of the filtered variables. The model stresses are computed using filtered variables and are compared to the corresponding exact values. The correlation between these values is seen as a model performance parameter. The comparison done here is at a single instant of time and there is no indication as to how the model will effect the filtered flow field in time, i.e., the modeled terms may correlate well with the corresponding exact values but the slightest difference between them could amplify in time, leading to large errors in the filtered field in an actual LES. The time history of the modeled terms could be very different from that of the exact terms and this is why a model which correlates well with filtered DNS field at a given instant of time may not be a good model after all. Also, in a LES, it is unreasonable to expect a point to point correlation with DNS or experiments, since only the large scale behavior is expected to be obtained correctly. Hence, as was also concluded recently by several researchers, such models are no better than phenemological models and further more they sometimes have problems with stability [13].

The spectral eddy viscosity model, when using a spectral cut-off filter has the following form.

$$\nu_t \sim \left[\frac{E(k_c)}{k_c}\right]^{\frac{1}{2}}, \qquad (4)$$

where E is the energy spectrum and k_c is the cut-off wavenumber. In theory, the spectral eddy viscosity depends on the wavenumber, but the above approximation is valid for the entire wavenumber range except for those wavenumber very close to the cut-off. (The spectral eddy viscosity has a cusp at the cut-off and an asymptotic behavior in the low wavenumber range). The above expression can be derived by introducing an effective eddy viscosity concept into the spectral energy transfer equations under the Eddy Damped Quasi-Normal Markovian approximation (see Chollet and Lesieur [14]). The assumption of isotropy has been made in arriving at the above equation, which necessitates the assumption of local isotropy of the subgrid scales when it is used in a LES.

Now, another assumption is made that the Kolmogorov inertial range exists at the cut-off wavenumber. In a LES, it is very unlikely that the dissipation range (Kolmogorov length scale) would be resolved since the purpose of LES is then lost. However, a restriction nevertheless exists at the other end of the inertial range,i.e., the cut-off wavenumber cannot lie in the energy containing wavenumber range (outside the $k^{-\frac{5}{3}}$ range). This limits the capability of LES unless some information about the infrared (energy containing) wavenumber spectrum is known apriori. There is no general form for this spectrum, even for a specific class of flow fields. Given the fact that inertial range exists at the cut-off, the energy spectrum at the cut-off and the eddy viscosity can be written as $E(k_c) \sim \epsilon^{\frac{2}{3}} k_c^{-\frac{5}{3}}$ and $\nu_t \sim \epsilon^{\frac{1}{3}} k_c^{-\frac{4}{3}}$. Similar expressions are obtained in the low wavenumber (infrared) limit when eddy viscosity concept is introduced in the inertial range energy transfer equations obtained using Renormalized Perturbation Theory (Kraichnan [15]).

The turbulent dissipation is yet to be determined. For this, the form of the subgrid scale energy spectrum is needed. The Kolmogorov spectrum is purely inertial and does not produce the required turbulent dissipation when extended to high wavenumbers. Hence, a more general form of the energy spectrum (see Pao [16]) valid in both inertial and dissipative ranges of the spectrum is considered here. This general form is

$$E(k) = \alpha \epsilon^{\frac{2}{3}} k^{-\frac{5}{3}} \exp\left[-\frac{3}{2}\alpha (k\eta)^{\frac{4}{3}}\right], \qquad (5)$$

where η is the Kolmogorov length scale. The dissipation spectrum is given by $D(k) = 2\nu k^2 E(k)$ and the total and the subgrid dissipation can be written as follows.

$$\epsilon = \int_0^\infty D(k)dk \qquad (6)$$

$$\epsilon^{sgs} = \int_{k_c}^\infty D(k)dk \qquad (7)$$

The form of the energy spectrum in eq.(5) is not really valid at low wavenumbers. So this form cannot be used to calculate dissipation at low wavenumbers. However, if the calculation is conducted using this form, the dissipation is

very low at low wavenumbers (energetic scales) as is the case in real flows. So the equation for total dissipation above, is a valid approximation. The turbulent dissipation can now be written as follows.

$$\epsilon \sim K^{\frac{3}{2}} k_c \tag{8}$$

For a LES in physical space, the relevant subgrid length scale would be the filter width Δ which is inversely proportional to the cut-off wavenumber k_c. So, the eddy viscosity in physical space, after using eq.(8) can be written as

$$\nu_t = C_\nu K^{\frac{1}{2}} \Delta, \tag{9}$$

which is same as the expression obtained if one uses dimensional arguments considering the subgrid kinetic energy and filter width as the relevant parameters for determining the subgrid eddy viscosity.

LES is a tool for modeling large scale characteristics of a flow field in an efficient manner. In turbulent flows, energy is usually drained into the small scales and what one needs to represent in a LES is the correct transfer of this energy. This energy transferred to small scales, is then dissipated using a model for subgrid dissipation. Since this expression for eddy viscosity is derived so as to lead to correct flux of energy across the cut-off wavenumber, it is exactly suited to the purpose of LES and hence the analytical approach outlined above serves to justify the use of eddy viscosity concept in a LES. The subgrid dissipation can now be written as

$$\epsilon^{sgs} = C_\epsilon \frac{K^{\frac{3}{2}}}{\Delta} \exp\left[-C_d \frac{\nu}{\nu_t}\right], \tag{10}$$

where C_ϵ and C_d are constants. The exponential term is close to unity since the eddy viscosity is much higher as compared to the kinematic viscosity for high Reynolds number flows. So the subgrid dissipation is not very different from the total dissipation. Similar forms for eddy viscosity and subgrid dissipation are arrived at by using two scale direct interaction approximation by Yoshizawa [17].

For the transport term, a gradient diffusion model based on eddy diffusivity model (with unit eddy Prandtl number) has been proposed and studied by Menon et al. Renormalization Group Theory (see Yakhot and Orszag [18]) when viewed in the low wavenumber limit as a LES theory, provides a justification for this approximation. . This approximation was found to model adequately well, the transport terms. Hence this is used in a similar form in this study.

The constants of proportionality in the expressions for eddy viscosity and subgrid dissipation, for a spectral cut-off filter, can be evaluated in terms of the Kolmogorov constant which serves as the constant of proportionality α. Studies have shown that the functional forms of LES models are independent of the type of filter used, except that the model constants differ. When using filters other than the spectral filter, the model constants are evaluated by comparing the LES results with experiments or DNS results. These constants, however, are not universal and differ with flow fields in general. This suggests that these constants also depend on the local(supergrid) structure of the flow field. It is, then appropriate to refer to them as coefficients rather than constants. A dynamic approach is applied here to evaluate these coefficients, thus removing the arbitrariness in prescribing these coefficients. The approach is based on the concept of subgrid stress similarity supported by experiments in jets (Liu et al. [19]). In this approach, a test filter(similar to the LES filter) of characteristic width 2Δ is defined and the corresponding filtered velocity field is denoted by $\tilde{U}_i$. This new velocity field is obtained by convolution of the LES filtered velocity with the test filter. The subgrid stress corresponding to the scales in between the grid filter width and the test filter width can be written as follows.

$$t_{ij} = \tilde{\overline{U_i}}\ \tilde{\overline{U_j}} - \tilde{\overline{U_i}}\,\tilde{\overline{U_j}} \tag{11}$$

and the corresponding dissipation is defined as

$$e = (\nu + \nu_t)\left[\frac{\partial \tilde{\overline{U_i}}}{\partial x_j}\frac{\partial \overline{U_i}}{\partial x_j} - \frac{\partial \tilde{\overline{U_i}}}{\partial x_j}\frac{\partial \tilde{\overline{U_i}}}{\partial x_j}\right] \tag{12}$$

Assuming stress similarity and the present model to be valid for length scales between Δ and 2Δ (which imposes a further restriction that the test filter width also lies in the inertial range of length scales), t_{ij} and e can be written as follows.

$$t_{ij} = -\frac{2}{3}\tilde{K}\delta_{ij} + 2\tilde{\nu_t}\tilde{\overline{S_{ij}}} \tag{13}$$

and

$$e = C_\epsilon \frac{\tilde{K}^{\frac{3}{2}}}{2\Delta}, \tag{14}$$

where $\tilde{K} = -\frac{1}{2}t_{ii}$ and $\tilde{\nu_t}$ is the eddy viscosity corresponding to the test filter of width 2Δ and is given by $C_\nu \tilde{K}^{\frac{1}{2}}(2\Delta)$. From eq.(14), the value of C_ϵ can be evaluated. There are, however, six equations represented by eq.(13) using which C_ν could be evaluated. This is a over-determined system of equations and in the present formulation, is solved using least-squares technique. These coefficients are then used for evaluation of eddy viscosity and to advance the dynamic equation for K in time, thus achieving complete closure.

The similarity assumed above is instantaneous. The local flow structure at any time, thus, has considerable effect on the evolution of the flow field although the derivation of the model is statistical. The Kolmogorov spectrum can be expected at the cut-off only as a probable state over several LES realizations. The instantaneous structure is determined by the super grid velocity field and this stress similarity approach serves as a way to introduce this dependence into LES. The spatial variation of the model coefficients evaluated using many of the dynamic approaches in the

past, was found to be oscillatory and lead to numerical instabilities. Various methods like filtering, spatial averaging were used to remove this oscillatory behavior. The present dynamic evaluation procedure is however completely localized and does not lead to any instabilities in integration. The present model, hence, is a considerable improvement over the existing LES models, as shown by Menon et al. [11].

4 Results and Conclusions

The LES model is used to simulate a co-flowing circular jet of Reynolds number (based on mean exit velocity and the nozzle exit diameter) of 7000. Mean exit velocity and nozzle diameter are both equal to 1.0, so that all quantities in these simulations can be considered non-dimensionalized. The co-flow velocity is 10 percent of the mean velocity at the nozzle exit plane. A 65x49x49 grid that resolves an axial distance of 15 diameters is used for the simulations.

Two types of inlet conditions are studied. In the first case, inlet conditions are prescribed as solenoidal coherent modes (corresponding to temporally sinusoidal forcing) superposed over axial mean velocity. Forcing frequecies of ω_o,$2.0\omega_o$,$3.0\omega_o$ and $5.0\omega_o$ are used, where ω_o is the frequency that is close to the jet preferred mode. The amplitude of forcing is set at 10 percent and a 4 percent random noise is added at the inflow. $K^{sgs} = -\frac{1}{2}C_m t_{ii}$ is prescribed as the inflow condition for the subgrid kinetic energy. C_m is a constant that is set equal to the model constant in the Meneveau scale similarity model. The simulations that are conducted without the model are termed Direct Numerical Simulations (DNS) though it is very unlikely that the grid resolution can resolve all the relevant length scales. In the second case, the inlet conditions corresponding to a cross plane of a temporally evolving pipe flow are used. The pipe flow is simulated on a uniform grid (over an axial distance of 5 diameters) and hence, the wall layer is not adequately resolved. The peak in the kinetic energy near the wall is however captured to a certain extent in this LES (see Fig.6). This type of inflow removes the arbitrariness in prescribing the turbulent kinetic energy, since, K^{sgs} coming in is correlated to the filtered velocity field through the same set of finite difference equations used in the LES of the jet. The characteristics of the inflow are shown in the Fig.6.

The resolved and the subgrid scale turbulent kinetic energies from the LES and DNS are shown in Fig.1 and Fig.2. The axial variation of resolved scale kinetic energy from DNS and LES along with the mean subgrid kinetic energy from the LES are plotted in Fig.1. The radial variations are plotted in Fig.2. As can be seen, the total turbulent kinetic energy (resolved scale and the subgrid) in the LES is found to exceed the turbulent kinetic energy in the DNS which indicates the presence of relevant scales that remain unresolved in the DNS. Due to the significant value of K^{sgs} in the shear layer, the shear layer growth is expected to be effected by the presence of the LES model. The ratio of eddy viscosity to the kinematic viscosity across the shear layer is plotted in Fig.3.

Longitudinal two point correlations of axial velocity are computed starting from the lip of the jet. The eigen decomposition of these correlations gives the information about the longitudinal modes corresponding to shear layer growth and the energy content in each mode. As can be seen in Fig.4, the most dominant mode (mode with highest energy) in LES is different from the same as predicted by DNS indicating the very different spatio-temporal behavior of the shear layer due to the presence of the model.

In Fig.5 are shown the eigen values corresponding to the most significant radial modes (which are found to be similar in LES and DNS) computed from radial velocity correlations at an axial distance of 12 diameters, are shown. The energy in the most dominant modes in LES and DNS is again found to differ and it is further seen that much of energy exists in the first few modes indicating the presence of vortical structures. This is an indication that the assumption of fully developed turbulence may not be valid in this region. It can be concluded that the use of a LES model leads to results differing significantly from those without the model but the accuracy of either of these is still an issue for the future research.

The evolution of the flow is found to be slightly different when turbulent inflow conditions are used. In this case, there is no shear layer peak in the subgrid kinetic energy. This is shown if Fig.7. The ratio of turbulent to kinematic viscosities is plotted at the same axial location in Fig.8. The subgrid kinetic energy stays almost constant along the axial line, while the resolved scale (component wise) turbulent kinetic energies are found to drop drastically downstream (see Fig.10). This feature can be observed in the case with forced inflow, but the sudden drop of resolved scale turbulent kinetic energy in that case could be attributed to filtering out of the non-solenoidal (in finite difference sense) and the noise (the spatio-temporal behavior that does not fall into the solution space of the present finite difference equations). In the present case, since, the subgrid kinetic energy and the velocity field form a solution of the finite difference LES equations, this behavior is not related to the inflow. It is likely that turbulent kinetic energy within the resolved scale is transported into the large scale shear layer structures (mean flow), thus, exhibiting a backscatter phenomena within the range of resolved scales. The backscatter of energy from the subgrid into the resolved scales, as mentioned earlier, cannot be accounted for in this LES model. This could be considered the reason as to why the subgrid kinetic energy does not drop in the downstream as much as the resolved scale turbulence. It is possible that this could hinder the growth of the shear layer as well.

The eigenvalues corresponding to the radial modes at two different axial locations can be seen in Fig.9. While the first mode has significantly high amount of energy than the other modes at the first location, the energy seems more dis-

tributed at the second axial location (which is downstream of the first). This indicates a possible breaking down of the large scale structure that is formed in the near field. When the break down is complete (which can be expected further downstream), the energy would possibly enter the small scales. The study of this phenomena needs to be undertaken using a LES which can resolves more axial distance.

The contours of vorticity (instantaneous) for the case of forced jet and turbulent inflow are plotted in Fig.11 and Fig.12 respectively. The coherent large structures due to forcing at the jet preferred mode if evident in Fig.11 where as Fig.12 shows more small scale structure due to turbulent inflow.

It is seen that the backscatter of energy plays an essential role in the evolution of the circular jet (forced or turbulent). Although the eddy viscosity turns out be negative at some of the points in the flow field due to a negative eddy viscosity coefficient, it cannot be expected that this indicates physical backscatter. As mentioned earlier, the backscatter terms in the spectral energy transfer equations have been ignored in the derivation of the eddy viscosity. So the backscatter seen in simulations using models such as the present one is heuristic and is not the physical backscatter one can expect in real flows. Further study of the backscatter phenomena and the subsequent modification of the LES model would be the next step in development of better simulation tools.

Acknowledgements

The authors are grateful for the financial support from the Fluid Dynamics Division of the Office of Naval Research under Grant N00014-93-1-0342 (monitored by Dr. P. Purtell). The computer time was provided by the DoD on the SGI Power Challenge Array at the HPC Center, Army Research Laboratories, Maryland.

References

1. W. M. Pitts, 1991, "Reynolds number effects on the mixing behavior of axisymmetric turbulent jets,"Experiments in Fluids 11, 135-141.
2. R. A. Antonio and R. W. Bilger.,1973, "An experimental investigation of an axisymmetric jet in a co-flowing air stream," J. Fluid Mech., vol. 61, pp 805-822.
3. J. C. Sautet and D. Stepowski., 1995, "Dynamic behavior of variable-density , turbulent jets in their near development fields," Phys. Fluids 7(11).
4. U. Schumann., 1975, "Subgrid scale model for finite difference simulations of turbulent flows in plane channels and annuli," J. Comp. Phys. 18, 376-404.
5. M. J. Pourquie and J. G. Eggels., 1993, "The use of three types of inflow conditions in the Large Eddy Simulation of a turbulent jet," FED-162, Engineering Applications of Large Eddy Simulations, ASME, 37-44.
6. P. R. Spalart., 1989, "Direct numerical simulation of a turbulent boundary layer up to Re=1400," J. Fluid Mech., 187,61-97.
7. M. V. Melander, F. Hussain, and A. Basu, 1991, "Breakdown of a circular jet into turbulence," Proceedings of the Eighth Symposium on Turbulent Shear Flows, Munich.
8. R. Verzicco and P. Orlandi, 1994, "Direct simulations of the transitional regime of a circular jet," Phys. Fluids 6(2).
9. Yan Zang, R. L. Street, and J. R. Koseff, 1994, "A non-staggered grid, fractional step method for the time-dependent incompressible Navier-Stokes equations in curvilinear coordinates," J. Comp. Phys. 114, 18-33.
10. S. Weeratunga and S. Menon., 1993, "Parallel computations of unsteady combustion in a Ramjet Engine," AIAA Paper 93-1914, AIAA/SAE/ASME/ASEE 29^{th} Joint Propulsion Conference and Exhibit, Monterey, CA.
11. S. Menon and W.-W. Kim, 1996, "High Reynolds number flow simulations using the localized dynamic subgrid scale model," AIAA Paper 96-0425, 34^{th} Aerospace Sciences Meeting and Exhibit, Reno, NV.
12. R. H. Kraichnan, 1964, "Kolmogorov's hypotheses and Eulerian turbulence theory," Phys. Fluids. 7,1723
13. J. Badrina, J. H. Ferziger, and W. C. Reynolds, 1991, "Improved subgrid scale models for large eddy simulations," AIAA paper 80-1357.
14. J. P.Chollet and M. Lesieur, 1981, "Parametrization of small scales of three-dimensional isotropic turbulence using spectral closures," J. Atmos. Sci., 38, 2747-2757.
15. R. H. Kraichnan, 1966, "Isotropic turbulence and inertial range structure," Phys. Fluids. 9, 1728.
16. Y. H. Pao, 1965, "Structure of turbulent velocity and scalar fields at large wavenumbers," Phys. Fluids 8, 1063.
17. A. Yoshizawa and K. Horiuti, 1985, "A statistically-derived subgrid-scale kinetic energy model for the Large Eddy Simulation of turbulent flows," J. Phys. Soc. Japan, Vol.54, 2834-2839.
18. V. Yakhot and S. Orszag., 1986, "Renormalization group methods in turbulence," J. Sci. Comput. 1,3.
19. S. Liu, C. Meneveau, and J. Katz, 1994, "On the properties of similarity subgrid scale models as deduced from measurements in a turbulent jet," J. Fluid Mech. 275, 83.

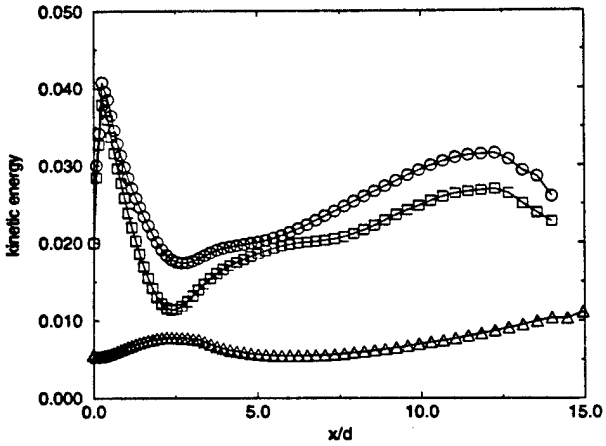


Figure 1: Axial variation of turbulent kinetic energy. ○ RMS velocity from the DNS,□ RMS velocity from the LES, △ K^{sgs} in the LES.

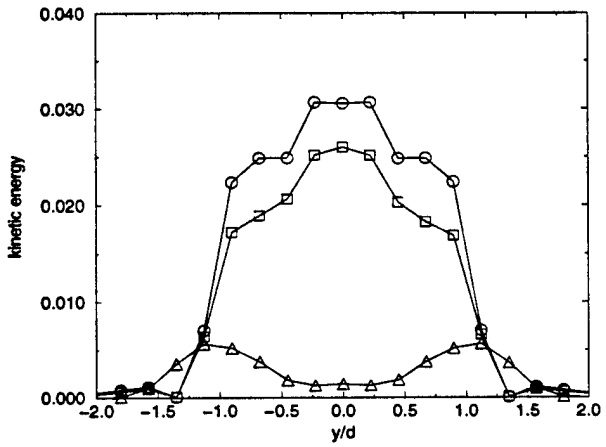


Figure 2: Radial variation of turbulent kinetic energy at x=7d. ○ RMS velocity from the DNS,□ RMS velocity from the LES, △ K^{sgs} in the LES.

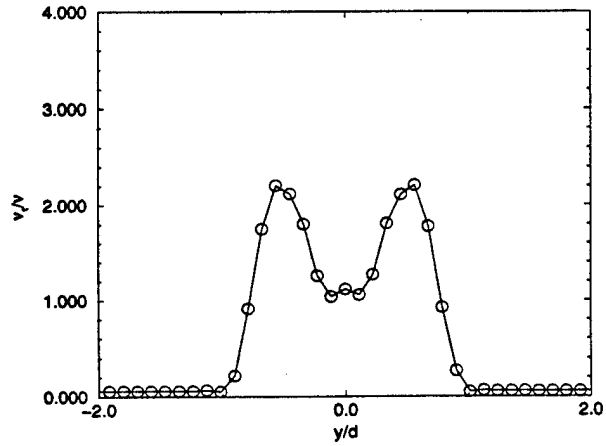


Figure 3: Relative magnitudes of eddy viscosity and kinematic viscosity in the shear layer

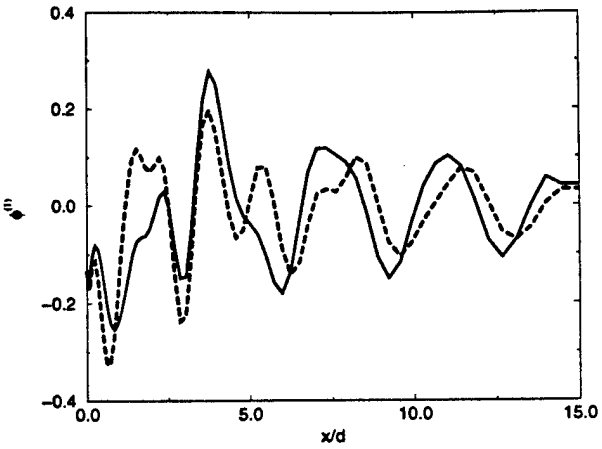


Figure 4: Most dominant longitudinal mode in the shear layer. solid line - DNS, dotted line - LES.

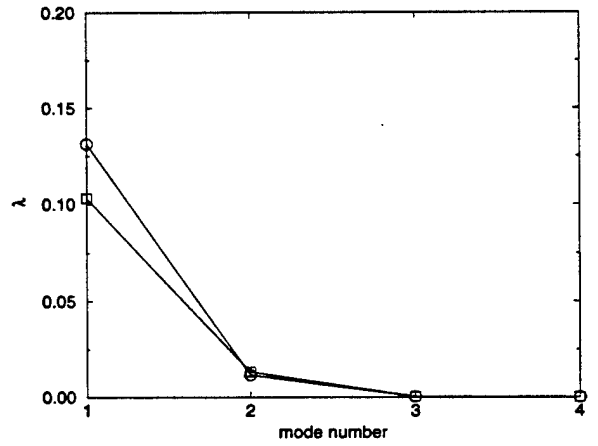


Figure 5: Eigen values of the radial eigenmodes at x=12d ○ DNS, □ LES.

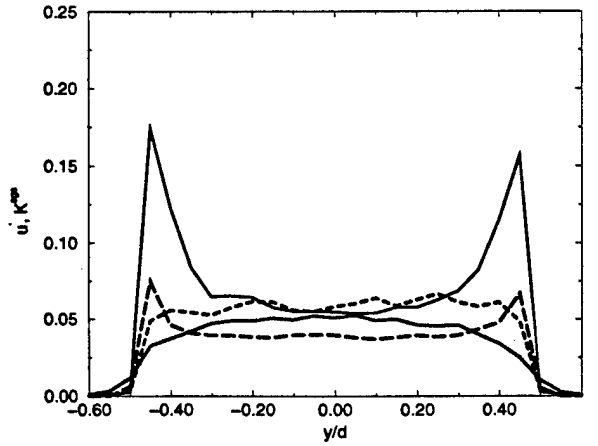


Figure 6: Single point statistics in a pipe (inflow for the jet) solid line urms, dotted line vrms, dashed line wrms , long-dashed K^{sgs}.

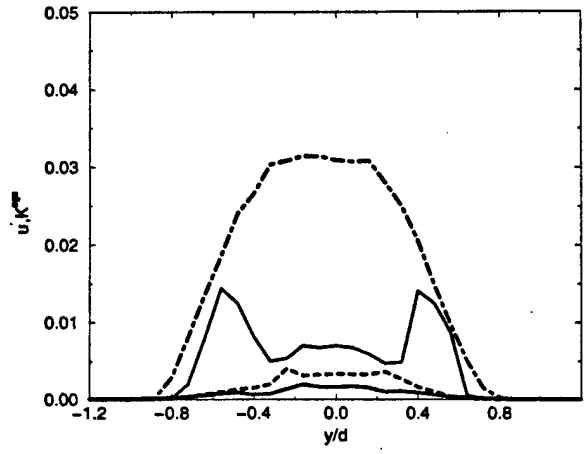


Figure 7: Radial variation of kinetic energies at x=6.0d. solid line urms, dotted line vrms, dashed line wrms , dotted-dashed K^{sgs}.

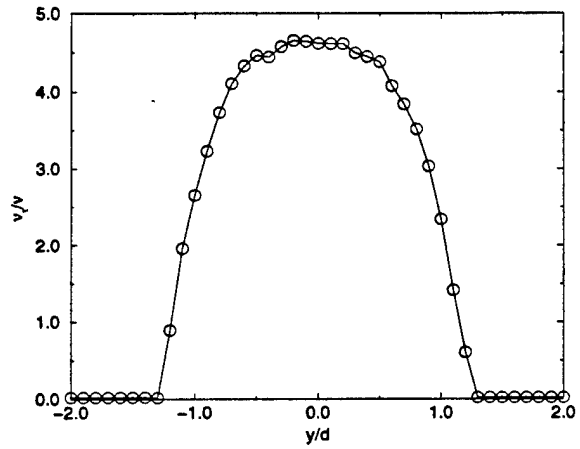


Figure 8: Relative magnitudes of eddy viscosity and kinematic viscosity in the shear layer (at x=6.0d).

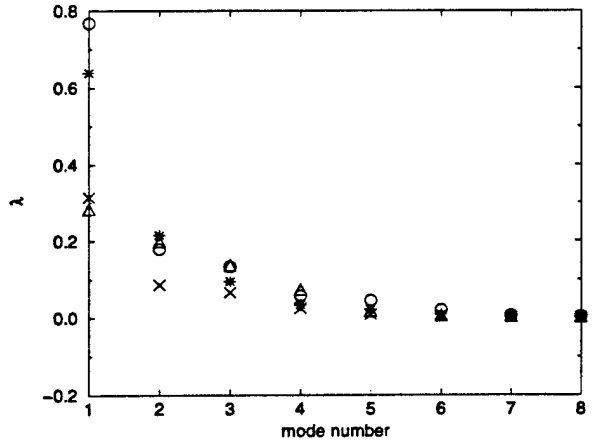


Figure 9: Eigen values of the radial eigenmodes. ○ DNS at x=7d, ∗ LES at x=7d △ DNS at x=10d, × LES at x=10d

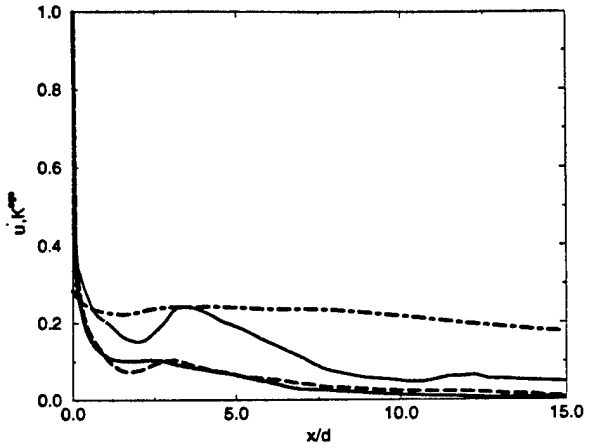


Figure 10: Axial variation of component-wise kinetic energies in a LES. solid line urms, dotted line vrms, dashed line wrms , dotted-dashed K^{sgs}.

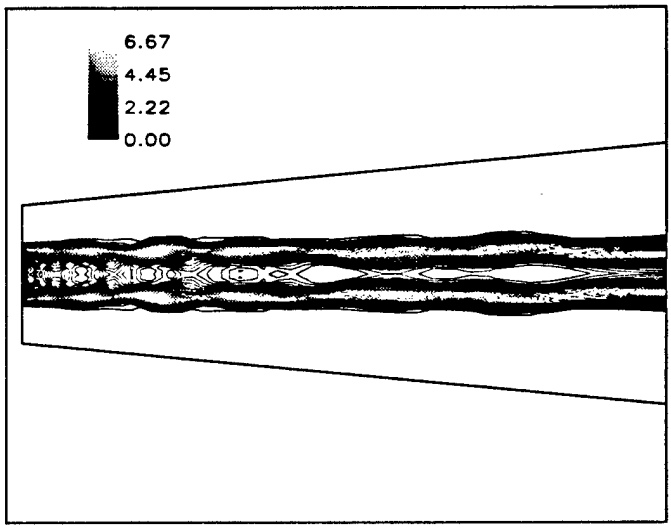


Figure 11: Contours of vorticity magnitude for the case of forced jet

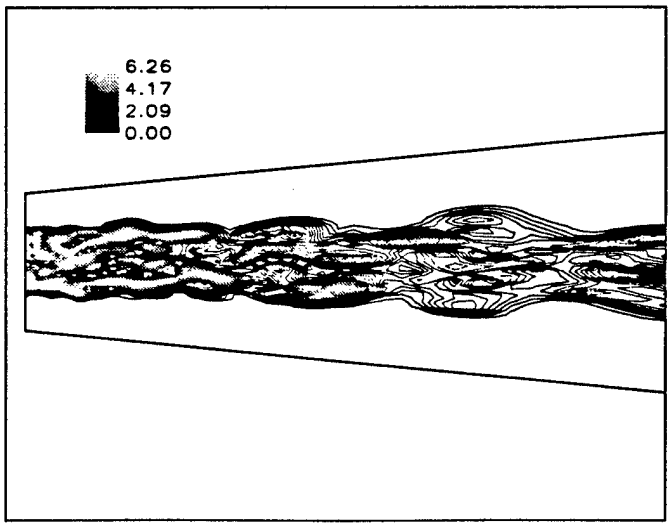


Figure 12: Contours of vorticity magnitude for the case of turbulent inflow

Pergamon

0045-7930(95)00036-4

Computers & Fluids Vol. 25, No. 2, pp. 165–180, 1996
Copyright © 1996 Elsevier Science Ltd
Printed in Great Britain. All rights reserved
0045-7930/96 $15.00 + 0.00

EFFECT OF SUBGRID MODELS ON THE COMPUTED INTERSCALE ENERGY TRANSFER IN ISOTROPIC TURBULENCE

S. MENON, P.-K. YEUNG and W.-W. KIM

School of Aerospace Engineering, Georgia Institute of Technology, Atlanta, GA 30332-0150, U.S.A.

(Received 6 March 1995; in revised form 30 August 1995)

Abstract—Direct and large eddy simulations of forced and decaying isotropic turbulence have been performed to investigate the behavior of subgrid models. Various subgrid models have been analyzed (i.e. Smagorinsky's eddy viscosity model, dynamic eddy viscosity model, dynamic one-equation model for the subgrid kinetic energy and scale-similarity model). *A priori* analysis showed that the subgrid stress and the subgrid energy flux predicted by the scale similarity model, and subgrid kinetic energy model (with fixed coefficients) correlate reasonably well with exact data, while the Smagorinsky's eddy viscosity model showed relatively poor agreement. However, the correlation for the scale similarity model decreased much more rapidly with decrease in grid resolution when compared to the subgrid kinetic energy model. The subgrid models were then used to carry out large-eddy simulations for a range of Reynolds number. When dynamic evaluation was incorporated, the correlation improved significantly. The dynamic subgrid kinetic energy model showed, consistently, a higher correlation for a range of Reynolds number when compared to the dynamic eddy viscosity model. These results demonstrate the capabilities of the dynamic one-equation model.

1. INTRODUCTION

Large-eddy simulation (LES) methods are currently being used to simulate a variety of flow problems. For such methods to perform adequately, subgrid models that faithfully represent the effects of the unresolved subgrid scales (SGS) on the resolved motion have to be developed and validated. The capability of the subgrid models can be determined by carrying out LES and comparing the predicted results (typically, ensemble or time-averaged properties) with experimental data. Good agreement would demonstrate the capability and validity of the chosen subgrid model. However, this approach does not provide any means to improve the subgrid model if poor agreement with experimental data occurs. Alternatively, the subgrid model(s) can be evaluated using direct numerical simulation (DNS) data, and then the subgrid model(s) can be used in an LES of the same flow field, by using coarse grids. Comparison of the LES results with the DNS data can then be used to determine the validity of the model. This approach, however, also has problems. Models validated using low Reynolds number DNS data (for simple flows) invariably show poor agreement with data when used to simulate high Reynolds number, complex flows.

In recent years, studies have identified some inherent limitations of subgrid models currently being employed for LES. For example, it has been shown that the "constant" in the popular eddy viscosity model of Smagorinsky has to be fine-tuned for every flow of interest. This problem was circumvented recently by using a dynamic procedure [1] which allows a direct evaluation of the constant as a part of the solution. The dynamic model has proven quite versatile, and results show that it can model correctly the behavior of subgrid stresses both near and away from the wall, and has a capability to model backscatter [1, 2]. However, even this model has some problems. Namely, the evaluation of the "constant" can result in numerical problems. Methods to address this limitation have been developed [2–4].

For LES of high Reynolds number flows, the typical grid resolution possible (due to computer resource limitations) can be quite coarse. In this case, a large dynamic range of scales, including "energy containing" scales of motion, can remain unresolved. It is not clear if eddy viscosity-type subgrid models will be able to model accurately the effects of these unresolved scales. Since a significant amount of turbulent kinetic energy may be present in the subgrid scales, the assumption

of balance between the energy production and the dissipation rate (an assumption implicit in the formulation of the eddy viscosity models) may be violated. Furthermore, reverse cascade of energy (the so-called backscatter) from the subgrid scales to the resolved scales could become significant, and anisotropy effects in the unresolved scales may have to be taken into account. Higher-order models, such as the one-equation model studied here, may be required to take these features into account.

In this paper, the effects of the form of the chosen subgrid model on the energy transfer process between the resolved and unresolved scales in LES will be investigated. The results of DNS and LES of forced and decaying isotropic turbulence is analyzed in both physical and spectral space. The goal of this research is to develop methods to analyze subgrid models without using any DNS information. This would enable investigation of the validity and the applicability of subgrid models in more complex flows which cannot be computed using DNS techniques.

2. NUMERICAL METHODS AND SUBGRID MODELS

Two simulation codes have been used in this research. A well-known pseudo-spectral code of Rogallo [5] has been used to obtain high resolution DNS data. However, no LES has been performed using this code. To carry out both LES and DNS, a finite-difference, Navier–Stokes solver, which is fifth-order accurate in space and second-order accurate in time, is used. The numerical algorithm is based on the artificial compressibility method. To obtain time-accuracy at each time step, pseudo-time iterations are carried out using a multigrid technique until the incompressibility condition has been met. The Kolmogorov-scaled energy and dissipation spectra obtained using the finite-difference code, were compared to the results obtained using the pseudo-spectral code. Very good agreement over nearly the entire wavenumber space was obtained [6]. Detailed evaluations of the various statistical quantities (such as the dissipation rate, skewness, etc.) also showed that the physical space code is capable of reproducing statistics very similar to those obtained by the spectral code.

Decaying and forced isotropic turbulence data obtained on both 64^3 and 128^3 grid resolutions have been employed for analysis. For the decaying case, the hydrodynamic field is allowed to evolve until a "realistic", self-similar state has been reached. This developed isotropic state is characterized by Kolmogorov similarity in the high wavenumber energy spectrum, power law decay of energy, and non-Gaussian velocity gradients. The decaying turbulence DNS data used in this paper is approximately at a Taylor-scale Reynolds number Re_λ of 20 (obtained on a 128^3 grid) and 10 (obtained on a 64^3 grid). DNS data at a Re_λ of around 90 obtained (on a 128^3 grid) using stochastic forcing [7], is also used for some analysis.

2.1. *Subgrid modeling in physical space*

In physical space, the incompressible Navier–Stokes equations are filtered using a spatial filter of characteristic width Δ (typically, the grid resolution) resulting in the filtered LES equations:

$$\frac{\partial \bar{u}_i}{\partial x_i} = 0, \tag{1a}$$

$$\frac{\partial \bar{u}_i}{\partial t} + \bar{u}_j \frac{\partial \bar{u}_i}{\partial x_j} = -\frac{\partial}{\partial x_j}\left[\frac{\bar{p}}{\rho}\delta_{ij} + \tau_{ij}\right] + \nu \nabla^2 \bar{u}_i, \tag{1b}$$

where $\bar{u}_i(\mathbf{x}, t)$ is the resolved velocity field, p and ρ are, respectively, the pressure and density, and ν is the kinematic viscosity. Here, the bar over the flow variable indicates the effect of the filtering process. The subgrid scale stress tensor τ_{ij} is defined as: $\tau_{ij} = \overline{u_i u_j} - \bar{u}_i \bar{u}_j$ and must be modeled. It has been shown [8] that proper choice of the filtering process is essential to maintain model consistency. Various types of filtering processes have been studied in the past [8, 9] such as the top hat, the Gaussian, and the Fourier cutoff filters. In the present study, we employ the top hat filter which is considered appropriate for finite-difference methods.

The goal of SGS modeling is to represent the SGS stress τ_{ij} in terms of the resolved field $\bar{u}_i(\mathbf{x}, t)$ in such a manner that the modeled SGS stresses represent, as much as possible, the exact stresses. In addition, the energy flux to the unresolved scales given by $E(\Delta) = -\tau_{ij}\bar{S}_{ij}$ must also be modeled reasonably well by the subgrid model. These issues will be addressed in this study.

2.1.1. Smagorinsk's eddy viscosity model. The most popular subgrid model is the algebraic eddy viscosity model originally proposed by Smagorinsky:

$$\tau_{ij} - \tfrac{1}{3}\delta_{ij}\tau_{kk} = -2\nu_t \bar{S}_{ij}, \tag{2}$$

where $\nu_T = C\Delta^2|\bar{S}|$ is the subgrid eddy viscosity, C is constant

$$\bar{S}_{ij} = \frac{1}{2}\left(\frac{\partial \bar{u}_i}{\partial x_j} + \frac{\partial \bar{u}_j}{\partial x_i}\right) \tag{3}$$

is the resolved rate-of-strain tensor, and $|\bar{S}| = |2\bar{S}_{ij}\bar{S}_{ij}|^{1/2}$. As noted above, the "constant" C has to be adjusted for different flows. For decaying isotropic turbulence a value of $C \approx 0.03$ has been suggested by Lilly [10] and is used here.

This model is denoted Model A for subsequent discussions.

2.1.2. Dynamic eddy viscosity model. In the dynamic modeling approach [1], a mathematical identity between the stresses resolved at the grid scale filter Δ and a test filter $\langle\Delta\rangle$ (typically $\sim 2\Delta$) is used to determine the model coefficient C as a part of the simulation. Thus, if the application of the test filter on any variable $\bar{\phi}$ is denoted by $\langle\bar{\phi}\rangle$, it can be shown that:

$$L_{ij} = T_{ij} - \langle\tau_{ij}\rangle = \langle\bar{u}_i\bar{u}_j\rangle - \langle\bar{u}_i\rangle\langle\bar{u}_j\rangle. \tag{4}$$

Here, $T_{ij} = \overline{\langle u_i u_j\rangle} - \langle\bar{u}_i\rangle\langle\bar{u}_j\rangle$ is defined using the test filter. Assuming that T_{ij} is similar to τ_{ij} results in an expression for T_{ij} as:

$$T_{ij} - \tfrac{1}{3}\delta_{ij}T_{kk} = -2\nu_T\overline{\langle\bar{S}_{ij}\rangle}, \tag{5}$$

where $\nu_T = C\langle\Delta\rangle^2|\langle\bar{S}\rangle|$. Combining equations (2), (4) and (5), an equation for C can be obtained:

$$L_{ij} - \tfrac{1}{3}\delta_{ij}L_{kk} = 2CM_{ij}, \tag{6}$$

where

$$M_{ij} = -(\langle\Delta\rangle^2|\langle\bar{S}\rangle|\overline{\langle\bar{S}_{ij}\rangle} - \Delta^2\langle|\bar{S}|\bar{S}_{ij}\rangle). \tag{7}$$

Equation (6) is a set of five independent equations for one unknown C. To minimize the error from solving this overdetermined system, Lilly [11] proposed a least square method which yields:

$$C = \frac{1}{2}\frac{L_{ij}M_{ij}}{M_{ij}M_{ij}}. \tag{8}$$

Studies have shown that the numerical value of C obtained from equation (8) can vary widely (and change sign) in the flow field. In addition, the denominator in equation (8) can become zero in some places. All these effects can (and do) result in numerical instability. Various methods have been proposed to resolve this problem. Typically, spatial averaging (usually only in the direction of flow homogeneity) is performed for both the numerator and denominator in equation (8). For homogeneous, isotropic turbulence averaging can be implemented over the entire computational domain. Thus, in the present implementation of the dynamic model, C is a function of time only.

This model is denoted Model B for subsequent discussions.

2.1.3. Subgrid kinetic energy model. A one-equation model for the subgrid kinetic energy

$$k_{sgs} = \tfrac{1}{2}(\overline{u_i^2} - \bar{u}_i^2)$$

in the following form:

$$\frac{\partial k_{sgs}}{\partial t} + \bar{u}_i\frac{\partial k_{sgs}}{\partial x_i} = -\tau_{ij}\frac{\partial \bar{u}_i}{\partial x_j} - C_\epsilon\frac{k_{sgs}^{3/2}}{\Delta} + \frac{\partial}{\partial x_i}\left(\frac{\nu_k}{\sigma_k}\frac{\partial k_{sgs}}{\partial x_i}\right) \tag{9}$$

has also been studied. Here, the three terms on the right-hand side of equation (9) represent, respectively, production, dissipation, and diffusion of the subgrid kinetic energy. The subgrid stresses τ_{ij} are modeled in terms of the SGS eddy viscosity ν_k as:

$$\tau_{ij} = -2\nu_k\bar{S}_{ij} + \tfrac{2}{3}k_{sgs}\delta_{ij} \tag{10}$$

where the SGS eddy viscosity is $\nu_k = C_k\sqrt{k_{sgs}}\Delta$. The constants are chosen, based on an earlier study [12], to be $C_k = 0.05$, $C_\epsilon = 1.0$ and $\sigma_k = 1.0$.

An important feature of this model is that no assumption of local balance between the subgrid scale energy production and dissipation rate has been made. Therefore, it is expected that this model would be much better than the algebraic eddy viscosity model in regions where local balance is violated. The results of this study (described below) clearly show this capability.

To investigate the behavior of the k_{sgs} model, the exact production, the dissipation, and the transport terms were computed by filtering the DNS data, and then correlated with the model terms in equation (9). The results (not shown) showed that the transport and the production terms in the model equation were correlated quite well with the exact terms (with a correlation greater than 0.6). However, the dissipation term was poorly correlated. This result agreed with the earlier observation that the dissipation model needs further improvement. This has been addressed using a dynamic procedure, which is outlined below.

This model is denoted Model C for subsequent discussions.

2.1.4. Dynamic subgrid kinetic energy model. The dynamic approach can be used to obtain appropriate values of the coefficients C_k and C_ϵ. To implement this method, the kinetic energy at the test filter level is obtained by using the trace of equation (4): $K = L_{ii}/2 + \langle k \rangle$. For the evolution equation for k, Ghosal *et al.* [4] formulated a dynamic localization procedure to determine the dissipation and the diffusion model coefficients. In the present study, the similarity assumption is expanded to model the dissipation term in the subgrid kinetic energy transport equation. This implies that not only the subgrid scale stress tensor but also the subgrid scale dissipation is assumed to satisfy the similarity assumption in consecutive resolutions. The diffusion model coefficient (defined here as $C_d = C_k/\sigma_k$) can also be determined dynamically using the similarity assumptions (this dynamic procedure is discussed in detail in [13]). However, since $\sigma_k = 1$ is usually adopted, especially, in homogeneous turbulence where the diffusion effect is not very significant, in the present study, $C_d = C_k$ is adopted for simplicity. Using a procedure similar to that outlined in Section 2.1.2, equations for both C_k and C_ϵ can be derived:

$$L_{ij} - \tfrac{1}{3}\delta_{ij}L_{kk} = -C_k(\langle\Delta\rangle K^{1/2}\langle\overline{S_{ij}}\rangle - \Delta\langle k^{1/2}\overline{S_{ij}}\rangle), \tag{11}$$

$$\nu\left(\left\langle\frac{\hat{c}\overline{u_i}}{\hat{c}x_j}\frac{\hat{c}\overline{u_i}}{\hat{c}x_j}\right\rangle - \frac{\hat{c}\langle\overline{u_i}\rangle}{\hat{c}x_j}\frac{\hat{c}\langle\overline{u_i}\rangle}{\hat{c}x_j}\right) = C_\epsilon\left(\frac{K^{3/2}}{\langle\Delta\rangle} - \frac{\langle k^{3/2}\rangle}{\Delta}\right). \tag{12}$$

Note that equation (12) is a scalar equation for a single unknown and, thus, the exact value of C_ϵ can be obtained without applying the least square method. Ghosal *et al.* [4] used a more complicated formulation for the dissipation model coefficient than equation (12). A simpler formulation in equation (12) is possible when the similarity concept is applied to the subgrid scale dissipation model. The validity of this application, however, does warrant further investigation. The obvious deficiency of the formulation (12) is that this formulation has an unphysical property of vanishing at high Reynolds numbers. This problem was recently overcome by a new localized dynamic formulation which is described in detail in Kim and Menon [13].

This model is denoted Model D for subsequent discussion.

2.1.5. Stochastic backscatter model. If subgrid scales contain energy-containing eddies, then backscatter of energy from the subgrid scales to the resolved scales may occur. Analysis of DNS data has shown that backscatter occurs over a significant portion of the grid points [14]. Furthermore, earlier studies [15, 16] have shown that the forward scatter (by the eddy viscosity term) and the backscatter are two distinct processes and, therefore, the two effects must be modeled separately. Using the results of Chasnov [15], a phenomenological model for stochastic backscatter was derived earlier [17] by assuming that the backscatter effect can be modeled by a random force which satisfies certain constraints. The resulting form of the backscatter contribution to the subgrid stress model can be written as:

$$\tau_{ij}^{bs} = C_{bs}\Pi\frac{\Delta^2}{\sqrt{\Delta t}}|\bar{S}|\bar{S}_{ij}^{1/2}. \tag{13}$$

Here, C_{bs} is a constant of order unity (here, $C_{bs} = 0.1$), Δt is the time step of the LES, and Π is a random number with zero mean and unit variance. This term, equation (13), can be added to any model for the forward scatter, i.e. equation (2) or (10). In the present study, the backscatter effects were investigated in conjunction with the k_{sgs} model (Model C) given in Section 2.1.3.

This combined model is denoted Model E for subsequent discussions. Recently, Carati *et al.* [18] applied the dynamic localization procedure to this combined model. However, this model is not included in this study.

2.1.6. Scale similarity model. A scale similarity model was recently proposed by Liu *et al.* [9] based on *a priori* analysis of high $Re_\lambda (=310)$ experimental data for a turbulent jet. This model is of the form:

$$\tau_{ij} = C_L f(I_{LS}) L_{ij}, \tag{14}$$

where the stress $L_{ij} = \langle \bar{u}_i \bar{u}_j \rangle - \langle \bar{u}_i \rangle \langle \bar{u}_j \rangle$ can be computed entirely from the resolved velocity field. Also, $f(I_{LS})$ is a scalar function defined below. The constant C_L was determined to be 0.45 using the high Re_λ data [9]. This model is similar to the scale similarity model proposed earlier by Bardina [19], and it can be shown that the energy flux to the subgrid scale $E_L = -L_{ij}\bar{S}_{ij}$ will exhibit both positive (forward scatter) and negative (backscatter) in the flow. However, it has been noted earlier [9, 19] and in the present study, that this type of similarity model does not dissipate sufficient energy due to too much backscattering. Hence, to control the backscatter, a scalar function $f(I_{LS})$ is defined in terms of I_{LS}, a dimensionless invariant:

$$I_{LS} = -\frac{L_{mn}\bar{S}_{mn}}{\sqrt{L_{ij}L_{ij}}\sqrt{\bar{S}_{ij}\bar{S}_{ij}}}. \tag{15}$$

Here, I_{LS} represents the alignment between L_{ij} and $\bar{S}_{ij}$. Various forms of the scalar function $f(I_{LS})$ were proposed by Liu *et al.* [9], but their validity in LES has not been investigated. Furthermore, the experimental data was a two-dimensional slice of the flow field and Liu *et al.* [9] had to make some assumptions to determine the contribution from the third dimension. In the present study *a priori* analysis of DNS results and LES results was carried out to evaluate this model. Various forms of backscatter control were also studied. However, for LES, $f(I_{LS})$ was chosen following the earlier suggestion [9] such that $f(I_{LS}) = [1 - \exp(-10I_{LS}^2)]$, if $I_{LS} \geq 0$, and $f(I_{LS}) = 0$, if $I_{LS} < 0$.

For subsequent discussion, the scale similarity model without backscatter control [i.e. with $f(I_{LS}) = 1$] is denoted Model F1 and with backscatter control is denoted Model F2.

During the study of high Reynolds number (e.g. $Re_\lambda = 100$) decaying turbulence, it was observed that the LES with the Model F1 would become numerically unstable. Therefore, some simulations were carried out using a mixed model which involved combining the eddy viscosity model, Model A with Model F1. This type of model is similar to the mixed model proposed earlier [19].

The mixed scale similarity model is denoted Model F3 for subsequent discussions.

2.2. Subgrid modeling in Fourier space

The Fourier space representation of the Navier–Stokes equations may be written as:

$$\left(\frac{\hat{c}}{\hat{c}t} + \nu k^2\right) u_n(\mathbf{k}) = N_n(\mathbf{k}), \tag{16}$$

where $u_n(\mathbf{k})$ is the velocity field in the Fourier space at a wavenumber mode $\mathbf{k}$ (of magnitude k), and $N_n(\mathbf{k})$ is the nonlinear term which includes the effects of advection, pressure and incompressibility [6].

In Fourier space, the various terms in the above equation can be decomposed into "resolved" and "subgrid" components in the wavenumber space by introducing a wavenumber cutoff at k_c. For example, the nonlinear term may be decomposed into [6, 20]:

$$N_n(\mathbf{k}) = N_n(\mathbf{k}|k_c) + N_n^s(\mathbf{k}|k_c)(k \leq k_c). \tag{17}$$

The resolved nonlinear term, $N_n(\mathbf{k}|k_c)$, represents contributions from those triad interactions that couple a resolved mode $k \leq k_c$ to two other resolved modes p and $k-p$ (i.e. with both $\mathbf{p}$ and $\mathbf{k}-\mathbf{p}$ in the resolved range below k_c). On the other hand, the rest of the triad interactions, which couple the resolved modes to subgrid modes (with at least one of $\mathbf{p}$ and $\mathbf{k}-\mathbf{p}$ in the subgrid range $k > k_c$), are represented by the subgrid nonlinear term, $N_n^s(\mathbf{k}|k_c)$.

Energy transfer between different scales is represented by triadic interactions. The total (rate of) energy transfer to a Fourier mode $\mathbf{k}$, due to its interactions with the subgrid scales, is given by $T^s(\mathbf{k}|k_c) = \mathrm{Re}[u_n^*(\mathbf{k})N_n(\mathbf{k}|k_c)]$, where the asterisk denotes complex conjugate and Re indicates the

real part. The subgrid transfer spectrum function is then given by:

$$T^s(k\,|k_c) = \sum_{k-\frac{\Delta k}{2} \leqslant |\mathbf{k}'| < k+\frac{\Delta k}{2}} T^s(\mathbf{k}'|k_c). \tag{18}$$

Here, $T^s(k\,|k_c)$ is a function of wavenumber magnitude k only, and the shell thickness Δk is taken as unity for convenience. Summation over spectral shells, denoted by $\Sigma_{\Delta k}$ for short, is also used in the formation of the energy spectrum function $E(k)$ from the energy of discrete Fourier modes:

$$E(k) = \frac{1}{2}\sum_{\Delta k} \mu_n(\mathbf{k}')u_n^*(\mathbf{k}').$$

The energy spectrum $E^L(k)$ of the resolved scales (i.e. for $k \leqslant k_c$, signified by superscript L) at wavenumber k evolves by:

$$\frac{\partial}{\partial t}E^L(k) = -2\nu k^2 E^L(k) + T(k\,|k_c) + T^s(k\,|k_c), \tag{19}$$

where $T(k\,|k_c)$ represents energy transfer from interactions with resolved scales only, and $T^s(k\,|k_c)$ represents interactions with subgrid modes which must be modeled in an LES.

2.2.1. Spectral eddy viscosity model. A spectral subgrid eddy viscosity can be defined as [20]:

$$\nu_e(k\,|k_c) = -\frac{T^s(k\,|k_c)}{2k^2E^L(k)}, \quad k \leqslant k_c. \tag{20}$$

The corresponding modeled subgrid nonlinear term is given by: $N_n^{sm}(\mathbf{k}\,|k_c) = -\nu_e(k\,|k_c)k^2u_n(\mathbf{k})$, and the modeled subgrid transfer is $T^m(\mathbf{k}|k_c) = \mathrm{Re}[u_n^*(\mathbf{k})N_n^{sm}(\mathbf{k}|k_c)]$.

It can be shown that this spectral, eddy viscosity model accounts for the total energy transfer to a spectral shell correctly [6]. However, this model assumes that energy and energy transfer have the same form of distribution within a given spectral shell. In other words, energy and energy transfer are assumed to be entirely in phase with each other in wavenumber space. This assumption, of course, deviates from the exact spectral equations.

3. RESULTS AND DISCUSSIONS

In this section, the results of the analysis in both spectral and physical space are discussed. In the present study, the analysis of the subgrid models is largely dependent on the correlation between the DNS and the LES results or between two different LES results. This type of correlation test has been used earlier [9, 20] and can provide the information on "how accurately can the subgrid model reproduce the local structure of the subgrid scale stress and energy transfer." However, the determination of "whether proper energy is dissipated or whether the correct turbulence statistics are predicted" cannot be addressed by this type of test. Therefore, the results of correlation tests are used here only to demonstrate that the models tested here are capable of

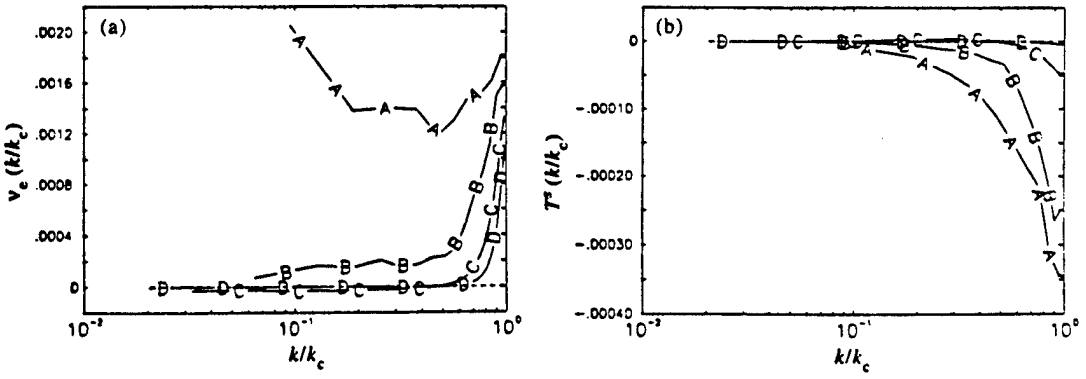


Fig. 1. The subgrid eddy viscosity and subgrid energy transfer computed from decaying isotropic turbulence DNS data for various values of k_c. Curves A–D are for $k_c = 10.5$, 15.5, 30.5 and 48.5, respectively. (a) Subgrid eddy viscosity, $\nu_e(k\,|k_c)$; (b) subgrid energy transfer, $T^s(k\,|k_c)$.

reproducing local subgrid stresses and energy transfer accurately. Given this evaluation, the next step would be to implement the chosen subgrid model in the actual problem of interest and then investigate its ability to predict "turbulence statistics", etc. This aspect of the study is reported elsewhere [13].

3.1. *Spectral space analysis*

Energy transfer information extracted from the DNS data was analyzed to determine the effect of a variable cutoff wavenumber k_c on energy transfer between the resolved (in an LES sense, $k \leqslant k_c$) and subgrid ($k \geqslant k_c$) scale ranges. The SGS eddy viscosity [equation (20)] and the subgrid energy transfer $T^s(k|k_c)$ computed using the DNS data for decaying isotropic turbulence (at $Re_\lambda \approx 20$) are shown in Fig. 1(a) and (b), respectively. It can be seen that the SGS eddy viscosity takes negative, albeit, small values at low k/k_c for relatively high values of the cutoff wavenumber. This indicates that the SGS energy transfer $T^s(k|k_c)$ takes on positive values—representing a nonnegligible backscatter of energy from the subgrid scales to the resolved scales. The eddy viscosity displays a cusp-like behavior at resolved wavenumbers approaching k_c, consistent with the results of Domaradzki [20] at higher Reynolds number. The formation of these cusps may be understood in terms of the local nature of energy transfer in turbulence. An active, forward-cascading transfer of energy occurring between scales close to k_c causes a large and negative value of $T^s(k|k_c)$ and, hence, a large and positive SGS eddy viscosity. The strength of this local transfer, which is evident in Fig. 1(b), depends, of course, on the energy in scales of size in the order of $1/k_c$ and, hence, weakens with increasing k_c.

In Fig. 1(a), it may be seen that the SGS eddy viscosity at the lowest cutoff wavenumber $k_c = 10.5$ (line A) has a much greater value than the data at higher spectral cutoffs. This is because a larger energy transfer to subgrid scales occurs as the spectral cutoff is moved to lower wavenumbers. That is, energy transfer between the larger (resolved) scales and the subgrid scales becomes much more significant if the subgrid range is expanded to include the intermediate scales that are closer to the larger scales. The upturn in line A at the low wavenumber end is partly a result of the fall-off in the energy spectrum as the low wavenumber limit is approached.

The data obtained using the forced isotropic turbulence data was also analyzed and discussed earlier [6]. The results showed that the cusp-like behavior of the SGS eddy viscosity near k_c is preserved, although more pronounced than for decaying turbulence. The influence of k_c on the magnitudes of the SGS eddy viscosity and subgrid transfer near k_c is qualitatively similar to decaying isotropic turbulence.

To assess the performance of the SGS eddy viscosity model [equation (20)], an important criterion is how well the energy transfer is predicted in physical space. The Fourier space considerations illustrated by equation (19) indicate (in homogeneous turbulence) that the space average of the energy transfer is reproduced exactly by this model. However, incorrect phase information in Fourier space translates to deviations from exact values at each grid point in physical space. A quantitative measure of model accuracy is the correlation coefficient between the exact and modeled SGS transfer in physical space, denoted by $T^s(\mathbf{x}|k_c)$ and $T^{sm}(\mathbf{x}|k_c)$, respectively. This correlation coefficient, $\rho(T^s, T^{sm})$, which is computed over all grid points in physical space, is shown in Fig. 2(a) as a function of the cutoff wavenumber k_c. Also shown is the corresponding correlation coefficient, averaged over the coordinate components, between the exact and modeled SGS nonlinear terms, denoted by $\rho(N^s, N^{sm})$.

Several observations may be made in Fig. 2(a). First, for all of the quantities considered, model performance improves steadily with increasing cutoff wavenumber. This is clearly consistent with the general expectation that SGS models should improve if a wider range of scales are resolved in an LES by increasing the number of grid points, leaving only the smallest scales to be modeled. Second, except at low cutoff wavenumbers, the nonlinear term is predicted more accurately than the energy transfer. Since in physical space this (subgrid) transfer is given by the dot product between the resolved velocity vector and the subgrid nonlinear vector, we may conclude that the alignment between these vectors is not well predicted. Third, the model produces better agreement with DNS data in the decaying case compared to the forced case. This is not surprising, since the artificial forcing has a distorting effect on energy transfer, especially at the large scales which generally dominate the correlation coefficients.

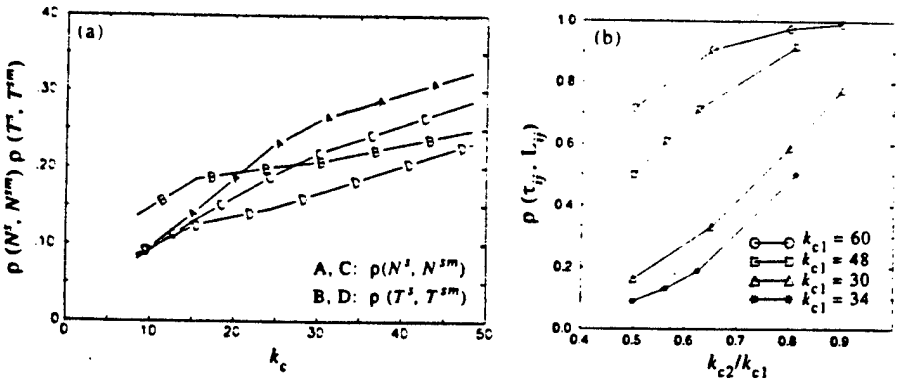


Fig. 2. Correlation between the exact and modeled quantities computed in physical space. (a) Spectral eddy viscosity model. Curves A and B are for decaying turbulence while curves C and D are for the forced case. (b) Scale similarity model (Model F1).

The scale similarity model (Model F1) was also studied in Fourier space. Since two filter operations are required to evaluate this model, two cutoff wave numbers are defined as k_{c1} and k_{c2}, where $k_{c2} < k_{c1}$. Using the decaying turbulence data obtained on the 128^3 grid (for which $k_{max} = 60$), the correlation of the exact subgrid stress τ_{ij} with the modeled subgrid stress [equation (14), with $f(I_{LS}) = 1$] was carried out. Figure 2(b) shows the correlation $\rho(\tau_{xx}, L_{xx})$ as a function of the ratio k_{c2}/k_{c1} for a range of values of k_{c1} and k_{c2}. This figure shows that for a fixed value of k_{c1}, the correlation decreases rapidly with decrease in the test cutoff wavenumber k_{c2}. Note that $k_{c2}/k_{c1} = 0.5$ is equivalent, in physical space, to a ratio between the test filter 2Δ and the grid filter Δ. Thus, it can be seen that there is a significant reduction in the correlation when the grid filter Δ (or equivalently, k_{c1}) is decreased. This implies that the scale similarity model prediction becomes quite poor as the grid is coarsened.

It has been observed in the present study and also noted earlier [9] that the scale similarity model can predict both forward scatter and backscatter. However, it is possible that the backscatter predicted by this model is not realistic. To determine this, the correlation between the negative values of the exact subgrid stresses and the scale similarity model was computed as a function of k_{c1} and k_{c2}. The results (not shown) indicate that for a fixed value of k_{c1}, a high correlation is observed only when k_{c2} is close to k_{c1}. The correlation was always lower than the correlation shown in Fig. 2(b) indicating that the negative parts are relatively less correlated. In addition, with decrease in k_{c1}, the correlation of the backscatter part dropped rapidly. These results suggest that the backscatter modeled by the scale similarity model is somewhat realistic, however, when the grid is coarsened (or $k_{c2} \ll k_{c1}$), a significant portion of the modeled backscatter could be nonphysical.

The spectral space analysis method was then used to analyze the behavior of some of the subgrid models. Figure 3(a) shows the Kolmogorov scaled energy spectra for the 64^3 DNS, and for the 32^3

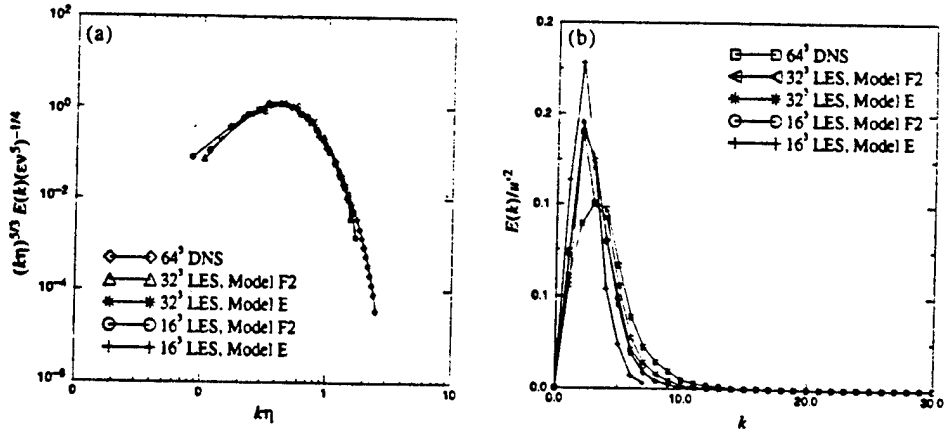


Fig. 3. Comparison of the energy spectra for DNS and LES with various subgrid models at $Re_\lambda = 10$. (a) Kolmogorov scaled energy spectra; (b) normalized energy spectra.

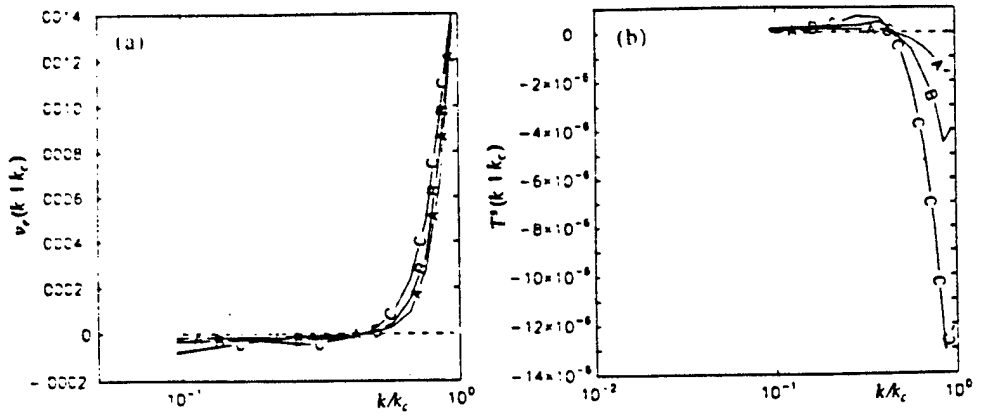


Fig. 4. The subgrid eddy viscosity and subgrid energy transfer computed from DNS and LES data for $k_c = 10.5$. Curve A: 32^3 LES, Model E; curve B: 32^3 LES, Model F2; curve C: 64^3 DNS. (a) Subgrid eddy viscosity, $\nu_e(k|k_c)$; (b) subgrid energy transfer, $T^s(k|k_c)$.

and 16^3 LES using the k_{sgs} model with stochastic backscatter (Model E), and the scale similarity model (Model F2) at a time $t = 12$ which corresponds to around 21.7 large eddy turnover time. The LES simulations were performed by first filtering the 64^3 initial field (i.e. at $t = 0$) in *physical space* into the LES grid using the top hat filter. Thus, at $t = 0$, all the initial fields were highly correlated in the physical space. (Results of the physical space analysis will be discussed in the next section.) However, in Fourier space, due to the form of the transfer function for the top hat filter, the initial energy spectra will be quite different for the direct and large eddy simulations. This should show up in the eventual evolution of the flow field when analyzed in Fourier space. However, if the simulations are self consistent, the Kolmogorov scaled spectra should exhibit similarity, as seen in Fig. 3(a).

Figure 3(b) shows the energy spectra (normalized by the kinetic energy) as a function of wavenumber. The disagreements between DNS and LES results are more apparent in this figure. The normalized energy spectra obtained using LES predict a higher peak energy at a lower wavenumber when compared to DNS data. Both Models E and F2 predict nearly the same peak value (about 25% higher than exact) and location with 32^3 resolution. However, as the grid is coarsened, the k_{sgs} model shows an energy peak larger than the similarity model. Further, near $k = k_{max}$, the energy in the high wavenumbers is much lower for the LES. These results suggest that the subgrid models are too dissipative.

The energy transfer in spectral space was also analyzed using the LES data. Using the DNS and LES fields shown in Fig. 3, the spectral eddy viscosity and the subgrid transfer at a cutoff wavenumber $k_c = 10$ was computed and is shown in Fig. 4(a) and (b), respectively. Note that for the DNS, $k_{max} = 30$, while for the LES, $k_{max} = 15$. Therefore, a k_c of 10 is in the range of resolved scales for all the simulations. Figure 4(a) shows that the spectral eddy viscosity behavior in all cases is nearly identical, suggesting that the LES models are behaving quite well. However, this is somewhat misleading. Figure 4(b) shows that at $k/k_c \rightarrow 1$ both models E and F2 predict lower negative values for the subgrid transfer $T^s(k|k_c)$. A low value for the transfer would result in a lower peak in the eddy viscosity. However, less energy is being transferred to the subgrid scales, as seen in Fig. 3(b). Therefore, the combination of low (negative) value of $T^s(k|k_c)$ and lower $E(k)$ near k_c, results in an eddy viscosity [from equation (20)] that appears to agree with the *a priori* results.

3.2. *Physical space analysis*

The analysis in physical space was carried out using methods that attempted to quantify the behavior of the models in terms of the resolution of the large-scale structures, and the correlation between the exact and the modeled stresses and energy flux to the subgrid scales. Although the *a priori* analysis was carried out on all the DNS data sets, only representative results are discussed below.

3.2.1. A priori analysis in physical space. Figure 5(a) shows contours of the subgrid energy flux $[E(\Delta) = -\tau_{ij}\bar{S}_{ij}]$ to the subgrid scales on a 32^3 grid obtained by filtering the 128^3 forced stationary turbulence data. This result is compared to the prediction by the k_{sgs} model without backscatter [Model C, Fig. 5(b)] and the scale similarity models, Model F1 [Fig. 5(c)] and Model F2 [Fig. 5(d)]. The contour interval is the same for all figures, and an arbitrary (but same) slice of the 3D field is shown. Comparison with the exact results [Fig. 5(a)] shows that there is significant similarity in regions with high positive transfer. However, only Model F1 [Fig. 5(c)] is capable of resolving regions with backscatter, although, the peak negative value is about 25% lower than in the exact case. The peak positive value also is not predicted very well. All models tested here are predicting positive peak values lower than the exact value. These results suggest that even when there

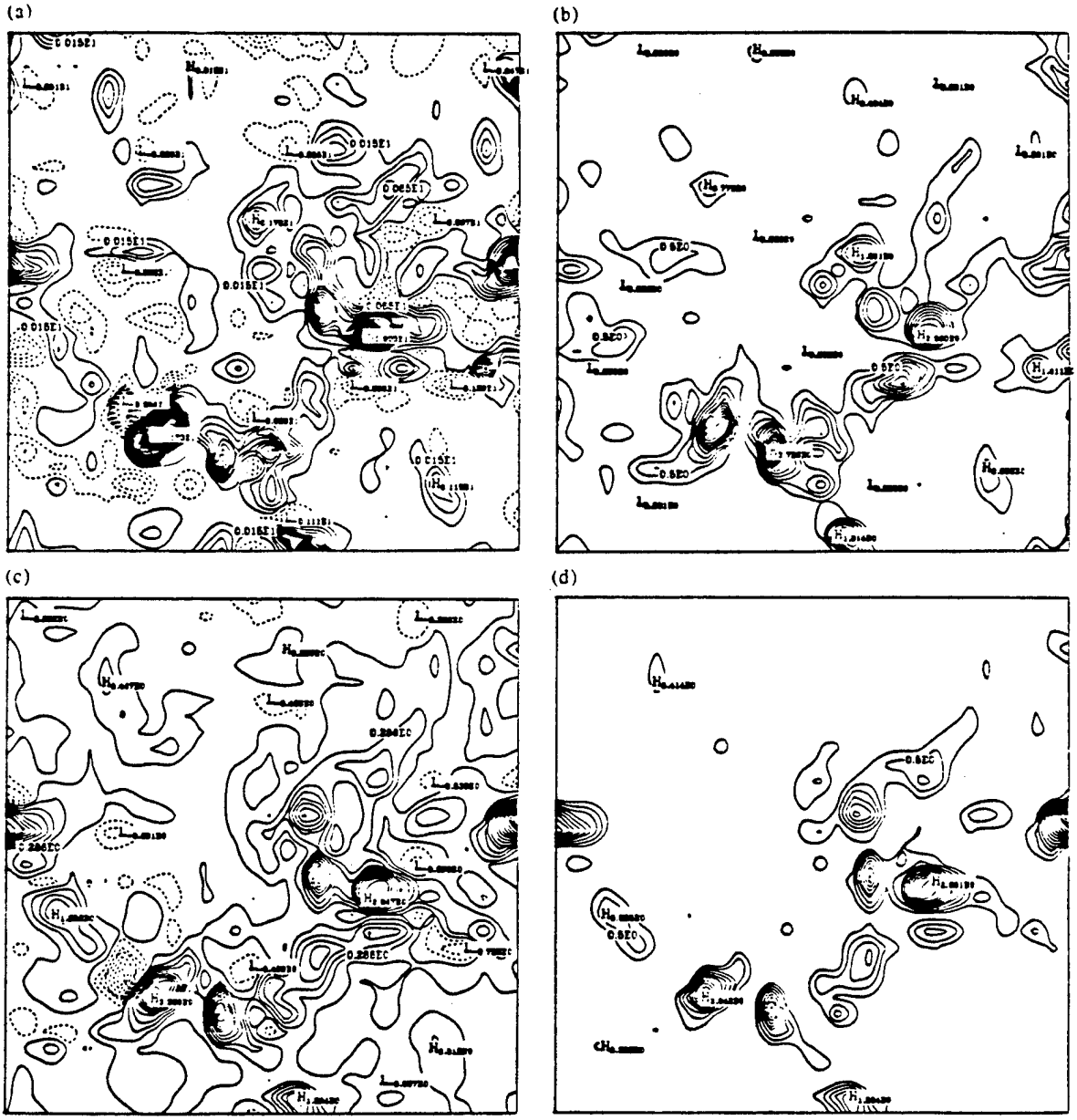


Fig. 5. Comparison of the contours of subgrid energy transfer for forced DNS data ($Re_\lambda = 90$) and subgrid model predictions on 32^3 grid. Same contour interval and locations shown for all cases. Solid contours indicate forward scatter and dotted contours indicate backscatter. (a) Exact energy transfer from DNS data; (b) energy transfer predicted by Model C; (c) energy transfer predicted by Model F1; (d) energy transfer predicted by Model F2.

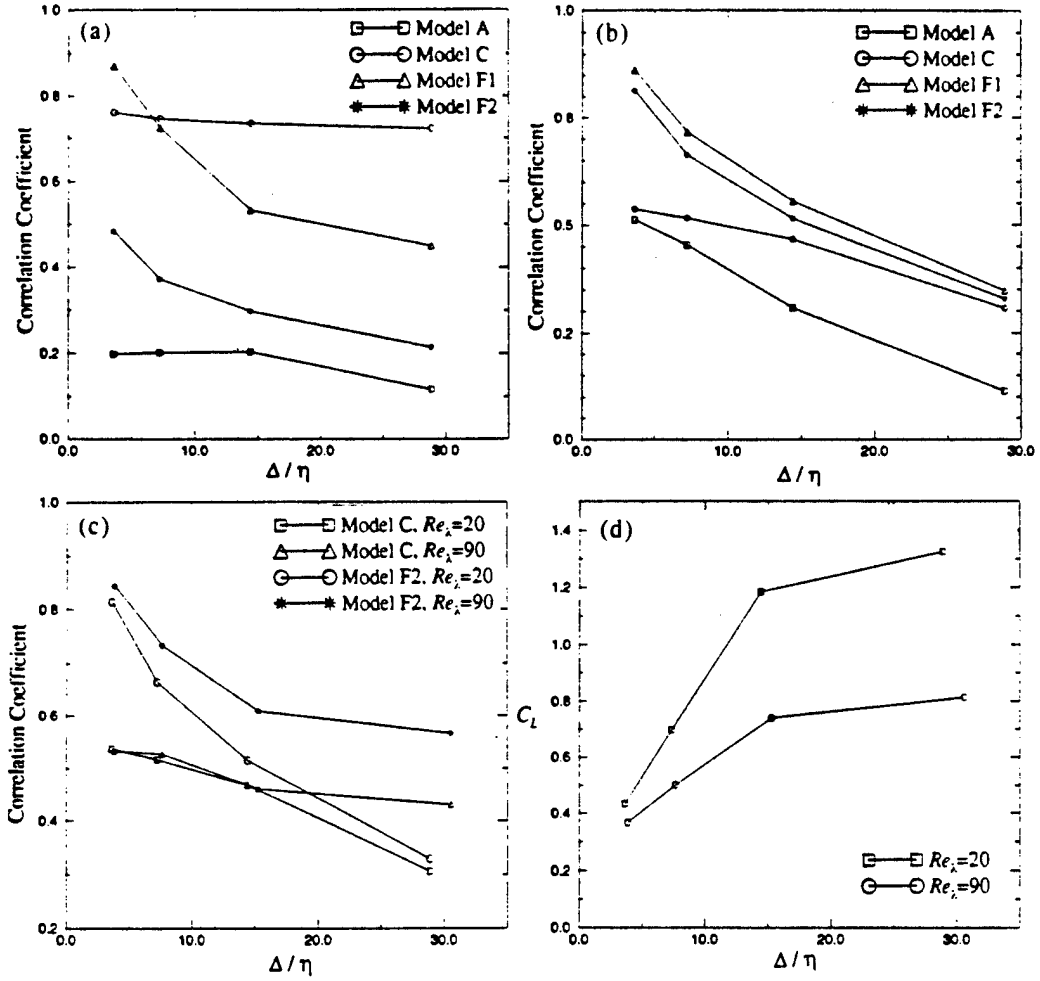


Fig. 6. Correlation between exact and modeled subgrid stress and energy transfer computed from 128^3 decaying turbulence DNS data. (a) Stress correlation at $Re_\lambda = 20$; (b) energy transfer correlation at $Re_\lambda = 20$; (c) energy transfer correlation at $Re_\lambda = 20$ and 90; (d) variation of C_L (Model F1 and F2).

is similarity between the resolved structures, the peak values predicted by subgrid models can be quite different from the exact values.

To further quantify the differences and the similarities between the model predictions and the exact values, the subgrid stress and the energy transfer correlations were computed. The stress correlation data indicates that the correlation decreases with an increase in filter width for all cases. Figure 6(a) shows the average correlation for the isotropic components of the subgrid stress tensor (i.e. τ_{ii}) as a function of filter width. The correlation for the similarity models (Models F1 and F2) decreases rapidly with increase in filter size when compared to other models. When backscatter control was imposed (Model F2), the correlation was lower. This suggests that some of the backscatter intrinsic in the scale similarity model may be realistic and this result is consistent with the data obtained earlier [9]. The eddy viscosity model of Smagorinsky (Model A) consistently showed the lowest correlation, as seen in earlier studies. On the other hand, the k_{sgs} model (Model C) showed a relatively high correlation for the stresses with only a weak dependence on the filter width. However, note that the high correlation is observed for the k_{sgs} model only for the isotropic stress components by virtue of the definition, equation (10). The correlation for the off-diagonal stress components was found to be quite low. Correlation analysis of the energy flux $(= -\tau_{ij}\bar{S}_{ij})$ is more relevant for present analysis and is discussed in more detail below.

Figure 6(b) shows the energy flux correlation for the models shown in Fig. 6(a) and (c) shows the energy flux correlation for the models at two different Reynolds numbers. Note that the higher Reynolds number case is obtained using stochastic forcing and therefore, direct comparison

of the forced and decaying turbulence cases is not intended in this figure. As noted earlier, the energy flux to the unresolved scales is defined as $E(\Delta) = -\tau_{ij}\bar{S}_{ij}$ at a filter width Δ for the exact energy flux. For the subgrid models, τ_{ij} is replaced by the appropriate model. For small values of Δ/η, where η is the Kolmogorov scale, the correlation for the scale similarity models (Model F1 and F2) is much higher than for the other models. The correlation decreases with increase in filter width for both Reynolds number with the largest decrease seen for the similarity models. On the other hand, the one-equation model (Model C) shows only a weak dependence on the filter width and Reynolds number. This suggests that the subgrid kinetic energy model may have good potential for application in coarse grid LES.

The decrease in the subgrid stress and energy transfer correlation for the similarity models with increase in filter width can be understood by noting that this model was developed based on analysis of very high Re_λ experimental data with at least a decade of wavenumbers in the inertial range. For the present DNS data, there is no appreciable inertial range, and this situation is even worse for the low Re_λ case. Furthermore, the model assumes that there is similarity between the stresses resolved at 2Δ grid and the stresses resolved at the Δ grid. In the present case, as the filter width increases (or as the grid coarsens), this assumption breaks down.

The energy flux at scales larger than Δ is also of interest. For example, it was shown [9] that the energy flux at a scale 2Δ can be represented from the "local" and "not-so-local" contributions. Using the Germano identity, the energy flux at 2Δ can be written as: $F(2\Delta) = -(L_{ij}\langle\bar{S}\rangle_{ij} + \langle\tau\rangle_{ij}\langle\bar{S}\rangle_{ij})$. The first term on the right-hand side of the above expression represents the "local" transfer of energy flux from large scales to scales between Δ and 2Δ, while the second term represents the energy transfer to the scales smaller than Δ. A correlation between these two terms was computed for various filter widths. The results (not shown for brevity) indicate a very high correlation around 0.8. A similar high correlation and behavior was observed by Liu *et al.* [9].

The coefficient C_L in Model F1 was determined by assuming that the correct amount of dissipation must be predicted by the model. Thus, $C_L = \langle\tau_{ij}\bar{S}_{ij}\rangle / \langle f(I_{LS})L_{ij}\bar{S}_{ij}\rangle$, where $\langle\ \rangle$ denotes ensemble averaging. A value of around 0.45 ± 0.15 was estimated for the high Reynolds number experimental data [9]. For the correlation analysis shown in Fig. 6(a)–(c), $C_L = 0.45$ was employed. Since, in the present study, a significant variation in the correlation was observed as a function of both the filter width and Re_λ, this coefficient was recomputed using the above noted relation. Figure 6(d) shows the variation of C_L as a function of filter width and Re_λ. The results suggest that this coefficient increases with increase in filter width and decrease in Re_λ. However, for small filter widths, the predicted value is well within the range of the value determined experimentally [9] in high Re_λ flows. The large variation in the value of C_L may be an artifact of the limited range of scales resolved in the present DNS data and the problems with the similarity model (discussed above) when the grid is coarsened. This issue needs further study.

A priori analysis of the DNS data at $Re_\lambda \approx 10$ was also carried out since this data is used for comparison with LES predictions (as discussed in Fig. 3). Comparison of the flow structures, and the stress and energy flux correlations showed a picture very similar to that seen at the higher Re_λ (and therefore is not shown).

3.2.2. A posteriori analysis in physical space. The subgrid models were implemented in LES using 32^3 and 16^3 grid resolutions. For LES, the flow field was initialized by the filtered initial field for the 64^3 DNS. Hence, at $t = 0$ the physical space fields were highly correlated (although, in Fourier space there was quite a bit of discrepancy). However, the results showed that as time evolved, the DNS and LES became uncorrelated due to the chaotic property of turbulence.

To analyze the LES results, the DNS data obtained on the 64^3 grid resolution, and the LES data obtained on the 32^3 grid were filtered to the 16^3 grid. The energy flux predicted from these two simulations at the 16^3 grid resolution was then compared to the model prediction in the actual 16^3 grid LES. The results showed that all the models predicted very poor correlation (less than 0.1) when the 16^3 grid LES was compared to the filtered DNS data set at the same grid level. The comparison between the two LES (16^3 and 32^3 grid resolution) showed that the energy transfer correlation for the scale similarity models (F1 and F2) was very low (around 0.12), while the k_{sgs} model (Model E) predicted a relatively higher value of around 0.35. This suggests that the k_{sgs} model appears to respond more consistently to the changes in grid resolution.

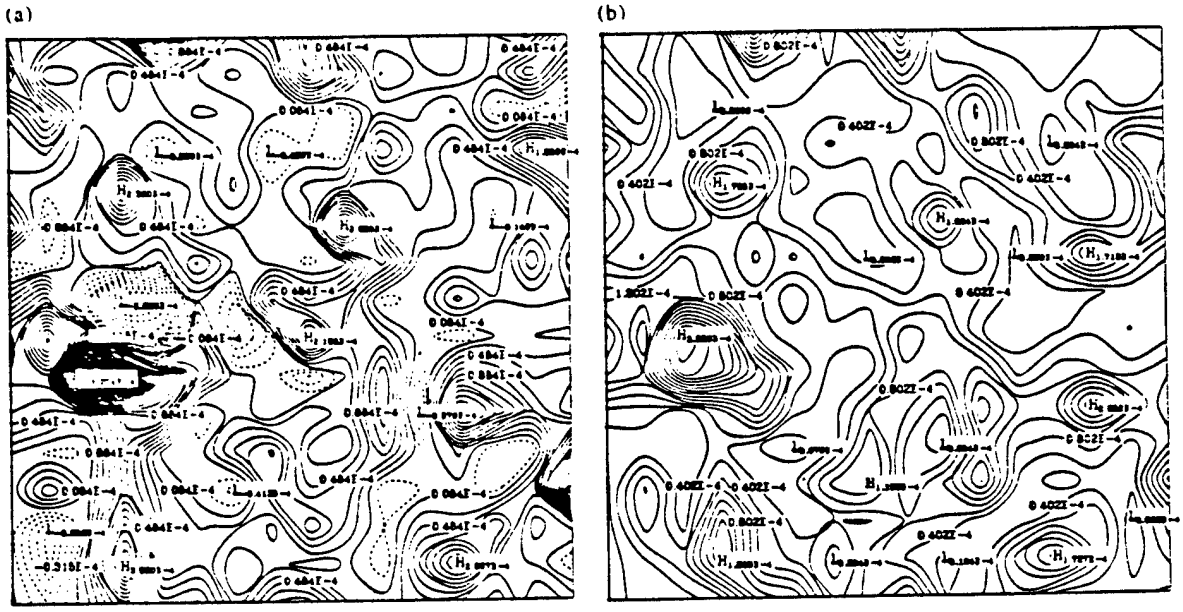


Fig. 7. Comparison of the exact and modeled subgrid energy transfer resolved on a 16^3 grid obtained using 64^3 decaying isotropic turbulence DNS data. Same contour interval and location shown. (a) Exact energy transfer from DNS data; (b) modeled energy transfer by Model C.

To visualize these results, Fig. 7(a) shows the contours of the energy transfer computed on the 16^3 grid by filtering the 64^3 DNS data. Figure 7(b) shows the contours [using the same contour interval as in Fig. 7(a)] of the *a priori* prediction by the k_{sgs} model (Model C) on the 16^3 grid using the same DNS data. Clearly, there is quite a good correlation between the two figures [as seen in Fig. 6(a) and (b)].

Figure 8(a) shows the contours of the energy transfer computed on the 16^3 grid by filtering the results of the 32^3 grid LES (using the Model C). Finally, Fig. 8(b) shows the energy transfer on the 16^3 grid obtained by carrying out LES using Model C in that grid. If the subgrid model was accurate, then all these figures should be highly correlated. As noted above, although the *a priori*

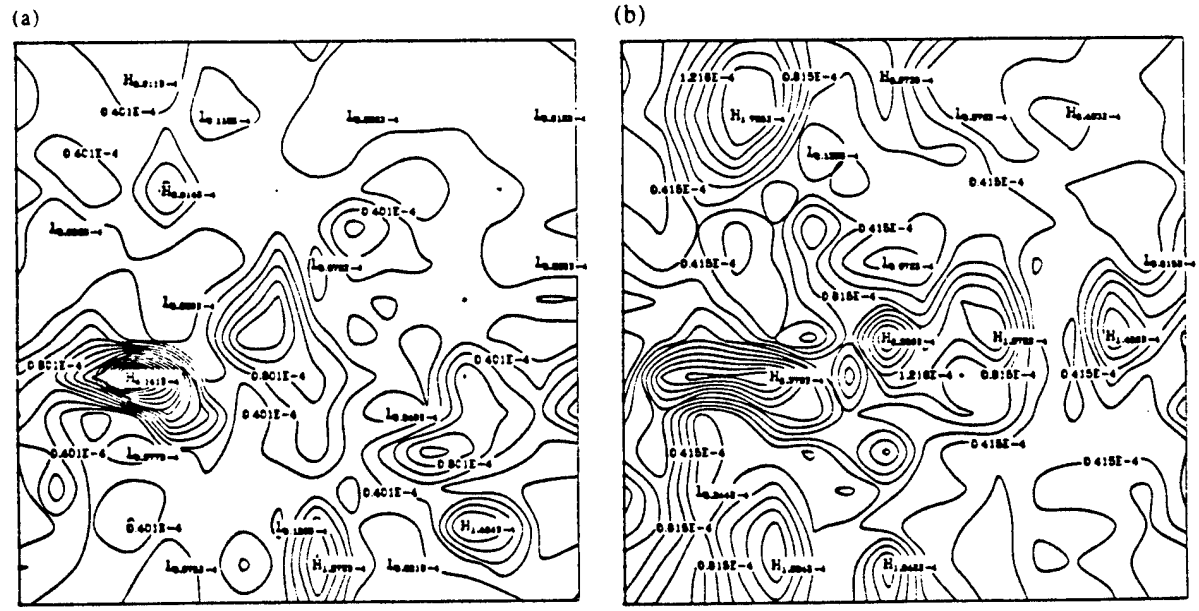


Fig. 8. Comparison of the subgrid energy transfer predicted by LES using Model C on a 16^3 grid. Same contour interval and location shown as in Fig. 7. (a) Energy transfer predicted using 32^3 LES data; (b) energy transfer modeled by Model C in 16^3 LES.

correlation was high [Fig. 7(a) and (b)], the correlation obtained using LES data was quite low [Fig. 8(a) and (b)]. However, it is worth noting these results were much better than the results obtained using Models A and F2 (not shown).

Figure 9(a) summarizes the above results for a range of Reynolds number. The computed correlation in the 16^3 grid for the various models is plotted as a function of the initial Reynolds number. The data shows that the correlation for all models is much lower in LES than in the *a priori* analysis. Furthermore, with increase in Re_λ, the correlation for all the models decreases. With backscatter modeling (Model E), a slightly higher value of the correlation was obtained when compared to the model without backscatter (Model C). This small change does not justify the inclusion of the backscatter term. However, this issue will be revisited at a later stage.

The above study showed that, although the one-equation model had some potential for application as a subgrid model, it still had some major problems. To determine if these problems could be removed, a series of calculations were carried out using the dynamic versions of the eddy viscosity model (Model B) and the dynamic one-equation model (Model D). The results obtained from these simulations were much more encouraging. To evaluate the self consistency of the dynamic models, the LES results obtained on the 32^3 grid were compared to the LES results obtained on the 16^3 grid. The flow fields from these two simulations can be related through the mathematical identity, equation (4). Thus, the modeled quantity $\langle u_i u_j \rangle$ obtained from the two data sets must be identical if the subgrid model has performed correctly at the two grid level.

Figure 9(b) shows the average value of the correlation for the anisotropic components of $\langle u_i u_j \rangle$ as a function of the Reynolds number. Clearly, the correlation is very high for both the dynamic models with values consistently in the 0.85–0.97 range. However, with increase in Reynolds number, the correlation for the dynamic eddy viscosity model decreases while the dynamic one-equation model maintains a high value. This result suggests that models that do not make the assumption of local equilibrium between energy production and dissipation rate (e.g. Model D) are superior to algebraic eddy viscosity type models (e.g. Model B). This result is very important since this implies that such models may be applicable for LES of high Reynolds number flows using relatively coarse grids (grid resolution restrictions are typically imposed due to computer resource limitations).

Figure 10(a) shows the variation of the dynamically evaluated constants (i.e. C, C_k, and C_ϵ) with time during the simulation for $Re_\lambda = 100$. Figure 10(b) shows the variation of the constants with Reynolds number. The model coefficients go through changes in the early stages of the turbulent flow development. However, as a realistic decaying isotropic field develops, the coefficients reach an asymptotic state. Also, the values of the coefficients at this asymptotic state are almost independent of Reynolds number [Fig. 10(b)], except for C_ϵ in Model D which is sensitive to both

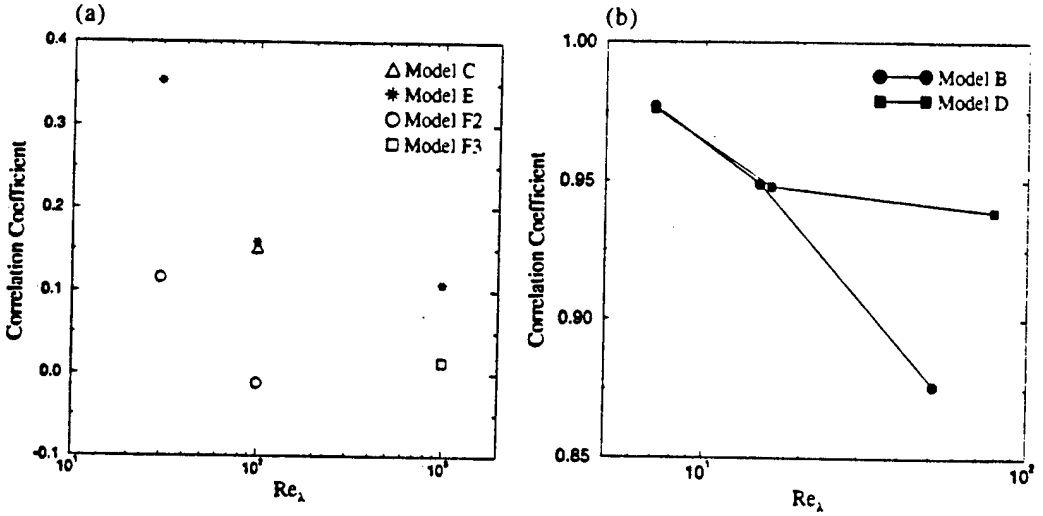


Fig. 9. Variation of subgrid energy transfer correlation with Re_λ. Correlation computed on 16^3 grid. (a) Subgrid models with fixed coefficients; (b) dynamic subgrid models.

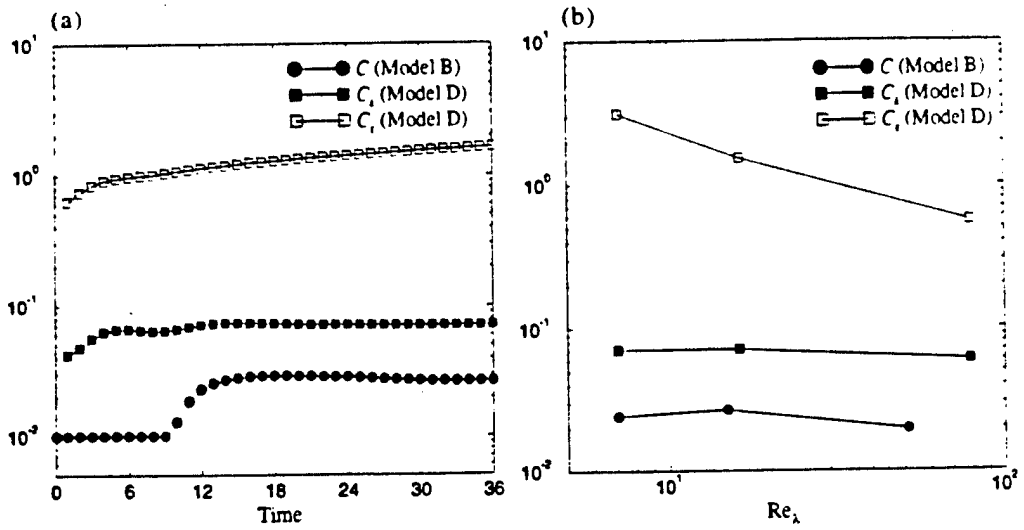


Fig. 10. The variation of the coefficients with time and Re_λ for the dynamic models. (a) Variation with time; (b) variation with Re_λ.

grid resolution and Reynolds number. The values of the constants are in good agreement with earlier results. For example, the Smagorinsky's constant C_S (which is the square-root of the dynamic model coefficient C) is around 0.16 which is quite close to 0.17, suggested by Lilly [10] for homogeneous, isotropic turbulence with cutoff in the inertial range. The dynamically determined value of $C_k \approx 0.065$ is also close to the value $C_k = 0.05$ recommended by Yoshizawa and Horiuti [12] based on their two-scale analysis of the two-scale direct interaction approximation.

4. CONCLUSIONS

Direct and large eddy simulations of forced and decaying isotropic turbulence have been performed using a pseudo spectral and a finite-difference code. Subgrid models that include a one-equation subgrid kinetic energy model with and without a stochastic backscatter forcing term and a new scale similarity model, have been analyzed in both Fourier space and physical space using high resolution DNS data. The spectral space correlation analysis of the modeled (by a spectral eddy viscosity) and exact nonlinear terms, and the subgrid energy transfer in physical space showed relatively low values. The correlation of the scale similarity model was much higher; however, the correlation decreased with decrease in the grid cutoff wave number (k_{c1}). This suggests that as the grid becomes coarse (i.e. Δ is large), the scale similarity model becomes less reliable.

In physical space, *a priori* analysis of the stress and energy transfer correlation between the exact value and the modeled terms was carried out for a range of Re_λ. Results show that the stress and energy flux predicted by subgrid models C and F2 correlates reasonably well with the DNS data, with the scale similarity model showing very high correlation for reasonable grid resolution. However, with decrease in grid resolution, the scale similarity model (Model F2) becomes more uncorrelated when compared to the kinetic energy model (Model C). This result is consistent with the observation made in spectral space.

When the subgrid models (with fixed coefficients) were used for LES, correlation with the DNS results do not improve even for the LES using models C and F2, which showed high correlation in the *a priori* test. This suggests that the results of *a priori* analysis cannot be used to predict the behavior of the subgrid models in actual LES. The analysis of the LES data obtained on very coarse grids showed that the scale similarity model behaves poorly when compared to the k_{sgs} model, which consistently showed relatively higher (albeit low) correlation. These results suggest that the scale similarity model can be used only for relatively fine grid resolution, whereas the kinetic energy model may be useful even in coarse grids. However, it was determined that to improve the one-equation model, the dissipation term in the transport equation has to be modeled more accurately.

To determine the performance of dynamic models, two models (the dynamic eddy viscosity model and the dynamic one-equation model) were implemented and LES was carried out for a range of Reynolds numbers. The correlation analysis of these simulations was carried out without using any DNS information. It was shown that both models consistently indicated a very high correlation even in coarse grids. However, with increase in Reynolds number, the correlation for the dynamic eddy viscosity model decreased while for the dynamic one-equation model there was not much change. This showed that models that do not assume local balance between the energy production and dissipation rate (as Model D) have a much better potential for modeling subgrid stresses in coarse grids even at relatively high Reynolds number. Furthermore, the application of the dynamic procedure to the one-equation model appears to have improved the modeled dissipation term in the original equation.

Acknowledgements—This work is supported by the Office of Naval Research under Grant No. N00014-93-1-0342. Computing time was provided by the Numerical Aerodynamic Simulation (NAS) at NASA Ames Research Center and is gratefully acknowledged.

REFERENCES

1. M. Germano, U. Piomelli, P. Moin and W. H. Cabot, A dynamic subgrid-scale eddy viscosity model. *Phys. Fluids A* **3**, 1760 (1991).
2. P. Moin, D. Carati, T. Lund, S. Ghosal and K. Akselvoll, Developments and applications of dynamic models for large eddy simulations of complex flows. *Proc. 74th AGARD FDP Symp. on Application of Direct and Large Eddy Simulation to Transition and Turbulence*, AGARD CP-551 (1995).
3. U. Piomelli and J. Liu, Large-eddy simulations of rotating channel flows using a localized dynamic model. *Phys. Fluids* **7**, 839 (1995).
4. S. Ghosal, T. S. Lund, P. Moin and K. Akselvoll, A dynamic localization model for large-eddy simulation of turbulent flows. *J. Fluid Mech.* **289**, 229 (1995).
5. R. S. Rogallo, Numerical experiments in homogeneous turbulence, NASA TM 81315 (1981).
6. S. Menon and P.-K. Yeung, Analysis of subgrid models using direct and large eddy simulations of isotropic turbulence. *Proc. 74th AGARD FDP Symp. on Application of Direct and Large Eddy Simulation to Transition and Turbulence*, AGARD CP-551 (1995).
7. V. Eswaran and S. B. Pope, An examination of forcing in direct numerical simulations of turbulence. *Comput. Fluids* **16**, 257 (1988).
8. U. Piomelli, P. Moin and J. H. Ferziger, Model consistency in large eddy simulation of turbulent channel flows. *Phys. Fluids* **31**, 1884 (1988).
9. S. Liu, C. Meneveau and J. Katz, On the properties of similarity subgrid-scale models as deduced from measurements in a turbulent jet. *J. Fluid Mech.* **275**, 83 (1994).
10. D. K. Lilly, On the application of the eddy viscosity concept in the inertial sub-range of turbulence, NCAR manuscript 123 (1966).
11. D. K. Lilly, A proposed modification of the germano subgrid-scale closure model. *Phys. Fluids* **4**, 633 (1992).
12. A. Yoshizawa and K. Horiuti, A statistically-derived subgrid scale kinetic energy model for large-eddy simulation of turbulent flows. *J. Phys. Soc. Japan* **54**, 2834 (1985).
13. W.-W. Kim and S. Menon, On the properties of a localized dynamic subgrid-scale model for large-eddy simulations. Submitted to *J. Fluid Mech.* (1995).
14. U. Piomelli, W. H. Cabot, P. Moin and S. Lee, Subgrid-scale backscatter in turbulent and transitional flows. *Phys. Fluids A* **3**, 1766 (1991).
15. J. R. Chasnov, Simulation of the Kolmogorov inertial subrange using an improved subgrid model. *Phys. Fluids A* **3**, 188 (1991).
16. C. E. Leith, Stochastic backscatter in a subgrid-scale model: plane shear mixing layer. *Phys. Fluids A* **2**, 297 (1990).
17. S. Menon, A numerical study of secondary fuel injection control of combustion instability in a ramjet. AIAA Paper 92-0777 (1992).
18. D. Carati, S. Ghosal and P. Moin, On the representation of backscatter in dynamic localization models. *Phys. Fluids* **7**, 606 (1995).
19. J. Bardina, J. H. Ferziger and W. C. Reynolds, Improved subgrid scale models for large eddy simulations. AIAA Paper 80-1357 (1980).
20. J. A. Domaradzki, W. Liu and M. E. Brachet, An analysis of subgrid scale interactions in numerically simulated isotropic turbulence. *Phys. Fluids A* **5**, 1747 (1993).

On the properties of a localized dynamic subgrid-scale model for large-eddy simulations

Won-Wook Kim and Suresh Menon

School of Aerospace Engineering

Georgia Institute of Technology

Atlanta, Georgia

November 1996

Abstract

A new dynamic model for large-eddy simulations of turbulent flows that provides localized (both in time and space) determination of the model coefficients has been developed using the subgrid-scale kinetic energy equation model. In the proposed model, the dynamic modeling approach originally introduced by Germano *et al.* is improved to make it more generally applicable. It is shown that the shortcomings of existing dynamic models can be resolved without significant increase in complications and computational cost. Moreover, analysis shows that the localized model coefficient determined by the proposed model is Galilean-invariant and very realizable. The properties of the model have been examined by conducting large-eddy simulations of various

turbulent flows such as decaying, forced, and rotating isotropic turbulence, and plane Couette flows. No adjustment of the model was required for the simulations of these various flows. The results show good agreement with existing experimental and direct numerical simulation data.

1 Introduction

The dynamic subgrid-scale (SGS) model of Germano *et al.* (1991) has been successfully used in large-eddy simulations (LES) to study numerous turbulent and transitional flows (Moin *et al.*, 1991; Akselvoll & Moin, 1993; Piomelli, 1993; Zang *et al.*, 1993; Wong & Lilly, 1994; El-Hady *et al.*, 1994; Squires & Piomelli, 1994). Several demonstrated features of this model have established the unique capabilities of the dynamic approach. The (dynamic) determination of the model coefficient as a part of the solution has removed the inability of the classical Smagorinsky model to parameterize accurately the unresolved SGS stresses in different turbulent flows with a single *universal* constant. Furthermore, the ability of the dynamic model to mimic backscatter of energy from the subgrid scales to the resolved scales in certain regions of the flow (consistent with filtering experiments by Piomelli *et al.* (1991) using direct numerical simulation (DNS) data of turbulent channel flows) and the demonstration of correct asymptotic behavior near a wall and in laminar flows have clearly established the dynamic methodology.

The dynamic methodology is independent of the choice of the SGS model. However, the predictive capability of this approach depends considerably on the choice of the SGS model. The Smagorinsky time-independent, algebraic eddy-viscosity model used in many of the

past studies has some well known limitations. For example, this model assumes equilibrium between SGS energy production and dissipation, and requires that the SGS stress tensor and the resolved-scale strain-rate tensor are aligned. However, the validity of these assumptions in general turbulent flows is questionable. In many past studies, the isotropic part of the SGS stress tensor (equivalent to 2/3 of the subgrid-scale kinetic energy) is added to pressure and is considered the grid-scale total pressure. Consequently, the computed velocity field is due to the influence of this grid-scale total pressure instead of just the pressure. In addition to these model-related limitations, the dynamic procedure assumes that the computed model coefficient is constant with respect to the test-scale filtering (this assumption can not be justified unless the model coefficient is constant throughout the whole flow field). The inconsistency of this assumption was pointed out earlier by Cabot & Moin (1993). Moreover, as discussed by Lund *et al.* (1993), the dynamic model exhibits numerical instability in some regions of the flow due to large fluctuations of the dynamic model coefficient and the prolonged presence of the negative model coefficient.

To resolve the limitations caused by the inherent nature of the base model, modifications such as the addition of the resolved stress term (Zang *et al.*, 1993; Vreman *et al.*, 1994b; Salvetti & Banerjee, 1995) or the explicit backscatter term (Carati *et al.*, 1995) to the Smagorinsky model, have been carried out. Piomelli & Liu (1995) proposed an iterative scheme (based on the time-splitting method) to remove the above noted inconsistency in the dynamic model formulation. Germano (1995) recently reformulated the model to make it statistically consistent. The ill conditioning problem (i.e., the numerical instability) has been overcome in simple flows such as isotropic turbulence by spatially averaging the model coefficient in directions of flow homogeneity. Since this is not possible in flows without any

direction of flow homogeneity, local averaging techniques also have been proposed (Meneveau *et al.*, 1996; Kim & Menon, 1995) for more complex flows. The prolonged presence of negative model coefficient has been avoided by introducing the SGS kinetic energy (e.g., Wong, 1992) which prevents backscatter whenever it becomes zero.

Although significant improvement has been obtained using these modifications, they are still incomplete (i.e., only parts of the problem have been resolved by each modification) and/or are based on *ad hoc* procedures. The dynamic localization model of Ghosal *et al.* (1995), which is based on a constrained variational approach, overcomes all the shortcomings of dynamic model. However, the computational cost associated with the iterative solution procedure for computing the model coefficients is quite significant.

In this paper, a dynamic model which can be applied to various turbulent flows without any adjustment of model parameters is proposed. This model is formulated in a mathematically consistent manner without employing *ad hoc* procedures and adopts only assumptions verified in experiments. The properties of this model are investigated using LES of various isotropic turbulent flows (such as decaying, forced, and rotating isotropic turbulence) and turbulent plane Couette flows. Comparison with past simulations and experimental data is carried out to quantify the capability of this model.

The details of the new dynamic subgrid-scale model, its application to various turbulent flows, and the employed numerical scheme are discussed in the following sections. In section 2, two typical dynamic models are described along with a discussion of their favorable and adverse features. In section 3, existing localized dynamic models are briefly discussed. Then, a new localized dynamic model that overcomes the limitations of the existing dynamic models is introduced (section 3.1 and section 3.2), followed by an analysis of its basic properties

(section 3.3). In section 4, the numerical method employed in this study is described. In section 5, the new model is applied to decaying (section 5.1), forced (section 5.2), and rotating (section 5.3) isotropic turbulent flows, and turbulent Couette flows (section 5.4). Conclusions are presented in section 6.

2 Dynamic subgrid-scale modeling

In LES, the flow variables are decomposed into a large-scale component (denoted by an overbar) and a small subgrid-scale component by applying a filtering operation:

$$\overline{f}(x_i) = \int f(x_i')G(x_i, x_i')dx_i' \tag{1}$$

where G is the filter function and the integral is extended over the entire domain. Applying the filtering operation (in the present study, a low-pass filter of a computational mesh is used, hence, the characteristic size of this filter is the grid width $\overline{\Delta}$), the incompressible Navier-Stokes equations for the evolution of the large-scale motions are obtained. The resulting governing equations are:

$$\frac{\partial \overline{u}_i}{\partial x_i} = 0 \tag{2}$$

$$\frac{\partial \overline{u}_i}{\partial t} + \overline{u}_j \frac{\partial \overline{u}_i}{\partial x_j} = -\frac{\partial}{\partial x_j}\left(\overline{p}\delta_{ij} + \tau_{ij}\right) + \nu \frac{\partial^2 \overline{u}_i}{\partial x_j \partial x_j} \tag{3}$$

where i $(= 1, 2, 3)$ indicates the spatial dimension and $\overline{u}_i(x_i, t)$ is the resolved velocity field. The effects of the small scales appear in the SGS stress tensor,

$$\tau_{ij} = \overline{u_i u_j} - \overline{u}_i \overline{u}_j \tag{4}$$

that must be modeled.

Eddy-viscosity models assume proportionality between the anisotropic part of the SGS stress tensor $\tau_{ij} - \frac{1}{3}\delta_{ij}\tau_{kk}$ and the resolved-scale strain-rate tensor $\overline{S}_{ij}$:

$$\tau_{ij} - \frac{1}{3}\delta_{ij}\tau_{kk} = -2\nu_T \overline{S}_{ij} \tag{5}$$

where ν_T is the eddy viscosity and

$$\overline{S}_{ij} = \frac{1}{2}\left(\frac{\partial \overline{u}_i}{\partial x_j} + \frac{\partial \overline{u}_j}{\partial x_i}\right) \tag{6}$$

Simple dimensional arguments suggest that the eddy viscosity ν_T should be parameterized by a product of a velocity and a length scale. In LES, the length scale is usually related to the filter size ($\overline{\Delta}$). However, the various proposed models differ in their prescription for the velocity scale. In the Smagorinsky model, the velocity scale is obtained by assuming that an equilibrium exists between energy production and dissipation in the small scales whereas, in one-equation model (Schumann, 1975; Yoshizawa & Horiuti, 1985; Menon *et al.*, 1996), a transport equation for the SGS kinetic energy is solved to obtain the velocity scale.

The eddy-viscosity models used in LES are similar to the eddy-viscosity models used in Reynolds-averaged Navier-Stokes simulation (RANS) approach. Similarity models developed by Bardina *et al.* (1980) and Liu *et al.* (1994) assume a similarity between turbulent stresses in consecutive scales or resolutions (e.g., similarity between the smallest resolved-scale stresses and the largest unresolved SGS stresses). Although these models reproduce the

structure of the SGS stresses rather well, they do not dissipate sufficient turbulent energy and, therefore, must be combined with the eddy-viscosity type models in order to have all of the desired properties. The resulting models are often called mixed models. In the mixed models, the major role of the similarity part is to cause backscattering of SGS energy, as noted by Horiuti (1989).

To date, two dynamic models have been suggested. One is the dynamic algebraic SGS model which incorporates the Smagorinsky model (Germano *et al.*, 1991), and the other is the dynamic one-equation SGS model based on the SGS kinetic energy (e.g., Wong, 1992). These models are described in the following two sections to facilitate subsequent discussion.

2.1 Dynamic Smagorinsky model (DSM)

The simplest SGS model which predicts the global energy transfer with acceptable accuracy is the algebraic eddy-viscosity model originally proposed by Smagorinsky (1963):

$$\tau_{ij} = -2C_S\overline{\Delta}^2 \left|\overline{S}\right| \overline{S}_{ij} + \frac{1}{3}\delta_{ij}\tau_{kk} \tag{7}$$

where the model coefficient C_S is equivalent to the square of the Smagorinsky constant and $\left|\overline{S}\right| = \left(2\overline{S}_{ij}\overline{S}_{ij}\right)^{1/2}$. In the classical approach, C_S requires adjustment for different flows. This was circumvented by the dynamic procedure (Germano *et al.*, 1991) which directly calculates C_S as a part of the solution by employing a mathematical identity between the SGS stresses (characterized by $\overline{\Delta}$) and the subtest-scale stresses (characterized by $\hat{\Delta}$, typically, $\hat{\Delta} = 2\overline{\Delta}$). Here, the test filter should be similar to the grid filter to conserve the similarity between the SGS stresses and the subtest-scale stresses. In the present study, we employ a top-hat test

filter which is considered appropriate for finite-difference methods in physical space. Thus, if the application of the test filter on any variable ϕ is denoted by $\widehat{\phi}$, it can be shown that,

$$L_{ij} = T_{ij} - \widehat{\tau}_{ij} = \widehat{\overline{u}_i \overline{u}_j} - \widehat{\overline{u}}_i \widehat{\overline{u}}_j \tag{8}$$

where

$$T_{ij} = \widehat{\overline{u}_i \overline{u}_j} - \widehat{\overline{u}}_i \widehat{\overline{u}}_j \tag{9}$$

is the subtest-scale stress tensor. Assuming similarity between the subtest-scale stresses and the SGS stresses, T_{ij} is modeled similar to τ_{ij}:

$$T_{ij} = -2C_S \widehat{\Delta}^2 \left|\widehat{\overline{S}}\right| \widehat{\overline{S}}_{ij} + \frac{1}{3}\delta_{ij} T_{kk} \tag{10}$$

Substitution of (7) and (10) into (8) results in

$$L_{ij} - \frac{1}{3}\delta_{ij} L_{kk} = -2C_S \widehat{\Delta}^2 \left|\widehat{\overline{S}}\right| \widehat{\overline{S}}_{ij} + \widehat{2C_S \overline{\Delta}^2 \left|\overline{S}\right| \overline{S}_{ij}} \tag{11}$$

This equation includes only one unknown quantity C_S, hence, it can be used to compute C_S. However, C_S can not be directly solved from (11) since C_S appears inside the test-filtering operator. In most of the past studies, an assumption that C_S *does not depend on the test filtering*, was made to extract C_S from the test-filter operator. Then, (11) can be rewritten:

$$L_{ij} - \frac{1}{3}\delta_{ij} L_{kk} = 2C_S M_{ij} \tag{12}$$

where

$$M_{ij} = -\left(\hat{\Delta}^2 \left|\hat{\overline{S}}\right| \hat{\overline{S}}_{ij} - \overline{\Delta}^2 \widehat{\left|\overline{S}\right| \overline{S}_{ij}}\right) \tag{13}$$

Equation (12) is a set of five independent equations for one unknown C_S. To minimize the error that can occur when solving this over-determined system, Lilly (1992) proposed a least-square method which yields

$$C_S = \frac{1}{2} \frac{L_{ij} M_{ij}}{M_{ij} M_{ij}} \tag{14}$$

As many researchers have pointed out, this original formulation of the dynamic model contains some shortcomings. First, this formulation has been derived using two fundamental assumptions. The primary assumption is that the model coefficient is a totally local variable (this is a sufficient condition for dynamic modeling) while the second assumption is that the model coefficient is constant with respect to the test-scale filtering (this assumption, implicit in (12), is valid only when the model coefficient is constant in whole flow field). Obviously, these two assumptions are in contradiction and, thus, *mathematically inconsistent.* Second, the equation (14) for C_S is ill-conditioned because the denominator of this expression (i.e., M_{ij}) is the difference between two model representations at different filter levels and, hence, can become very small (even though the difference between the corresponding exact quantities is supposed to be finite) causing numerical instability. Finally, the prolonged occurrence of negative model coefficient in some locations of the flow field has also been known to cause numerical instability (Lund *et al.*, 1993).

In this paper, we refer to this model (which is identical to original Germano *et al.*'s dynamic model) as the dynamic Smagorinsky model (DSM).

2.2 Dynamic k_{sgs}-equation model (DKM)

A one-equation model for the subgrid-scale kinetic energy,

$$k_{sgs} = \frac{1}{2}\left(\overline{u_k u_k} - \overline{u}_k \overline{u}_k\right) \tag{15}$$

in the following form (e.g., Schumann, 1975),

$$\frac{\partial k_{sgs}}{\partial t} + \overline{u}_i \frac{\partial k_{sgs}}{\partial x_i} = -\tau_{ij}\frac{\partial \overline{u}_i}{\partial x_j} - \varepsilon_{sgs} + \frac{\partial}{\partial x_i}\left(\nu_T \frac{\partial k_{sgs}}{\partial x_i}\right) \tag{16}$$

has been studied recently (Menon *et al.*, 1996). In (16), the three terms on the right hand side represent, respectively, the production, the dissipation, and the diffusion of k_{sgs}. Note that, in the model of the diffusion term, the direct effect of ν has been dropped and, furthermore, in the original model of this term, ν_T/σ_k (when σ_k is a constant) is used in place of ν_T. However, since the SGS diffusion of k_{sgs} is usually small compared to the other terms (i.e., the SGS energy production, the SGS energy dissipation, and the resolved-scale advection), $\sigma_k = 1$ is commonly adopted (e.g., Wong, 1992; Yoshizawa, 1993). Note that the dynamic procedure can also be applied to determine σ_k (or an equivalent diffusion model coefficient) as described in appendix A.

In the k_{sgs}-equation model, the SGS stress tensor τ_{ij} and the eddy viscosity ν_T are usually modeled as

$$\tau_{ij} = -2C_\tau \overline{\Delta} k_{sgs}^{1/2} \overline{S}_{ij} + \frac{1}{3}\delta_{ij}\tau_{kk} \tag{17}$$

where $\tau_{kk} = 2k_{sgs}$ and

$$\nu_T = C_\tau \overline{\Delta} k_{sgs}^{1/2} \tag{18}$$

Here, C_τ is an adjustable coefficient to be determined dynamically. Equation (16) is closed by providing a model for the SGS dissipation rate term, ε_{sgs}. Using simple scaling arguments, ε_{sgs} is usually modeled as

$$\varepsilon_{sgs} = C_\varepsilon \frac{k_{sgs}^{3/2}}{\overline{\Delta}} \tag{19}$$

where, C_ε is another coefficient also to be determined dynamically.

In the following, the dynamic procedures for C_τ and C_ε are described. These procedures need the subtest-scale kinetic energy which can be defined from the trace of (8):

$$K = \frac{1}{2} L_{kk} + \hat{k}_{sgs} \tag{20}$$

The subtest-scale stress tensor T_{ij} is modeled using K as:

$$T_{ij} = -2C_\tau \hat{\Delta} K^{1/2} \hat{\overline{S}}_{ij} + \frac{1}{3}\delta_{ij} T_{kk} \tag{21}$$

where $T_{kk} = 2K$. Using a procedure similar to that outlined in section 2.1, a set of equations for C_τ can be derived, so that:

$$L_{ij} - \frac{1}{3}\delta_{ij} L_{kk} = 2C_\tau N_{ij} \tag{22}$$

where

$$N_{ij} = -\left(\hat{\Delta} K^{1/2} \hat{\overline{S}}_{ij} - \overline{\Delta \widehat{k_{sgs}^{1/2} \overline{S}_{ij}}} \right) \tag{23}$$

As before, C_τ can be computed by applying the least-square method to (22),

$$C_\tau = \frac{1}{2}\frac{L_{ij}N_{ij}}{N_{ij}N_{ij}} \tag{24}$$

To determine the coefficient C_ε, a mathematical identity, similar to (8), between the dissipation rates of k_{sgs} and K can be constructed. Thus,

$$F = E - \hat{\varepsilon}_{sgs} = \nu\left(\widehat{\frac{\partial\overline{u}_i}{\partial x_j}\frac{\partial\overline{u}_i}{\partial x_j}} - \frac{\partial\hat{\overline{u}}_i}{\partial x_j}\frac{\partial\hat{\overline{u}}_i}{\partial x_j}\right) \tag{25}$$

where

$$\varepsilon_{sgs} = \nu\left(\overline{\frac{\partial u_i}{\partial x_j}\frac{\partial u_i}{\partial x_j}} - \frac{\partial\overline{u}_i}{\partial x_j}\frac{\partial\overline{u}_i}{\partial x_j}\right) \tag{26}$$

$$E = \nu\left(\widehat{\overline{\frac{\partial u_i}{\partial x_j}\frac{u_i}{\partial x_j}}} - \frac{\partial\hat{\overline{u}}_i}{\partial x_j}\frac{\partial\hat{\overline{u}}_i}{\partial x_j}\right) \tag{27}$$

can be used by substituting the model for ε_{sgs} (19), and a similar model for E,

$$E = C_\varepsilon\frac{K^{3/2}}{\hat{\Delta}} \tag{28}$$

to obtain:

$$C_\varepsilon = \frac{F}{\left(K^{3/2}/\hat{\Delta} - \widehat{k_{sgs}^{3/2}/\Delta}\right)} \tag{29}$$

As is seen, C_ε is computed from a scalar relation without applying any approximation.

Note that the above dynamic modeling procedure is basically the same as described in Wong (1992) except for the fact that, in the present approach, the subtest-scale kinetic

energy K has been directly evaluated from the algebraic relation (20) while in Wong (1992), an extra transport equation for K was solved to compute K. In the present formulation, the mathematical inconsistency and the ill-conditioning problem noted earlier for the DSM approach still exist. The primary advantage of this approach is that, by using the SGS kinetic energy in the formulation, the prolonged presence of negative C_τ is no longer the source of numerical instability. There is, however, a new problem with this approach since C_ϵ has the unphysical property of vanishing at high Reynolds numbers. The remedy for this problem will be given in section 3.

In this paper, we refer to this model as the dynamic k_{sgs}-equation model (DKM).

3 Localized dynamic k_{sgs}-equation model (LDKM)

As noted in section 2, both Germano *et al.*'s dynamic formulation and the dynamic one-equation model suffer from numerical instability caused by the ill-conditioned model coefficients and by the prolonged presence of negative model coefficient (observed only in the DSM). This problem has been circumvented in the past by spatially averaging the model coefficient in directions of flow homogeneity (e.g., Germano *et al.*, 1991; Moin *et al.*, 1991). Recently, Meneveau *et al.* (1996) suggested a Lagrangian-averaging scheme applied along particle trajectories for flows without any directions of homogeneity. This approach is based on the hypothesis that the SGS model coefficient at a given point should depend on the history of the flow along the trajectory leading to that point because turbulent eddies are expected to evolve along this pathline. This model was tested in homogeneous and channel turbulent flows. In homogeneous flows, the results were as good as the volume-averaged

dynamic model; while in channel flows, the predictions were superior to those of the conventional plane-averaged dynamic model. It was reported that this model required only about 10% more computational cost than the conventional spatial-averaged dynamic model. However, whether it is spatial or local Lagrangian averaging, the concept of averaging is still an artifact that is employed primarily to control the numerical instability. A true dynamic model should evaluate the model coefficients locally without any *ad hoc* averaging.

Such a localized model, applicable to inhomogeneous flows, was recently demonstrated by Ghosal *et al.* (1995) (following their notation, this model is denoted DLM(k)). They introduced a variational formulation to rigorously derive integral equations for the model coefficient as a function of position and time, and demonstrated that by solving these integral equations iteratively, the numerical instability resulting from the ill-conditioning problem can be effectively suppressed. Furthermore, this model demonstrated realizability of the subgrid-scale kinetic energy (obtained by solving a transport equation for the subgrid-scale kinetic energy). This ensured that the prolonged presence of negative model coefficient is no longer a source for numerical instability. However, these improvements were achieved at a significant additional cost. Carati *et al.* (1995) reported that the DLM(k) required 67% more CPU time than the standard Smagorinsky model while the conventional spatial-averaged dynamic Smagorinsky model required only 4% more CPU time. This is due to the computational effort required to solve two integral equations iteratively and the solution of the transport equation for the subgrid-scale kinetic energy. DLM(k) has been tested (so far) in isotropic turbulence and has demonstrated its capability by showing a good agreement with experimental data.

In the following two sections, we described a different approach for obtaining the model

coefficients locally and dynamically.

3.1 Rationale for the present approach

As mentioned earlier, the production of the SGS kinetic energy, $k_{sgs} = (\overline{u_k u_k} - \overline{u}_k \overline{u}_k)/2$, is by $-\tau_{ij}(\partial \overline{u}_i/\partial x_j)$ at the large scales whereas it is dissipated by ε_{sgs} (26) at the small scales. Here the energy levels $\overline{u}_k \overline{u}_k$ and $\overline{u_k u_k}$ represent, respectively, the levels where the large- and the small-scale energy transfers occur. In turbulence modeling, the appropriate velocity scale (or time scale) and length scale corresponding to these energy levels are used to parameterize energy production and dissipation. For example, the appropriate velocity scale is obviously the square root of k_{sgs} both for energy production and dissipation, and the length scale characterizing the large-scale (resolved) energy level ($\overline{u}_k \overline{u}_k$) is the grid resolution $\overline{\Delta}$ (since the energy level $\overline{u}_k \overline{u}_k$ is directly resolved by the grid). However, the length scale required to characterize the small-scale energy level ($\overline{u_k u_k}$) is unknown and, therefore, a closure assumption is needed. Note that since the energy dissipation at the small scales is essentially controlled by the energy transfer from the large scales (energy is neither produced nor dissipated inside the domain bounded by these two energy transfer processes), it is assumed that both the velocity and the length scales for the small-scale energy dissipation can be approximated by those for the large-scale production process (although this assumption is reasonable and often invoked, the resulting model for the small-scale energy dissipation is known to be inadequate). As a result, $\overline{\Delta}$ and k_{sgs} (in addition to $\overline{S}_{ij}$, when the eddy-viscosity assumption is adopted) are employed to model both the large- and small-scale energy production/dissipation processes. Models resulting from this parameterization are

shown in (17) and (19).

We now consider the equivalent energy production and dissipation processes at the test-filter level. At the test-filter level, the subtest-scale kinetic energy $K = (\widehat{\overline{u_k}\overline{u_k}} - \widehat{\overline{u}}_k\widehat{\overline{u}}_k)/2$ exists but is unknown. This kinetic energy is produced at the large scales by $-T_{ij}(\partial\widehat{\overline{u}}_i/\partial x_j)$ but its dissipation process is more complicated. To demonstrate this, we first note that K can be decomposed into two distinct components: the resolved (by grid) energy, $\left(\overline{u}_k\overline{u}_k - \widehat{\overline{u}}_k\widehat{\overline{u}}_k\right)/2$, and the unresolved energy, $\left(\widehat{\overline{u_k}\overline{u_k}} - \overline{u}_k\overline{u}_k\right)/2$. This partitioning can be understood by noting that since the flow field at the test-filter level has been constructed by filtering the grid-resolved field, the property of the test-filtered field depends to a major extent on the grid-filtered field. Especially when dissipation is considered, the test-filtered quantities should recognize the dissipation effect at the scale characterized by $\overline{\Delta}$ in addition to the molecular dissipation which occurs at the unresolved range. Thus, the dissipation of the subtest-scale kinetic energy K (denoted by E) must be due to both the molecular viscosity ν and the eddy viscosity ν_T. This results in the following expression for E:

$$E = (\nu + \nu_T)\left(\frac{\partial\overline{u}_i}{\partial x_j}\frac{\partial\overline{u}_i}{\partial x_j} - \frac{\partial\widehat{\overline{u}}_i}{\partial x_j}\frac{\partial\widehat{\overline{u}}_i}{\partial x_j}\right) + \nu\left(\widehat{\frac{\partial u_i}{\partial x_j}\frac{u_i}{\partial x_j}} - \frac{\partial\overline{u}_i}{\partial x_j}\frac{\partial\overline{u}_i}{\partial x_j}\right) \tag{30}$$

The two terms on the right hand side of (30) represent, respectively, the dissipation of the resolved part of K by the effective viscosity $(\nu + \nu_T)$ and the dissipation of the unresolved-scale part energy of K purely due to the molecular viscosity. Note that if (30) is used instead of (27) to determine C_ε in the DKM (described in section 2.2), the resulting C_ε will not have the unphysical property of vanishing at high Reynolds number since the effective viscosity $(\nu + \nu_T)$ remains non-zero even at the infinite Reynolds number limit. The large- and small-

scale energy transfers resulting in K can be modeled in the similar manner as described above, with the resulting models shown in (21) and (28).

By invoking similarity between τ_{ij} and T_{ij}, and between ε and E, the model coefficients can be determined. In this approach, the model coefficients, C_τ and C_ε, are obtained by implicitly representing L_{ij} in (8) and F in (25) in terms of the difference between two different filter-level model representations (i.e., $T_{ij}^{\text{model}} - \widehat{\tau}_{ij}^{\text{model}}$ and $E^{\text{model}} - \widehat{\varepsilon}_{sgs}^{\text{model}}$, respectively). Note that although the expressions (8) and (25) are exact relations, the model representations of differences lose their physical relevance more quickly than the individually modeled quantities. This causes the ill-conditioning problem and results in numerical instability.

3.2 Formulation of the present model

Given the problems with the dynamic models described above, we seek an alternate method for the dynamic determination of the model coefficients. Recently, Liu *et al.* (1994) observed significant similarity between τ_{ij} and L_{ij} by analyzing experimental data obtained in the far field of a turbulent round jet at a reasonably high Reynolds number, $Re_\lambda \approx 310$. The experimental data showed that the correlation between these two stress tensors was quite high. Therefore, they suggested an appropriate SGS model based on this scale similarity: $\tau_{ij} = C_k L_{ij}$ where C_k is an adjustable constant (a value of 0.45 ± 0.15 was suggested by Liu *et al.* (1994) based on experimental data). However, as mentioned earlier, such scale-similarity models do not provide sufficient dissipation to be directly applicable. Here, since we are interested in high Reynolds number flows, we assume that this similarity between τ_{ij} and L_{ij} will exist in flows of interest (provided of course, that proper grid resolution is employed

to ensure that cut-offs for both the grid and test filters are located in the scale-similarity range). Further, we assume that the scale-similarity concept can be extended to the similarly defined dissipation rates, ε_{sgs} and e (defined below). With these assumptions, we define a (numerically) resolved kinetic energy at the test-filter level:

$$k_{test} = \frac{1}{2}\left(\widehat{\overline{u}_k\overline{u}_k} - \widehat{\overline{u}}_k\widehat{\overline{u}}_k\right) \tag{31}$$

(note that, $k_{test} = L_{kk}/2$). This energy is similar to k_{sgs}. However, it is produced at the large scales by $-L_{ij}(\partial\widehat{\overline{u}}_i/\partial x_j)$ where $L_{ij} = \widehat{\overline{u}_i\overline{u}_j} - \widehat{\overline{u}}_i\widehat{\overline{u}}_j$ and is dissipated by:

$$e = (\nu + \nu_T)\left(\widehat{\frac{\partial\overline{u}_i}{\partial x_j}\frac{\partial\overline{u}_i}{\partial x_j}} - \frac{\partial\widehat{\overline{u}}_i}{\partial x_j}\frac{\partial\widehat{\overline{u}}_i}{\partial x_j}\right) \tag{32}$$

at the small scales. Again, $(\nu+\nu_T)$ is used in the above expression since k_{test} is fully resolved at the test-filter level and, thus, must be dissipated by both the eddy viscosity and the molecular viscosity. Obviously, $k_{test}^{1/2}$ is the characteristic velocity scale for both the large- and small-scale energy transfer processes and the characteristic length scale of the large-scale energy transfer is $\widehat{\Delta}$ (since this energy transfer occurs at the energy level $\widehat{\overline{u}}_k\widehat{\overline{u}}_k$ and is fully resolved at the test-filter level). However, as before, the characteristic length scale for the dissipation process at the small scales is still unknown even though the kinetic energy k_{test} is dissipated at the energy level $\widehat{\overline{u}_k\overline{u}_k}$ (which is located in the resolved-scale range between $\overline{\Delta}$ and $\widehat{\Delta}$). Hence, a closure assumption is still needed to model e.

Consider first the closure for τ_{ij}. As noted above, experiments suggest that τ_{ij} and L_{ij} have excellent correlation. Thus, we assume that both τ_{ij} and L_{ij} can be represented in a similar manner using appropriately defined parameters. Since τ_{ij} is modeled in terms of

grid-resolved quantities as

$$\tau_{ij} = -2C_\tau \overline{\Delta} k_{sgs}^{1/2} \overline{S}_{ij} + \frac{1}{3}\delta_{ij}\tau_{kk} \tag{17}$$

we consider a similar representation for L_{ij} as

$$L_{ij} = -2C_\tau \widehat{\Delta} k_{test}^{1/2} \widehat{\overline{S}}_{ij} + \frac{1}{3}\delta_{ij} L_{kk} \tag{33}$$

where all quantities are defined at the test-filter level. Whereas (17) contains two unknowns τ_{ij} and C_τ, (33) contains only C_τ as the unknown. Thus, (33) can be viewed as an explicit (albeit, over-determined) model representation for C_τ in terms of quantities resolved at the test-filter level. Since (33) is an over-determined system, least-square method is still required to obtain C_τ:

$$C_\tau = \frac{1}{2}\frac{L_{ij}\sigma_{ij}}{\sigma_{ij}\sigma_{ij}} \tag{34}$$

where

$$\sigma_{ij} = -\widehat{\Delta} k_{test}^{1/2} \widehat{\overline{S}}_{ij} \tag{35}$$

We see that the expressions for C_τ (24) and (34) are similar in form except for the definitions of N_{ij} and σ_{ij}. Whereas N_{ij} is the difference between two models evaluated at the two filter levels, σ_{ij} is determined completely from quantities at the test-filter level. Furthermore, although N_{ij} results from a model approximation to the exact Germano *et al.*'s mathematical identity, σ_{ij} results from a model based on the assumption that τ_{ij} and L_{ij} are similar. The

applicability of the similarity assumption and the appropriateness of (33) is verified in the present study by carrying out LES of various flows.

Similarity between the dissipation rates ε_{sgs} at the grid-filter level and e at the test-filter level is also invoked in the present approach to obtain the dissipation model coefficient. Thus, using

$$e = C_\epsilon \frac{k_{test}^{3/2}}{\widehat{\Delta}} \tag{36}$$

C_ϵ is determined from the expression:

$$C_\epsilon = \frac{(\nu + \nu_T)\,\widehat{\Delta}\left[\widehat{(\partial\overline{u}_i/\partial x_j)\,(\partial\overline{u}_i/\partial x_j)} - \left(\partial\widehat{\overline{u}}_i/\partial x_j\right)\left(\partial\widehat{\overline{u}}_i/\partial x_j\right)\right]}{k_{test}^{3/2}} \tag{37}$$

By adopting the similarity assumption between τ_{ij} and L_{ij}, the present model is formulated without employing any mathematically inconsistent or *ad hoc* procedure. There are some positive aspects to this approach. The denominators of (34) and (37) contain only well defined quantities and, therefore, the ill-conditioning problem (seen in the earlier models such as the DSM and the DKM) is significantly relieved (as demonstrated in the numerical studies described below). Also, the dynamically determined C_ϵ from (37) does not have the unphysical property of vanishing at high Reynolds numbers. From computational standpoint, the cost of the dynamic procedure is not significant (about the same as that for the DSM) due to its simplicity. The additional computational cost is primarily due to the inclusion of a transport equation for k_{sgs}.

In the following, we refer to this model as the localized dynamic k_{sgs}-equation model (LDKM) to emphasize its ability to employ localized model coefficients.

3.3 Properties of the present model

Before testing the LDKM by implementing it in actual simulations, properties of the model are examined from a theoretical point of view. Recently, Vreman *et al.* (1994a) noted that SGS models should share some basic properties with the exact SGS stress tensor τ_{ij} to successfully predict this unresolved quantity. They presented three properties of τ_{ij} that SGS models should satisfy as a necessary condition. First, since τ_{ij} is a symmetric tensor, the model of τ_{ij} should also be symmetric. Second, as the filtered Navier-Stokes equations are Galilean invariant, they should retain this property even after τ_{ij} is replaced by the model. Finally, since τ_{ij} should remain positive definite for positive filters, the model for τ_{ij} should remain positive definite as well, if a positive filter is applied. As it turns out, the first requirement is satisfied by all SGS models discussed here. However, the latter two requirements have to be checked, especially when a new SGS model is being considered. The ability of the proposed LDKM to satisfy all of these requirements is discussed below.

The Navier-Stokes equations, as well as their filtered LES form (3), exhibit Galilean invariance. As Speziale (1985) has argued, the SGS stress tensor must be modeled with terms which are Galilean invariant so that the resulting LES equations of motion for the large eddies retain the same form in all inertial frames of reference. The Galilean invariance of the SGS model can be examined by employing the following transformations,

$$\begin{aligned} x_i^* &= x_i + Ut + C \\ t^* &= t \end{aligned} \tag{38}$$

where U and C are any constant vectors. This transformation yields a frame of reference

in which the motion differs by a constant translational velocity U. Hence, if x_i constitutes an inertial frame of reference, then x_i^* also represents the class of inertial frame of reference. By differentiating (38) and substituting them into the definition of the SGS kinetic energy (15), it can be shown that $k_{sgs}^* = k_{sgs}$. Since U is constant, the strain-rate tensor $\overline{S}_{ij}$ is invariant. Consequently, it is clear that the models for τ_{ij} (17), ν_T (18), and ε_{sgs} (19) are also invariant. The direct substitution of these results into (16) can be used to show that the SGS kinetic-energy equation (16) is also Galilean invariant (Kim, 1996). This analysis can be extended to the test-filter level to show that the subtest-scale kinetic energy K, the test-filter level strain-rate tensor $\widehat{\overline{S}}_{ij}$, L_{ij} in (33), and e in (36) are all Galilean invariant. Finally, by direct substitution of these results, it can be shown that

$$C_\tau^* = C_\tau \tag{39}$$

$$C_\varepsilon^* = C_\varepsilon$$

In addition to Galilean invariance, the ability of the model to satisfy the realizability conditions (Schumann, 1977) is also examined. These conditions for the SGS stress tensor $\tau_{\alpha\beta}$ (the summation convention is not applied here) have been described earlier by Vreman *et al.* (1994a), by proving that the tensor $\tau_{\alpha\beta}$ forms a Grammian matrix which is always positive semidefinite. Hence, $\tau_{\alpha\beta}$ is positive semidefinite (this is the strictest requirement for realizability of the model for $\tau_{\alpha\beta}$) and the realizability conditions given by the following inequalities hold,

$$\tau_{\alpha\alpha} \geq 0 \tag{40}$$

$$\tau_{\alpha\beta}^2 \leq \tau_{\alpha\alpha}\tau_{\beta\beta} \tag{41}$$

However, this proof is only valid if positive filters such as the top-hat or Gaussian filters are employed. If the spectral cut-off filter is applied, this proof is not valid. (Note that in the dynamic approach, the grid filter is implemented in physical space as a low-pass filter of computational mesh which is believed to be a positive filter. Therefore, the resulting SGS stress tensor $\tau_{\alpha\beta}$ is positive definite. If the spectral cut-off filter is used for the test filter, the subtest-scale stress tensor can become locally negative definite and the dynamic approach becomes inconsistent.)

Since the low-pass filter makes $\tau_{\alpha\beta}$ positive definite, it is consistent to require that the model of $\tau_{\alpha\beta}$ should be positive definite as well. In LDKM, the base model (i.e., the SGS kinetic-energy equation model) is formulated so that the SGS kinetic energy remains positive during the simulation. This was also shown earlier by Ghosal *et al.* (1995). Thus, this base model for the LDKM is realizable. The only unanswered question is whether the dynamically determined model coefficients can guarantee that the model for $\tau_{\alpha\beta}$ satisfies the realizability conditions expressed by the two inequalities (40 and 41). The first inequality (40) requires that the quantity determined by a single velocity component remains positive whereas the second inequality (41) prescribes bounds for the cross correlation between two different velocity components. Earlier, Schumann (1977) suggested that in addition to the realizability constraints noted above, $\det(\tau_{\alpha\beta}) \geq 0$ also needs to be satisfied to demonstrate realizability in the strictest sense. Although this condition was not verified in the results reported here, more recent studies here (Nelson & Menon, in preparation) and elsewhere

(Fureby & Tabor, in preparation) show that the proposed localized model also enforces $\det(\tau_{\alpha\beta}) \geq 0$ at the grid points where the other two realizability conditions are satisfied.

We first examine the inequality, (40). Equation (17) can be rewritten for $\tau_{\alpha\alpha}$ as follows,

$$\tau_{\alpha\alpha} = -2C_\tau \overline{\Delta} k_{sgs}^{1/2} \overline{S}_{\alpha\alpha} + \frac{2}{3} k_{sgs} \tag{42}$$

where $\overline{S}_{\alpha\alpha}$ denote the eigenvalues of the strain-rate tensor which are assumed to be ordered as $\overline{S}_{11} \geq \overline{S}_{22} \geq \overline{S}_{33}$, for convenience. The signs of the eigenvalues of the strain-rate tensor can be determined from the incompressibility condition ($\overline{S}_{11} + \overline{S}_{22} + \overline{S}_{33} = 0$) so that the largest eigenvalue $\overline{S}_{11} \geq 0$, the smallest eigenvalue $\overline{S}_{33} \leq 0$, and, $\overline{S}_{22}$ can have either sign. The direct substitution of these results into the first realizability condition (40) gives the following condition:

$$\frac{k_{sgs}^{1/2}}{3\overline{\Delta}\,\overline{S}_{33}} \leq C_\tau \leq \frac{k_{sgs}^{1/2}}{3\overline{\Delta}\,\overline{S}_{11}} \tag{43}$$

where $\overline{S}_{33}$ has negative sign and, hence, the lower bound is also negative.

Another set of bounds for C_τ is obtained by substituting (17) into the second realizability condition (41) (for brevity, the sum of all three independent relations is considered, therefore, the following is a necessary condition for (41)),

$$\nu_T^2 \left(\overline{S}_{12}^2 + \overline{S}_{23}^2 + \overline{S}_{31}^2\right) \leq \nu_T^2 \left(\overline{S}_{11}\overline{S}_{22} + \overline{S}_{22}\overline{S}_{33} + \overline{S}_{33}\overline{S}_{11}\right) + \frac{1}{3} k_{sgs}^2 \tag{44}$$

The first term in the right hand side of (44) can be rewritten using the incompressibility condition as:

$$\nu_T^2\left(\overline{S}_{12}^2+\overline{S}_{23}^2+\overline{S}_{31}^2\right) \leq -\frac{1}{2}\nu_T^2\left(\overline{S}_{11}^2+\overline{S}_{22}^2+\overline{S}_{33}^2\right)+\frac{1}{3}k_{sgs}^2 \tag{45}$$

Combining the terms which contain the strain-rate tensor and substituting the definition $\left|\overline{S}\right| = \left(2\overline{S}_{ij}\overline{S}_{ij}\right)^{1/2}$ yields

$$\nu_T^2\left|\overline{S}\right|^2, \leq \frac{4}{3}k_{sgs}^2 \tag{46}$$

Finally, the upper and the lower bounds for C_τ are obtained by substituting the definition of ν_T:

$$-\frac{2}{\sqrt{3}}\frac{k_{sgs}^{1/2}}{\overline{\Delta}\left|\overline{S}\right|} \leq C_\tau \leq \frac{2}{\sqrt{3}}\frac{k_{sgs}^{1/2}}{\overline{\Delta}\left|\overline{S}\right|} \tag{47}$$

The two conditions, (43) and (47) give the realizable range for the dynamically determined model coefficient C_τ. The model coefficient C_τ should, therefore, fall inside this range for the LDKM to become a realizable model of the SGS stress tensor. This was verified in the present study by simulating the experiment of decaying isotropic turbulence of Comte-Bellot & Corsin (1971) (detailed description of this flow field will be presented in section 5.1). It was observed that more than 99.9% (for the 48^3 grid resolution), 99.8% (for the 32^3 grid resolution), and 99.6% (for the 24^3 grid resolution) of the grid points satisfy both realizability conditions, (43) and (47), at the same time during the entire simulation. Therefore, it appears that the LDKM satisfies these realizability conditions reasonably well. In comparison, Ghosal *et al.* (1995) reported that the DLM(k) satisfied the first realizability condition, (43), at about 95% of the grid points in the simulation of this experiment using a 48^3 grid resolution.

4 Numerical method

Spectral methods are very accurate and, therefore, used extensively for turbulent flow simulations, especially for DNS. However, spectral methods cannot be used for simulations of flows in complex geometry. For such flows, numerical methods defined in the physical space like finite-difference methods (FDM) and finite-volume methods (FVM) are more appropriate. However, it is important to ensure that these physical space methods have high enough accuracy for turbulent simulations. A highly accurate methodology applicable to complex flows was demonstrated by Rai & Moin (1991). Their approach used a non-conservative form of the unsteady, incompressible Navier-Stokes equations, (2) and (3), and, hence, it is appropriate only for simulations of flow fields without discontinuity. The present study is limited to such flows and, therefore, a similar methodology is adopted here.

Following Rai & Moin (1991), the convective terms are approximated using fifth-order accurate, upwind-biased finite differences with a seven-point stencil. For example, the first term in the $\overline{u}$-momentum equation, $\overline{u}\frac{\partial \overline{u}}{\partial x}$, is evaluated as,

$$(\overline{u}\overline{u}_x)_{i,j,k} = \frac{\overline{u}_{i,j,k}}{120\overline{\Delta}}\left(-6\overline{u}_{i+2,j,k} + 60\overline{u}_{i+1,j,k} + 40\overline{u}_{i,j,k} - 120\overline{u}_{i-1,j,k} + 30\overline{u}_{i-2,j,k} - 4\overline{u}_{i-3,j,k}\right) \tag{48}$$

if $\overline{u}_{i,j,k} > 0$, and

$$(\overline{u}\overline{u}_x)_{i,j,k} = \frac{\overline{u}_{i,j,k}}{120\overline{\Delta}}\left(4\overline{u}_{i+3,j,k} - 30\overline{u}_{i+2,j,k} + 120\overline{u}_{i+1,j,k} - 40\overline{u}_{i,j,k} - 60\overline{u}_{i-1,j,k} + 6\overline{u}_{i-2,j,k}\right) \tag{49}$$

if $\overline{u}_{i,j,k} < 0$, on a uniform grid. Here, subscript x indicates differentiation with respect to x. The remaining convective terms are evaluated in a similar manner.

The viscous terms are computed using central differences. By applying the fourth-order accurate, half-points differencing, the first viscous term in the u-momentum equation, $\frac{\partial}{\partial x}\left(\nu_{eff}\frac{\partial \overline{u}}{\partial x}\right)$, is discretized as

$$\left[\left(\nu_{eff}\overline{u}_x\right)_x\right]_{i,j,k} = \frac{1}{24\Delta}\left[\begin{array}{l} -\left(\nu_{eff}\overline{u}_x\right)_{i+3/2,j,k} + 27\left(\nu_{eff}\overline{u}_x\right)_{i+1/2,j,k} \\ -27\left(\nu_{eff}\overline{u}_x\right)_{i-1/2,j,k} + \left(\nu_{eff}\overline{u}_x\right)_{i-3/2,j,k} \end{array}\right] \tag{50}$$

where $\nu_{eff} = \nu + \nu_T$. Also, $\overline{u}_x$ which is defined at the half-points is computed using the same fourth-order accurate finite differences given as

$$\left(\overline{u}_x\right)_{i+1/2,j,k} = \frac{1}{24\Delta}\left(-\overline{u}_{i+2,j,k} + 27\overline{u}_{i+1,j,k} - 27\overline{u}_{i,j,k} + \overline{u}_{i-1,j,k}\right) \tag{51}$$

$\left(\nu_{eff}\right)_{i+1/2,j,k}$ is interpolated using the information on same stencil which was used to evaluated $\left(\overline{u}_x\right)_{i+1/2,j,k}$, so as to retain high-order accuracy. Thus, the discretization of the viscous terms uses seven grid points and, therefore, the viscous terms are approximated to sixth-order accuracy on uniform grids. The velocity derivative terms in the continuity equation and the pressure derivative terms in the momentum equations are computed using central differences and a five-point stencil (fourth-order accuracy).

Unlike central-difference schemes, all the upwind and upwind-biased differences have leading truncation error terms that are dissipative in nature. In fact, some (low-order accurate) upwind (-biased) schemes are known to be highly dissipative. This can overwhelm the physical dissipation in the turbulent flow and, therefore, needs to be carefully evaluated. Figure 1(a) shows the time variation of the turbulent kinetic energy in decaying isotropic turbulence (the detailed description of this flow field will be given later in section 5.1). Results obtained on a 48^3 grid resolution using fifth-order accurate upwind-biased finite differences

(implemented with and without employing the LDKM) are shown together with the experimental data. It can be clearly observed that the numerical dissipation of the finite-difference scheme is much lower than the turbulent dissipation. This is an essential requirement for a turbulence-simulation code. As shown, the LES data agree with experimental data only when the SGS model is turned on. This demonstrates the need and the capability of the SGS model. For comparison, the results without the SGS model obtained using a well known pseudo-spectral code (Rogallo, 1981) with a "2/3 dealiasing rule" is also plotted (obtained from figure 1 in Carati *et al.* (1995)). Note that the simulation results which are obtained without employing any turbulence model from both FDM and spectral codes should not be considered as the DNS results since the 48^3 grid resolution is too coarse to resolve all the turbulence scales (as mentioned later in section 5.1, at least 384^3 grid resolution is required for the actual DNS of this particular case). The present finite-difference method appears to be less dissipative than the spectral method. This is somewhat surprising since the spectral method is known to have very little dissipation. Deviations in the initial energy distribution (in the spectral space) between the current implementation and Carati *et al.*'s may be responsible for the difference between two cases. It can be observed from the comparison, however, that the dissipation in the current finite-difference method is comparable to that of the spectral method. Figure 1(b) shows unscaled energy spectra at the instant $t^* = 4.98$ and $t^* = 8,69$ obtained in the current calculation of the decaying isotropic turbulence implemented with and without employing the LDKM. At $t^* = 4.98$, without the model the spectrum shows that the energy builds up at the high-wavenumber end. As time evolves, the prediction without the model worsens at all wavenumber.

The major difference between the incompressible and the compressible Navier-Stokes

formulation is the lack of a time derivative term in the continuity equation in the incompressible formulation. Therefore, satisfying the mass conservation equation is the primary issue in solving the incompressible equations. Physically, incompressible flow is characterized by the elliptic behavior of the (infinite speed) pressure waves. The pressure field is desired as a part of the solution. This can be achieved by introducing the artificial compressibility method, originally proposed by Chorin (1967). The main advantage of this approach is that, by introducing artificial unsteady term into the continuity equation, efficient solution algorithms developed for time-dependent compressible flows can be utilized to compute incompressible flows. In this formulation, the continuity equation is modified by adding a pseudo-time derivative of the pressure term which results in hyperbolic-parabolic type of time-dependent equations together with the unsteady momentum equations,

$$\frac{1}{\beta^2}\frac{\partial p}{\partial \tau} + \frac{\partial \overline{u}_i}{\partial x_i} = 0 \tag{52}$$

Here, β is a prescribed parameter which represents an artificial speed of sound and τ is the pseudo-time variable which is not related to the physical time t. The choice of β is crucial in determining convergence and stability properties of the numerical scheme. Since β has the dimensions of a speed, it cannot be a universal constant. For instance, if the nondimensionalized governing equations are employed, β is also nondimensionalized by a reference velocity. Therefore, the optimal β will depend on the choice of the reference velocity. Following the work of Turkel (1987), many researchers chose β^2 to be slightly larger than $\overline{u}^2 + \overline{v}^2 + \overline{w}^2$ as an optimal choice. However, in general, the superiority of this choice of β over a constant β has not been verified. In the present study, both a constant

β and a variable β, i.e., $\beta^2 = C\,(\overline{u}^2 + \overline{v}^2 + \overline{w}^2)$ (where C is a constant of order unity) have been evaluated. It was determined that for most of the problems studied here, a constant β provided better convergence.

The time-accurate capability is obtained by adding pseudo-time velocity derivatives to the momentum equations (Rogers & Kwak, 1989),

$$\frac{\partial q}{\partial \tau} = -\frac{\partial q}{\partial t} - R(q) \tag{53}$$

where q denotes the velocity vector $q = [\overline{u}, \overline{v}, \overline{w}]^T$ and R represents the residual in the momentum equations which includes convective and viscous terms. In this unsteady formulation, the governing equations are marched in the pseudo time (i.e., subiterated) until the divergence-free flow field is obtained. Therefore, the artificial compressibility does not corrupt the physical-time solution as long as the pseudo-time solution converges to a steady state at each physical-time level. The integration in the pseudo time is carried out by an explicit method based on a 5-stage Runge-Kutta time-stepping scheme with the coefficients (0.059, 0.145, 0.273, 0.5, 1.0) which are considered appropriate for upwind schemes. The physical-time derivatives in the momentum equations are computed using a second-order backward difference that results in an implicit scheme,

$$\frac{\partial q}{\partial \tau} = -\frac{3q^{n+1} - 4q^n + q^{n-1}}{2\Delta t} - R(q^{n+1}) \tag{54}$$

where the superscript n denotes the physical-time level.

It should be noted that, in the present approach, a non-staggered grid (i.e., both velocity and pressure are defined at the grid points) is used, and the velocity derivatives in the

continuity equation and the pressure derivatives in the momentum equations are central-differenced. Therefore, velocity and pressure are decoupled, that is, the pressure is computed by excluding the influence of velocity at that point, and vice versa. (This kind of decoupling is not present in compressible flows due to the density-velocity coupling.) This decoupling generates high-frequency (odd-even decoupling type) oscillations. Here, these high-frequency oscillations in the velocity field are controlled by the implicit smoothing of the upwind-biased scheme (used to compute the convective terms in momentum equations) without unduly affecting the accuracy of the solution. To control the high-frequency oscillations in the pressure field, some higher-order artificial dissipation terms are typically added. However, the addition of artificial dissipation terms needs to be avoided in turbulence simulations since it may contaminate the turbulence behavior. To solve this problem, Harlow & Welch (1965) introduced a staggered grid. This problem was also solved by using special interpolation techniques such as momentum interpolation (Majumdar, 1988) and elliptic-corrected linear interpolation (Armfield, 1991). In the present study, however, high-frequency oscillations in the pressure field were not significant since for all test problems considered here, a statistically constant pressure field existed. Therefore, no attempt was made to eliminate the pressure oscillations.

To accelerate the convergence in pseudo-time marching at each physical-time step, efficient acceleration techniques developed for explicit steady-state solvers, such as local time-stepping, residual smoothing, and multigrid are employed. Local time-stepping involves using the locally maximum allowable time step. The stability limit of the basic scheme can be extended by employing residual smoothing as first demonstrated by Jameson (1983). In most cases, with residual smoothing CFL=5 was possible for the pseudo-time iteration.

Convergence can be further accelerated by also incorporating the full approximation storage (FAS) scheme based multigrid method as proposed by Brandt (1981). The basic idea is to solve the governing equations on a sequence of successively coarser grids to speed up the propagation of the fine-grid corrections. This has two advantages. First, the computational effort per time step is reduced on a coarser grid. Second, the use of coarser grids tracks the evolution on a larger scale, with the consequence that global equilibrium can be more rapidly attained (i.e., the system residuals can be more rapidly reduced). In the case of an explicit time-stepping scheme, this manifests itself as successively larger time steps as the solution procedure moves to the coarser grids, without violating the stability limit. Auxiliary coarser grids are introduced by doubling the grid spacing. The detailed description of FAS multigrid method can be found in Brandt (1981) and Jameson (1983). It is worth noting that the turbulent eddy viscosity on coarse grids is evaluated by injecting the subgrid-scale turbulent kinetic energy and the dynamically determined model coefficients from the fine grid instead of solving a transport equation on the coarse grids.

In practice, a solution is considered converged if the root-mean-square of the pressure and velocity changes decrease less than 10^{-6} since, in most cases, further iterations to reduce these quantities do not noticeably change the solution. Both the eddy viscosity and the model coefficients are computed at each pseudo-time step. Usually, the model coefficients adjust themselves quickly and remain almost constant during pseudo-time iterations.

5 Results and discussion

The LDKM developed in this study has been applied to decaying (section 5.1), forced (section 5.2), and rotating (section 5.3) isotropic turbulent flows,and turbulent plane Couette flows (section 5.4). Before discussing these simulation results, it is worthwhile to investigate the effects of the top-hat filtering on the results. The DNS data used for this purpose have been obtained by simulating a Taylor-Green vortex flow which has spatial symmetries (that are preserved in time as the flow evolves). Thus, the information in a fractional part of the periodic box is sufficient to describe the whole flow field by using symmetric boundary condition (Brachet *et al.*, 1983). In this study, the impermeable box ($0 \leq x, y, z \leq \pi$) of the Taylor-Green vortex flow has been simulated. The flow field develops from the initial condition,

$$\begin{aligned} \overline{u} &= \sin(x)\cos(y)\cos(z) \\ \overline{v} &= -\cos(x)\sin(y)\cos(z) \\ \overline{w} &= 0 \end{aligned} \tag{55}$$

At time $t = 0$, the flow is two-dimensional but becomes three-dimensional for all times $t > 0$. This flow is considered a simple flow field in which the generation of small scales and the resulting turbulence can be studied.

Figure 2 shows the unscaled energy and dissipation spectra of an effectively 128^3 DNS (actually simulated using the 64^3 grid resolution in a π-box) data at $t = 29$. At this time, turbulence is well developed and no energy is left in the range of wavenumbers $k \leq 1$. The Taylor microscale Reynolds number Re_λ is approximately 32. Note that, in the present

study, energy spectra (and some other results) are plotted in unscaled form. DNS results are usually scaled using the Kolmogorov length scale. This scaling is meaningful for DNS data. However, in LES, it is not straightforward to evaluate the value of the Kolmogorov length scale (it can be estimated only in an approximate manner). Furthermore, the Kolmogorov scaling may not be suitable for the LES results since the dissipation range is not resolved in the LES domain.

Figures 3(a) and (b) show the energy spectra of the 64^3 and 32^3 LES, respectively, which are compared with the energy spectra of 128^3 DNS and the filtered 128^3 DNS (filtering was performed using the top-hat filter) at $t = 29$. All LES (using the LDKM, the volume-averaged DKM, and the volume-averaged DSM) are initialized by first filtering the 128^3 DNS flow field down to the LES resolution using the top-hat filter at $t = 9$ (by this time, turbulence begins to decay due to the viscous damping and realistic turbulence is about to develop). As shown, the LES energy spectra are closer to the filtered 128^3 DNS spectrum than the 128^3 DNS energy spectrum itself. The difference (at the wavenumber range below the cut-off wavenumber, k_c) between the 128^3 DNS data and the filtered 128^3 DNS data is the result of using the top-hat filter which yields a significant contribution to the subgrid-scale energy from the lower wavenumbers than k_c (when the Fourier cut-off filter is employed, the subgrid-scale energy is entirely due to the wavenumbers larger than k_c). The LES data compare well with the filtered DNS data since the LES implemented by the current FDM code implicitly employs the top-hat filter by virtue of the numerical discretization. It can be deduced from this study that for meaningful comparison between LES predictions and DNS data, the DNS data must be filtered down to the same resolution as LES.

5.1 Decaying isotropic turbulence

The experiment of decaying isotropic turbulence of Comte-Bellot & Corsin (1971) is simulated to demonstrate the capability of the LDKM in predicting the decay of turbulent energy. First, the grid resolutions required for both DNS and LES are investigated by computing the resolved energy at each grid resolution (i.e., by numerically integrating the experimental spectrum between wavenumbers zero to the maximum wavenumber resolved by the grid resolution). The results are summarized in table 1. To accurately resolve all turbulence scales (i.e., for DNS), at least a 384^3 grid resolution, in which more than 99% of turbulent kinetic energy is resolved, is needed. For LES, the chosen grid resolution must be consistent with the basic assumption of LES that the resolved scales contain most of the turbulent energy. In the simulation of this experiment, Ghosal *et al.* (1995) concluded that the 48^3 grid resolution is the smallest possible resolution for LES since, at grid resolutions coarser than 48^3, a significant number of energy-containing eddies reside in the unresolved scales. As a result, the dynamic Smagorinsky model (DSM) could not accurately predict the energy decay. Therefore, the simulation of this experiment using a grid resolution coarser than 48^3 (i.e., when the subgrid scales contain more than 30% of total turbulent kinetic energy) is a good test case to measure the quality of the proposed SGS model. For this purpose, three grid resolutions (48^3, 32^3, and 24^3) are used for the simulations implemented here.

In the experiment, measurements of the energy spectra were carried out at three locations downstream of the grid (which generated the turbulence in the wind tunnel). At the first measuring station, the Reynolds number based on the Taylor microscale and the integral scale were, respectively, 71.6 and 187.9 (these values decreased to 60.7 and 135.7, respectively, at

the last measuring station). By assuming a constant mean velocity across the wind tunnel cross section, the elapsed time of the turbulent field, traveling at the mean velocity, from some reference location can be obtained. Thus, the spatial evolution of turbulence can be converted to a temporally evolving state, more specifically, a decaying isotropic turbulence inside a cubical box which is moving with the mean flow velocity. The size of the box is chosen to be greater than the integral length scale of the measured real turbulence. The statistical properties of turbulence inside the box are believed to be realistic even after applying periodic boundary conditions for numerical implementation. All experimental data are nondimensionalized by the reference length scale $10M/2\pi$ (where $M = 5.08cm$ is the mesh size of the grid) and the reference time scale 0.1 *sec* for computational convenience. By this nondimensionalization, the three measuring locations correspond to the three dimensionless time levels, t^* =2.13, 4.98 and 8.69, respectively.

The initial velocity field (primarily the amplitudes of the velocity Fourier modes) is chosen to match the three-dimensional energy spectrum at the first experimental station. The phases of Fourier modes are chosen to be random so that the initial velocity field satisfy Gaussian statistics. The initial pressure is assumed to be uniform throughout the flow field and the initial SGS kinetic energy is estimated by assuming the similarity between the SGS kinetic energy and the resolved-scale energy at the test-filter level. Thus, at t^* =2.13,

$$k_{sgs} \approx \frac{C_k}{2}\left(\widehat{\overline{u}_k\overline{u}_k} - \hat{\overline{u}}_k\hat{\overline{u}}_k\right) \tag{56}$$

where the constant C_k is determined by matching the total amount of k_{sgs} to be the same as the exact amount of the energy remaining above the cut-off wavenumber at the first

measuring station of the experiment. (If the magnitude of the exact SGS kinetic energy is not known, a value of C_k (0.45 ± 0.15) given by Liu *et al.* (1994) for the stress-similarity model, $\overline{u_i u_j} - \overline{u}_i \overline{u}_j = C_k \left(\widehat{\overline{u}_i \overline{u}_j} - \widehat{\overline{u}}_i \widehat{\overline{u}}_j \right)$, can be used. The initial SGS kinetic energy can also be estimated by adopting the similarity concept used in the dynamic procedure. This procedure is described in appendix B.)

Although the above procedure for generating the initial condition looks reasonable, the generated turbulent field may not be sufficiently realistic. Carati *et al.* (1995) suggested that a practical way to make the initial field more realistic, is to let the flow evolve for a few physical time steps (in this study, 5 time steps) and then multiply all Fourier modes by an appropriate real number to scale the velocity field to be consistent with the experimental spectrum. This additional procedure for initial conditions ensures that the (somewhat arbitrarily prescribed) flow variables become closely correlated to each other.

Figure 4 shows the decay of the resolved turbulent kinetic energy computed using the LDKM at three grid resolutions, 48^3, 32^3, and 24^3. The results are compared with the predictions of the volume-averaged DSM at the 48^3 grid resolution and the experimental data of Comte-Bellot & Corsin (1971). The predictions of both models (at the 48^3 grid resolution) are in good agreement with the experiment.

As is well known, the turbulent kinetic energy undergoes a power law decay, i.e., $E \sim (t^*)^r$, in the asymptotic self-similar regime. Table 2 shows this decay exponent r which is obtained from a least-square fit to each data set. The results predicted by the other models (DSM, DLM(k), and DLM(S)) are also shown in the table as given in Carati *et al.* (1995). DSM(S) denotes the stochastic dynamic localization model (see Carati *et al.* (1995), for a detailed description of this model). These results confirm the agreement between the

predictions of LES and the experiment. More importantly, the results of the LDKM at all three grid resolutions used (even for the 24^3 grid resolution where about a half of the turbulent kinetic energy is not resolved) show consistency in predicting the energy decay. This ability of the model to predict accurately the turbulence decay with coarse grids has important implications for application to complex and high Reynolds number flows where a significant amount of turbulent energy could be unresolved.

The computed and experimental three-dimensional energy spectra resolved at the three different grid resolutions, 48^3, 32^3, and 24^3, are shown in figures 5(a) (at $t^* = 4.98$) and (b) (at $t^* = 8.69$). Both of the LDKM and the volume-averaged DSM predict the spectra reasonably well. More interestingly, the LDKM predicts the spectra consistently well for all three grid resolutions. Some discrepancies between the experimental and LES-predicted energy spectra are observed around the cut-off wavenumber. These discrepancies are primarily due to the top-hat filter (implicitly adopted in the present FDM code), as explained in figures 3(a) and (b). Direct comparison between experimental and LES-predicted energy spectra is meaningful only when the full-resolution, experimental data is filtered down to the LES grid resolution. This was not possible here since the experimental flow field was not available.

5.2 Forced isotropic turbulence

A statistically stationary isotropic turbulence is simulated using a 32^3 grid resolution. The main purpose of this simulation is to examine whether a low resolution LES using the LDKM can reproduce the statistics (of the large-scale motions) of a realistic, high Reynolds number turbulent flow. The results are compared with the existing high resolution DNS

data by Vincent & Meneguzzi (1991) and Jimenez *et al.* (1993) obtained at $Re_\lambda \approx 150$ and $Re_\lambda \approx 170$, respectively.

A statistically stationary turbulent field is obtained by forcing the large scales as was done by Kerr (1985). In this study, the initial value of all Fourier modes with wavenumber components equal to 1 is kept fixed. The initial condition is obtained by generating a random realization of the energy spectrum (e.g., Briscolini and Santangelo, 1994),

$$E(k) = C\frac{k^4}{1+(k/k_0)^{5/3+4}} \tag{57}$$

where k_0=1 and C is a constant which normalizes the initial total energy to be 0.5. In isotropic turbulence, there are some generally accepted parameters characterizing the flow such as the Taylor microscale Reynolds number, the integral-scale Reynolds number, and the large-eddy turnover time. For an accurate estimate of these parameters, the full resolution DNS data are required. Strictly speaking, there is no way to exactly evaluate these quantities from LES data. Therefore, the characteristic parameters are computed here in an approximate manner.

The energy dissipation rate ε can be roughly estimated using the property of the forced turbulence since, in the forced isotropic turbulence, the energy dissipation rate is balanced with the energy injection rate by the external force. The energy injection rate can be easily determined from the external force added into the field and the velocity field at the wavenumber component equal to 1 where the external force is applied. The total energy E_{tot} involved in the cascade process is estimated by assuming that the energy spectrum obeys the Kolmogorov law $E(k) = C_K\varepsilon^{2/3}k^{-5/3}$ (where $C_K \approx 1.5$ is the Kolmogorov constant),

$$E_{tot} = \int_{k_0}^{\infty} E(k)dk = C_K \varepsilon^{2/3} \int_{k_0}^{\infty} k^{-5/3} dk = \frac{3}{2} C_K \varepsilon^{2/3} k_0^{-2/3} \tag{58}$$

The root-mean-square velocity u_{rms} is defined as

$$u_{rms}^2 = \frac{2}{3} E_{tot} \tag{59}$$

and the Taylor microscale λ is defined here as

$$\lambda^2 = 15 \nu_{eff} u_{rms}^2 / \varepsilon \tag{60}$$

where ν_{eff} denotes the effective viscosity $(\nu + \nu_T)$ instead of the molecular viscosity. The integral scale ℓ is

$$\ell = \frac{\pi}{2u_{rms}^2} \int_{k_0}^{\infty} k^{-1} \left(C_K \varepsilon^{2/3} k^{-5/3} \right) dk = \frac{3\pi}{10} \frac{C_K \varepsilon^{2/3} k_0^{-5/3}}{u_{rms}^2} \tag{61}$$

Finally, the Taylor microscale Reynolds number is defined as $Re_\lambda = u_{rms}\lambda/\nu_{eff}$, the integral-scale Reynolds number as $Re_\ell = u_{rms}\ell/\nu_{eff}$, and the large-eddy turnover time as $\tau = \ell/u_{rms}$.

In this study, LES are implemented under two different flow conditions. One is characterized by $Re_\lambda \approx 260$, $Re_\ell \approx 2400$, and $\tau \approx 3.7$; the other is characterized by $Re_\lambda \approx 80$, $Re_\ell \approx 220$, and $\tau \approx 4$. The simulations have been run for 27 and 25 large-eddy turnover times, respectively. To ensure statistical independence, 20 fields are used for statistical analysis for both cases with the time interval between successive fields larger than (or at least same as) one large-eddy turnover time.

Figure 6 shows the temporal evolution of the mean resolved turbulent kinetic energy. After an initial decaying period (i.e., after $t \approx 20$), the mean turbulent kinetic energy

remains at almost the same level, reflecting a balance between forcing at the large scales (the energy injection rate) and dissipation at the small scales (the energy dissipation rate). This energy equilibrium period of time is used for statistical analysis because it is close to a statistically steady state.

Figure 7(a) shows the probability distribution of velocity differences, $\delta u(r) = \overline{u}(x+r) - \overline{u}(x)$, for various values of length scale r (note that all values of r used here are comparable with inertial range scales). Here, δu is normalized so that $\sigma^2 = \widetilde{\delta u^2} = 1$. The LES results (using the LDKM at $Re_\lambda \approx 260$) clearly show that the distribution changes from a non-Gaussian (which has tails) to a Gaussian, as r increases. The same behavior of the distribution was observed in the high resolution DNS of Vincent & Meneguzzi (1991). In addition to the basic agreement regarding the development of the non-Gaussian statistics, the LES accurately predicts the probability of each bin. Figure 7(b) shows good agreement between the distributions for $r = 0.39$ obtained from the LES and the DNS, except for deviations in the tail regions. However, as is well known, the tails of the non-Gaussian distribution develop mainly due to small-scale fluctuations. Therefore, the deviations between the LES and the DNS results in the tails are somewhat natural; since in LES, most small scales are not resolved and even the resolved portion of small scales lies under the strong influence of the top-hat filter implicitly adopted in the FDM code.

Statistics of velocity and its derivatives are also investigated. While the statistics of velocity are the property of the large scales which are mostly resolved in LES, the statistics of velocity derivative are the property of the dissipation range scales which are not resolved by LES. Therefore, a direct comparison of the velocity derivative statistics from LES and DNS data does not agree well. A more useful comparison could have been possible if the

DNS field is filtered down to the LES resolution. Unfortunately, the filtered DNS data are not available, therefore, the DNS statistics of velocity derivative obtained from the full resolution simulations (shown in table 3) are being used only as a qualitative measure for the LES results. We computed the nth-order moments of the velocity and its derivative distributions using

$$S_n = \frac{\widetilde{x^n}}{\widetilde{x^2}^{n/2}} \tag{62}$$

Here, "$\sim$" denotes ensemble averaging. The results of these calculations are summarized in table 3. The results of the 512^3 DNS ($Re_\lambda \approx 170$), the 240^3 DNS ($Re_\lambda \approx 150$), and the 64^3 LES ($Re_\lambda \approx 140$) are obtained from Jimenez *et al.* (1993), Vincent & Meneguzzi (1991), and Briscolini & Santangelo (1994), respectively. (Note that these authors employ different definitions of Re_λ. However, the values reported by the authors are used here without any correction.) The 64^3 LES (Briscolini & Santangelo, 1994) was implemented using the Kraichnan's eddy viscosity where the small scales are parameterized reproducing a self-similar range of energy in spectral space. Two different Reynolds number cases were studied using the same grid resolution to investigate the effect of the Reynolds number on the statistics. As shown in the table, the velocity statistics appear not to depend on either the grid resolutions or the Reynolds numbers simulated. However, the velocity derivative statistics are highly influenced by the grid resolutions employed (it can be observed from the table that the values of the velocity derivative statistics are consistently decreased as the grid resolution is reduced from 512^3 to 32^3). In LES, the Reynolds number effects on the velocity derivative statistics are not captured (in the DNS of Jimenez *et al.* (1993), an

increase with Reynolds number increase was observed), since these statistics are strongly determined by the grid resolution employed.

Figures 8(a) and (b) show the temporal evolution of the model coefficient C_τ and the dissipation model coefficient C_ϵ (locally evaluated coefficients are volume-averaged for presentation). The LDKM predicts $C_\tau \approx 0.056$ and $C_\epsilon \approx 0.33$ for the higher Reynolds number case ($Re_\lambda \approx 260$) and $C_\tau \approx 0.05$ and $C_\epsilon \approx 0.44$ for the lower Reynolds number case ($Re_\lambda \approx 80$). These values are similar to those suggested by Grötzbach & Schumann (1979) ($C_\tau \approx 0.042$ and $C_\epsilon \approx 0.63$) and Yoshizawa & Horiuti (1985) ($C_\tau \approx 0.05$ and $C_\epsilon \approx 1$), especially for C_τ. Following suggestions of Lilly (1967), Schmidt & Schumann (1989) determined the values of the coefficients to be $C_\tau \approx 0.086$ and $C_\epsilon \approx 0.85$. These values are notably larger but may work well for very high Reynolds numbers. Note that in the Reynolds-averaged turbulence models, a generally adopted value for C_τ is about 0.09 which is significantly larger than that for LES. There are, however, some discrepancies in C_ϵ which may be because C_ϵ is more sensitive to the details of flow fields. Also, the dynamic coefficients may depend on the numerical scheme employed, more specifically, on the dissipative nature of the scheme (in this study, numerical dissipation caused by upwind-biased schemes is significantly reduced by employing the high-order accurate scheme). From these figures, it can be concluded that, in the LES of (forced) isotropic turbulence on a given (fixed) grid resolution, a larger value of C_τ and a smaller value of C_ϵ are required as the Reynolds number is increased.

Figure 9 shows that the fraction of grid points where the model coefficient C_τ is negative (indicating energy backscatter). In the present LES, about 20% fraction of grid points have negative model coefficient throughout the simulation. For comparison, an earlier study by Carati *et al.* (1995) reported that the DLM(k) predicts negative model coefficient in about

13% fraction of grid points for a similar forced isotropic simulation.

5.3 Rotating isotropic turbulence

The principal effect of system rotation on isotropic turbulence is to alter the nonlinear interactions among turbulence scales. The system rotation inhibits energy transfer from large to small scales and, thus, leads to a reduction in turbulence dissipation and an associated decrease in the decay rate of turbulence energy. However, prediction of these phenomena by RANS turbulence models is not possible unless modifications are made to take rotation effects into account (see Speziale *et al.* (1992) for a review on this issue). On the other hand, according to Bardina *et al.* (1985) who simulated rotating homogeneous turbulence using the standard Smagorinsky model, LES is capable of predicting the effects of system rotation without any modification. This was confirmed by Squires & Piomelli (1994). They simulated both initially isotropic turbulence and turbulent channel flow subjected to system rotation using the spatial-averaged (along homogeneous directions) DSM without any adjustment of model parameters.

In this study, we simulate the experiment of rotating homogeneous turbulence of Jacquin *et al.* (1990). The effect of system rotation on the large-scale velocity field can be easily included by adding the Coriolis term $2\epsilon_{ij3}\Omega\overline{u}_j$ to the right hand side of (3). Here, ϵ_{ijk} is Levi-Civita's alternating tensor. The resulting equations represent the governing equations of large-scale motions in a reference frame rotating with constant angular velocity Ω about the z-axis.

Four different cases, $\Omega = 0$, 15.7, 31.4, and 62.8 rad/sec, were simulated using the 32^3

grid resolution. In general, rotation rates are characterized in terms of Rossby number, $Ro \sim$ (velocity scale)/($2\Omega\times$length scale). However, the characteristic velocity and length scales reported in the experiment are the mean velocity and the mesh size of the grid used for turbulence generation, respectively, whereas these scales are not appropriate for the present LES. Therefore, the dimensional parameter Ω is used to discuss the effects of increasing rotation rates.

The same initial field, which was used for the simulation of decaying isotropic turbulence described in section 5.1, is adopted. The total energy and the time scale of this initial state have been scaled to match those of Jacquin *et al.*'s (1990) experiment at the imaginary origin of realistic turbulence where the grid wakes are believed to completely mix together. The imaginary origin is assumed to be $x/M = 2.6$ (M denotes the mesh size of the grid) as given by the authors for $\Omega = 0\ rad/sec$ and $M = 1.5\ cm$.

The decay of the resolved-scale turbulent kinetic energy for various rotation rates are compared to the experimental data of Jacquin *et al.* (1990) in figure 10. These results clearly demonstrate the principal effect of system rotation on isotropic turbulence, that is, increasing rotation rate decreases the decay rate of turbulent kinetic energy. As shown, LES predictions of this phenomenon are in good agreement with the experimental data.

In figure 11, the rotation effect on the three-dimensional energy spectra is examined. As observed in the experiment (see Jacquin *et al.* (1990)), with an increase in rotation rate, more and more energy remains in the low wavenumber range while slightly more energy is dissipated in the high wavenumber range. This observation can be explained by noting that as a result of decreasing nonlinear energy transfer from large to small scales, energy loss due to the molecular viscosity in the high wavenumber range can not be adequately replaced by

transfer of energy from the large-scales. Thus, the energy in the high wavenumber scales decay somewhat faster for higher rotation rates. Note that increasing energy backscatter caused by system rotation also contributes in part to these results.

The variation of the model coefficient due to rotation is shown in figures 12 and 13. Figure 12 shows the time evolution of C_τ (a) and C_ϵ (b) subjected to four different rates of rotation. Consistent with the earlier results in figures 10 and 11, both C_τ and C_ϵ become smaller for higher rotation rates due to the significant reduction in the overall energy transfer into (by C_τ) and among (by C_ϵ) subgrid scales.

The positive and negative contributions to C_τ are shown in figure 13(a). The mean value of each contribution is computed by dividing the sum of each contribution by the number of grid points involved in the corresponding contribution. As the rotation rate is increased, the mean positive coefficient is decreased while the mean negative coefficient remains almost unchanged. This indicates that the relative role of backscatter (represented by negative coefficient) becomes stronger for higher rotation rates. Figure 13(b) shows the fraction of grid points which experience backscatter. For higher rotation rates, more grid points are involved in backscatter. Therefore, the actual amount of energy backscatter also increases appreciably with increase in rotation rates (this is considered to be only a rough estimate since the amount of energy transfer is not determined solely by the model coefficient).

Figures 14 (a) and (b) show the instantaneous vorticity magnitude isosurfaces (gray-shaded structures) together with the shaded contours (color-shaded plane) of the dynamically determined model coefficient in an (x,z) plane at $x/M \approx 75$ (the last measurement location). The model coefficient is divided into three ranges: the high dissipation ($C_\tau > 0.1$), the normal dissipation ($0 < C_\tau < 0.1$), and the backscatter ($C_\tau < 0$) ranges. Non-rotating ($\Omega = 0$ rad/s)

and highly rotating ($\Omega = 62.8$ rad/s) cases are shown in figures 14 (a) and (b), respectively. In the non-rotating case, the high dissipation and the backscatter regions are almost equally (and randomly) distributed. However, in the rotating case, larger regions of backscatter are seen in comparison to the high dissipation regions. As shown, the energy backscatter occurs in extended (and spatially correlated) regions since it is determined in a deterministic manner based on a resolved-scale information. Although the energy forward scatter (dissipation) can be accurately estimated from the resolved-scale field, the energy backscatter can be predicted more accurately only by using the unresolved-scale field (this SGS information is not available in the LES). Thus, the SGS effects are recognized by the resolved-scale field as random inverse-cascading forcing processes. This suggests that inclusion of backscatter into LES may be possible using stochastic forcing models as suggested by many researchers, most recently by Schumann (1995).

5.4 Turbulent Plane Couette Flow

Turbulent plane Couette flow is driven by shear generated at two infinite flat walls which are in rectilinear, parallel movement relative to each other. A distinguished feature of this flow is that it has a constant shear stress across the entire channel (all the other turbulent shear flows near walls have a thin constant shear stress layer very close to the wall). In plane Couette flow, (since most of turbulent energy production occurs in the constant shear stress layer) turbulence production is finite across the channel (even though it still has a maximum close to the wall), whereas, in channel flows maximum turbulence production occurs close to the wall and then rapidly decreases towards zero at the channel centerline. This feature

of the flow is a direct consequence of zero mean pressure gradient throughout the flow and makes it significantly different from pressure-driven shear flows.

The experiments of Bech *et al.* (1995) and Aydin & Leuthersser (1987, 1991) were simulated. In the simulations, only the upper wall (at $y/h = 1$) was moving with a constant velocity U_w while the lower wall (at $y/h = -1$) was fixed. The chosen Reynolds number $\mathrm{Re} = U_w h/\nu$ (where h is the channel half height) was 2600, while the Reynolds number $\mathrm{Re}_\tau = U_\tau h/\nu$ based on the wall-shear velocity $U_\tau = (\nu dU/dy|_{wall})^{1/2}$, was 81. The computational domain was $4\pi h \times 2h \times 2\pi h$ in the streamwise, normal, and spanwise directions, respectively. The grid resolution was $48 \times 48 \times 32$ with uniform spacing in the streamwise and spanwise directions. While in the normal direction, the grid was stretched using a 6% linear stretching in order to improve the resolution in the near-wall regions. Computational meshes are around $21.1\Delta y^+$ in the streamwise direction, $15.8\Delta y^+$ in spanwise direction, and the resolution in the normal direction is $1.6\Delta y^+$, next to the wall, with stretching so that the maximum grid size is $6.1\Delta y^+$. At the wall boundaries, no-slip conditions were used and in the homogeneous (streamwise and spanwise) directions, periodic conditions were imposed. The initial field was constructed of the laminar mean velocity profile with finite-amplitude velocity fluctuations superimposed. After about $150h/U_w$, the flow reaches a statistically steady state. Statistics were obtained by ensemble averaging for another $55h/U_w$.

Before time-averaged statistics obtained from the LES are presented, it is worthwhile to describe how the (time-averaged) Reynolds stresses are calculated from the LES field. By ensemble-averaging the LES governing equations (3), the Reynolds stresses are defined as follows,

$$R_{ij} = \widetilde{\overline{u_i u_j}} - \tilde{\bar{u}}_i \tilde{\bar{u}}_j \tag{63}$$

where "$\sim$" denotes ensemble averaging. In the above expression, $\overline{u_i u_j}$ is an unknown quantity but it can be estimated using the SGS model, i.e., $\overline{u_i u_j} = \tau_{ij}^{\text{model}} + \overline{u}_i \overline{u}_j$. Note that if the turbulence intensities are calculated using $u_{rms} = (\widetilde{\overline{u}\,\overline{u}} - \tilde{\overline{u}}\,\tilde{\overline{u}})^{0.5}$ instead of $u_{rms} = (\widetilde{\overline{u}\,\overline{u}} - \tilde{\overline{u}}\,\tilde{\overline{u}})^{0.5}$, the SGS contribution to the turbulence intensities will be totally neglected.

Figure 15 shows the mean velocity distribution. For comparison, experimental data obtained by Aydin & Leutheusser (1987) at Re =2600 and Bech *et al.* (1995) at Re =2520, and DNS results by Bech *et al.* (1995) at Re =2600 are also plotted in figure 15(a). The DNS (Bech *et al.*, 1995) was carried out using a $256 \times 70 \times 256$ grid resolution. The agreement between the LES and the experimental data is excellent both in the wall region and in the center of the channel. In figure 15(b), the mean velocity is plotted in a semi-logarithm form, normalized by the viscous scale. As shown, the velocity profile is clearly divided into a viscous sublayer, a buffer region, and a logarithm part. For comparison, the following universal velocity-distribution law for smooth-wall conditions is also plotted,

$$U^+ = A \ln y^+ + B \tag{64}$$

where $U^+ = U/U_\tau$, $y^+ = yU_\tau/\nu$ and A is the inverse of the von Kármán constant. The constants appearing in the equation have the universal values: A =2.5 and B =5.5. The LES results align well with the straight line with only small deviations. The logarithmic region extends to the center of the channel, a feature observed in the experiments and also captured here.

In figure 16, turbulence intensities obtained from LES, DNS, and experiments are shown (only the moving wall part is presented). The LES results show overall good agreement

with the DNS and experimental data except for some deviations of the normal component in the region close to the wall. The highest intensity is observed in the streamwise component which has a maximum at $y^+ \approx 13$ whereas (unlike the plane Poiseuille flow) the other components monotonically increase to a constant value in the center of the channel. In the present simulation, the ratio of the velocity fluctuations v_{rms}/u_{rms} ≈0.65 is obtained (this value lies in between the value of 0.6 obtained by Aydin & Leuthersser (1991) and the value of 0.67 obtained by Bech *et al.* (1995)).

In figure 17(a), the time-averaged distribution of the model coefficient is plotted. Without employing the exponential damping of Van Driest (1956), the smooth variation of the model coefficient is obtained close to the wall. When approaching the core region, the model coefficient monotonically increases to a constant level (≈ 0.055) which matches well with the value predicted by the forced isotropic turbulence simulation at high Reynolds number (section 5.2). Figure 17(b) shows the time-averaged distribution of the dissipation model coefficient. Close to the wall, the dissipation model coefficient rapidly increases indicating the pronounced effects of the small-scale dissipation. However, it also approaches a constant level in the core region.

In figure 18, the model coefficient distribution is redrawn in a logarithm form to closely examine the model behavior in the wall region. This figure confirms the exponential decay in the wall region. The constant model coefficient (here 0.055 is used to match with the present calculation at the core region) distributions are also plotted combined with the exponential damping function as proposed by Moin & Kim (1982),

$$C_\tau = 0.055[1 - \exp(-y^+/A^+)] \tag{65}$$

and by Piomelli *et al.* (1987),

$$C_\tau = 0.055[1 - \exp(-(y^+)^3/(A^+)^3)]^{1/2} \tag{66}$$

with wall damping constant $A^+ = 25$. These damping functions were determined from *a priori* test (where the exact SGS quantities are calculated from exact DNS data and then the modeled quantities are evaluated by comparing with the exact ones) developed by Clark *et al.* (1979). In most cases, however, the results obtained from the *a priori* test can not be confirmed by *a posteriori* test (where the SGS model is actually implemented in an LES code and then the results of the simulation are evaluated) since, in an *a priori* test, the results are obtained by completely ignoring the dynamics at the cut-off. The present results also show some discrepancies with the damping functions based on *a priori* test. According to the present LES results, the following damping function seems to represent more accurately the distribution of model coefficient in the wall region,

$$C_\tau = 0.055[1 - \exp(-(y^+)^2/(A^+)^2)] \tag{67}$$

Figure 19 (a) shows the isosurfaces (gray-shaded region) of instantaneous streamwise velocity fluctuation (u''=0.06) together with the shaded contours (color-shaded plane) of the dynamically determined model coefficient in (x,y) and (y,z) planes. The model coefficient is divided into three ranges: the high dissipation ($C_\tau > 0.1$), the normal dissipation ($0 < C_\tau < 0.1$), and the backscatter ($C_\tau < 0$) ranges. As was observed in high resolution DNS fields (e.g., Lee & Kim, 1991), the entire flow field contains the streaky structures elongated along the flow direction which are analogous to the streaks observed in the viscous sublayer of a turbulent boundary layer. These streaks are believed to be responsible for the production

of turbulence. In the turbulent plane Couette flow, the streaky structures clearly exist in the core region though they are somewhat distorted. Both the high dissipation and the backscatter regions are observed in a significant amount of domain.

Figure 19(b) shows the isosurfaces (gray-shaded region) of instantaneous normal velocity fluctuation (v''=0.024) together with the shaded contours (color-shaded plane) of the dynamically determined dissipation model coefficient in (x,y) and (y,z) planes. The dissipation model coefficient is divided into three ranges: $C_\epsilon > 2$, $1 < C_\epsilon < 2$, and $C_\epsilon < 1$. The elongated structures are not noticeable as much as in the streamwise velocity fluctuation case. The regions of high level of the dissipation model coefficient are distributed uniformly across the channel.

5.5 Conclusions

In this study, a new localized dynamic model has been developed and its properties have been studied in detail. This model is formulated using the subgrid-scale kinetic energy equation model as a base model. As in other dynamic models, two different filter levels are introduced to dynamically determine the model coefficient. However, in the present model, similarity between the subgrid-scale stress tensor and the test-scale Leonard stress tensor is used to obtain the coefficient, while in the earlier dynamic models, the (Germano *et al.*'s) mathematical identity was used to implicitly model the test-scale Leonard stress tensor in terms of the difference between two different filter level models.

The scale-similarity assumption used here allows the present subgrid-scale model to overcome some of the inherent deficiencies of the earlier dynamic models. The instability caused

by the prolonged presence of negative model coefficients is also prevented in the LDKM by explicitly computing the subgrid-scale kinetic energy. It has been demonstrated that the localized model coefficients obtained from the LDKM are Galilean-invariant and very realizable. The proposed LDKM is also quite simple and efficient in comparison with the existing dynamic localization model (based on the subgrid-scale kinetic energy) by Ghosal *et al.* (1995).

The subgrid-scale model proposed here has been successfully applied to various isotropic and shear-driven turbulent flows. It has been demonstrated that the energy decay rate in decaying isotropic turbulence can be accurately predicted in good agreement with experimental data. The LES results confirmed the power law decay which was observed in the experimental data. Furthermore, three different coarse grid LES showed consistency in predicting the energy decay. The present model was then applied to forced (statistically stationary) high-Reynolds-number isotropic turbulence. The LES results were in good agreement with the high resolution DNS data and clearly demonstrated the accurate prediction of velocity statistics and the development of the non-Gaussian statistics. Finally, LES prediction of the characteristic effect of system rotation on an initially isotropic turbulence showed a good agreement with the experiment. The dynamic model coefficients were also shown to respond correctly to the changes in the large-scale motions caused by system rotation.

In the simulation of the turbulent Couette flows, the LDKM has demonstrated its capability by capturing correctly the behavior near solid walls without any adjustments of the model. The mean velocity distribution and turbulent intensities were very accurately predicted and compared well with the existing experimental and DNS data. It was also shown that the prediction of the mean velocity profile confirmed the universal velocity-distribution

law for smooth wall conditions clearly showing the division into a viscous sublayer, a buffer region, and a logarithm part. Furthermore, the (time-averaged) dynamically determined model coefficients showed correct asymptotic behaviors near solid walls by confirming the exponential decay suggested by Van Driest (1956). However, the damping function determined from the present LES data was different with the damping functions estimated based on *a priori* test using DNS data.

This work was supported by the Fluid Dynamics Division of the Office of Naval Research under grant N00014-93-1-0342, monitored by Dr. L. P. Purtell. Computing time was provided by the DoD High Performance Computing (HPC) Centers: Army Research Laboratory (ARL), Naval Oceanographic Office (NAVOCEANO), and Army Engineer Waterways Experiment Station (CEWES).

A Dynamic determination of the diffusion model coefficient

The diffusion term in the transport equation for k_{sgs}, (16), can be rewritten as:

$$\frac{\partial}{\partial x_i}\left(D_i + \nu\frac{\partial k_{sgs}}{\partial x_i}\right) \tag{A 1}$$

Here, the exact expression and the model of D_i at the grid-filter level are given by

$$\begin{aligned} D_i &= -\left(\overline{\rho u_i} - \overline{\rho}\,\overline{u}_i\right) - \left(\overline{u_i k_{tot}} - \overline{u}_i\overline{k}_{tot}\right) + \overline{u}_j\left(\overline{u_i u_j} - \overline{u}_i\overline{u}_j\right) \\ &= C_d\overline{\Delta}k_{sgs}^{1/2}\frac{\partial k_{sgs}}{\partial x_i} \end{aligned} \tag{A 2}$$

where, $k_{tot} = \frac{1}{2}u_k u_k$ and $C_d = C_\tau/\sigma_k - \nu/(\overline{\Delta} k_{sgs}^{1/2})$ which is defined here as a diffusion model coefficient. Using the procedure described in section 3.3, the following expression for the diffusion flux at the test-filter level is obtained,

$$\begin{aligned} d_i &= -\left(\widehat{\overline{p}\,\overline{u}_i} - \hat{\overline{p}}\,\hat{\overline{u}}_i\right) - \left(\widehat{\overline{u}_i \overline{k}_{tot}} - \hat{\overline{u}}_i \hat{\overline{k}}_{tot}\right) + \hat{\overline{u}}_j \left(\widehat{\overline{u}_i \overline{u}_j} - \hat{\overline{u}}_i \hat{\overline{u}}_j\right) \\ &= C_d \hat{\Delta} k_{test}^{1/2} \frac{\partial k_{test}}{\partial x_i} \end{aligned} \qquad \text{(A 3)}$$

where, $\overline{k}_{tot} = \frac{1}{2}\overline{u_k u_k} = \frac{1}{2}\overline{u}_k \overline{u}_k + k_{sgs}$ and $k_{test} = \frac{1}{2}\left(\widehat{\overline{u}_k \overline{u}_k} - \hat{\overline{u}}_i \hat{\overline{u}}_i\right)$. (A 3) does not include any other unknowns except C_d, hence, C_d can be determined directly from (A 3). However, since (A 3) is a set of three independent equations for one unknown C_d, the least-square method can be used to solve this over-determined system as was done to determine C_τ. Thus,

$$C_d = \frac{d_i \left(\partial k_{test}/\partial x_i\right)}{\hat{\Delta} k_{test}^{1/2} \left(\partial k_{test}/\partial x_i\right)\left(\partial k_{test}/\partial x_i\right)} \qquad \text{(A 4)}$$

B Dynamic estimate of the initial k_{sgs}

As shown by Lilly (1967), the standard Smagorinsky model (with fixed coefficient) has been derived from the SGS kinetic energy model by assuming equilibrium of the SGS energy production and dissipation. With this assumption, the SGS energy can be described in terms of the grid width and the resolved-scale strain-rate tensor without employing a transport equation for k_{sgs}. This description is easily obtained by comparing (7) with (17),

$$k_{sgs} = \frac{1}{2}\left(\overline{u_k u_k} - \overline{u}_k \overline{u}_k\right) \approx C\overline{\Delta}^2 \left|\overline{S}\right|^2 \qquad \text{(B 1)}$$

The test-filter level energy can also be described in a similar manner,

$$k_{test} = \frac{1}{2}\left(\widehat{\overline{u}_k\overline{u}_k} - \hat{\overline{u}}_k\hat{\overline{u}}_k\right) \approx C\hat{\Delta}^2\left|\hat{\overline{S}}\right|^2 \tag{B 2}$$

Now, a dimensionless coefficient C can be evaluated from (B 2),

$$C \approx \frac{k_{test}}{\hat{\Delta}^2\left|\hat{\overline{S}}\right|^2} \tag{B 3}$$

By substituting (B 3) into (B 1), we get

$$k_{sgs} \approx \frac{\overline{\Delta}^2\left|\overline{S}\right|^2}{\hat{\Delta}^2\left|\hat{\overline{S}}\right|^2} k_{test} \tag{B 4}$$

(B 4) can provide a dynamic estimate of k_{sgs} when the initial k_{sgs} is unknown. The description for k_{sgs} in (B 4) is the same as in (56), except that (B 4) contains a variable coefficient while (56) contains a fixed coefficient C_k. By analogy between (B 4) and (56), C_k can be evaluated from the resolved-scale information in LES data,

$$C_k \approx \frac{\overline{\Delta}^2\left|\overline{S}\right|^2}{\hat{\Delta}^2\left|\hat{\overline{S}}\right|^2} \tag{B 5}$$

Using the LES data of the forced isotropic turbulence (section 5.2), (B 5) predicts $C_k \approx 0.49$ for higher Reynolds number case ($Re_\lambda \approx 260$) and $C_k \approx 0.45$ for lower Reynolds number case ($Re_\lambda \approx 80$). These values are in very good agreement with that given by Liu *et al.* (1994). In their work, $C_k = 0.45 \pm 0.15$ was obtained from a high Reynolds number ($Re_\lambda \approx 310$) experimental data of a free jet.

References

[1] Akselvoll, K. & Moin, P. 1993 Application of the dynamic localization model to large-eddy simulation of turbulent flow over a backward facing step. In *Engineering Applications of Large Eddy Simulations* (ed. U. Piomelli & S. Ragab). ASME-FED v. 162, p. 1.

[2] Armfield, S. W. 1991 Finite difference solution of the Navier-Stokes equations on staggered and non-staggered grids. *Comput. Fluids* **20**, 1.

[3] Aydin, E. M. & Leutheusser, H. J. 1987 Experimental investigation of turbulent plane Couette flow. *ASME Forum on Turbulent Flows, FED* v. 51, p. 51.

[4] Aydin, E. M. & Leutheusser, H. J. 1991 Plane-Couette flow between smooth and rough walls. *Exps Fluids* **11**, 302.

[5] Bardina, J., Ferziger, J. H. & Reynolds, W. C. 1980 Improved subgrid scale models for large eddy simulation. *AIAA Paper* 80-1357.

[6] Bardina, J., Ferziger, J. H. & Rogallo, R. S. 1985 Effect of rotation on isotropic turbulence: computation and modeling. *J. Fluid Mech.* **154**, 321.

[7] Bech, K. H., Tillmark, N., Alfredsson, P. H. & Andersson, H. I. 1995 An investigation of turbulent plane Couette flow at low Reynolds numbers. *J. Fluid Mech.* **286**, 291.

[8] Brachet, M. E., Meiron, D. I., Orszag, S. A., Nickel, B. G., Morf, R. H. & Frisch, U. 1983 Small-scale structure of the Taylor Green Vortex. *J. Fluid Mech.* **130**, 411.

[9] Brandt, A. 1981 Guide to multigrid development. In *Lecture Notes in Mathematics* v. 960. Springer-Verlag, p. 220.

[10] Briscolini, M. & Santangelo, P. 1994 The non-Gaussian statistics of the velocity field in low-resolution large-eddy simulations of homogeneous turbulence. *J. Fluid Mech.* **270**, 199.

[11] Cabot, W. H.. & Moin, P. 1993 Large eddy simulation of scalar transport with the dynamic subgrid-scale model. In *Large Eddy Simulation of Complex Engineering and Geophysical Flows* (ed. B. Galperin & S. A. Orszag). Cambridge University Press, p. 411.

[12] Carati, D., Ghosal, S. & Moin, P. 1995 On the representation of backscatter in dynamic localization models. *Phys. Fluids* **7**, 606.

[13] Chorin, A. J. 1967 A numerical method for solving incompressible viscous flow problems. *J. Comput. Phys.* **2**,12.

[14] Clark, R. A., Ferziger, J. H. & Reynolds, W. C. 1979 Evaluation of subgrid-scale models using an accurately simulated turbulent flow. *J. Fluid Mech.* **91**, 1.

[15] Comte-Bellot, G. & Corsin, S. 1971 Simple Eulerian time correlation of full- and narrow-band velocity signals in grid-generated, 'isotropic' turbulence. *J. Fluid Mech.* **48**, 273.

[16] El-Hady, N. M., Zang, T. A. & Piomelli, U. 1994 Application of the dynamic subgrid-scale model to axisymmetric transitional boundary layer at high speed. *Phys. Fluids* **6**, 1299.

[17] Germano, M., Piomelli, U., Moin, P. & Cabot, W. H. 1991 A dynamic subgrid-scale eddy viscosity model. *Phys. Fluids* A **3**, 1760.

[18] Germano, M. 1995 A statistical formulation of the dynamic model. Submitted to *Phys. Fluids.*

[19] Ghosal, S., Lund, T. S., Moin, P. & Akselvoll, K. 1995 A dynamic localization model for large-eddy simulation of turbulent flows. *J. Fluid Mech.* **286**, 229.

[20] Grötzbach, G. & Schumann, U. 1979 Direct numerical simulation of turbulent velocity, pressure, and temperature fields in channel flows. In *Turbulent Shear Flows 1* (ed. F. Durst, B. E. Launder, F. W. Schmidt & J. H. Whitelaw). Springer-Verlag, p. 370.

[21] Harlow, F. H. & Welch, J. E. 1965 Numerical calculation of time-dependent viscous incompressible flow with free surfaces. *Phys. Fluids* **8**, 2182.

[22] Horiuti, K. 1989 The role of the Bardina model in large eddy simulation of turbulent channel flow. *Phys. Fluids* A **1**, 426.

[23] Jacquin, L., Leuchter, O., Cambon, C. & Mathieu, J. 1990 Homogeneous turbulence in the presence of rotation. *J. Fluid Mech.* **220**, 1.

[24] Jameson, A. 1983 Solution of the Euler equations for two dimensional transonic flow by a multigrid method. *Appl. Math. Comp.* **13**, 327.

[25] Jimenez, J., Wray, A. A., Saffman, P. S. & Rogallo, R. S. 1993 The structure of intense vorticity in isotropic turbulence. *J. Fluid Mech.* **255**, 65.

[26] Kerr, R. M. 1985 Higher order derivative correlations and the alignment of small-scale structures in isotropic numerical turbulence. *J. Fluid Mech.* **153**, 31.

[27] Kim, W.-W. 1996 A New Dynamic Subgrid-Scale Model for Large-Eddy Simulation of Turbulent Flows. Ph. D. Thesis, School of Aerospace Engineering, Georgia Institute of Technology, Atlanta, Georgia.

[28] Kim, W.-W. & Menon S. 1995 A new dynamic one-equation subgrid-scale model for large-eddy simulations. *AIAA Paper 95-0356, AIAA 33rd Aerospace Sciences Mtg, Reno, NV.*

[29] Lee, M. J. & Kim, J. 1991 The structure of turbulence in a simulated plane Couette flow. *Proc. 8th Symp. on Turbulent Shear Flows*, p. 5-3-1.

[30] Lilly, D. K. 1967 The representation of small-scale turbulence in numerical simulation experiments. In *Proc. IBM Sci. Comput. Symp. on Environmental Sci.* (ed. H. H. Goldstine). IBM Form no. 320-1951, p. 195.

[31] Lilly, D. K. 1992 A proposed modification of the Germano subgrid-scale closure method. *Phys. Fluids* **4**, 633.

[32] Liu, S., Meneveau, C. & Katz, J. 1994 On the properties of similarity subgrid-scale models as deduced from measurements in a turbulent jet. *J. Fluid Mech.* **275**, 83.

[33] Lund, T. S., Ghosal, S. & Moin, P. 1993 Numerical experiments with highly-variable eddy viscosity models. In *Engineering Applications of Large Eddy Simulations* (ed. U. Piomelli & S. Ragab). ASME-FED v. 162, p. 7.

[34] Majumdar, S. 1988 Role of underrelaxation in momentum interpolation for calculation of flow with nonstaggered grids. *Numer. Heat Transfer* **13**, 125.

[35] Meneveau, C., Lund, T. S. & Cabot, W. 1996 A Lagrangian dynamic subgrid-scale model of turbulence. *J. Fluid Mech.* **319**, 353.

[36] Menon, S., Yeung, P.-K. & Kim, W.-W. 1996 Effect of subgrid models on the computed interscale energy transfer in isotropic turbulence. *Comput. Fluids*, **25**, 165.

[37] Moin, P. & Kim, J. 1982 Numerical investigation of turbulent channel flow. *J. Fluid Mech.* **118**, 341.

[38] Moin, P., Squires, K., Cabot, W. & Lee, S. 1991 A dynamic subgrid-scale model for compressible turbulence and scalar transport. *Phys. Fluids* A **3**, 2746.

[39] Piomelli, U., Ferziger, J. H. & Moin, P. 1987 Models for large eddy simulations of turbulent channel flows including transpiration. Report TF-32, Stanford University, Dept. of Mechanical Engineering.

[40] Piomelli, U., Cabot, W. H., Moin, P. & Lee S. 1991 Subgrid-scale backscatter in turbulent and transitional flows. *Phys. Fluids* A **3**, 1766.

[41] Piomelli, U. 1993 High Reynolds number calculations using the dynamic subgrid-scale stress model. *Phys. Fluids* A **5**, 1484.

[42] Piomelli, U. & Liu, J. 1995 Large-eddy simulation of rotating channel flows using a localized dynamic model. *Phys. Fluids* **7**, 839.

[43] Rai, M. M. & Moin, P. 1991 Direct simulations of turbulent flow using finite-difference schemes. *J. Comput. Phys.* **96**, 15.

[44] Rogallo, R. S. 1981 Numerical experiments in homogeneous turbulence. *NASA Tech. Memo.* 81315.

[45] Rogers, S. E. & Kwak, D. 1989 Numerical solution of the incompressible Navier-Stokes equations for steady and time-dependent problems. *AIAA Paper 89-0463.*

[46] Salvetti, M. V. & Banerjee, S. 1995 *A priori* tests of a new dynamic subgrid-scale model for finite-difference large-eddy simulations. *Phys. Fluids* A **7**, 2831.

[47] Schmidt, H. & Schumann, U. 1989 Coherent structure of the convective boundary layer derived from large-eddy simulations. *J. Fluid Mech.* **200**, 511.

[48] Schumann, U. 1975 Subgrid scale model for finite difference simulations of turbulent flows in plane channels and annuli. *J. Comput. Phys.* **18**, 376.

[49] Schumann, U. 1977 Realizability of Reynolds-stress turbulence models. *Phys. Fluids* **20**, 721.

[50] Schumann, U. 1995 Stochastic backscatter of turbulence energy and scalar variance by random subgrid-scale fluxes. *J. Fluid Mech.* **451**, 293.

[51] Smagorinsky, J. 1963 General circulation experiments with the primitive equations. I. The basic experiment. *Month. Wea. Rev.* **91**, 99.

[52] Speziale, C. G. 1985 Galilean invariance of subgrid-scale stress models in the large-eddy simulation of turbulence. *J. Fluid Mech.* **156**, 55.

[53] Speziale, C. G., Raj, R. & Gatski, T. B. 1992 Modeling the dissipation rate in rotating turbulent flows. In *Studies in Turbulence* (ed. T. B. Gatski, S. Sarkar & C. G. Speziale). Springer-Verlag, p. 129.

[54] Squires, K. & Piomelli, U. 1994 Dynamic modeling of rotating turbulence. In *Turbulent Shear Flows 9* (ed. F. Durst, N. Jasagi, B. E. Launder, F. W. Schmidt & J. H. Whitelaw). Springer-Verlag, p. 73.

[55] Turkel, E. 1987 Preconditioned methods for solving the incompressible and low speed compressible equations. *J. Comput. Phys.* **72**, 277.

[56] Van Driest, E. R. 1956 On the turbulent flow near a wall. *J. Aerospace Sci.* **23**, 1007.

[57] Vincent, A. & Meneguzzi, M. 1991 The spatial structure and statistical properties of homogeneous turbulence. *J. Fluid Mech.* **225**, 1.

[58] Vreman, B., Geurts, B. & Kuerten, H. 1994a Realizability conditions for the turbulent stress tensor in large-eddy simulation. *J. Fluid Mech.* **278**, 351.

[59] Vreman, B., Geurts, B. & Kuerten, H. 1994b On the formulation of the dynamic mixed subgrid-scale model. *Phys. Fluids* **6**, 4057.

[60] Wong, V. C. 1992 A proposed statistical-dynamic closure method for the linear or nonlinear subgrid-scale stresses. *Phys. Fluids* A **4**, 1080.

[61] Wong, V. C. & Lilly, D. K. 1994 A comparison of two dynamic subgrid closure methods for turbulent thermal convection. *Phys. Fluids* **6**, 1016.

[62] Yoshizawa, A & Horiuti, K. 1985 A statistically-derived subgrid-scale kinetic energy model for the large-eddy simulation of turbulent flows. *J. Phys. Soc. Jpn.* **54**, 2834.

[63] Yoshizawa, A. 1993 Bridging between eddy-viscosity-type and second-order models using a two-scale DIA. *Proc. 9th Symp. on Turbulent Shear Flows*, p. 23-1-1.

[64] Zang, Y., Street, R. L. & Koseff, J. R. 1993 A dynamic mixed subgrid-scale model and its application to turbulent recirculating flows. *Phys. Fluids* A **5**, 3186.

List of tables

Table 1 Turbulent kinetic energy resolved by various grid resolutions. Results are obtained by numerically integrating the energy spectrum for the decaying isotropic turbulence experiment of Comte-Bellot & Corsin (1971).

Table 2 Decay exponent r of the power law decay $E \sim (t^*)^r$ in isotropic turbulence. Experimental data are computed from the energy spectra given by Comte-Bellot & Corsin (1971). Results of DSM, DLM(k), and DLM(S) are adopted from Carati *et al.* (1995).

Table 3 Higher-order moments of a velocity component u and its longitudinal and transverse derivatives, $\partial u/\partial x$ and $\partial u/\partial y$, in forced isotropic turbulence. The nth-order moments are denoted by S_n. Results of 512^3 DNS, 240^3 DNS, and 64^3 LES are adopted from Jimenez *et al.* (1993), Vincent & Meneguzzi (1991), and Briscolini & Santangelo (1994), respectively.

List of figures

Figure 1 (a) Decay of resolved turbulent kinetic energy and (b) energy spectra in decaying isotropic turbulence. Spectral code results of Carati *et al.* (1995) (no model case) and experimental data of Comte-Bellot & Corsin (1971) are also plotted in (a).

Figure 2 Energy spectrum $E(k)$ and dissipation spectrum $2\nu k^2 E(k)$ obtained from 128^3 DNS of Taylor-Green vortex flow at $t = 29$.

Figure 3 Energy spectra obtained from (a) 64^3 LES and (b) 32^3 LES (using various dynamic SGS models) of Taylor-Green vortex flow at $t = 29$. Energy spectra of filtered 128^3 DNS fields are also plotted.

Figure 4 Decay of turbulent kinetic energy in isotropic turbulence, resolved by LES with three different grid resolutions. Experimental data of Comte-Bellot & Corsin (1971) are also plotted.

Figure 5 Energy spectra of decaying isotropic turbulence predicted by LES with three different grid resolutions at (a) $t^* = 4.98$ and (b) $t^* = 8.69$. Experimental data of Comte-Bellot & Corsin (1971) are also plotted.

Figure 6 Time evolution of mean resolved kinetic energy in 32^3 LES of forced isotropic turbulence at two different Reynolds numbers.

Figure 7 Probability distribution of normalized velocity difference for (a) five different scales (r) and (b) $r = 0.39$ predicted by 32^3 LES of forced isotropic turbulence. High resolution DNS results of Vincent & Meneguzzi (1991) are also plotted in (b).

Figure 8 Time evolution of (a) the model coefficient and (b) the dissipation model coefficient dynamically determined by 32^3 LES of forced isotropic turbulence at two different Reynolds numbers.

Figure 9 Time variation of negative model coefficient fraction resulting from 32^3 LES of forced isotropic turbulence at two different Reynolds numbers.

Figure 10 Decay of resolved turbulent kinetic energy in 32^3 LES of rotating isotropic turbulence for various rotation rates. Experimental data of Jacquin *et al.* (1990) are also plotted.

Figure 11 Energy spectra obtained from 32^3 LES of rotating isotropic turbulence for various rotation rates.

Figure 12 Time variation of (a) the model coefficient and (b) the dissipation model coefficient determined from 32^3 LES of rotating isotropic turbulence for various rotation rates.

Figure 13 Time variation of (a) mean positive/negative contributions to the model coefficient and (b) negative model coefficient fraction resulting from 32^3 LES of rotating isotropic turbulence for various rotation rates.

Figure 14 Instantaneous vorticity magnitude isosurfaces (gray-shaded structures) obtained from 32^3 LES of rotating isotropic turbulence at (a) $\Omega = 0 rad/s$ and (b) $\Omega = 62.8 rad/s$. Shaded contours (color-shaded plane) of the dynamically determined model coefficient are also drawn in an (x, z) plane. The model coefficient is divided into three ranges: the high dissipation ($C_\tau > 0.1$), the normal dissipation ($0 < C_\tau < 0.1$), and the backscatter ($C_\tau < 0$) ranges.

Figure 15 (a) Mean velocity distribution and (b) mean velocity distribution in a semi-logarithm form normalized with viscous scales obtained from turbulent plane Couette flow simulation. Experimental data of Aydin & Leutheusser (1987) (Re = 2600) and Bech *et al.* (1995) (Re = 2520), and DNS results of Bech *et al.* (1995) (Re = 2600) are also plotted in (a). In (b), universal velocity-distribution law for smooth wall conditions is plotted for comparison.

Figure 16 Turbulence intensities obtained from turbulent plane Couette flow simulation. Experimental data of Aydin & Leutheusser (1991) (Re = 2600) and Bech *et al.* (1995) (Re = 2520), and DNS results of Bech *et al.* (1995) (Re = 2600) are also plotted.

Figure 17 Time-averaged distribution (across the channel) of (a) the model coefficient and (b) the dissipation model coefficient, obtained from turbulent plane Couette flow simulation.

Figure 18 Time-averaged distribution (across the channel) of the model coefficient in a logarithm form (normalized with viscous scales) obtained from the turbulent plane Couette flow simulation. Some exponential damping functions are also drawn for comparison.

Figure 19 (a) Isosurfaces (gray-shaded structures) of instantaneous streamwise velocity fluctuation obtained from turbulent plane Couette flow simulation. Shaded contours (color-shaded plane) of the dynamically determined model coefficient are also drawn in (x, y) and (y, z) planes. The model coefficient is divided into three ranges: the high dissipation ($C_\tau > 0.1$), the normal dissipation ($0 < C_\tau < 0.1$), and the backscatter ($C_\tau < 0$) ranges. (b) Isosurfaces (gray-shaded structures) of instantaneous normal velocity fluctuation together with shaded contours (color-shaded plane) of the dynamically determined dissipation model coefficient in (x, y) and (y, z) planes.

Table 1. Turbulent kinetic energy resolved by various grid resolutions. Results are obtained by numerically integrating the energy spectrum for the decaying isotropic turbulence experiment of Comte-Bellot & Corsin (1971).

Grid resolution	Resolved energy (%)
512^3	99.8
384^3	99.5
256^3	98.4
192^3	96.6
128^3	92.2
96^3	87.3
64^3	78.3
48^3	70.3
32^3	59.3
24^3	49.7
16^3	35.1
12^3	24.4
8^3	10.5

Table 2. Decay exponent r of the power law decay $E \sim (t^*)^r$ in isotropic turbulence. Experimental data are computed from the energy spectra given by Comte-Bellot & Corsin (1971). Results of DSM, DLM(k), and DLM(S) are adopted from Carati *et al.* (1995).

Grid resolution	48^3	32^3	24^3
Experiment	-1.20	-1.16	-1.12
LDKM	-1.17	-1.13	-1.09
DSM	-1.27		
DLM(k)	-1.28		
DLM(S)	-1.17		

Table 3. Higher-order moments of a velocity component u and its longitudinal and transverse derivatives, $\partial u/\partial x$ and $\partial u/\partial y$, in forced isotropic turbulence. The nth-order moments are denoted by S_n. Results of 512^3 DNS, 240^3 DNS, and 64^3 LES are adopted from Jimenez *et al.* (1993), Vincent & Meneguzzi (1991), and Briscolini & Santangelo (1994), respectively.

	u		$\partial u/\partial x$ ($\partial u/\partial y$)			
	S_4	S_6	S_3	S_4	S_5	S_6
512^3 DNS ($\mathrm{Re}_\lambda \approx 170$)	2.80	12.5	-0.525	6.1	-12.0	125
				(9.4)		(370)
240^3 DNS ($\mathrm{Re}_\lambda \approx 150$)			-0.5	5.9	-9.0	90
			(-0.04)	(8.0)		
64^3 LES ($\mathrm{Re}_\lambda \approx 140$)			-0.35			
			(0.06)	(4.5)		
32^3 LDKM ($\mathrm{Re}_\lambda \approx 260$)	2.78	11.9	-0.317	3.47	-3.48	23.4
			(-0.005)	(4.87)	(-0.109)	(49.9)
32^3 LDKM ($\mathrm{Re}_\lambda \approx 80$)	2.80	12.1	-0.302	3.59	-3.57	25.8
			(0.028)	(4.93)	(0.233)	(51.3)
Gaussian	3.0	15.0	0.0	3.0	0.0	15.0
			(0.0)	(3.0)	(0.0)	(15.0)

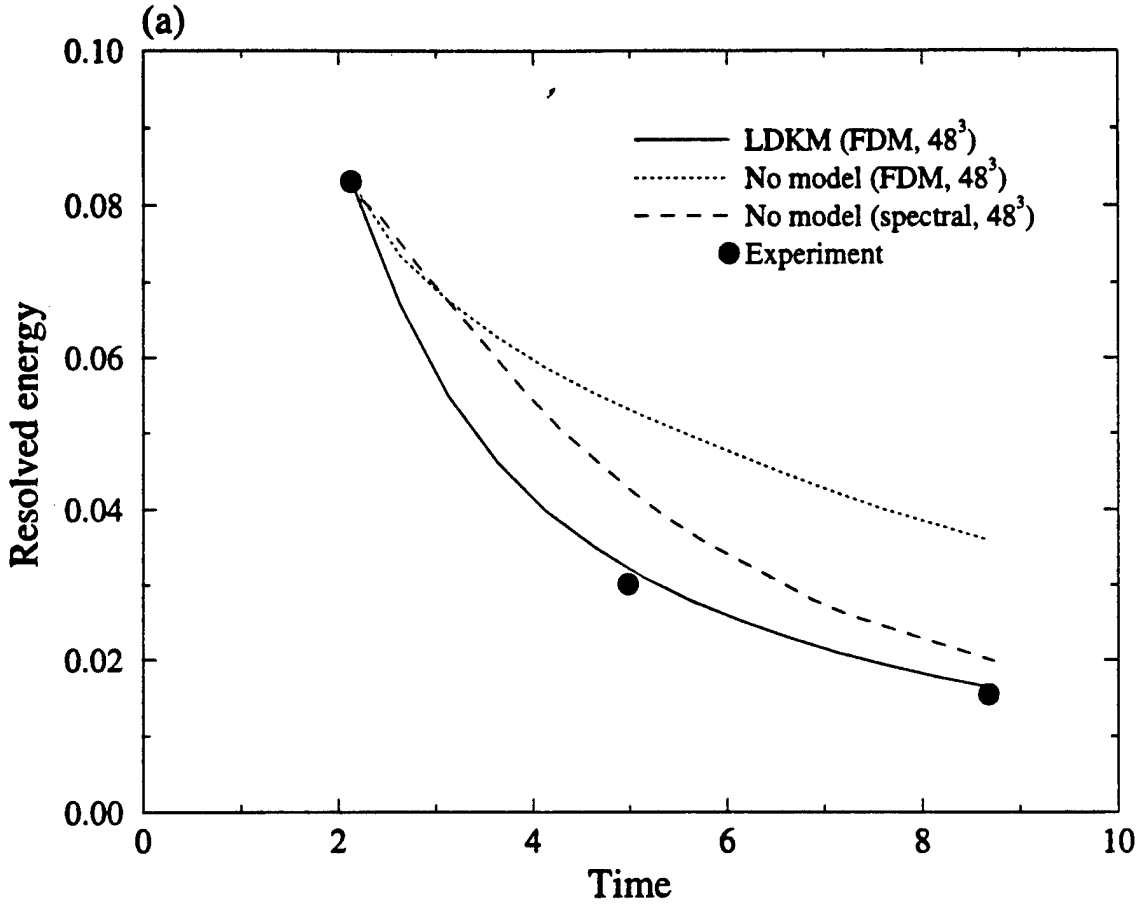

(a)
0.10
0.08
0.06
0.04
0.02
0.00
Resolved energy
0
2
4
6
8
10
Time
LDKM (FDM, 48³)
No model (FDM, 48³)
No model (spectral, 48³)
Experiment

Figure 1(a)

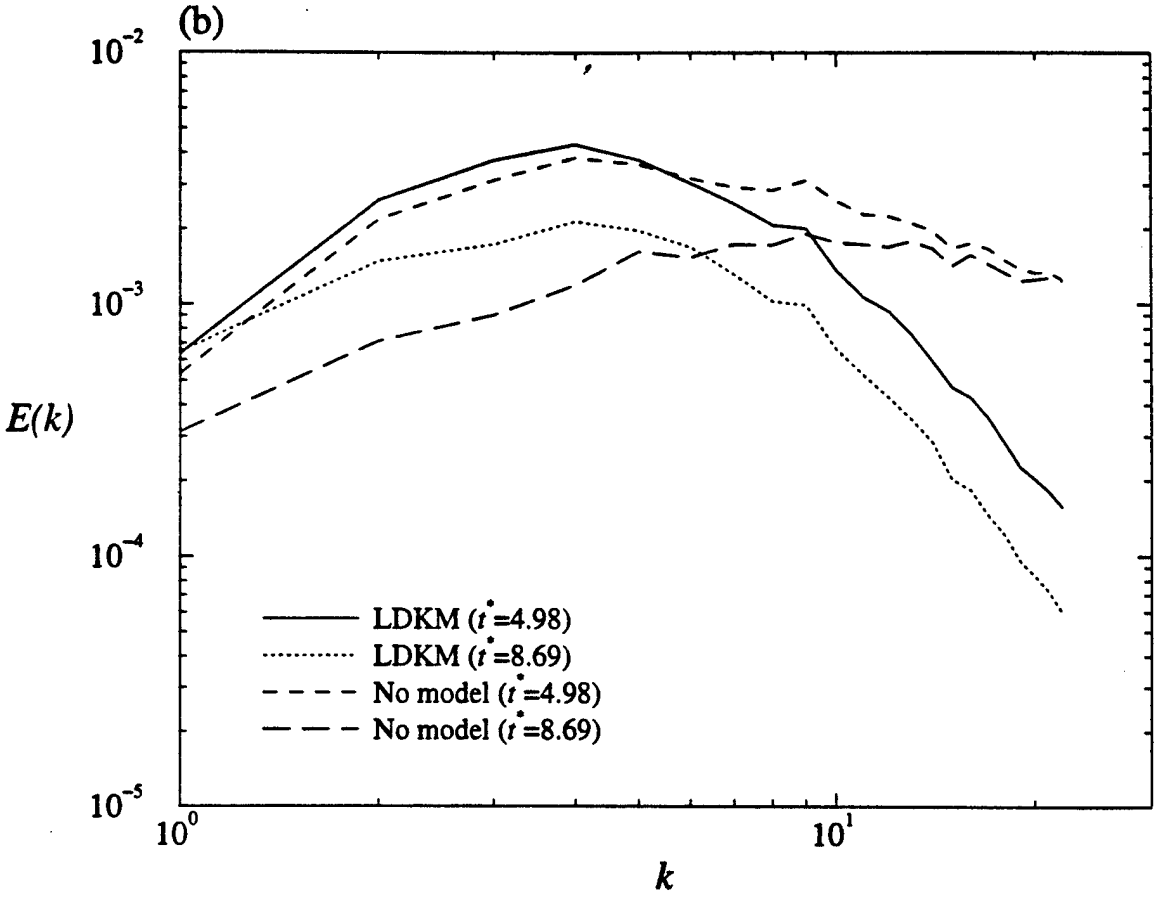

(b)
10^{-2}
10^{-3}
10^{-4}
10^{-5}
$E(k)$
10^{0}
10^{1}
k
LDKM (t^*=4.98)
LDKM (t^*=8.69)
No model (t^*=4.98)
No model (t^*=8.69)

Figure 1(b)

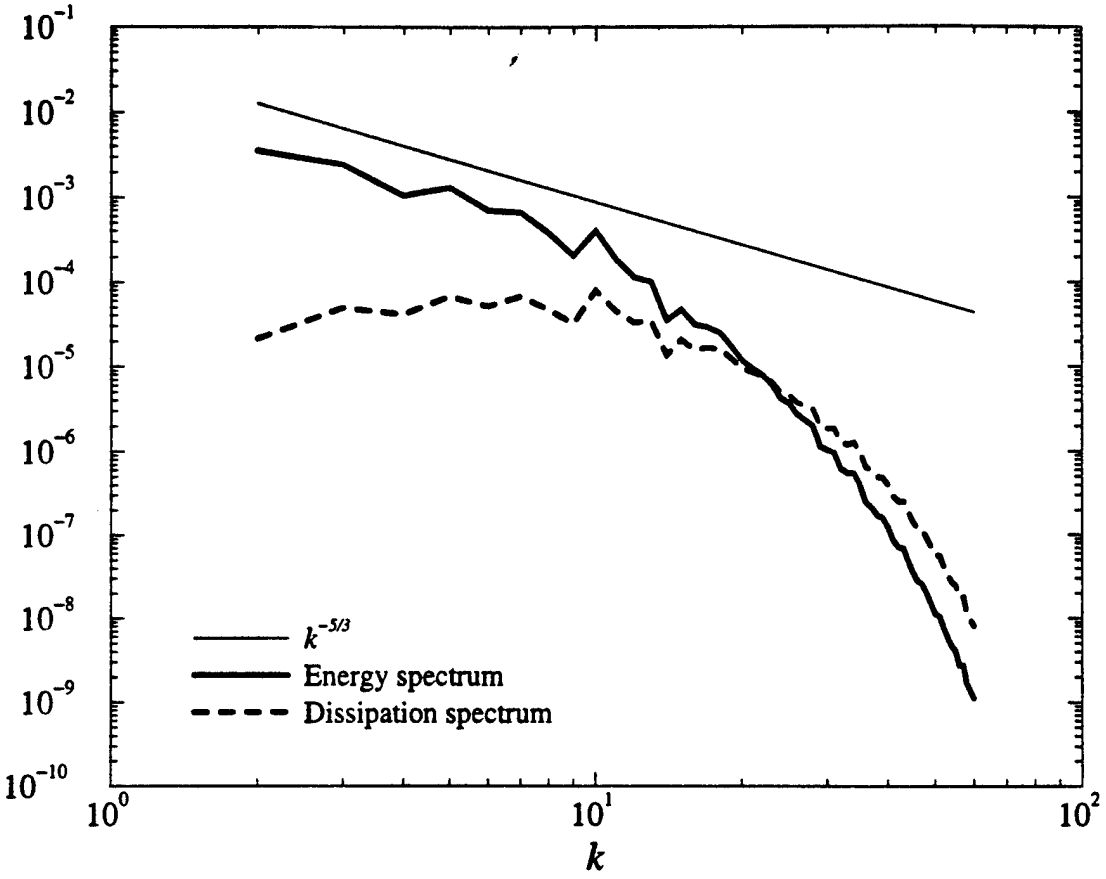

10^{-1}
10^{-2}
10^{-3}
10^{-4}
10^{-5}
10^{-6}
10^{-7}
10^{-8}
10^{-9}
10^{-10}
10^{0}
10^{1}
10^{2}
k
$k^{-5/3}$
Energy spectrum
Dissipation spectrum

Figure 2

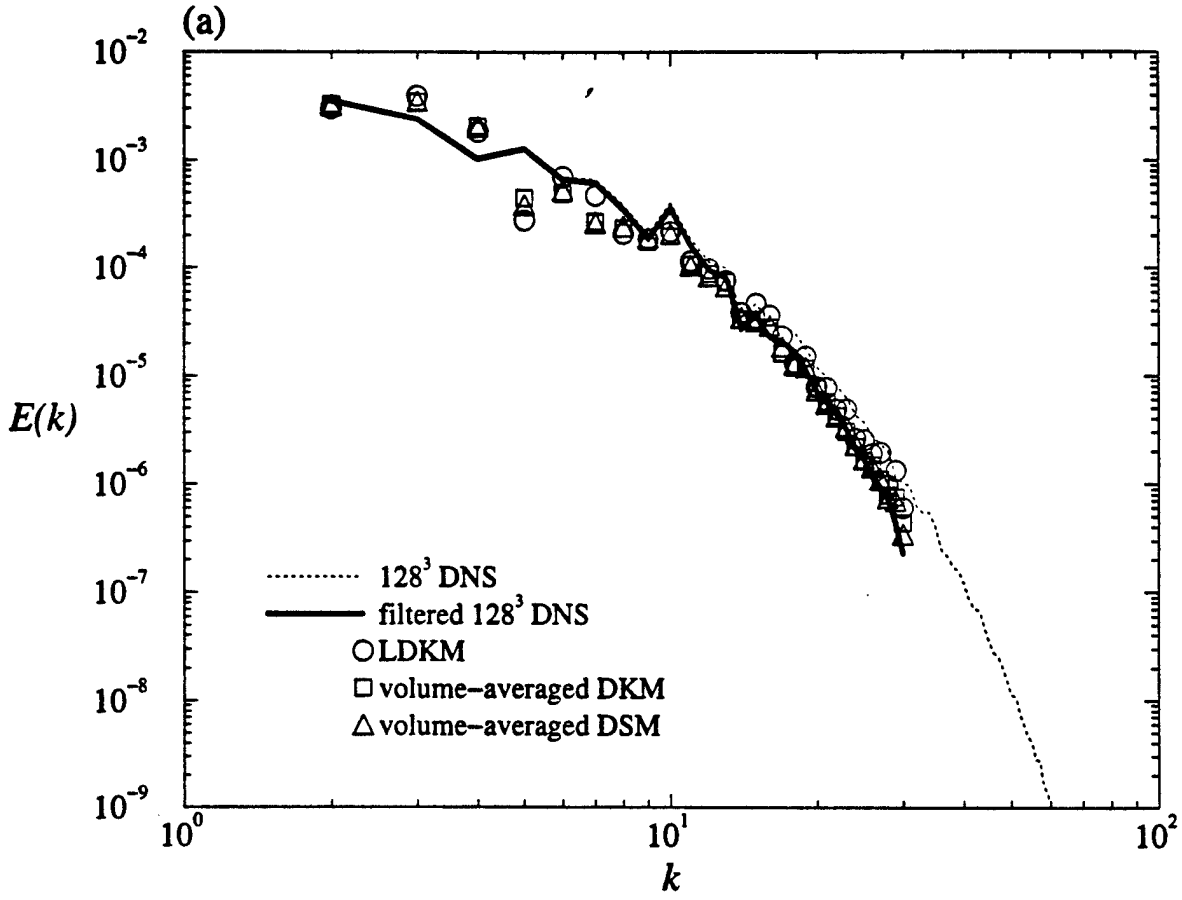

(a)
10^{-2}
10^{-3}
10^{-4}
10^{-5}
10^{-6}
10^{-7}
10^{-8}
10^{-9}
E(k)
10^{0}
10^{1}
10^{2}
k
128^3 DNS
filtered 128^3 DNS
LDKM
volume–averaged DKM
volume–averaged DSM

Figure 3(a)

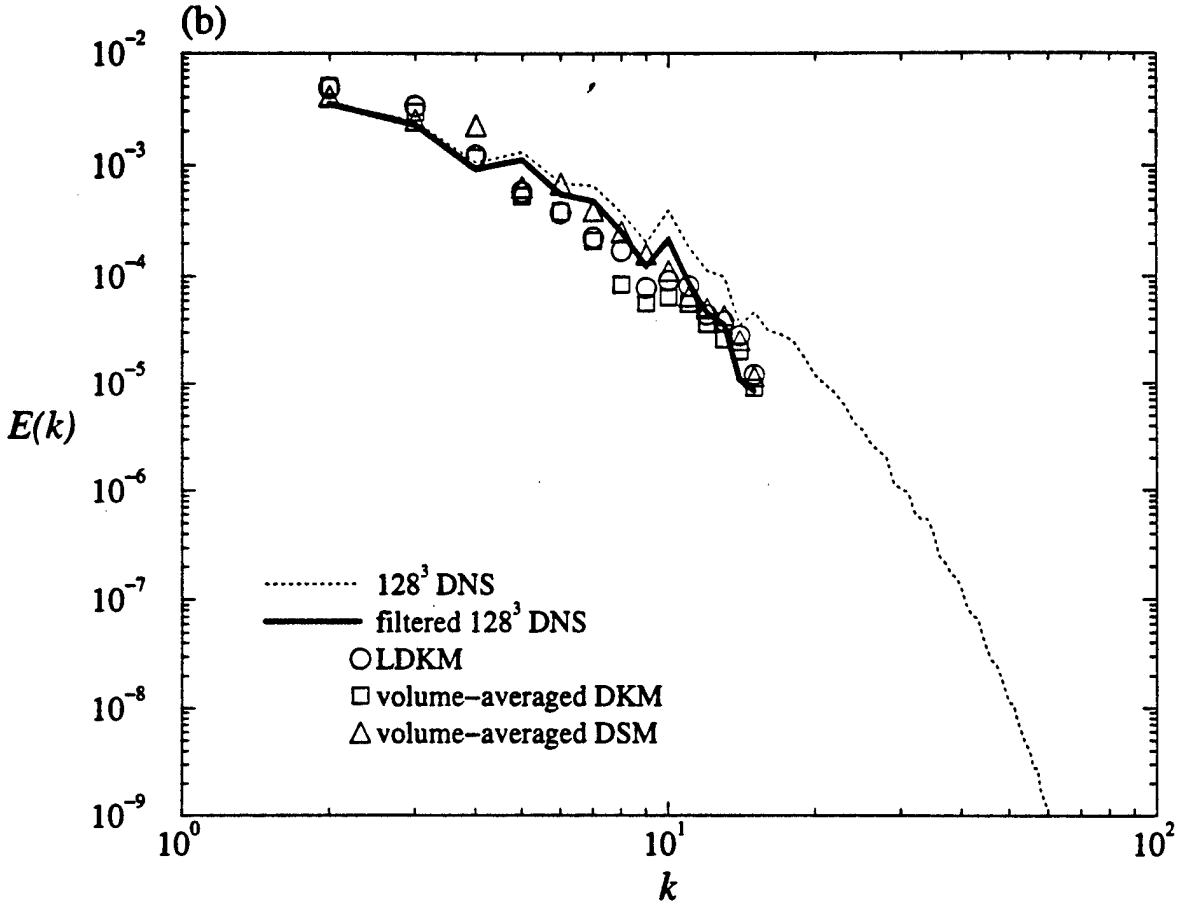

(b)
10^{-2}
10^{-3}
10^{-4}
10^{-5}
10^{-6}
10^{-7}
10^{-8}
10^{-9}
E(k)
10^{0}
10^{1}
10^{2}
k
128^3 DNS
filtered 128^3 DNS
LDKM
volume–averaged DKM
volume–averaged DSM

Figure 3(b)

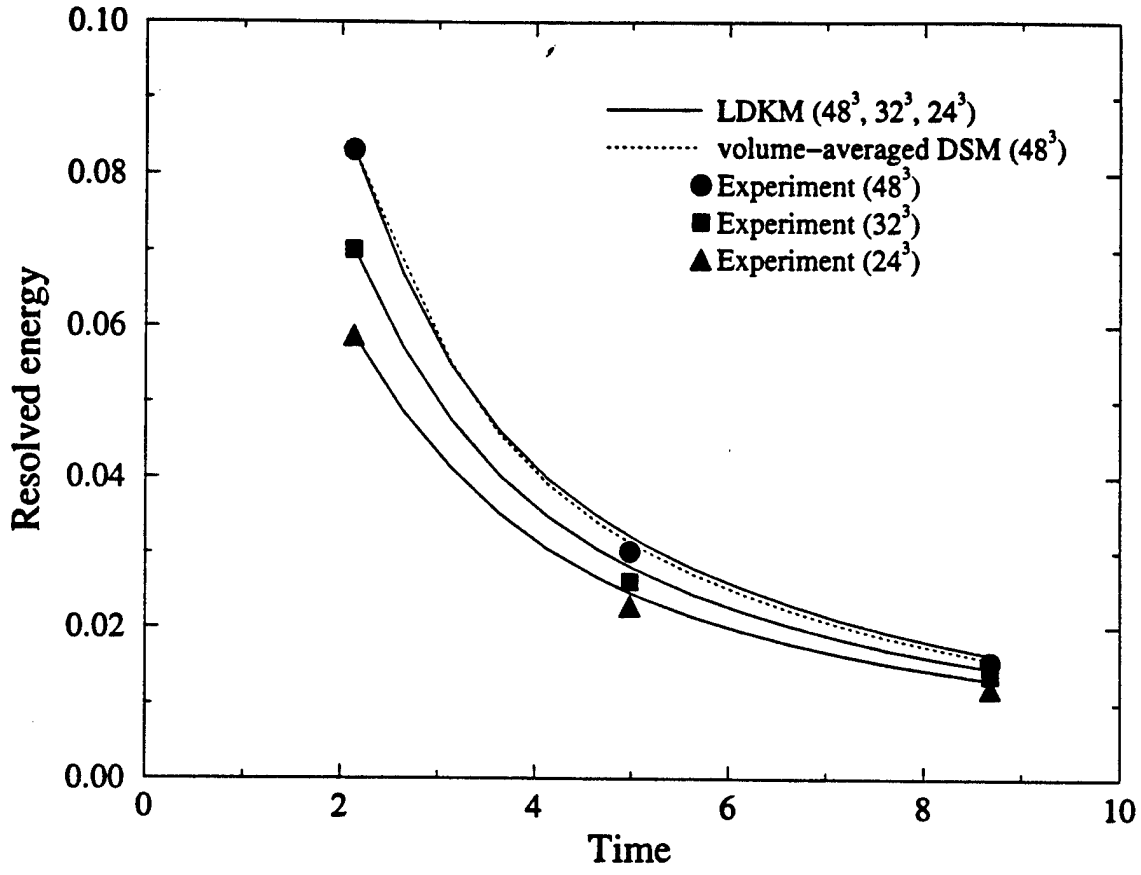

0.10
0.08
0.06
0.04
0.02
0.00
Resolved energy
0
2
4
6
8
10
Time
LDKM (48³, 32³, 24³)
volume–averaged DSM (48³)
Experiment (48³)
Experiment (32³)
Experiment (24³)

Figure 4

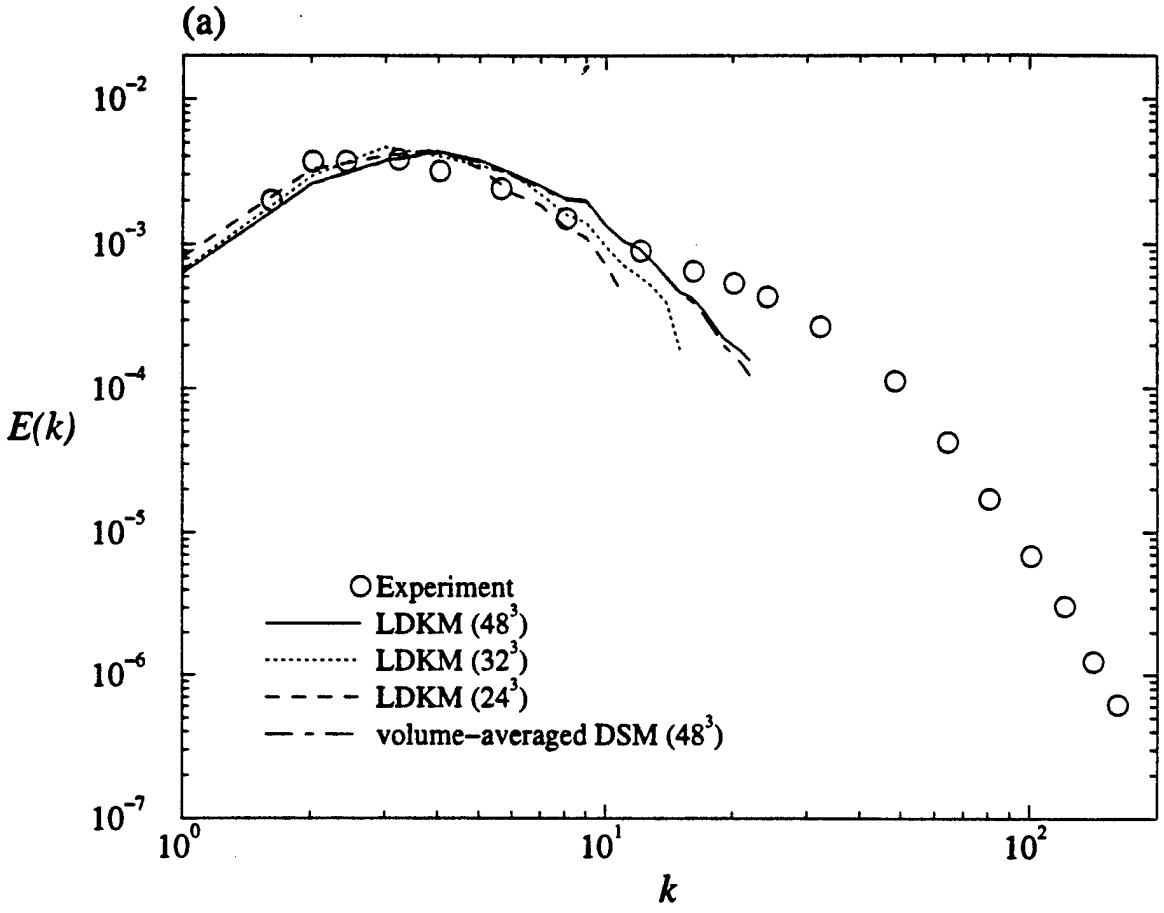

(a)
10^{-2}
10^{-3}
10^{-4}
10^{-5}
10^{-6}
10^{-7}
E(k)
10^{0}
10^{1}
10^{2}
k
Experiment
LDKM (48^3)
LDKM (32^3)
LDKM (24^3)
volume-averaged DSM (48^3)

Figure 5(a)

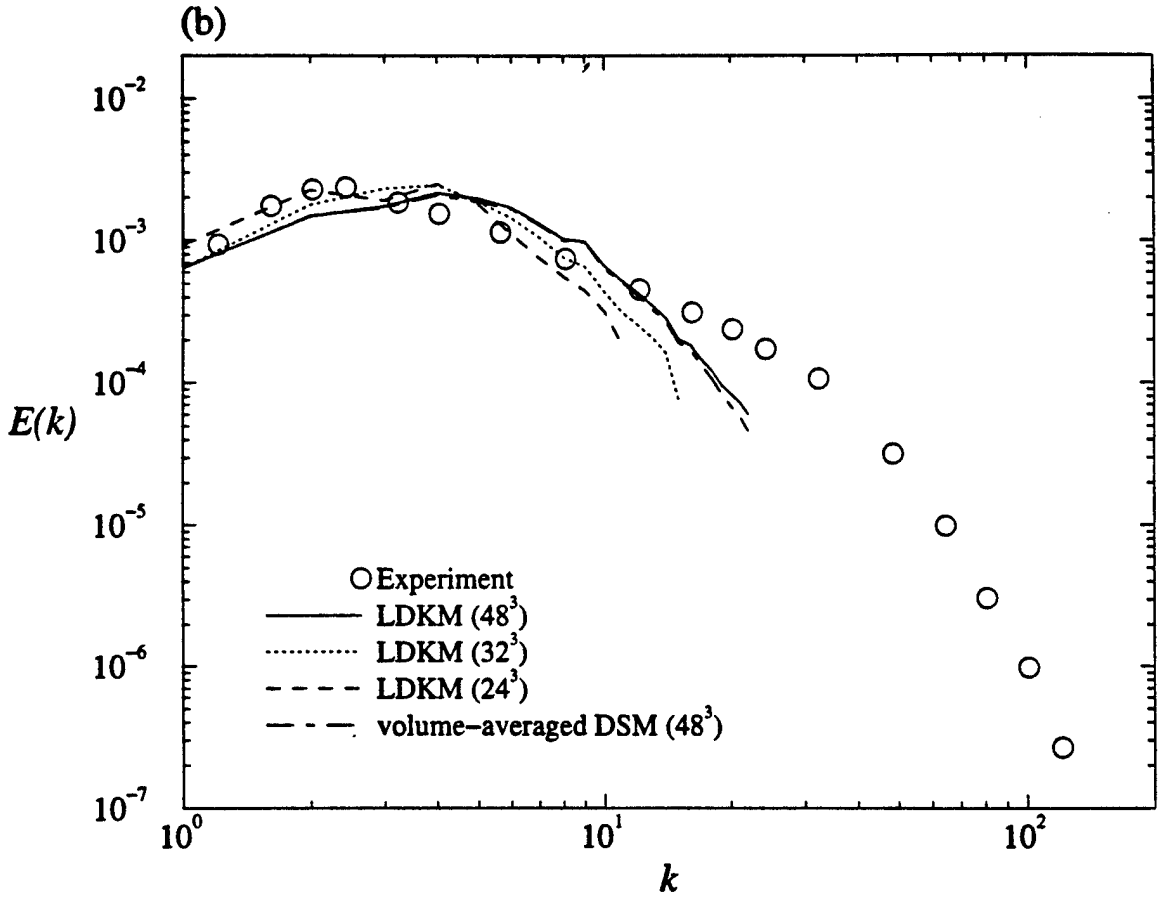

(b)
10^{-2}
10^{-3}
10^{-4}
10^{-5}
10^{-6}
10^{-7}
E(k)
10^{0}
10^{1}
10^{2}
k
Experiment
LDKM (48^3)
LDKM (32^3)
LDKM (24^3)
volume-averaged DSM (48^3)

Figure 5(b)

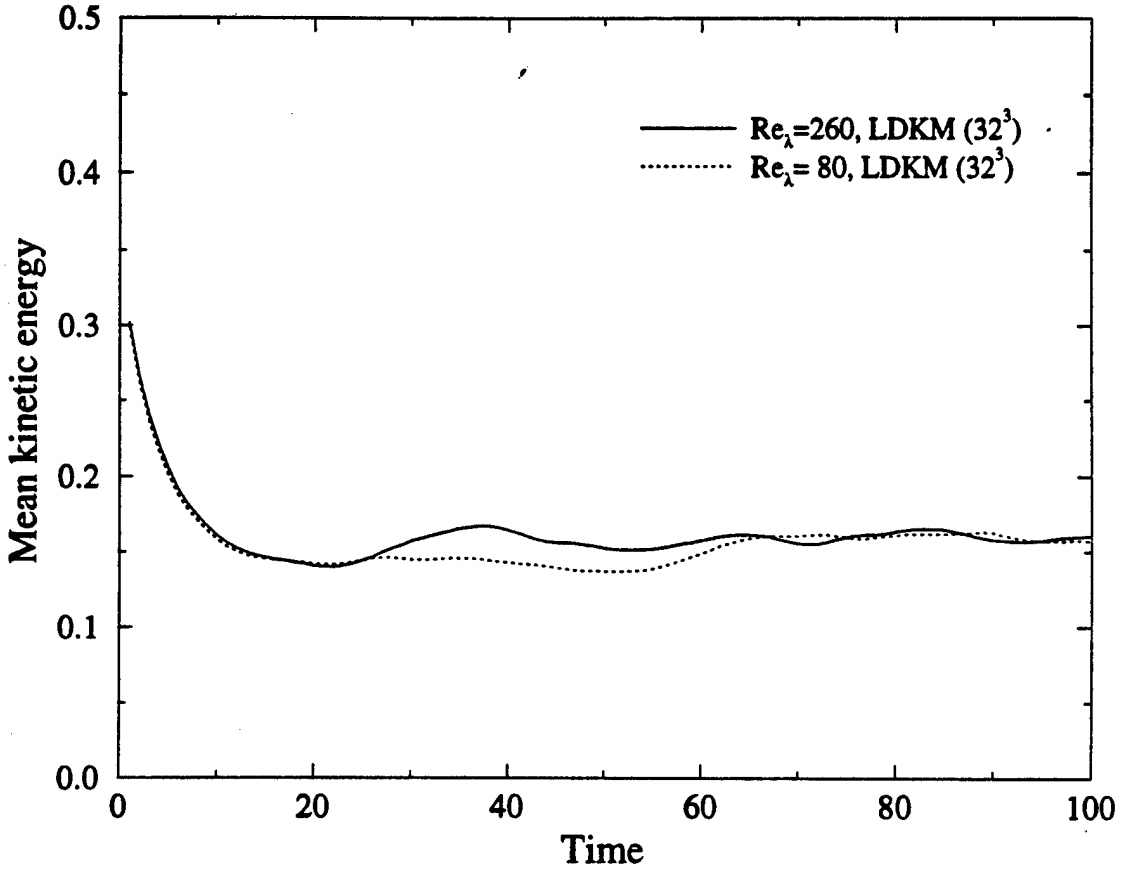

0.5
0.4
0.3
0.2
0.1
0.0
Mean kinetic energy
0
20
40
60
80
100
Time
Re$_\lambda$=260, LDKM (32^3)
Re$_\lambda$= 80, LDKM (32^3)

Figure 6

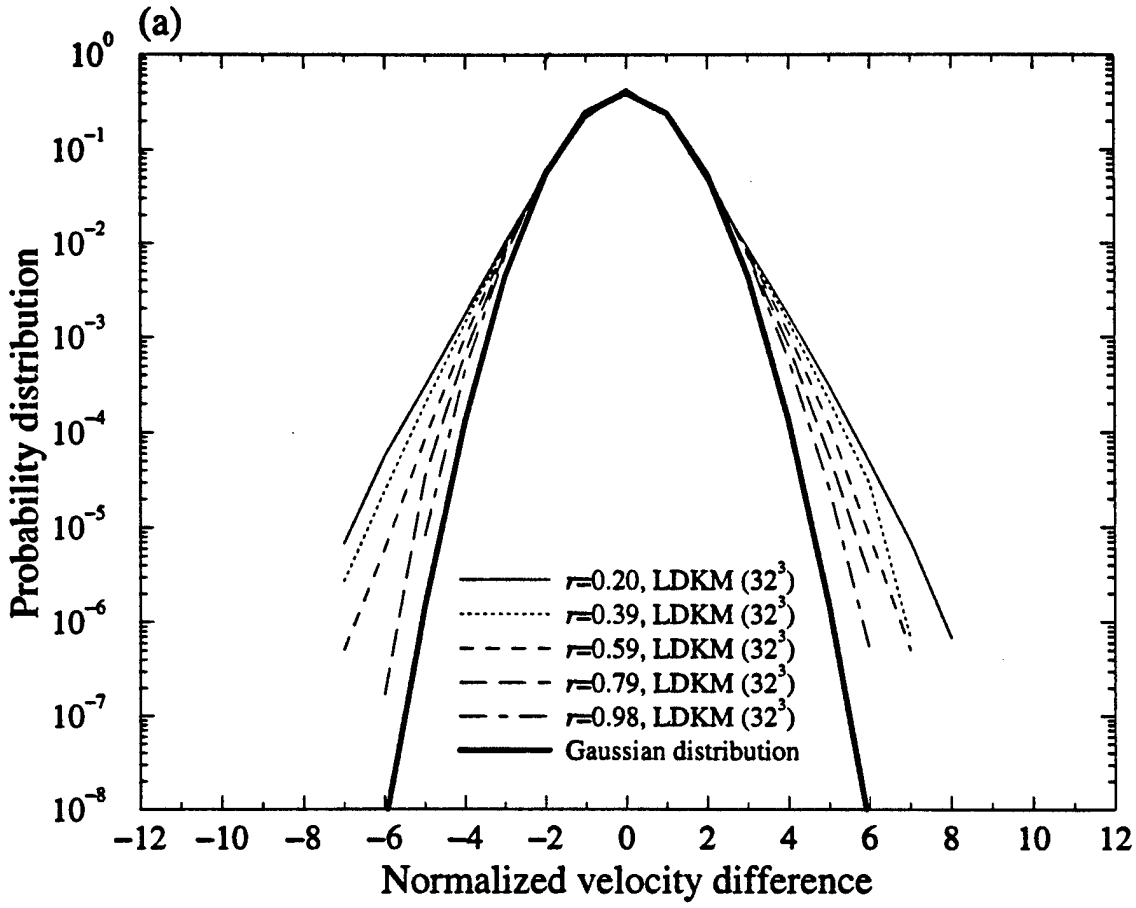

(a)
Probability distribution
Normalized velocity difference
r=0.20, LDKM (32^3)
r=0.39, LDKM (32^3)
r=0.59, LDKM (32^3)
r=0.79, LDKM (32^3)
r=0.98, LDKM (32^3)
Gaussian distribution

Figure 7(a)

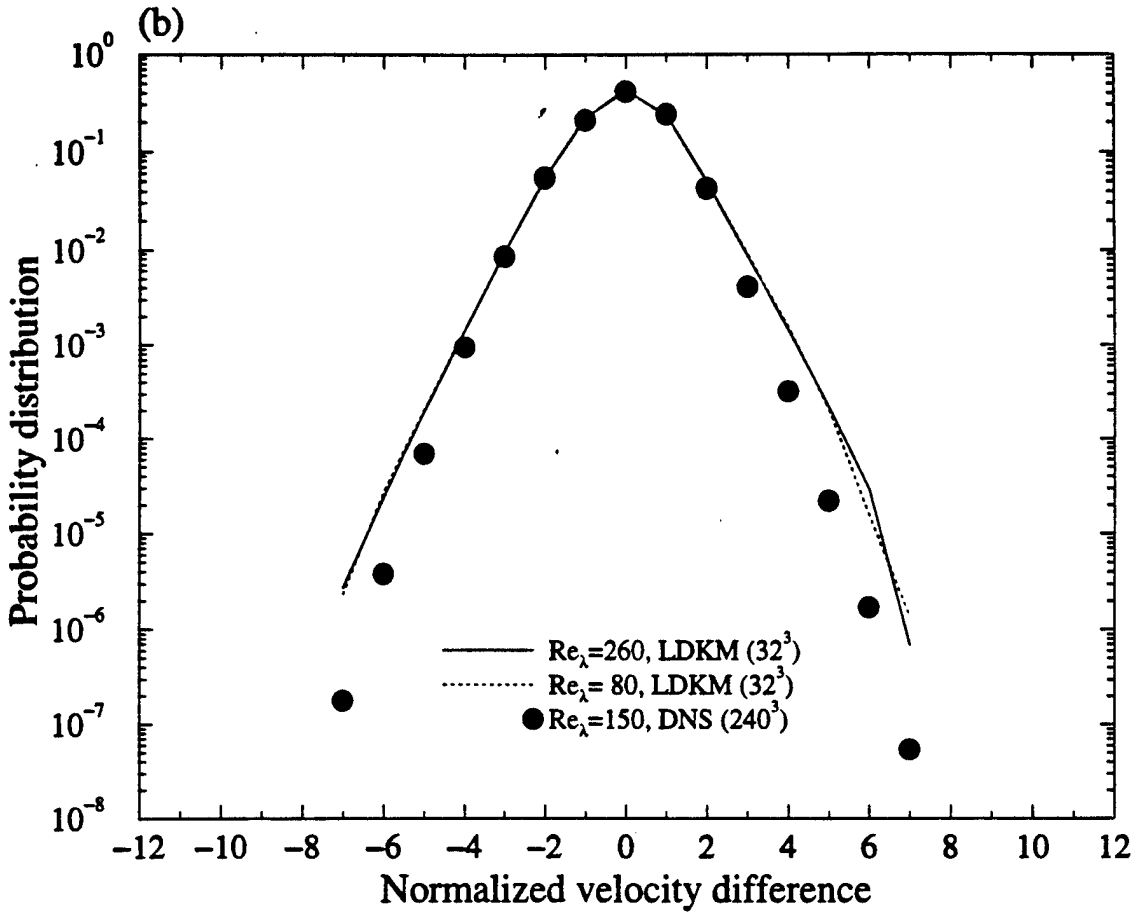

(b)
Probability distribution
Normalized velocity difference
Re$_\lambda$=260, LDKM (32^3)
Re$_\lambda$= 80, LDKM (32^3)
Re$_\lambda$=150, DNS (240^3)

Figure 7(b)

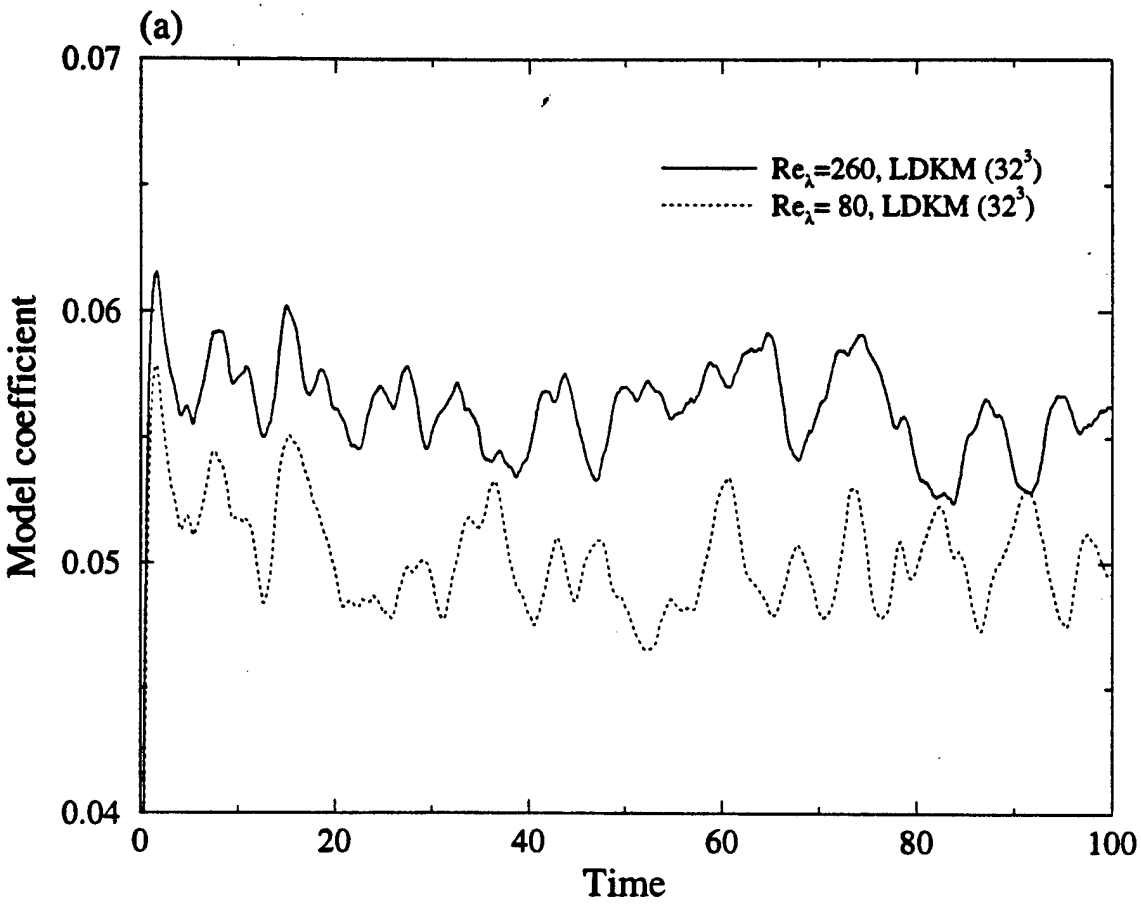

(a)
0.07
0.06
0.05
0.04
Model coefficient
0
20
40
60
80
100
Time
Re$_\lambda$=260, LDKM (32^3)
Re$_\lambda$= 80, LDKM (32^3)

Figure 8(a)

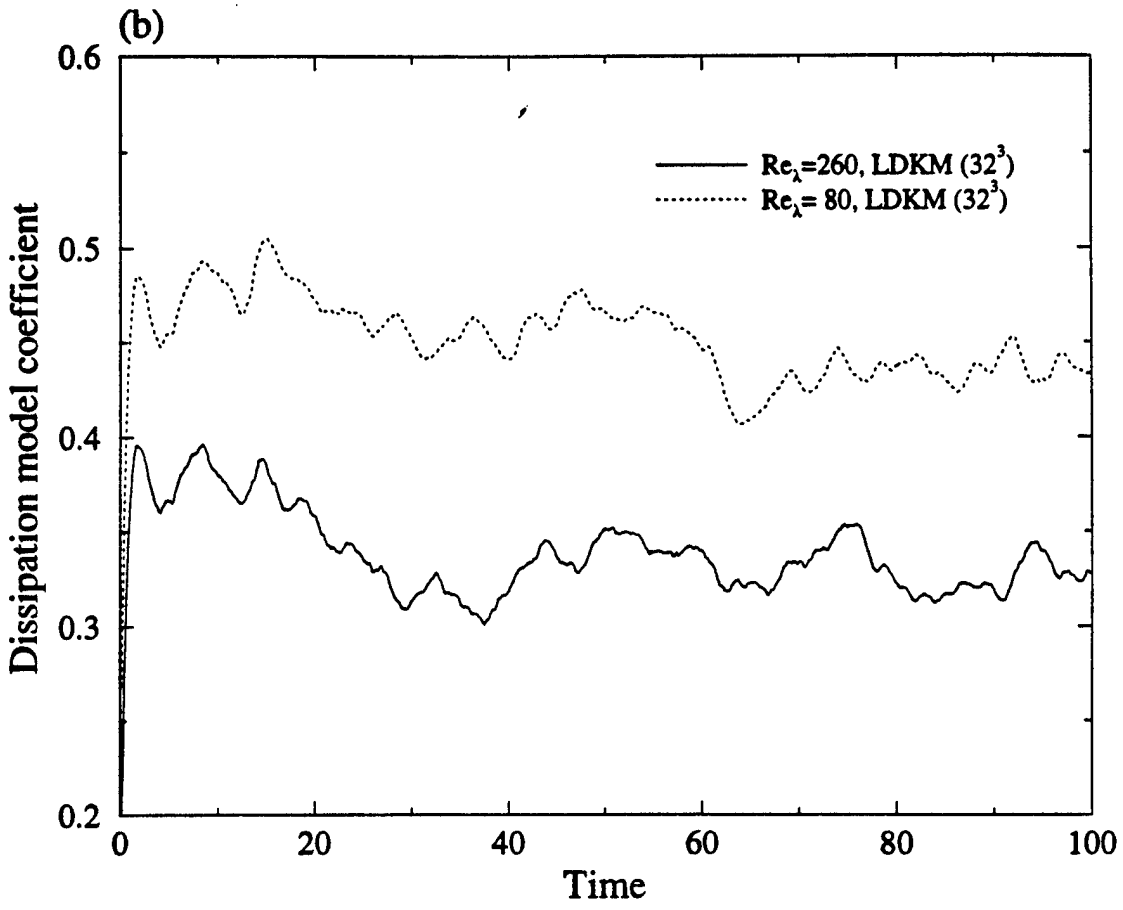

(b)
0.6
0.5
0.4
0.3
0.2
Dissipation model coefficient
0
20
40
60
80
100
Time
Re$_\lambda$=260, LDKM (32^3)
Re$_\lambda$= 80, LDKM (32^3)

Figure 8(b)

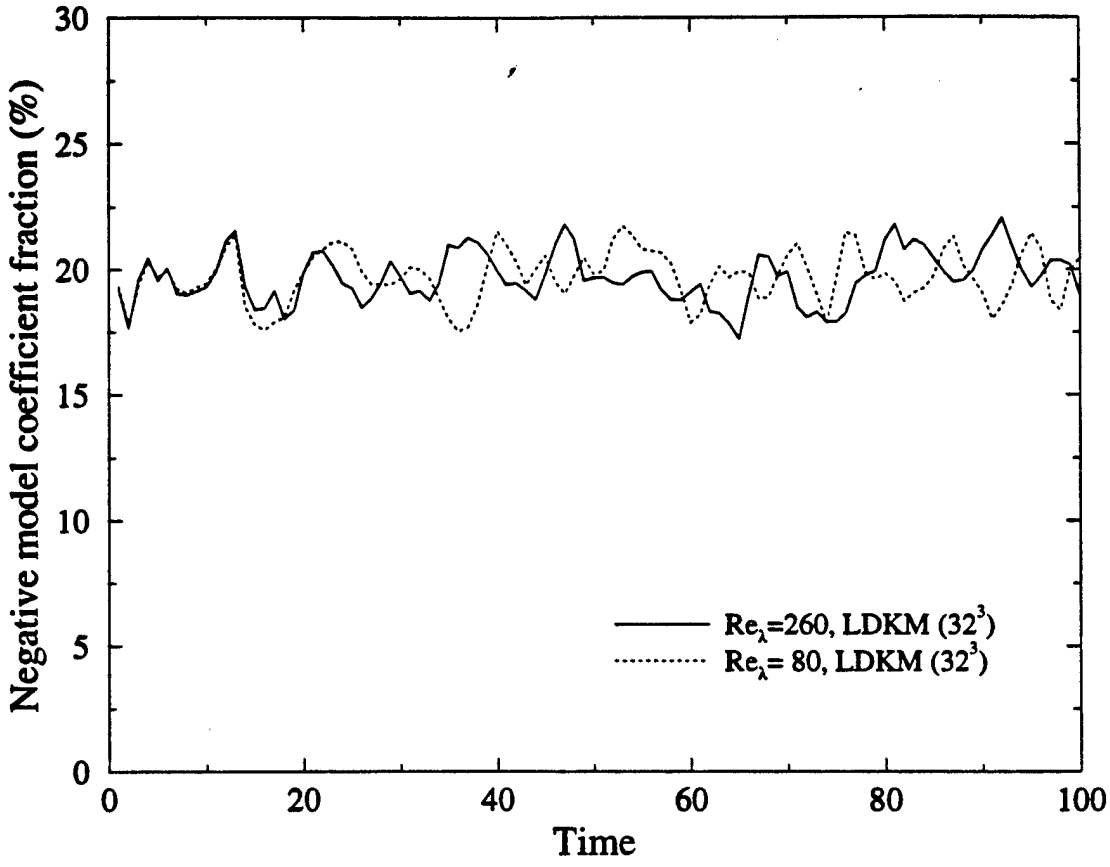

Negative model coefficient fraction (%)
30
25
20
15
10
5
0
0
20
40
60
80
100
Time
Re$_\lambda$=260, LDKM (32^3)
Re$_\lambda$= 80, LDKM (32^3)

Figure 9

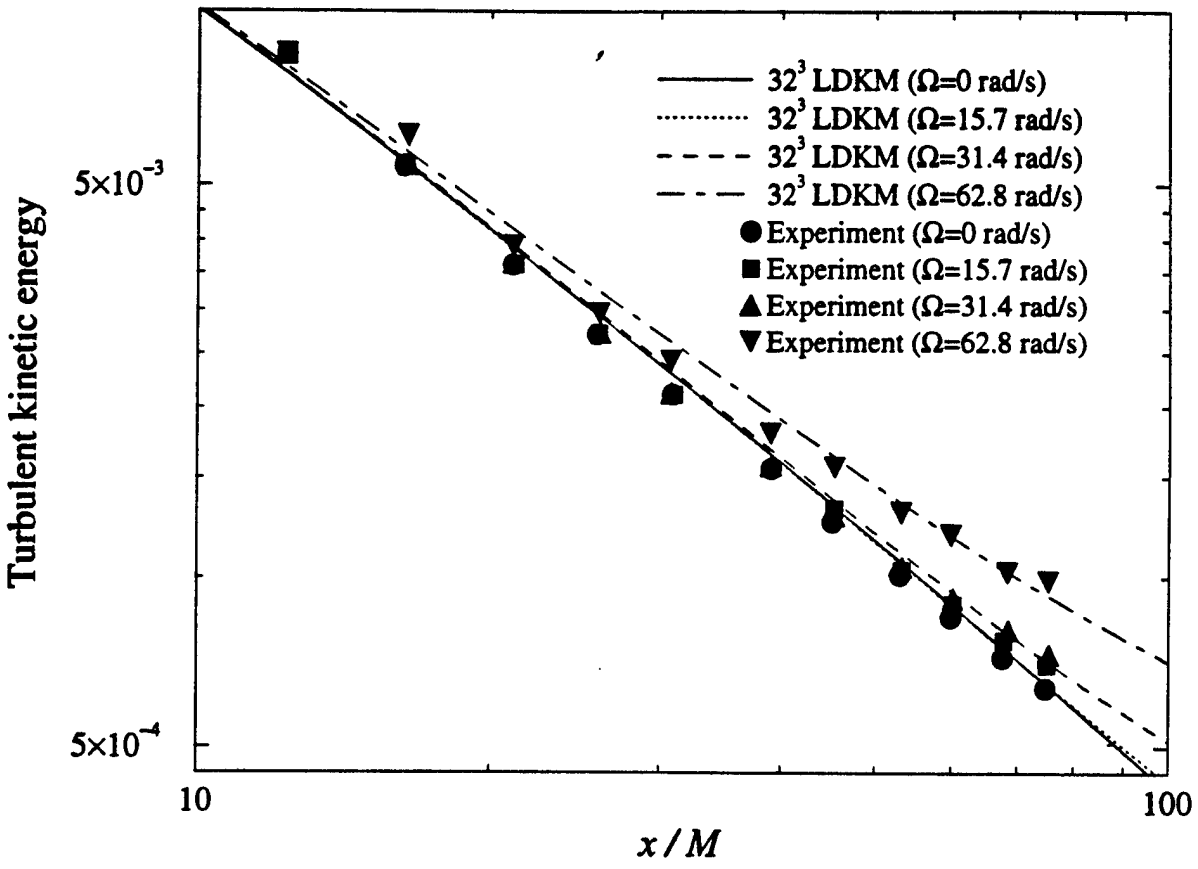

Turbulent kinetic energy
5×10⁻³
5×10⁻⁴
10
100
x / M
32³ LDKM (Ω=0 rad/s)
32³ LDKM (Ω=15.7 rad/s)
32³ LDKM (Ω=31.4 rad/s)
32³ LDKM (Ω=62.8 rad/s)
Experiment (Ω=0 rad/s)
Experiment (Ω=15.7 rad/s)
Experiment (Ω=31.4 rad/s)
Experiment (Ω=62.8 rad/s)

Figure 10

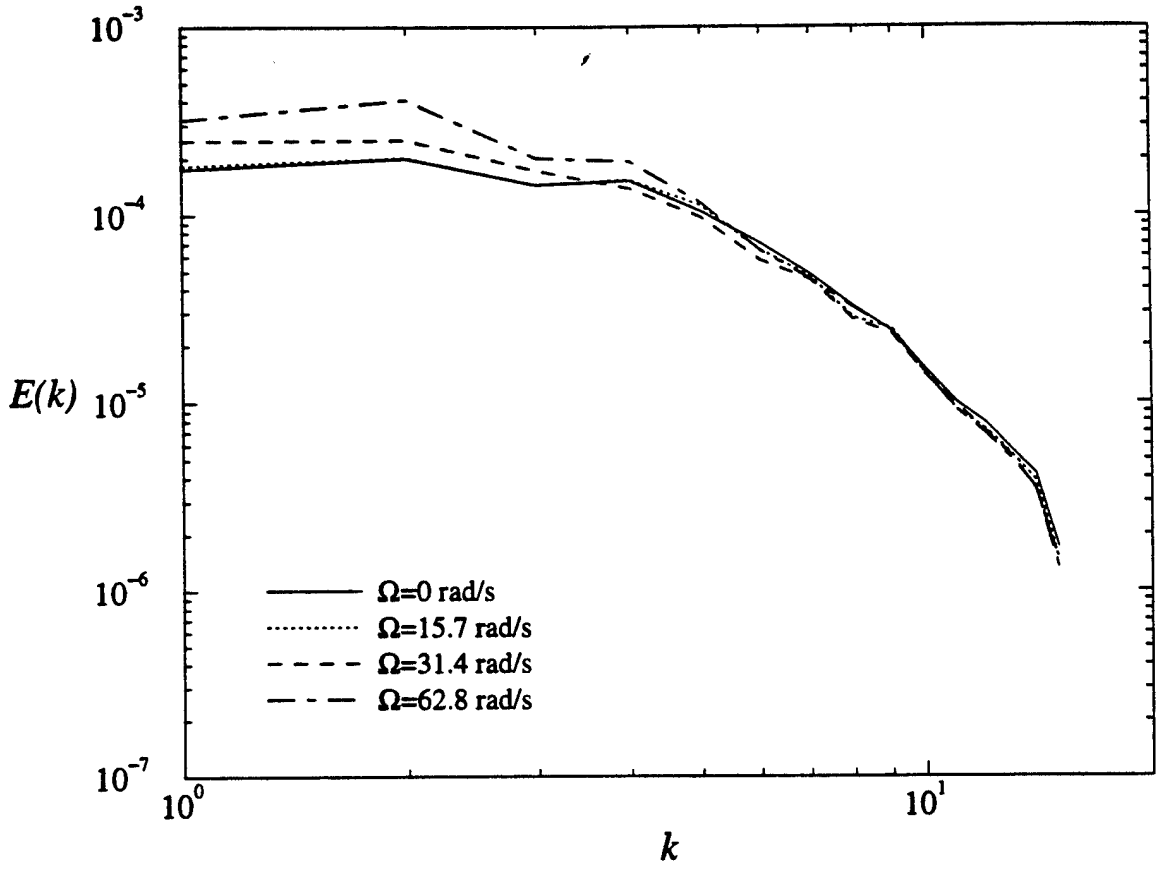

10^{-3}
10^{-4}
10^{-5}
10^{-6}
10^{-7}
$E(k)$
10^{0}
10^{1}
k
Ω=0 rad/s
Ω=15.7 rad/s
Ω=31.4 rad/s
Ω=62.8 rad/s

Figure 11

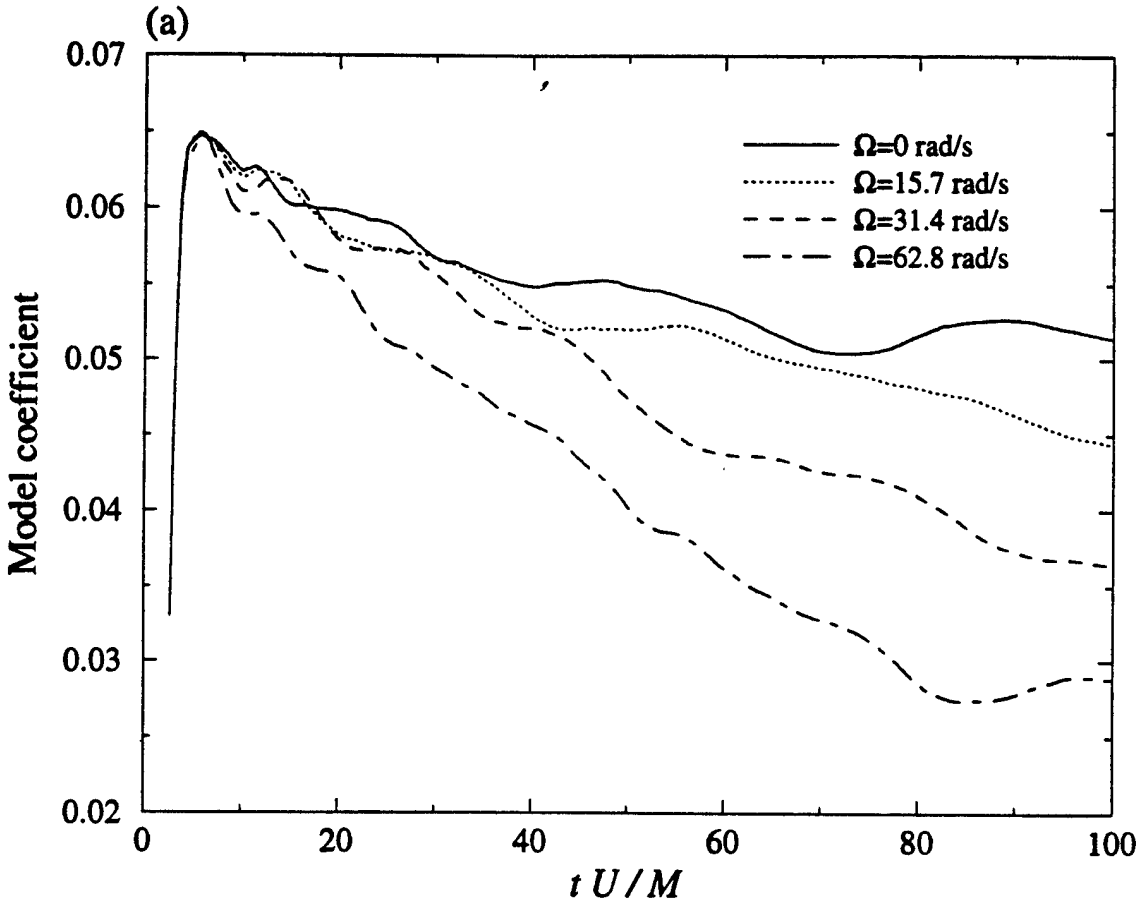

(a)
0.07
0.06
0.05
0.04
0.03
0.02
Model coefficient
0
20
40
60
80
100
t U / M
Ω=0 rad/s
Ω=15.7 rad/s
Ω=31.4 rad/s
Ω=62.8 rad/s

Figure 12(a)

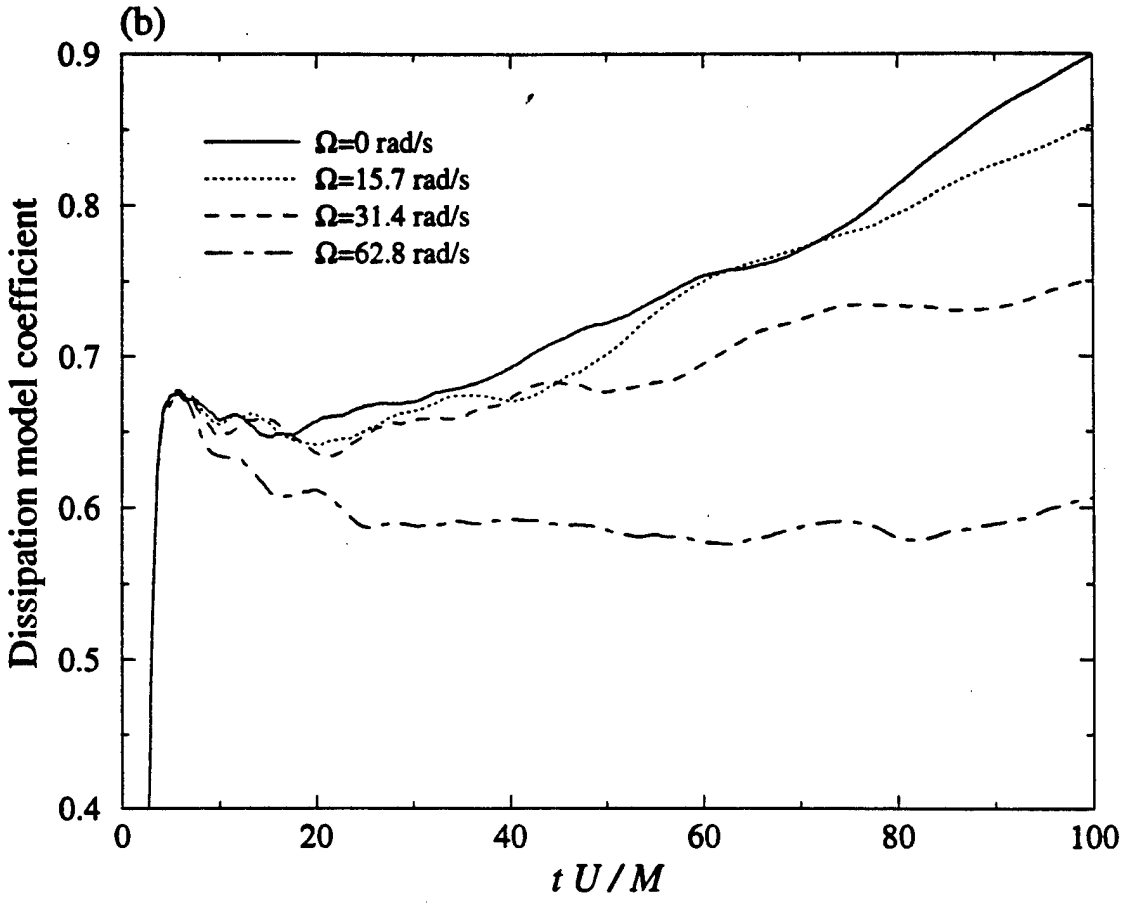

(b)
0.9
0.8
0.7
0.6
0.5
0.4
Dissipation model coefficient
Ω=0 rad/s
Ω=15.7 rad/s
Ω=31.4 rad/s
Ω=62.8 rad/s
0
20
40
60
80
100
t U / M

Figure 12(b)

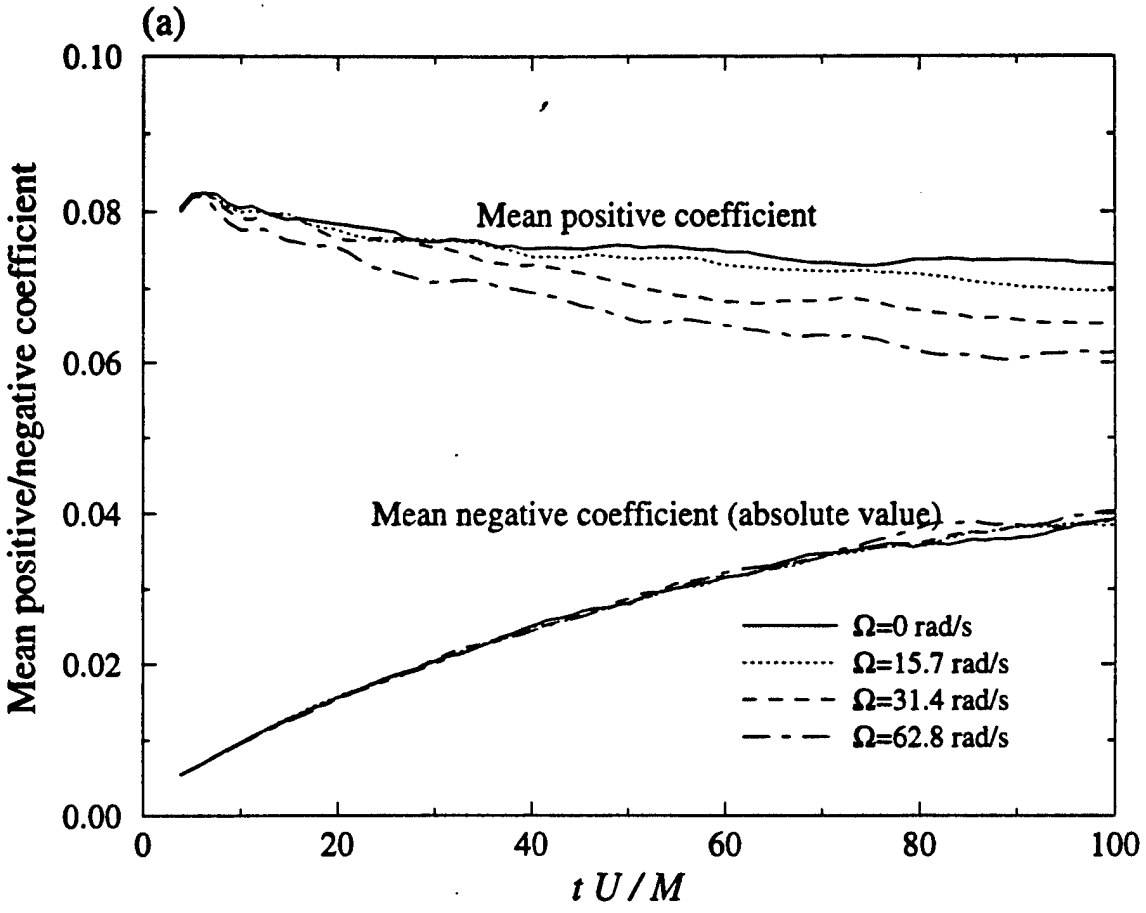

(a)
0.10
0.08
0.06
0.04
0.02
0.00
Mean positive/negative coefficient
Mean positive coefficient
Mean negative coefficient (absolute value)
Ω=0 rad/s
Ω=15.7 rad/s
Ω=31.4 rad/s
Ω=62.8 rad/s
0
20
40
60
80
100
t U / M

Figure 13(a)

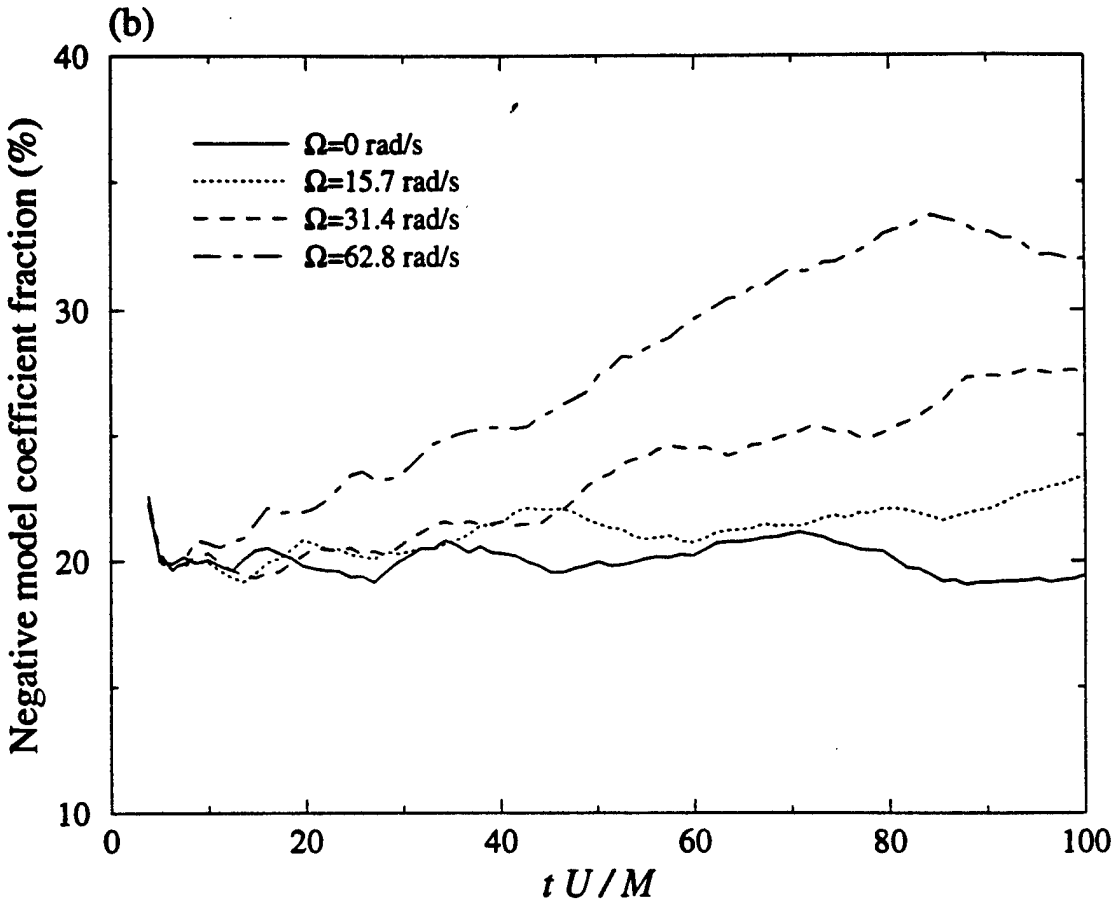

(b)
Ω=0 rad/s
Ω=15.7 rad/s
Ω=31.4 rad/s
Ω=62.8 rad/s
Negative model coefficient fraction (%)
40
30
20
10
0
20
40
60
80
100
t U / M

Figure 13(b)

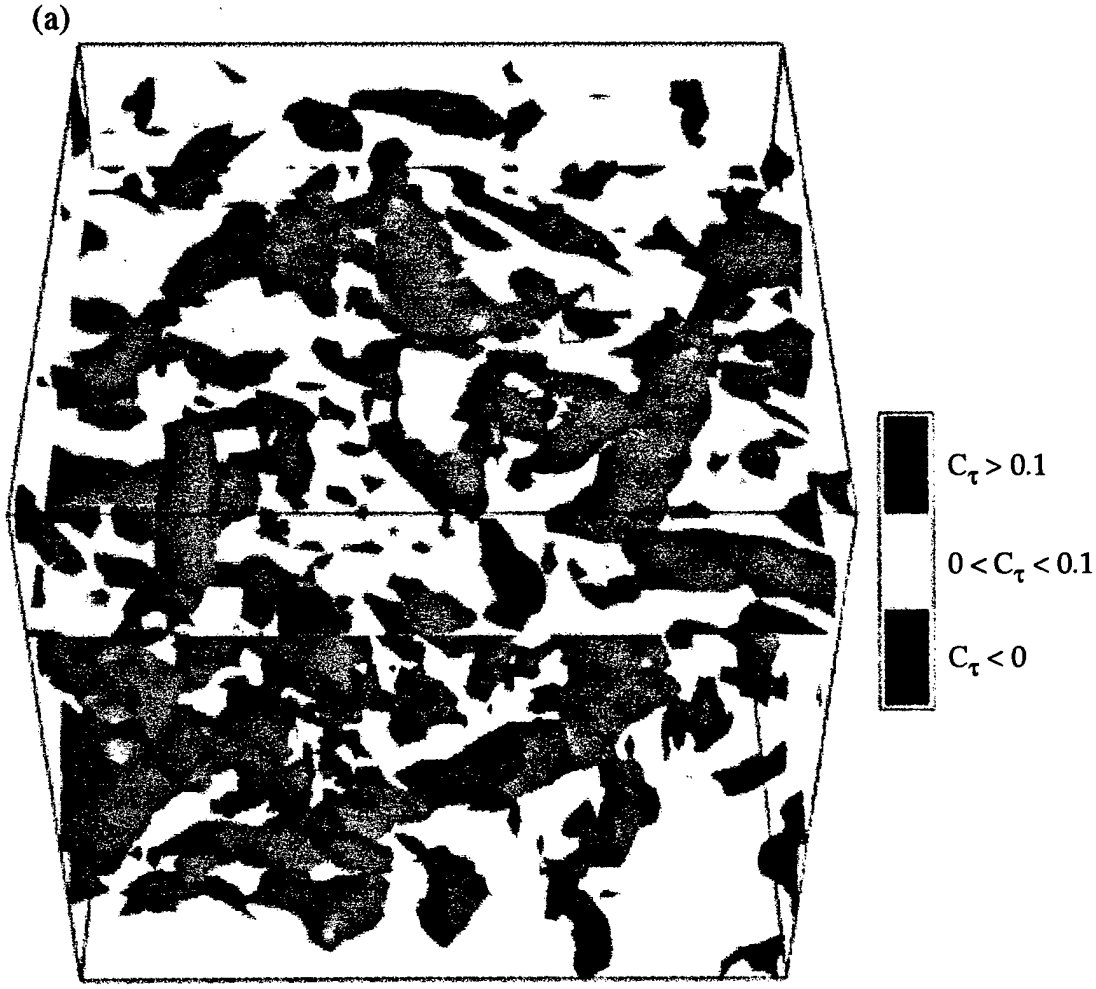


Figure 14(a)

(b)

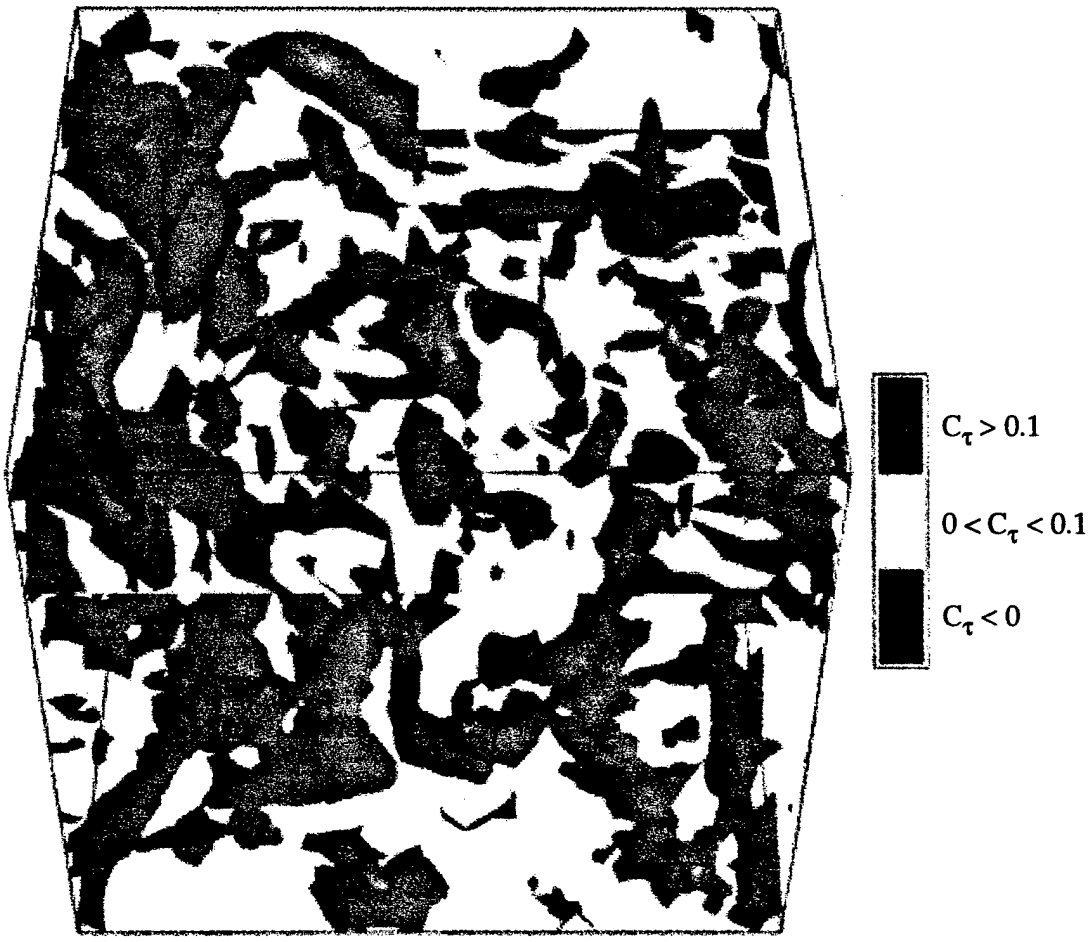


Figure 14 (b)

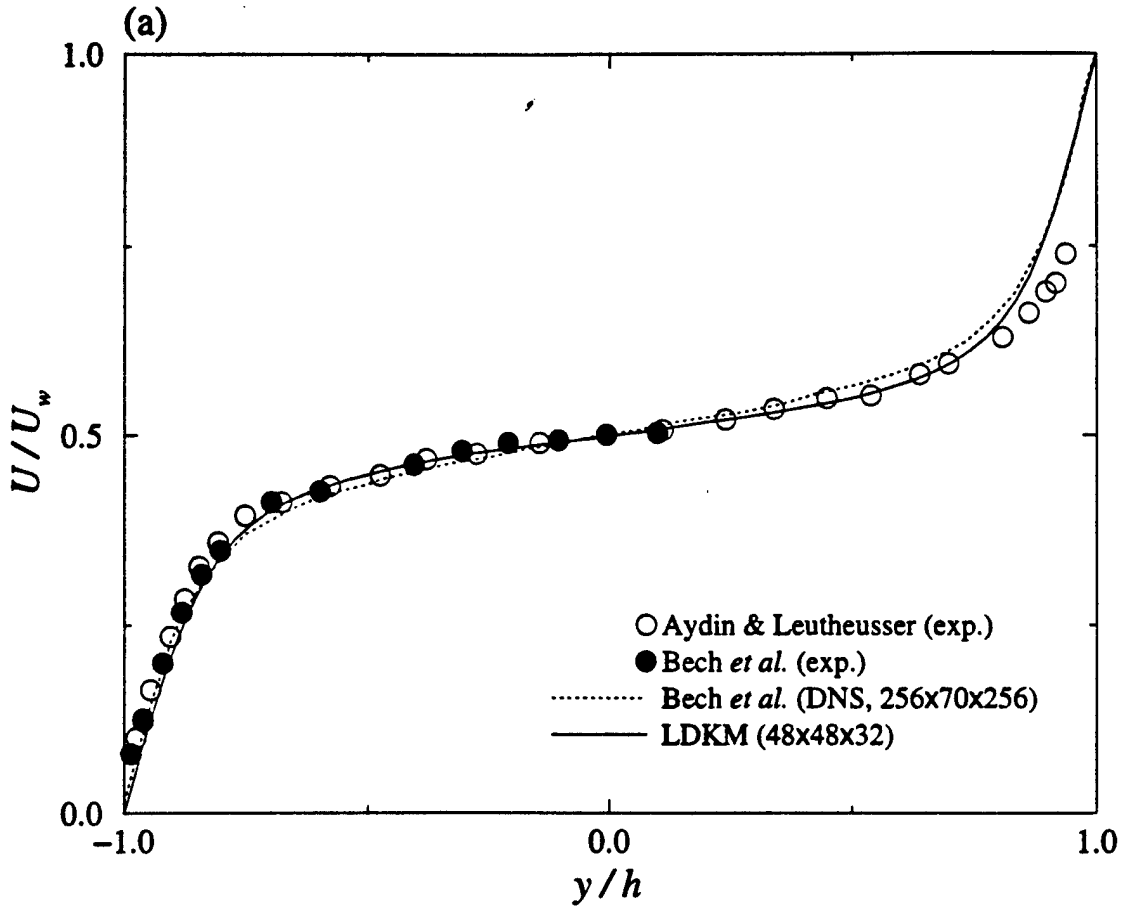

(a)
1.0
0.5
0.0
U/U*
−1.0
0.0
1.0
y/h
Aydin & Leutheusser (exp.)
Bech et al. (exp.)
Bech et al. (DNS, 256x70x256)
LDKM (48x48x32)

Figure 15(a)

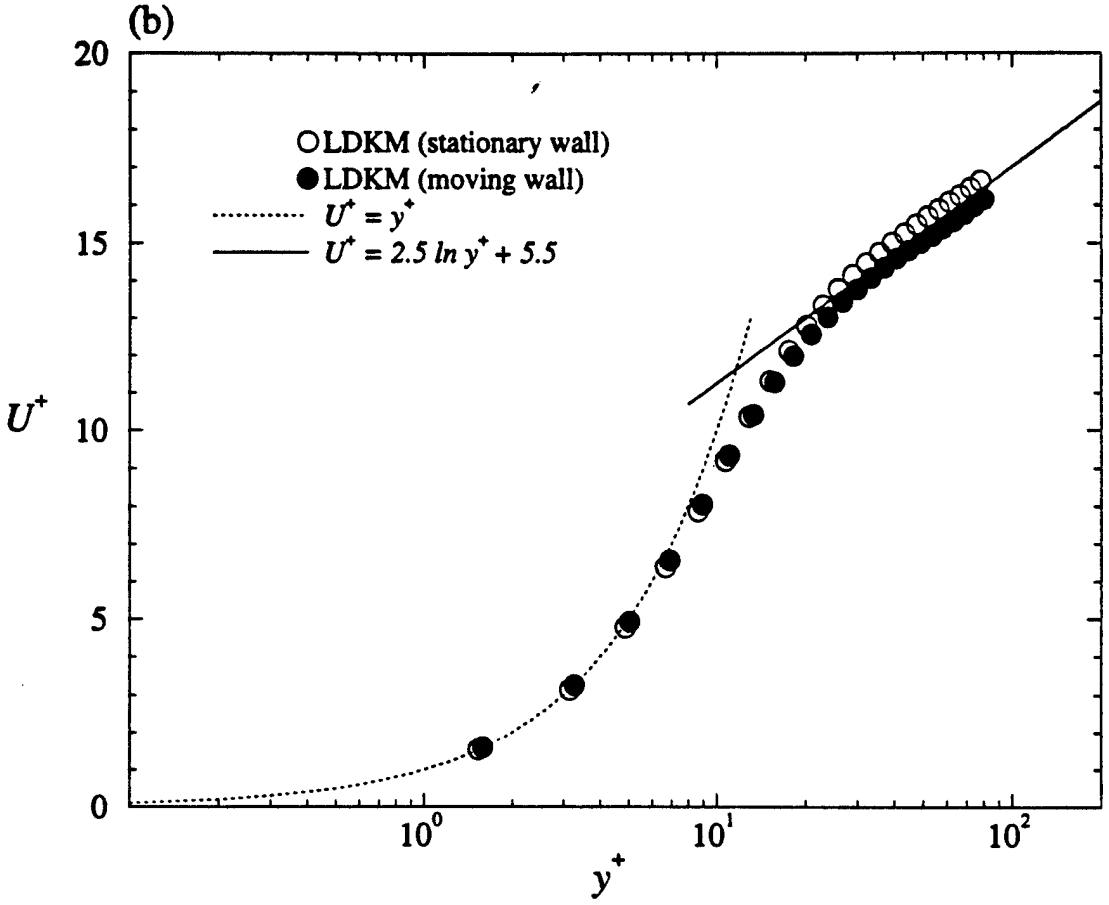

(b)
20
15
10
5
0
U^+
LDKM (stationary wall)
LDKM (moving wall)
$U^+ = y^+$
$U^+ = 2.5 \ln y^+ + 5.5$
10^0
10^1
10^2
y^+

Figure 15(b)

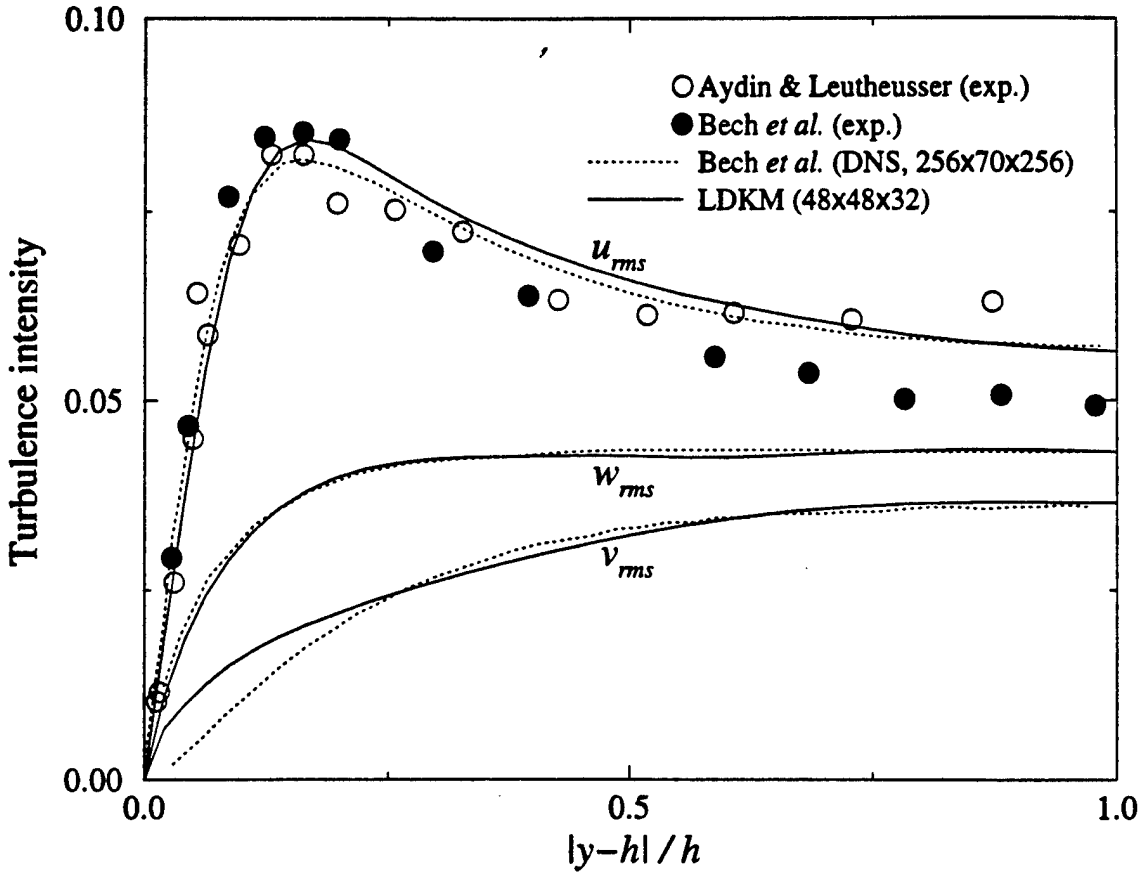

0.10
0.05
0.00
0.0
0.5
1.0
Turbulence intensity
|y−h| / h
Aydin & Leutheusser (exp.)
Bech et al. (exp.)
Bech et al. (DNS, 256x70x256)
LDKM (48x48x32)
u_{rms}
w_{rms}
v_{rms}

Figure 16

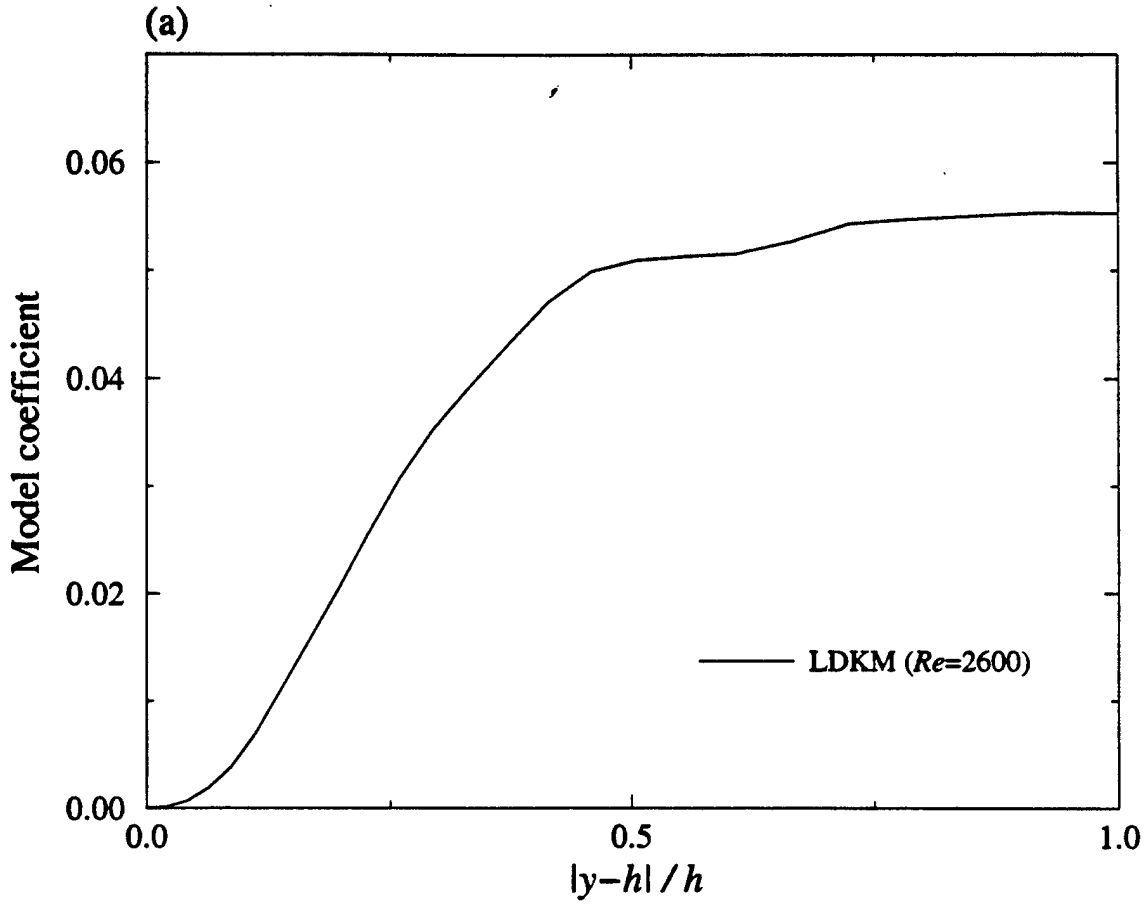


Figure 17(a)

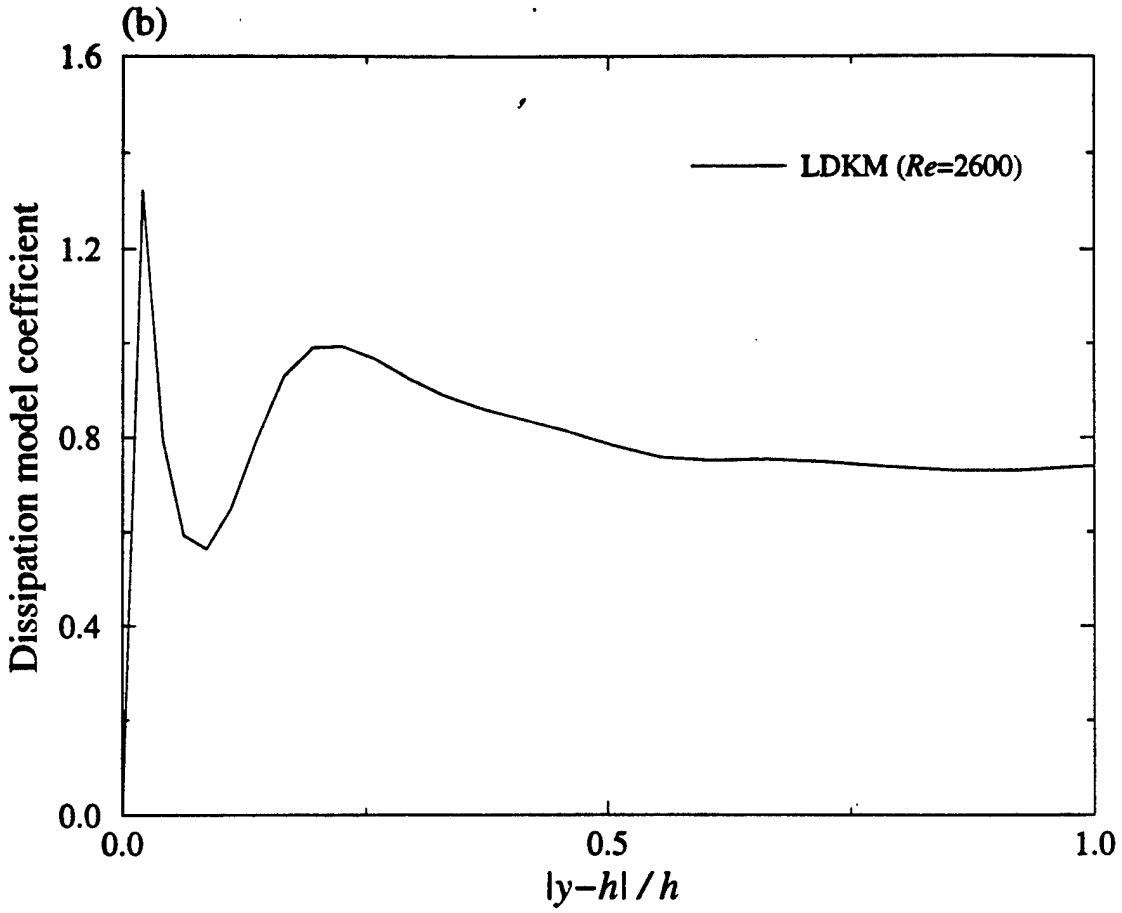

(b)
1.6
1.2
0.8
0.4
0.0
0.0
0.5
1.0
Dissipation model coefficient
|y−h| / h
LDKM (Re=2600)

Figure 17(b)

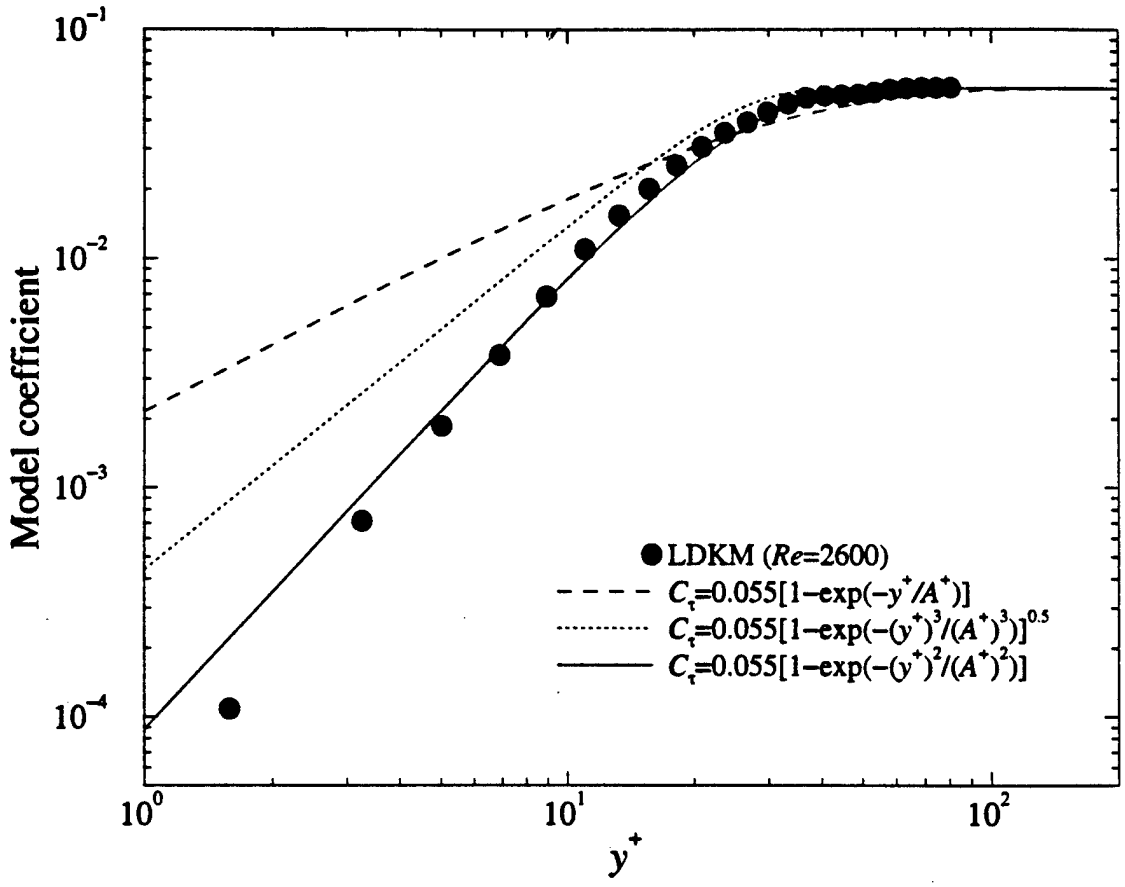

Model coefficient
10^{-1}
10^{-2}
10^{-3}
10^{-4}
10^{0}
10^{1}
10^{2}
y^+
LDKM (Re=2600)
C_τ=0.055[1−exp(−y^+/A^+)]
C_τ=0.055[1−exp(−$(y^+)^3/(A^+)^3$)]$^{0.5}$
C_τ=0.055[1−exp(−$(y^+)^2/(A^+)^2$)]

Figure 18

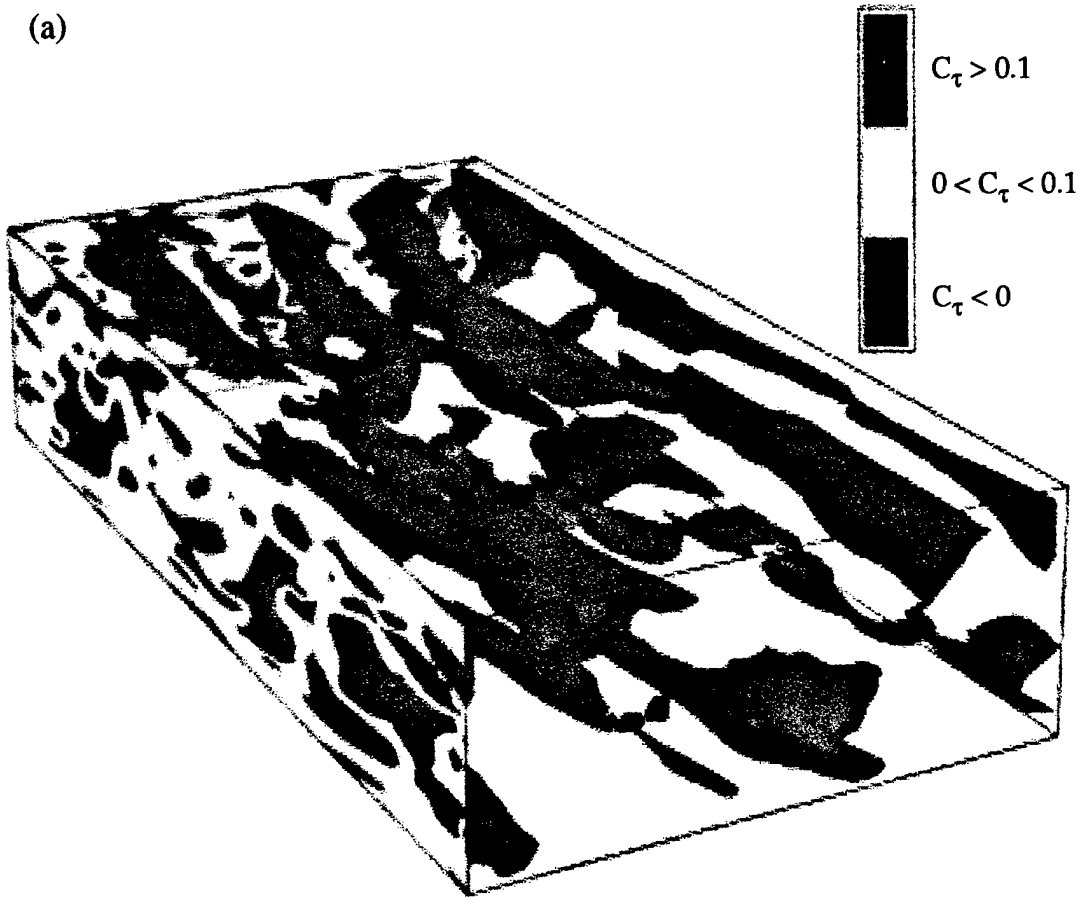


Figure 19(a)

(b)

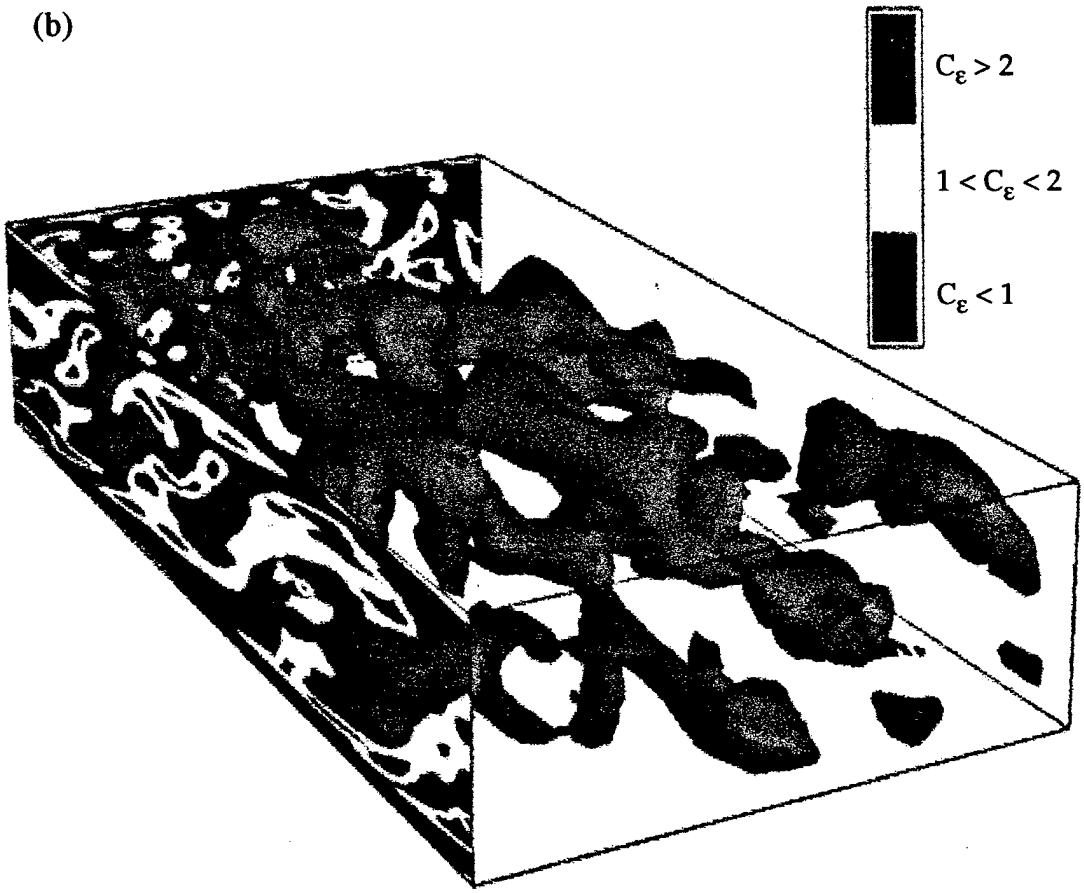


Figure 19(b)

Simulations of Spatially Evolving Compressible Turbulence Using a Local Dynamic Subgrid Model

A Thesis

Presented to

The Academic Faculty

by

Christopher C. Nelson

in Partial Fulfillment

of the Requirements for the Degree

Doctor of Philosophy in Aerospace Engineering

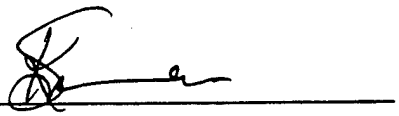
Georgia Institute of Technology

December 1997

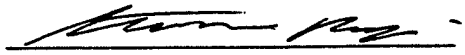
Copyright © 1997 by Christopher C. Nelson

Simulations of Spatially Evolving Compressible Turbulence Using a Local Dynamic Subgrid Model

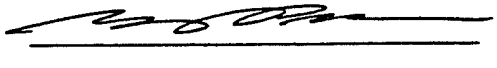
Approved:



Suresh Menon, Chairman



Stephen M. Ruffin



Pui-Kuen Yeung

Date Approved 9/5/97

Dedication

This is for Connie.

ACKNOWLEDGEMENTS

This dissertation is a work that has been many years in the making, and it would not have been possible at all without the help and encouragement of a great many people.

First on the list is Dr. Suresh Menon, who took me on when I was an "orphaned" graduate student and stuck with me through the years of "this code doesn't work" and "I found another bug." Thanks for not giving up on me, and also for not lowering the standards. In addition, I would like to thank Dr. Stephen Ruffin and Dr. Pui-Kuen Yeung for being on my Thesis Advisory Committee and to Dr. Lakshmi Sankar and Dr. Fotis Sotiropoulos for being on the Reading Committee. Thanks are also due to Dr. Robert Roach, who introduced to me the idea of numerical methods in fluid mechanics as a career option. He's also the one who convinced me that a Ph.D. was not only a good thing, but that it was something that even I could do.

The financial support of the Fluid Dynamics Division of the Office of Naval Research is gratefully acknowledged. The Air Force Office of Scientific Research also provided funding under the Focused Research Initiative, for which I am very grateful. This work would have taken several years longer than it has without the generous provision of computer time by the following Department of Defense Major Shared Resource Centers: the Aeronautical Systems Center at Wright-Patterson Air Force Base, the Army Research Laboratory at Aberdeen, Maryland, the Naval

Oceanographic Office at Stennis Space Center, and the Army Corps of Engineers Waterways Experiment Station at Vicksburg, Mississippi.

I also want to say a heartfelt "Thank you!" to all the guys in the lab (past and present). Those hours spent mulling with me over why my codes were not giving the answers I expected planted the seeds of many an insight. And even when there was no tangible result, just having someone there to listen to my ranting was a huge help. Special thanks go to Bill Calhoon: you will never know how timely some of your phone calls and e-mails were.

Another source of support and encouragement that I want to acknowledge is my family. It's been a long haul, but they have always stood with me. Thanks for all your prayers. My wife has shown superhuman patience in putting up with years of "surely I'll graduate next year." Her belief in my abilities and unfailing support has been instrumental in keeping me going on more than one occasion. Not only that, but her ability to produce culinary wonders on a GRA's income is the envy of the lab.

Finally, I want to acknowledge my Creator in bringing all these people and resources together at the right time and the right place so that this Ph.D. could become a reality.

> *Unless the Lord builds the house, those who build it labor in vain. Unless the Lord watches over the city, the watchman stays awake in vain.*

TABLE OF CONTENTS

DEDICATION iii

ACKNOWLEDGEMENTS iv

CONTENTS vii

LIST OF TABLES viii

LIST OF FIGURES xix

NOMENCLATURE xx

SUMMARY xxiv

CHAPTER

I INTRODUCTION 1
- 1.1 Effect of Compressibility on Turbulence 2
- 1.2 Numerical Simulation of Turbulence 6
- 1.3 Objectives of the Current Study 10
- 1.4 Outline of the Study 11

II FORMULATION OF THE PROBLEM 13
- 2.1 The Navier-Stokes Equations 13
- 2.2 The LES Equations 17

III CLOSURE OF THE SUBGRID TERMS 24
- 3.1 The LES State Equation 26
- 3.2 Closure of the LES Continuity Equation 30
- 3.3 Closure of the LES Momentum Equation 34
- 3.4 The k-Equation Model 41
- 3.5 Closure of the LES Energy Equation 53

IV NUMERICAL SCHEME 59
- 4.1 Derivation of the New 2-4 Method 62
- 4.2 Implementation of the New 2-4 Scheme in a Three Dimensional Compressible LES Code 71

V Near-Incompressible Regime Simulations 75
5.1 Lamb Vortex 75
5.2 Decaying Isotropic Turbulence 76

VI Simulations of Compressible Isotropic Turbulence 101
6.1 Decaying Isotropic Turbulence 101
6.2 Forced Isotropic Turbulence 123

VII Simulations of Spatially Developing Mixing Layers . . . 138
7.1 Simulation Specifications 141
7.2 Inflow and Exit Boundary Effects 145
7.3 Resolution Dependance 150
7.4 Sampling Time Effects 155
7.5 Model Effects 159
7.6 Simulation Results 175

VIII Conclusions and Recommendations 205

Appendix A The Filtering Operation and Large Eddy Simulation 209

Appendix B Formulation of the Problem using Favre Filtering 216
B.1 Derivation of the LES Equations 216
B.2 Closure of the Subgrid Terms 220

Appendix C Inflow Turbulence 239

Appendix D Alternate Subgrid Stress Tensor Model Coefficient 251

References 255

Vita 268

List of Tables

6.1 Test cases for the investigation into the effect of initial Mach and Reynolds number on model behavior 113

7.1 Flow parameters for spatial mixing layer cases 143

7.2 Boundary Effects Cases 145

7.3 Grids Employed for Resolution Tests 150

List of Figures

3.1 Contours of the state equation subgrid term $(R\left(\overline{\rho T} - \bar{\rho}\bar{T}\right))$ computed from a direct simulation of decaying compressible isotropic turbulence 26

3.2 Normalized density contours in a direct simulation of decaying compressible isotropic turbulence 27

3.3 Mach number contours in a direct simulation of decaying compressible isotropic turbulence 28

3.4 Probability density function of the state equation subgrid term relative to the local value of the exact pressure 29

3.5 History of pressure fluctuations in decaying compressible isotropic turbulence 29

3.6 Contours of the x-direction continuity equation subgrid term (c_x^{sgs}) normalized by reference momentum $(\rho_{ref} u_{ref})$ 31

3.7 Probability density function of the x-component of the continuity equation subgrid term relative to the reference momentum. 32

3.8 Contours of $\tau_{xx}^{sgs^{(c)}}$ as estimated from a DNS of compressible decaying isotropic turbulence- data normalized by reference quantities $(\rho_{ref} u_{ref}^2)$ 37

3.9 Contours of $\tau_{xx}^{sgs^{(i)}}$ as estimated from a DNS of compressible decaying isotropic turbulence- data normalized by reference quantities $(\rho_{ref} u_{ref}^2)$ 38

3.10 Probability density function of the "compressible" subgrid stress tensor $(\tau_{xx}^{sgs^{(c)}})$ term relative to reference quantities 39

3.11 Probability density function of the "incompressible" subgrid stress tensor $(\tau_{xx}^{sgs^{(i)}})$ term relative to reference quantities 40

3.12 Contours of $E_x^{sgs^{(c)}}$ normalized by reference quantities $(\rho_{ref} H_{ref} u_{ref})$ as estimated from a DNS of compressible decaying isotropic turbulence 56

4.1 Resolved kinetic energy predicted by various numerical schemes run without subgrid models compared with the experimental results of Comte-Bellot and Corrsin 61

4.2 Schematic of curvilinear grid spacing definitions 70

4.3 Comparison of Linear Stability Limits of the New 2-4 Scheme with the Gottlieb-Turkel Algorithm 71

5.1 Decay of enstrophy in 2-D isotropic turbulence 78

5.2 History of the enstrophy dissipation rate in 2-D isotropic turbulence 78

5.3 Behavior of the integral-scale Reynolds number in 2-D isotropic turbulence 79

5.4 Decay of resolved turbulent kinetic energy in isotropic turbulence simulated using a Favre filter formulation compared with experimental results of Comte-Bellot and Corrsin 81

5.5 Decay of resolved turbulent kinetic energy in isotropic turbulence compared with experimental results of Comte-Bellot and Corrsin . 82

5.6 Energy spectra of decaying isotropic turbulence with and without subgrid model 83

5.7 Comparison of energy spectra from LES with experimental data of Comte-Bellot and Corrsin 84

5.8 Comparison of the energy spectrum at the final station in the Comte-Bellot and Corssin experiment with simulated energy spectra . . . 86

5.9 Comparison of resolved kinetic energy in Comte-Bellot and Corrsin experiment with LES using different forms for c_ϵ 87

5.10 Comparison of subgrid kinetic energy predictions from simulations with differing c_ϵ with experimental results 87

5.11 Evolution of the average Mach number in near incompressible decaying isotropic turbulence 88

5.12 Normalized RMS of turbulent density fluctuations in near-incompressible decaying isotropic turbulence 89

5.13 Resolved kinetic energy in near-incompressible decaying isotropic turbulence 89

5.14 $\frac{\partial v}{\partial y}$ flatness history in near-incompressible decaying isotropic turbulence 90

5.15 $\frac{\partial v}{\partial y}$ skewness history in near-incompressible decaying isotropic turbulence 90

5.16 Mean value of c_ν in near-incompressible decaying isotropic turbulence 92

5.17 Mean value of positive c_ν in near-incompressible decaying isotropic turbulence 92

5.18 Mean value of negative c_ν in near-incompressible decaying isotropic turbulence 93

5.19 Time trace of the fraction of points in the domain with negative values of c_ν in near-incompressible decaying isotropic turbulence . . 93

5.20 Mean value of c_ε in near-incompressible decaying isotropic turbulence 94

5.21 Mean value of c_e in near-incompressible decaying isotropic turbulence 95

5.22 Evolution of modelled subgrid kinetic energy equation production and dissipation terms in near-incompressible, decaying isotropic turbulence 96

5.23 The evolution of the mean of c_e as computed using different methods in near-incompressible decaying isotropic turbulence 98

5.24 The effect of different forms of c_ε on the resolved kinetic energy in near-incompressible, decaying isotropic turbulence 99

5.25 The effect of different forms of c_ε on the subgrid kinetic energy in near-incompressible, decaying isotropic turbulence 99

5.26 The effect of different forms of c_ε on the modelled production and dissipation of k^{sgs} in near-incompressible, decaying isotropic turbulence 100

6.1 Mean Mach number in compressible decaying isotropic turbulence . 102

6.2 Normalized RMS of density fluctuations in compressible decaying isotropic turbulence 103

6.3 Evolution of resolved kinetic energy in compressible decaying isotropic turbulence 103

6.4 Evolution of $\frac{\partial v}{\partial y}$ flatness in compressible decaying isotropic turbulence 104

6.5 Evolution of $\frac{\partial v}{\partial y}$ skewness in compressible decaying isotropic turbulence 104

6.6 Evolution of mean c_ν in compressible decaying isotropic turbulence 106

6.7 Average of positive c_ν values in compressible decaying isotropic turbulence 106

6.8 Average of negative c_ν values in compressible decaying isotropic turbulence 107

6.9 Fraction of points with negative c_ν values in compressible decaying isotropic turbulence 107

6.10 Average value of the dissipation model coefficient in compressible decaying incompressible turbulence 108

6.11 Evolution of the mean of the energy equation subgrid model coefficient in compressible decaying isotropic flow 109

6.12 History of the modelled production and dissipation contributions to the subgrid kinetic energy equation for compressible decaying isotropic turbulence 110

6.13 The evolution of the mean of c_ε as computed by two different methods in compressible decaying isotropic turbulence 110

6.14 The effects of different algorithms for c_ε on the modelled production and dissipation of k^{sgs} in compressible, decaying isotropic turbulence 111

6.15 The effect of different methods to compute c_ε on the subgrid kinetic energy in compressible, decaying isotropic turbulence 111

6.16 The effect of different methods to compute c_ε on the mean Mach number in compressible, decaying isotropic turbulence 112

6.17 Mach number history for cases with different initial Reynolds and Mach numbers in decaying compressible isotropic turbulence 114

6.18 Evolution of normalized density fluctuations for different initial Reynolds and Mach numbers in decaying compressible isotropic turbulence 115

6.19 Resolved kinetic energy traces for different initial Mach and Reynolds numbers in decaying compressible isotropic turbulence 116

6.20 Subgrid kinetic energy traces for different initial Mach and Reynolds numbers in decaying compressible isotropic turbulence 116

6.21 Evolution of the mean sugrid stress tensor model coefficient for different initial Mach and Reynolds numbers in decaying compressible isotropic turbulence 117

6.22 Evolution of the mean of positive c_ν for different initial Mach and Reynolds numbers in decaying compressible isotropic turbulence . . 117

6.23 Evolution of the mean of negative c_ν for different initial Mach and Reynolds numbers in decaying compressible isotropic turbulence . . 118

6.24 Fraction of points with negative c_ν for different initial Mach and Reynolds numbers in decaying compressible isotropic turbulence . . 118

6.25 Average value of the dissipation model coefficient for different initial Mach and Reynolds numbers in decaying compressible isotropic turbulence 119

6.26 Average value of the energy equation subgrid model coefficient for different initial Mach and Reynolds numbers in decaying compressible isotropic turbulence 120

6.27 Average value of the modelled subgrid kinetic energy production term for different initial Mach and Reynolds numbers in decaying compressible isotropic turbulence 121

6.28 Average value of the modelled subgrid kinetic energy dissipation for different initial Mach and Reynolds numbers in decaying compressible isotropic turbulence 122

6.29 Evolution of the mean resolved kinetic energy in forced isotropic turbulence 124

6.30 Evolution of the average subgrid kinetic energy in forced isotropic turbulence 125

6.31 Mean values of the modelled subgrid kinetic energy production and dissipation terms for Case 1 125

6.32 Mean values of the modelled subgrid kinetic energy production and dissipation terms for Case 2 126

6.33 The mean Mach number as a function of time in forced isotropic turbulence 128

6.34 Evolution of the normalized RMS of density fluctuations in forced isotropic turbulence 129

6.35 Evolution of the mean of the subgrid stress tensor model coefficient in forced isotropic turbulence 130

6.36 The fraction of points with a negative subgrid stress model coefficient as a function of time in forced isotropic turbulence. 131

6.37 Time evolution of the mean of the dissipation model coefficient in forced isotropic turbulence 132

6.38 Time trace of the average value of the energy equation subgrid model coefficient 133

6.39 The evolution of the mean of c_ϵ as computed by different methods in forced isotropic turbulence 134

6.40 Mean values of the modelled k^{sgs} production and dissipation terms for Case 1 recomputed using the alternate form for c_ϵ 135

6.41 Mean values of the modelled k^{sgs} production and dissipation terms for Case 2 recomputed using the alternate form for c_ϵ 135

6.42 The effect of different means of computing c_ϵ on the predicted subgrid kinetic energy in forced isotropic turbulence 136

6.43 The effect of different means of computing c_ϵ on the resolved kinetic energy in forced isotropic turbulence 136

6.44 The effect of different means of computing c_ϵ on the mean Mach number in forced isotropic turbulence 137

7.1 Schematic of the spatial mixing layer computational domain 144

7.2 Predicted growth of Case 2 mixing layer for different boundary treatments 147

7.3 Predicted normalized streamwise velocity profiles ($x = 210mm$) of Case 2 mixing layer for different boundary treatments 148

7.4 Predicted streamwise turbulent intensity ($x = 210mm$) of Case 2 mixing layer for different boundary treatments 148

7.5 Predicted velocity skewness profiles ($x = 210mm$) of Case 2 mixing layer for different boundary treatments 149

7.6 Predicted growth of Case 2 mixing layer for different grid resolutions 152

7.7 Predicted normalized streamwise mean velocity profiles ($x = 210mm$) of Case 2 mixing layer for different grid resolutions 152

7.8 Predicted streamwise turbulent intensity profiles ($x = 210mm$) of Case 2 mixing layer for different grid resolutions 153

7.9 Predicted velocity skewness profiles ($x = 210mm$) of Case 2 mixing layer for different grid resolutions 153

7.10 Predicted velocity flatness profiles ($x = 210mm$) of Case 2 mixing layer for different grid resolutions 154

7.11 Effect of sampling time on the predicted growth ($x = 210mm$) of the Case 2 mixing layer 156

7.12 Effect of sampling time on the predicted normalized streamwise velocity profiles ($x = 210mm$) in the Case 2 mixing layer 157

7.13 Effect of sampling time on the predicted streamwise turbulence intensity profiles ($x = 210mm$) in the Case 2 mixing layer 157

7.14 Effect of sampling time on the Reynolds stress profiles ($x = 210mm$) in the Case 2 mixing layer 158

7.15 Effect of sampling time on the predicted streamwise velocity skewness profiles ($x = 210mm$) in the Case 2 mixing layer 158

7.16 Effect of sampling time on the predicted streamwise velocity flatness profiles ($x = 210mm$) in the Case 2 mixing layer 159

7.17 Predicted growth of Case 2 mixing layer for different values of a_0 . 161

7.18 Predicted normalized streamwise mean velocity profiles ($x = 210mm$) of Case 2 mixing layer for different values of a_0 161

7.19 Predicted streamwise turbulence intensity profiles ($x = 210mm$) of Case 2 mixing layer for different values of a_0 162

7.20 Predicted velocity skewness profiles ($x = 210mm$) of Case 2 mixing layer for different values of a_0 162

7.21 Predicted growth of Case 1 mixing layer for different algorithms for computing c_ν 164

7.22 Predicted normalized streamwise mean velocity profiles ($x = 150mm$) of Case 1 mixing layer for different algorithms for computing c_ν . . 164

7.23 Predicted turbulent intensity profiles ($x = 150mm$) of Case 1 mixing layer for different algorithms for computing c_ν 165

7.24 Predicted velocity skewness profiles ($x = 150mm$) of Case 1 mixing layer for different algorithms for computing c_ν 165

7.25 Predicted velocity flatness profiles ($x = 150mm$) of Case 1 mixing layer for different algorithms for computing c_ν 166

7.26 Predicted growth of Case 1 mixing layer for different algorithms for computing c_ε 168

7.27 Predicted normalized streamwise mean velocity profiles ($x = 150mm$) of Case 1 mixing layer for different algorithms for computing c_ε . . 168

7.28 Predicted streamwise turbulent intensity profiles ($x = 150mm$) of Case 1 mixing layer for different algorithms for computing c_ϵ 169

7.29 Predicted velocity skewness profiles ($x = 150mm$) of Case 1 mixing layer for different algorithms for computing c_ϵ 169

7.30 Predicted velocity flatness profiles ($x = 150mm$) of Case 1 mixing layer for different algorithms for computing c_ϵ 170

7.31 Predicted growth of Case 1 mixing layer for constant coefficient model versus the dynamic model 172

7.32 Predicted normalized streamwise velocity profiles ($x = 150mm$) of Case 1 mixing layer for constant versus dynamic coefficients 173

7.33 Predicted streamwise turbulent intensity profiles ($x = 150mm$) of Case 1 mixing layer for constant versus dynamic coefficients 173

7.34 Predicted streamwise velocity skewness profiles ($x = 150mm$) of Case 1 mixing layer for constant versus dynamic coefficients 174

7.35 Predicted streamwise velocity flatness profiles ($x = 150mm$) of Case 1 mixing layer for constant versus dynamic coefficients 174

7.36 Concentrations of a passive scalar in x-y planes of spatially developing mixing layers 177

7.37 Contours of streamwise vorticity and passive scalar concentration in the Case 1 mixing layer ($x = 49mm$) 178

7.38 Contours of streamwise vorticity and passive scalar concentration in the Case 2 mixing layer ($x = 49mm$) 179

7.39 Streamwise vorticity contours in a fully developed flow field of the Case 1 spatial mixing layer 180

7.40 Contours of the spanwise component of vorticity in the fully developed fully developed Case 1 spatial mixing layer 181

7.41 Streamwise vorticity contours in a fully developed flow field of the Case 2 spatial mixing layer 182

7.42 Spanwise vorticity contours in a fully developed flow field of the Case 1 spatial mixing layer 183

7.43 Streamwise evolution of pressure fluctuation spectra in the Case 1 mixing layer 186

7.44 Streamwise evolution of pressure fluctuation spectra in the Case 2 mixing layer 187

7.45 Contours of k^{sgs} and vorticity magnitude in the Case 1 mixing layer 188

7.46 Contours of k^{sgs} and vorticity magnitude in the Case 2 mixing layer 188

7.47 Contours of c_ν in the Case 2 mixing layer 189

7.48 Regions of "backscatter" in the Case 2 mixing layer 189

7.49 Contours of the k^{sgs} dissipation model coefficient for the Case 2 mixing layer 190

7.50 Comparison of simulated and experimental momentum thickness growth in spatial mixing layers (Grid 2) 191

7.51 Momentum thickness growth rates in spatial mixing layers 192

7.52 Comparison of simulated and experimental shear layer thickness growth in spatial mixing layers (Grid 2) 193

7.53 Comparison of simulated and experimental vorticity thickness growth in spatial mixing layers (Grid 2) 193

7.54 Normalized mean velocity profiles in the Case 1 spatial mixing layer 194

7.55 Streamwise turbulence intensity profiles in the Case 1 spatial mixing layer 195

7.56 Lateral turbulence intensity profiles in the Case 1 spatial mixing layer 196

7.57 Reynolds stress profiles in the Case 1 spatial mixing layer 196

7.58 Streamwise velocity skewness profiles in the Case 1 spatial mixing layer 197

7.59 Streamwise velocity flatness profiles in the Case 1 spatial mixing layer 198

7.60 Normalized mean velocity profiles in the Case 2 spatial mixing layer 199

7.61 Streamwise turbulent intensity profiles in the Case 2 spatial mixing layer 200

7.62 Lateral turbulent intensity profiles in the Case 2 spatial mixing layer 201

7.63 Reynolds stress profiles in the Case 2 spatial mixing layer 201

7.64 Streamwise velocity skewness profiles in the Case 2 spatial mixing layer 202

7.65 Streamwise velocity flatness profiles in the Case 2 spatial mixing layer 203

7.66 Maximum turbulence intensities and Reynolds stress versus convective Mach number 204

C.1 Conceptualization of the inflow turbulence approximation technique 241

NOMENCLATURE

Roman Symbols

a_0 "Compressibility" viscosity scaling factor

a_c "Compressibility" viscosity scaling function

c_e Energy equation subgrid model coefficient

c_i^{sgs} Continuity equation subgrid term

c_p Specific heat at constant pressure

c_v Specific heat at constant volume

c_ϵ Subgrid kinetic energy dissipation model coefficient

c_ν Subgrid stress tensor model coefficient

e Internal energy

E Total energy

$E_i^{sgs^{(i)}}$ "Incompressible" portion of the energy equation subgrid term

$E_i^{sgs^{(c)}}$ "Compressible" portion of the energy equation subgrid term

G Filter function

H Total enthalpy

k Kinetic energy (section 3.4.1)

k Wavenumber

$\bar{k}$ Filtered kinetic energy

$\overline{k^*}$ Resolved LES kinetic energy

k^{sgs} Subgrid kinetic energy

K_1 Curve fit coefficient on "compressibility" viscosity scaling function

M_1 High speed side Mach number (spatial mixing layer)

M_2 Low speed side Mach number (spatial mixing layer)

M_c Convective Mach number

n_k Cell face unit normal vector

p Static pressure

Pr Prandtl number

R Gas constant

R_e Reynolds number

R_{e_Δ} Cell Reynolds number

R_{e_λ} Reynolds number based on Taylor microscale

R_{e_ℓ} Reynolds number based on integral length scale

$R_{e_{\min}}$ Minimum cell Reynolds number (for "compressibility" viscosity)

R_{uv} Reynolds stress tensor ("uv" component)

S_{ij} Resolved rate of strain tensor

S_p Pressure switch (for "compressibility" viscosity)

t Time

$\bar{t}_{ij}$ Resolved viscous stress tensor

T Absolute temperature

$\hat{T}_{ij}$ Viscous stress tensor computed using test-filtered quantities

u Streamwise component of velocity

u_i Velocity vector

u_θ Tangential velocity

U^* Normalized mean velocity

U_1 High speed side velocity (spatial mixing layer)

U_2 Low speed side velocity (spatial mixing layer)

U_c Convective velocity

v Vertical component of velocity

w Lateral component of velocity

x Streamwise physical space coordinate

x_i Spatial coordinate vector

y Vertical physical space coordinate

z Lateral physical space coordinate

Greek Symbols

δ_{ij} Kronecker delta function

δ_ω Vorticity thickness

Δ Local characteristic grid spacing

$\hat{\Delta}$ Characteristic length of test filter

ϵ Dissipation of subgrid kinetic energy

γ Ratio of specific heats

κ Thermal conductivity

μ Molecular viscosity

μ_t Eddy (a.k.a. turbulent) viscosity

ν Kinematic viscosity

ν_c "Compressibility" viscosity

ν_{eff} Effective viscosity

ν_t Eddy (a.k.a. turbulent) "kinematic" viscosity

ν_{uc} "Unresolvable curvature" viscosity

ρ Density

σ_u, σ_v Turbulent intensity (u component and v component)

τ Characteristic time

τ_{ij} Viscous stress tensor

τ_{ij}^{sgs} Subgrid stress tensor

$\tau_{ij}^{(c)}$ "Compressible" part of the subgrid stress tensor

$\tau_{ij}^{(i)}$ "Incompressible" part of the subgrid stress tensor

θ Momentum thickness

Summary

The objective of this work is to enable the "time-accurate" simulation of turbulent flows in realistic geometries at previously unattainable Reynolds numbers. The cases chosen for this work are spatially evolving turbulent mixing layers. The large eddy simulation (LES) approach was chosen as the theoretical framework for this work. There are two essential components for successful unsteady simulations of high Reynolds number turbulent flows. First, it is necessary to have a numerical scheme which is not overly dissipative; otherwise the physics of the flow are overwhelmed by numerical effects. Secondly, an accurate subgrid model is required to remove turbulent energy from the resolved scales in a manner which approaches that of the actual cascade of turbulent energy.

To address the first requirement, a MacCormack-type scheme has been developed which has low intrinsic dissipation. This scheme is very similar to the Gottlieb-Turkel 2-4 algorithm, but is truly fourth order in space (on a uniform grid). The numerical dissipation of this scheme has been found to be sufficiently low to allow the study of the high Reynolds number phenomena of interest here.

The second factor has been addressed by the development of a new dynamic model for large eddy simulations (LES) of compressible turbulent flows. It allows the model coefficients to be calculated in a completely localized fashion. In the near-incompressible limit, this model gradually approaches the form of an incompressible model. Thus, it is potentially applicable across the full range of compressibility.

The properties of the model have been examined by LES of various turbulent flows, such as decaying and forced isotropic turbulence for a range of Mach numbers and Reynolds numbers. As expected, near the incompressible limit, the model behaves much like a similar incompressible model, and in the compressible regime, the model gives reasonable results over a considerable range of Mach and Reynolds numbers. For fully developed turbulent flows, the modelled subgrid stress tensor has been found to satisfy all of the realizability conditions over the vast majority of the domain.

Finally, the model has been applied to the problem of interest: LES of very high Reynolds number spatial mixing layers. Even with relatively coarse non-uniform grids, the results are in reasonable agreement with experimental data. Appropriate growth rates are observed for the mean quantities, and the turbulent intensities and Reynolds stresses are also consistent with experimental data. The results show that as the mixing layer develops downstream of the splitter plate, self-similarity in the mean flow is achieved relatively quickly, while, for the turbulent moments, this is delayed until further downstream.

In conclusion, the applicability of LES to the simulation of spatially developing compressible flows at high Reynolds number has been demonstrated. Depending on what quantities are being measured, reasonable data can be obtained even on very coarse grids. A dynamic model, such as the one used in this work, enhances the ability of the scheme to capture higher moments of turbulence.

CHAPTER I

INTRODUCTION

Turbulence is a phenomenon which occurs in almost all fluid flows, often changing their character radically. It is characterized by regions of seemingly random fluctuations in flow quantities (though it is assumed that they are deterministic and governed by the Navier-Stokes equations). Despite its prevalence and over a century of research into its nature, this phenomenon is still not fully understood. In large part, this is due to the nonlinearity of the equations, the chaotic nature of the phenomenon, and the fact that it occurs over such a large range of temporal and spatial scales. An example of this latter point is the wake of an airplane, which is likely to have scales of motion which range in size from that of the airplane itself to near-microscopic lengths. As the current work deals primarily with compressible turbulence, the features of incompressible flow will be discussed only by way of contrast with compressible findings. For details on the theory of incompressible turbulence, the interested reader may refer to any of the numerous books that have been written on the subject (*e.g.*, [1] [2] [3]). Some of the important findings on the effects of compressibility on turbulence are now briefly summarized. For more details, see the review by Lele [4] and the references therein.

1.1 Effect of Compressibility on Turbulence

Birch and Eggars [5] noted that compressible mixing layers grow slower than would be expected from incompressible theory. They believed that the mean density gradient was the cause. The experiments by Brown and Roshko [6] for low velocity mixing layers with variable density and Papamoschou and Roshko [7] for compressible mixing layers, coupled with the theory of Bogdanoff [8] showed that the primary cause of the reduced growth rate was actually linked to compressibility. Papamoschou and Roshko introduced the convective Mach number as a parameter for collapsing normalized growth rate data. This variable has been moderately successful in parameterizing normalized growth rates as found in experiments. Nevertheless, significant scatter remains. It has been hypothesized that this could be due to several factors: the sensitivity of the mixing layer to background disturbances, variable realizations of self-preserving flow, wind tunnel variability, and uncertainty in the normalizing incompressible growth rate. In addition, it may be that more than one parameter is necessary [4].

Not only mixing layers, but almost all flows show a decrease in the growth of turbulent kinetic energy due to compressibility. Several ideas have been presented to account for this. Papamoschou [9] speculated that this was due to eddy shocklets: regions of strong compression caused by the turbulent motion which would increase energy dissipation. This has been associated with the dilatation dissipation term in the Reynolds averaged turbulent kinetic energy equation. A similar term exists in the LES subgrid kinetic energy equation. Zeman [10] and Sarkar *et al.* [11] used this idea and developed models for the dilatation dissipation term which were added to standard k-ε models. These models were able to predict a reduction in

mixing layer growth rate with increased compressibility. Brankovic and Zeman [12] used a similar model for compression corner simulations. Wilcox [13] combined the two models to develop an improved version. These corrections, however, are not universally applicable [14]. Very little work, however, has been conducted for the equivalent LES terms. Spyropoulos and Blaisdell [15] claimed that such work is not needed, since the dynamic models already seem to adjust for compressibility effects. Their work, however, did not investigate strongly compressible flows, so the limitations of the dynamic model, if any, were not thoroughly tested.

The importance of eddy shocklets was called into question by Sandham and Reynolds [16] who were unable to find any such structures in 3-D DNS of temporal mixing layers. They suggested, rather, that linear stability theory accounted for most of the observed decrease in mixing layer growth rates [17]. Furthermore, linear theory correctly predicted the increasing three dimensionality of mixing layers as convective Mach number increases. This was found to be due to oblique (three-dimensional) instability modes becoming dominant at high compressibility, whereas two dimensional modes dominate at lower convective Mach numbers. Shocklets being unsteady, intermittent, and nonlinear phenomena, the ability of linear stability theory to predict this trend in mixing layers may be taken as further evidence that eddy shocklets are not of critical importance in determining the reduction of growth in mixing layers.

Experimental evidence for eddy shocklets has been, up to this point, completely lacking for co-flowing shear layers. Vreman *et al.* [18] have reported eddy shocklets in simulations of confined mixing layers with high convective Mach number. While dilatation-dissipation was found to increase in the vicinity of these structures, the overall contribution of this term to total dissipation was quite small (less than

ten percent). At times when no shocklets were present, the dilatation-dissipation was found to contribute less than one percent of the total dissipation. Lee *et al.* [19] observed eddy shocklets in direct simulations of decaying isotropic turbulence. These shocklets obey the normal shock jump conditions. Lee *et al.* believed that the reduction in kinetic energy growth was due to these structures. In confined countercurrent mixing layer experiments, Papamoschou [20] observed what appear to be eddy shocklets, but no evidence for shocklets was found in similar experiments for unconfined countercurrent shear layers [21] [22]. Therefore, while the debate is far from settled, it appears that eddy shocklets alone cannot account for the reduction in turbulent kinetic energy associated with compressibility.

Sarkar *et al.* [11] also attributed some of the kinetic energy growth rate reduction to the action of pressure-dilatation, and derived a model for this term for Reynolds averaged Navier-Stokes solvers. Similar work was reported by Speziale *et al.* [23]. A related term occurs in the subgrid kinetic energy equation, but currently, very little work that deals with this phenomenon in an LES context has been reported. The work by Koutmos *et al.* [24], who used a model proposed by Schumann, is one of the few papers which touch on the subject. The pressure dilatation has been found to be either positive or negative and is considered an isentropic process; in the absence of mean acceleration and volume change, it is observed to act as an exchange between turbulent kinetic energy and the internal energy [4]. Ristoricelli [25] found that this exchange was mediated by the acoustics of the flow. For compressible decaying isotropic turbulence, however, the pressure dilatation was found to be generally positive, and its contribution to dissipation was not significant [19].

A third mechanism was proposed for the observed reduction in kinetic energy growth rates which involved the reduction in Reynolds shear stress anisotropy. This

reduction results in decreased turbulent energy production [26]. Subsequent to the dilatation-dissipation and pressure-dilatation modelling work mentioned above, Sarkar has apparently come to new conclusions regarding the importance of these phenomena. He has found in direct simulations of homogeneous shear flow that the reduction in kinetic energy growth is primarily due to the reduced level of energy production, not due to any explicitly dilatational effects [27] [28]. While pressure-dilatation and dilatation-dissipation were found to increase with compressibility, they did not add appreciably to the overall dissipation. Sarkar has proposed the gradient Mach number as a parameter (in addition to the turbulent Mach number) to characterize the effects of compressibility. He noted that such effects are diminished in boundary layers, as compared to mixing layers- a fact which is accounted for if the gradient Mach number is a characteristic flow parameter. The author has not yet seen any models which have made use of this parameter.

Lee, Lele, and Moin [19] found that the effects of variable viscosity on turbulent properties were negligible for decaying compressible isotropic turbulence. This, however, is not the ideal case for testing this phenomenon. It is thought that a reacting mixing layer, or some other flow with extreme temperature gradients, would be a better means of determining the importance of variable viscosity, but work of this nature has not yet been published.

Direct acoustic energy loss may be significant for hypersonic boundary layers, but Lele [4] reported that this result was not conclusive. Otherwise, acoustic energy loss phenomena have not been seen to significantly affect turbulent flows.

1.2 Numerical Simulation of Turbulence

In numerical simulations of turbulent flows, in order to fully capture the physics of the flow, one must be able to resolve all of the scales of motion. Such a simulation is called a direct numerical simulation (DNS). Currently, DNS is impossible for all but the most simple problems, and this situation is likely to continue for the foreseeable future. Therefore, in order to study realistic flows, various approximations are introduced. The most common approach in the past has been to average the governing equations over time. This results in the Reynolds-Averaged Navier-Stokes (RANS) equations. Since a solution is sought only for the mean flow quantities, the entire effect of the turbulent fluctuations must be modelled. No information about the temporal behavior of the flow is available from such a solution, unless the flow is such that the "mean" quantities are changing with time (*e.g.*, a pitching airfoil).

A wide variety of turbulence models are available for use with RANS flow solvers. The standard (unmodified) $k-\varepsilon$ and $k-\omega$ models have been shown to be unable to correctly predict the effects of compressibility on turbulence. As mentioned in the previous section, attempts have been made to develop terms which, when added to standard RANS turbulence models, would correct for the effects of compressibility (*e.g.* [11] [10] [13]). These modifications (usually applied to $k-\varepsilon$ models) have been successful within the limited class of problems for which they were developed. When applied to different configurations, however, they have not proven to be very generalizable [29]. Furthermore, even when they give accurate predictions, only steady-state information is obtained. For information about transients, another approach is required.

In order to perform time-accurate numerical simulations of high Reynolds number flows, the concept of large eddy simulation (LES) has been introduced. In this approach, unsteady motion which can be resolved by the grid is to be captured, and only the effect of unresolvable scales are modelled. It has been observed that the effect of the flow configuration is mostly on the large scales of motion, while the smaller scales are more isotropic. Since LES only attempts to model the effects of these smaller, more isotropic, scales, the models thus developed offer at least the possibility of being more generally applicable than their RANS counterparts, which must capture the effects of all scales of motion. A brief summary of LES efforts to date is now presented. For a more detailed overview of LES, see the papers by Ferziger [30], Rogallo and Moin [31], Yoshizawa [32], Reynolds [33], Piomelli [34], and Lesieur and Métais [35].

Several approaches have been taken for modelling the effects of the subgrid scales on the resolved flow. The most common has been to introduce an eddy (or turbulent) viscosity and to treat the subgrid effects as an additional "viscous" stress. Smagorinsky's [36] approach modelled the velocity scale in the turbulent viscosity as a function of the resolved strain rate; variations of this approach are still the most common. Schumann [37] introduced the subgrid kinetic energy, which was governed by its own transport equation, as a means of computing a characteristic turbulent velocity. For spectral codes, a spectral eddy viscosity [38] model is often used. More recently, models have been developed for a physical-space analog of the spectral eddy viscosity; these are called structure function models [35]. A completely different approach to subgrid modelling has used the idea of scale-similarity to model small scale effects [39] [40]. The eddy viscosity approach has been combined with similarity models to form mixed models [41]. Another application of the similarity

concept has been in the formulation of dynamic models, which use the smallest resolved scales to compute values for the subgrid model coefficients [42] [43] [44].

Leslie and Quarini [45] confirmed Kraichnan's [38] claim that eddy viscosity was a reasonable way to model subgrid effects, but suggested that a better way to approach subgrid scale modelling is to treat the backscatter separately from the forward cascade of energy. Several models have been formulated which attempt this (*e.g.*, [46]). It has been noted that dynamic models, however, by allowing the model coefficient to become negative, contain a built in mechanism that permits a certain backscatter-like behavior [47]. Of course, modelling backscatter as a negative viscosity is not necessarily the best approach, but the prediction of a negative model coefficient could be used as a guide for regions where some other backscatter model should be applied. Schumann [46] states, however, that such models are "deterministic functions of the resolved fields, and, hence, miss to represent the stochastic nature of backscatter."

Early efforts in LES used Reynolds averaging to eliminate the Leonard and cross stresses, and modelled only the Reynolds stresses [48] [49] [50]. Later work computed the Leonard stresses directly and modelled the cross and Reynolds stresses (as in [51]). In 1985, Speziale [52] pointed out that many then-common practices in subgrid modelling were not Galilean invariant, which violated the fundamental character of the governing equations. Only the Bardina model [39], when the model constant had a value of unity, satisfied this condition. Partly as a result of this, more recent work has tended to treat the subgrid stress tensor as a whole, rather than separate it into Leonard, cross and Reynolds stresses (*e.g.*, [53] [43] [54]).

Compressible large eddy simulation began with Yoshizawa [55] who used an asymptotic expansion about an incompressible state to extend an incompressible

model to the weakly compressible regime. Erlebacher *et al.* [56], derived a subgrid model that was more consistent in that it made no such assumptions about the character of the compressibility. This work split the subgrid stress tensor into Leonard, cross, and Reynolds stresses, as discussed above. They proposed using a Bardina-type similarity model for the cross stresses. A compressible extension to Smagorinsky's model was used for the deviatoric component of the Reynolds stresses; the isotropic part was modelled using Yoshizawa's model. The Leonard stresses were computed directly. The subgrid heat flux was similarly split, with the "Leonard" heat fluxes being computed directly, similarity being used for the cross stress, and a gradient transport model being used for the "Reynolds" heat flux term. Moin *et al.* [57] developed a compressible version of Germano's dynamic model [42]. The basic model for this case was an algebraic eddy diffusion model, similar to that which Erlebacher *et al.* used for the Reynolds stress terms, but the methodology of Germano [58] was used to dynamically compute the model coefficients. This model has been used by several researchers for simple compressible flows, but continues to be limited by numerical instability which requires *ad hoc* averaging of the coefficients (*e.g.*, [54] [59]). Recently, several local dynamic models have been developed for incompressible flows (*e.g.*, [60] [43] [61] [44]).

The results of LES have been found to be sensitive to the choice of numerical scheme [62]. Even schemes which are normally (in RANS applications) thought of as "low dissipation" have been found to be overly dissipative in an LES context [63]. Of course, with enough resolution, almost any scheme can be made to yield acceptable results, and a wide variety of methods have been used in the past. Among these are fifth order upwind-biased finite difference methods [63], second order MacCormack schemes [64], sixth-order compact schemes [65], and modified Gudunov schemes [66],

to name only a few. As one attempts to simulate flows with ever higher Reynolds numbers, however, the problem of numerical dissipation becomes more critical. It quickly becomes impractical to keep adding points to the grid in order to keep the cell Reynolds number low enough for dissipative schemes to obtain reasonable results. Thus, for these cases, the numerical scheme must be chosen with care. This topic is discussed further in Chapter IV.

1.3 Objectives of the Current Study

As has been shown above, there is still a lack of consensus as to the underlying physics of the effects of compressibility on turbulence. The reasons for the reduced turbulent kinetic energy in compressible flows are still being debated. Although experimental techniques are constantly being improved, the current state of the art is unable to provide all of the data needed to resolve these issues. Computational techniques are called upon to investigate issues that experimental techniques cannot address. Unfortunately, here too, the state of the art is not yet at a stage where it can provide all of the needed data. Thus, further development is needed in both the experimental and computational approaches. This work attempts to advance computational capabilities by developing a numerical scheme and associated turbulence models that can simulate flows with reasonable accuracy at previously unfeasible Reynolds numbers.

To this end, the following objectives must be met:

- Formulate a new dynamic subgrid scale model for compressible flows. The approach that is chosen for this follows the work of Kim [67]. The model coefficients should be computed in a local manner. This model should be no

more expensive than other dynamic schemes, and yield comparable or better results for a variety of test problems.

- Develop a higher order numerical scheme with very low inherent numerical dissipation. It is believed that a scheme of this sort (low dissipation) is needed in order to accurately capture very high Reynolds number flows with relatively coarse grids. Otherwise, numerical dissipation swamps the viscous and subgrid terms, with the result that the solution is corrupted.

- Demonstrate the model's capability in near-incompressible isotropic turbulence, and show that it correctly duplicates the results of Kim's model for this regime.

- Test the model's ability to correctly capture compressibility effects in isotropic turbulence (decaying and forced) over a range of Mach and Reynolds numbers.

- Demonstrate the application of the model to flows of more practical interest by simulating very high Reynolds number spatially developing mixing layers for various convective Mach numbers.

1.4 Outline of the Study

The remainder of this dissertation is organized in the following manner. Chapter II introduces the governing equations of LES and the subgrid terms which require closure. Next, Chapter III discusses the models used to close these terms as well as the method used to dynamically compute the model coefficients. The numerical scheme used in this study is described in Chapter IV. The results from simulations near the incompressible limit are presented in Chapter V. Following that, Chapter

VI discusses results from simulations of compressible, homogeneous, isotropic turbulence. Spatially evolving compressible mixing layers are investigated in Chapter VII. In addition to testing the effect of different model configurations, the computational results are compared with experimental findings. Finally, Chapter VIII presents the conclusions derived from this study and recommendations for future work.

CHAPTER II

FORMULATION OF THE PROBLEM

In this chapter, the governing equations are presented, along with the assumptions made in their formulation. Several underlying assumptions are made, however, which apply to all the types of flow to be discussed in this dissertation. First, it is assumed that the fluid medium is a continuum. In other words, the smallest scales of interest (*e.g.*, the Kolmogorov scales of turbulence) are taken to be much greater than the mean free path of the molecules which make up the medium. Also, the medium is treated in a homogeneous manner in the sense that the exact chemical composition of the fluid is ignored. Finally, the fluid medium is taken to be a calorically perfect gas; thus, the equation of state for a perfect gas is used.

2.1 The Navier-Stokes Equations

The Navier-Stokes equations represent the most fundamental level of physics to be considered here. It is assumed that these equations accurately capture the behavior of fluids at all scales. They are a mathematical description of the following concepts:

1. Conservation of mass- mass is neither created nor destroyed.

2. Conservation of momentum- the fluid flow obeys Newton's second law of motion.

3. Conservation of energy- energy is neither created nor destroyed, though it may change its form.

The continuity equation requires conservation of mass and is written in tensor form as:

$$\frac{\partial \rho}{\partial t} = -\frac{\partial \rho u_i}{\partial x_i} \tag{2.1}$$

The momentum equation requires that the force on a control volume equal the time rate of change of its momentum. Put in tensor form, this becomes:

$$\frac{\partial \rho u_i}{\partial t} = -\frac{\partial}{\partial x_j}(\rho u_i u_j) - \frac{\partial p}{\partial x_i} + \frac{\partial \tau_{ij}}{\partial x_j} \tag{2.2}$$

In the above equation, τ_{ij} is the viscous stress tensor. For a Newtonian fluid, Stokes' hypothesis may be used to express this as:

$$\tau_{ij} = 2\mu \left[\frac{1}{2}\left(\frac{\partial u_i}{\partial x_j} + \frac{\partial u_j}{\partial x_i} \right) - \frac{1}{3}\frac{\partial u_k}{\partial x_k}\delta_{ij} \right] \tag{2.3}$$

Since the fluid is assumed to have a uniform chemistry, the viscosity, μ, is taken to be a function of temperature only. In this work, Sutherland's law will be used:

$$\mu \approx \frac{C_1 T^{\frac{3}{2}}}{T + C_2} \tag{2.4a}$$

$$\text{for SI units, } C_1 = 1.458e-6 \tag{2.4b}$$

$$C_2 = 110.4 \tag{2.4c}$$

The energy equation describes the balance of energy throughout a fluid. In tensor form, this equation may be written as follows:

$$\frac{\partial \rho E}{\partial t} = -\frac{\partial}{\partial x_i}\left(\rho E + p\right) u_i + \frac{\partial u_j \tau_{ij}}{\partial x_i} + \frac{\partial}{\partial x_i}\left(\kappa \frac{\partial T}{\partial x_i}\right) \tag{2.5}$$

As with the viscosity, the assumption of uniform chemistry implies that thermal conductivity is a function of temperature only

$$\kappa = \frac{\gamma c_v \mu\left(T\right)}{\mathrm{Pr}} \tag{2.6}$$

In the above equation, the ratio of specific heats (γ), the Prandtl number (Pr), and the specific heat at constant volume (c_v) are all assumed to be constant.

At this point there are five equations (continuity, u-momentum, v-momentum, w-momentum, and energy) plus three auxiliary equations describing the viscosity, the heat transfer coefficient, and the viscous stress tensor. These equations, however, involve seven flow variables: density, total energy, the three velocity components, pressure, and temperature. Therefore additional information is needed to close the system.

The total energy of the fluid per unit mass may be expressed in terms of internal energy and kinetic energy:

$$E = e + \frac{1}{2} u_i u_i \tag{2.7}$$

Assuming that the flow is calorically perfect, the internal energy may be related to temperature using:

$$e = c_v T \tag{2.8}$$

Finally, the temperature, density, and pressure are assumed to behave according the equation of state for a perfect gas:

$$p = \rho R T \tag{2.9}$$

With these relations, the system of equations is closed, but because they have no known general analytic solution, they must be solved numerically. If the Navier-Stokes equations are solved on a computational grid with sufficient resolution to capture all relevant scales of fluid motion, then the solution is called a direct numerical simulation (DNS). Unfortunately, for engineering problems, it is almost never practical (or even possible) to use such a grid. Therefore, further assumptions must be introduced in order to reduce this resolution requirement.

2.2 The LES Equations

The approach that is taken for this work is known as large eddy simulation (LES). As discussed in Chapter I, the idea behind LES is to capture all the scales of motion which the grid is capable of resolving and only introduce models to account for the effects of the scales which are unresolved. Central to this is the concept of filtering. The purpose of filtering is to separate the resolved scales from the unresolved. Leonard [49] defined a filtering operation with a uniform characteristic filter width Δ (in one dimension) in physical space as:

$$\bar{\phi}(x) = \int_{-\infty}^{\infty} G(x-\xi)\,\phi(\xi)\,d\xi \tag{2.10}$$

Note that, although the notation is similar to the time averaging used in formulating the Reynolds-Averaged Navier-Stokes equations, this is a spatial operation, not temporal (unless otherwise noted). The original field (ϕ) can therefore be defined as the filtered field plus a "subgrid" term:

$$\phi = \overline{\phi} + \phi' \tag{2.11}$$

The function G in equation 2.10 is the "filter function," which is a spatial analog of the spectral transfer function. According to Ghosal [68], a filter function may be any function, defined on an infinite domain, which satisfies the following requirements:

1. $G(-\xi) = G(\xi)$

2. $\int_{-\infty}^{\infty} G(\xi)\, d\xi = 1$

3. $G(\xi) \to 0$ as $|\xi| \to \infty$ such that all moments $\int_{-\infty}^{\infty} G(\xi)\, \xi^n d\xi$ $(n \geq 0)$ exist

4. $G(\xi)$ is "small" outside $\left(-\frac{\Delta}{2}, \frac{\Delta}{2}\right)$

One important result of choosing such a function is that:

$$\overline{\frac{\partial \phi}{\partial x}} = \frac{\partial \bar{\phi}}{\partial x} \tag{2.12}$$

See Appendix A for a more complete discussion of filtering.

2.2.1 The Equations of Motion for LES

The governing equations for LES are derived by filtering the Navier-Stokes equations. As discussed in Appendix A, the specific form of the filter function that will take the exact continuous Navier-Stokes equations and yield the LES equations (in the discrete form in which they are actually solved numerically) is not known. For a finite volume scheme such as this one, a box filter is a reasonable approximation, but relationships between derivatives are not preserved on the LES field (*e.g.*, a continuous velocity field which is divergence-free will not remain so after filtering to an LES grid). Therefore, it must be assumed that such a filter exists, and that equation 2.12 holds. Given this, the standard approach to deriving the LES equations defines

a corresponding Favre filter (in space) as:

$$\widetilde{\phi} = \frac{\overline{\rho\phi}}{\overline{\rho}} \tag{2.13}$$

The use of a Favre filter is very convenient from the standpoint of keeping the equations as simple as possible, but there are drawbacks. The primary limitation of Favre filtering is that experimental data is not density weighted. Further, Chen, Riley, and McMurtry ([69]) have shown that there can be significant differences between "straight" filtered and Favre filtered data. The objective of the current work is to extend LES capabilities closer to the realm of "practical" problems; for such cases, comparison with experimental results is a requirement. Therefore, the approach taken here is to avoid Favre filters, despite the additional complexity in the equations. One beneficial side-effect of this choice is that the equations in "straight" filtered form offer more guidance for modelling [70]. A more conventional approach to the derivation of the LES equations and their closure is covered in Appendix B

The LES continuity equation is, therefore, obtained by filtering equation 2.1:

$$\frac{\partial \bar{\rho}}{\partial t} = -\frac{\partial \bar{\rho}\bar{u}_i}{\partial x_i} - \frac{\partial}{\partial x_i}\left(\overline{\rho u_i} - \bar{\rho}\bar{u}_i\right) \tag{2.14}$$

Similarly, the momentum equation becomes:

$$\frac{\partial \bar{\rho}\bar{u}_i}{\partial t} = -\frac{\partial}{\partial x_j}\left(\overline{\rho u_i u_j} - \bar{\rho}\bar{u}_i\bar{u}_j\right) - \frac{\partial \bar{p}}{\partial x_i} + \frac{\partial \bar{t}_{ij}}{\partial x_j} - \frac{\partial}{\partial x_j}\left(\overline{\rho u_i u_j} - \bar{\rho}\bar{u}_i\bar{u}_j\right) + \frac{\partial}{\partial x_j}\left(\overline{\tau}_{ij} - \bar{t}_{ij}\right) - \frac{\partial}{\partial t}\left(\overline{\rho u_i} - \bar{\rho}\bar{u}_i\right) \tag{2.15}$$

The resolved viscous stress tensor in the above equation takes the following form:

$$\bar{t}_{ij} = 2\bar{\mu}\left[\frac{1}{2}\left(\frac{\partial \bar{u}_i}{\partial x_j} + \frac{\partial \bar{u}_j}{\partial x_i}\right) - \frac{1}{3}\frac{\partial \bar{u}_k}{\partial x_k}\delta_{ij}\right] \tag{2.16}$$

The viscosity in the above expression is assumed to follow equation 2.4 (using the resolved temperature, $\bar{T}$). The other viscous term in equation 2.15, $\overline{\tau}_{ij}$, is simply the filter of the exact viscous stress tensor (2.3). Next, the energy equation may be written as:

$$\begin{aligned}\frac{\partial \bar{\rho}\bar{E}}{\partial t} = & -\frac{\partial}{\partial x_i}\left(\bar{\rho}\bar{E} + \bar{p}\right)\bar{u}_i - \frac{\partial}{\partial x_i}\left(\overline{\rho E u_i} - \bar{\rho}\bar{E}\bar{u}_i\right) - \frac{\partial}{\partial x_i}\left(\overline{p u_i} - \bar{p}\bar{u}_i\right) \\ & + \frac{\partial}{\partial x_i}\left(\bar{u}_j\bar{t}_{ij}\right) + \frac{\partial}{\partial x_i}\left(\overline{u_j\tau_{ij}} - \bar{u}_j\bar{t}_{ij}\right) \\ & + \frac{\partial}{\partial x_i}\left(\bar{\kappa}\frac{\partial \bar{T}}{\partial x_i}\right) + \frac{\partial}{\partial x_i}\left(\overline{\kappa\frac{\partial T}{\partial x_i}} - \bar{\kappa}\frac{\partial \bar{T}}{\partial x_i}\right) \\ & - \frac{R}{\gamma - 1}\frac{\partial}{\partial t}\left(\overline{\rho T} - \bar{\rho}\bar{T}\right) - \frac{1}{2}\frac{\partial}{\partial t}\left(\overline{\rho u_i u_i} - \bar{\rho}\bar{u}_i\bar{u}_i\right) + \frac{\partial}{\partial t}\left(\bar{\rho}k^{sgs}\right)\end{aligned} \tag{2.17}$$

The total energy is here defined as:

$$\tilde{E} = \tilde{e} + \frac{1}{2}\tilde{u}_i\tilde{u}_i + k^{sgs} \tag{2.18}$$

The subgrid kinetic energy, k^{sgs}, is defined as the effect of the subgrid scales on the kinetic energy of the resolved field:

$$k^{sgs} = \frac{1}{2}\left(\overline{u_i u_i} - \tilde{u}_i\tilde{u}_i\right) \tag{2.19}$$

The LES thermal conductivity ($\tilde{\kappa}$) and internal energy ($\tilde{e}$) are, like viscosity, assumed to be functions (see equations 2.6 and 2.8) of the filtered temperature. Finally, the LES equation of state is written as:

$$\overline{p} = \overline{\rho}R\tilde{T} + R\left(\overline{\rho T} - \overline{\rho}\tilde{T}\right) \tag{2.20}$$

2.2.2 Identification of Subgrid Terms

In the above LES equations there are several terms which are not directly computable in a numerical simulation. These terms must either be modeled or neglected in order to close the system of equations. Such terms will now be briefly identified, and the next chapter will discuss the models which will be used to close the equations.

The continuity equation contains one subgrid term: $(\frac{\partial}{\partial x_i}(\overline{\rho u_i} - \bar{\rho}\bar{u}_i))$. This term is purely a compressible phenomenon related to the correlation between density and velocity fluctuations. It may also be rewritten in terms of the difference between the Favre filtered and "straight" filtered velocity. The LES state equation (2.20) also has a single subgrid term $(R(\overline{\rho T} - \bar{\rho}\bar{T}))$. This term may be thought of as a measure of the correlation of subgrid density and temperature fluctuations or as a pressure associated with subgrid fluctuations. Alternatively, it may be rewritten in terms of the difference between the Favre filtered and "straight" filtered temperature.

There are three subgrid terms in the LES momentum equation (2.15) which require closure. The first $(\frac{\partial}{\partial x_j}(\overline{\rho u_i u_j} - \bar{\rho}\bar{u}_i\bar{u}_j))$ arises from the convection terms. Like the Reynolds stress term of the Reynolds-averaged Navier-Stokes equations, this term has been observed, at least in regions of forward energy transfer, to behave, on average, much like a viscous stress [45] [38]. Thus, it is frequently written in terms of the so-called subgrid stress tensor, which is defined as:

$$\tau_{ij}^{sgs} = (\overline{\rho u_i u_j} - \bar{\rho}\bar{u}_i\bar{u}_j) \tag{2.21}$$

Another subgrid term $(\frac{\partial}{\partial x_j}(\overline{\tau}_{ij} - \bar{t}_{ij}))$ arises from the viscous terms because, unlike incompressible fluids, the viscosity is not a constant in compressible flows. Thus, $\bar{\tau}_{ij}$ contains unknown terms involving the correlation between the viscosity and velocity derivatives (*e.g.*, $\overline{\mu\frac{\partial u_i}{\partial x_j}}$). The final subgrid term in the momentum equation $(\frac{\partial}{\partial t}(\overline{\rho u_i} - \bar{\rho}\bar{u}_i))$ arises from the filtering of the time derivative and is very similar to the subgrid term from the continuity equation.

The LES energy equation (2.17) contains seven subgrid terms. The first of these ($\frac{\partial}{\partial x_i}\left(\overline{\rho E u_i} - \bar{\rho}\tilde{E}\tilde{u}_i\right)$) arises from the convection term. The second term is a pressure-velocity correlation term ($\frac{\partial}{\partial x_i}\left(\overline{pu_i} - \bar{p}\tilde{u}_i\right)$) which is also related to convection. The third is a viscous subgrid term ($\frac{\partial}{\partial x_i}\left(\overline{u_j\tau_{ij}} - \tilde{u}_j\tilde{t}_{ij}\right)$). This term involves the transfer of subgrid kinetic energy by viscous effects. The next term ($\frac{\partial}{\partial x_i}\left(\overline{\kappa\frac{\partial T}{\partial x_i}} - \tilde{\kappa}\frac{\partial\tilde{T}}{\partial x_i}\right)$) represents the subgrid heat flux. The last three terms all arise from the filtering of the density-weighted total energy (ρE). The first of these terms ($\frac{R}{\gamma-1}\frac{\partial}{\partial t}\left(\overline{\rho T} - \bar{\rho}\tilde{T}\right)$) is similar to that seen in the state equation (2.20); it involves the correlation between density and temperature. The next ($\frac{1}{2}\frac{\partial}{\partial t}\left(\overline{\rho u_i u_i} - \bar{\rho}\tilde{u}_i\tilde{u}_i\right)$) can be rewritten in terms of the diagonal of the subgrid stress tensor defined above (2.21). Also, the time variation of the subgrid kinetic energy ($\frac{\partial}{\partial t}\left(\bar{\rho}k^{sgs}\right)$) appears. Finally, the subgrid kinetic energy (k^{sgs}) which appears here and in the definition of total energy (equation 2.18) is not directly available either.

CHAPTER III

CLOSURE OF THE SUBGRID TERMS

As discussed in section 2.2.2, the LES equations require closure before they can be implemented in a code. The majority of the work in this area has concentrated on the closure of the momentum equations- specifically, the modelling of the subgrid stress tensor. Most compressible LES work in the past has been based on the compressible Smagorinsky model (*e.g.* [71] [56] [72] [62] [73] [74]) or some dynamic extension thereof (*e.g.* [57] [59] [75] [15]). Others (*e.g.* [76] [40] [77]) have examined "mixed" models which combine a compressible extension of Bardina's similarity model [39] with a compressible Smagorinsky-type model.

It should be noted that recently several papers have been published which claim to perform LES using no explicit subgrid model at all. This idea came about as researchers noted that, in many cases, the effect of the viscous terms and subgrid models was minimal. This was because the numerical dissipation inherent in many schemes is larger in magnitude than the combined viscous and conventional subgrid model terms. Despite this, the results for many of these cases were quite reasonable [66] [78] [79]. It has even been shown that some algorithms (notably the Piecewise Parabolic Method) mimic the behavior of a dissipative subgrid model [80]. The approach would seem, however, to have limited application to high Reynolds number flows since the numerical dissipation of such schemes will overwhelm the physics of the flow unless the cell Reynolds number is kept relatively small. Also, simulations

performed by Silveira-Neto *et al.* [81] for backward-facing steps did not give good agreement with experiment. Therefore, while such "pseudo-direct" simulations (also called "coarse grid DNS") may give good results in some situations (depending on what is being measured), they must be used with care.

All of the above approaches work well for many cases, but they have their drawbacks. The dynamic models are frequently not as stable as desired [44], but without dynamic computation of the model coefficients, eddy diffusion models are not very accurate [46]. Many of the methods used to get around these problems are complex and expensive (*e.g.* [61]) or involve some sort of *ad hoc* averaging (*e.g.* [57]). Similarly, researchers working with the Reynolds-averaged Navier-Stokes equations have encountered limitations when trying to extend simple algebraic models (which are usually designed and calibrated for boundary layers) to more general flow situations, especially those with complex geometries and/or regions of separated or recirculating flow [82]. This has prompted the development of higher order models based on transport equations for turbulent quantities. These models offer a more generally applicable approach, though they are not without their drawbacks. Therefore, in this study, a one-equation model with dynamic coefficients has been developed for LES. It is believed that this approach will prove more "portable" to different flow geometries than the more conventional algebraic models. The current model is based on the work of Schumann [37], Yoshizawa and Horiuti [83], Weeratunga and Menon [84], Menon and Yeung [85], Kim and Menon [?], and Kim [67].

3.1 The LES State Equation

The present approach to the derivation of the LES equations yields, as was shown in Chapter II, a subgrid term associated with the state equation $(R(\overline{\rho T} - \bar{\rho}\tilde{T}))$. This term may be thought of as representing a pressure associated with subgrid fluctuations. Alternatively, one can rewrite it in terms of the difference between the Favre and "straight filtered" temperature. This quantity is therefore expected to be relatively small, except in regions of extreme compression or expansion.

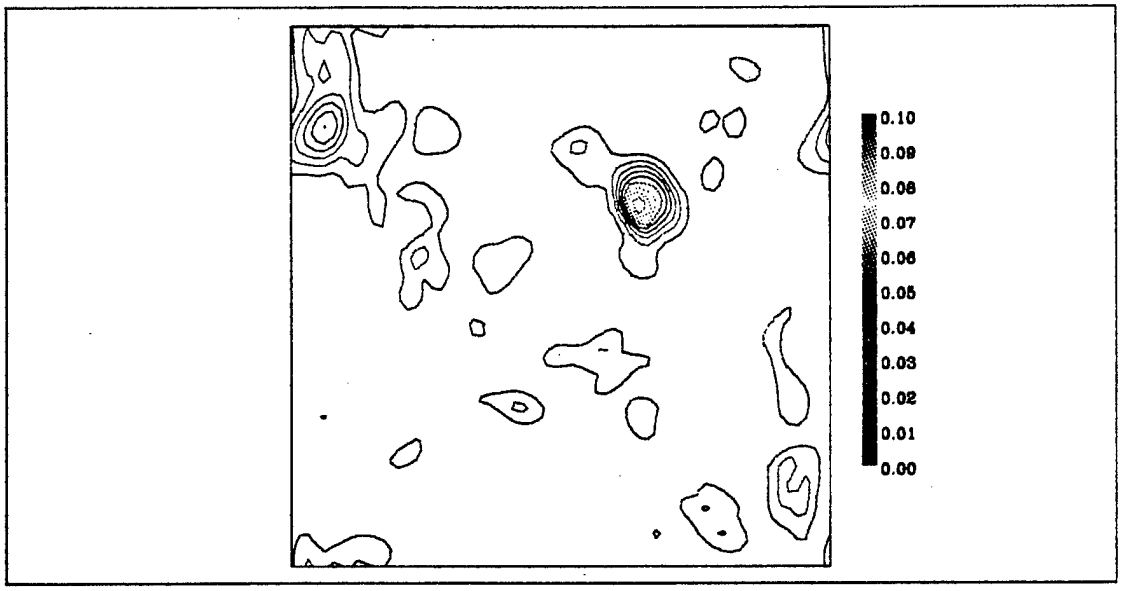


Figure 3.1: Contours of the state equation subgrid term $(R(\overline{\rho T} - \bar{\rho}\tilde{T}))$ computed from a direct simulation of decaying compressible isotropic turbulence

An estimate of this term was obtained using data from a direct simulation of decaying compressible isotropic turbulence simulation (described in more detail in

section 6.1.1). The "subgrid pressure" was computed using a box filter with a characteristic length of 4Δ; no coarsening of the data was performed. Contours of the result, relative to a reference pressure, are plotted in figure 3.1. It should be noted that the peak shown in this plot is the maximum in the entire domain. Figure 3.2 shows the corresponding density contours (normalized by a reference density) for the same plane. As expected, a strong compression region is visible at the location corresponding to the peak value of the subgrid term. This region corresponds to an eddy shocklet, as can be seen in figure 3.3, which shows the corresponding Mach number contours.

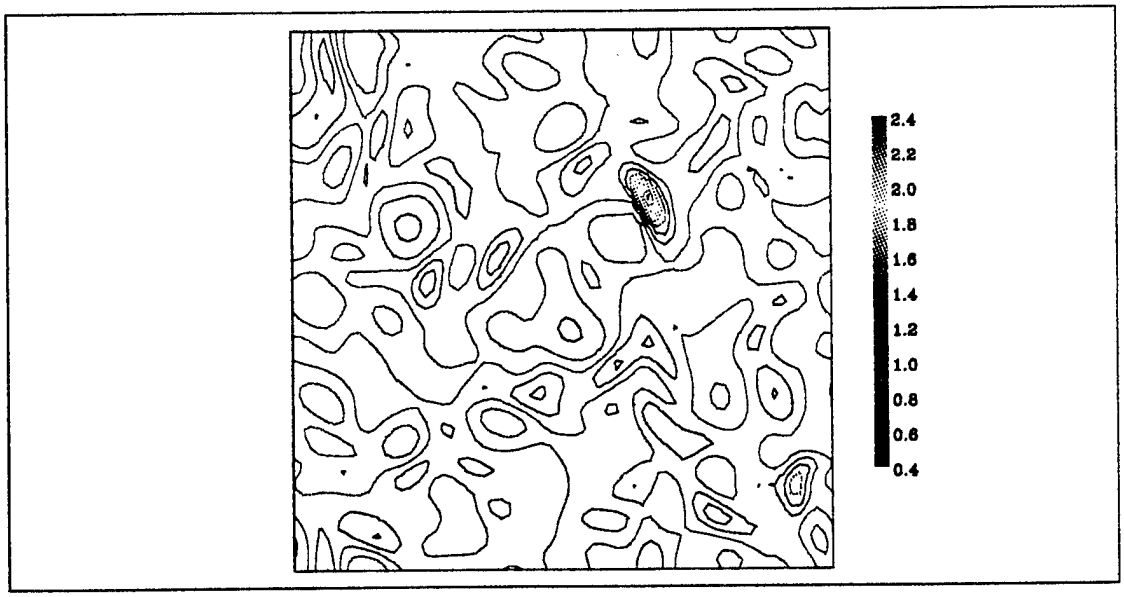


Figure 3.2: Normalized density contours in a direct simulation of decaying compressible isotropic turbulence

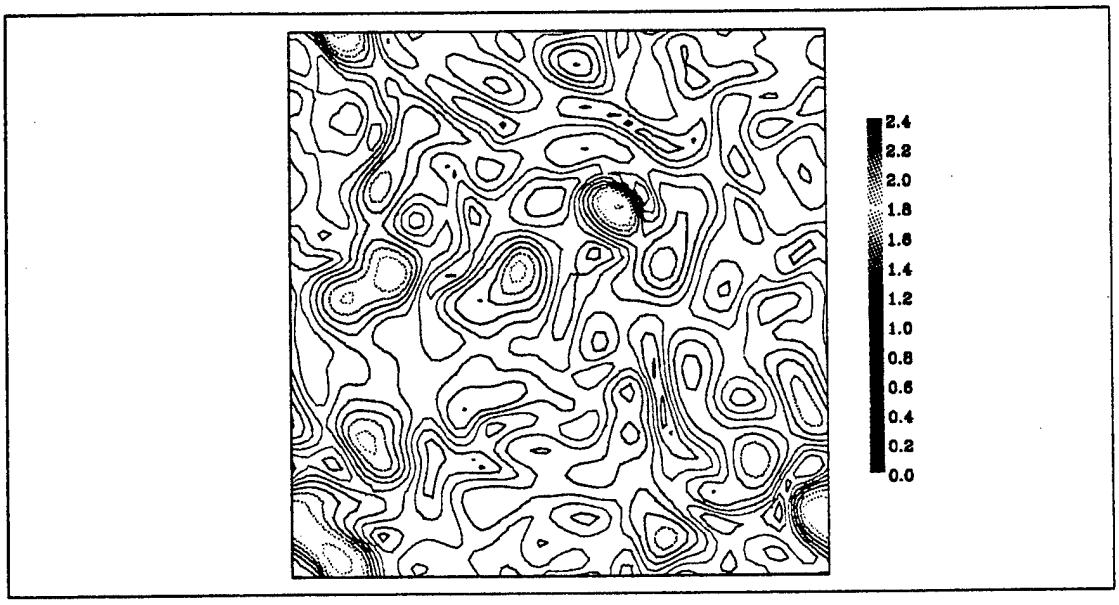


Figure 3.3: Mach number contours in a direct simulation of decaying compressible isotropic turbulence

The relative importance of the subgrid term in a more general sense is shown in figure 3.4 by a PDF of the "subgrid pressure" as a fraction of the exact pressure ($\bar{p}$). The maximum value of the subgrid term for this field was 7.5 percent of the exact pressure. As can be seen, the average value was much less than one percent. Therefore, at the moment, this "subgrid pressure" is assumed to be small, and the term is neglected. The validity of this assumption is illustrated by figure 3.5, which shows that the LES correctly captures the behavior (and magnitude) of the pressure. It should be noted that the DNS flow field which was used above had pressure fluctuations whose RMS was about 15 percent of the reference pressure. Of course, these examples are in the simplest of flows; a more complex configuration might yield a different result.

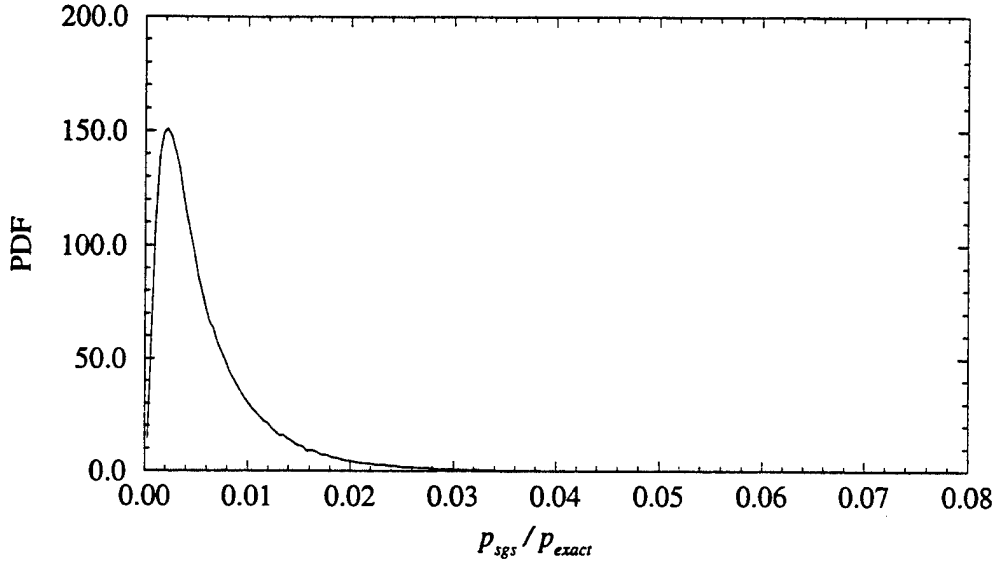


Figure 3.4: Probability density function of the state equation subgrid term relative to the local value of the exact pressure

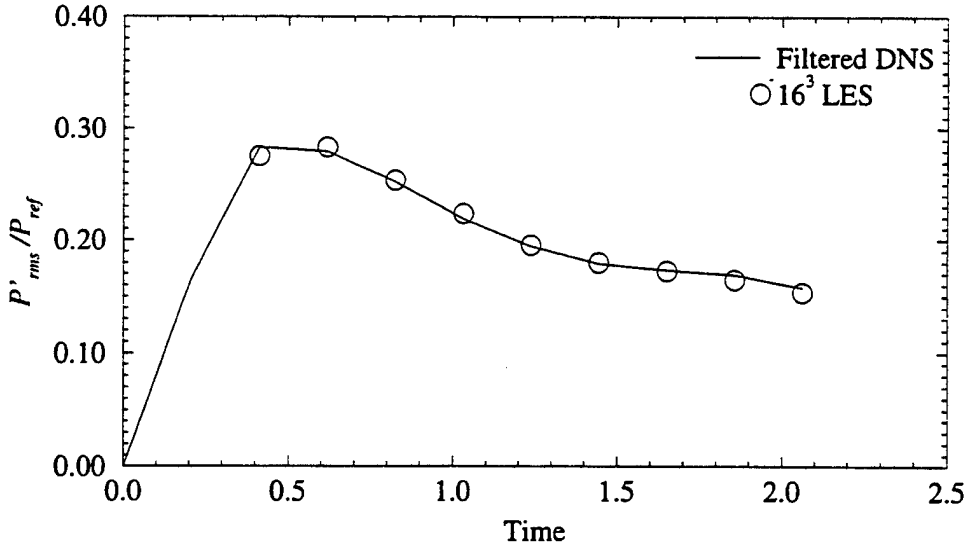


Figure 3.5: History of pressure fluctuations in decaying compressible isotropic turbulence

3.2 Closure of the LES Continuity Equation

The density-velocity correlation term which appears in the LES continuity equation (2.14) is a purely compressible phenomenon. Thus, the incompressible equations contain no direct analog of this term which can be used as a guide for its closure. Some properties, however, can be deduced *a priori*. First, this subgrid term (somewhat arbitrarily designated c_i^{sgs}) may rewritten as the difference between the Favre filtered and "straight filtered" velocity:

$$c_i^{sgs} = \overline{\rho u_i} - \bar{\rho}\bar{u}_i = \bar{\rho}\left(\tilde{u} - \bar{u}\right) \tag{3.1}$$

Obviously, since this term appears only in the compressible equations, any model for it should vanish for a constant density flow. Also, this term is expected to be most significant in regions of strong compression, such as a shock. This is in keeping with the findings of Chen *et al.* [69], who investigated the differences between Favre filtering and conventional filtering in the context of RANS simulations of combustion. They found that the differences between $\tilde{u}$ and $\bar{u}$ were virtually undetectable in regions with mild density gradients. When density is varying more abruptly, it can be argued, in a fashion similar to that used for the mixing length model of turbulent heat flux [1], that the contribution of this term should be proportional to the mean density gradient.

Qualitative evidence for this may be seen in figure 3.6, which shows the contours of the x-component of c_i^{sgs} on the same plane and computed from the same DNS flowfield as the above density contour plot (figure 3.2). Note that, again, the

subgrid term clearly peaks at the shocklet, and other regions of larger than average magnitude (*e.g.* the upper left and lower right corners) are also associated with rapid changes in density). The probability density function of this term is shown in figure 3.7. In figure 3.4, the magnitude of the state equation subgrid term remained below two percent of the exact pressure for the vast majority of points. In the case of the continuity equation subgrid term, the magnitude is significantly higher. Although the majority of points cluster in the vicinity of zero, the wings of the PDF indicate that a significant number of points see a magnitude of up to seven percent of the reference momentum. Thus, this term is obviously significant and cannot be neglected.

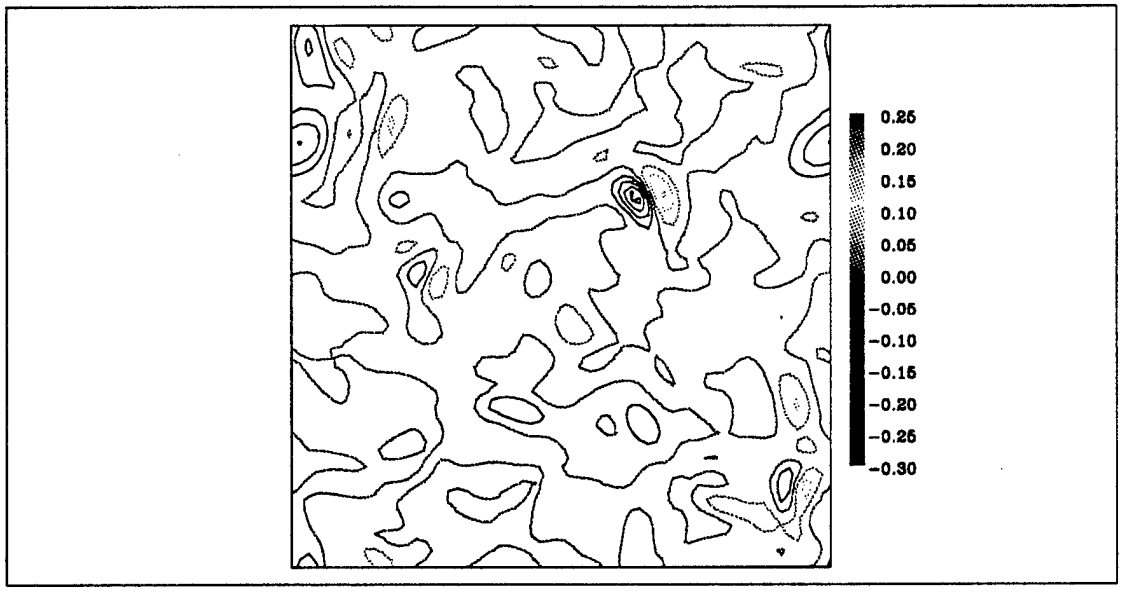


Figure 3.6: Contours of the x-direction continuity equation subgrid term (c_x^{sgs}) normalized by reference momentum ($\rho_{ref} u_{ref}$)

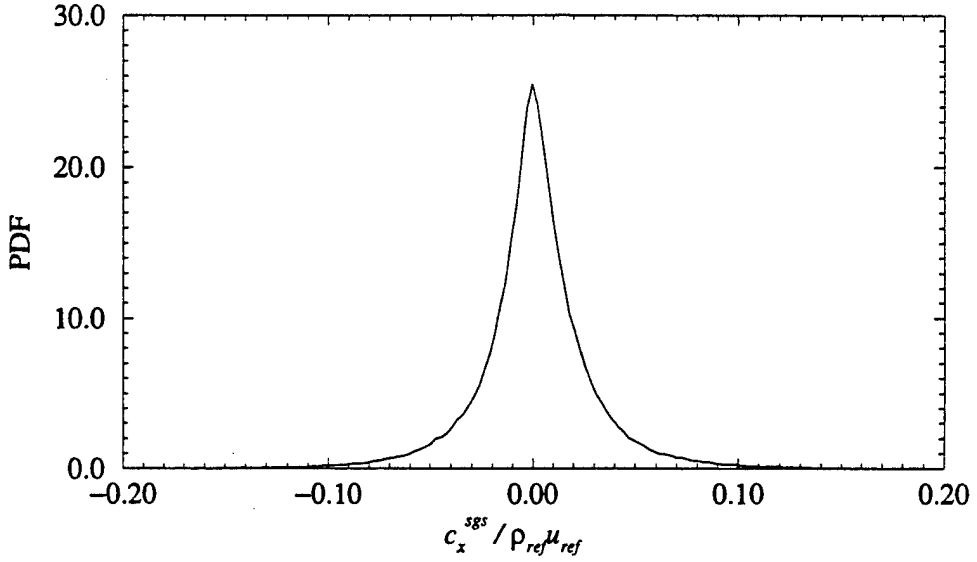


Figure 3.7: Probability density function of the x-component of the continuity equation subgrid term relative to the reference momentum.

In light of this, a gradient diffusion model is adopted for this term:

$$c_i^{sgs} = \overline{\rho u_i} - \bar{\rho}\tilde{u}_i \approx -\nu_c \frac{\partial \bar{\rho}}{\partial x_i} \tag{3.2}$$

The scaling factor in the above equation (ν_c- designated the "compressibility viscosity") is formulated in the following manner. Since this term is expected to be significant only near shocks, a switch is used to prevent excessive dissipation from being added to regions where the mean flow is smooth. It is defined in a discrete sense in a manner similar to that developed by MacCormack and Baldwin [86].On

the i-faces, for example, it may be written:

$$S_{p_{i+\frac{1}{2},j,k}} = \max\left(S_{p_{i,j,k}}, S_{p_{i+1,j,k}}\right) \tag{3.3a}$$

$$\text{where } S_{p_{i,j,k}} = \frac{|p_{i+1,j,k} - 2p_{i,j,k} + p_{i-1,j,k}|}{p_{i+1,j,k} + 2p_{i,j,k} + p_{i-1,j,k}} \tag{3.3b}$$

A characteristic length and velocity can be used to obtain the correct dimensions for this term. As a length, the grid spacing, Δ, is employed. The characteristic velocity is defined as the magnitude of the velocity normal to the cell face. Finally, a scaling factor is added to allow the model to be "tuned" to some degree. This factor is not simply set and held constant, because it is desired that as the cell Reynolds number decreases (*i.e.*, as the simulation is able to resolve a larger and larger fraction of the turbulent scales) this term should approach zero, even in regions of high compression. Therefore, a method is required by which the coefficient can adapt itself to the local Reynolds number.

In this case, numerical experiments on the one-dimensional non-linear Burger's equation have been used to obtain the specific form for the scaling factor. The Burger's equation is used as a model problem to test the behavior of the numerical scheme (with an added dissipation term similar to the proposed model) in the presence of sharp gradients, such as those found at shocks. The exact solution (a hyperbolic tangent) is compared to the numerically obtained solution to find an optimal value for the scaling factor for different cell "Reynolds" numbers. A curve fit is applied to the resulting data to obtain an analytic expression for the scaling

factor (at a cell face):

$$\nu_c = a_c S_p \left|\bar{u}_k n_k\right| \Delta \tag{3.4}$$

$$\text{where } a_c = \begin{cases} a_0 \exp\left[\frac{-1}{K_1\left(R_{e_\Delta} - R_{e_{\min}}\right)}\right] & R_{e_\Delta} > R_{e_{\min}} \\ 0 & R_{e_\Delta} \leq R_{e_{\min}} \end{cases} \tag{3.5}$$

$$R_{e_\Delta} = \frac{\left|\bar{u}_k n_k\right| \Delta}{\nu + \nu_t} \tag{3.6}$$

In the above equations, n_k represents the unit normal vector of the cell face for which ν_c is being calculated. From the aforementioned curve fit, the value used for K_1 is 0.257, and the minimum cell Reynolds number is 1.67. The scaling coefficient, a_0, was determined by a trial-and-error method. A value of 0.60 has been used for this work. The sensitivity of solutions to the choice of a_0 will be addressed in a later chapter.

The modelled LES continuity equation may now be written as:

$$\frac{\partial \bar{\rho}}{\partial t} = -\frac{\partial \bar{\rho}\bar{u}_i}{\partial x_i} + \frac{\partial}{\partial x_i}\left(\nu_c \frac{\partial \bar{\rho}}{\partial x_i}\right) \tag{3.7}$$

3.3 Closure of the LES Momentum Equation

3.3.1 The Subgrid Stress Tensor Model

The approach used in this work to model the subgrid stress tensor (defined in equation 2.21) is a compressible extension of Kim's incompressible model (see Kim

[67]). The first step is to consider the original incompressible model:

$$\tau_{ij}^{sgs} = \overline{u_i u_j} - \bar{u}_i \bar{u}_j \approx -2\nu_t \bar{S}_{ij} + \frac{2}{3} k^{sgs} \delta_{ij} \tag{3.8}$$

For compressible flow simulations, the above model is extended by multiplying by the filtered density and making slight modifications so the model more closely resembles the compressible viscous stress tensor. The left hand side of such an expression, however, does not represent the complete subgrid stress tensor as defined in equation 2.21. This component of τ_{ij}^{sgs} will be called the "incompressible" portion of the subgrid stress tensor ($\tau_{ij}^{sgs^{(i)}}$):

$$\tau_{ij}^{sgs^{(i)}} = \bar{\rho}\left(\overline{u_i u_j} - \bar{u}_i \bar{u}_j\right) \approx -2\bar{\rho}\nu_t \left(\bar{S}_{ij} - \frac{1}{3}\bar{S}_{kk}\delta_{ij}\right) + \frac{2}{3}\bar{\rho} k^{sgs} \delta_{ij} \tag{3.9}$$

In the above equation, $\bar{S}_{ij}$ represents the resolved rate of strain tensor:

$$\bar{S}_{ij} = \frac{1}{2}\left(\frac{\partial \bar{u}_i}{\partial x_j} + \frac{\partial \bar{u}_j}{\partial x_i}\right) \tag{3.10}$$

Following the reasoning of Schumann [37], the turbulent viscosity, ν_t, is approximated as:

$$\nu_t \approx c_\nu \sqrt{k^{sgs}} \Delta \tag{3.11}$$

In the above equation, c_ν is a model coefficient, and Δ is, again, a characteristic length that represents the resolution available on the numerical grid (in this case, the local grid spacing). The subgrid kinetic energy, k^{sgs}, is obtained by solving an equation for its transport in parallel with the other LES equations. The details of this equation are discussed in section 3.4.

The use of the grid spacing, Δ, as the characteristic length of the subgrid scales amounts to assuming that the numerical scheme is capable of resolving everything larger than this length. Of course, this is not accurate. At a minimum, it might appear that the length scale should be at least 2Δ (representing the local Nyquist frequency). This alone, however, would have a negligible effect, since the dynamic coefficient evaluation would tend to neutralize such a practice. Some researchers (*e.g.*, Leslie and Quarini [45]) have suggested that going one step further and explicitly pre-filtering the equations (with a filter of width 2Δ) before applying finite-difference algorithms would be more appropriate. Others, such as Germano [58], note that LES results appear to be relatively insensitive to the particular choice of filtering method (explicitly applied or implicit in the scheme). In light of this, the current work has followed the customary practice of using the discretization/numerical algorithm as the filter and assuming a characteristic length equal to the grid spacing.

3.3.2 Additional Momentum Equation Subgrid Models

The additional component of the subgrid stress tensor will be designated the "compressible" portion:

$$\tau_{ij}^{sgs^{(c)}} = \overline{\rho u_i u_j} - \overline{\rho u_i u_j} \tag{3.12}$$

It will be combined with all other effects of compressibility in the momentum equation, and this "lumped" subgrid term will then be approximated by a single model (as discussed below). As with the above state equation and continuity equation subgrid terms, this type of subgrid effect arises from the differences between Favre and "straight" filtering. Therefore these effects are expected to be highly localized to regions of strong density gradients. As an example of this, contours of $\tau_{xx}^{sgs^{(c)}}$ are plotted in figure 3.8. Again, the same DNS data field that was used in computing the state equation and continuity equation subgrid terms is used to approximate this quantity, and the same plane is plotted. Note that this term is only one part of the quantity which is being modelled, but it serves to illustrate the point. The other terms show a similar behavior.

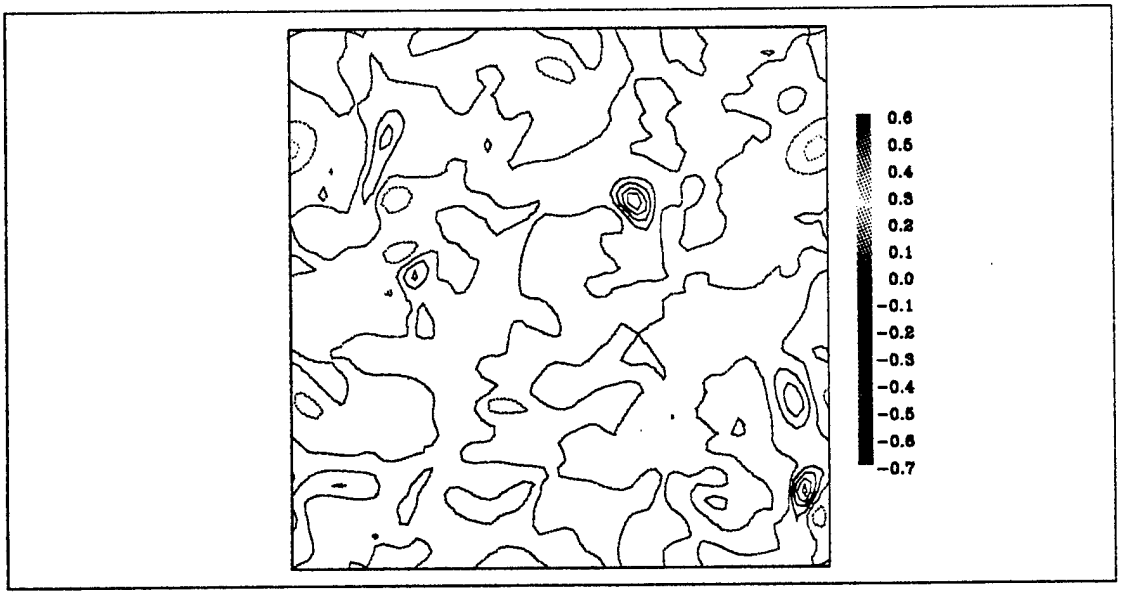


Figure 3.8: Contours of $\tau_{xx}^{sgs^{(c)}}$ as estimated from a DNS of compressible decaying isotropic turbulence- data normalized by reference quantities $(\rho_{ref} u_{ref}^2)$

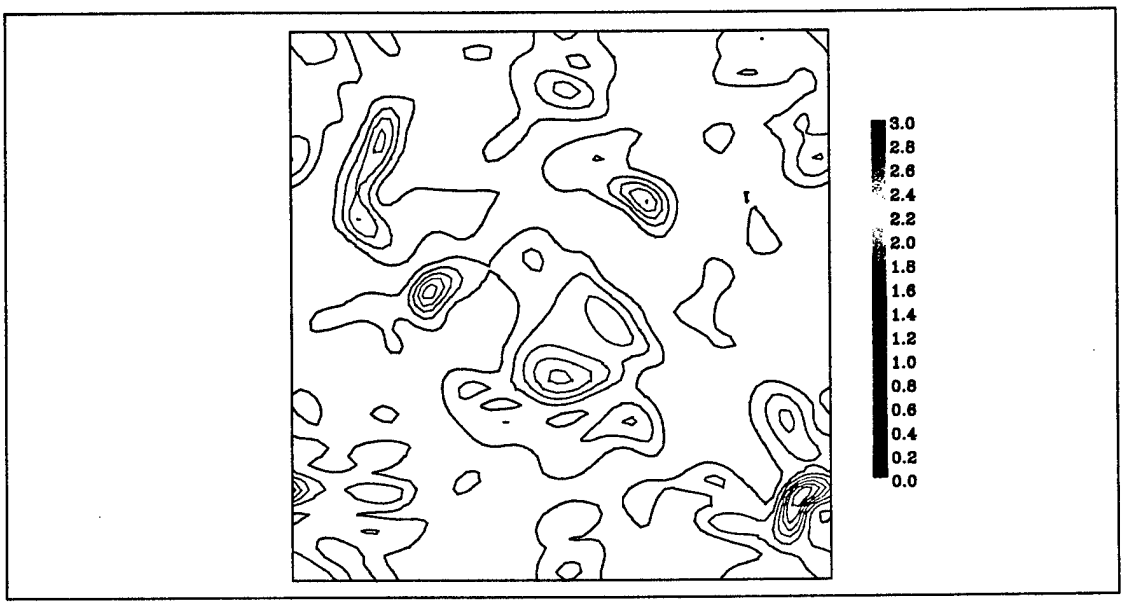


Figure 3.9: Contours of $\tau_{xx}^{sgs^{(i)}}$ as estimated from a DNS of compressible decaying isotropic turbulence- data normalized by reference quantities $(\rho_{ref} u_{ref}^2)$

As expected, a prominent peak is apparent in the vicinity of the shocklet, while elsewhere the magnitude is comparatively small. For comparison purposes, the analogous "incompressible" subgrid stress tensor term is shown in figure 3.9. Although a peak is found in the region of the shocklet, the major "activity" is found elsewhere for the "incompressible" term. Also note that this component of the "incompressible" subgrid stress tensor has positive values only (as do all of the diagonal elements of this tensor).

The magnitude of the "incompressible" term is also seen to be significantly larger than the "compressible" subgrid tensor; this is further illustrated by the PDF's of these fields shown in figures 3.10 and 3.11. For this field, the RMS of $\tau_{xx}^{sgs^{(c)}}$ was roughly 0.05, while $\tau_{xx}^{sgs^{(i)}}$ had an RMS value of 0.29. At this point in the simulation,

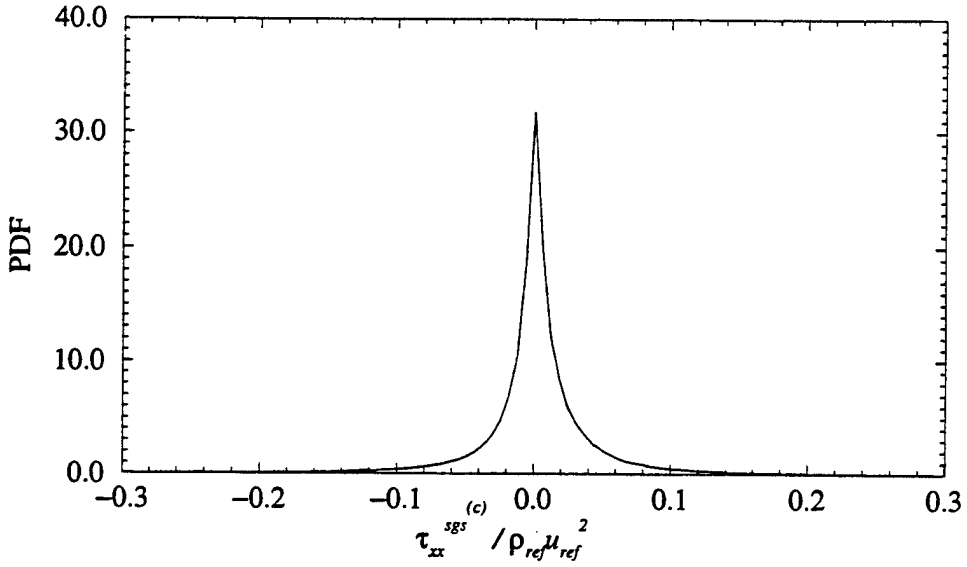


Figure 3.10: Probability density function of the "compressible" subgrid stress tensor ($\tau_{xx}^{sgs^{(c)}}$) term relative to reference quantities

the filtered DNS field shows density fluctuations whose RMS is in the vicinity of 12 percent. Obviously, in a more compressible flow, it is expected that the magnitude of the "compressible" part of the subgrid stress tensor would be larger. In general, however, this and all other specifically "compressible" effects in the momentum equation are expected to remain less important than the "incompressible" subgrid stress tensor (and, needless to say, the resolved terms) because velocity fluctuations are usually larger than density fluctuations.

In summary, it is noted that the effects of compressibility not accounted for by the "incompressible" subgrid stress tensor exist only in the presence of density variations and are expected to be significant only in the vicinity of strong pressure gradients (or in shocks). Therefore, the model for these terms should be triggered by the presence

of shocks. Further, since shocks have been observed in both experiment and direct simulations to have a dissipative effect on turbulence, this term is modelled as an additional dissipation term, as follows:

$$M_{ij}^{sgs^{(c)}} \approx -2\bar{\rho}\nu_c \left(\bar{S}_{ij} - \frac{1}{3}\bar{S}_{kk}\delta_{ij} \right) \tag{3.13}$$

The "viscosity" in the above expression (ν_c) is the same as used for the closure of the LES continuity equation (3.4). Note that this "compressible" term becomes vanishingly small in the limit of incompressible flow, in which case Kim's model is recovered.

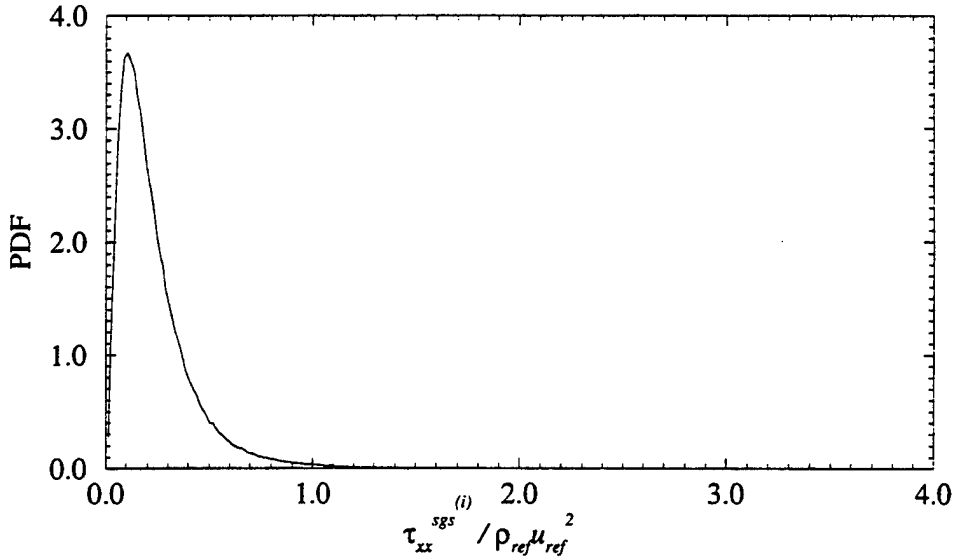


Figure 3.11: Probability density function of the "incompressible" subgrid stress tensor ($\tau_{xx}^{sgs^{(i)}}$) term relative to reference quantities

3.3.3 The Modelled Momentum Equation

Since the viscous terms are usually small for high Reynolds number flows, and the viscosity, though not constant, does not generally vary radically (flames being an obvious exception), the viscous subgrid term in the LES momentum equation (2.15) expected to be small compared with the other terms. Therefore, it is neglected in the current work. The modelled momentum equation can therefore be written as:

$$\frac{\partial \bar{\rho}\bar{u}_i}{\partial t} = -\frac{\partial}{\partial x_j}\left(\bar{\rho}\bar{u}_i\bar{u}_j\right) - \frac{\partial \bar{p}}{\partial x_i} + \frac{\partial \bar{t}_{ij}}{\partial x_j} - \frac{\partial \tau_{ij}^{sgs^{(i)}}}{\partial x_j} - \frac{\partial M_{ij}^{sgs^{(c)}}}{\partial x_j} \tag{3.14}$$

3.4 The k-Equation Model

3.4.1 The Compressible Subgrid Kinetic Energy Equation

The compressible subgrid kinetic energy equation is derived by the combination of two equations: the Navier-Stokes kinetic energy equation and the LES resolved kinetic energy equation. The Navier-Stokes kinetic energy equation is constructed by contracting the Navier-Stokes momentum equation (2.2) with the velocity vector and subtracting the continuity equation (2.1) multiplied by the kinetic energy. After some rearranging, this results in:

$$\frac{\partial \rho k}{\partial t} = -\frac{\partial}{\partial x_i}\rho k u_i - u_i\frac{\partial p}{\partial x_i} + u_i\frac{\partial \tau_{ij}}{\partial x_j} \tag{3.15}$$

In the above equations, k is the kinetic energy of the flow:

$$k = \frac{1}{2} u_i u_i \tag{3.16}$$

Similar operations performed on the LES continuity (2.14) and momentum (2.15) equations result in the LES resolved kinetic energy equation:

$$\begin{aligned} \frac{\partial \overline{\rho k^*}}{\partial t} &= -\frac{\partial}{\partial x_i}\left(\overline{\rho k^*}\bar{u}_i\right) - \bar{u}_i \frac{\partial \bar{p}}{\partial x_i} + \bar{u}_i \frac{\partial \bar{t}_{ij}}{\partial x_j} + \bar{u}_i \frac{\partial}{\partial x_j}\left(\bar{\tau}_{ij} - \bar{t}_{ij}\right) - \bar{u}_i \frac{\partial \tau_{ij}^{sgs}}{\partial x_j} \\ &\quad -\bar{u}_i \frac{\partial}{\partial t}\left(\overline{\rho u_i} - \bar{\rho}\bar{u}_i\right) + \frac{\bar{u}_j \bar{u}_j}{2} \frac{\partial}{\partial x_i}\left(\overline{\rho u_i} - \bar{\rho}\bar{u}_i\right) \end{aligned} \tag{3.17}$$

The resolved kinetic energy, $\overline{k^*}$, is defined as:

$$\overline{k^*} = \frac{1}{2} \bar{u}_i \bar{u}_i \tag{3.18}$$

The subgrid kinetic energy equation is formed by filtering equation 3.15 and then subtracting equation 3.17 from the result. After rearranging some terms, the following expression may be written:

$$\begin{aligned}\frac{\partial \bar{\rho} k^{sgs}}{\partial t} &= -\frac{\partial}{\partial x_i}\left(\bar{\rho} k_i^{sgs} \bar{u}_i\right) - \left(\overline{u_i \frac{\partial p}{\partial x_i}} - \bar{u}_i \frac{\partial \bar{p}}{\partial x_i}\right) + \left(\overline{u_i \frac{\partial \tau_{ij}}{\partial x_j}} - \bar{u}_i \frac{\partial \bar{\tau}_{ij}}{\partial x_j}\right) \\ &\quad -\frac{\partial}{\partial x_i}\left(\overline{\rho k u_i} - \bar{\rho}\bar{k}\bar{u}_i\right) + \frac{\partial \bar{u}_j \tau_{ij}^{sgs}}{\partial x_i} - \tau_{ij}^{sgs}\frac{\partial \bar{u}_j}{\partial x_i} \\ &\quad -\frac{\partial}{\partial t}\left(\overline{\rho k} - \bar{\rho}\bar{k}\right) + \bar{u}_i \frac{\partial}{\partial t}\left(\overline{\rho u_i} - \bar{\rho}\bar{u}_i\right) - \frac{\bar{u}_j \bar{u}_j}{2}\frac{\partial}{\partial x_i}\left(\overline{\rho u_i} - \bar{\rho}\bar{u}_i\right) \quad (3.19)\end{aligned}$$

3.4.2 Closure of the Subgrid Kinetic Energy Equation

The above form of the equation contains several terms which require closure. The method used to accomplish this is a compressible extension of the incompressible subgrid k-equation model developed by Kim [67]. In this approach, the right-hand side of the above equation is modelled as the combination of five terms which represent different physical phenomena: resolved convective transport, subgrid transport, production, dissipation, and additional compressibility effects.

The first of these, the resolved convective transport is computed exactly:

$$\text{Convective Transport} = -\frac{\partial}{\partial x_i}\left(\bar{\rho} k_i^{sgs} \bar{u}_i\right) \quad (3.20)$$

All other transport terms are combined and modelled as a single term:

$$\text{Subgrid Transport} \approx \frac{\partial}{\partial x_i}\left(\bar{\rho}\nu_t \frac{\partial k^{sgs}}{\partial x_i}\right) \quad (3.21)$$

The subgrid kinetic energy production rate is computed as:

$$\text{Production} \approx -\tau_{ij}^{sgs^{(i)}} \frac{\partial \bar{u}_j}{\partial x_i} \tag{3.22}$$

The production term is computed using the model for the "incompressible": subgrid stress tensor (equation 3.9).

The viscous subgrid term encompasses two phenomena: dissipation of subgrid kinetic energy and viscous transport. Since the viscous transport is modelled as a part of the general subgrid transport term (3.21), only the dissipation is modelled explicitly. This model, is derived using simple scaling arguments, as:

$$\text{Dissipation} \approx -\overline{\rho} c_\epsilon \frac{(k^{sgs})^{\frac{3}{2}}}{\Delta} \tag{3.23}$$

It should be noted that this dissipation is not identical to the physical dissipation of turbulent kinetic energy. In fact, the modelled subgrid kinetic energy is really only that portion of unresolved energy in the flow which affects the resolved flow. Thus, the dissipation referred to here is the rate at which this energy is either dissipated or transferred to scales too small to affect the resolved flow. Thus, it can be argued that even in an inviscid flow, "dissipation" would be present. This point will be further discussed below.

Finally, the additional effects of compressibility are modelled as:

$$\text{Compressibility Effects} \approx \frac{\partial}{\partial x_i}\left(\bar{\rho}\nu_c \frac{\partial k^{sgs}}{\partial x_i}\right) \tag{3.24}$$

Combining these terms, the modelled subgrid kinetic energy equation may now be written as:

$$\frac{\partial \overline{\rho} k^{sgs}}{\partial t} = -\frac{\partial}{\partial x_i}\left(\bar{\rho} k^{sgs} \bar{u}_i\right) + \frac{\partial}{\partial x_i}\left(\overline{\rho}\left(\nu_t + \nu_c\right)\frac{\partial k^{sgs}}{\partial x_i}\right) - \tau_{ij}^{sgs^{(i)}}\frac{\partial \bar{u}_j}{\partial x_i} - \overline{\rho} c_\varepsilon \frac{\left(k^{sgs}\right)^{\frac{3}{2}}}{\Delta} \tag{3.25}$$

where the "incompressible" subgrid stress tensor, $\tau_{ij}^{sgs^{(i)}}$, is given by equation 3.9, the turbulent viscosity, ν_t, is given by equation 3.11, and the "compressibility viscosity" (ν_c) is given by equation 3.4.

3.4.3 Dynamic Calculation of Model Coefficients

The modelled subgrid kinetic energy equation, as derived above, contains two model coefficients (c_ν and c_ε). Rather than specifying these coefficients, they will be computed dynamically as discussed in the following sections. The idea behind dynamic modeling is to use information from the resolved field to estimate the unresolved effects. The underlying assumption is that the subgrid scales behave very much like the smallest resolved scales. This proposition has been experimentally validated for the subgrid stress tensor by Liu *et al.* [40] for the case of free jets. The subgrid model coefficient is therefore determined by the use of a similarity model. To do this, a "test" filter is defined. This filter (denoted by a circumflex- *e.g.* $\widehat{\phi}$)

must have a characteristic length, $\widehat{\Delta}$, larger than the grid resolution. Usually $\widehat{\Delta}$ is taken to be twice the size of the local grid spacing (Δ), but this is somewhat arbitrary. Tests by Spyropoulos and Blaisdell [15] have shown that the results are relatively insensitive to the characteristic length of the test filter. Coefficients may then be computed by comparing quantities that are resolved in the LES flow field but not by a corresponding "test" filtered field.

The Dissipation Model Coefficient In order to compute the dissipation model coefficient, it is necessary to obtain an expression for the subgrid kinetic energy dissipation rate. In the incompressible subgrid kinetic energy equation, the viscous term is easily split into transport and dissipation components:

$$\overline{u_i \frac{\partial \tau_{ij}}{\partial x_j}} - \bar{u}_i \frac{\partial \bar{\tau}_{ij}}{\partial x_j} = \nu \frac{\partial}{\partial x_j}\left(\frac{\partial k^{sgs}}{\partial x_j}\right) - \nu\left(\overline{\frac{\partial u_i}{\partial x_j}\frac{\partial u_i}{\partial x_j}} - \frac{\partial \bar{u}_i}{\partial x_j}\frac{\partial \bar{u}_i}{\partial x_j}\right) \tag{3.26}$$

The first term on the right hand side is the incompressible subgrid viscous transport, and the second term is the subgrid kinetic energy dissipation rate. A similar rearrangement can be performed for the compressible terms:

$$\overline{u_j \frac{\partial \tau_{ij}}{\partial x_i}} - \bar{u}_j \frac{\partial \bar{\tau}_{ij}}{\partial x_i} = \left(\overline{\frac{\partial u_j \tau_{ij}}{\partial x_i}} - \frac{\partial \bar{u}_j \bar{\tau}_{ij}}{\partial x_i}\right) - \left(\overline{\tau_{ij}\frac{\partial u_j}{\partial x_i}} - \bar{\tau}_{ij}\frac{\partial \bar{u}_j}{\partial x_i}\right) \tag{3.27}$$

The first term on the right-hand side is a transport term, and as such, is included in the "subgrid transport" model term (equation 3.21). The second term governs the dissipation of subgrid kinetic energy. At this point, unfortunately, the situation

becomes less straightforward than for the incompressible equations. The dissipation term may be rewritten as:

$$\begin{aligned}\overline{\tau_{ij}\frac{\partial u_j}{\partial x_i}} - \overline{\tau}_{ij}\frac{\partial \bar{u}_j}{\partial x_i} &= \overline{\left(\mu\left[\frac{\partial u_i}{\partial x_j}+\frac{\partial u_j}{\partial x_i}\right]-\frac{2}{3}\mu\frac{\partial u_k}{\partial x_k}\delta_{ij}\right)\frac{\partial u_j}{\partial x_i}} \\ &\quad - \overline{\left(\mu\left[\frac{\partial u_i}{\partial x_j}+\frac{\partial u_j}{\partial x_i}\right]-\frac{2}{3}\mu\frac{\partial u_k}{\partial x_k}\delta_{ij}\right)}\frac{\partial \bar{u}_j}{\partial x_i} \end{aligned} \tag{3.28}$$

In the incompressible form of the subgrid kinetic energy equation, the viscosity is a constant, and can be taken outside the filtering operations. As mentioned previously, the viscosity is not constant in compressible flows. An approximate expression, for the purposes of modelling, can be constructed by assuming the viscosity to be locally invariant. This is a reasonable assumption except in the presence of extreme mean temperature gradients and is consistent with the treatment of the viscous terms in the momentum equation. Note that the assumption is not that the viscosity is constant throughout the domain, only that the resolved viscous stress tensor ($\bar{t}_{ij}$) is equivalent to the filtered exact stress tensor ($\bar{\tau}_{ij}$). Therefore, the subgrid kinetic energy dissipation term and its model may be written (approximately) as follows:

$$\varepsilon^{\bar{\Delta}} \approx \overline{\tau_{ij}\frac{\partial u_j}{\partial x_i}} - \bar{t}_{ij}\frac{\partial \bar{u}_j}{\partial x_i} \approx \overline{\rho} c_\varepsilon \frac{(k^{sgs})^{\frac{3}{2}}}{\Delta} \tag{3.29}$$

By use of the "test" filter on the resolved field and assuming similarity as discussed above, one can construct an analogous "test-field" dissipation as follows:

$$\varepsilon^{\hat{\Delta}} \approx \widehat{\bar{t}_{ij}\frac{\partial \bar{u}_j}{\partial x_i}} - \widehat{T}_{ij}\frac{\partial \widehat{\bar{u}}_j}{\partial x_i} \approx \frac{c_\epsilon \widehat{\bar{\rho}}}{\widehat{\Delta}}\left(\widehat{\frac{\bar{u}_k \bar{u}_k}{2}} - \frac{\widehat{\bar{u}}_k \widehat{\bar{u}}_k}{2}\right)^{\frac{3}{2}} \tag{3.30}$$

In the above equation, the viscous stresses resolved on the test filtered field are defined as:

$$\widehat{T}_{ij} = \widehat{\bar{\mu}}\left(\frac{\partial \widehat{\bar{u}}_i}{\partial x_j} + \frac{\partial \widehat{\bar{u}}_j}{\partial x_i} - \frac{2}{3}\frac{\partial \widehat{\bar{u}}_k}{\partial x_k}\delta_{ij}\right) \tag{3.31}$$

Note that all of the terms, except the model coefficient, in equation 3.30 can be determined from the resolved field. Therefore, an expression for the coefficient may now be written:

$$c_\epsilon = \frac{\widehat{\Delta}\left(\widehat{\bar{t}_{ij}\frac{\partial \bar{u}_j}{\partial x_i}} - \widehat{T}_{ij}\frac{\partial \widehat{\bar{u}}_j}{\partial x_i}\right)}{\widehat{\bar{\rho}}\left(\widehat{\frac{\bar{u}_k \bar{u}_k}{2}} - \frac{\widehat{\bar{u}}_k \widehat{\bar{u}}_k}{2}\right)^{\frac{3}{2}}} \tag{3.32}$$

In his work, Kim found that the above approach tends to underpredict values of c_ϵ [67]. It may be argued that this is due to the idea, mentioned above, that the subgrid kinetic energy modelled here is only that portion of unresolved turbulence which directly affects the resolved field. Thus, for a high Reynolds number flow (or inviscid flow), the dissipation model should account for more than just the

physical dissipation of turbulent kinetic energy. Kim argued that because the test-filtered "subgrid" kinetic energy contains energy that is resolved on the grid, the "dissipation" of this test-filtered energy is controlled by both the molecular viscosity and the eddy viscosity. Therefore, an alternative expression for this coefficient may be written as:

$$c_\epsilon = \frac{(\bar{\mu} + \mu_t)\,\widehat{\Delta}\left(\widehat{\bar{t}_{ij}\frac{\partial \bar{u}_j}{\partial x_i}} - \widehat{T}_{ij}\frac{\partial \widehat{\bar{u}}_j}{\partial x_i}\right)}{\bar{\mu}\widehat{\bar{\rho}}\left(\frac{\widehat{\bar{u}_k\bar{u}_k}}{2} - \frac{\widehat{\bar{u}}_k\widehat{\bar{u}}_k}{2}\right)^{\frac{3}{2}}} \tag{3.33}$$

The turbulent viscosity in the above equation is computed as $\bar{\rho}\nu_t$, where ν_t is given by equation 3.11. The effect of this modification (and whether or not it is needed) is discussed in later chapters.

The Subgrid Stress Tensor Model Coefficient The process for determining the coefficient (c_ν) in the subgrid stress tensor model is similar to that shown above. For the first approach mentioned in section 3.3, this is as follows. First, the trace-free portion of the "incompressible" subgrid stress tensor and its model (equations 2.21 and 3.9) are written:

$$\bar{\rho}\left(\overline{u_i u_j} - \bar{u}_i\bar{u}_j\right) - \frac{1}{3}\bar{\rho}\left(\overline{u_k u_k} - \bar{u}_k\bar{u}_k\right)\delta_{ij} \approx -2c_\nu\bar{\rho}\nu_t\left(\bar{S}_{ij} - \frac{1}{3}\bar{S}_{kk}\delta_{ij}\right) \tag{3.34}$$

Next, using the "test" filter and assuming similarity as in section 3.4.3, an analogous "test-field" expression may be written:

$$\begin{aligned} & \widehat{\bar{\rho}}\left(\widehat{\bar{u}_i\bar{u}_j} - \widehat{\bar{u}}_i\widehat{\bar{u}}_j\right) - \frac{1}{3}\widehat{\bar{\rho}}\left(\widehat{\bar{u}_k\bar{u}_k} - \widehat{\bar{u}}_k\widehat{\bar{u}}_k\right)\delta_{ij} \\ \approx\ & -2c_\nu\widehat{\Delta}\widehat{\bar{\rho}}\left(\frac{\widehat{\bar{u}_k\bar{u}_k}}{2} - \frac{\widehat{\bar{u}}_k\widehat{\bar{u}}_k}{2}\right)^{\frac{1}{2}}\left(\widehat{\bar{S}}_{ij} - \frac{\widehat{\bar{S}}_{kk}}{3}\delta_{ij}\right) \end{aligned} \tag{3.35}$$

The "test" field resolved rate of strain tensor in equation 3.35 is defined as:

$$\widehat{\bar{S}}_{ij} = \frac{1}{2}\left[\frac{\partial\widehat{\bar{u}}_i}{\partial x_j} + \frac{\partial\widehat{\bar{u}}_j}{\partial x_i}\right] \tag{3.36}$$

Equation 3.35 is actually overspecified since there are six independent tensor components, but only one unknown (c_ν). Thus, it must be contracted. The current work follows the approach of Lilly [87], who used a least squares approach to obtain an expression for the dynamic coefficient of a Germano [42] algebraic model. The first step is to write an expression for the model error:

$$\begin{aligned} \mathrm{E}_{ij} \ =\ & \widehat{\bar{\rho}}\left(\widehat{\bar{u}_i\bar{u}_j} - \widehat{\bar{u}}_i\widehat{\bar{u}}_j\right) - \frac{1}{3}\widehat{\bar{\rho}}\left(\widehat{\bar{u}_k\bar{u}_k} - \widehat{\bar{u}}_k\widehat{\bar{u}}_k\right)\delta_{ij} \\ & +2c_\nu\widehat{\Delta}\widehat{\bar{\rho}}\left(\frac{\widehat{\bar{u}_k\bar{u}_k}}{2} - \frac{\widehat{\bar{u}}_k\widehat{\bar{u}}_k}{2}\right)^{\frac{1}{2}}\left(\widehat{\bar{S}}_{ij} - \frac{\widehat{\bar{S}}_{kk}}{3}\delta_{ij}\right) \end{aligned} \tag{3.37}$$

This can be written in simplified form as:

$$\mathrm{E}_{ij} = L_{ij} + 2c_\nu D_{ij} \tag{3.38}$$

$$\text{where } L_{ij} = \widehat{\bar{\rho}}\left(\widehat{\bar{u}_i\bar{u}_j} - \widehat{\bar{u}}_i\widehat{\bar{u}}_j\right) - \frac{1}{3}\widehat{\bar{\rho}}\left(\widehat{\bar{u}_k\bar{u}_k} - \widehat{\bar{u}}_k\widehat{\bar{u}}_k\right)\delta_{ij} \tag{3.39}$$

$$\text{and } D_{ij} = \widehat{\Delta}\widehat{\bar{\rho}}\left(\frac{\widehat{\bar{u}_k\bar{u}_k}}{2} - \frac{\widehat{\bar{u}}_k\widehat{\bar{u}}_k}{2}\right)^{\frac{1}{2}}\left(\widehat{\bar{S}}_{ij} - \frac{\widehat{\bar{S}}_{kk}}{3}\delta_{ij}\right) \tag{3.40}$$

Next, the error is contracted with itself to form:

$$\mathrm{E}_{ij}\mathrm{E}_{ij} = L_{ij}L_{ij} + 4c_\nu D_{ij}L_{ij} + 4c_\nu^2 D_{ij}D_{ij} \tag{3.41}$$

In order for the RMS of the error to be a minimum, the derivative of equation 3.41 with respect to the model coefficient must be zero:

$$\frac{\partial \mathrm{E}_{ij}\mathrm{E}_{ij}}{\partial c_\nu} = 0 = 4D_{ij}L_{ij} + 8c_\nu D_{ij}D_{ij} \tag{3.42}$$

Using the above expression, the model coefficient can now be computed:

$$c_\nu = \frac{-L_{ij}D_{ij}}{2D_{ij}D_{ij}} \tag{3.43}$$

Because only positive filters are used in this work (*i.e.* the filter function, G, in equation 2.10 is always positive), the so-called "incompressible" part of the subgrid stress tensor must be positive semidefinite. Therefore, the model coefficient, c_ν, is constrained such that the resulting modelled tensor, $\tau_{ij}^{sgs^{(i)}}$ has this property. The conditions which enforce this are known as the "realizability" conditions [88]. These may be stated as follows:

$$\tau_{\alpha\alpha}^{sgs^{(i)}} \geq 0 \text{ for } \alpha \in \{1,2,3\} \tag{3.44a}$$

$$\left|\tau_{\alpha\beta}^{sgs^{(i)}}\right|^2 \leq \tau_{\alpha\alpha}^{sgs^{(i)}} \tau_{\beta\beta}^{sgs^{(i)}} \text{ for } \alpha,\beta \in \{1,2,3\} \tag{3.44b}$$

$$\det\left(\tau_{ij}^{sgs^{(i)}}\right) \geq 0 \tag{3.44c}$$

Note that, unlike conventional tensor notation, repeated indices in the above expressions do not indicate summation.

For well-resolved, fully developed turbulent flows, these constraints have been found to require adjustments to c_ν at fewer than five percent of the grid points at any given time. Frequently, less than one percent need adjusting. In several isotropic cases, by the end of the simulation, only a handful of points (or none at all) were being affected. Some of the spatial cases, however, required more adjustment. This is attributed to the imperfect turbulent inflow conditions as well as the coarseness of the grid away from the region of interest. Within the core regions, very little adjustment of this nature was required.

In addition, since the concept of negative viscosity is dubious at best (in theory) and numerically destabilizing (in practice), the subgrid stress tensor model coeffi-

cient is constrained so that the resulting effective viscosity is positive:

$$\nu_{eff} = \nu + \nu_t \geq 0 \tag{3.45}$$

3.5 Closure of the LES Energy Equation

While much work has been published on the closure of the LES momentum equation, the LES energy equation (2.17) has received comparatively little attention. Erlebacher *et al.* [56] proposed a model which involved splitting the subgrid heat flux into Leonard, cross, and Reynolds heat fluxes. This author, however, is unaware of any detailed examination of this model. Moin *et al.* [57] proposed an eddy diffusion model for the entire term. They also used a dynamic model coefficient which was computed after the fashion of Germano *et al.* [42]. This technique, though very powerful, proved to be somewhat unstable and required *ad hoc* averaging. Again, not many results were presented which dealt specifically with the energy closure. Spyropoulos and Blaisdell [15] also used this model; in addition, they compared dynamic coefficients calculated by the method of Germano *et al.* with those computed using Lilly's [87] least squares technique. They reported that, considering the simulations as a whole, Lilly's method gave slightly better answers than the original Germano technique, but still an *ad hoc* averaging was used to prevent numerical instability. The temperature spectra that were presented indicate, however, that the model was appropriately preventing the buildup of temperature oscillations in high wavenumbers. The present work uses a similar approach, but as will be shown, the coefficient is computed in a purely local fashion.

3.5.1 Derivation of the LES Energy Equation Model

The LES energy equation (2.17), as mentioned above, has several terms that require closure. Using the definition of total enthalpy,

$$H = E + \frac{p}{\rho} \tag{3.46}$$

two of these subgrid terms can be combined as follows:

$$-\frac{\partial}{\partial x_i}\left(\overline{\rho E u_i} - \bar{\rho}\tilde{E}\tilde{u}_i\right) - \frac{\partial}{\partial x_i}\left(\overline{p u_i} - \bar{p}\bar{u}_i\right) = -\frac{\partial}{\partial x_i}\left(\overline{\rho H u_i} - \bar{\rho}\tilde{H}\tilde{u}_i\right) \tag{3.47}$$

This term is then split (similar to the subgrid stress tensor) into an "incompressible" component and a "compressible" part:

$$\frac{\partial}{\partial x_i}\left(\overline{\rho H u_i} - \bar{\rho}\tilde{H}\tilde{u}_i\right) = \frac{\partial}{\partial x_i}\bar{\rho}\left(\overline{H u_i} - \tilde{H}\tilde{u}_i\right) + \frac{\partial}{\partial x_i}\left(\overline{\rho H u_i} - \bar{\rho}\overline{H u_i}\right) \tag{3.48}$$

Obviously, since the energy equation is generally not considered in incompressible flows, both components are, in this sense, "compressible." The "compressible" term (the second term on the right-hand side of the above equation), however, is entirely dependant on the variation of density. In regions of uniform density, this term vanishes, whereas the "incompressible" term, being less dependant on density fluctuations, may remain.

The "incompressible" portion of the above subgrid term is modelled, in a similar manner as in the Favre filtering approach, using an eddy diffusion assumption, as:

$$E_i^{sgs^{(i)}} = \bar{\rho}\left(\overline{Hu_i} - \bar{H}\bar{u}_i\right) \approx -c_e\bar{\rho}\sqrt{k^{sgs}}\Delta\frac{\partial\tilde{H}}{\partial x_i} \tag{3.49}$$

In this model, the coefficient, c_e, combines the subgrid stress tensor model coefficient and the turbulent Prandtl number that were present in the other models mentioned above. This greatly reduces the numerical instability of the model when c_e is computed dynamically.

As was done with the momentum equation, the effect of the "compressible" term is combined with all the other compressibility effects in the energy equation and modelled as a single term. This term, as with similar terms in the continuity and momentum equations, is assumed to be small away from regions of sharp density gradients. This is illustrated for the case of $E_x^{sgs^{(c)}}$ in figure 3.12. Note that this is only one part of this term, but the others, also arising from the differences between Favre and "straight" filtering, show a similar behavior. Again, the DNS data used to compute this term is the same as was used in previous sections.

Similar to the effects of compressibility in the other equations, this combined term is expected to have a dissipative effect on the flowfield. Note, however, that total enthalpy is generally constant through a shock. Thus, derivatives of total enthalpy are inappropriate scaling quantities for modelling these terms. Therefore the additional effects of compressibility are modelled as an additional heat conduc-

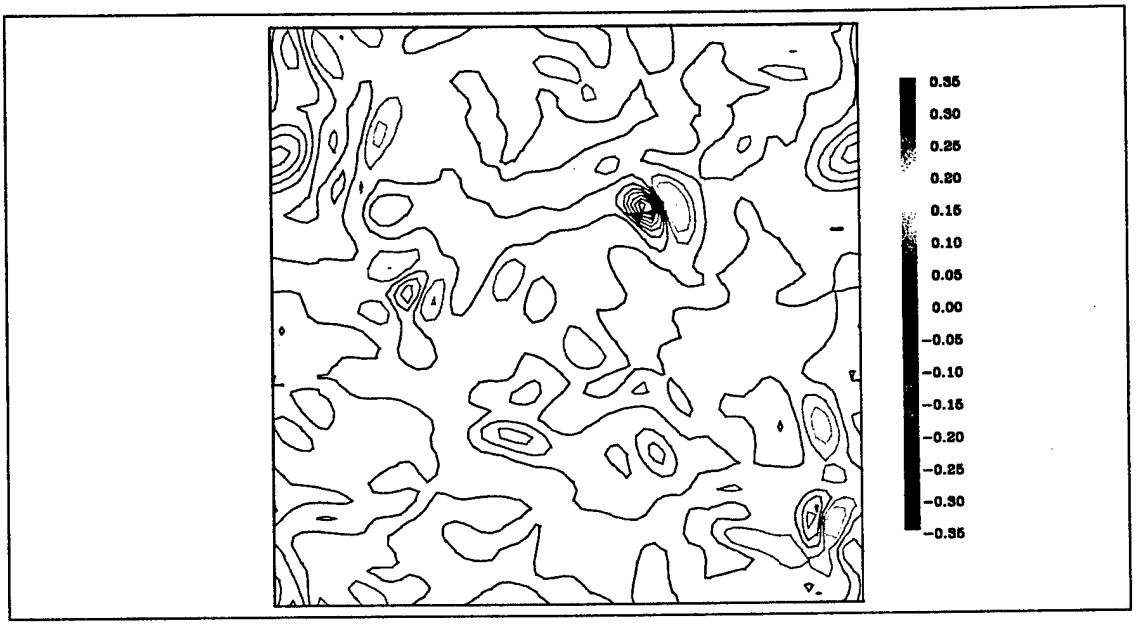


Figure 3.12: Contours of $E_x^{sgs^{(c)}}$ normalized by reference quantities $(\rho_{ref} H_{ref} u_{ref})$ as estimated from a DNS of compressible decaying isotropic turbulence

tion term in the following manner:

$$\text{Compressibility Effects} \approx -\frac{\gamma c_v \bar{\rho} \nu_c}{\text{Pr}} \frac{\partial \bar{T}}{\partial x_i} \tag{3.50}$$

In the above equation, ν_c, is the same "compressibility" viscosity that was used previously (equation 3.4). Despite the similar appearance, the specific heat at constant volume, c_v, in the above expression, should not be confused with the subgrid stress tensor model coefficient, c_ν.

The next term to be dealt with is the thermal conduction subgrid term $(\frac{\partial}{\partial x_i}\left(\overline{\kappa \frac{\partial T}{\partial x_i}} - \bar{\kappa}\frac{\partial \bar{T}}{\partial x_i}\right))$. Similar to the assumptions made in section 3.4.3, the thermal

conductivity is assumed to be locally constant. Under these conditions, the conduction subgrid term vanishes; therefore, it is neglected. In addition, the subgrid viscous transport term is also neglected. This is a reasonable assumption for high Reynolds number flows. In such conditions, viscous terms are generally small relative to convective terms, and the viscous subgrid transport term is smaller still.

Thus the modelled LES energy equation may now be written as:

$$\begin{aligned}\frac{\partial \bar{\rho}\bar{E}}{\partial t} &= -\frac{\partial}{\partial x_i}\left(\bar{\rho}\bar{E}+\bar{p}\right)\bar{u}_i + \frac{\partial}{\partial x_i}\left(c_e\bar{\rho}\sqrt{k^{sgs}}\Delta\frac{\partial \bar{H}}{\partial x_i}\right) + \frac{\partial}{\partial x_i}\left(\bar{u}_j\bar{t}_{ij}\right) \\ &\quad + \frac{\partial}{\partial x_i}\left(\left[\bar{\kappa}+\frac{\gamma c_v \bar{\rho}\nu_c}{\mathrm{Pr}}\right]\frac{\partial \bar{T}}{\partial x_i}\right) \end{aligned} \tag{3.51}$$

3.5.2 Dynamic Computation of the Energy Equation Subgrid Model Coefficient

The method for dynamically computing c_e is similar to that described in section 3.4.3. By assuming similarity between the subgrid and the highest resolved wavenumbers, the following expression may be written:

$$\hat{\bar{\rho}}\left(\widehat{\bar{H}\bar{u}_i} - \hat{\bar{H}}\hat{\bar{u}}_i\right) \approx -c_e\hat{\bar{\rho}}\left(\frac{\widehat{\bar{u}_k\bar{u}_k}}{2} - \frac{\hat{\bar{u}}_k\hat{\bar{u}}_k}{2}\right)^{\frac{1}{2}}\hat{\Delta}\frac{\partial \hat{\bar{H}}}{\partial x_i} \tag{3.52}$$

As with the derivation of the dynamic subgrid stress tensor model coefficient (equation 3.35), the above equation is overspecified. Thus, as before, a least squares method is used to contract it so that a single equation for the model coefficient, c_e,

may be obtained. First, the error in equation 3.52 is written as:

$$E_i = n_i + c_e d_i \tag{3.53}$$

$$\text{where } n_i = \widehat{\bar{\rho}}\left(\widehat{\bar{H}\bar{u}_i} - \widehat{\bar{H}}\widehat{\bar{u}_i}\right) \tag{3.54}$$

$$d_i = \widehat{\bar{\rho}}\left(\frac{\widehat{\bar{u}_k\bar{u}_k}}{2} - \frac{\widehat{\bar{u}}_k\widehat{\bar{u}}_k}{2}\right)^{\frac{1}{2}} \widehat{\Delta}\frac{\partial\widehat{\bar{H}}}{\partial x_i} \tag{3.55}$$

Next, the error, E_i, is contracted with itself to yield:

$$E_i E_i = n_i n_i + 2c_e n_i d_i + c_e^2 d_i d_i \tag{3.56}$$

As before, to minimize the error, the derivative of this equation with respect to the model coefficient must be zero:

$$\frac{\partial E_i E_i}{\partial c_e} = 0 = 2n_i d_i + 2c_e d_i d_i \tag{3.57}$$

Solving this equation for c_e yields:

$$c_e = \frac{n_i d_i}{d_i d_i} \tag{3.58}$$

Chapter IV

Numerical Scheme

Several algorithms were examined in an effort to find an appropriate numerical method for the solution of the LES equations for the problems to be examined in this dissertation. The methods that were evaluated were a standard MacCormack scheme [89], the so-called MacCormack 2-4 method of Gottlieb and Turkel [90], a new MacCormack-type 2-4 schème, a 2nd order Steger-Warming flux vector splitting method [91], and two Advection Upstream Splitting Method (AUSM) schemes [92]: a 3rd order and a 5th order [93]. In tests of decaying homogeneous isotropic turbulence, the two 2-4 schemes were found to be superior to the other methods examined. For the classes of problems investigated in this work, the other methods were found to be significantly less accurate and more dissipative, with the result that the turbulent structures were unacceptably "smeared."

An example of the effect of numerical dissipation is shown in figure 4.1, which plots the decay of resolved kinetic energy as predicted by the higher order MacCormack-type schemes and the 5th order AUSM scheme- all run without any subgrid models- as compared to the experimental results of Comte-Bellot and Corrsin. For more details about this case, see Section 5.2.2. Without a model, the 2-4 schemes show significantly less energy decay than the experiment predicted, but the AUSM scheme, because of it's much higher level of numerical dissipation, obtains results which mimic the experiment. If one could rely on the numerical scheme's dissipation

to damp the resolved energy at the correct rate, then subgrid models would be unnecessary. Unfortunately, there are no guarantees that this will take place. In this case, for example, while the resolved energy is being dissipated as the solution progresses, AUSM's results do not match the experiment. Thus a subgrid model is still necessary. If the cell Reynolds number can be kept low enough, the effects of numerical dissipation will remain sufficiently small that the subgrid model can still function. The Reynolds number for this case, for instance, while high enough to make DNS difficult, is still comparatively low, and the numerical dissipation has not exceeded the actual dissipation observed in the experiment. For a truly high Reynolds number flow, however, it is easy to see that the dissipation in the AUSM scheme would overwhelm the viscous and turbulent forces to the extent that no subgrid model could compensate enough to obtain the correct results.

Of course, there is an almost limitless supply of other schemes which could be considered. In particular, Essentially Non-Oscillatory (ENO) schemes might perform well for the types of problems of interest here [94], but due to time constraints, they have not been examined. Also, recent work with Dispersion-Relation-Preserving (DRP) schemes at NASA Lewis has shown great promise for acoustic applications [95], with work beginning on applying these schemes to LES. Again, due to time constraints, these have not been examined.

The MacCormack 2-4 method has been used by numerous researchers for a variety of problems since it was introduced. When they introduced the scheme, Gottlieb and Turkel [90] demonstrated it on one-dimensional wave propagation and shock problems. Turkel [96] presented similar one-dimensional results, and also reported the results of some two-dimensional simulations: the linear equation of elasticity and the linearized magnetohydrodynamic equations. In 1985, Bayliss *et*

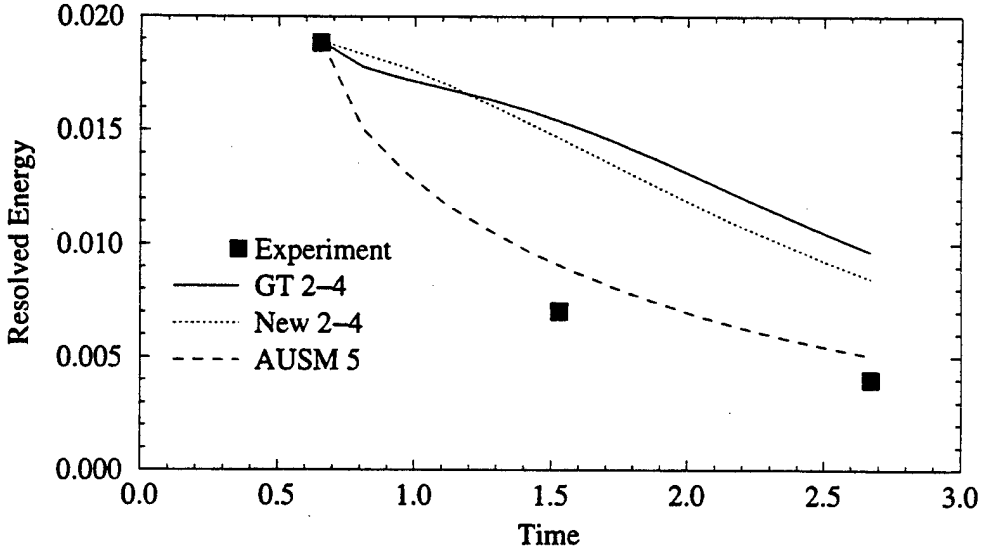


Figure 4.1: Resolved kinetic energy predicted by various numerical schemes run without subgrid models compared with the experimental results of Comte-Bellot and Corrsin

al. [97] applied the scheme to the compressible Navier-Stokes equations; two solutions were discussed: the steady-state solution of a supersonic flat plate boundary layer and the propagation of a disturbance through a subsonic flat plate boundary layer. Hariharan and Lester [98] used such an algorithm to study acoustic shocks in variable area ducts. Tang, Komerath, and Sankar [99], as well as Tuncer and Sankar [100], simulated laminar supersonic spatial mixing layers using this method. In addition, Comte *et al.* [101] used such a code for direct simulation of temporal (compressible) mixing layers. Similarly, Sheen, Sreedhar, and Ragab [102] applied the algorithm to LES of temporal mixing layers.

The Gottlieb and Turkel algorithm has also been widely used in the field of computational aeroacoustics. Some examples from one recent conference include papers by Martin [103]; Scott, Hariharan, and Mankbadi [104]; Viswanathan and Sankar [105]; and Hudson and Long [106]. Another example is the work of Gamet and Estivalezes [107], who applied the scheme to the aeroacoustics of jets. Thus, the MacCormack 2-4 method (sometimes augmented with artificial dissipation) has been found to provide reasonable stability without unduly sacrificing accuracy in a wide variety of applications. Therefore it was chosen as the basis for the algorithm used in this work.

The Gottlieb and Turkel 2-4 method, as it was originally presented, is inapplicable to finite volume solvers on generalized grids. Gamet and Estivalezes [107] describe an equivalent reformulation of the algorithm which does not have this problem. The current work uses a similar approach.

4.1 Derivation of the New 2-4 Method

To start with, consider the following one-dimensional (in space) equation:

$$\frac{\partial q}{\partial t} + \frac{\partial f}{\partial x} = 0 \tag{4.1}$$

For the above model equation, the MacCormack family of predictor-corrector algorithms may be written as:

$$q_i^* = q_i^n - \frac{\Delta t}{\Delta x}\left(f_{i+\frac{1}{2}}^{+(n)} - f_{i-\frac{1}{2}}^{+(n)}\right) \tag{4.2a}$$

$$q_i^{n+1} = \frac{1}{2}\left[q_i^n + q_i^* - \frac{\Delta t}{\Delta x}\left(f_{i+\frac{1}{2}}^{-(*)} - f_{i-\frac{1}{2}}^{-(*)}\right)\right] \tag{4.2b}$$

The above algorithm is written with forward differencing (denoted by the "+" superscript) on the predictor step and backward differencing (denoted by the "−" superscript) on the corrector step. For time dependant problems, alternate iterations would use backward differencing first, followed by forward differencing on the corrector step in order to minimize any biasing due to the differencing.

4.1.1 The Original MacCormack Scheme

If the original second order MacCormack scheme is to be implemented, then the values of the fluxes at the cell faces are given as:

$$f_{i+\frac{1}{2}}^{+} = f_{i+1} \tag{4.3a}$$

$$f_{i+\frac{1}{2}}^{-} = f_i \tag{4.3b}$$

In order to investigate the order of the scheme, the model equation is linearized by setting

$$f = Aq \tag{4.4}$$

where A is a constant propagation speed. First, equation 4.4 is substituted into equation 4.3. Next, the resulting expressions are substituted into equation 4.2, which is in turn rewritten as a single step algorithm which takes q^n and yields q^{n+1}. After rearranging some terms and making use of Taylor series expansions, the second order MacCormack scheme applied to the linearized model equation can now be shown to be equivalent to an exact solution of the following equation:

$$\frac{\partial q}{\partial t} + \frac{\partial f}{\partial x} = -\frac{\Delta t^2}{6}\frac{\partial^3 q}{\partial t^3} - \frac{\Delta x^2}{6}\frac{\partial^3 f}{\partial x^3} - \frac{\Delta t\,\Delta x^2 A}{24}\frac{\partial^4 f}{\partial x^4} + H.O.T. \tag{4.5}$$

The terms on the right hand side of the above equation represents the truncation error of the scheme. Thus, the original MacCormack scheme is seen to be second order accurate in time and space.

4.1.2 The Gottlieb-Turkel Algorithm

If a higher order scheme is desired, then the values at the faces are extrapolated in such a manner that, when the predictor and corrector steps (equations 4.2a and 4.2b) are combined, the spatial operator becomes a central difference derivative of the desired order. Thus, for a scheme equivalent to the Gottlieb and Turkel

algorithm, one would use:

$$f^+_{i+\frac{1}{2}} = \frac{1}{6}(7f_{i+1} - f_{i+2}) \tag{4.6a}$$

$$f^-_{i+\frac{1}{2}} = \frac{1}{6}(7f_i - f_{i-1}) \tag{4.6b}$$

An expression analogous to equation 4.5 may be obtained for the Gottlieb-Turkel algorithm:

$$\frac{\partial q}{\partial t} + \frac{\partial f}{\partial x} = -\frac{\Delta t^2}{6}\frac{\partial^3 q}{\partial t^3} - \frac{\Delta t \Delta x^2 A}{18}\frac{\partial^4 f}{\partial x^4} + \frac{\Delta x^4}{30}\frac{\partial^5 f}{\partial x^5} + H.O.T. \tag{4.7}$$

Again, the right hand side represents the truncation error of the scheme. Thus the Gottlieb-Turkel algorithm is seen to be second order accurate in time. In space, the leading error term ($\frac{\Delta t \Delta x^2 A}{18}\frac{\partial^4 f}{\partial x^4}$) is not so straightforward due to the presence of Δt in the expression. The time step is related to the grid spacing by the CFL condition:

$$\Delta t = CFL\frac{\Delta x}{A} \tag{4.8}$$

After substituting the above expression into equation 4.7, one obtains:

$$\frac{\partial q}{\partial t} + \frac{\partial f}{\partial x} = -\frac{\Delta t^2}{6}\frac{\partial^3 q}{\partial t^3} - CFL\frac{\Delta x^3}{18}\frac{\partial^4 f}{\partial x^4} + \frac{\Delta x^4}{30}\frac{\partial^5 f}{\partial x^5} + H.O.T. \tag{4.9}$$

For explicit schemes, such as this one, $CFL \simeq 1$. Thus, the leading spatial error is seen to be third order. Therefore, the MacCormack "2-4" scheme is actually a "2-3" scheme.

4.1.3 The New 2-4 Scheme

The extrapolations shown in equation 4.6 are not the only ones possible. A new scheme has been developed which uses the following interpolations to obtain fluxes at cell faces:

$$f^+_{i+\frac{1}{2}} = \frac{1}{6}(2f_i + 5f_{i+1} - f_{i+2}) \tag{4.10a}$$

$$f^-_{i+\frac{1}{2}} = \frac{1}{6}(2f_{i+1} + 5f_i - f_{i-1}) \tag{4.10b}$$

A differential equation which corresponds to this scheme as applied to the linearized model problem may be expressed as:

$$\frac{\partial q}{\partial t} + \frac{\partial f}{\partial x} = -\frac{\Delta t^2}{6}\frac{\partial^3 q}{\partial t^3} + \frac{\Delta x^4}{30}\frac{\partial^5 f}{\partial x^5} - \frac{\Delta t \Delta x^4 A}{30}\frac{\partial^6 f}{\partial x^6} + H.O.T. \tag{4.11}$$

From the above equation, it is observed that the new 2-4 scheme is second order accurate in time and fourth order accurate in space.

4.1.4 Computing Viscous Terms

The above examples dealt only with convection terms. If the equation to be solved includes a viscous term, the current scheme adds in the viscous flux to the

convective flux in such a way that when the predictor and corrector steps are combined, the viscous term will recover a fourth order central difference form. To demonstrate this, consider the following linear equation:

$$\frac{\partial q}{\partial t} + A\frac{\partial q}{\partial x} - \mu\frac{\partial^2 q}{\partial x^2} = 0 \tag{4.12}$$

For the above equation, the viscous contribution to the fluxes is:

$$f^+_{v_{i+\frac{1}{2}}} = -\frac{\mu}{6\Delta x}\left(-q_{i+2} + 8q_{i+1} - 7q_i\right) \tag{4.13a}$$

$$f^-_{v_{i+\frac{1}{2}}} = -\frac{\mu}{6\Delta x}\left(q_{i-1} - 8q_i + 7q_{i+1}\right) \tag{4.13b}$$

Computing an equivalent differential equation for this case yields:

$$\begin{aligned}\frac{\partial q}{\partial t} + A\frac{\partial q}{\partial x} - \mu\frac{\partial^2 q}{\partial x^2} = & -\frac{\Delta t^2}{6}\frac{\partial^3 q}{\partial t^3} + A\frac{\Delta x^4}{30}\frac{\partial^5 q}{\partial x^5} - A^2\frac{\Delta t \Delta x^4}{30}\frac{\partial^6 q}{\partial x^6} \\ & -\mu^2\frac{\Delta t \Delta x^2}{72}\frac{\partial^6 q}{\partial x^6} + \mu\frac{\Delta x^4}{90}\frac{\partial^6 q}{\partial x^6} + \mu A\frac{7\Delta t \Delta x^4}{120}\frac{\partial^7 q}{\partial x^7} \\ & + H.O.T.\end{aligned} \tag{4.14}$$

In this form the scheme's order of accuracy is not readily apparent. Thus, the above equation will be rewritten using equation 4.8 and the following definition of the cell

Reynolds number:

$$R_{e_{\Delta x}} = \frac{A\Delta x}{\mu} \tag{4.15}$$

After the previously mentioned substitutions and rearranging some terms, equation 4.14 may be expressed as:

$$\begin{aligned} 0 \;=\; & \left(\frac{\partial q}{\partial t} + \frac{\Delta t^2}{6}\frac{\partial^3 q}{\partial t^3}\right) + A\left(\frac{\partial q}{\partial x} - \frac{\Delta x^4}{30}\frac{\partial^5 q}{\partial x^5} + CFL\frac{\Delta x^5}{30}\frac{\partial^6 q}{\partial x^6}\right) \\ & -\mu\left(\frac{\partial^2 q}{\partial x^2} + \frac{CFL\,\Delta x^4}{72R_{e_{\Delta x}}}\frac{\partial^6 q}{\partial x^6} - CFL\frac{7\Delta x^5}{120}\frac{\partial^7 q}{\partial x^7}\right) + H.O.T. \end{aligned} \tag{4.16}$$

From this expression, it can be seen that the scheme remains strictly fourth order accurate in space as long as the cell Reynolds number is greater than the CFL number (which is typically 0.25).

4.1.5 Modification of the New 2-4 Scheme for Generalized Coordinate Systems

All of the above derivations have implicitly assumed that the grid spacing was uniform. If the grid stretching rate is small, the error introduced by the nonuniform mesh is limited. Unfortunately, for three-dimensional problems of general interest, one can rarely afford a grid with a maximum stretching of no more than four to six percent. On grids with severe stretching, the error thus introduced can even cause the code to crash (with either the new 2-4 scheme or the Gottlieb-Turkel algorithm). Therefore a modified interpolation has been developed which attempts to take into

account the nonuniform distribution of grid points:

$$f^{+}_{i+\frac{1}{2}} = \frac{1}{3}\left[2\left(1-\frac{\Delta_i^{(1)}}{\Delta_i}\right)f_i + \left(1+\frac{\Delta_i-\Delta_i^{(1)}}{\Delta_{i+1}}+2\frac{\Delta_i^{(1)}}{\Delta_i}\right)f_{i+1} - \frac{\Delta_i-\Delta_i^{(1)}}{\Delta_{i+1}}f_{i+2}\right] \tag{4.17a}$$

$$f^{-}_{i+\frac{1}{2}} = \frac{1}{3}\left[2\left(1-\frac{\Delta_i-\Delta_i^{(1)}}{\Delta_i}\right)f_{i+1} + \left(1+\frac{\Delta_i^{(1)}}{\Delta_{i-1}}+2\frac{\Delta_i-\Delta_i^{(1)}}{\Delta_i}\right)f_i - \frac{\Delta_i^{(1)}}{\Delta_{i-1}}f_{i-1}\right] \tag{4.17b}$$

In the above equations (see figure 4.2), Δ_i is the distance from the cell center at point i to the cell center at $i+1$, and $\Delta_i^{(1)}$ is the distance from the cell center at i to the cell face at $i+\frac{1}{2}$. Note that the above expression reduces to equation 4.10 in the limit as $\Delta_i \rightarrow \Delta$ and $\Delta_i^{(1)} \rightarrow \frac{\Delta}{2}$.

4.1.6 Strengths and Weaknesses of the New 2-4 Scheme

This method has several advantages over the original Gottlieb-Turkel algorithm. First, it is truly fourth order accurate in space (for uniform grids), while the Gottlieb-Turkel algorithm is technically only third order accurate. Also, with the implementation of the variable grid interpolation, the new scheme is more accurate and stable on curvilinear grids. Also, the current scheme is less dissipative than the original 2-4 scheme, which is especially important when simulating time-dependant phenomena such as turbulence. This very lack of dissipation, however, is the scheme's Achilles' heel, because it leads to instability at high Reynolds numbers.

A linear stability analysis has been performed, and the results are plotted in figure 4.3. As can be seen in the plot, as the cell Reynolds number becomes large, the maximum stable CFL number becomes steadily smaller for the new scheme,

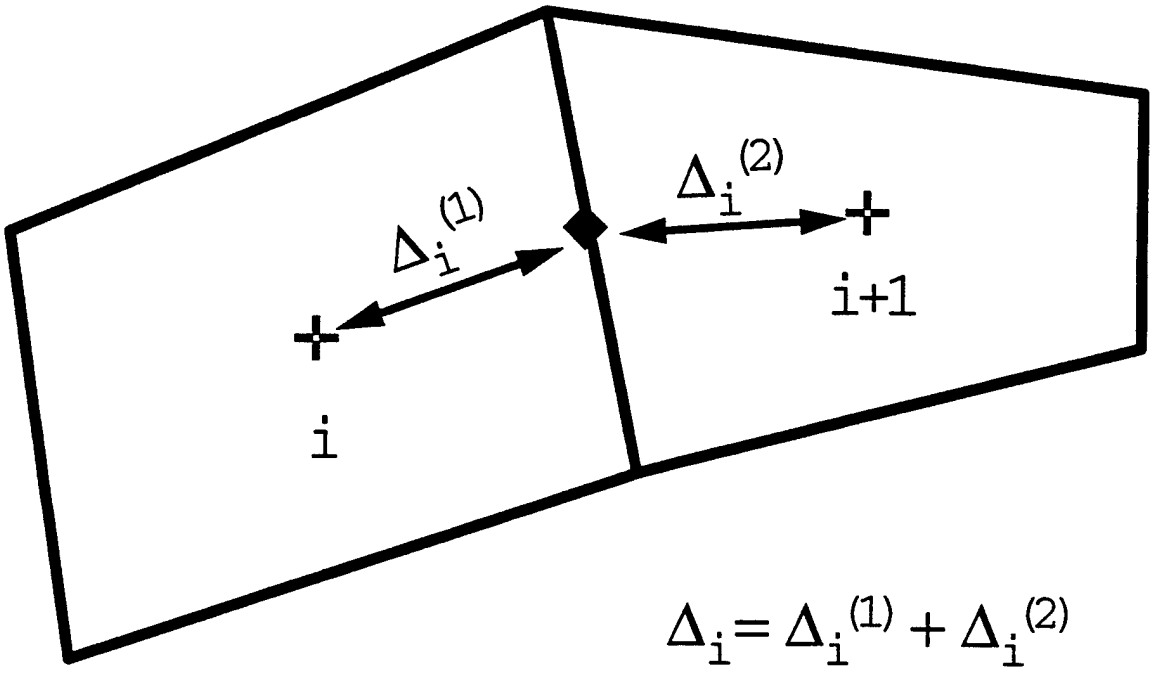


Figure 4.2: Schematic of curvilinear grid spacing definitions

whereas the Gottlieb-Turkel algorithm maintains roughly the same level of stability throughout the region that was investigated. For many applications, this would be an unacceptable limitation, but for LES, this weakness may in fact be a strength. In an LES, the subgrid model is supposed to account for the unresolved scales of motion by transferring energy from the resolved scales to the subgrid at the proper rate. In the absence of a subgrid model (as was the case for figure 4.3), energy should build up at the smallest resolved scales. Thus, the physics of a high Reynolds number flow should make the scheme increasingly unstable.

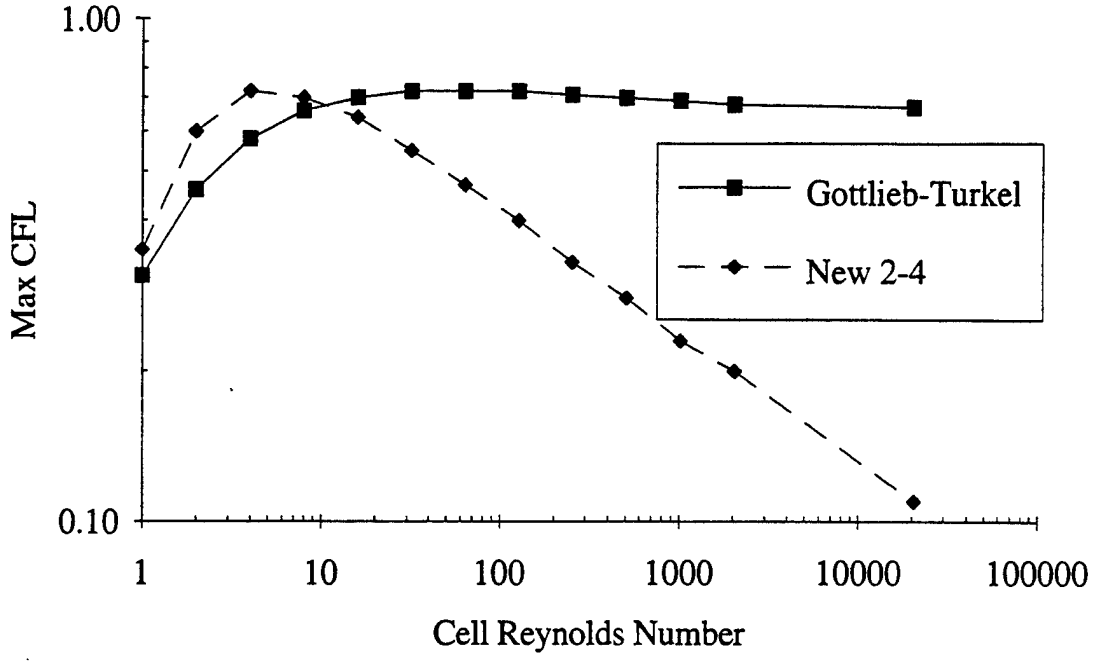


Figure 4.3: Comparison of Linear Stability Limits of the New 2-4 Scheme with the Gottlieb-Turkel Algorithm

4.2 Implementation of the New 2-4 Scheme in a Three Dimensional Compressible LES Code

The algorithm described in the previous section has been implemented in a finite volume sense to solve the modelled compressible LES equations (3.7, 3.14, 3.51, and 3.25) for three dimensional flows. Since finite volume schemes are well known, the details of the implementation will not be discussed except to deal with those issues which are not necessarily obvious.

In computing the cell-face fluxes (both viscous and inviscid), this code interpolates the conserved quantities (*e.g.*, density and momentum) from cell centers to cell

faces using equation 4.17. Any quantities which are needed at the cell faces (*e.g.*, velocity and temperature) are then computed from these interpolated conserved variables.

Viscous derivatives in the direction normal to the cell face are computed as shown in equation 4.13. Rather than having different metrics for the forward- and backward-biased face-normal derivatives, a single "average" metric is computed that represents the combined effect of the predictor and corrector steps. On an i-face, for example, the following metric would be used:

$$\left(\frac{\partial x}{\partial \xi}\right)_{i-face} = \frac{-x_{i+2} + 15\left(x_{i+1} - x_{i-1}\right) + x_{i-2}}{12} \tag{4.18}$$

For such a scheme, in the limit of the linear case, the viscous terms will be uniformly fourth order accurate, as shown above in section 4.1.4. The transverse derivatives are computed by a fourth order central difference algorithm using cell face values.

In implementing the dynamic subgrid models discussed in Chapter III, the model coefficients are calculated at cell centers and then simple averaging is used to obtain cell face values. In order to compute the model terms, a characteristic length (Δ) is required. This, as mentioned before, is usually taken to be the grid size. In the case of a nonuniform mesh, however, the grid spacing is not the same in each direction. Therefore, the cube root of the cell volume is used as the characteristic length for non-uniform grids. Obviously this is only one of several possible definitions of the characteristic length. The effect of methods of calculating Δ is not expected to be large, however, because the dynamic calculation of the model coefficients would act to minimize any differences. The dynamic model coefficients are computed only

once per iteration, rather than for both the predictor and corrector steps. This is in no way an approximation, since the scheme is designed such that the equations of motion are fully satisfied only at the end of each predictor-corrector sequence.

In order to prevent numerical problems, a small number, α, (typically 10^{-12} multiplied by appropriate reference quantities) is added to the denominator of the expressions for the dynamic model coefficients (equations 3.32, 3.43, and 3.58) to prevent the expressions from becoming singular. If the proper reference quantities are used in scaling α, then this will avoid numerical instability but add no appreciable error into the solution. As a further protection from numerical instability, the subgrid kinetic energy is not permitted to decrease below a level which is specified as a reference kinetic energy multiplied by a small number (again, usually 10^{-12}). Also, it is not permitted to increase to a level that would force the temperature to become negative (in practice this is not really problem).

Experience has shown that prolonged negative values of c_e can cause unphysical temperature spikes; therefore this coefficient is constrained to be positive (or zero). Extreme positive values of c_e have also been observed to cause problems. Thus, this coefficient is not allowed to exceed a cutoff value (set somewhat arbitrarily as 20 for the current work). This limitation generally affects only a handful of points at any given time. For the isotropic cases reported in this work, this cutoff was not needed at all.

The production and dissipation terms are implemented as source terms in a central difference fashion. Finally, it should be noted that the derivatives of total enthalpy in equation 3.51 are not actually computed. Instead, to save storage, they are rewritten in terms of velocity and temperature derivatives. The x-derivative, for

example, becomes:

$$\frac{\partial \widetilde{H}}{\partial x} = \gamma c_v \frac{\partial \widetilde{T}}{\partial x} + \widetilde{u}\frac{\partial \widetilde{u}}{\partial x} + \widetilde{v}\frac{\partial \widetilde{v}}{\partial x} + \widetilde{w}\frac{\partial \widetilde{w}}{\partial x} \tag{4.19}$$

Since these derivatives are already available (from the viscous terms), the additional cost associated with this computation is minimal.

CHAPTER V

NEAR-INCOMPRESSIBLE REGIME SIMULATIONS

5.1 Lamb Vortex

In order to validate the code and numerically investigate the order of accuracy of the new 2-4 scheme, a two-dimensional Lamb vortex has been simulated. The Lamb vortex is a decaying incompressible laminar vortex whose solution is given by:

$$u_\theta = \Gamma_0 \frac{1 - e^{\frac{-r^2}{4\nu t}}}{2\pi r} \tag{5.1a}$$

$$p = \int_0^r \frac{\rho u_\theta^2}{r'} dr' \tag{5.1b}$$

For this case only, the code has been rewritten to use dual time-stepping [108]. For comparison, the Gottlieb-Turkel 2-4 algorithm [90] and a fifth order AUSM scheme [93] were similarly implemented. These codes have been run on three different uniform grids (64×64, 96×96, and 128×128) for the same flow conditions: $M_{ref} = 0.05$, $\nu_{ref} = 0.02$, and domain size, $L = 20$. Each case has been run for a single outer time step of 0.1 seconds (beginning at a time of 15 seconds). The reason for running only one outer time step is to isolate, as much as possible, the error due to spatial discretization from the error due to time marching. Next, the solution is examined to find the maximum error in regions away from the boundaries. By

comparing the error for the three different grids and assuming that the time marching error is constant for all three, the order of the scheme can be determined. Of the three schemes, the fifth order AUSM scheme, as expected, has the highest order of accuracy: 4.1. The next best is the new 2-4 scheme, which is order 3.8. Finally, the Gottlieb-Turkel algorithm is found to be order 2.9. Interestingly, in absolute terms, the peak error of the new 2-4 scheme was almost two orders of magnitude smaller on the finest grid than either of the other two schemes. This is attributed to the very low level of dissipation inherent in the scheme. Since the case was not run beyond the first outer time step (error from the boundary conditions quickly corrupts the results), it is not known if the new 2-4 scheme would maintain this high level of accuracy relative to the other schemes.

5.2 Decaying Isotropic Turbulence

5.2.1 Direct Simulation of Two Dimensional Turbulence

As a further validation of the new 2-4 scheme, it was applied to the direct simulation of two dimensional, decaying homogeneous isotropic turbulence. This case was designed to duplicate one of the runs published by Herring *et al.* [109] (designated Case I in the paper). The original case was run using a spectral code with a grid resolution of 128×128 (in spectral space). Following the standard rule of thumb regarding comparison of Taylor series based codes with spectral codes, the current scheme was run with twice the resolution in each direction. For additional comparison, this case was also run with the Gottlieb-Turkel scheme.

As shown in figure 5.1, the enstrophy predictions of both finite volume schemes are in excellent agreement with the spectral data of Herring *et al.* The time scale for

this plot (and subsequent plots for this case) has been non-dimensionalized using a reference time:

$$\tau = \frac{L}{U_0} \tag{5.2}$$

In the above equation, L is the initial integral length scale, and U_0 is a reference velocity, which was set by Herring *et al.* as one meter per second. All three schemes also predict very similar enstrophy dissipation rates, as shown in figure 5.2. Reasonable agreement is found for predictions of the integral-scale Reynolds number, as shown in figure 5.3. For the latter part of the simulation, however, the two finite volume methods differ slightly from the spectral data. Since both finite volume schemes show the same behavior, these disparities are thought to be due, at least in part, to differences in the initial conditions between the Herring *et al.* simulations and the current work.

As these figures show, the new 2-4 scheme is found to match the results of the Gottlieb-Turkel algorithm very closely; in fact, on most of the plots it is difficult to distinguish any differences between the two. Also, both finite volume schemes are in reasonable agreement with the spectral data. Therefore, the new 2-4 scheme is taken to be validated in terms of solving the unsteady Navier-Stokes equations. The next step is to examine the scheme as it is applied to the solution of the LES equations.

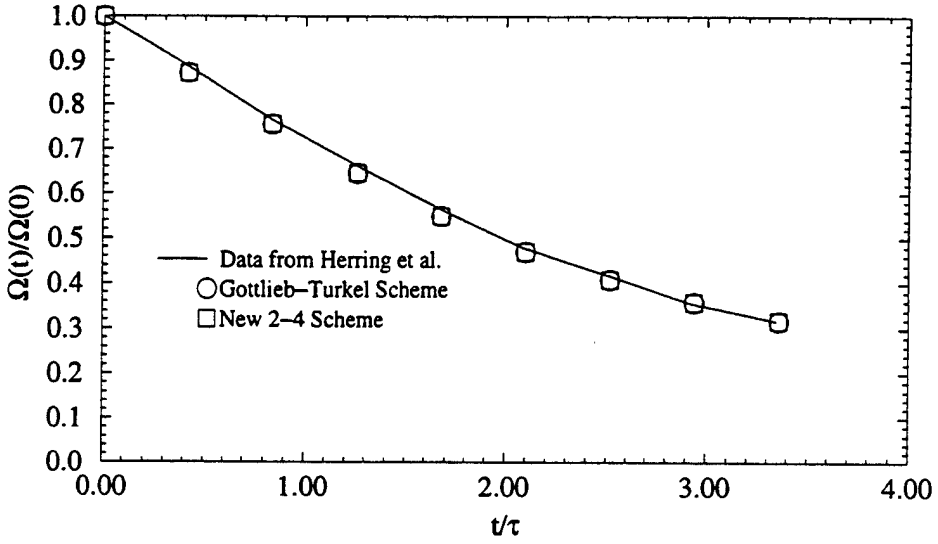


Figure 5.1: Decay of enstrophy in 2-D isotropic turbulence

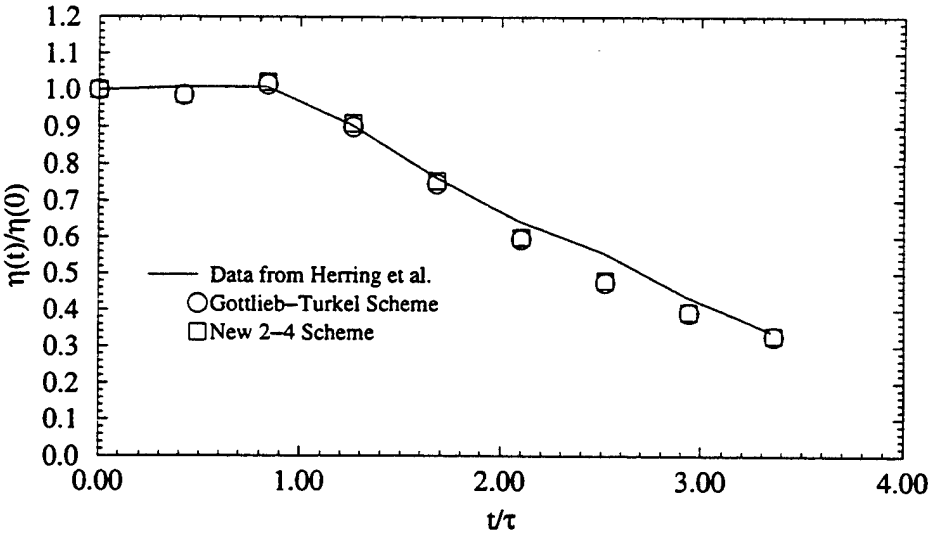


Figure 5.2: History of the enstrophy dissipation rate in 2-D isotropic turbulence

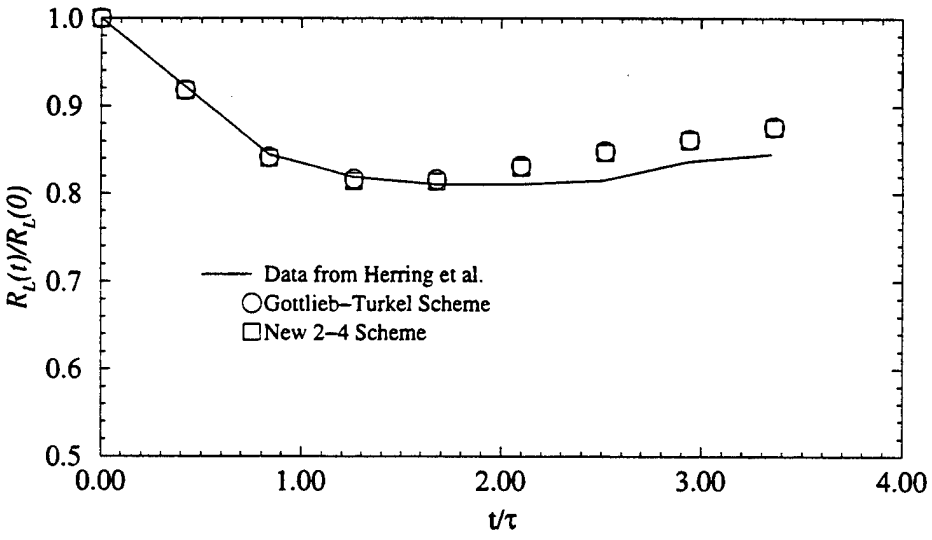


Figure 5.3: Behavior of the integral-scale Reynolds number in 2-D isotropic turbulence

5.2.2 Comparison with Grid Turbulence Experimental Data

To further validate the numerical scheme and as an initial test of the subgrid model, cases have been run which replicate the grid turbulence experiments of Comte-Bellot and Corrsin [110]. In the experiment, measurements were taken at three locations downstream of a turbulence generating grid. The experimental data have been non-dimensionalized by a reference length ($l^* = 10M$) and a reference time scale ($t^* = \frac{64M}{U_0}$). The mean velocity ahead of the turbulence generating grid (U_0) was 10 meters per second and the mesh spacing (M) was 5.08 cm. A decaying isotropic turbulence numerical experiment that is equivalent to Comte-Bellot and Corrsin's work can be constructed by assuming that the flow in the wind tunnel has a constant mean velocity and ignoring any wall effects. The isotropic turbulence is visualized as a cubical box with periodic boundary conditions being carried along by the mean flow. Thus, the three streamwise locations for which experimental data is available are associated with three points in time in the decaying isotropic simulation. These points can be computed as the time it would take for the mean flow to convect the hypothetical box of turbulence from some reference point to the given experimental measuring point.

The domain size for such a simulation must be chosen such that the "box" is large enough for the integral length scale to be resolved; in this case, each side is taken to be the reference length (l^*). The simulations are begun at a point in time corresponding to the first experimental measurement station. The initial velocity field matches the experimental spectrum at this location and is computed to be divergence-free. The initial pressure, density, and temperature are constant throughout the domain. The reference Mach number is set, for convenience, as 0.1.

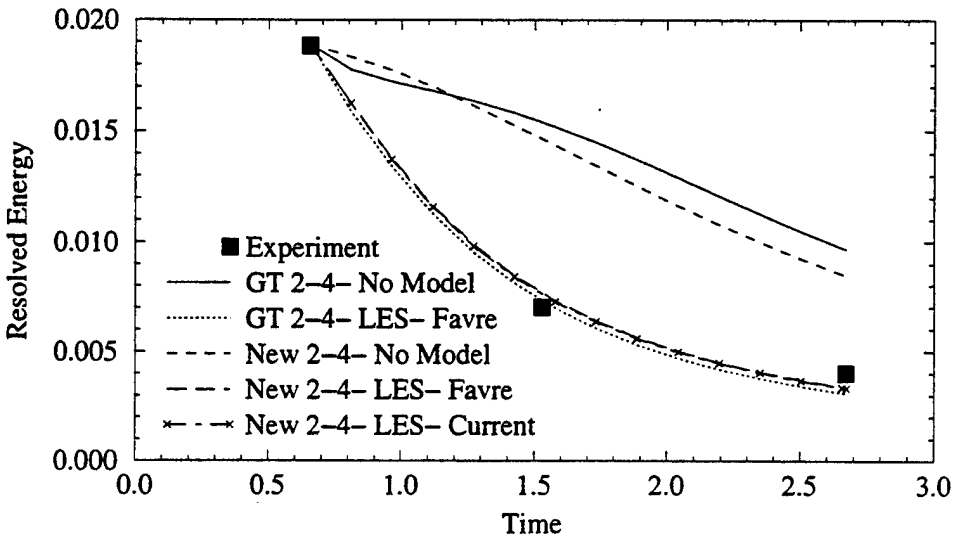


Figure 5.4: Decay of resolved turbulent kinetic energy in isotropic turbulence simulated using a Favre filter formulation compared with experimental results of Comte-Bellot and Corrsin

The initial subgrid kinetic energy field is computed using a similarity assumption as follows:

$$k^{sgs} \approx \frac{C_k}{2}\left(\widehat{\widetilde{u}_i\widetilde{u}_i} - \widehat{\widetilde{u}}_i\widehat{\widetilde{u}}_i\right) \tag{5.3}$$

The constant, C_k, in the above expression is computed such that the total amount of k^{sgs} in the field matches the amount predicted by the experimental spectrum for the given computational grid. Although the above procedure yields visually reasonable results, the subgrid kinetic energy is not necessarily correlated to the resolved field properly. To improve the initial conditions, the technique of Carati, Ghosal, and

Moin [47] is implemented: the field is allowed to evolve for a short time (50 iterations in this case), and then it is re-scaled to again match the initial spectrum as given in the experiment. This allows the subgrid kinetic energy field to adjust to the resolved velocities, and *vice versa.*

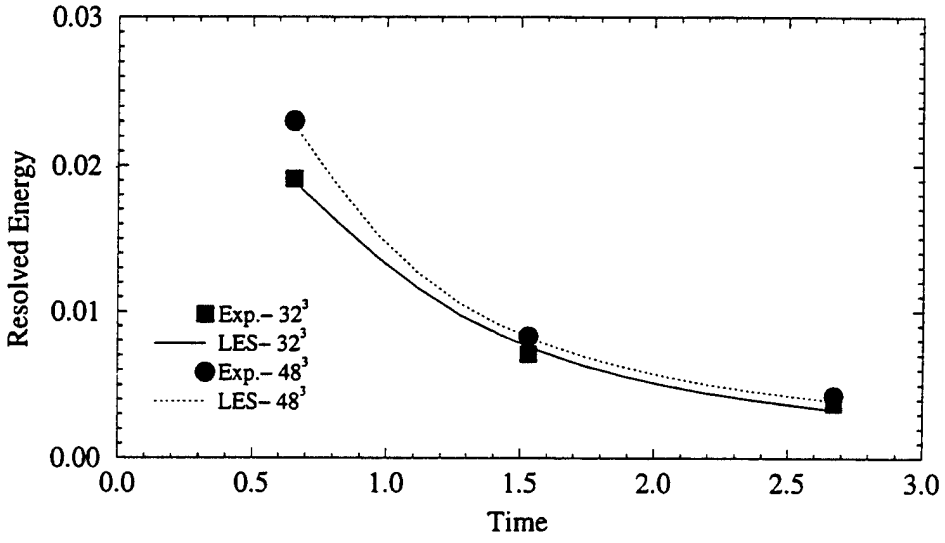


Figure 5.5: Decay of resolved turbulent kinetic energy in isotropic turbulence compared with experimental results of Comte-Bellot and Corrsin

The first simulations were run on a $32 \times 32 \times 32$ grid for both the Gottlieb-Turkel algorithm and the new 2-4 scheme. At this grid resolution, only 59.3 percent of the energy in the experimental spectrum is resolved [67]. Thus, 40.7 percent of the energy lies in the subgrid. Ghosal *et al.* [61] found that for this case, the lower limit of resolution was $48 \times 48 \times 48$, but Kim [67] was able to capture important features of the flow with much smaller grids. Since the current subgrid model is a

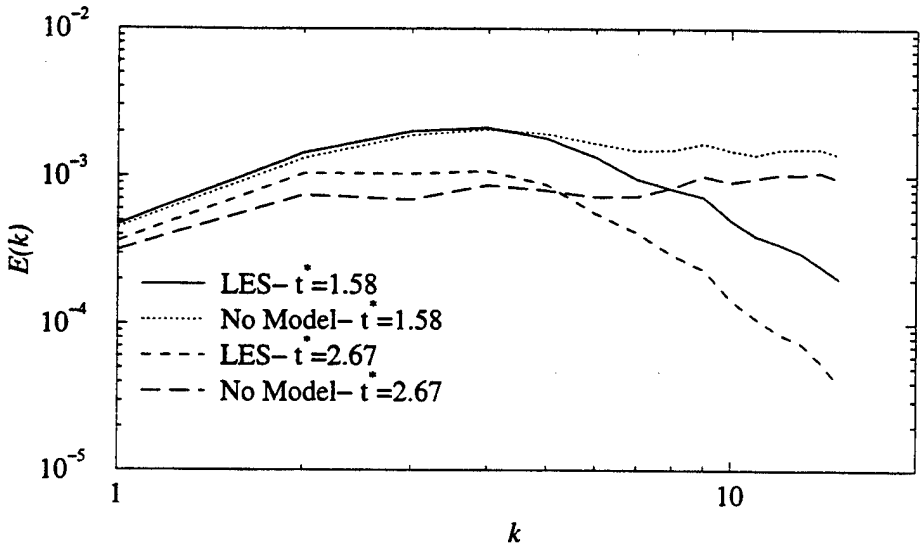


Figure 5.6: Energy spectra of decaying isotropic turbulence with and without subgrid model

compressible extension of Kim's work, the present scheme should be able to obtain similar results to Kim's in the near-incompressible regime.

Figure 5.4 shows the decay of resolved kinetic energy in the domain. For comparison, the Gottlieb-Turkel algorithm was run along with the new 2-4 scheme. In addition, two different LES schemes were compared: the current model (as described in Chapters II and III) and a more conventional Favre filtered approach (described in Appendix B). In the incompressible limit both formulations should reduce to the same scheme, and this is, in fact, what is observed. The significance of this plot, therefore, lies not so much in the details of the particular mathematical formulation employed, but rather in the comparison between the two numerical schemes and the runs with and without subgrid models. First, both numerical methods yield very

similar results. With the subgrid model turned on, the Gottlieb-Turkel algorithm does dissipate kinetic energy faster, but the differences are minor. Thus, the new 2-4 scheme will be taken as validated, and henceforth it is used exclusively. The second point to note is that without a subgrid model, both algorithms deviate radically from the experimental data. This verifies that the subgrid model is having an effect on the flowfield, and that this effect is in some way beneficial. As a corollary, this also demonstrates that the numerical scheme is not overly dissipative.

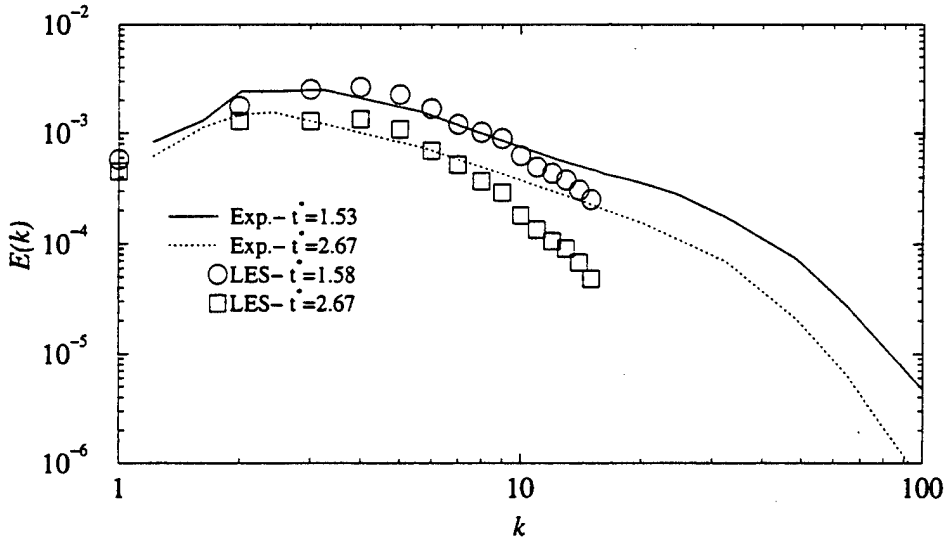


Figure 5.7: Comparison of energy spectra from LES with experimental data of Comte-Bellot and Corrsin

The current scheme (as derived in Chapters II and III) was used to simulate the same case for two different grid resolutions ($32 \times 32 \times 32$ and $48 \times 48 \times 48$). The resolved kinetic energy history is shown in figure 5.5 compared to data derived

from the truncated experimental energy spectra. As expected, although the lower resolution case is in reasonable agreement with experiment, the higher resolution case shows improved results.

As was seen in figure 5.4, without a proper subgrid model these algorithms do not capture the energy decay rate correctly. The reason for this is a build-up of kinetic energy in the highest resolved wavenumbers due to the artificial termination of the turbulent energy cascade. This is clearly illustrated in figure 5.6. The same LES kinetic energy spectra are compared to the corresponding (unfiltered) experimental spectra in figure 5.7. These results are in reasonable agreement, especially when the coarseness of the grid is considered. The drop-off shown by the LES results is characteristic of finite-volume algorithms. This is because, in using such an algorithm, an implicit filtering operation is being performed, similar to a box filter. In consequence, the resolved LES field tends to take on spectra characteristic of box filtered data. The box filter's spectral admittance function (with a cutoff wavenumber k_c) is of the form $\frac{\sin\frac{\pi k}{k_c}}{\pi k}$. Therefore, a gradual drop in resolved energy as one approaches the cutoff wavenumber is to be expected in a finite volume LES field. Figure 5.8 shows the effect of grid resolution on the final predicted kinetic energy spectrum. As expected, the results from the higher resolution case agree more closely with the experiment, although, once again, a noticeable drop-off in the higher wavenumbers is present.

The effects of using the modified form of the dynamic dissipation coefficient (equation 3.33) are shown in figure 5.9. The alternate form of c_ε results in faster dissipation of subgrid kinetic energy. Thus, as can be seen, the eddy viscosity is smaller, and turbulent dissipation of resolved energy is decreased. This difference is shown more dramatically in figure 5.10; without the modification to c_ε, the subgrid

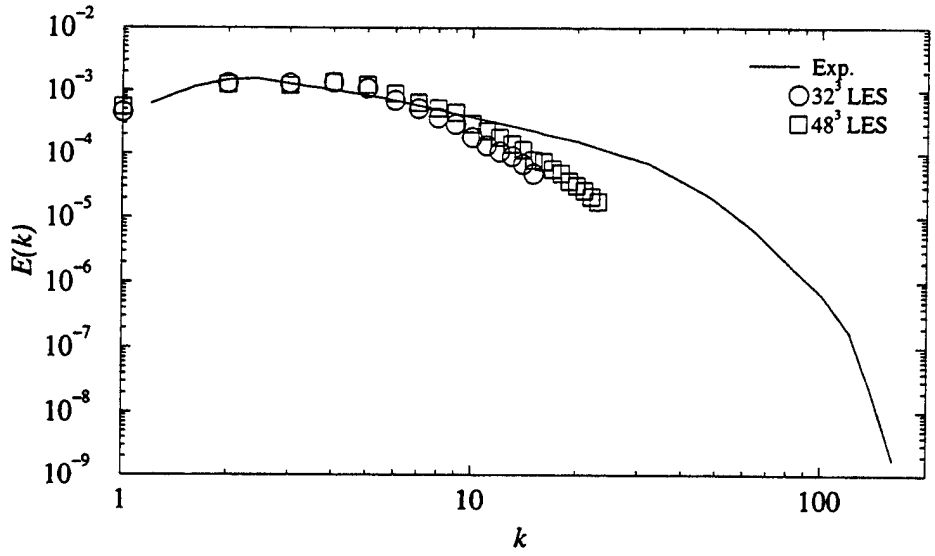


Figure 5.8: Comparison of the energy spectrum at the final station in the Comte-Bellot and Corssin experiment with simulated energy spectra

kinetic energy's magnitude is badly overpredicted, and the trends are wrong as well. With the modification, the behavior is much closer to that of the experiment, although there is still much room for improvement.

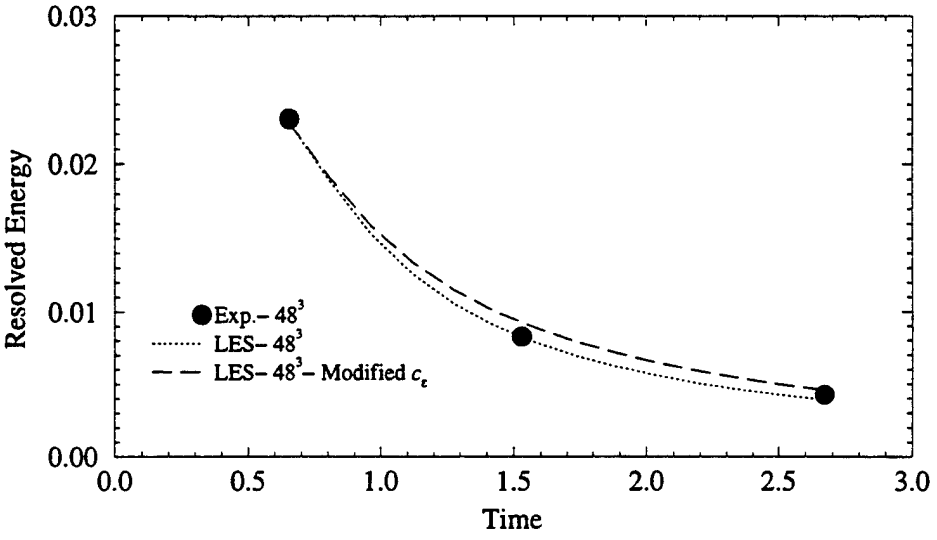


Figure 5.9: Comparison of resolved kinetic energy in Comte-Bellot and Corrsin experiment with LES using different forms for c_ϵ

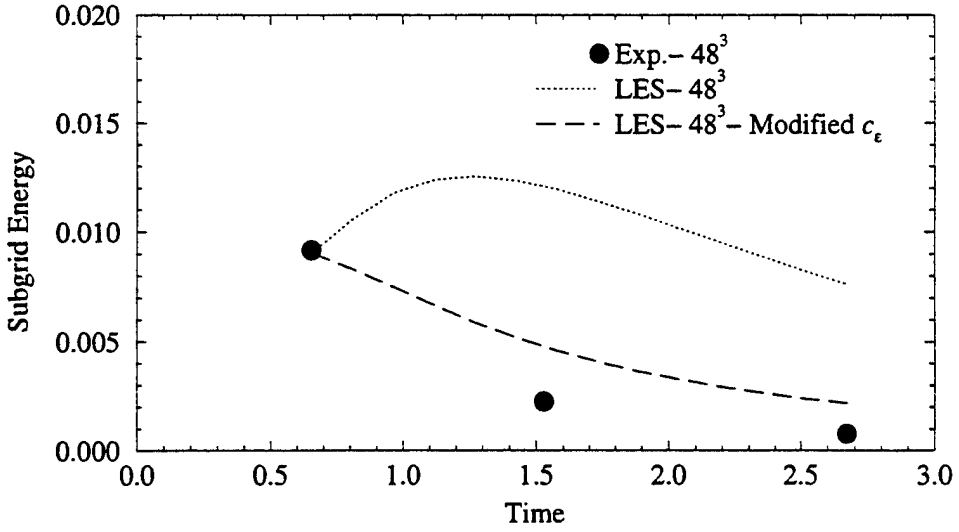


Figure 5.10: Comparison of subgrid kinetic energy predictions from simulations with differing c_ϵ with experimental results

5.2.3 Comparison with DNS

A direct numerical simulation of near-incompressible decaying isotropic turbulence has been run on a $64 \times 64 \times 64$ grid. The domain is a cube with sides of length 2π meters. The initial Taylor Reynolds number of the flow is 37.8 and the initial turbulent Mach number is 0.159. By the end of the simulation ($t = 10$ seconds), the Taylor Reynolds number has decreased to roughly 10.5. A corresponding LES is run on a $16 \times 16 \times 16$ grid. Initial conditions for the LES are generated by filtering (using a box filter) a "snapshot" of the flow field from early in the DNS (one second after the start).

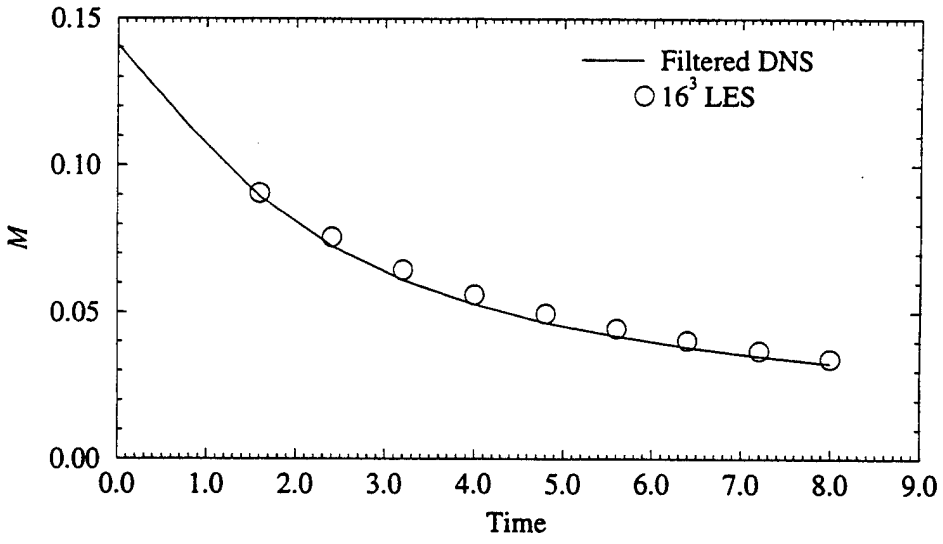


Figure 5.11: Evolution of the average Mach number in near incompressible decaying isotropic turbulence

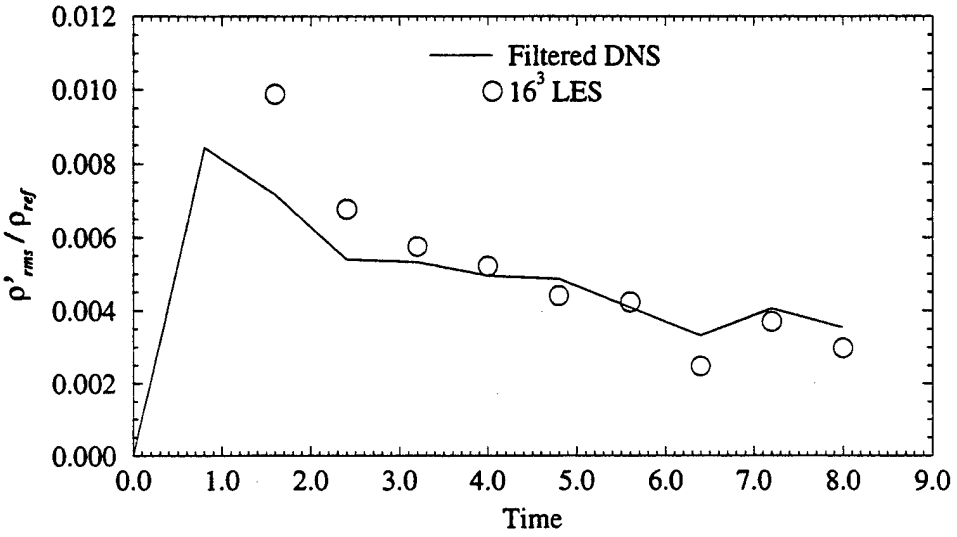


Figure 5.12: Normalized RMS of turbulent density fluctuations in near-incompressible decaying isotropic turbulence

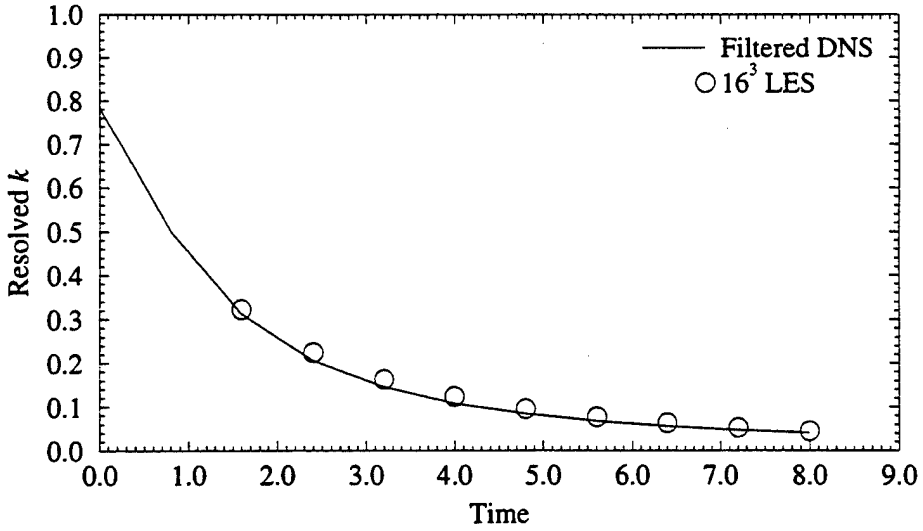


Figure 5.13: Resolved kinetic energy in near-incompressible decaying isotropic turbulence

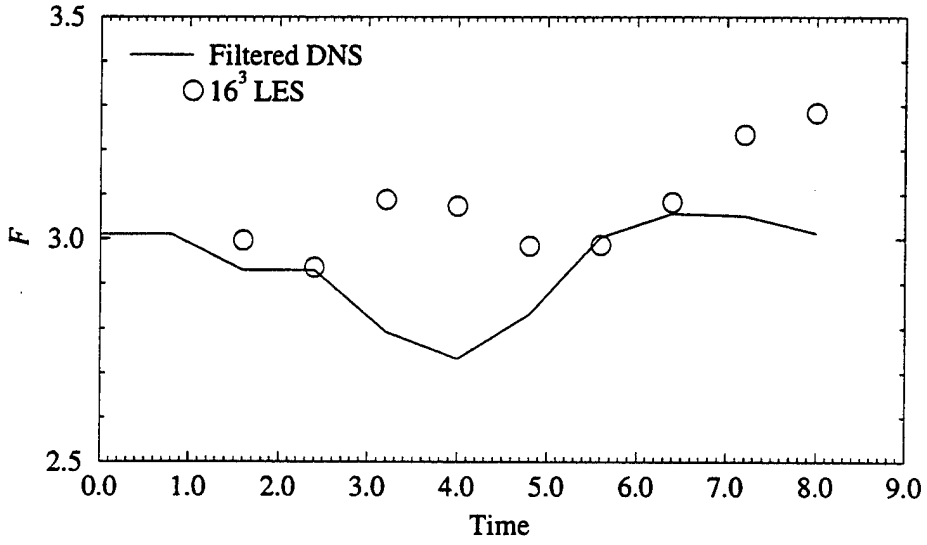


Figure 5.14: $\frac{\partial v}{\partial y}$ flatness history in near-incompressible decaying isotropic turbulence

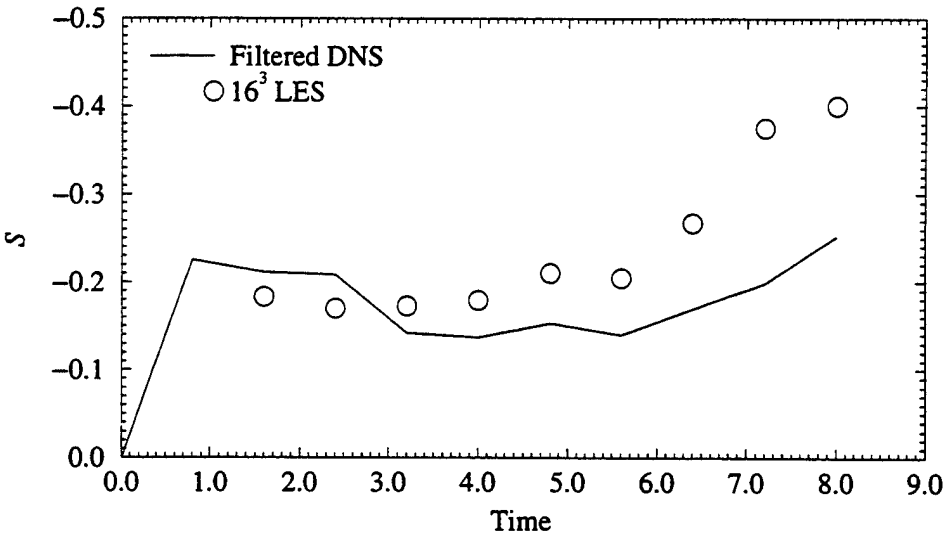


Figure 5.15: $\frac{\partial v}{\partial y}$ skewness history in near-incompressible decaying isotropic turbulence

The incompressible nature of the flow is shown in figures 5.11 and 5.12. The LES correctly predicts the evolution of the average Mach number, which starts at around 0.14 and decays to less than 0.04. Note that the temporal axis on all of these plots has been non-dimensionalized by the initial integral-scale eddy turnover time of the DNS data:

$$\tau = \left(\frac{l}{u_{rms}} \right)_{t=0} \tag{5.4}$$

For the current case, this time was found to be roughly 1.25 seconds. Except for an initial overshoot, which may be (at least partly) the result of the initial conditions not satisfying the LES equations fully, the model correctly predicts the decay of the RMS of the density fluctuations, which peak at about one percent and then decay to less than 0.4 percent of the mean density. Figure 5.13 shows that the LES accurately predicts the decay of the resolved kinetic energy. The energy has been non-dimensionalized by the initial kinetic energy in the DNS flow field.

Despite the poor resolution of the LES, it is also able to properly capture some of the characteristics of the higher moments of the flow. Sample traces of the velocity derivative flatness and skewness (results for $\frac{\partial v}{\partial y}$ are plotted here) are shown in figures 5.14 and 5.15. While the agreement is not perfect, the LES does predict the approximate magnitude of the flatness and the overall trends of the skewness. It should be noted, however, that these values are much closer to a Gaussian distribution than the unfiltered DNS data. This property of LES results (and filtered fields in general) must be kept in mind when analyzing such data.

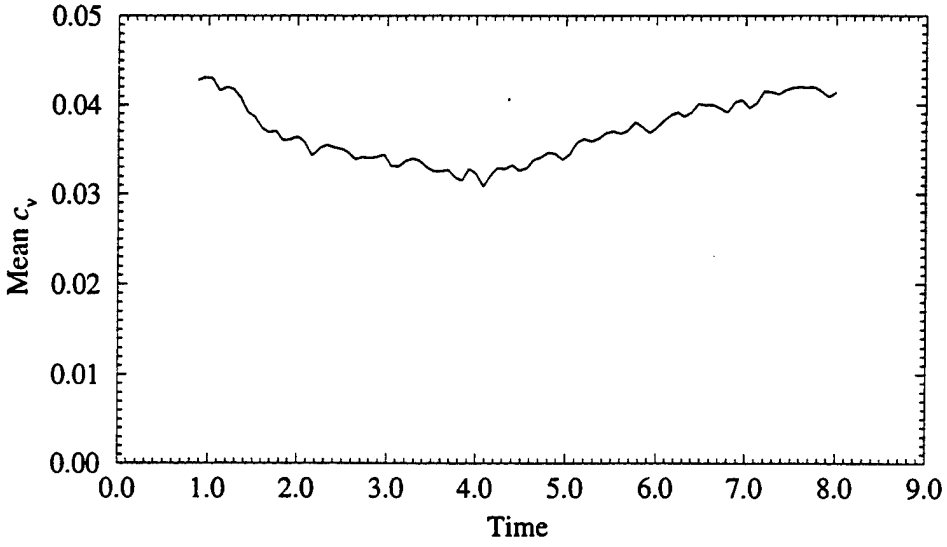


Figure 5.16: Mean value of c_ν in near-incompressible decaying isotropic turbulence

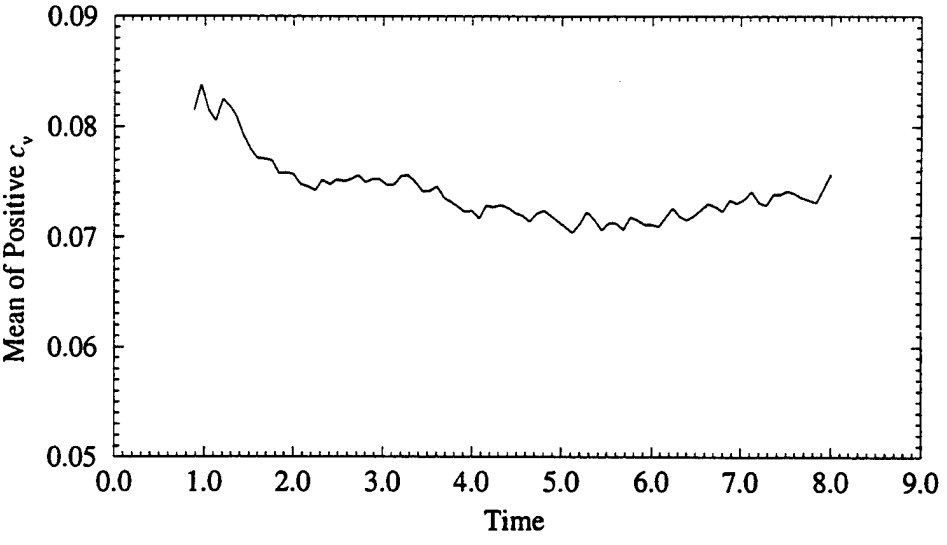


Figure 5.17: Mean value of positive c_ν in near-incompressible decaying isotropic turbulence

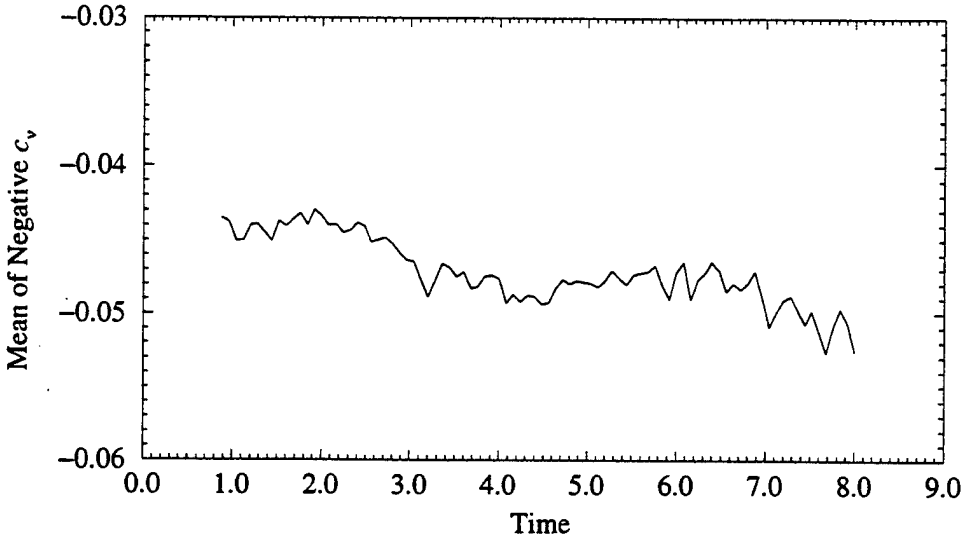


Figure 5.18: Mean value of negative c_ν in near-incompressible decaying isotropic turbulence

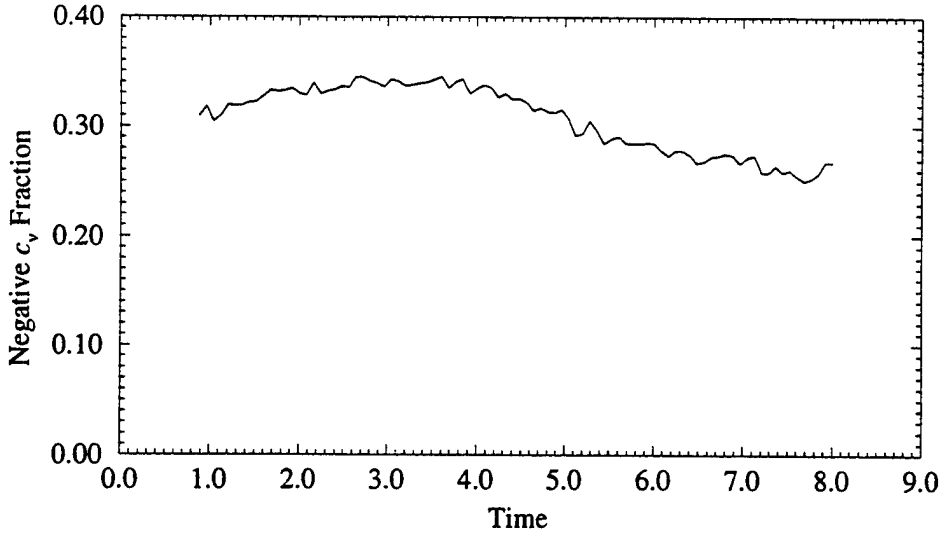


Figure 5.19: Time trace of the fraction of points in the domain with negative values of c_ν in near-incompressible decaying isotropic turbulence

The behavior of the subgrid stress tensor model coefficient, c_ν, is examined in figures 5.16, 5.17, 5.18, and 5.19. These plots show that the model coefficient remains relatively stable throughout the simulation. The overall mean value ranges between 0.03 and 0.045. This is a significant variation, but this variation occurs only gradually. When considering only the positive values of c_ν, the mean starts around 0.083 and then decreases until it seems to stabilize around 0.074. When only negative values are used, the average coefficient value shows a generally decreasing trend (from -0.043 to -0.052). This is accompanied, however, by a decreasing number of points with negative values. After reaching a peak of about 35 percent, the fraction of grid cells with negative coefficient values drops steadily. At the end of the simulation, roughly 27 percent of the points have negative values of c_ν.

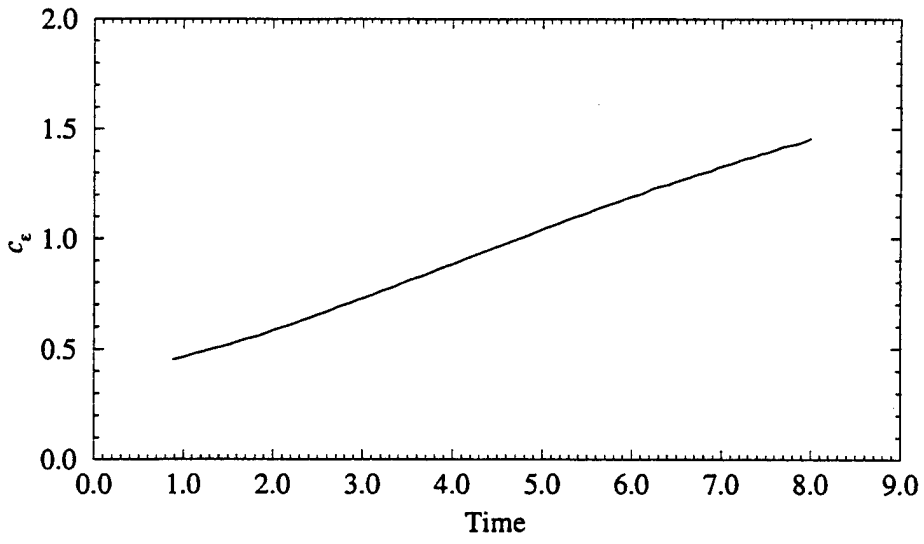


Figure 5.20: Mean value of c_ε in near-incompressible decaying isotropic turbulence

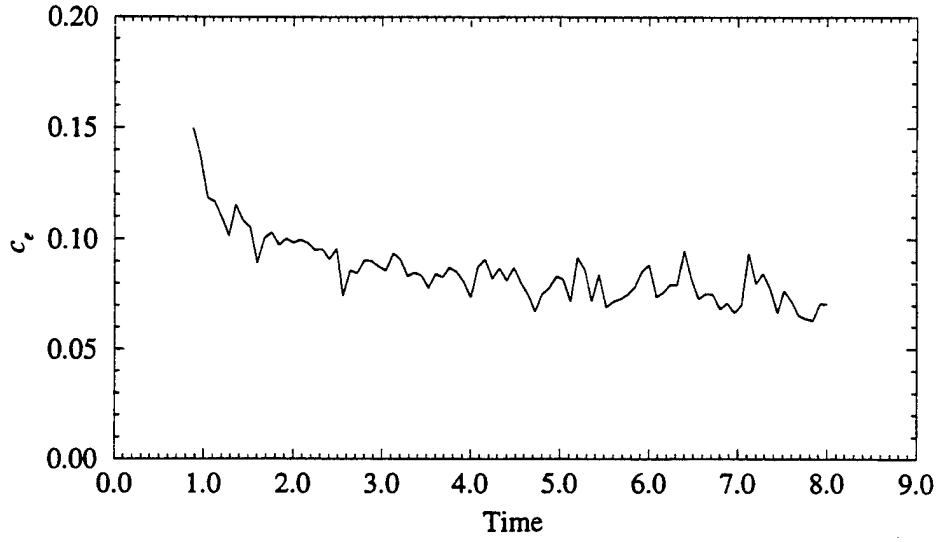


Figure 5.21: Mean value of c_e in near-incompressible decaying isotropic turbulence

The mean values of the other two model coefficients, c_ϵ and c_e, are plotted in figures 5.20 and 5.21. The dissipation model coefficient is shown to grow linearly from a value of 0.5 to 1.5 over the course of the simulation. This is due to the decreasing Reynolds number of the flow, which means that there should be progressively less subgrid kinetic energy. The dissipation coefficient therefore increases to ensure that whatever subgrid kinetic energy is produced dissipates at a faster rate. At such low levels of compressibility, the energy equation does not have much of an effect on the flow, and consequently the energy equation subgrid model does not have much effect either. However, it is important that in such circumstances, the model remains well behaved (*i.e.* not become unstable). In this case, the energy model coefficient decreases from an initial value of about 0.15 to the vicinity of 0.07.

No stability problems were encountered with the energy equation subgrid model for this case.

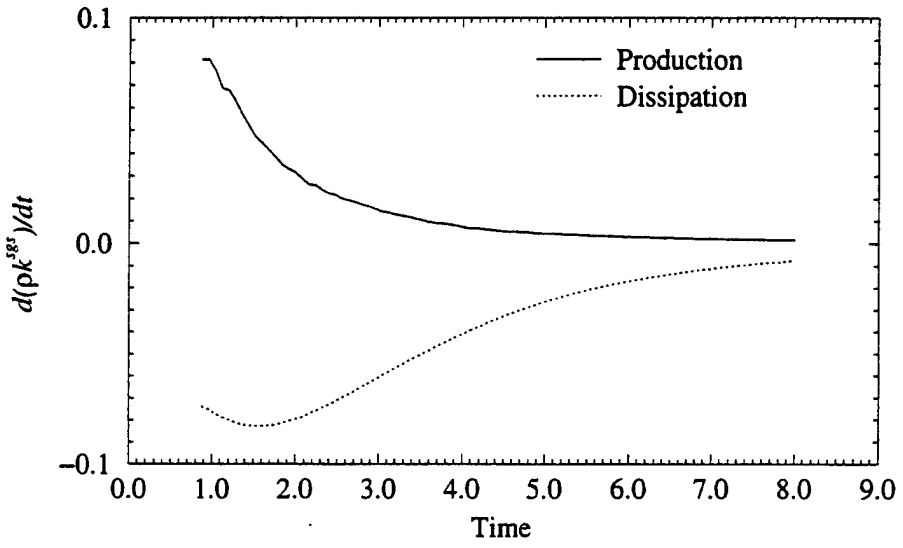


Figure 5.22: Evolution of modelled subgrid kinetic energy equation production and dissipation terms in near-incompressible, decaying isotropic turbulence

The subgrid kinetic energy equation production and dissipation terms are plotted in figure 5.22. The vertical axis has been non-dimensionalized by the quantity $\frac{\rho_{ref} k_{ref}}{\tau}$. The values plotted represent the respective contributions of the production and dissipation models to $\frac{\partial \rho k^{sgs}}{\partial t}$. Although the two terms are initially almost equal, the production drops off quickly, while the dissipation magnitude continues to increase for about one large eddy turnover time before it too asymptotically approaches zero. It should be noted that the other terms in the modelled subgrid kinetic energy equation do not contribute to the production or dissipation of subgrid

kinetic energy. Their mean values are many orders of magnitude less than the two terms plotted here. This is not to say that they are unimportant, because their RMS values are typically of the same order as the modelled production and dissipation (or even larger). Their function, however, is only to modify the rate of k^{sgs} transport, they do not create or destroy subgrid energy. Of course, the production term here does not actually represent a true production of turbulent kinetic energy. Rather, it represents the rate of transfer of turbulent kinetic energy from resolved scales into the subgrid. Similarly, the dissipation does not necessarily represent the physical dissipation of turbulent kinetic energy. Rather, it may be thought of as representing the rate at which that portion of unresolved energy which affects the resolved flow is being dissipated or transferred to scales which do not directly affect the resolved field.

The impact of computing the dissipation coefficient using the alternate formulation (equation 3.33 as opposed to the original form equation 3.32) on the average magnitude of this term is appreciable, as shown in figure 5.23. This does not, however, translate to significant differences in resolved-scale flow quantities. For instance, the average resolved kinetic energy decays at almost the same rate (see figure 5.24). Again, however, the corresponding subgrid kinetic energy is significantly different (see figure 5.25). As can be seen in the figure, the modified form results in better predictions of the subgrid kinetic energy, although there is still deviation from the *a priori* results from DNS. As one would expect, the modified coefficient has a large effect on the modelled subgrid kinetic energy dissipation (shown in figure 5.26). With the alternate form, the dissipation curve becomes more nearly a mirror image of the production. Whereas the modelled production is initially larger in magnitude than the dissipation when the original algorithm is used,

the modified c_ϵ results in the magnitude of the average dissipation being larger than that of the production for the entire simulation.

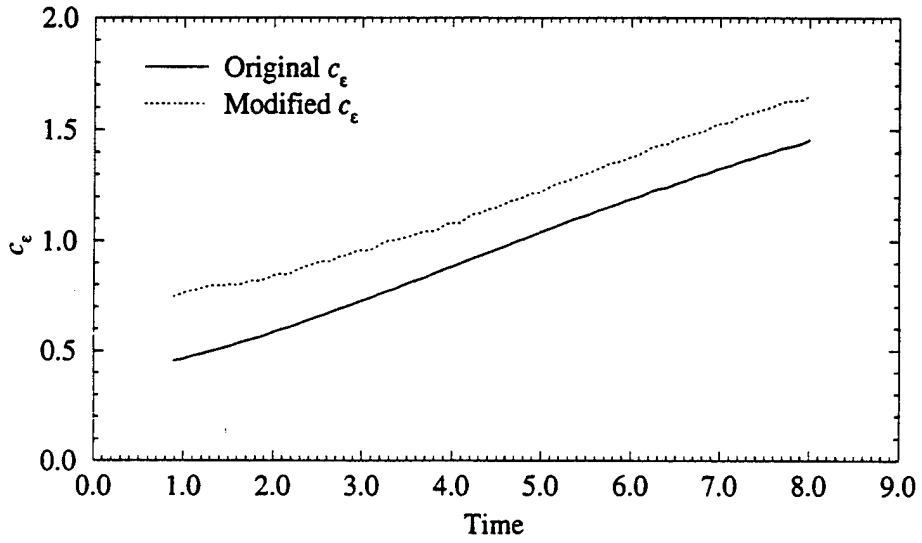


Figure 5.23: The evolution of the mean of c_e as computed using different methods in near-incompressible decaying isotropic turbulence

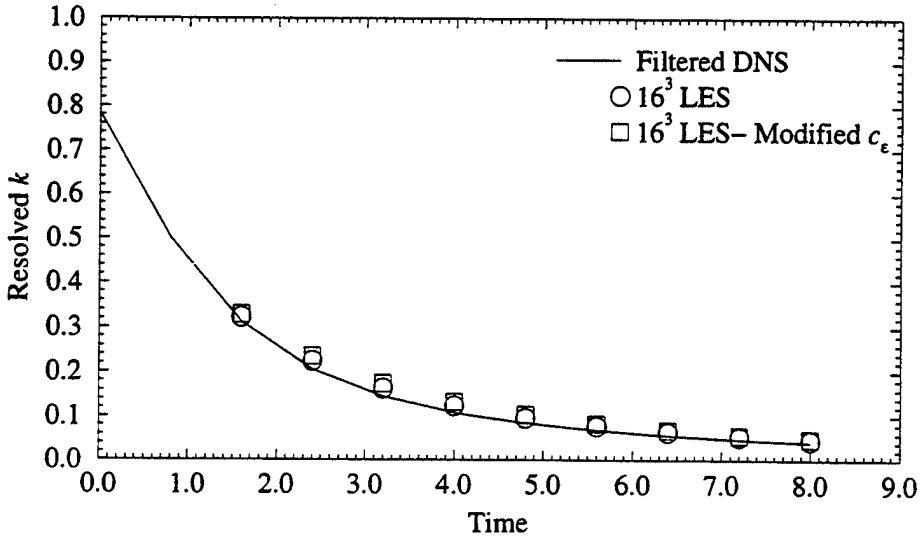


Figure 5.24: The effect of different forms of c_ε on the resolved kinetic energy in near-incompressible, decaying isotropic turbulence

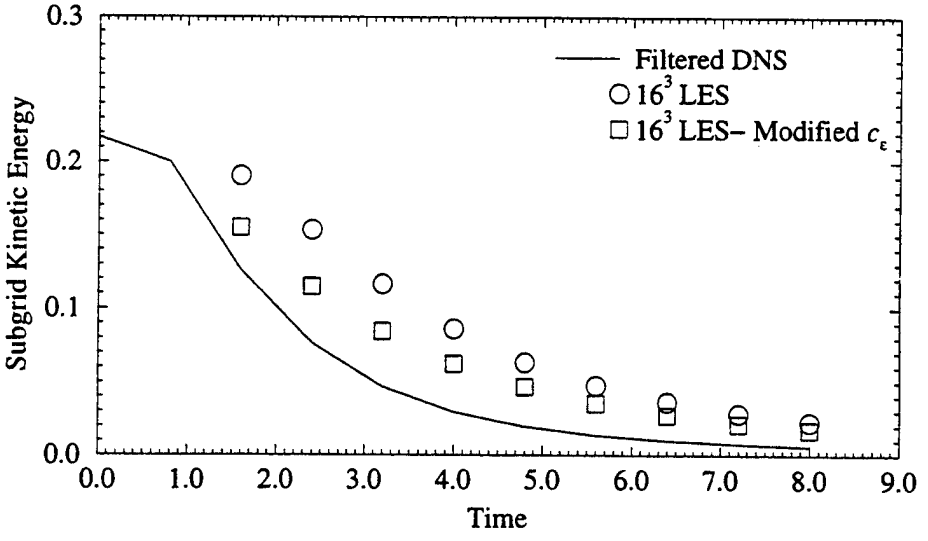


Figure 5.25: The effect of different forms of c_ε on the subgrid kinetic energy in near-incompressible, decaying isotropic turbulence

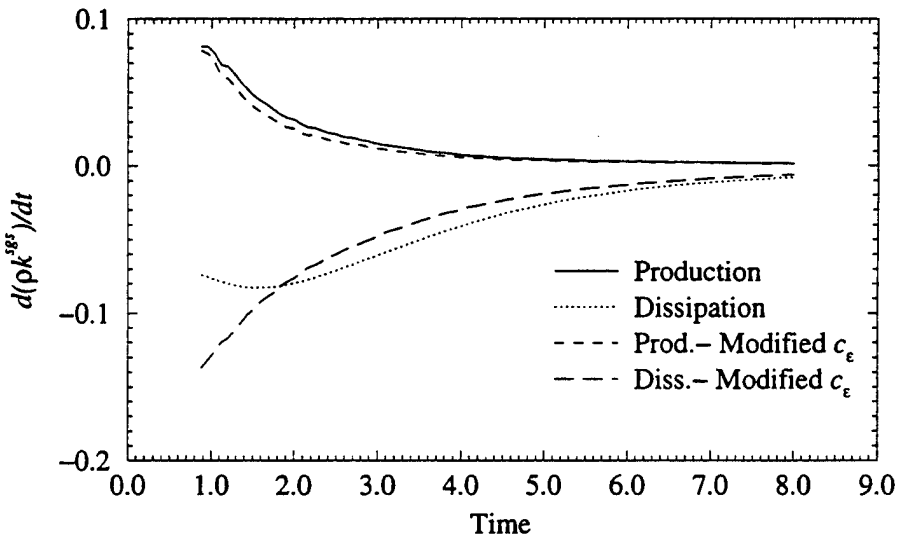


Figure 5.26: The effect of different forms of c_ε on the modelled production and dissipation of k^{sgs} in near-incompressible, decaying isotropic turbulence

Chapter VI

Simulations of Compressible Isotropic Turbulence

6.1 Decaying Isotropic Turbulence

6.1.1 Comparison with DNS

In order to examine the behavior of the model as the flow becomes more compressible, results are presented from simulations of compressible decaying isotropic turbulence. First, a DNS is run on a $64 \times 64 \times 64$ grid. As before, the domain is taken to be a cube with sides of length 2π meters. The initial Taylor Reynolds number of the flow is 34.9, and the initial turbulent Mach number is 0.826. By the end of the simulation, the Taylor Reynolds number has decreased to roughly 12.5. Note that a similar drop in Taylor Reynolds number occurred in the near-incompressible case, but in this case, the total simulation runs for roughly two large eddy turnover times (1.25 seconds), whereas the near-incompressible run covered about eight turnover times (10 seconds). This is due to the well known damping effect that compressibility has on turbulent kinetic energy. A snapshot of the DNS solution is taken after it has run a short time (0.1 seconds in this case). This is filtered (using a box filter) and coarsened, as for the incompressible case in section 5.2.3, to provide initial conditions for an LES, which is run on a $16 \times 16 \times 16$ grid.

The current scheme is well able to capture the mean features of the flow, as illustrated in figures 6.1, 6.2, and 6.3. Figure 6.1 shows the decay of the mean resolved Mach number. Note that the temporal axis has been non-dimensionalized

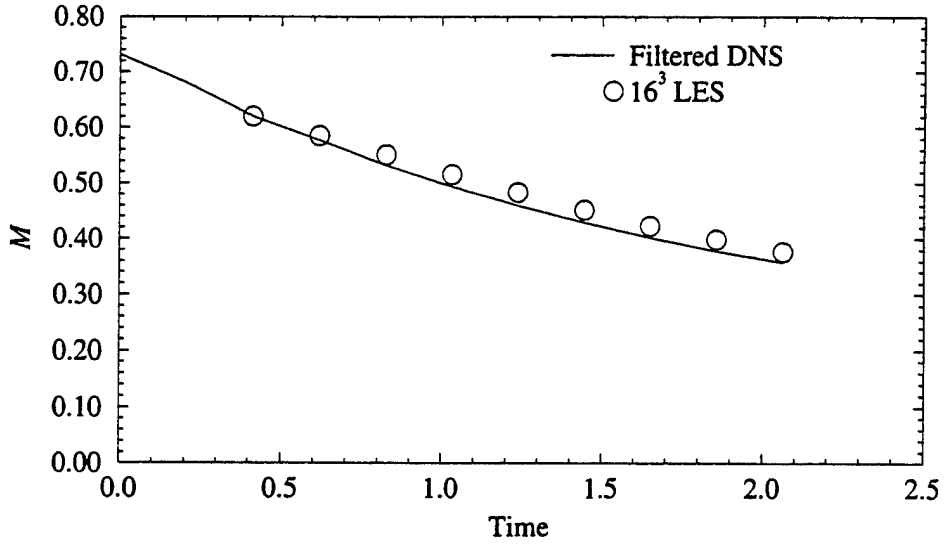


Figure 6.1: Mean Mach number in compressible decaying isotropic turbulence

by the initial large eddy turnover time of the DNS (in this case $\tau = 0.6$ seconds). Reasonable agreement is shown between the LES and the filtered DNS solution for the entire duration of the simulation. The density fluctuations are also accurately predicted, as shown in figure 6.2. The resolved kinetic energy evolution (normalized by the direct simulation's initial kinetic energy) is shown in figure 6.3. Again, agreement between the LES and filtered DNS results is quite good. The model also does a reasonable job at capturing some of the higher moments of the flow. The magnitude of the velocity derivative flatness, shown in figure 6.4 is correctly predicted, although some of the trends are not correct. The LES-predicted skewness of the resolved velocity derivative field compares somewhat better to the DNS results (up until the last two measuring points), as shown in figure 6.5. Note again, however,

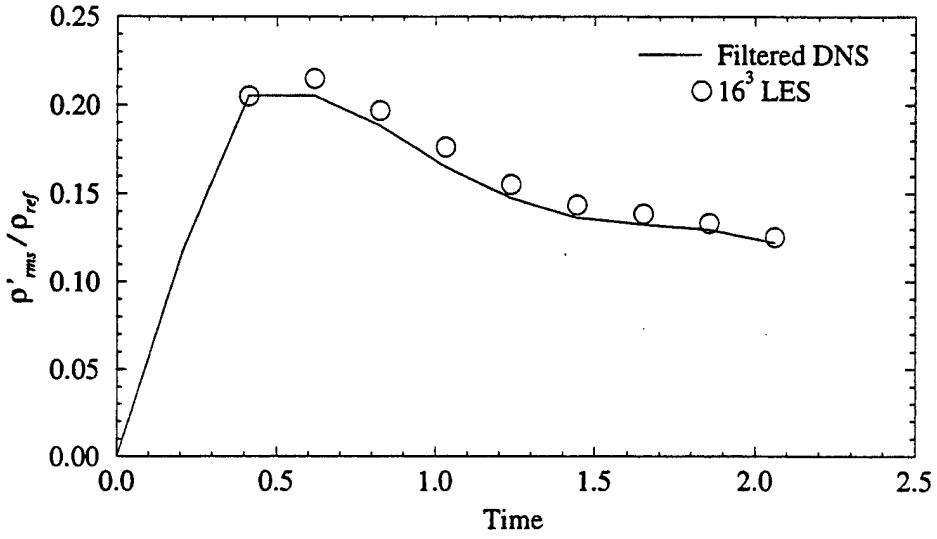


Figure 6.2: Normalized RMS of density fluctuations in compressible decaying isotropic turbulence

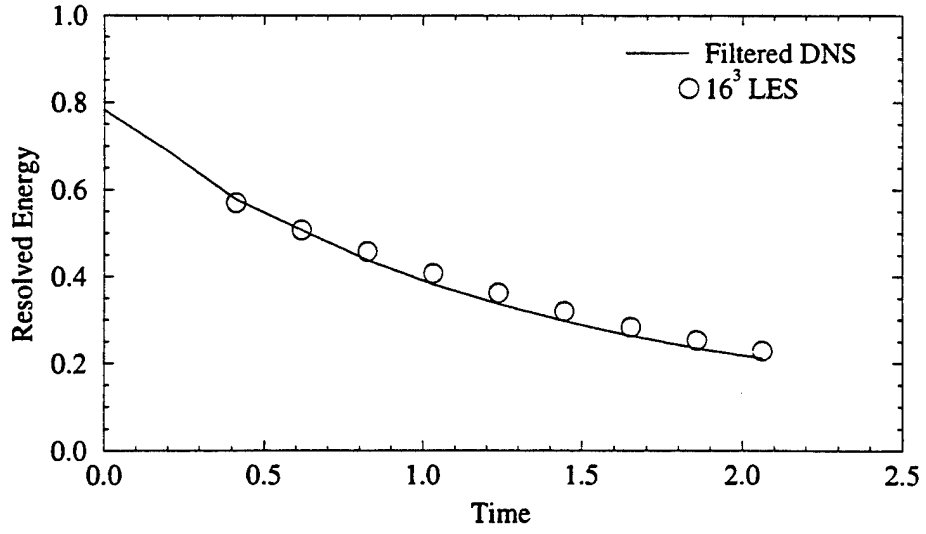


Figure 6.3: Evolution of resolved kinetic energy in compressible decaying isotropic turbulence

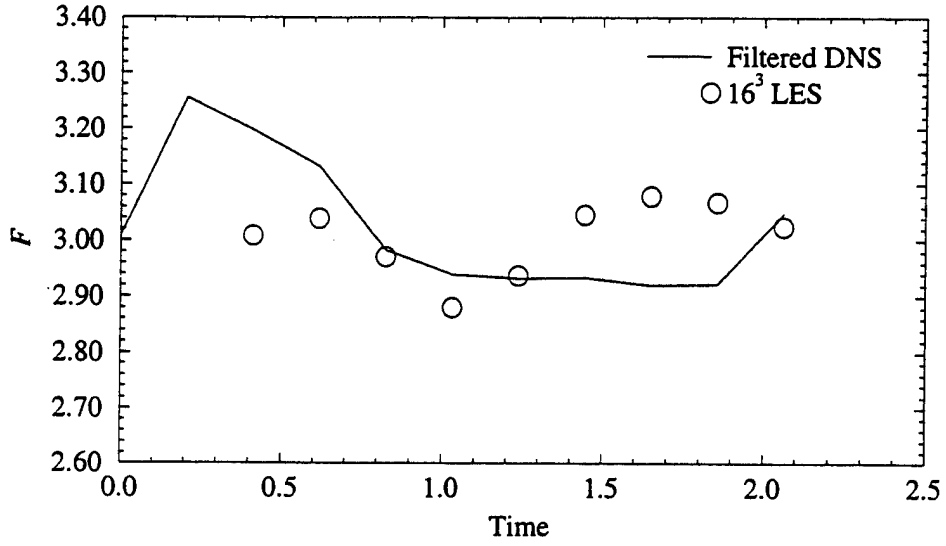


Figure 6.4: Evolution of $\frac{\partial v}{\partial y}$ flatness in compressible decaying isotropic turbulence

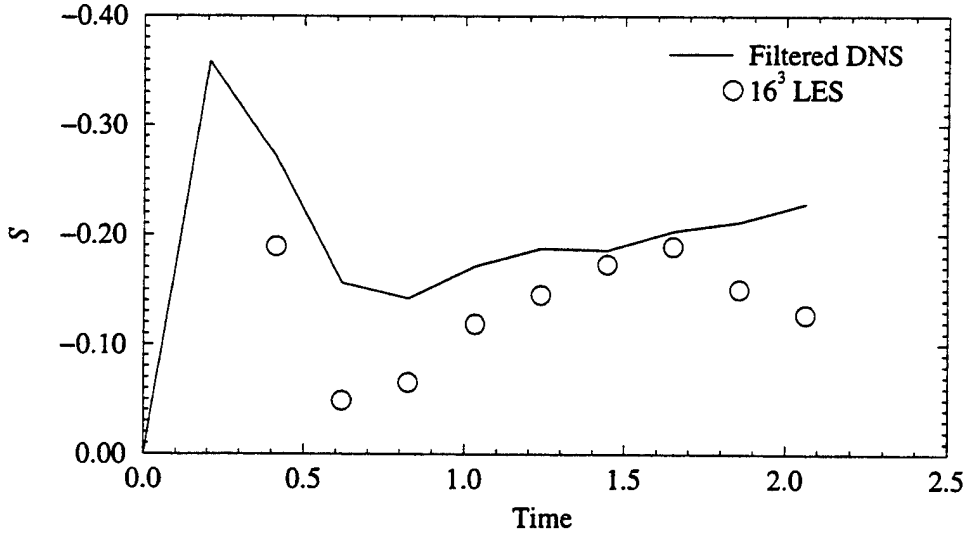


Figure 6.5: Evolution of $\frac{\partial v}{\partial y}$ skewness in compressible decaying isotropic turbulence

that both the LES and filtered DNS fields are much closer to Gaussian than the unfiltered DNS.

The mean valued of the subgrid stress tensor model coefficient (c_ν), after an initial drop, increases steadily as the simulation progresses, as shown in figure 6.6. The same sort of behavior is also observed when considering only positive values of the coefficient, as shown in figure 6.7. The mean of the negative values of c_ν range, in a less predictable manner, between -0.045 and -0.055, as shown in figure 6.8. This case has a somewhat larger fraction of points with negative stress tensor model coefficient values than the near-incompressible case discussed in section 5.2.3. The current case, shown in figure 6.9, predicts roughly 35 to 40 percent of the points with negative values at any given time, whereas the incompressible case predicted somewhat more than 25 percent at the end of the simulation. This would appear to be counter-intuitive, because compressible turbulence is thought to be more dissipative, and negative coefficients are associated with reduced dissipation. Indeed, the average value of c_ν is somewhat less for the compressible case than the incompressible. There is, however, a tendency for the coefficients to be somewhat larger in magnitude, as illustrated by figures 6.7 and 6.8 as compared to figures 5.17 and 5.18. Thus, the model predicts a higher rate of energy transfer in the turbulent energy cascade (both forward and backward) for the compressible case.

The evolution of the mean value of the dissipation model coefficient is shown in figure 6.10. As in the incompressible case, the coefficient starts with a value of about 0.5 and increases linearly from there. In this case, however, the mean value does not reach as high a level as in the incompressible case. The slope, however, is higher. The behavior of the energy subgrid model is shown in figure 6.11. In this

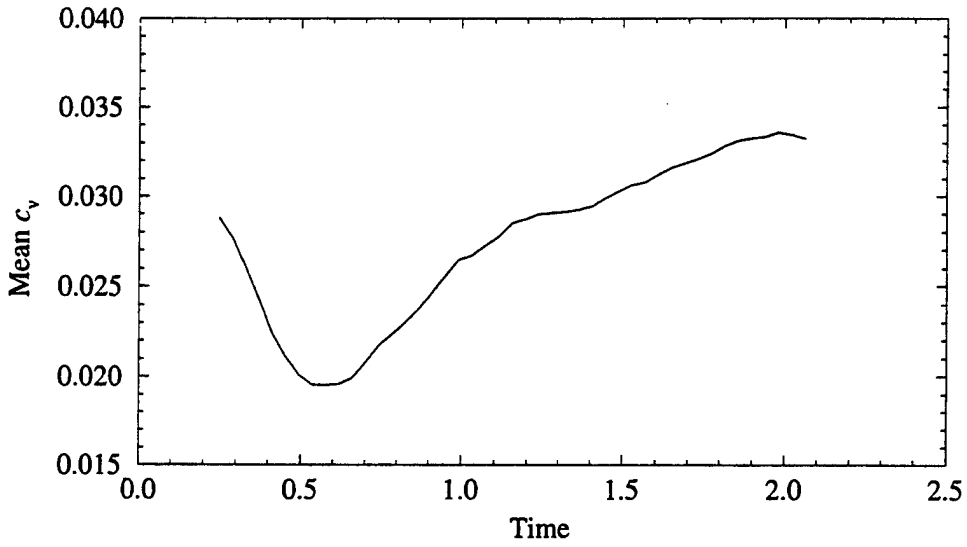


Figure 6.6: Evolution of mean c_ν in compressible decaying isotropic turbulence

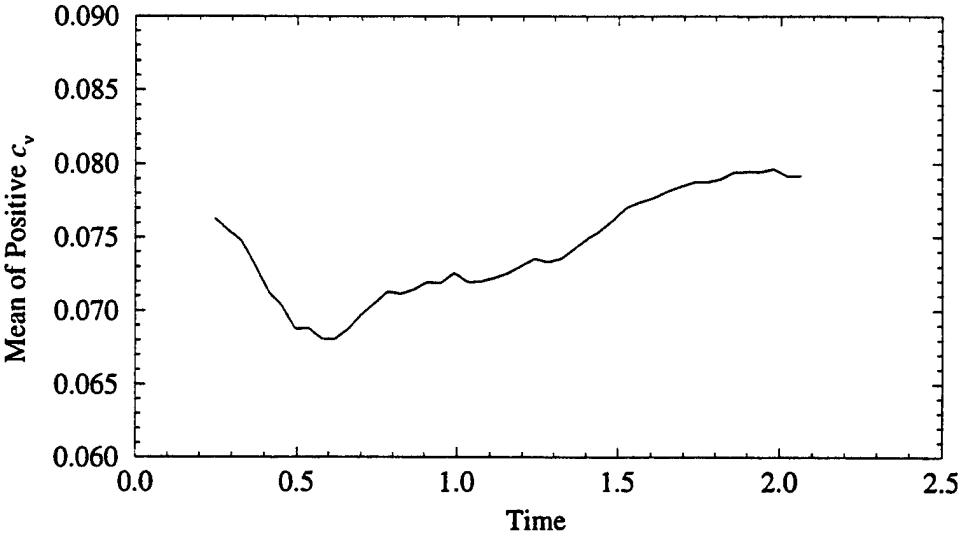


Figure 6.7: Average of positive c_ν values in compressible decaying isotropic turbulence

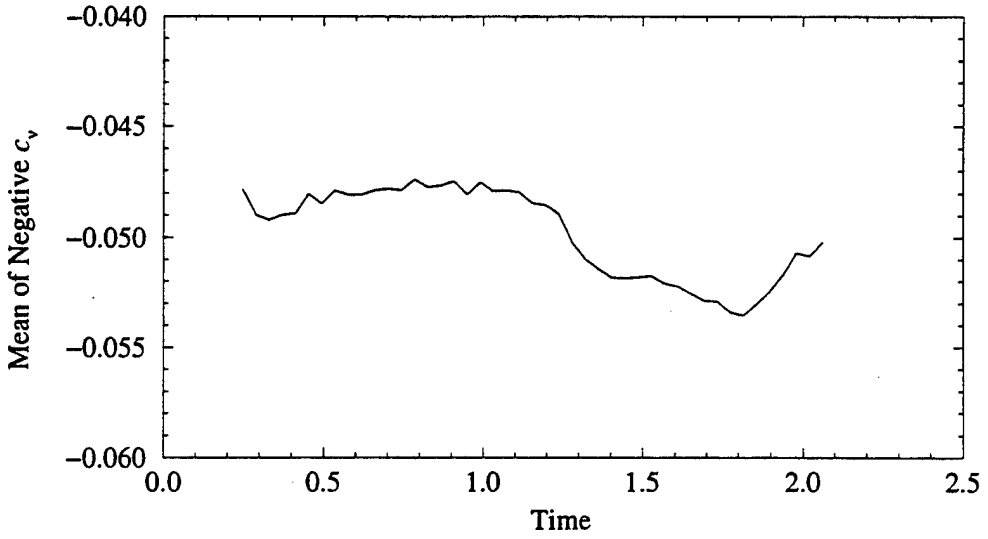


Figure 6.8: Average of negative c_ν values in compressible decaying isotropic turbulence

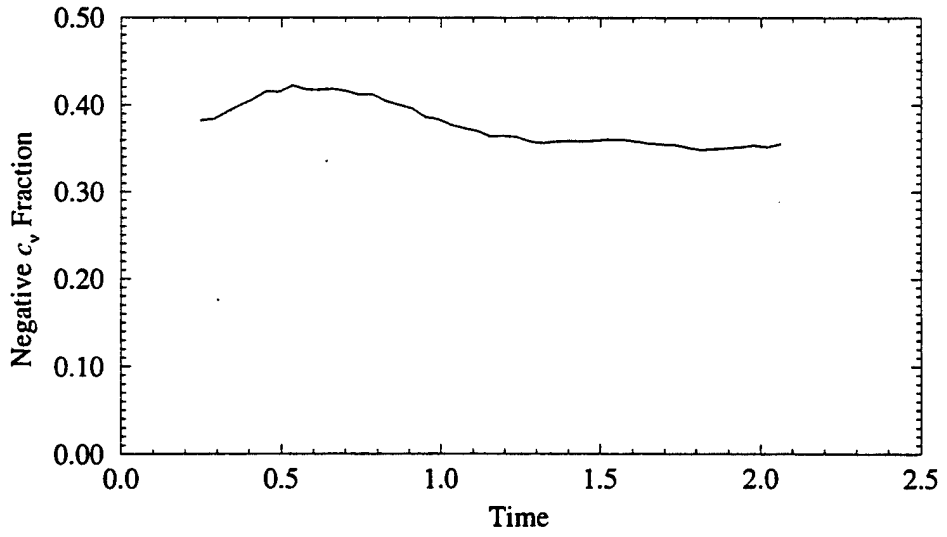


Figure 6.9: Fraction of points with negative c_ν values in compressible decaying isotropic turbulence

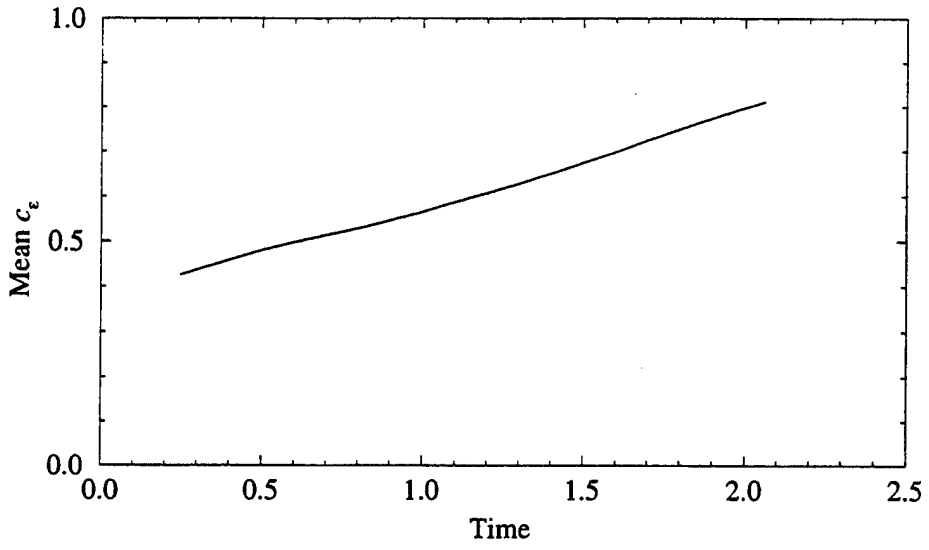


Figure 6.10: Average value of the dissipation model coefficient in compressible decaying incompressible turbulence

case, the model coefficient does not decrease as does the incompressible case (see figure 5.21), remaining in the vicinity of 0.1.

The mean predicted contributions of the modelled subgrid kinetic energy equation production and dissipation terms (from equation 3.25) are shown in figure 6.12. Whereas these terms both approached zero for the incompressible case, in this case the magnitude of the dissipation term remains relatively large throughout the simulation compared with the production term.

As with the incompressible decaying isotropic turbulent flows (Sections 5.2.2 and 5.2.3), the effect of using the alternate method to compute the subgrid kinetic energy dissipation model coefficient has been investigated for this case. Again, the difference in coefficient magnitude is significant, as illustrated in figure 6.13. This

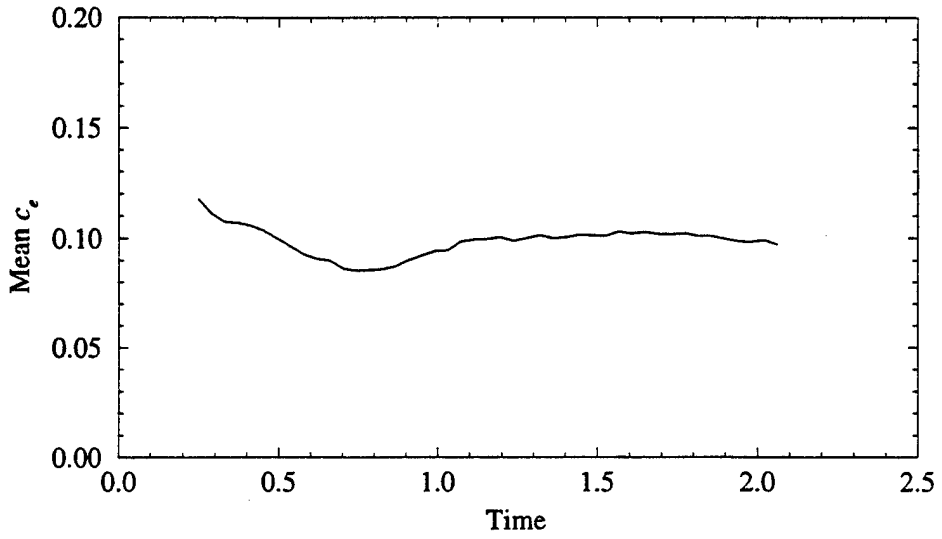


Figure 6.11: Evolution of the mean of the energy equation subgrid model coefficient in compressible decaying isotropic flow

results in an increase to the modelled dissipation in the early stages of the simulation (see figure 6.14). This in turn reduces the amount of subgrid kinetic energy in the flow, although it is still significantly different from the levels computed *a priori* from DNS data (figure 6.15). These differences in subgrid quantities do not correspond, however, to large differences in the resolved field. The Mach number, for instance, behaves almost identically with the alternate form as with the original algorithm (see figure 6.16).

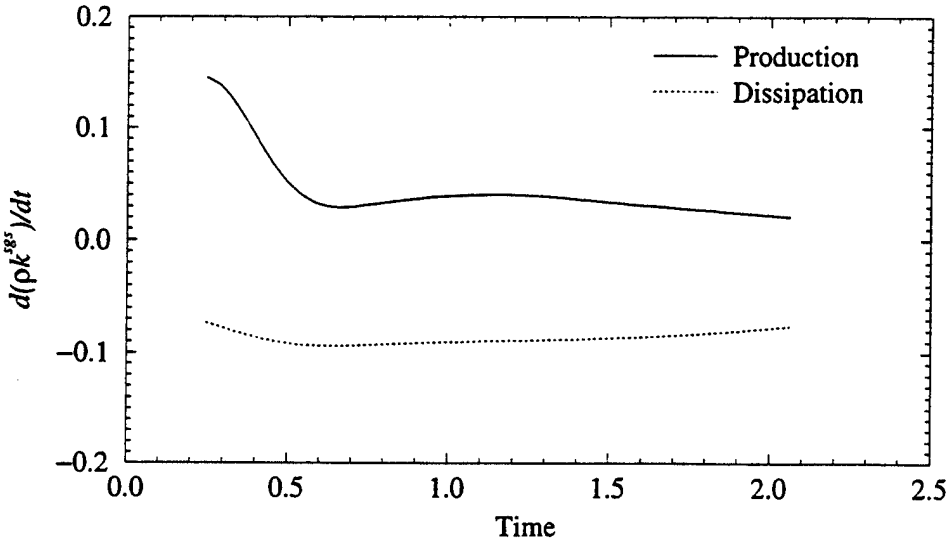


Figure 6.12: History of the modelled production and dissipation contributions to the subgrid kinetic energy equation for compressible decaying isotropic turbulence

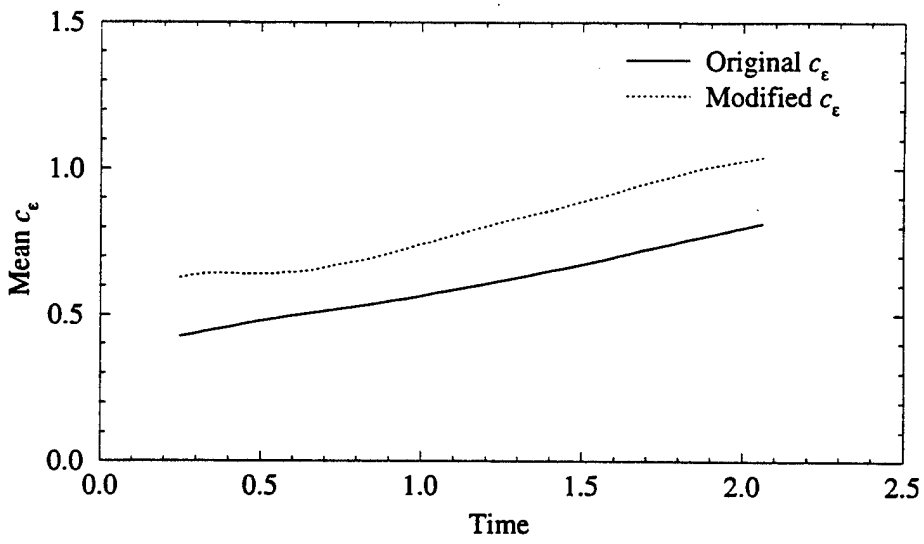


Figure 6.13: The evolution of the mean of c_ϵ as computed by two different methods in compressible decaying isotropic turbulence

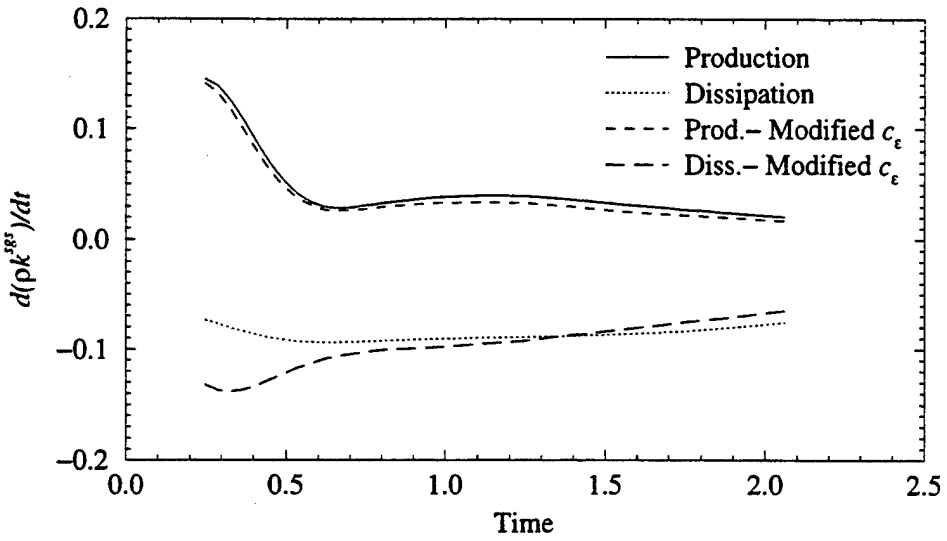


Figure 6.14: The effects of different algorithms for c_ε on the modelled production and dissipation of k^{sgs} in compressible, decaying isotropic turbulence

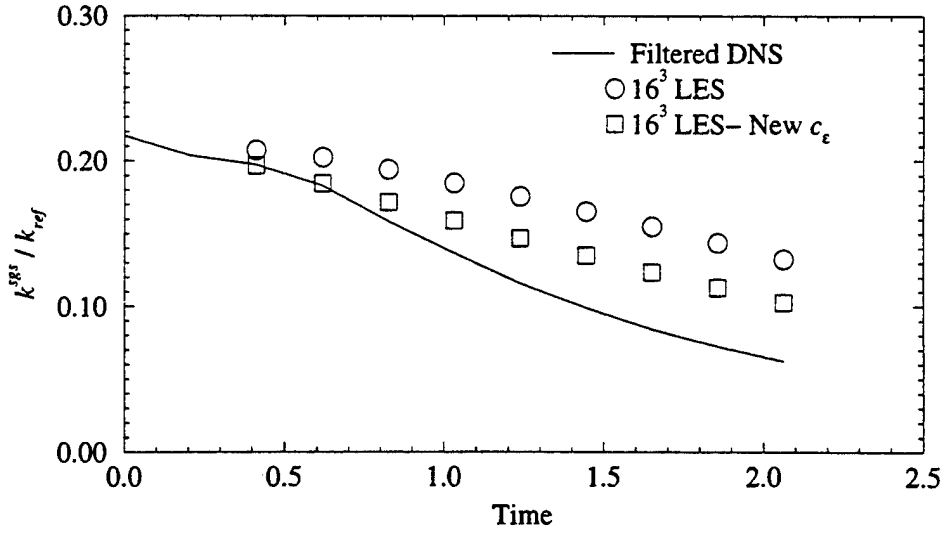


Figure 6.15: The effect of different methods to compute c_ε on the subgrid kinetic energy in compressible, decaying isotropic turbulence

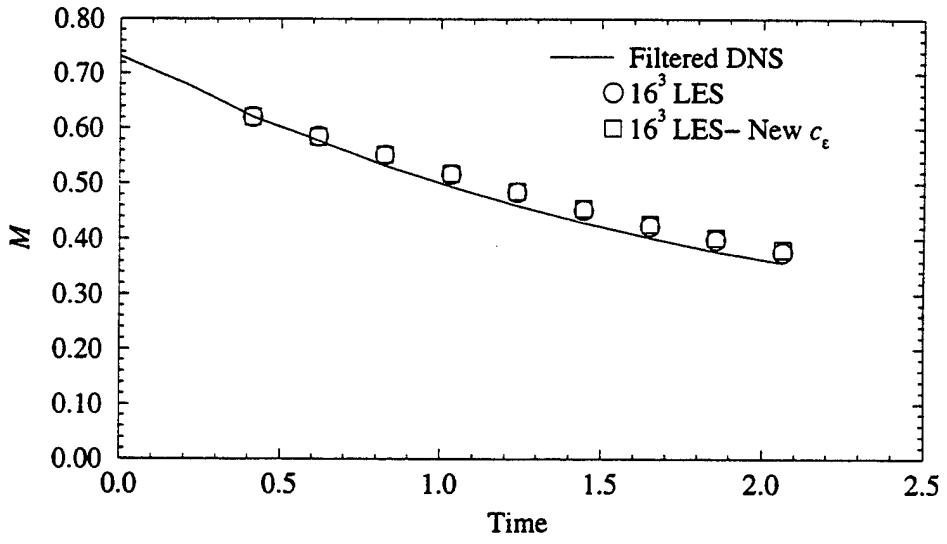


Figure 6.16: The effect of different methods to compute c_ϵ on the mean Mach number in compressible, decaying isotropic turbulence

6.1.2 Reynolds Number and Mach Number Tests

To gain a better understanding of the effects of Mach number and Reynolds number on isotropic turbulence and the current model, a series of numerical tests were conducted. The same domain (a cube with 2π meter sides), grid ($32 \times 32 \times 32$), and initial velocity field were used in each case, but the thermodynamic variables were manipulated to yield different initial Mach and Reynolds numbers. Simulations were run for three different values of the average initial Mach number and two initial Reynolds numbers (see Table 6.1). The initial pressure, temperature, and density fields are constant.

Table 6.1: Test cases for the investigation into the effect of initial Mach and Reynolds number on model behavior

Case	M_t	R_{e_L}	$R_{e_{l_0}}$
I	0.4	900	86.2
II	0.6	900	86.2
III	0.8	900	86.2
IV	0.4	1350	129.3
V	0.6	1350	129.3
VI	0.8	1350	129.3

The evolution of the mean Mach number for the six cases is shown in figure 6.17. As expected, a higher Reynolds number corresponds with a lower Mach number decay rate, though the difference is not great. Also, the suppression of turbulence due to compressibility is visible in that the higher Mach number flows experience a greater absolute drop in the average Mach number. The effect of turbulent Mach number on the development of density fluctuations is directly visible in figure 6.18.

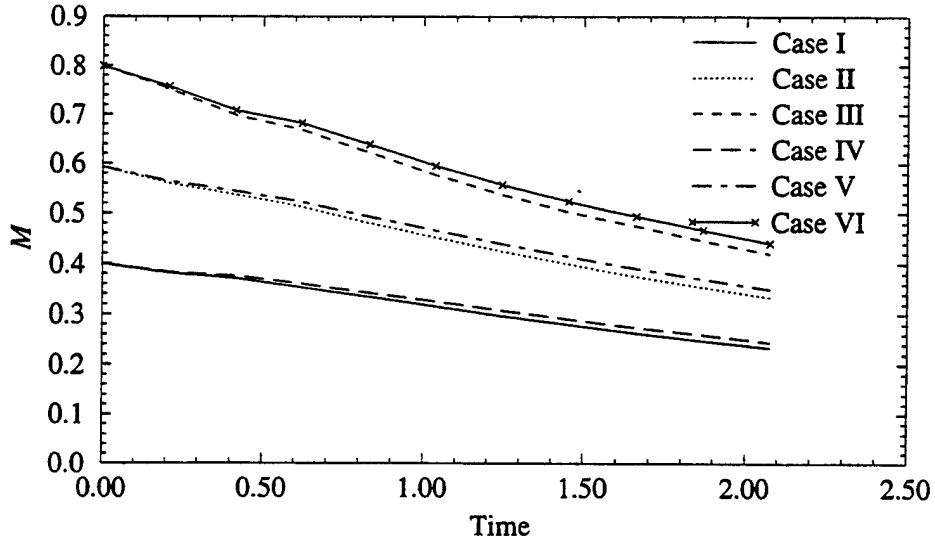


Figure 6.17: Mach number history for cases with different initial Reynolds and Mach numbers in decaying compressible isotropic turbulence

Again, a slight effect of Reynolds number is visible as the fluctuation level for the higher Reynolds number simulations remains slightly higher than that of the corresponding lower Reynolds number run.

The behavior of the kinetic energy for these tests is shown in figures 6.19 and 6.20. As expected, as the Mach number increases, the energy of the flow is decreased. Conversely, as the Reynolds number is increased, the kinetic energy of the flow remains at a higher level. The impact of the Reynolds number is most visible in the subgrid kinetic energy. This is due to the strong dependance of the dissipation model on viscosity.

The mean of the subgrid stress tensor model coefficient (c_ν) is shown in figure 6.21. Though no clear trend with Mach number is visible, the magnitude clearly

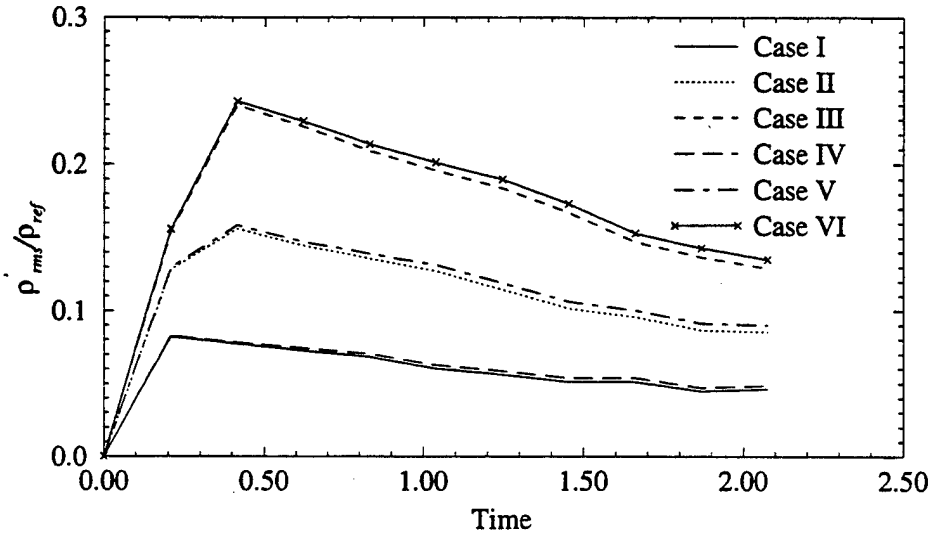


Figure 6.18: Evolution of normalized density fluctuations for different initial Reynolds and Mach numbers in decaying compressible isotropic turbulence

increases with Reynolds number. This a somewhat artificial trend, however. When only the positive elements of c_ν are considered, as in figure 6.22, this trend is not present. Instead, this plot shows that the cases with the highest compressibility seem, on average, to compute consistently higher values of the coefficient than the other runs. The Reynolds number dependance does show up strongly in the negative components of the coefficient field, as shown in figure 6.23. This is due to the constraint that the effective viscosity must always be positive (or zero). For the higher Reynolds number runs (cases IV, V, and VI), the kinematic viscosity was smaller than for the lower Reynolds number tests (cases I, II, and III); consequently, the aforementioned constraint was more restrictive for the former runs. Therefore, with negative values more tightly constrained, the overall mean value shows a rise for

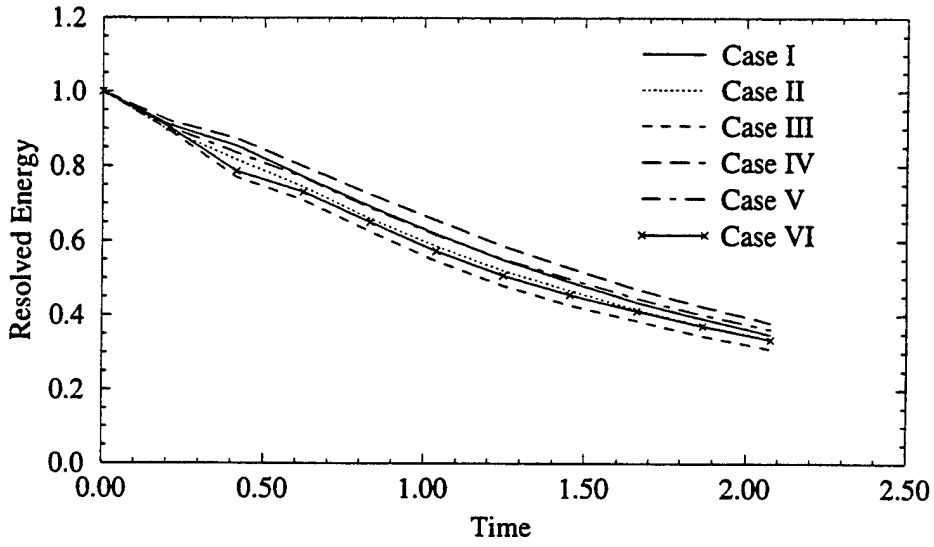


Figure 6.19: Resolved kinetic energy traces for different initial Mach and Reynolds numbers in decaying compressible isotropic turbulence

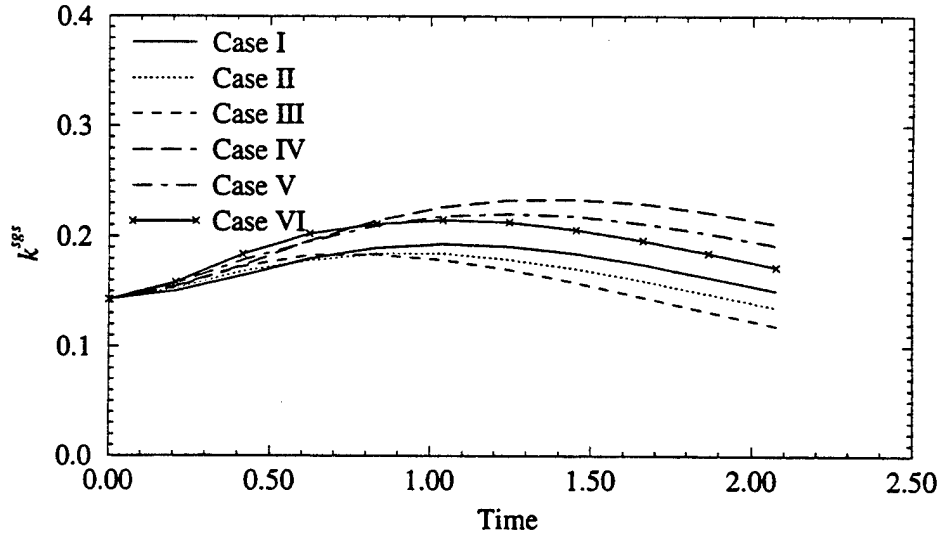


Figure 6.20: Subgrid kinetic energy traces for different initial Mach and Reynolds numbers in decaying compressible isotropic turbulence

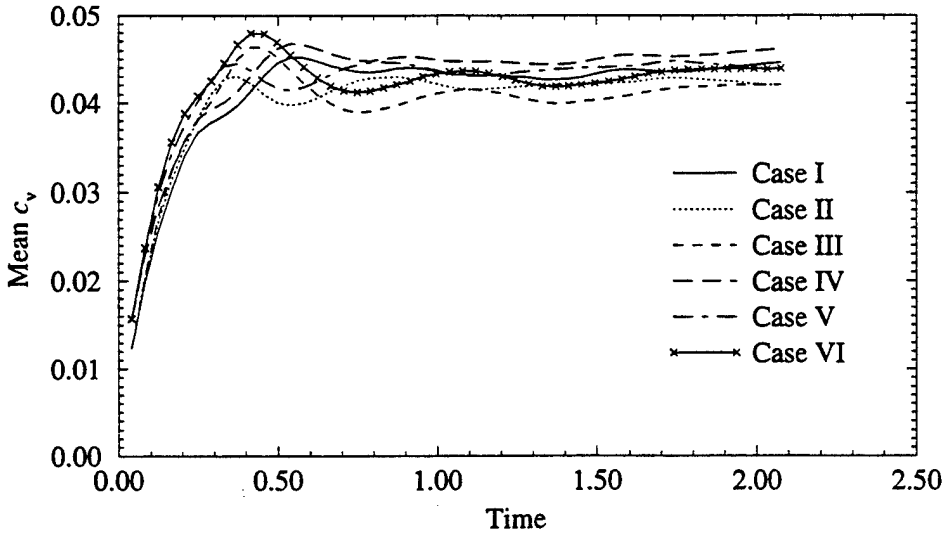


Figure 6.21: Evolution of the mean sugrid stress tensor model coefficient for different initial Mach and Reynolds numbers in decaying compressible isotropic turbulence

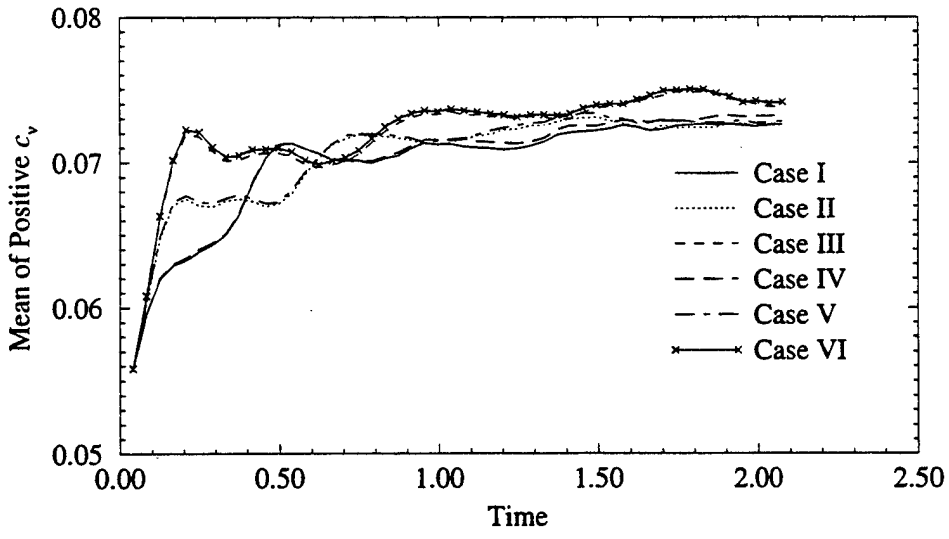


Figure 6.22: Evolution of the mean of positive c_ν for different initial Mach and Reynolds numbers in decaying compressible isotropic turbulence

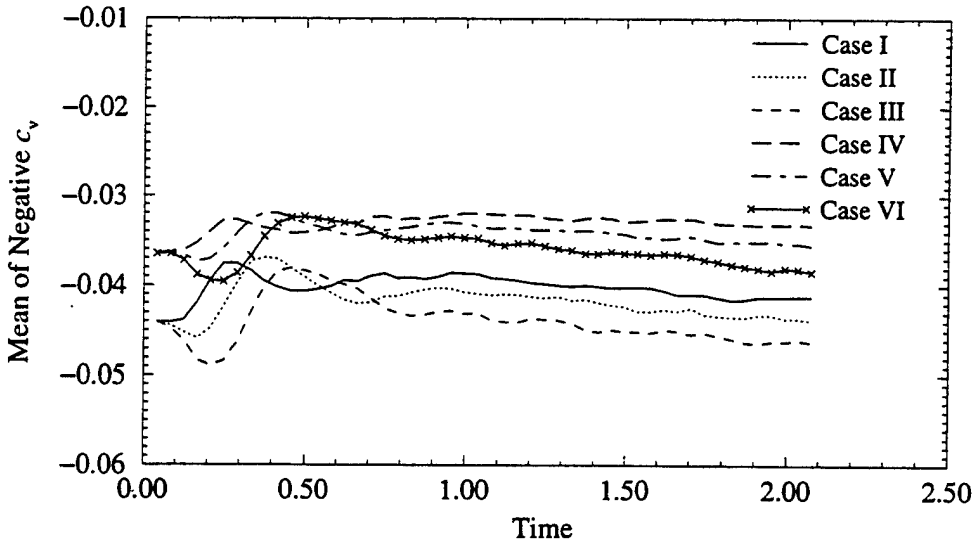


Figure 6.23: Evolution of the mean of negative c_ν for different initial Mach and Reynolds numbers in decaying compressible isotropic turbulence

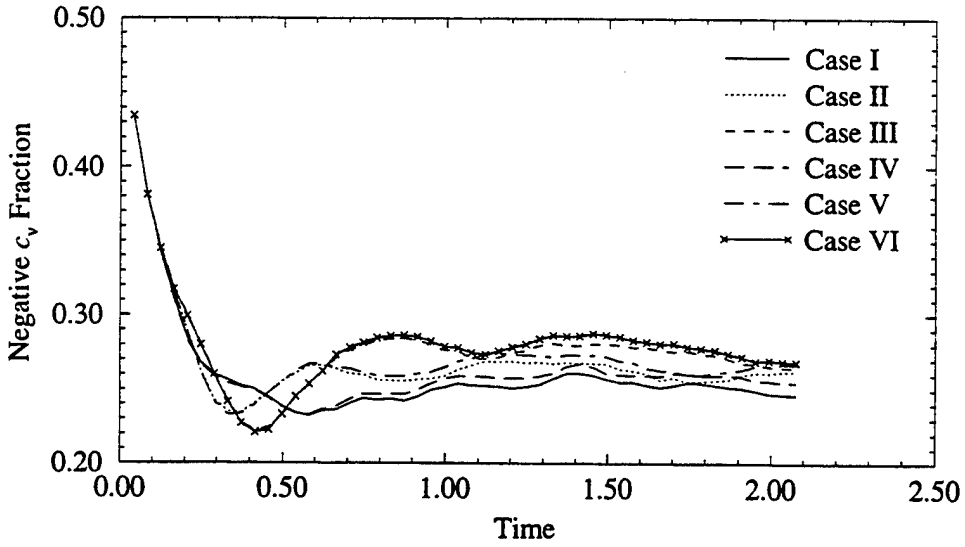


Figure 6.24: Fraction of points with negative c_ν for different initial Mach and Reynolds numbers in decaying compressible isotropic turbulence

the higher Reynolds number cases. In addition, for a given Reynolds number, figure 6.23 shows an increase in the magnitude of the negative coefficients as the Mach number increases. The fraction of points with negative coefficient values does not appear to depend strongly on Reynolds number, as shown in figure 6.24. There is, however, a slight, but noticeable, decrease in the number of negative points with rising Mach number.

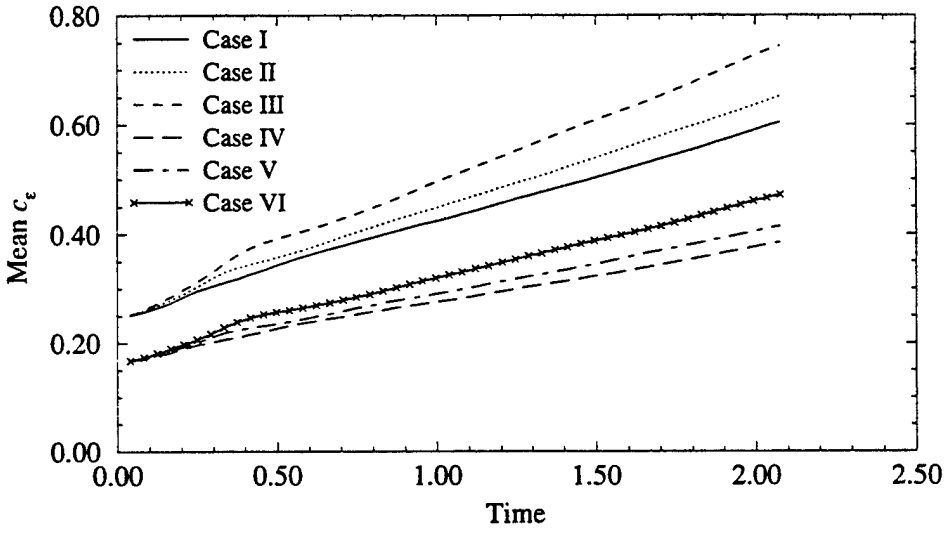


Figure 6.25: Average value of the dissipation model coefficient for different initial Mach and Reynolds numbers in decaying compressible isotropic turbulence

Given the formulation of the dynamic subgrid dissipation model coefficient (equation 3.32), one would expect a strong negative correlation of this coefficient with Reynolds number; in other words, an increase in the dissipation coefficient is expected with increasing viscosity. This is, in fact, what is observed, as shown

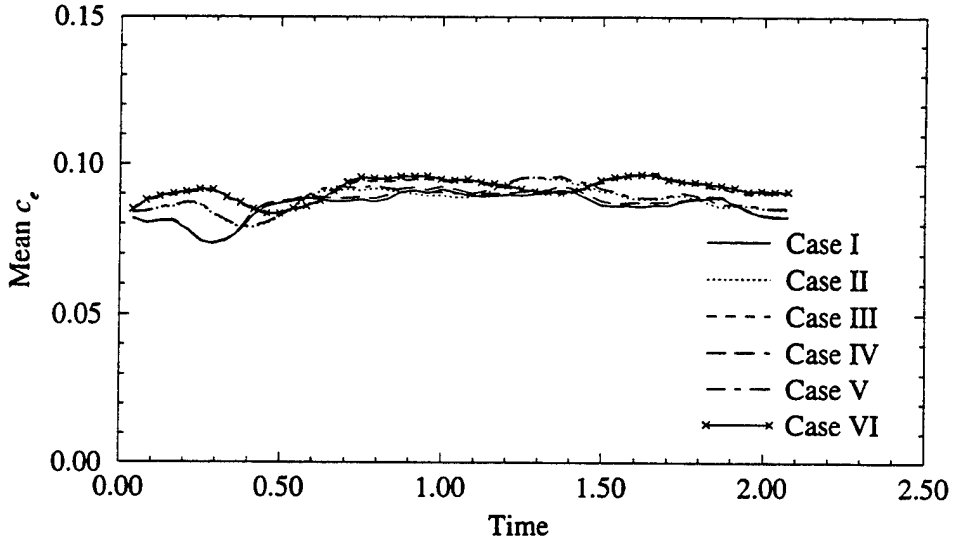


Figure 6.26: Average value of the energy equation subgrid model coefficient for different initial Mach and Reynolds numbers in decaying compressible isotropic turbulence

in figure 6.25. There is also an increase in the coefficient's mean value with Mach number. The mean of the energy equation subgrid model coefficient does not appear to have any strong dependance on either Mach number or Reynolds number (figure 6.26). Although the initial values for these cases showed a rise in the mean coefficient value with increasing Mach number, this dependance does not last throughout the simulations. The mean value for all cases stayed in the vicinity of 0.08-0.10 once the flow was established.

The behavior of the modelled subgrid kinetic energy production and dissipation terms is shown in figures 6.27 and 6.28. From these plots a striking difference is noted between the behavior of these terms early in the simulations and that found later on. Production, for instance, is predicted as being much higher for the

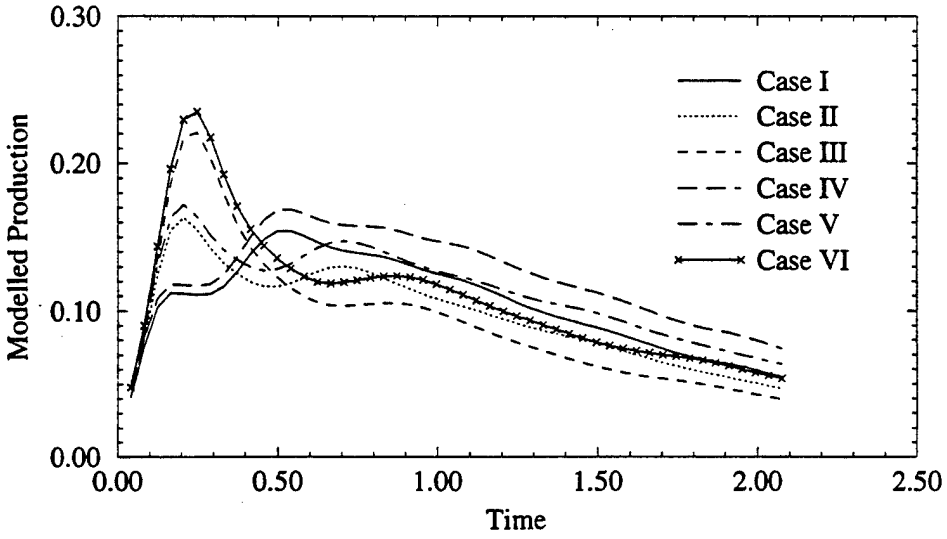


Figure 6.27: Average value of the modelled subgrid kinetic energy production term for different initial Mach and Reynolds numbers in decaying compressible isotropic turbulence

higher Mach numbers early in the simulation, but after half an eddy turnover time, this situation reverses itself, and the lower Mach number cases are seen to have the greatest production. At the same time, the effect of the Reynolds number, at first negligible, becomes more important, with the higher Reynolds number cases "producing" more subgrid kinetic energy. The modelled dissipation, however, shows a strong dependance on Reynolds number from the very beginning. As with the production, the dissipation is seen at first to have increased magnitude in the higher Mach number cases. Gradually, however, the lower Mach number cases catch up and finally surpass the higher Mach number simulations.

It is difficult to draw firm conclusions about the affect of compressibility on the production and dissipation of turbulent kinetic energy from these simulations. In

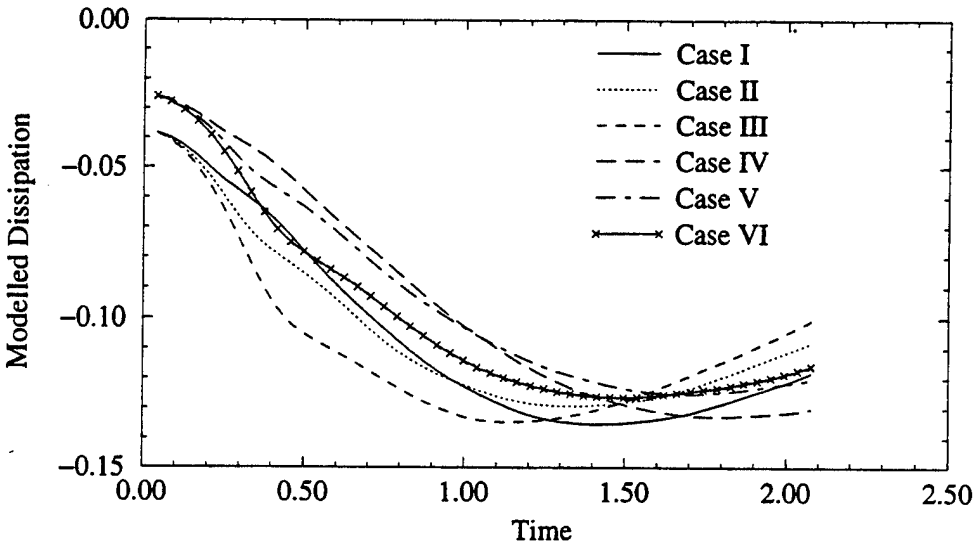


Figure 6.28: Average value of the modelled subgrid kinetic energy dissipation for different initial Mach and Reynolds numbers in decaying compressible isotropic turbulence

the first place, the initial conditions are merely a random, divergence-free realization of a fairly arbitrary energy spectrum. Thus, the early behavior of the flow cannot be considered truly turbulent. At some point, it is assumed, the simulation approaches the character of real turbulence, but exactly when this takes place is not necessarily easy to say. If one assumes that this happens sometime between half a turnover time and a full turnover time, then it is still difficult to say what the effect of compressibility is, because the unphysical initial development may have "corrupted" the solution (for these purposes). Despite these uncertainties, it appears that the production rate is generally decreased by increasing compressibility. There may also be an associated increase of dissipation associated with increasing compressibility,

but this observation is made more tenuous than that for the production because, by the end of the simulations, the situation has been reversed.

Note also that it is not clear that the quantities labelled "production" and "dissipation" in these cases are at all related to the actual production and dissipation of turbulent kinetic energy. It is perhaps better to call them energy transfer rates at the limit of grid resolution ("production" of subgrid kinetic energy) and at the limit of scales which affect resolved scales ("dissipation" of subgrid kinetic energy). Looked at in this light, they have more to say about the energy cascade process than the actual creation or destruction of turbulent kinetic energy.

6.2 Forced Isotropic Turbulence

Statistically stationary turbulence was simulated on a low resolution (32^3) grid to examine the characteristics of the model in a medium to high Reynolds number, moderate Mach number regime. The domain was taken to be a cube with sides of length 2π. The statistically stationary turbulent field is obtained by forcing the low wavenumber components in a similar manner as Kim [67]. This forcing is done by holding fixed the value of all velocity Fourier modes with wavenumber magnitude less than 1.5. The flow was initialized as a random, divergence-free field with the following energy spectrum:

$$E(k) = C\frac{k^4}{1+\left(\frac{k}{k_0}\right)^{5/3+4}} \tag{6.1}$$

The peak wavenumber, k_0, had a value of one, and C was a constant which normalized the field to match a specified u_{rms}. Two cases (denoted Case 1 and Case 2) were run. The first was a weakly compressible, relatively low Reynolds number case. The statistically steady state velocity field from this case was scaled and used as initial conditions for a more compressible, higher Reynolds number case.

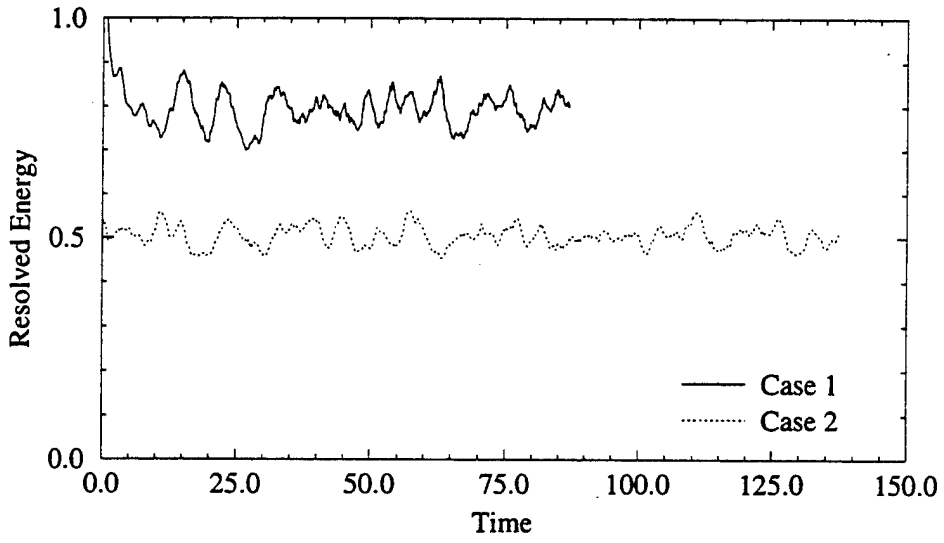


Figure 6.29: Evolution of the mean resolved kinetic energy in forced isotropic turbulence

Since this is LES, it is not possible to directly compute many of the parameters which are commonly used to characterize isotropic turbulence (*e.g.*, the Taylor Reynolds number). These will be approximated in the following manner. Once a statistically steady state has been reached, mean flow quantities are obtained by averaging spatially to obtain a single mean value for a given point in time. Mean

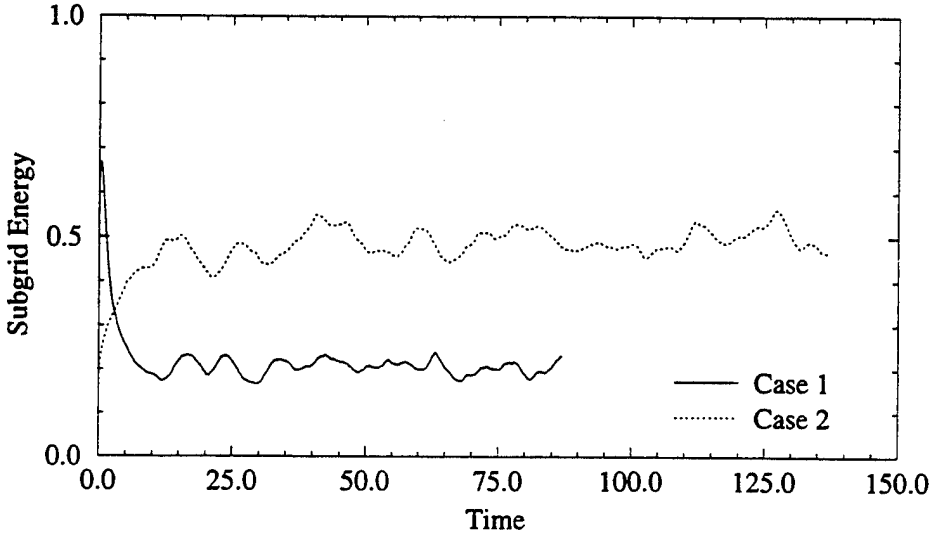


Figure 6.30: Evolution of the average subgrid kinetic energy in forced isotropic turbulence

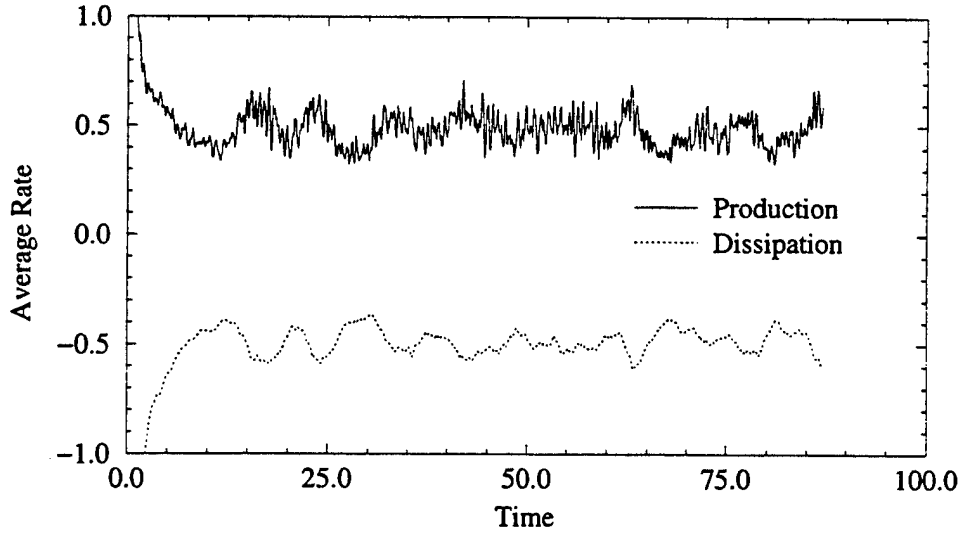


Figure 6.31: Mean values of the modelled subgrid kinetic energy production and dissipation terms for Case 1

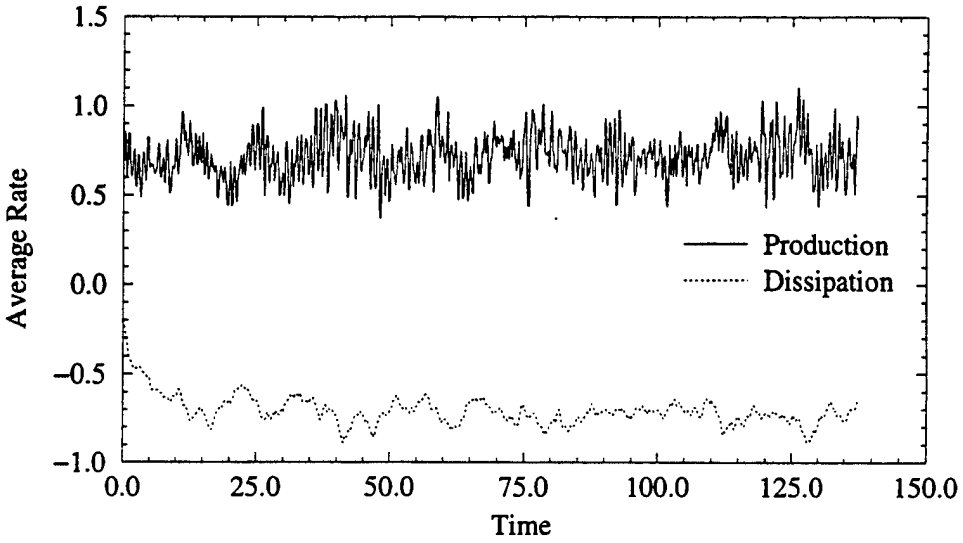


Figure 6.32: Mean values of the modelled subgrid kinetic energy production and dissipation terms for Case 2

values from several points in time can then be averaged to obtain approximations for the steady state mean values of the flow. The average energy dissipation rate, ε, is estimated in this fashion from the mean energy injection rate. An estimate for the mean turbulent kinetic energy (E_{tot}) of the flow can be obtained by finding the steady state value of the subgrid kinetic energy and adding that to the average resolved kinetic energy. The RMS of velocity can be related to the mean total kinetic energy as:

$$u_{rms}^2 = \frac{2}{3} E_{tot} \tag{6.2}$$

The effective viscosity $(\nu + \nu_t)$ can be computed from equations 3.11 and 2.4 using steady state values of the subgrid stress tensor model coefficient (c_ν), subgrid kinetic energy, and temperature. With this, the Taylor microscale is approximated as:

$$\lambda^2 \approx \frac{15\nu_{eff}\, u_{rms}^2}{\varepsilon} \tag{6.3}$$

A corresponding integral length scale is approximated as:

$$\ell \approx \frac{3\pi E_{tot}}{10 u_{rms}^2 k_0} \tag{6.4}$$

Using the above analysis, the Taylor Reynolds number for Case 1 was approximately 266 and the integral length scale Reynolds number was roughly 622. The integral scale eddy turnover time was computed to be 1.84 seconds. Case 1 was, therefore, run for roughly 85 large eddy turnover times. For Case 2, the approximate Taylor Reynolds number was much higher: 1586. The integral scale Reynolds number was found to be roughly 2457. The integral scale turnover time for Case 2 was about 1.42 seconds; therefore, the simulation was run for more than one hundred turnover times after stationary flow was achieved.

The instantaneous mean resolved and subgrid kinetic energy (normalized by E_{tot}) are shown in figures 6.29 and 6.30, respectively. After an initial relaxation period, the average resolved kinetic energy in the domain remains roughly constant, as shown in figure 6.29. This reflects the balance between forcing and dissipation. Similarly, the subgrid kinetic energy history is shown in figure 6.30. By comparing

figure 6.30 with figure 6.29 the relative proportion of resolved to unresolved energy can be determined. As expected, the higher Reynolds number case (Case 2) has a much greater proportion of energy in the subgrid. It can be seen that the subgrid holds about twenty percent of the energy of the flow for Case 1. For Case 2, this fraction was significantly higher: around fifty percent.

The energy balance is further depicted in figure 6.31 which shows mean values of the subgrid kinetic energy production and dissipation model terms (see equation 3.25) as a function of time for Case 1. Figure 6.32 shows similar data for Case 2. As it should be, the production largely mirrors the dissipation, though it is interesting to note that there is a much greater level of high frequency fluctuation in the former quantity. The data in these plots has been non-dimensionalized by $\rho_{ref}\varepsilon$.

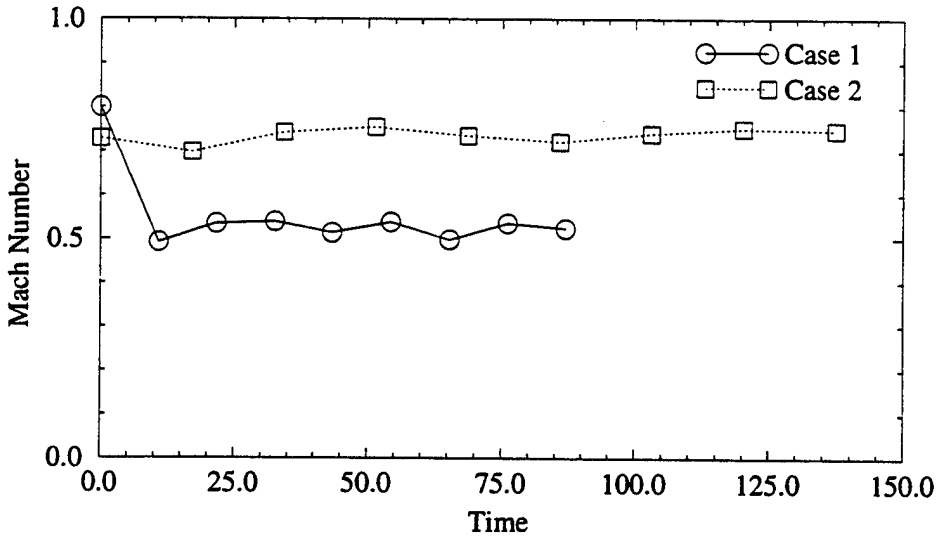


Figure 6.33: The mean Mach number as a function of time in forced isotropic turbulence

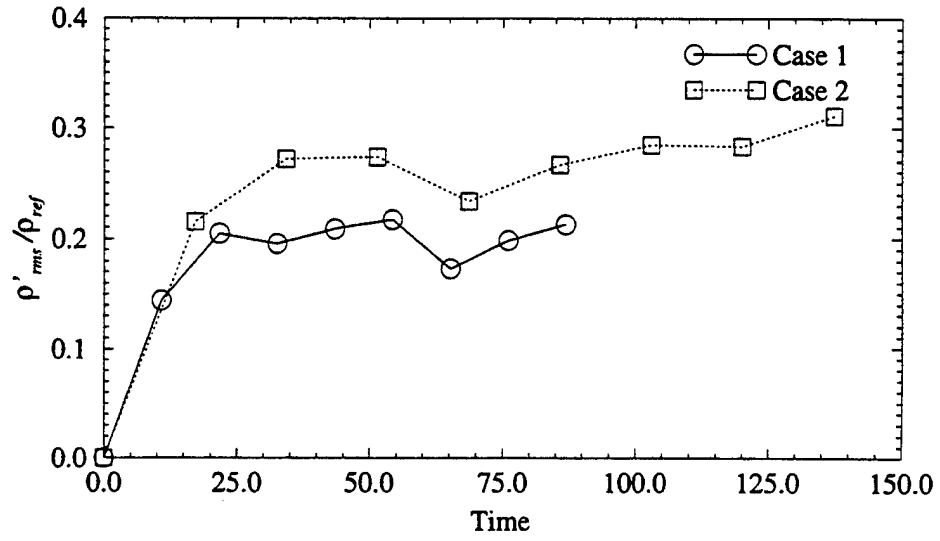


Figure 6.34: Evolution of the normalized RMS of density fluctuations in forced isotropic turbulence

The averaged (in space) Mach number for Case 1 started near 0.8, but decreased to a stable value of roughly 0.5, as is shown in figure 6.33. Peak Mach numbers averaged around 1.2-1.5 after the stationary state had been reached. Thus, the flow may be said to be at least weakly compressible. For Case 2, the mean Mach number is roughly 0.75, which is well into the compressible region. For this case, the peak Mach numbers for the statistically steady state flow hovered in the region of 1.8-2.4.

The compressibility of the flow is further reflected in the density fluctuation history, which is shown in figure 6.34. The fluctuations reached a steady state value of 20 percent of the reference density for Case 1. This is in line with the decaying isotropic turbulence results which Spyropoulos and Blaisdell [15] reported for an initial turbulence Mach number of 0.4 and an initial compressibility factor of 0.1.

For that case, the RMS of density fluctuations peaked at roughly 15 percent. While one must be careful in comparing forced simulations with decaying simulations, at least it appears that this level of density fluctuation is reasonable. For Case 2, the density fluctuations are, as expected, somewhat higher: around 25 to 30 percent.

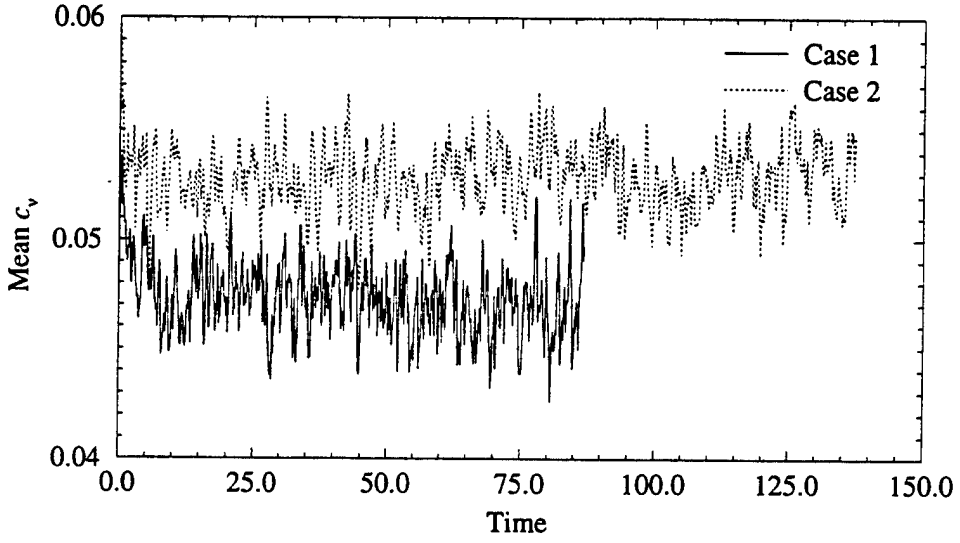


Figure 6.35: Evolution of the mean of the subgrid stress tensor model coefficient in forced isotropic turbulence

The subgrid stress tensor model coefficient, c_ν, reached a steady-state value of roughly 0.047 in Case 1, as is shown in figure 6.35. Case 2 stabilizes in the vicinity of 0.053. This is reasonably close to the results that Kim [67] obtained for forced incompressible isotropic turbulence. In Kim's cases, the coefficient stabilized in the region of 0.05 and 0.055. The fraction of points with a negative coefficient value,

shown in figure 6.36, is somewhat higher than that reported by Kim: about thirty percent for both cases, as opposed to roughly twenty percent for Kim.

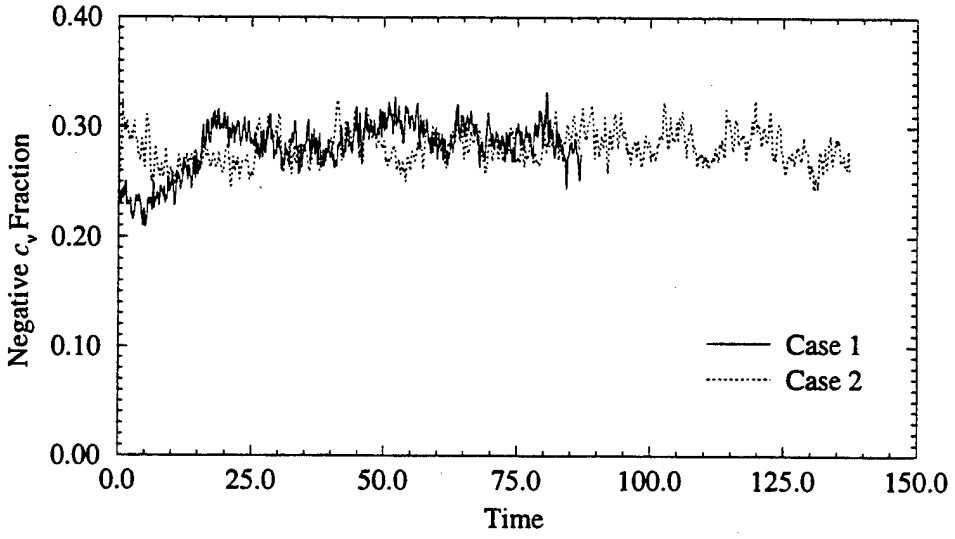


Figure 6.36: The fraction of points with a negative subgrid stress model coefficient as a function of time in forced isotropic turbulence.

The steady state values of the dissipation model coefficients were roughly 0.33 and 0.44 for the incompressible cases reported by Kim. The present results, shown in figure 6.37 level off at roughly 0.2 for Case 1. Case 2 reaches a steady state value of roughly 0.05. The reason for this drastic difference is not clear, although it is certain that the Reynolds number plays a large role. In Kim's cases, the higher Reynolds number case also had a lower dissipation model coefficient, though the difference was not so great. The behavior of the energy equation subgrid model

coefficient is shown in figure 6.38. As can be seen, it reaches a stable value in the region of 0.09 for Case 1 and 0.10 for Case 2.

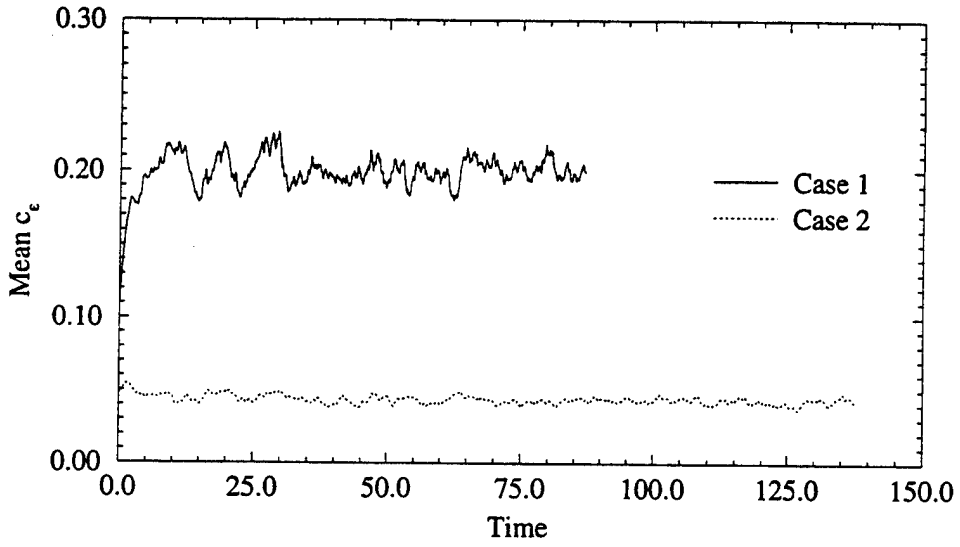


Figure 6.37: Time evolution of the mean of the dissipation model coefficient in forced isotropic turbulence

The effect of using the alternate expression for c_ϵ (equation 3.33 instead of equation 3.32) has been investigated for both of the above cases. As seen in the decaying isotropic cases, the effect on the coefficient magnitude is quite large (see figure 6.39). This difference has a measurable effect on the estimated Reynolds numbers. For Case 1, the new estimate of the Taylor Reynolds number is 214 (down from 266), while for Case 2 it was down from 1546 to 674. The estimated integral scale Reynolds numbers were similarly effected: down from 622 to 593 for Case 1, and from 2457 to 1967 for Case 2. The effect of these changes on the modelled production and

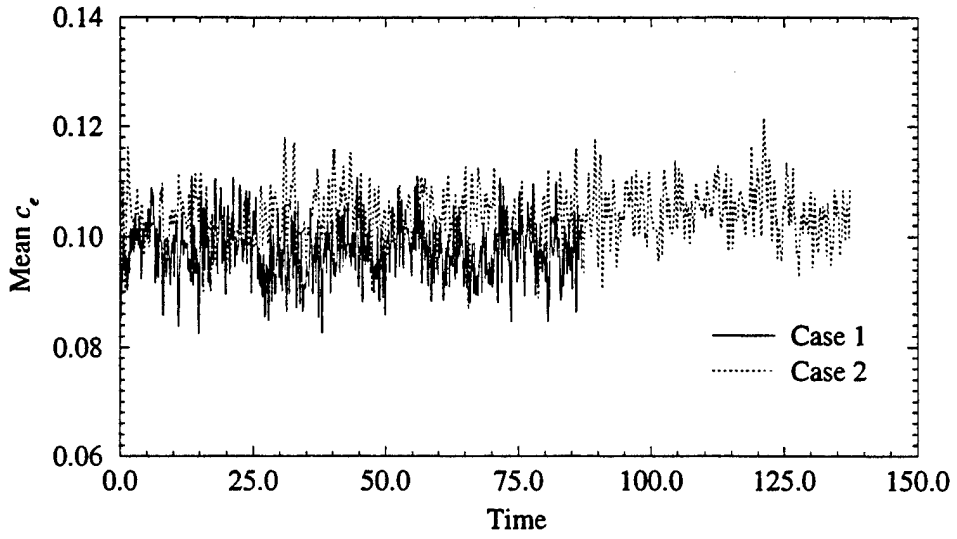


Figure 6.38: Time trace of the average value of the energy equation subgrid model coefficient

dissipation terms may be seen by comparing figures 6.40 and 6.41 with figures 6.31 and 6.32. From these figures, it is apparent that for the lower Reynolds number case (Case 1), the effect is quite small, but for Case 2, the magnitude of both the non-dimensionalized production and dissipation are reduced by a third.(from 0.75 to 0.5). The relative amount of subgrid kinetic energy (to E_{tot}) was greatly affected, as shown in figure 6.42. For Case 1, the amount was cut in half, while for Case 2, the new level was less than one third of the original. As a result of these changes, the relative proportion of resolved kinetic energy increased for both cases to the vicinity of 90 percent of E_{tot} (see figure 6.43). Despite such large changes in the above quantities, the resolved flow variables were not, in general, significantly affected.

The mean Mach number, for instance, was unchanged, as shown in figure 6.44. The other resolved field variables were similarly unchanged.

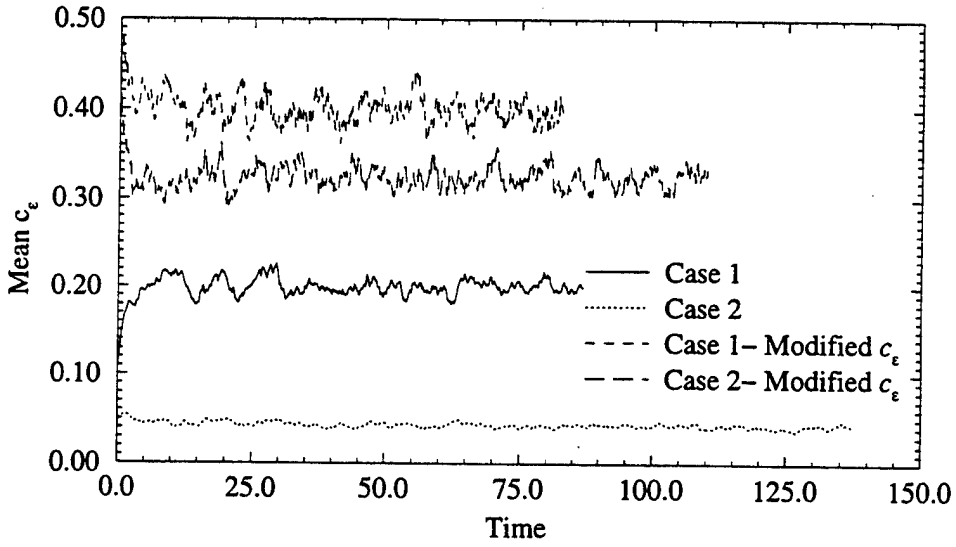


Figure 6.39: The evolution of the mean of c_ε as computed by different methods in forced isotropic turbulence

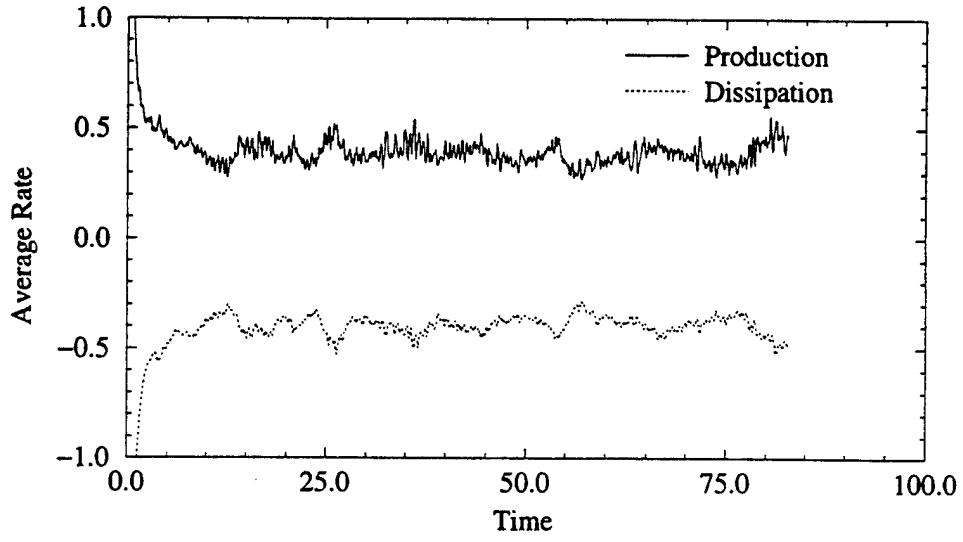


Figure 6.40: Mean values of the modelled k^{sgs} production and dissipation terms for Case 1 recomputed using the alternate form for c_ε

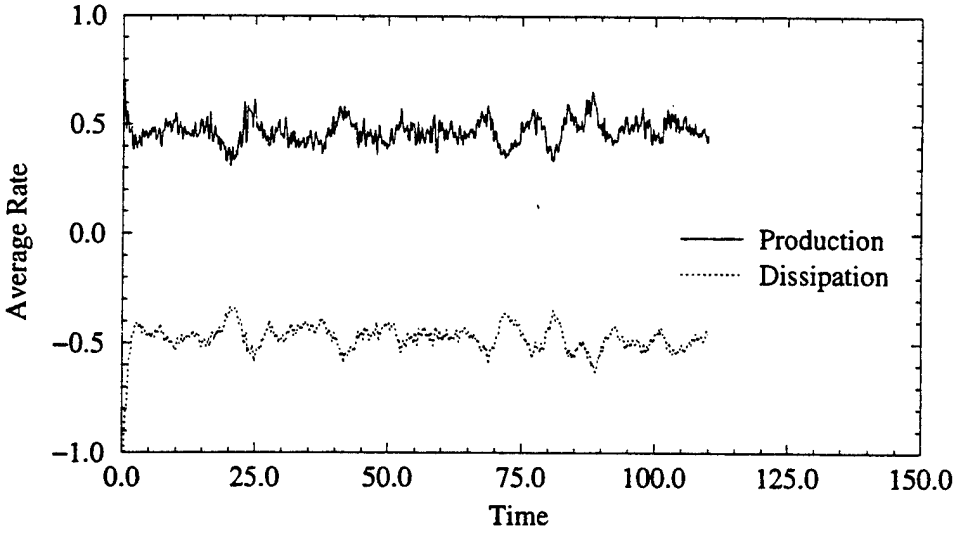


Figure 6.41: Mean values of the modelled k^{sgs} production and dissipation terms for Case 2 recomputed using the alternate form for c_ε

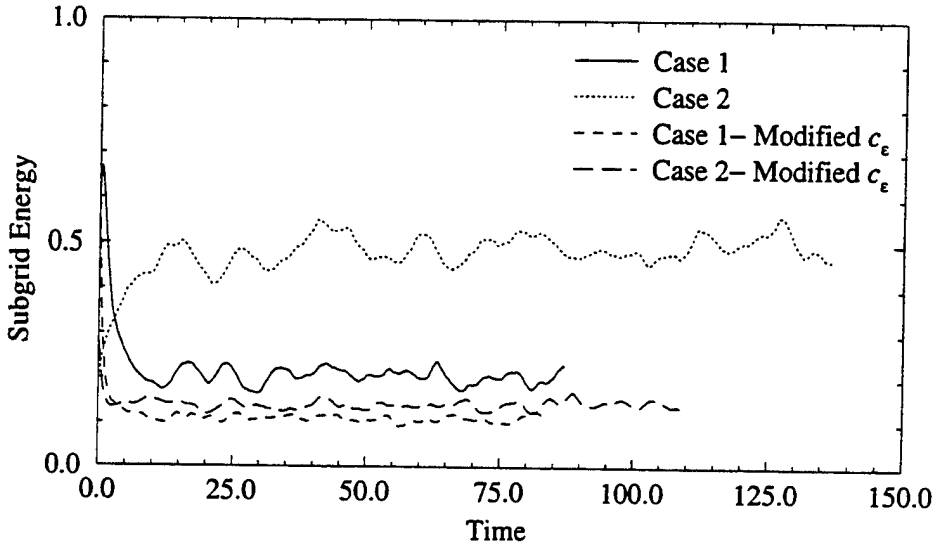


Figure 6.42: The effect of different means of computing c_ε on the predicted subgrid kinetic energy in forced isotropic turbulence

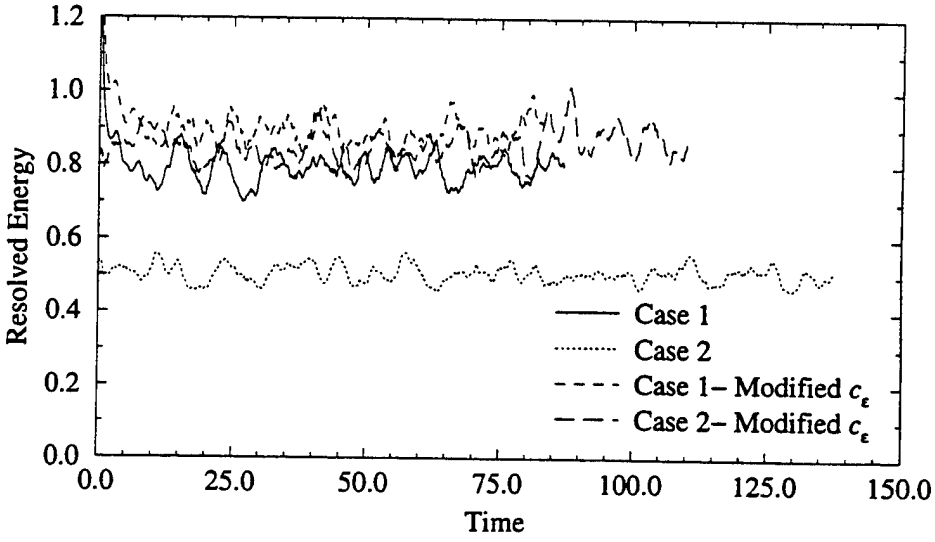


Figure 6.43: The effect of different means of computing c_ε on the resolved kinetic energy in forced isotropic turbulence

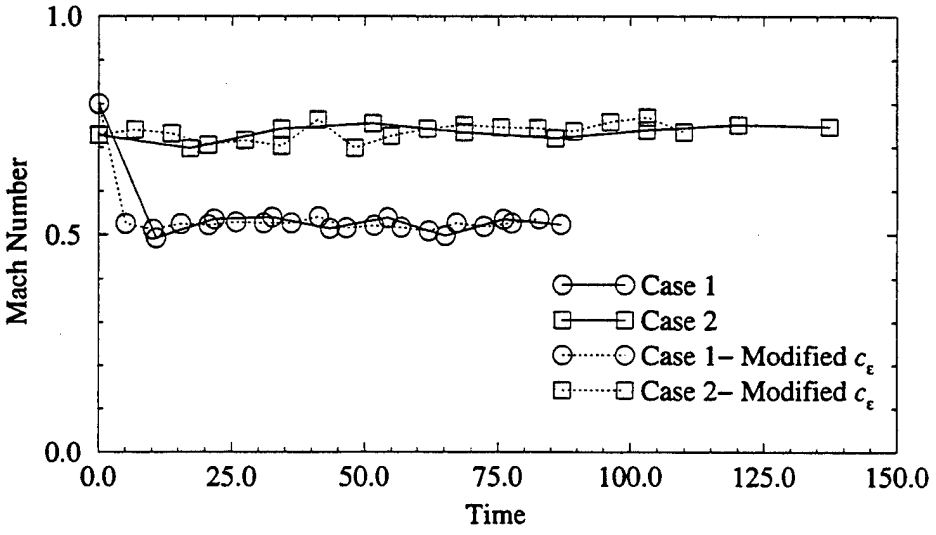


Figure 6.44: The effect of different means of computing c_ε on the mean Mach number in forced isotropic turbulence

CHAPTER VII

SIMULATIONS OF SPATIALLY DEVELOPING MIXING LAYERS

In order to test the capabilities of the code and the dynamic model more fully, spatially developing mixing layers are simulated. The dynamics of large turbulent structures in incompressible mixing layers have been examined by Brown and Roshko [6]. They found large roller type structures which have distinct core and braid regions which are related to Kelvin-Helmholtz instability waves which emanate from the tip of the splitter plate [111]. Winant and Browand [112] suggest that perturbations induce vertical velocities in the vorticity layer, which causes it to become periodically thicker and thinner. Eventually, the vortical regions become pinched off and form the well defined roller structures mentioned above. The growth of structures in a mixing layer, according to Hussain [113] occurs through three mechanisms:

1. Entrainment of freestream fluid [114] [115].
2. Vortex pairing [114].
3. Vortex tearing [113].

Hussain suggests that the turbulent energy cascade is not a factor in mixing layer growth, but Moser and Rogers [116] disagree, based on direct simulations of incompressible temporal mixing layers. Intuitively, it would seem obvious that the turbulent cascade would affect the growth rate. The turbulent cascade removes

energy from the larger vortices which are involved in the pairing process mentioned above, so it is hard to imagine that this does not affect the growth rate.

Studies of compressible mixing layers have been relatively uncommon compared to incompressible flows, and there is still some debate over the fundamental physics associated with these flows. The convective Mach number, introduced by Papamoschou and Roshko [7], has been found to be reasonably successful in parameterizing compressible mixing layer results. This quantity is a Mach number which is defined with respect to a frame of reference travelling with an average large structure in the flow. The convective velocity at which large structures typically travel is derived by assuming that a stagnation point (with respect to the moving frame of reference) exists, and that streamlines from the two free streams reach stagnation isentropically. The resulting expression for the convective velocity is given as:

$$U_c = \frac{a_1 U_2 + a_2 U_1}{a_1 + a_2} \tag{7.1}$$

Convective Mach numbers can therefore be defined using information from either stream:

$$M_{c_1} = \frac{U_1 - U_c}{a_1} \tag{7.2}$$

$$M_{c_2} = \frac{U_c - U_2}{a_2} \tag{7.3}$$

More recently, Papamoschou [9] has suggested that, although the convective Mach number correlates mixing layer growth rate data relatively well, the isentropic

assumption used in deriving it is not always accurate. For highly compressible cases, the convective Mach numbers of the two streams are not the same; one is sonic or supersonic, and the other is low subsonic. For the two cases discussed here, however, the experimental data indicates that the convective Mach as defined above will adequately parameterize the growth rates [117]; therefore the above definitions are employed for this study.

Large structures have been observed in compressible mixing layers by many researchers (*e.g.*, [118] [119] [120] [121]). Clemens and Mungal [119] reported finding braid and core type structures in mixing layers with convective Mach numbers less than 0.5. They found that increasing convective Mach number increased the three dimensionality of the flow. In a later paper, Clemens and Mungal [122] report that the PDFs of mixture fraction are narrower for higher compressibility. Shau and Dolling [123], working with a low compressibility ($M_c = 0.38$) mixing layer, found that structures align at an angle $35° - 50°$ from the mean flow direction on the high speed side. On the low speed side, the alignment was 90° from the mean flow. The experimental work of Samimy and Elliott [124] [125] with compressible mixing layers showed that as the convective Mach number increases, the magnitude and extent of the turbulence decreases. Goebel and Dutton [126] found, however, that only the lateral turbulence intensity decreased in magnitude. Mixing layers confined in a channel have been seen to display new instability modes, caused by mixing layer instabilities interacting with channel acoustics [127] [128] [129].

There are numerous methods for measuring mixing layer growth. Three common ones are used for the current work. The first is called the shear layer thickness. It

is computed from a normalized mean velocity field:

$$U^* = \frac{\overline{u} - U_2}{U_1 - U_2} \tag{7.4}$$

In the above expression, $\overline{u}$ represents the time-averaged velocity in the streamwise direction. The shear layer thickness (b) at a given streamwise station is computed as the distance between the point where the value of U^* is 0.1 and the point where it reaches 0.9. The second measure is the momentum thickness, which is computed as:

$$\theta = \frac{1}{\rho_1} \int_{-\infty}^{\infty} \overline{\rho} U^* \left(1 - U^*\right) dy \tag{7.5}$$

As in equation 7.4, the overbar in the above equation represents a time-averaged quantity (in this case, density). Finally, the vorticity thickness, as used by Brown and Roshko [6], is computed as:

$$\delta_\omega = \frac{U_1 - U_2}{\left(\frac{\partial \overline{u}}{\partial y}\right)_{\max}} \tag{7.6}$$

7.1 Simulation Specifications

The current simulations attempt to duplicate the compressible mixing layer experiments of Samimy and Elliott [124] [121] [117] [130] [131] [132] [133] [125]

[134]. Two experiments were simulated. The incoming flow parameters for these two cases are summarized in Table 7.1. The Reynolds number (per meter) for these cases was 9.4×10^6 and 9.1×10^6 for Case 1 and Case 2, respectively.

The original experiments were conducted in a high Reynolds number blowdown tunnel. This dual stream tunnel has a 152.4 *mm* by 152.4 *mm* test section. A 3.175 *mm* thick steel splitter plate separates the two streams. The low speed side of this plate has a 1° angle machined over the final 125 *mm* ahead of the test section. The width of the splitter plate at its trailing edge is about 0.5 *mm*. Optical access of the test section can be arranged for areas up to 500 *mm* in length and 80 *mm* high. The velocity measurements to which the current LES results are compared were taken using a two-component coincident laser Doppler velocimetry (LDV) system. Both the high-speed and the low-speed flows were seeded with atomized silicone oil less than one micron in diameter. The LDV results presented here are based on 2048 samples per channel (corrected for velocity bias). This small sample size is thought to be responsible for some of the scatter seen in the experimental results [124].

Liou *et al.* [66] also simulate one of these cases (Case 1). They use a two dimensional solver with no subgrid model (*i.e.*, a "pseudo-direct" simulation). The coarsest grid employed for the current 3-D simulations (discussed below) has less than half the points of their "grid independent" resolution (402×202). Despite this disparity in resolution, the current runs, even on the extremely coarse grids, obtain similar mixing layer growth and much better turbulent profiles (due to the difference between two and three dimensional flow). Ameur and Chollet [135] have run 3-D "pseudo-direct" simulations of a third case ($M_c = 0.64$) using a hybrid piecewise parabolic method (PPM). Like Liou *et al.*, they did not include any viscous terms and employed a much finer grid ($200 \times 180 \times 50$) than any employed here. In addition,

they do not model the splitter plate, and no comparisons are made between their results and the experimental data. This particular case was not simulated for the current study because the supersonic stream is run in an underexpanded state, resulting in a shock-expansion pattern which may influence the development of the shear layer.

Table 7.1: Flow parameters for spatial mixing layer cases

Case	T_0 (K)	P_{0_1} (kPa)	M_1	M_2	M_c	U_1 (m/s)	$\frac{U_2}{U_1}$	$\frac{\rho_2}{\rho_1}$	δ (mm)
1	291.0	314.0	1.80	0.51	0.52	479.5	0.355	0.638	8.0
2	276.0	722.0	3.01	0.45	0.86	597.7	0.246	0.370	9.2

The computational domain employed for these simulations is shown conceptually in figure 7.1. It starts just upstream of the splitter plate lip, and ends 0.4 meters downstream of the lip. As with the experiments, the splitter plate is 0.5 mm thick at the lip. The 1° angle on the subsonic side of the splitter plate is ignored, however; this surface is assumed to be aligned horizontally for the LES. The splitter plate is treated as a no-slip, adiabatic wall. The full height of the experimental rig (152.4 mm) is simulated, but the upper and lower boundaries are treated as slip-walls, since the grid does not have adequate resolution to resolve the boundary layers. Only the middle 76 mm (out of 152 mm) are computed in the spanwise direction, and periodic boundary conditions are used in this direction. This was done for convenience rather than any requirement of the code or the subgrid models. The flow at the outflow boundary is computed, using the characteristic form of the governing equations, after the manner of Thompson [136] and Poinsot and Lele

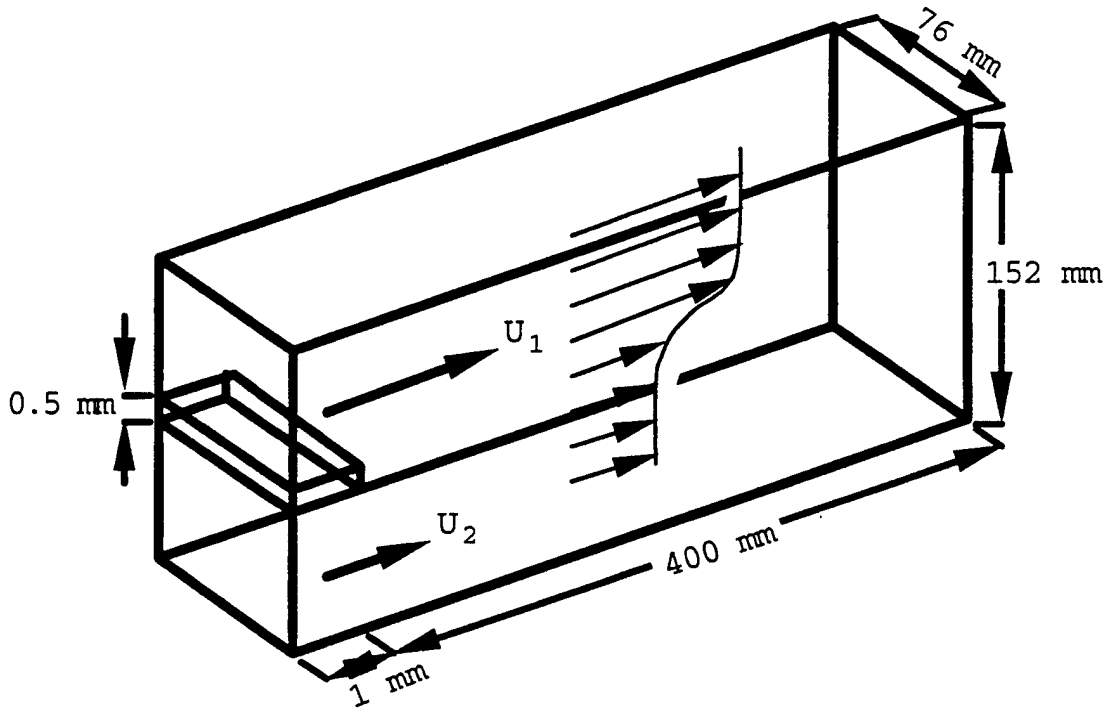


Figure 7.1: Schematic of the spatial mixing layer computational domain

[137]. Initial (mean) conditions for the incoming boundary layers are computed using a 2-D boundary layer equation solver. The inflow on the supersonic side is fully specified, while on the subsonic side, a characteristic boundary condition is used. In order to better match the experimental predictions, pseudo-turbulence was added at the inflow boundaries. The details of this are given in Appendix C. On the finest grid employed in this study, the resolution at the inflow boundary was sufficient to allow 18-20 points in the high speed side boundary layer, and about ten points on the low speed side.

In order to compute time averaged quantities for comparison with the experimental results, mean flow fields (and higher moments) are developed in the following

manner. The cases are run until the starting vortex leaves the domain. The length of time required for this is used as a reference flow-through time. Then, the gathering of statistical quantities is initiated. For most of the cases presented here, these quantities are gathered for two flow-through periods. Since the flow is periodic in the spanwise (z) direction, the mean fields thus developed can be averaged across the domain to give a single plane of mean data. This vastly decreases the amount of time required for a good statistical sample (as discussed below).

7.2 Inflow and Exit Boundary Effects

As previously mentioned (in Chapter I), the success of linear stability analysis in predicting the growth rate of compressible mixing layers [17] [16] leads one to conclude that such growth is driven by the shear layer instability modes; the turbulence of the incoming streams is thought to play a relatively minor role. It is important, however, to verify that the results of the simulations are not highly sensitive to the pseudo-turbulence which is introduced through the inflow boundaries. In addition, one must ensure that the influence of the outflow boundary on the region of interest is minimal. A series of three test cases (of the Case 2 mixing layer) was run in order to investigate these issues. These runs are summarized in Table 7.2.

Table 7.2: Boundary Effects Cases

Case	Resolution	Inflow Turb.	Domain Size
BC1	$60 \times 40 \times 16$	2.5%	Normal
BC2	$70 \times 40 \times 16$	2.5%	w/ Exit Region
BC3	$70 \times 40 \times 16$	3.0%	w/ Exit Region

Because of the extremely coarse grid used for these cases, it was found that the dynamic energy equation model coefficient was destabilizing the flow; therefore, they were run with the following alternative definition:

$$c_e = \frac{c_\nu}{\mathrm{Pr}_t} \tag{7.7}$$

It must be emphasized that the issue of accuracy as compared with experiment is not being addressed in this section. The issue here is the consistency of the solution with varying boundary treatment.

The first case (BC1) was run using the domain discussed above. The other two cases used the same grid, but with an extended exit region of highly stretched cells which increased the domain length by about 75%. Case BC3 also had an increased level of inflow pseudo-turbulence (20% more all across the inlet) compared to the standard level of freestream inflow turbulence of 2.5 percent (from Elliott [117]). All three cases were run using the same time step, and all were run for the same number of iterations.

Figure 7.2 shows that the predicted shear layer growth is almost identical for all three cases. The normalized streamwise mean velocity profiles are likewise almost indistinguishable (figure 7.3). Slight differences are visible in the streamwise turbulent intensity profiles (figure 7.4), but these are not significant. Somewhat greater differences are visible in the higher moments; the velocity skewness, for example, shows a decrease in the magnitude of the peak on the high speed side of the mixing layer with the addition of an exit region. Similarly, increasing the incoming pseudo-turbulence tends to increase the skewness on the low speed side of the mixing layer.

In general, however, these simulations gave very similar results. Therefore, in the interests of saving CPU time, the smaller domain size is employed for the remainder of these cases. Likewise, the intensity of the incoming pseudo-turbulence of the other simulations presented in this chapter is fixed at 2.5 percent in the freestream.

One note of caution must be added, however. All three tests were run on very coarse grids. With better resolution, it is possible that the resulting increase of smaller structures reaching the outflow boundary could result in contamination of the upstream flow. In practice, no signs of this were seen on the finer grids (as shown in the following section), but since these effects can be very subtle, the possibility cannot be ruled out.

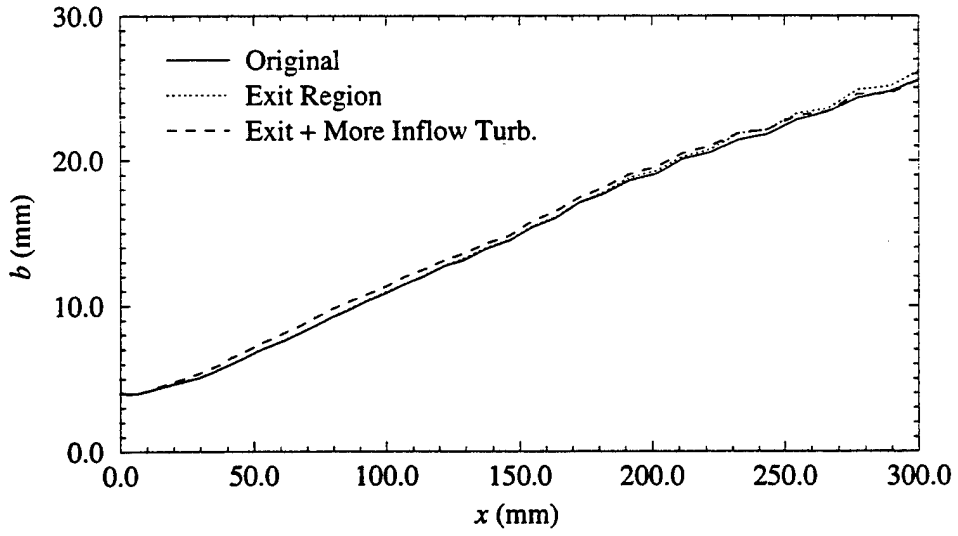


Figure 7.2: Predicted growth of Case 2 mixing layer for different boundary treatments

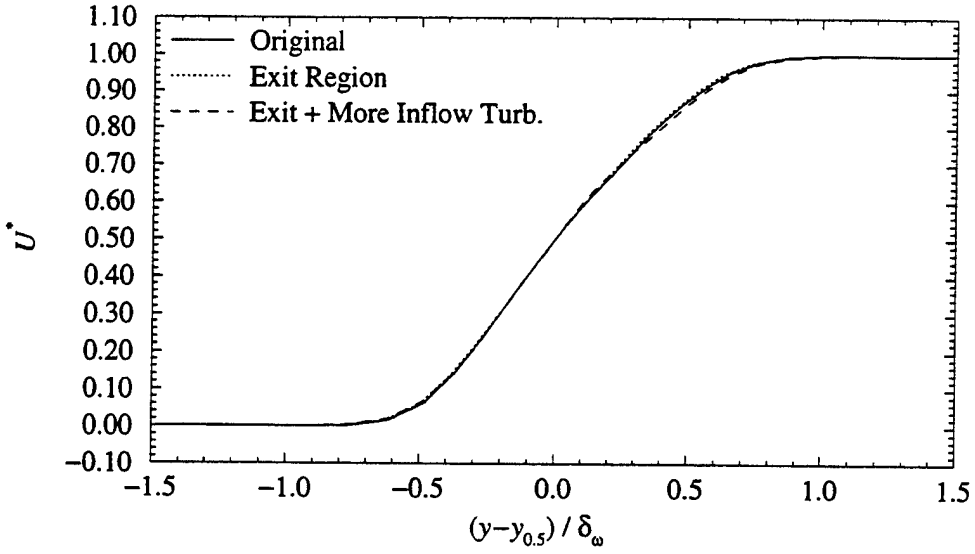


Figure 7.3: Predicted normalized streamwise velocity profiles ($x = 210mm$) of Case 2 mixing layer for different boundary treatments

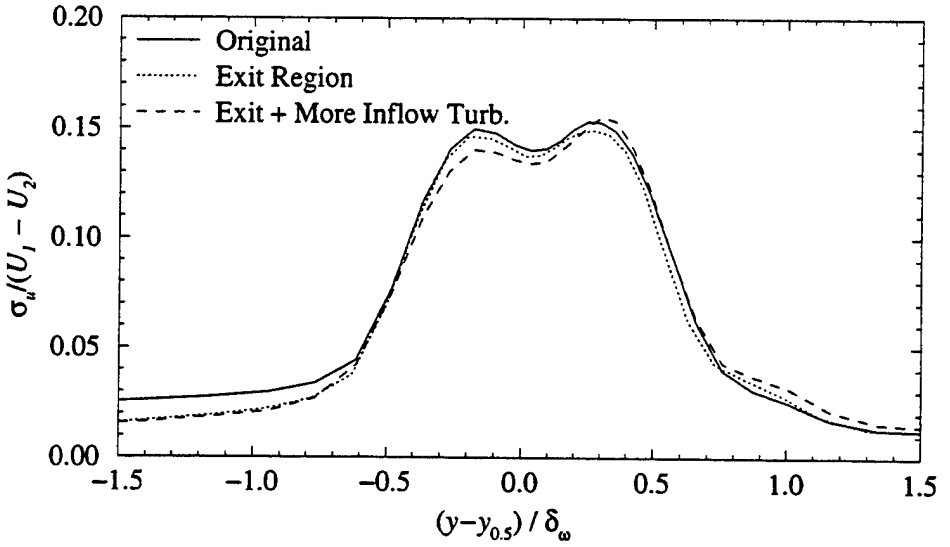


Figure 7.4: Predicted streamwise turbulent intensity ($x = 210mm$) of Case 2 mixing layer for different boundary treatments

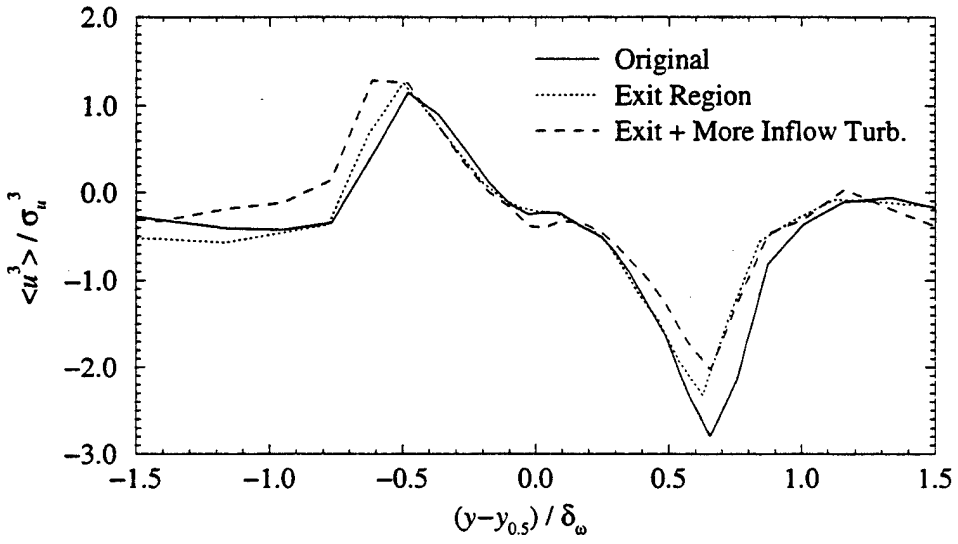


Figure 7.5: Predicted velocity skewness profiles ($x = 210mm$) of Case 2 mixing layer for different boundary treatments

7.3 Resolution Dependance

The question of consistency in a simulation does not end with establishing that the boundaries are not unduly influencing the solution. Another issue which must be addressed is whether or not the grid resolution is sufficient that the solution is "grid independent." To some extent, the idea of "grid independence" is a misnomer when placed in an LES context. By definition, any LES will be dependant on the grid resolution, because that is what determines the transition from resolved to subgrid scales. The only way to have a truly "grid independent" solution in such a case is to run a DNS! Nevertheless, in order to verify that the large scales of motion are being simulated properly, it is important to establish that the LES is converging in a consistent and gradual manner with increasing resolution.

To this end, three different grid resolutions have been used in simulations of the Case 2 mixing layer (see table 7.3). As above, the issue is the consistency of the solutions, not their accuracy. The results of these tests indicate that, at least for the lower moments of the flow, a reasonable level of "grid independence" is achieved for Grids 2 and 3.

Table 7.3: Grids Employed for Resolution Tests

ID	Resolution	Points
Grid 1	$60 \times 40 \times 16$	38,400
Grid 2	$90 \times 60 \times 32$	172,800
Grid 3	$120 \times 90 \times 48$	518,400

The shear layer thickness development is shown in figure 7.6. For the regions of primary interest (up till about $300mm$ behind the splitter plate) the medium and fine resolution grids give very similar results. Similar agreement is shown in the normalized streamwise velocity profiles (figure 7.7). In fact, for this variable, even Grid 1 gives "grid independent" results. The streamwise turbulent intensity (figure 7.8), however, shows significant differences between Grid 1 and the other two simulations. These differences are even greater for the velocity skewness profiles (in figure 7.9). For this variable, even Grid 2 starts to show variance from the Grid 3 results, although the difference between Grids 2 and 3 is less than that between Grids 1 and 2. Very similar behavior is seen for the velocity flatness profiles shown in figure 7.10. Note, however, the large amount of noise on the high speed side of the mixing layer. Though not shown clearly here (due to the truncated spatial axis), this noise is definitely related to grid resolution, since the magnitude of the fluctuations decreases with grid resolution. It is not surprising that such fluctuations are observed; outside the mixing layer region, the grid cell sizes increase while both turbulent scales and intensity decrease. Therefore, results for the higher moments of the flow are not reliable outside the core of the mixing layer.

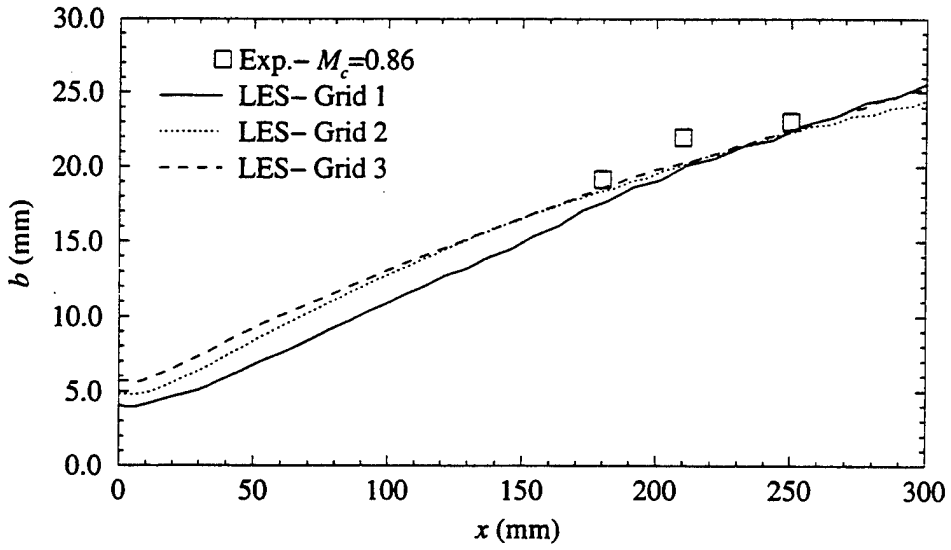


Figure 7.6: Predicted growth of Case 2 mixing layer for different grid resolutions

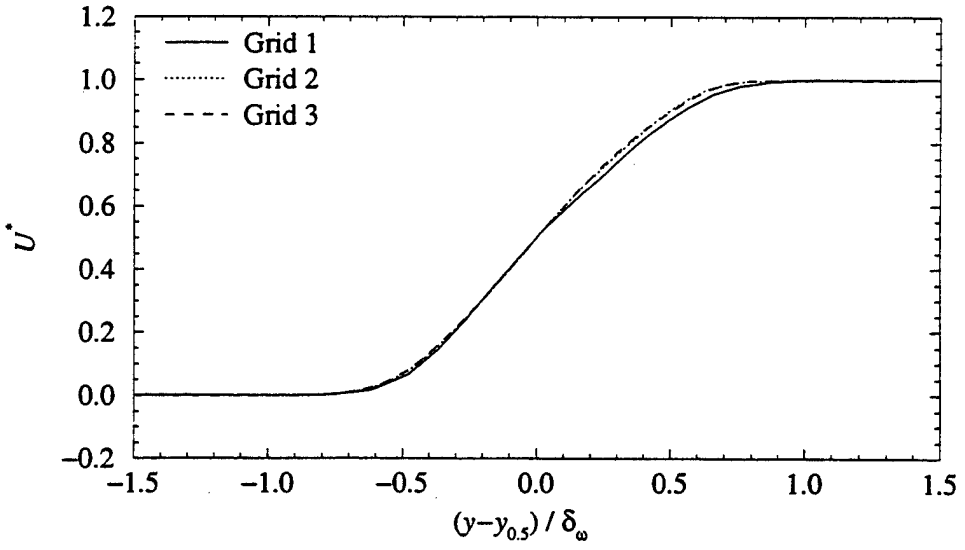


Figure 7.7: Predicted normalized streamwise mean velocity profiles ($x = 210mm$) of Case 2 mixing layer for different grid resolutions

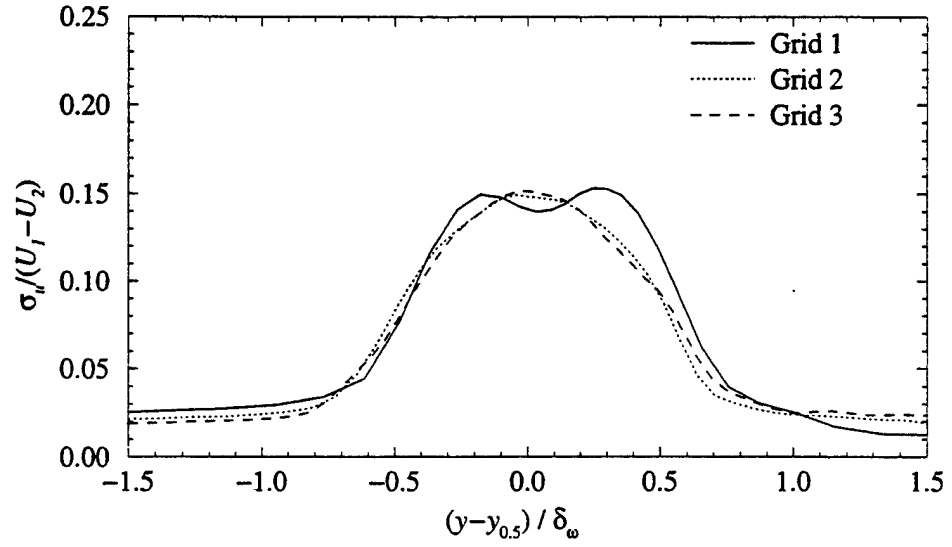


Figure 7.8: Predicted streamwise turbulent intensity profiles ($x = 210mm$) of Case 2 mixing layer for different grid resolutions

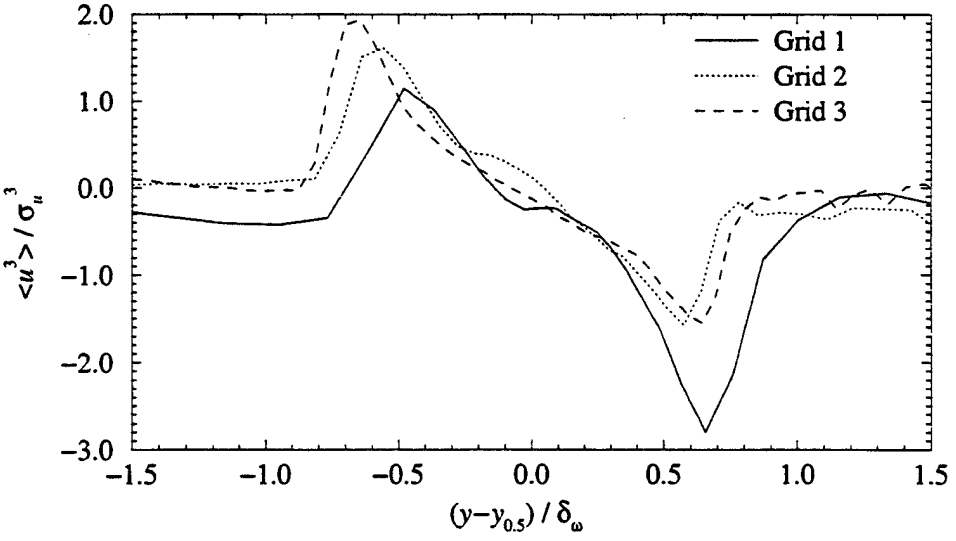


Figure 7.9: Predicted velocity skewness profiles ($x = 210mm$) of Case 2 mixing layer for different grid resolutions

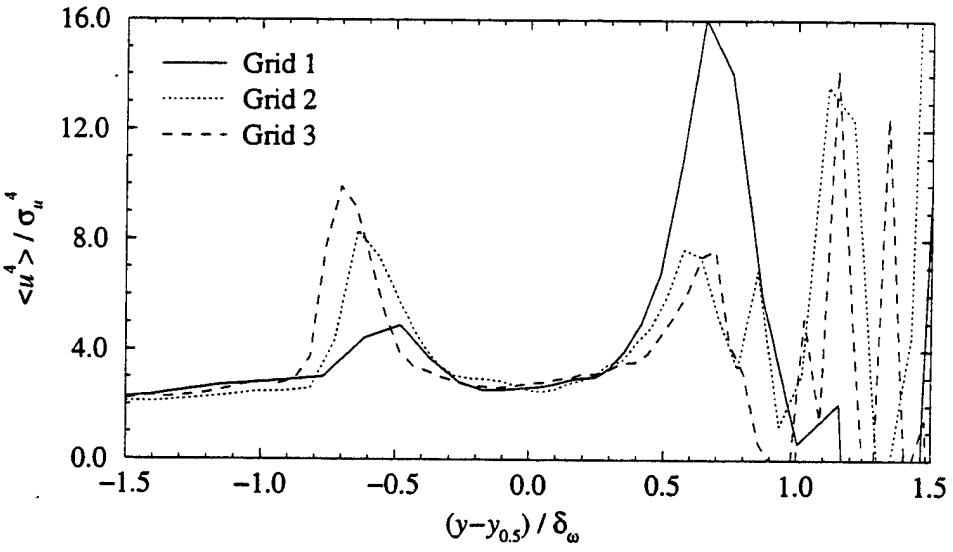


Figure 7.10: Predicted velocity flatness profiles ($x = 210mm$) of Case 2 mixing layer for different grid resolutions

7.4 Sampling Time Effects

It is important, when gathering statistical data, that the sample size be large enough that the results are essentially invariant to further sampling. For a conventional unsteady simulation, this would require taking statistics for five to ten flow-through times. In most cases presented here, as mentioned above, statistics were only taken over two flow-through times. This is not as bad as it might seem at first glance, because the homogeneous transverse direction in these simulation flows allows these statistical fields to be averaged across all the k-planes. Nevertheless, valid questions can be raised about the adequacy of the sampling time, especially in light of the noise present in the velocity flatness results presented above. Therefore, to investigate this issue, one of the Case 2 mixing layer cases (on Grid 2) has been restarted and run for two additional flow-through times.

The resulting data shows that for the lower moments of the flow the statistical sample is quite adequate. For example, the shear layer thickness (figure 7.11) is virtually unchanged in the region of interest. Similarly, in figure 7.12, almost no change is discernible in the streamwise velocity profiles. The streamwise turbulent intensity profiles, shown in figure 7.13, reveal some small differences in the core region of the mixing layer. More puzzling is the apparent increase of the intensity of the turbulence in the low speed freestream. This, however, does not appear to have any significant effect on the mixing layer itself. The cross components of the Reynolds stress tensor (the uv component of which is shown in figure 7.14) do not seem to be similarly affected; this term is almost unchanged.

Not too surprisingly, more significant changes begin to appear in the higher moments. The streamwise velocity skewness profiles (see figure 7.15), for instance,

are essentially unchanged in the region from -0.5 to 0.5 (measured in the normalized y-coordinates), but show significant differences in the regions outside this core region. The same trend is shown, in an even more exaggerated fashion, for the velocity flatness (figure 7.16). This is of lesser importance, however, because these quantities are suspect outside the core of the mixing layer in any case. Thus, it appears that, at least for the purposes of the initial trade-off studies, two flow-through times of sampling is sufficient. For the final results, however, the simulations have been run as long as possible in order to better resolve the higher moments of the flow.

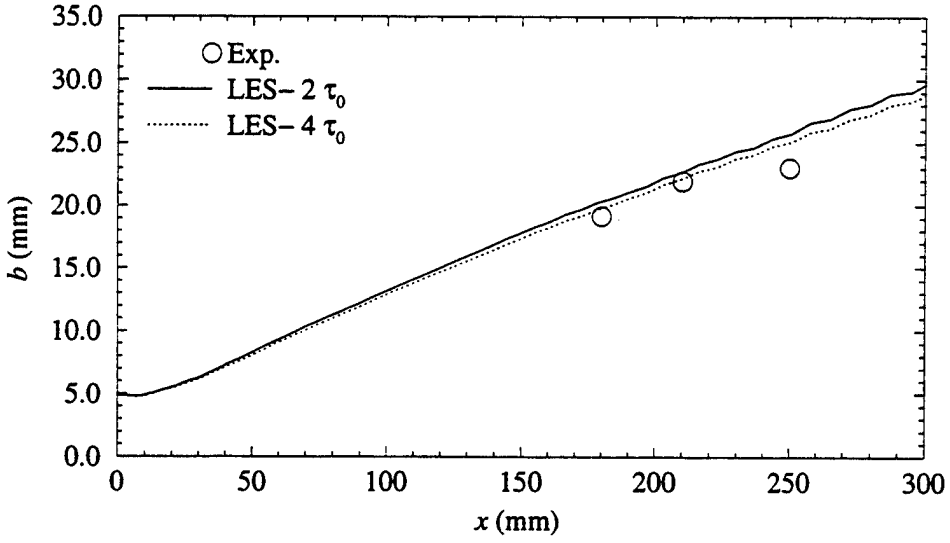


Figure 7.11: Effect of sampling time on the predicted growth ($x = 210mm$) of the Case 2 mixing layer

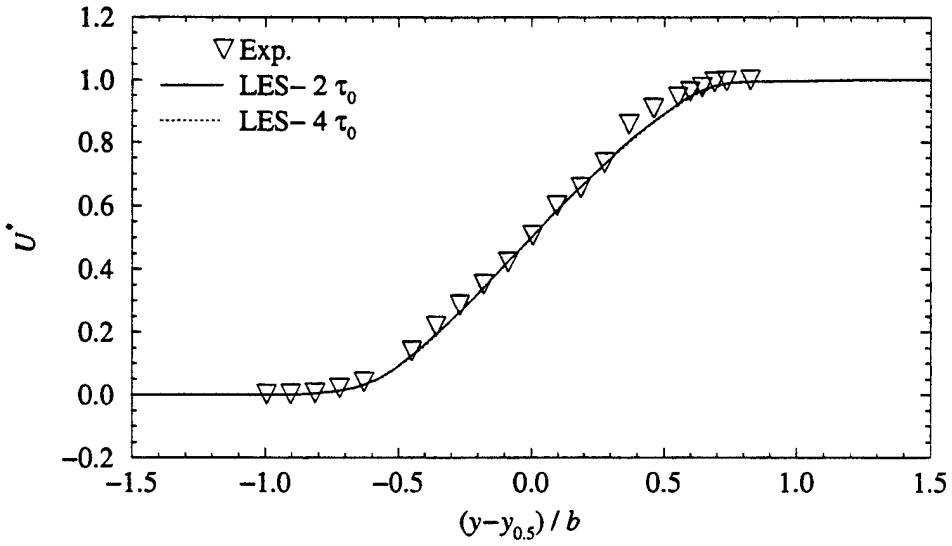


Figure 7.12: Effect of sampling time on the predicted normalized streamwise velocity profiles ($x = 210mm$) in the Case 2 mixing layer

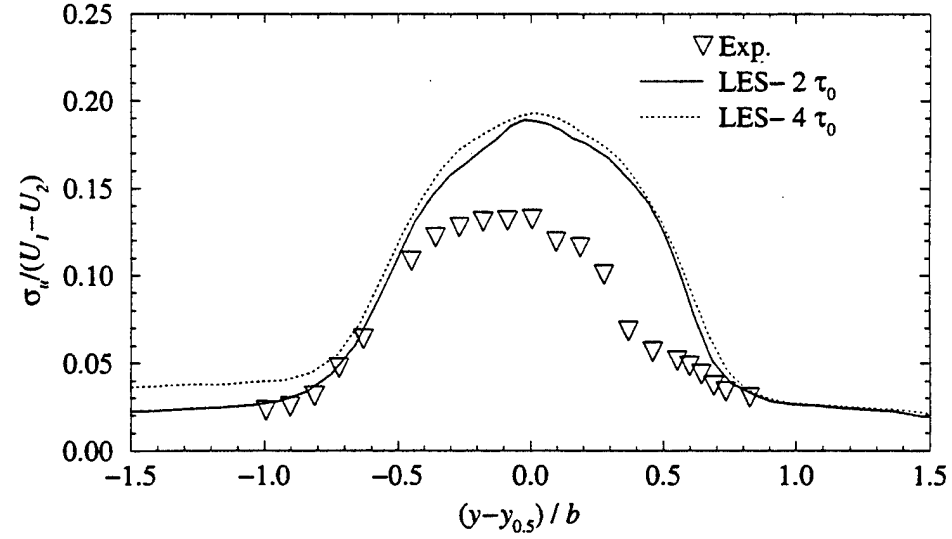


Figure 7.13: Effect of sampling time on the predicted streamwise turbulence intensity profiles ($x = 210mm$) in the Case 2 mixing layer

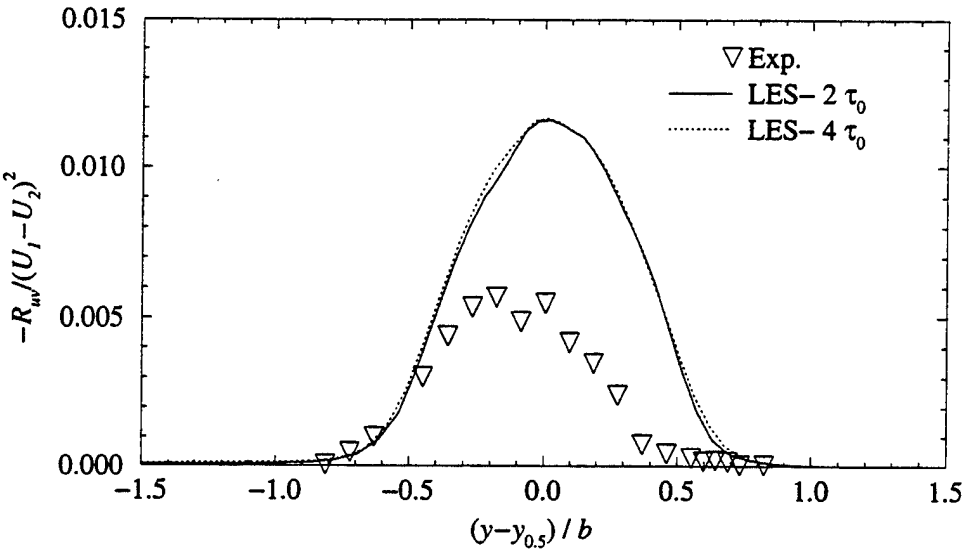


Figure 7.14: Effect of sampling time on the Reynolds stress profiles ($x = 210mm$) in the Case 2 mixing layer

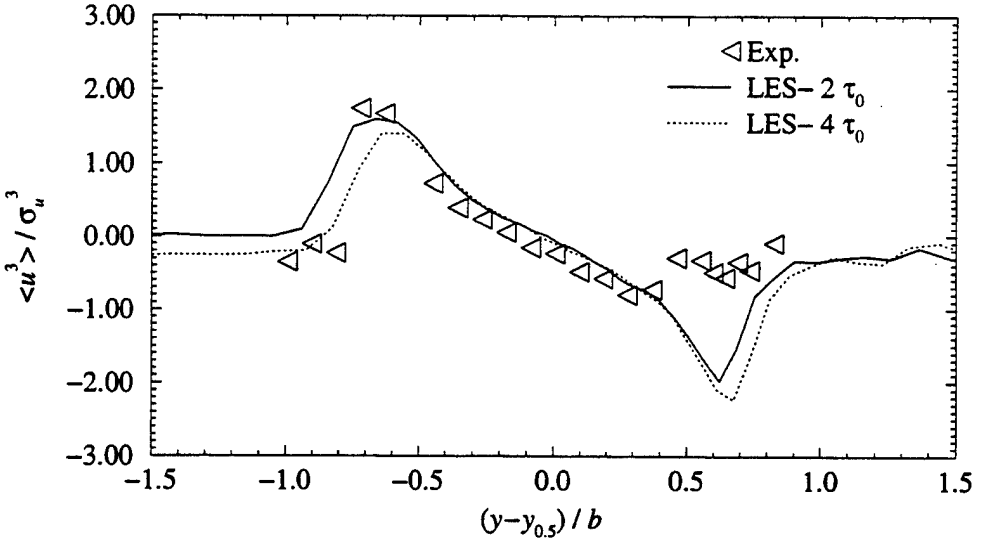


Figure 7.15: Effect of sampling time on the predicted streamwise velocity skewness profiles ($x = 210mm$) in the Case 2 mixing layer

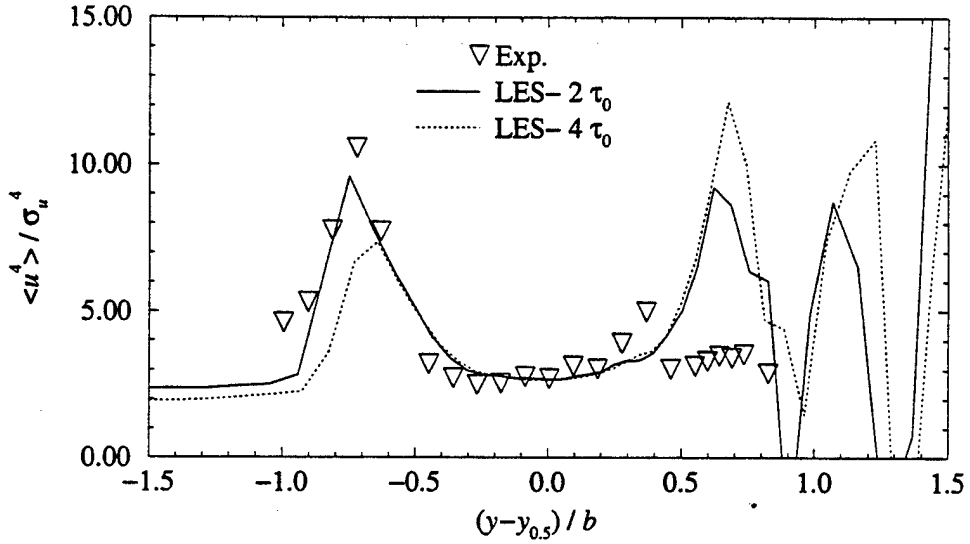


Figure 7.16: Effect of sampling time on the predicted streamwise velocity flatness profiles ($x = 210mm$) in the Case 2 mixing layer

7.5 Model Effects

7.5.1 Varying the "Compressibility" Viscosity Scaling Factor

In Chapter III, the "compressibility" viscosity is defined, and its scaling coefficient (a_0) is given there as 0.6 for the current work. This value seems to give good results, but one may legitimately question how sensitive the results are to this term. Ideally, the "compressibility" viscosity is only significant in the vicinity of sudden changes in density. Therefore, in general it is expected that while locally significant, it should not dominate the global development of the flow.

To verify that this is, in fact, true, the Case 2 mixing layer (on Grid 1) was re-run with a_0 set to 0.35 instead of 0.6. The results indicate that the model is performing as

expected. Figure 7.17 shows the predicted shear layer thickness growth for both the original simulation and the current test. As can be seen, there is almost no difference between the two runs. Similarly, the normalized streamwise velocity profiles (figure 7.18) show little change with a_0. Some small variations appear in plots of the streamwise turbulent intensity (figure 7.19) near the peak values. Overall, however, very little difference is observed. Finally, the velocity skewness curves (figure 7.20) show similar behavior, although the lower value of a_0 corresponds to an increased skewness magnitude. Although the grid is too coarse to expect much accuracy for these higher moments, it should be noted that the skewness profiles predicted by the original simulation ($a_0 = 0.6$) are closer to the experimentally observed values.

It is concluded, therefore, that the results are relatively insensitive to the exact setting of the "compressibility" viscosity scaling coefficient. For the remaining cases, the originally suggested value of 0.6 is used.

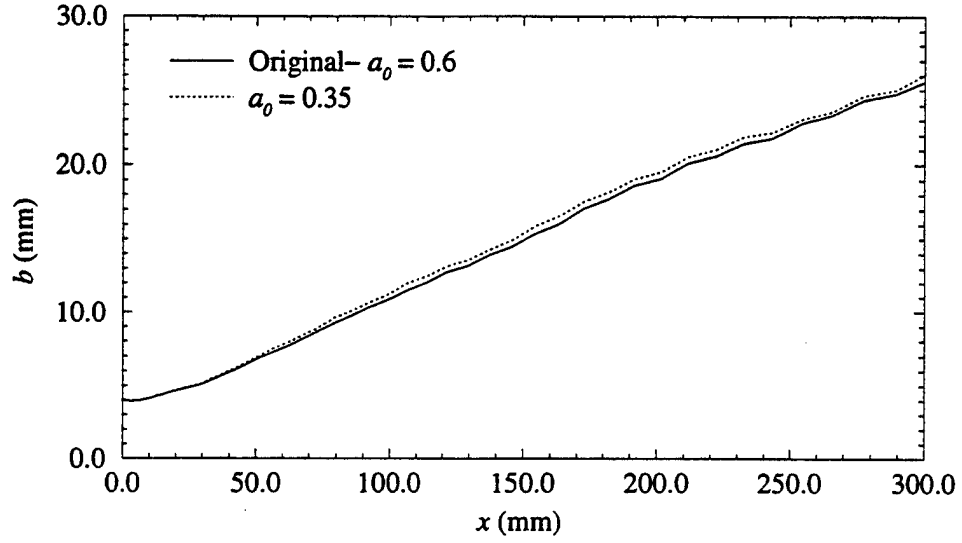


Figure 7.17: Predicted growth of Case 2 mixing layer for different values of a_0

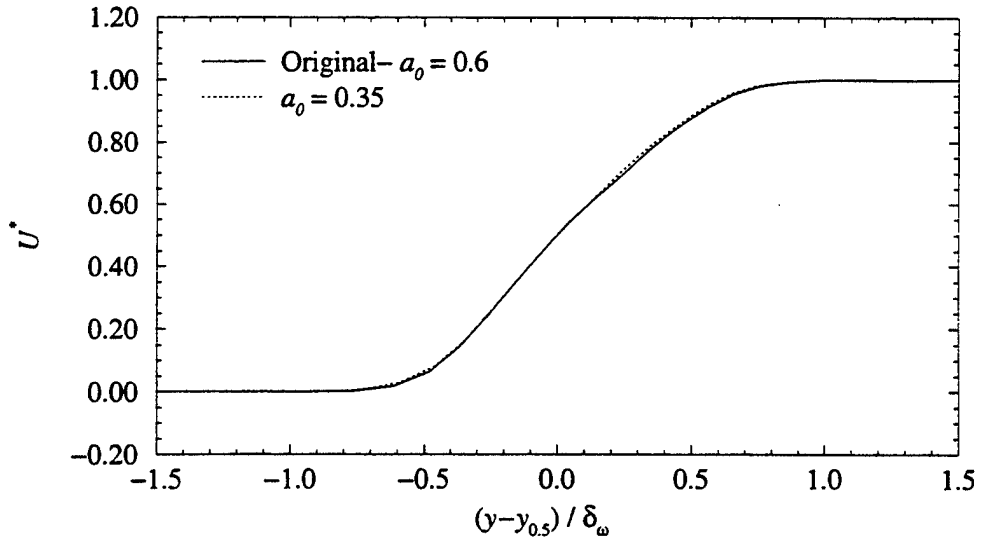


Figure 7.18: Predicted normalized streamwise mean velocity profiles ($x = 210mm$) of Case 2 mixing layer for different values of a_0

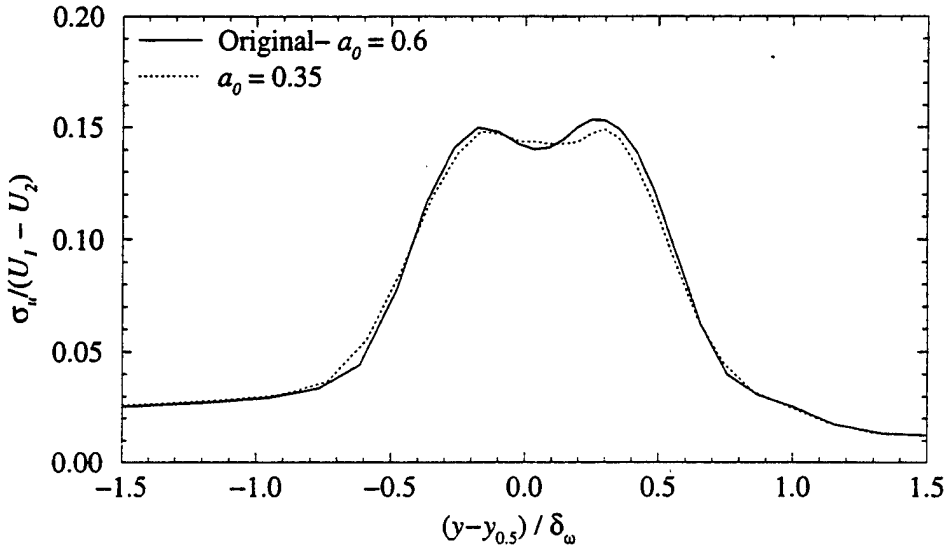


Figure 7.19: Predicted streamwise turbulence intensity profiles ($x = 210mm$) of Case 2 mixing layer for different values of a_0

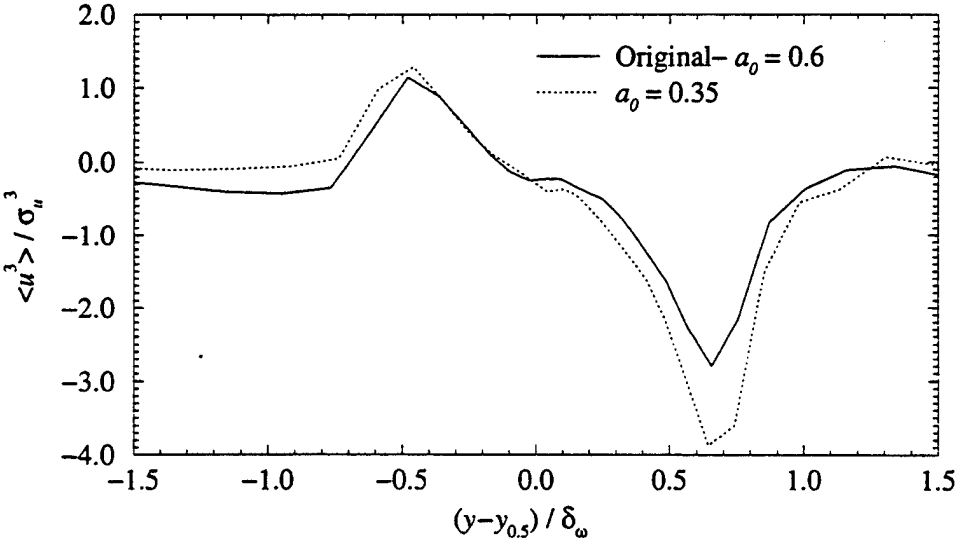


Figure 7.20: Predicted velocity skewness profiles ($x = 210mm$) of Case 2 mixing layer for different values of a_0

7.5.2 Using an Alternate Form of the Subgrid Stress Tensor Model Coefficient

The form of the subgrid stress tensor model coefficient derived in Section 3.4.3 is only one of many possibilities. One obvious alternative is given in Appendix D. This latter approach treats the subgrid stress tensor as a whole, rather than splitting it into "compressible" and "incompressible" parts. The effects of using this alternate form rather than the originally proposed algorithm have been explored in simulations of the Case 1 mixing layer on Grid 2.

While the two expressions for c_ν are very similar, they produce noticeably different results. Figure 7.21 shows that the alternate form predicts significantly less mixing layer growth than the original algorithm. The normalized streamwise velocity profiles, however, remain very similar (see figure 7.22). As shown in figure 7.23, the turbulent intensity level is significantly less when using the alternate algorithm. The streamwise velocity skewness on the high speed side of the mixing layer is poorly predicted by the alternate algorithm, as shown in figure 7.24. The corresponding flatness curve (see figure 7.25) is similarly distorted. Note, however, that (as shown above in Section 7.4) both curves show extremely large error as one moves outside the mixing layer.

On the basis of these results, the alternate form of c_ν is found to be inferior to the original form found in Section 3.4.3. Therefore, this latter formulation is used for the remainder of the runs.

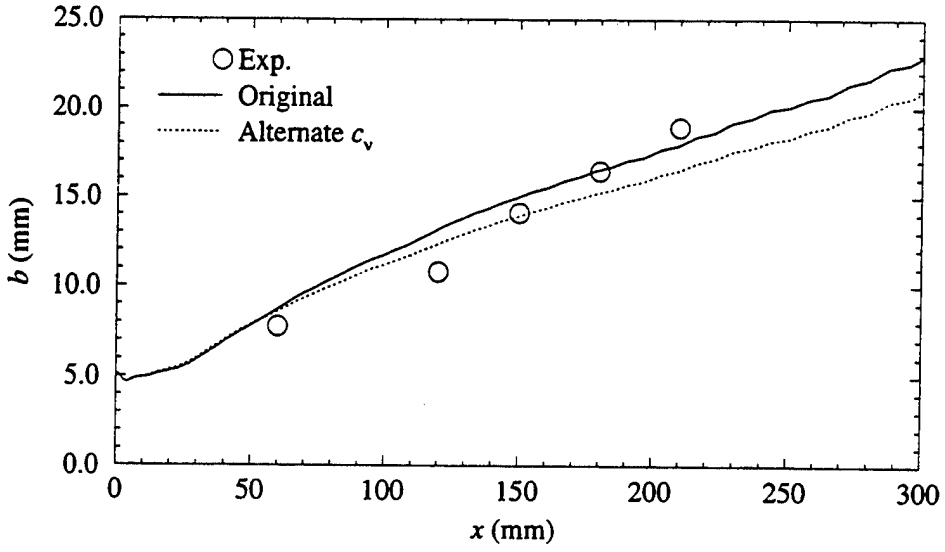


Figure 7.21: Predicted growth of Case 1 mixing layer for different algorithms for computing c_ν

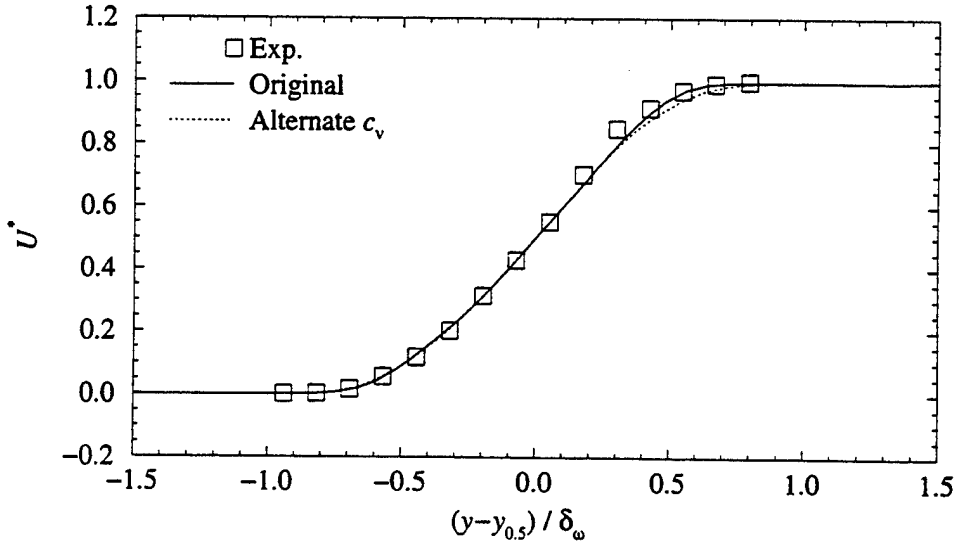


Figure 7.22: Predicted normalized streamwise mean velocity profiles ($x = 150mm$) of Case 1 mixing layer for different algorithms for computing c_ν

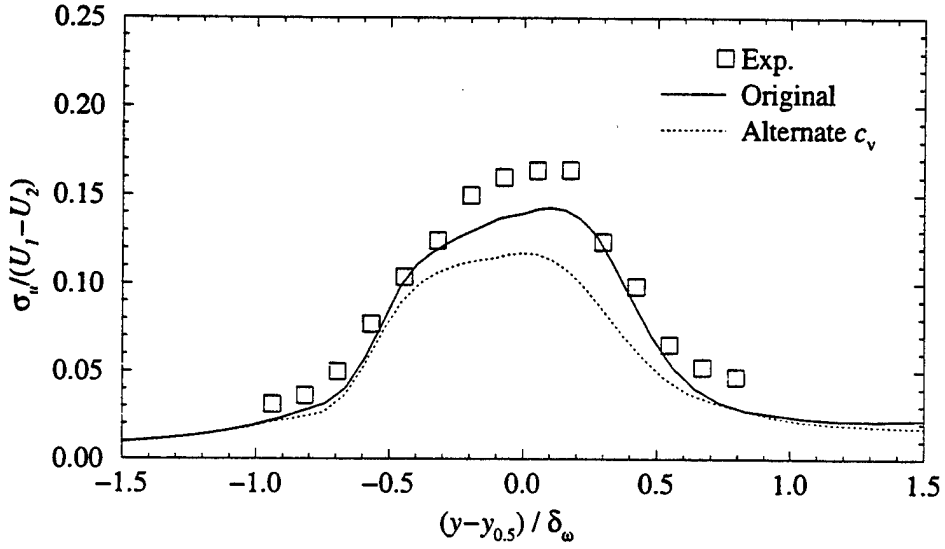


Figure 7.23: Predicted turbulent intensity profiles ($x = 150mm$) of Case 1 mixing layer for different algorithms for computing c_ν

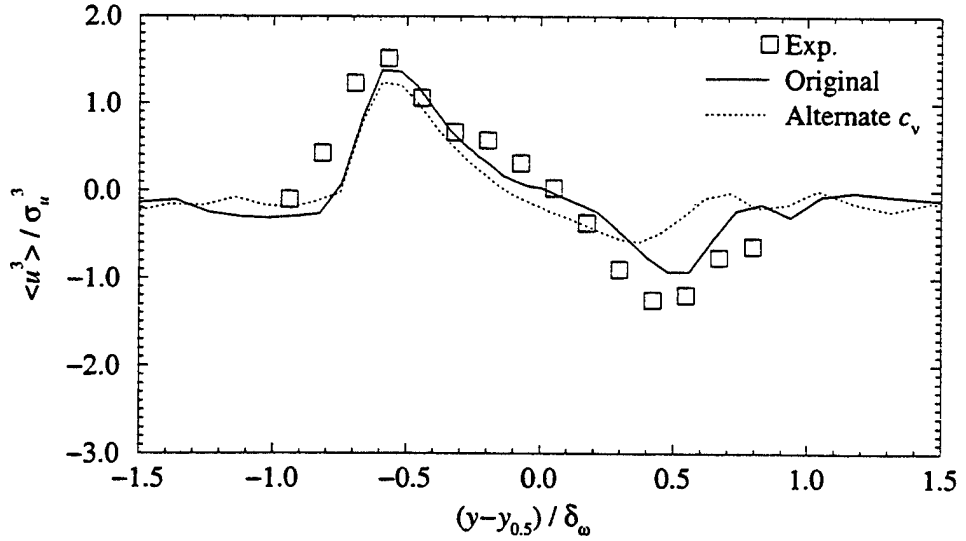


Figure 7.24: Predicted velocity skewness profiles ($x = 150mm$) of Case 1 mixing layer for different algorithms for computing c_ν

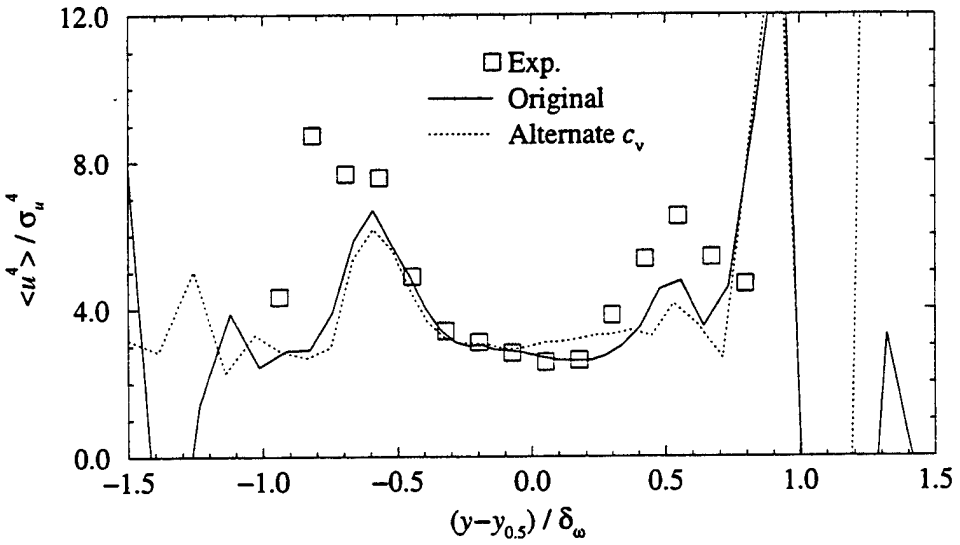


Figure 7.25: Predicted velocity flatness profiles ($x = 150mm$) of Case 1 mixing layer for different algorithms for computing c_ν

7.5.3 Using a Different Subgrid Kinetic Energy Dissipation Coefficient Equation

In Section 3.4.3, two alternatives were proposed for the dynamic computation of the subgrid kinetic energy dissipation model coefficient (equations 3.32 and 3.33). The effect of switching these two algorithms was tested on the Case 1 mixing layer (on Grid 2). The results indicate that this issue has a significant impact on the predicted mixing layer development.

Figure 7.26 shows that the computed shear layer thickness is quite different, depending on which algorithm is used. The original algorithm seems to do a better job at predicting the absolute thickness of the layer, but the alternate form is much better at predicting the slope. Both equations yield good predictions of the streamwise velocity profile, as shown in figure 7.27. The streamwise turbulent intensity is not as well predicted (see figure 7.28). The original form of the dissipation coefficient significantly underpredicts this quantity, while the alternate equation overpredicts it. Overall, the alternate form appears to do a slightly better job at predicting the turbulent intensity.

It is in the higher moments, however, that the superiority of the alternate formulation begins to reveal itself. The streamwise velocity skewness, for example (figure 7.29), shows much better agreement with experiment when the alternate equation is used. The same behavior is observed in the flatness profiles, shown in figure 7.30. In addition, though not shown here, the original dissipation coefficient resulted in drastic overprediction of the subgrid kinetic energy. The alternate form results in much more physically meaningful values of subgrid kinetic energy, though they are still somewhat high. Therefore, the alternate form of the dissipation coefficient is used for all subsequent simulations.

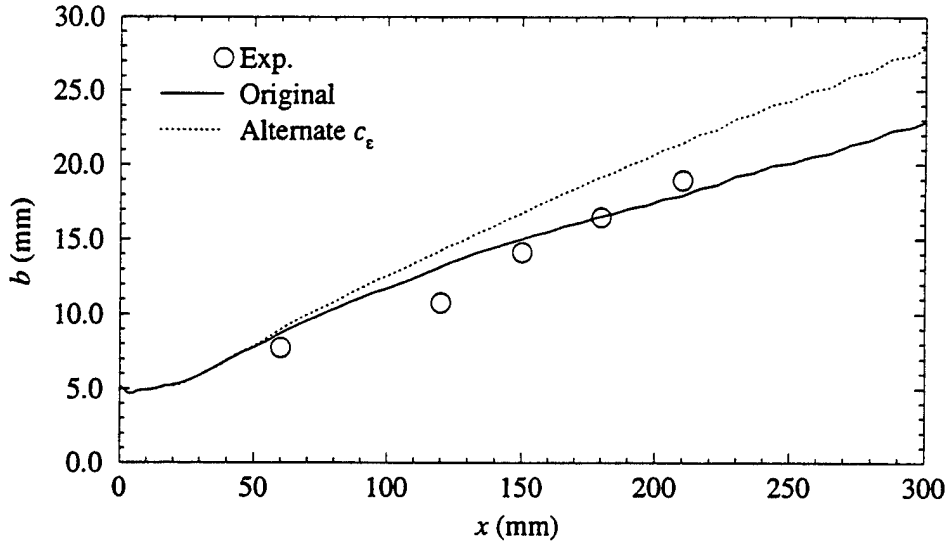


Figure 7.26: Predicted growth of Case 1 mixing layer for different algorithms for computing c_ε

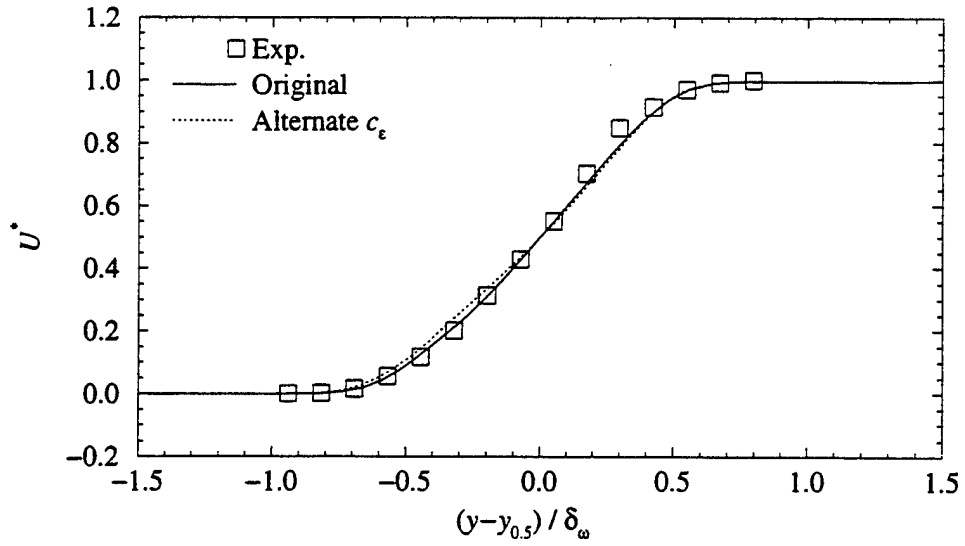


Figure 7.27: Predicted normalized streamwise mean velocity profiles ($x = 150mm$) of Case 1 mixing layer for different algorithms for computing c_ε

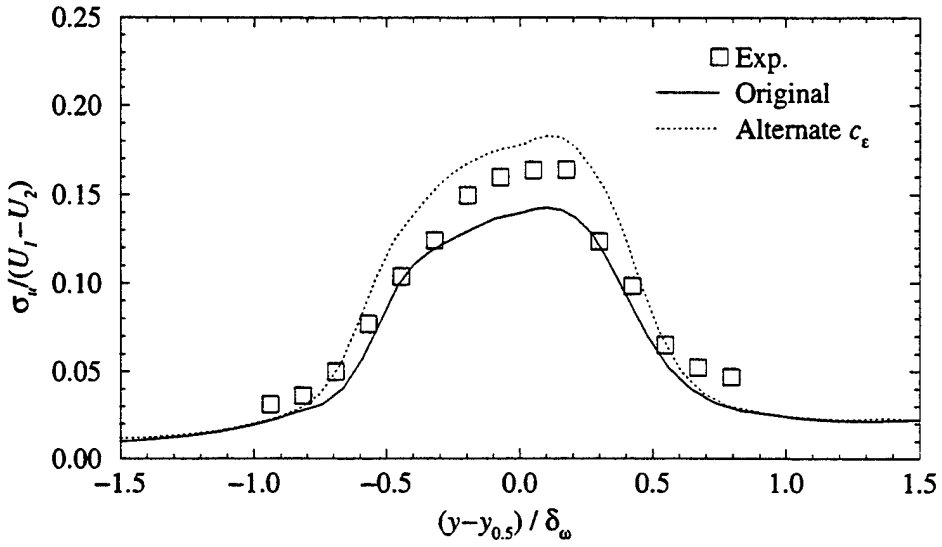


Figure 7.28: Predicted streamwise turbulent intensity profiles ($x = 150mm$) of Case 1 mixing layer for different algorithms for computing c_ε

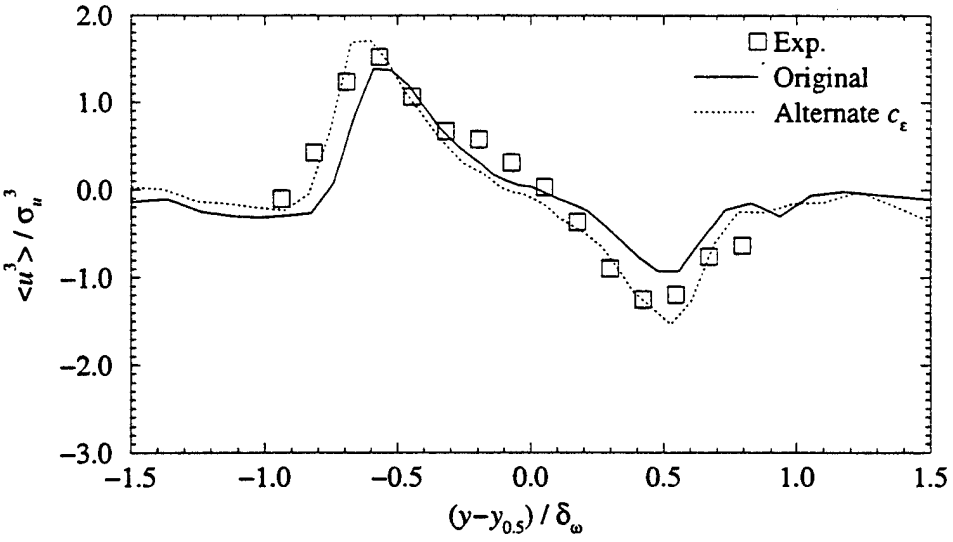


Figure 7.29: Predicted velocity skewness profiles ($x = 150mm$) of Case 1 mixing layer for different algorithms for computing c_ε

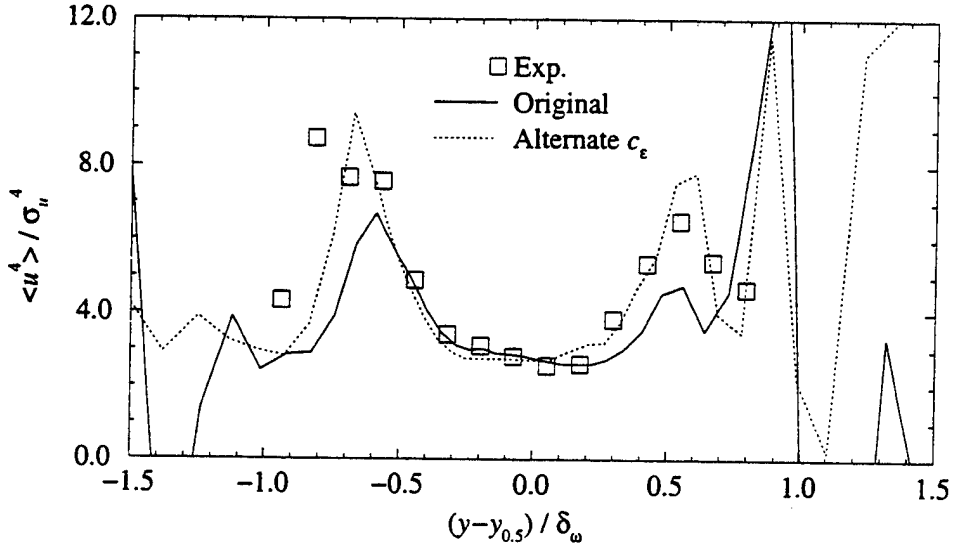


Figure 7.30: Predicted velocity flatness profiles ($x = 150mm$) of Case 1 mixing layer for different algorithms for computing c_ε

7.5.4 Running with Constant Model Coefficients

From the beginning of this work, it has been assumed that a dynamic subgrid model will yield more accurate results in simulations turbulent flows at very high Reynolds number than simply using constant model coefficients. In order to verify this assertion, the Case 1 mixing layer case (on Grid 2) has been run using the k-equation model with constant coefficients. The model coefficients were set based on the suggested values of [37]. The subgrid stress tensor model coefficient (c_ν) was fixed at 0.0854, the dissipation coefficient (c_ε) was held at 0.916, and the turbulent Prandtl number was set at 0.9. The "compressibility" viscosity was computed, as usual, with a_0 of 0.6. The results of this run were then compared with the best combination of dynamic models (from Section 7.5.3).

Somewhat surprisingly, the constant coefficient model does almost as good a job as the dynamic model for the lower moments of the flow. This is illustrated in figure 7.31, which shows that the shear layer thickness predictions of the two runs were almost identical, although the growth rate of the constant coefficient run was slightly less. The normalized streamwise velocity contours (shown in figure 7.32) are likewise extremely close. Some small deviations in the results become apparent in the streamwise turbulent intensity profiles shown in figure 7.33. The dynamic model does a somewhat better job at predicting this quantity, although the differences are slight.

The real advantage of the dynamic model shows up when the higher moments of the flow are considered. Figure 7.34 shows skewness profiles as predicted by the two schemes. The dynamic model does a significantly better job here, while the constant coefficient model overpredicts the peaks on this curve. A similar phenomenon is seen

on a plot of the streamwise velocity flatness (figure 7.35). Thus, while the constant coefficient model does a good job, the dynamic model offers a distinct improvement. Since the dynamic model is still in a fairly early stage of development, one expects that with further refinement, even better results could be achieved.

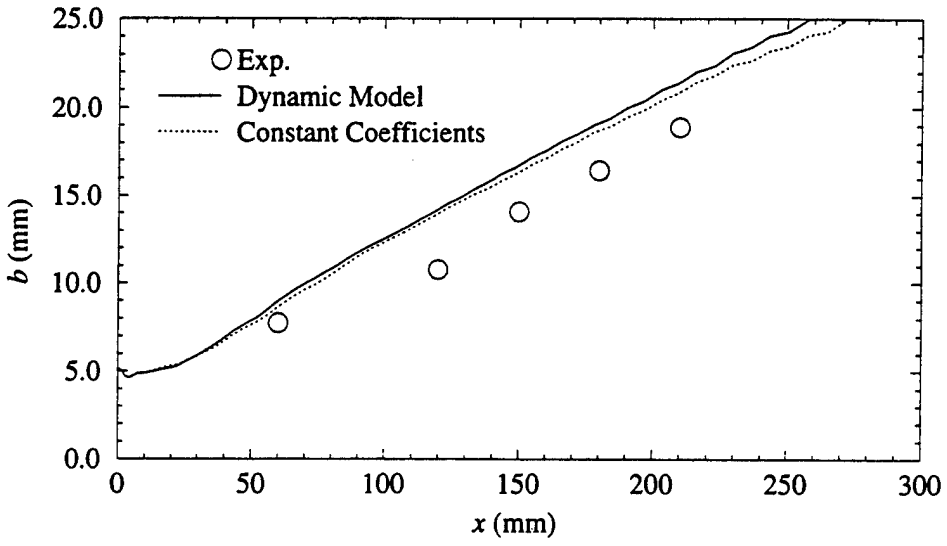


Figure 7.31: Predicted growth of Case 1 mixing layer for constant coefficient model versus the dynamic model

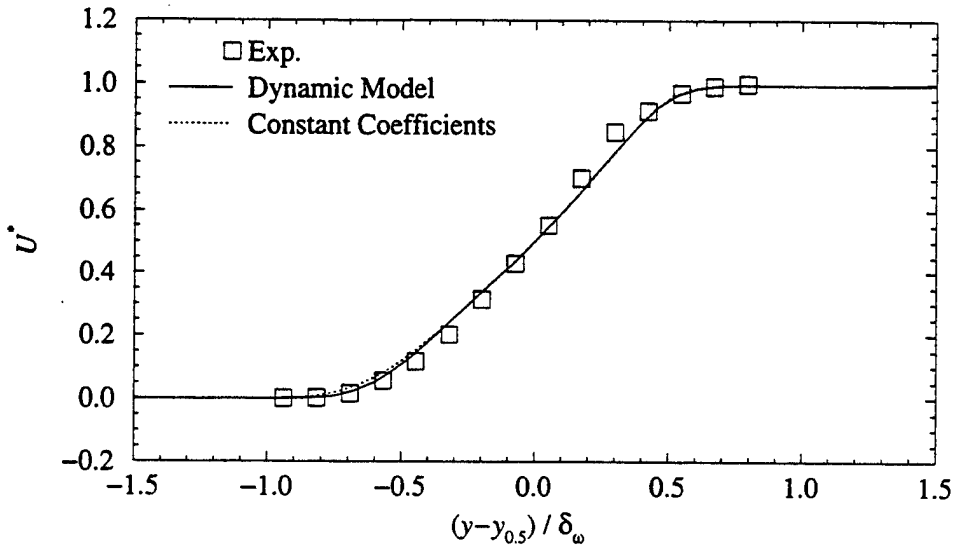


Figure 7.32: Predicted normalized streamwise velocity profiles ($x = 150mm$) of Case 1 mixing layer for constant versus dynamic coefficients

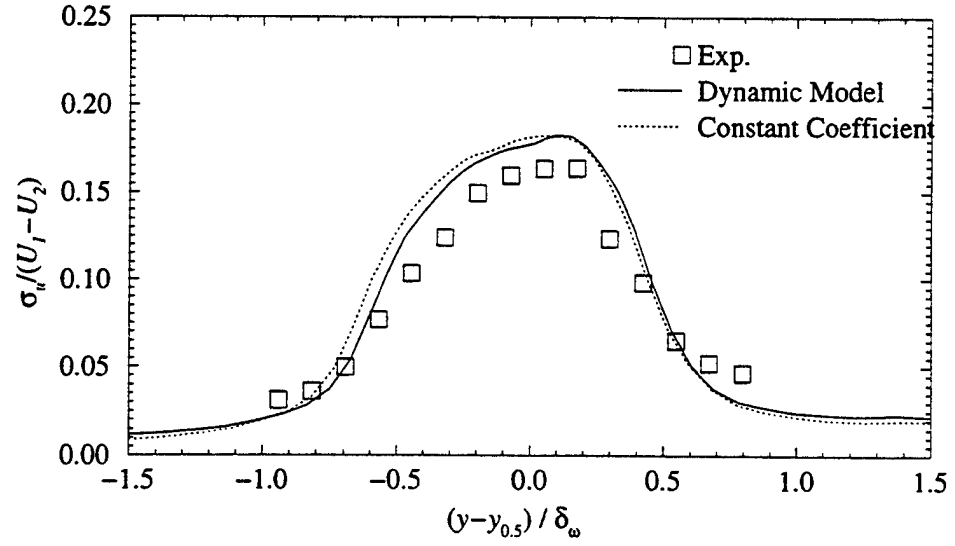


Figure 7.33: Predicted streamwise turbulent intensity profiles ($x = 150mm$) of Case 1 mixing layer for constant versus dynamic coefficients

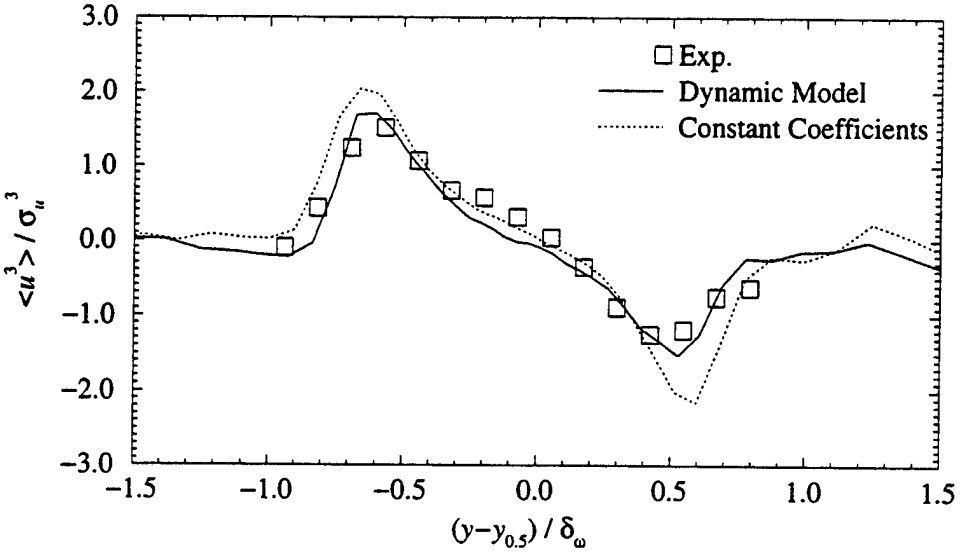


Figure 7.34: Predicted streamwise velocity skewness profiles ($x = 150mm$) of Case 1 mixing layer for constant versus dynamic coefficients

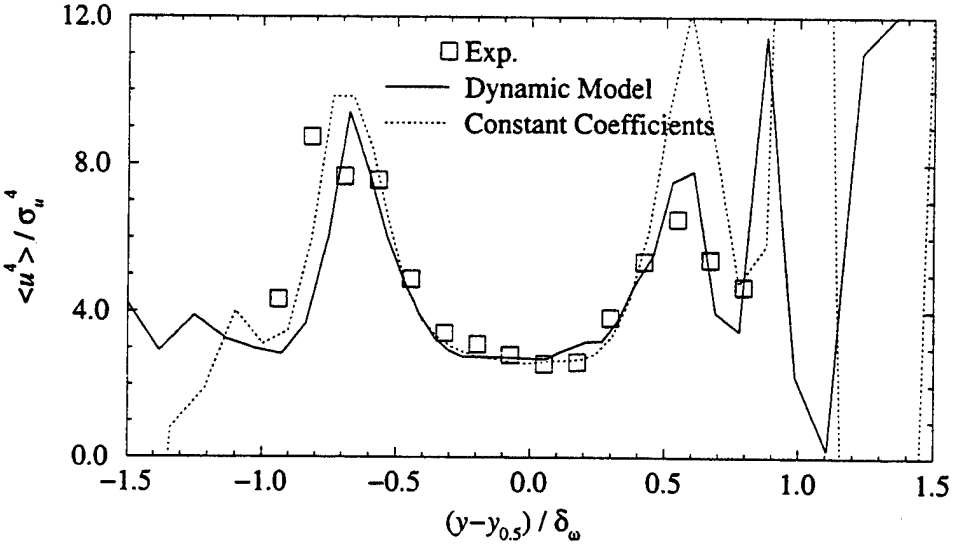


Figure 7.35: Predicted streamwise velocity flatness profiles ($x = 150mm$) of Case 1 mixing layer for constant versus dynamic coefficients

7.6 Simulation Results

Thus, of the model options considered above, the best combination is to use the standard value for a_0 (0.6), compute c_ν as described in Section 3.4.3, and use the alternate form (equation 3.33) for the dissipation coefficient. All subsequent results will be from simulations using these options (unless otherwise noted). Having established the model configuration to be used, it is applied to the simulation of the two mixing layers being examined. The Case 1 mixing layer may be considered a flow with low to moderate compressibility effects. The Case 2 mixing layer, however, is well into the compressible regime. Thus, by comparing the two, it should be possible to determine some of the effects of compressibility on the development of turbulent mixing layers (and turbulent flows in general).

In the remainder of this chapter, the results from the "final" model configuration on the finest grid are presented. These have been divided into two groups. First, qualitative results are presented and compared with the experimental and theoretical findings. The second section contains quantitative comparisons of the LES with Elliott's experimental data. As discussed in Chapter I, the primary motivation for the development of LES was to enable the numerical investigation of the effects of transients in high Reynolds number flows. RANS solvers (with the appropriate turbulence model) are capable of predicting the mean conditions, but they give no direct insight into the unsteady elements of the flow. This limitation can be overcome in part by making use of the turbulence model. Thus, the modelled Reynolds stress tensor and related quantities such as turbulent intensity can be computed. In contrast, a large eddy simulation allows a direct view of at least the larger scales of the unsteady flow field. A wealth of information is, therefore, potentially available

in LES which is simply not possible to obtain in RANS simulations. In this case, while RANS could provide much of the quantitative data (although a standard $k-\varepsilon$ or $k-\omega$ model does not predict the higher moments such as skewness and flatness), none of the qualitative comparisons could be made.

7.6.1 Qualitative Comparisons

As mentioned in Chapter I, one of the major prediction of linear stability theory [17] is that the braid-and-core structures that are so prominent in low speed mixing layers should give way to a more random-appearing three-dimensional flow structure with increasing compressibility. This is due to oblique instability modes becoming increasingly dominant. This is shown in figure 7.36 by the contours of the concentration of a passive scalar for the two cases. The Case 1 mixing layer, because it has a more coherent structure (particularly in the first half of the domain), shows evidence of roller-type vortical structures in the entrainment patterns of the passive scalar. The Case 2 mixing layer, however, while it evidences a great deal of mixing, does not show the same regular pattern of entrainment, indicating that the flow is indeed more three-dimensional.

The streamwise vorticity plays a large role in the mixing process in these shear layers. This is illustrated in figure 7.37 by superimposing contours of the passive scalar concentration (black and white lines) on contours of streamwise vorticity (shaded color) in a y-z plane. As one would expect, the mixing region coincides with the region of intense vorticity. Noted on the figure are pairs of counter-rotating vortices. These pairs have the effect of sucking up unmixed air (from the lower stream) into the mixing region, causing the contours of the passive scalar concentration to move up. Similar vortex pairs are simultaneously pulling unmixed scalar (from the

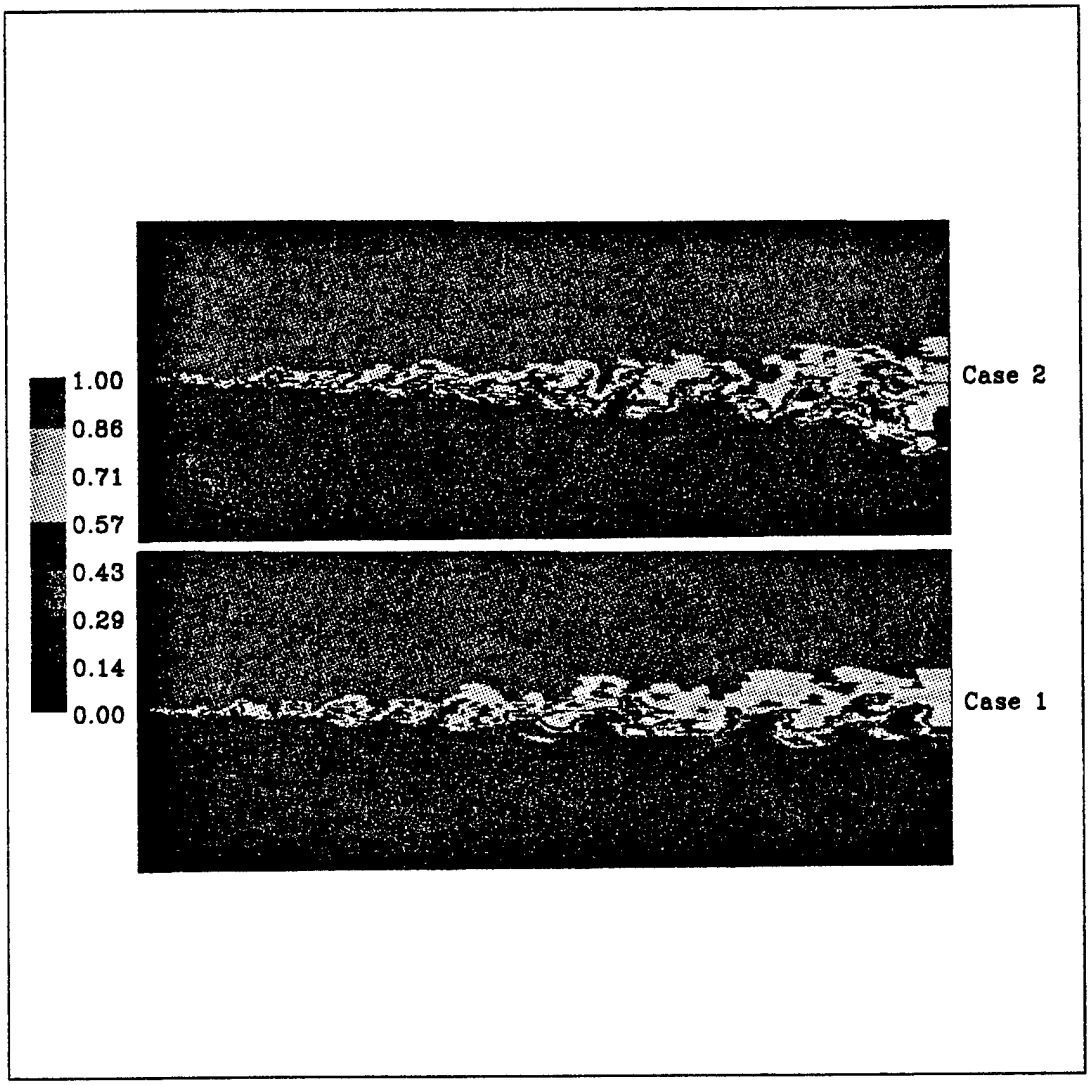


Figure 7.36: Concentrations of a passive scalar in x-y planes of spatially developing mixing layers

upper stream) into the mixing region. Together this vortical activity is responsible for the characteristic "S"-curves seen in the concentration contours.

A similar plot for the Case 2 mixing layer is shown in figure 7.38. Because the flow is more "broken up," however, the mixing takes place only in the lower two-thirds

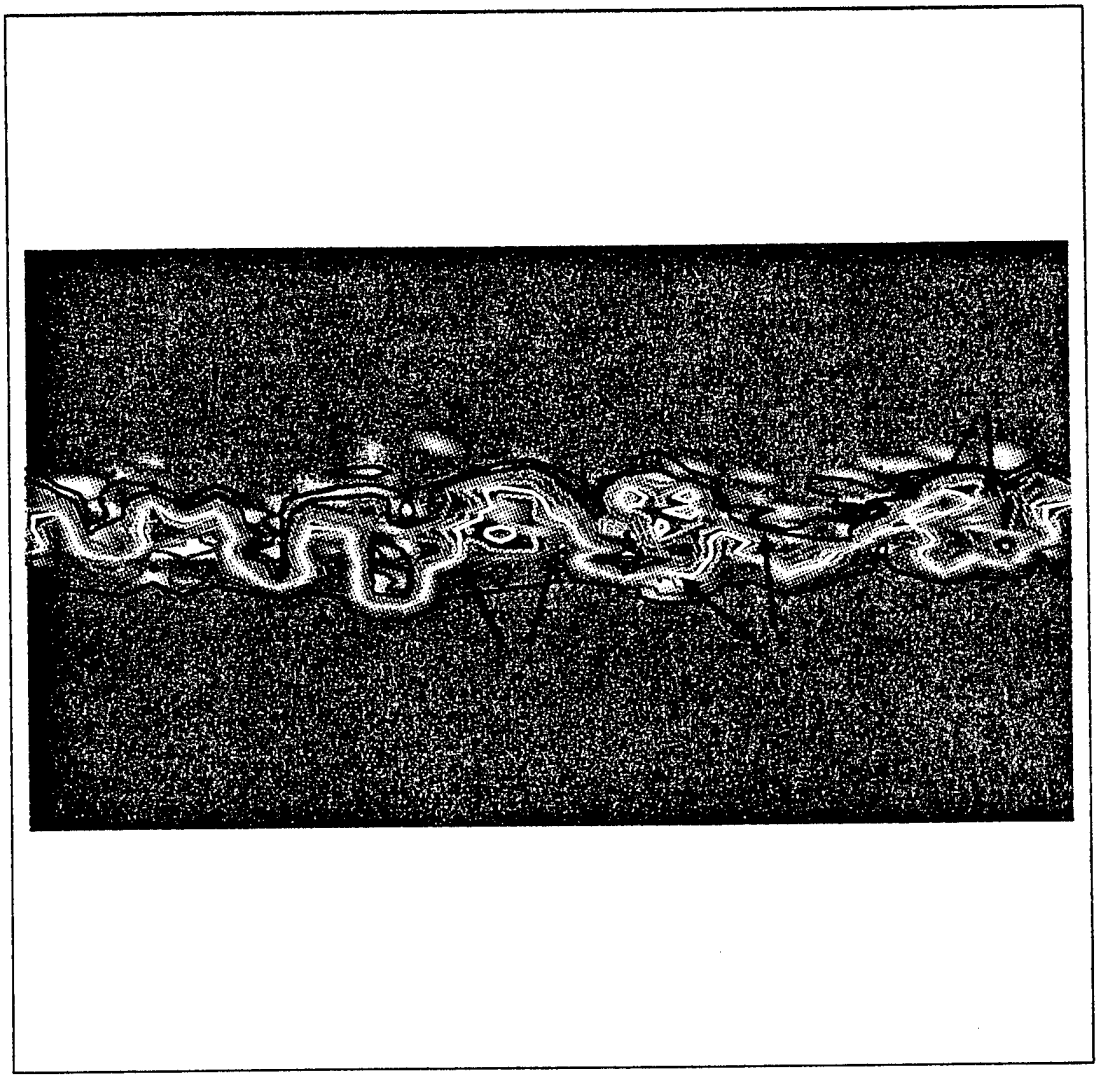


Figure 7.37: Contours of streamwise vorticity and passive scalar concentration in the Case 1 mixing layer ($x = 49mm$)

of the region of high vorticity. This is also responsible for the increased wrinkling of the contours and the lack of apparent correlation between counter-rotating vortices and the concentration contour lines.

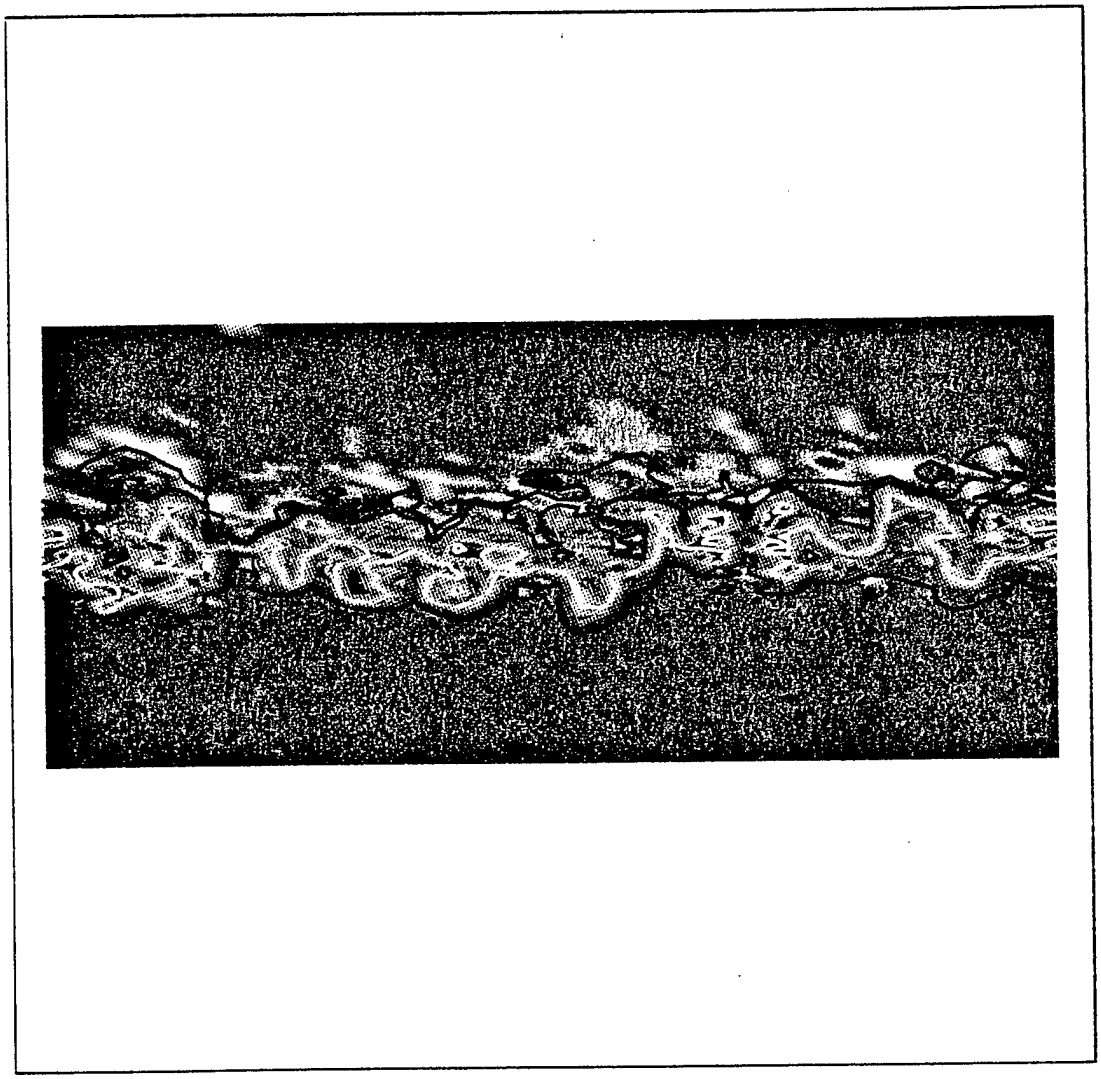


Figure 7.38: Contours of streamwise vorticity and passive scalar concentration in the Case 2 mixing layer ($x = 49mm$)

Figure 7.39 shows a snapshot of the streamwise vorticity in the flow field on several $y-z$ planes for Case 1, as well as one cross-section in the $x-y$ plane. Figure 7.40 shows, for the same flow field, the spanwise component of vorticity at the same locations. As expected. both plots show a pattern of coherent structures which

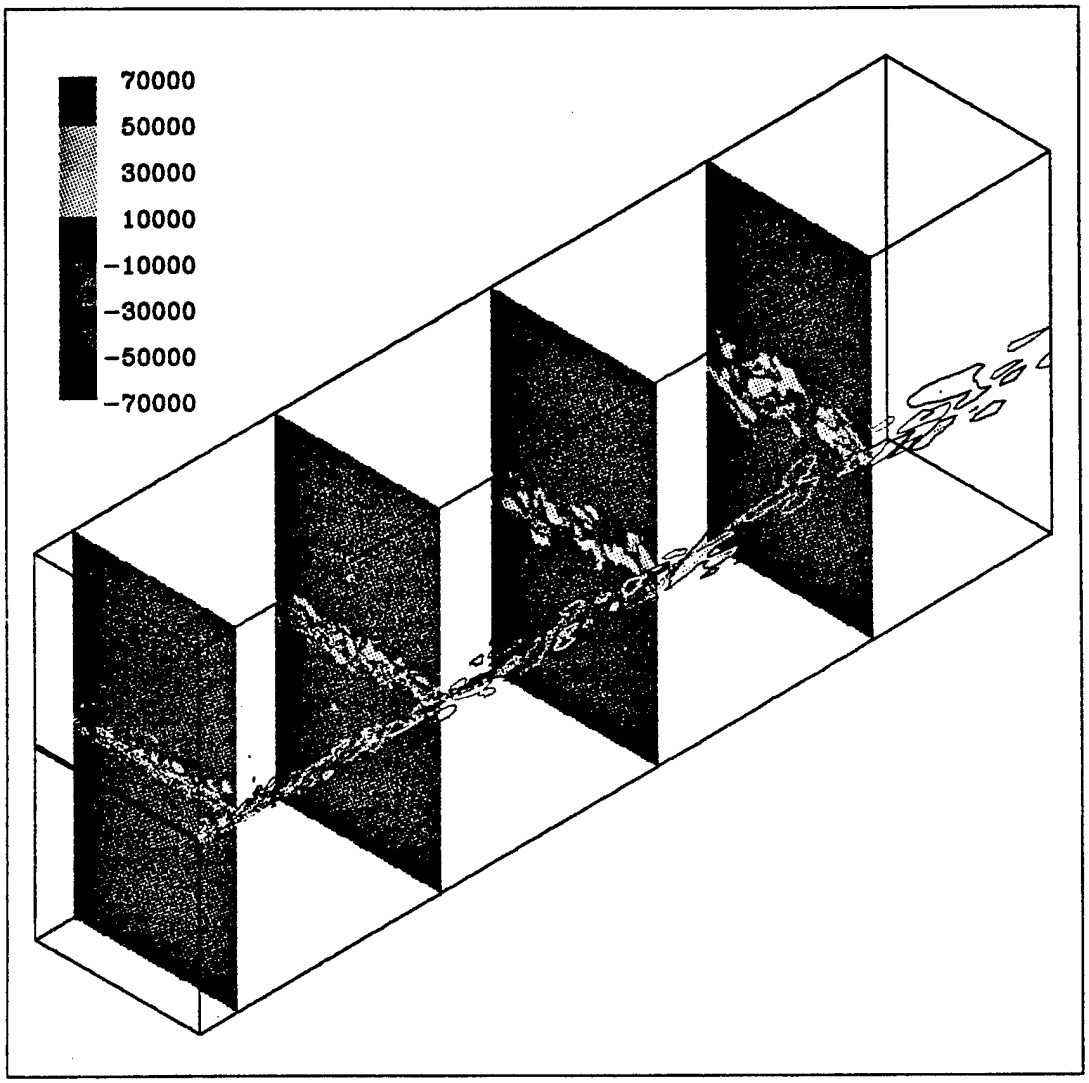


Figure 7.39: Streamwise vorticity contours in a fully developed flow field of the Case 1 spatial mixing layer

increase linearly in size as the flow moves downstream. The results are in accord with the predictions of linear theory [17] in that the spanwise vorticity strength dissipates as the structures move downstream, reflecting the reduced growth rate of the two-dimensional energy modes compared to three-dimensional modes. The

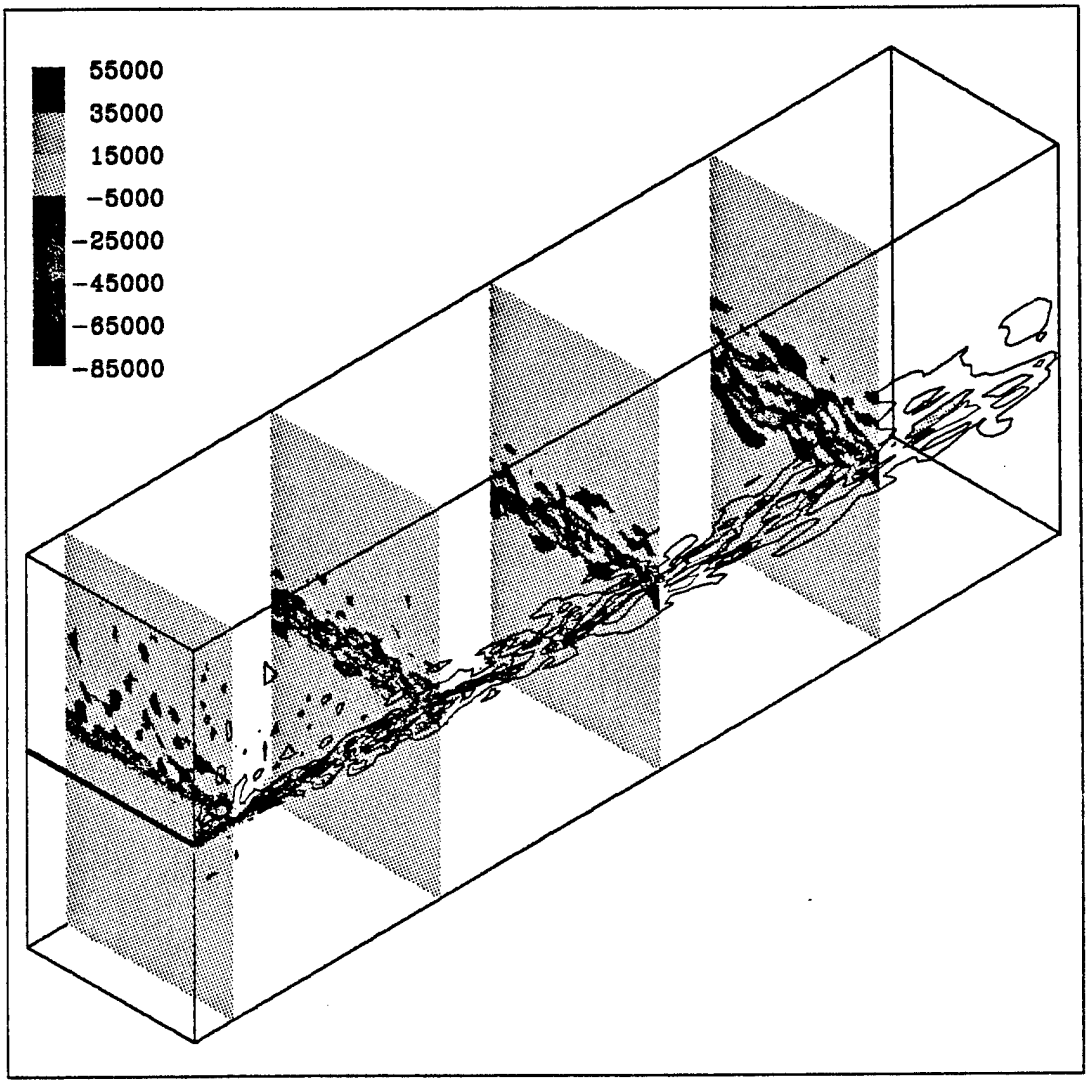


Figure 7.40: Contours of the spanwise component of vorticity in the fully developed fully developed Case 1 spatial mixing layer

streamwise vorticity, which is energized by the three-dimensional modes, maintains its intensity and, though the structures grow in size, they do not lose their coherence to the same degree as the spanwise vorticity structures. Similar behavior is shown

in the Case 2 mixing layer (see figures 7.41 and 7.42). For the higher speed case, however, the structures are somewhat smaller and more random in appearance.

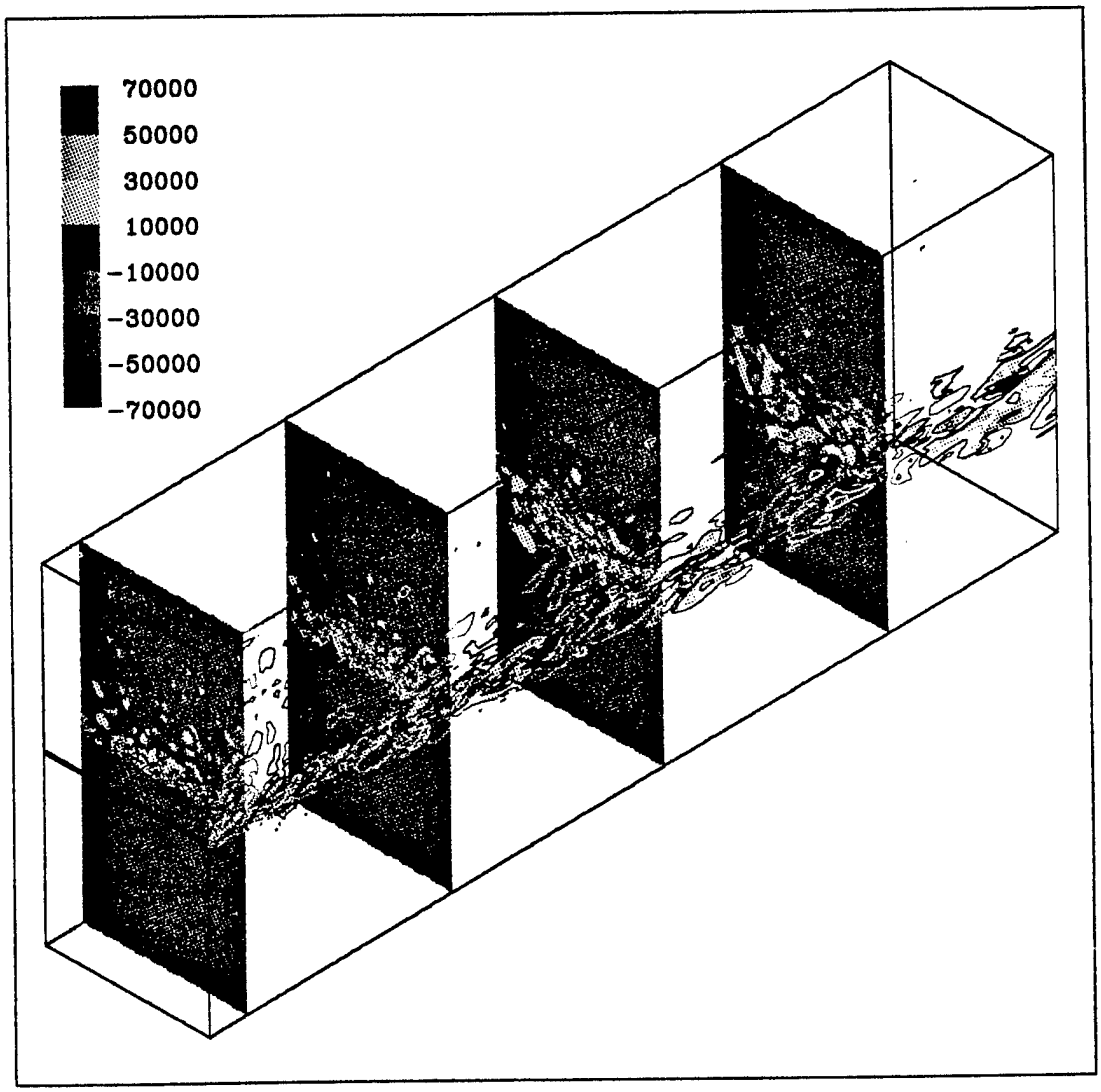


Figure 7.41: Streamwise vorticity contours in a fully developed flow field of the Case 2 spatial mixing layer

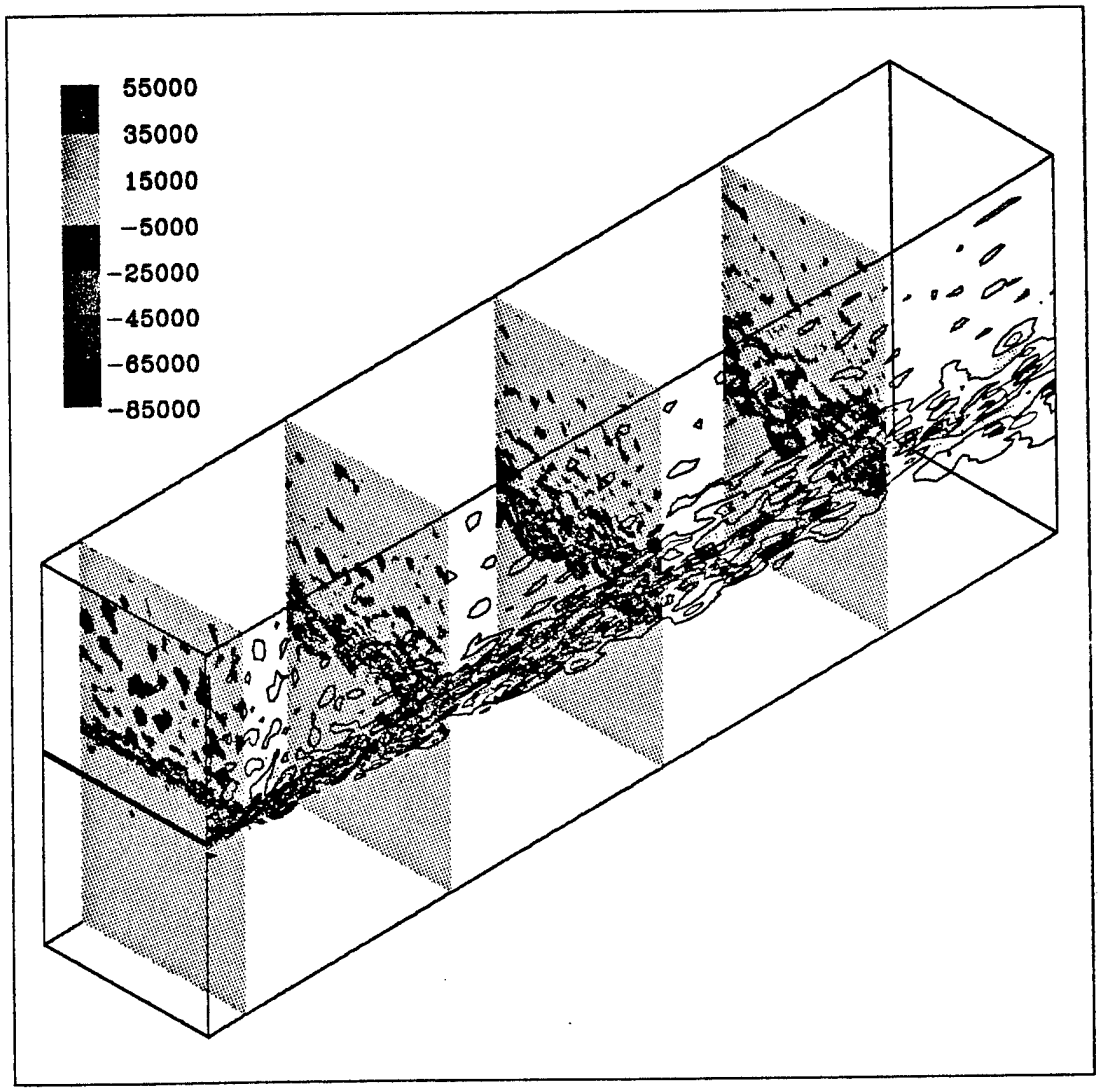


Figure 7.42: Spanwise vorticity contours in a fully developed flow field of the Case 1 spatial mixing layer

The streamwise evolution of pressure fluctuation spectra is shown in figure 7.43 for Case 1. These spectra have been taken as near to the bottom edge ($y - y_{0.5}/\delta_\omega = -0.47$) of the mixing layer as possible. It has not been possible to accomplish this exactly, since the sampling points must be determined in advance of the simulation. For Case 1, the sampling points allow for reasonably good comparison with experimental results. Unfortunately, for Case 2, the choice of sampling points is not as good. Each spectrum has been normalized by the total amount of energy of that particular spectrum. Elliott reports that the initial peak "...is between 9-13 kHz and decreases in frequency towards the fully developed region to 4-7 kHz." The same behavior is observed in the LES. For the Case 2 mixing layer, the experiment showed that the portion of the spectrum which contains significant energy is much broader than for Case 1. This general trend is also observed in the Case 2 mixing layer simulations (figure 7.44). This signifies less temporal organization of the structures at the higher convective Mach number.

The simulated subgrid kinetic energy of these mixing layers is highly correlated to the vorticity of the flow. In figure 7.45, the subgrid kinetic energy (black contour lines) is superimposed on a plot of the vorticity magnitude for the fully developed region of the Case 1 mixing layer (flow is from left to right). The strong correlation of these two quantities is obvious. The same behavior is readily apparent in figure 7.46, which shows the same quantities for Case 2.

The behavior of the model coefficients has been found to be almost isotropic for these cases. As an example of this, contours of c_ν for the Case 2 mixing layer are shown in figure 7.47. Although some grid effects are visible in the presence of smaller "structures" wherever the grid points are clustered, the field generally appears "random" in that no obvious correlations with other flow properties can

be discerned. Some of this is due, no doubt, to the addition of pseudo-isotropic turbulence to the two freestreams, but it is surprising that, allowing for grid effects, the mixing layer is not discernible in these cases. When one examines the locations of negative coefficient values (shown in figure 7.48 for Case 2), however, a slight trend can be discerned in that there appears to be a larger fraction of negative values in the freestreams. In the vicinity of the mixing layer itself, generally positive values are seen. Note that the apparent homogeneity of the model coefficient does not imply that the subgrid stress tensor is, on average, uniform in these flows, because the subgrid viscosity is also dependant on the subgrid kinetic energy which, as has been shown, is largely confined to the mixing layer.

Because of its strong dependance on the stress tensor model coefficient, the dissipation model coefficient exhibits much the same behavior (shown in figure 7.49). Again, there is no apparent difference between the behavior of the coefficient in the mixing layer and in the freestreams (although some grid effects are visible).

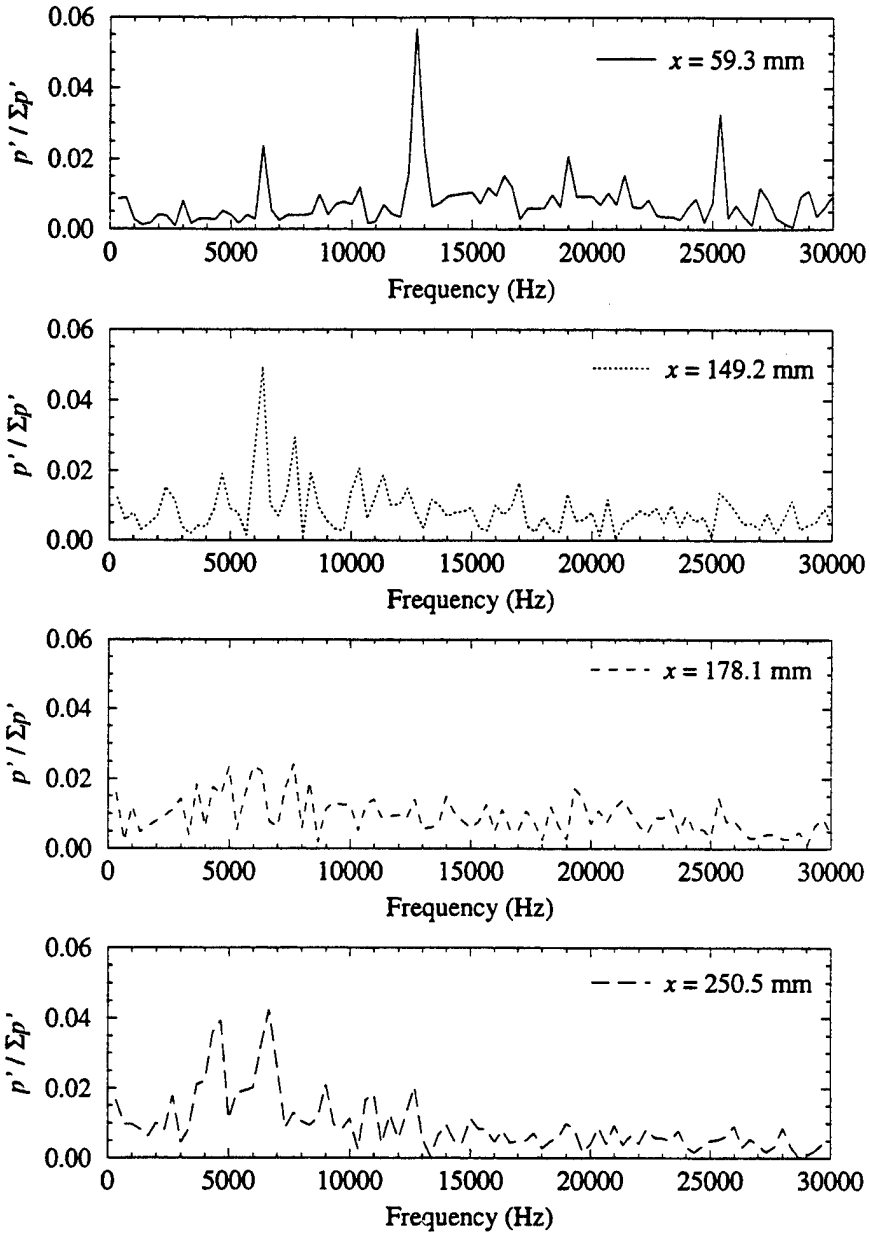


Figure 7.43: Streamwise evolution of pressure fluctuation spectra in the Case 1 mixing layer

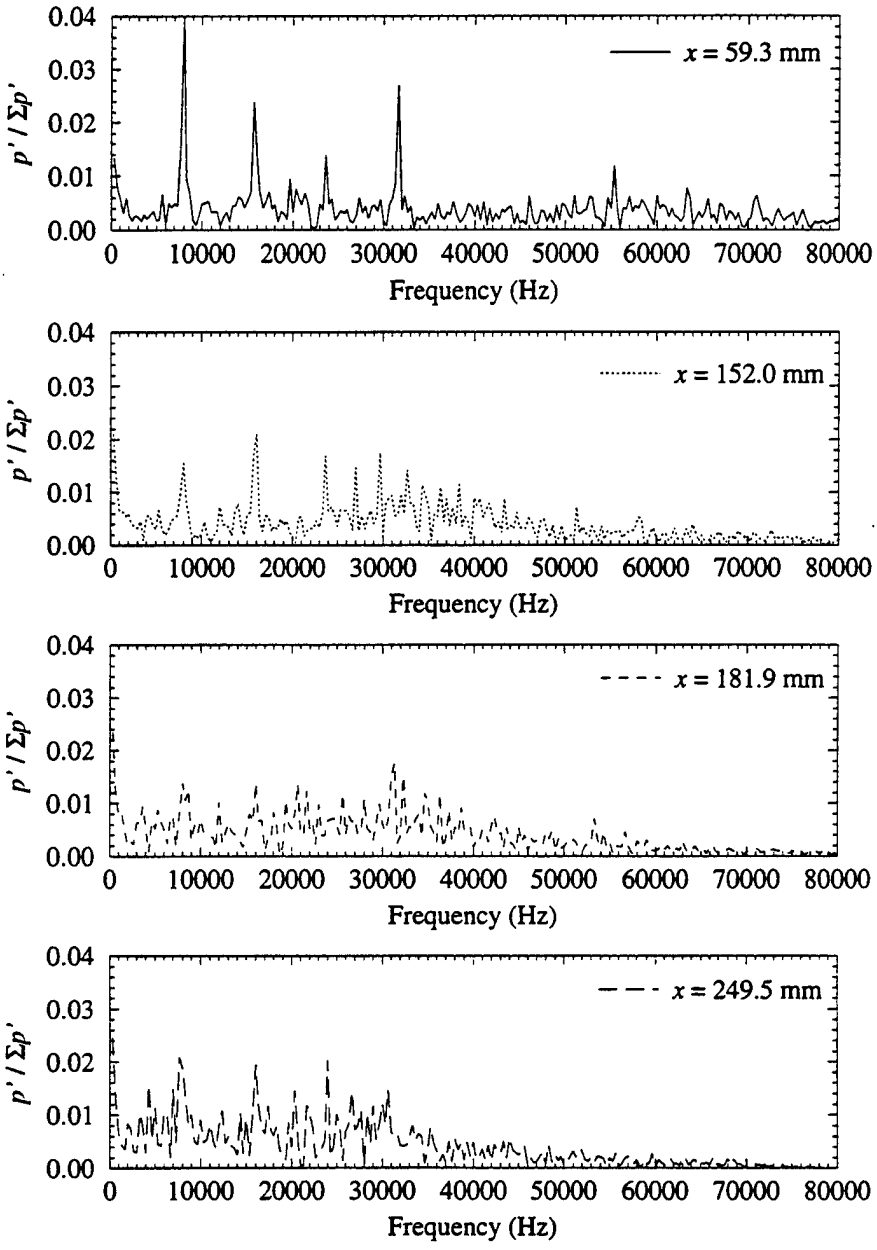


Figure 7.44: Streamwise evolution of pressure fluctuation spectra in the Case 2 mixing layer

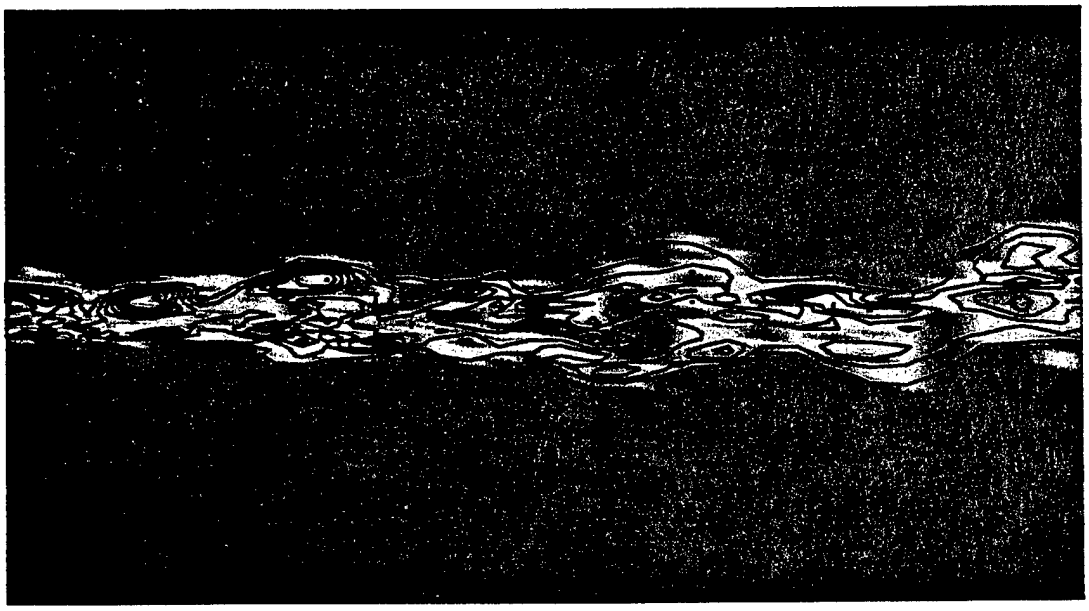


Figure 7.45: Contours of k^{sgs} and vorticity magnitude in the Case 1 mixing layer

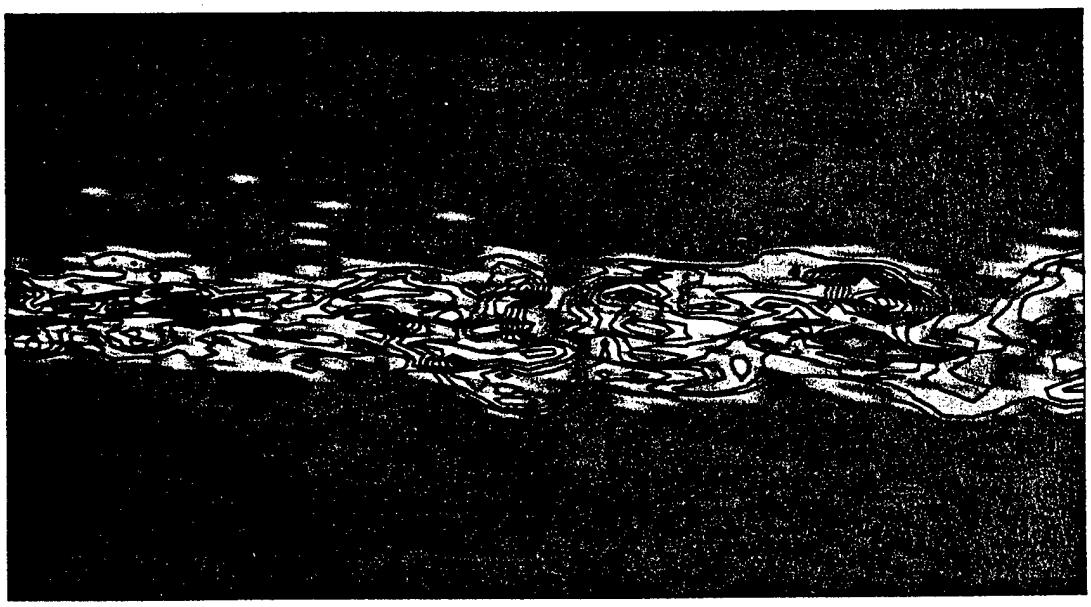


Figure 7.46: Contours of k^{sgs} and vorticity magnitude in the Case 2 mixing layer

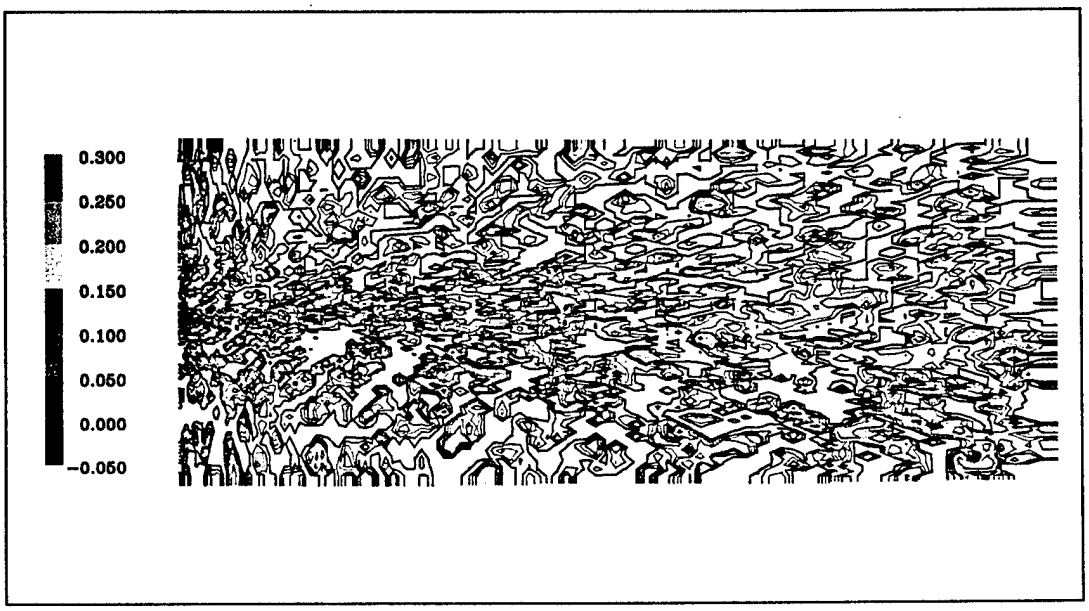


Figure 7.47: Contours of c_ν in the Case 2 mixing layer

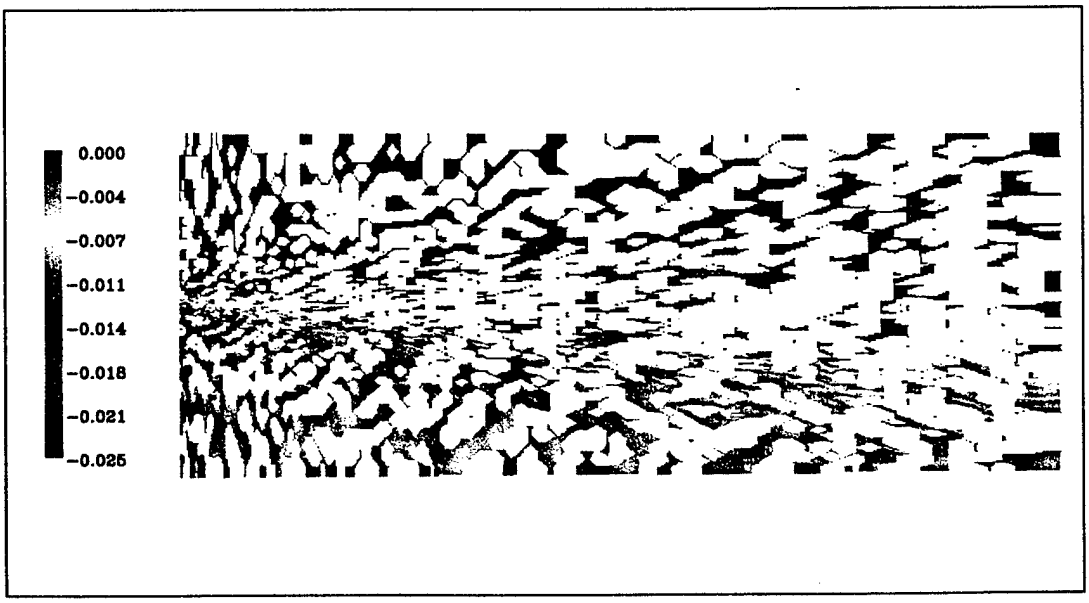


Figure 7.48: Regions of "backscatter" in the Case 2 mixing layer

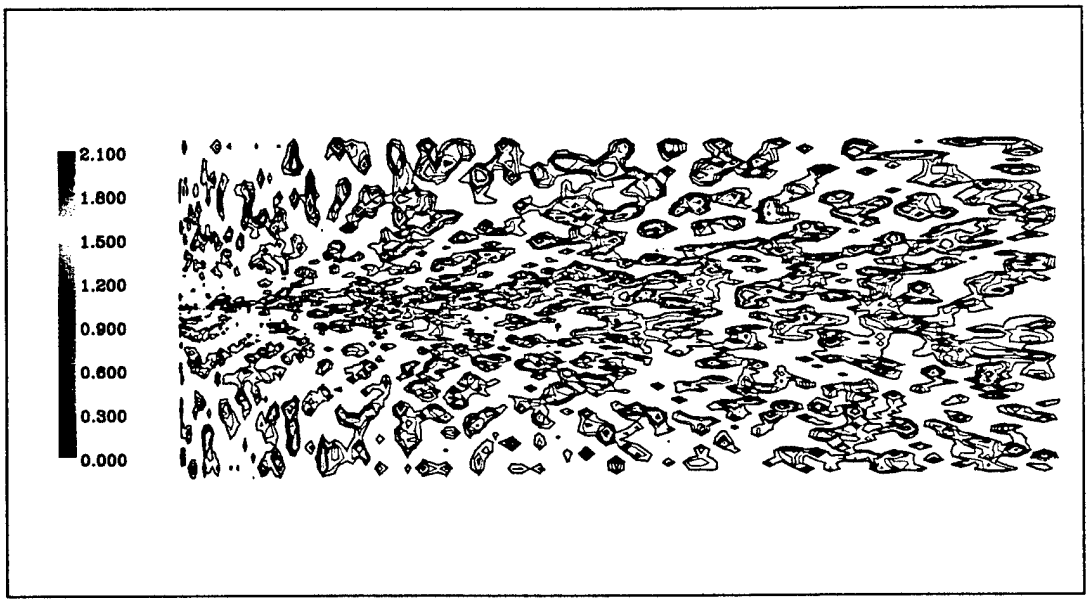


Figure 7.49: Contours of the k^{sgs} dissipation model coefficient for the Case 2 mixing layer

7.6.2 Quantitative Evaluations

Despite the relatively coarse grid at even the highest resolutions, the results are surprisingly good when compared to experiment. The momentum thickness as a function of position downstream of the splitter plate (for Grid 2 after averaging over two flow-through times), shown in figure 7.50, is reasonably well captured by the LES. The effect of compressibility is shown in the decrease in thickness for the higher convective Mach number case. The growth rate is also close to experimental values, as shown in figure 7.51. The values shown here must be used with caution, however, since, at least in Elliott's case, they are based on data from only three streamwise locations. The LES results, naturally, use more points, but they are still sensitive to the choice of locations on which the regression is performed.

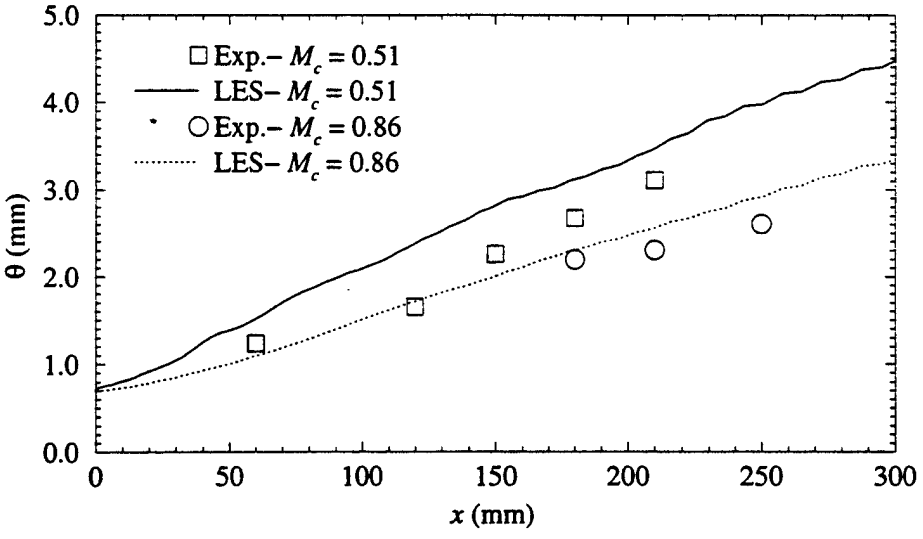


Figure 7.50: Comparison of simulated and experimental momentum thickness growth in spatial mixing layers (Grid 2)

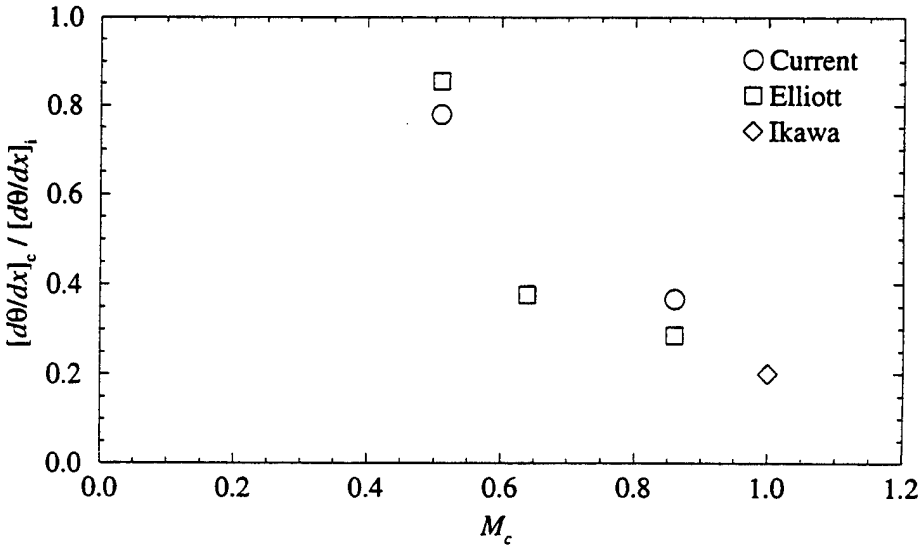


Figure 7.51: Momentum thickness growth rates in spatial mixing layers

The shear layer thickness growth as a function of position downstream of the splitter plate is also in reasonable agreement with experimental results for both cases, as shown in figure 7.52. The linear nature of the growth is well resolved, as is the approximate magnitude, but the differences between the two cases are not well resolved. This is due primarily to the Case 1 mixing layer, which is somewhat overpredicted.

The vorticity thickness, in figure 7.53, is not in as close agreement with experiment as are the shear layer thickness and momentum thickness. Agreement with experiment is reasonable for Case 1, but for Case 2, a decrease in growth rate is observed beginning around $150mm$ downstream of the splitter plate. The reasons for this are not clear, because the same behavior is not observed in the other measures of mixing layer thickness. In general, this quantity tends to display more devia-

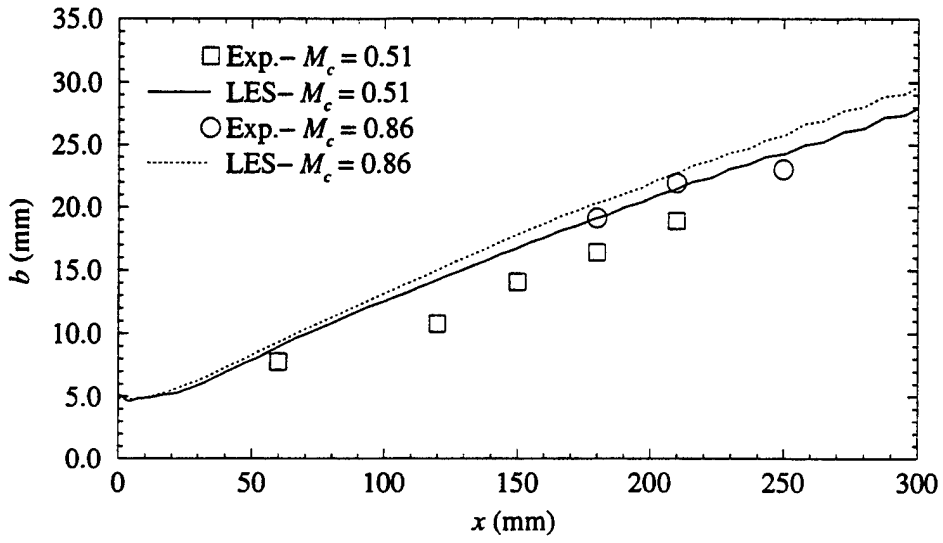


Figure 7.52: Comparison of simulated and experimental shear layer thickness growth in spatial mixing layers (Grid 2)

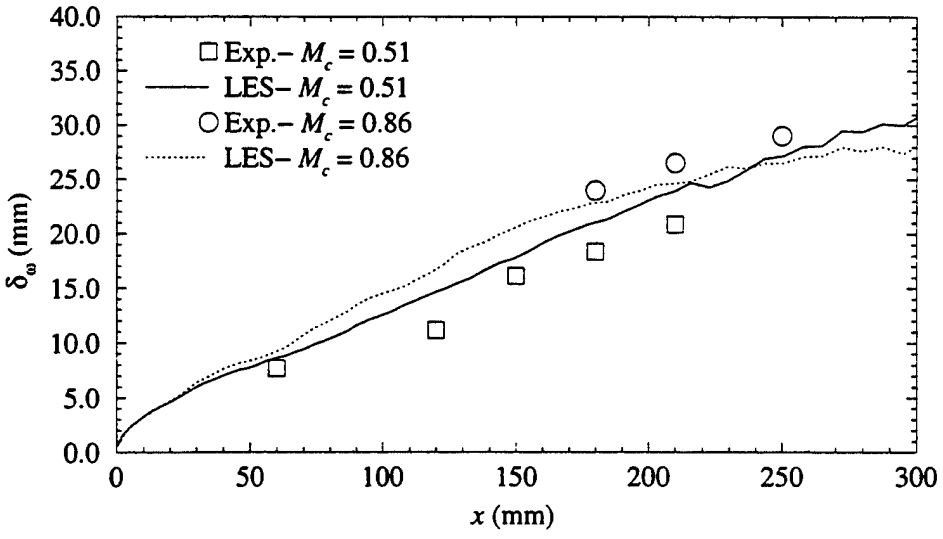


Figure 7.53: Comparison of simulated and experimental vorticity thickness growth in spatial mixing layers (Grid 2)

tions from linear growth than the others. Insufficient sampling time is one possible explanation for this behavior, but this has not been verified.

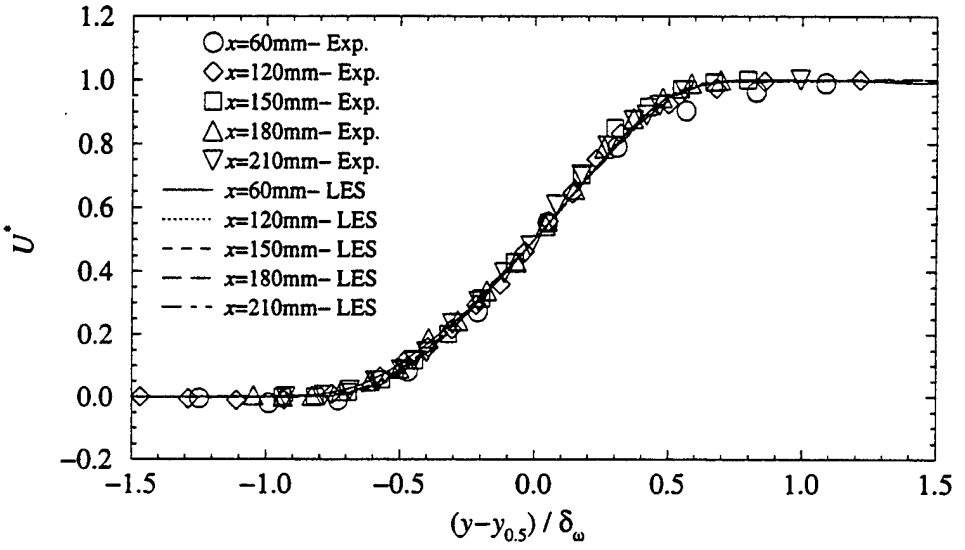


Figure 7.54: Normalized mean velocity profiles in the Case 1 spatial mixing layer

In general, the simulation results for Case 1 (on Grid 3 with averaging over roughly 2.5 flow-through times) agree very well with experiment. Normalized velocity profiles for Case 1 at various streamwise stations are plotted in figure 7.54. The agreement with the experimental data is excellent. As the figure shows, the self-similar character of the mean flow is well resolved by the current scheme.

Turbulent quantities are also in good agreement with experiment. Figure 7.55 shows streamwise turbulent intensity profiles at the same locations as for the previous figure. Both the peak magnitude and the overall distribution of turbulence are well predicted compared to the experiment. The width is correct, as is the shape

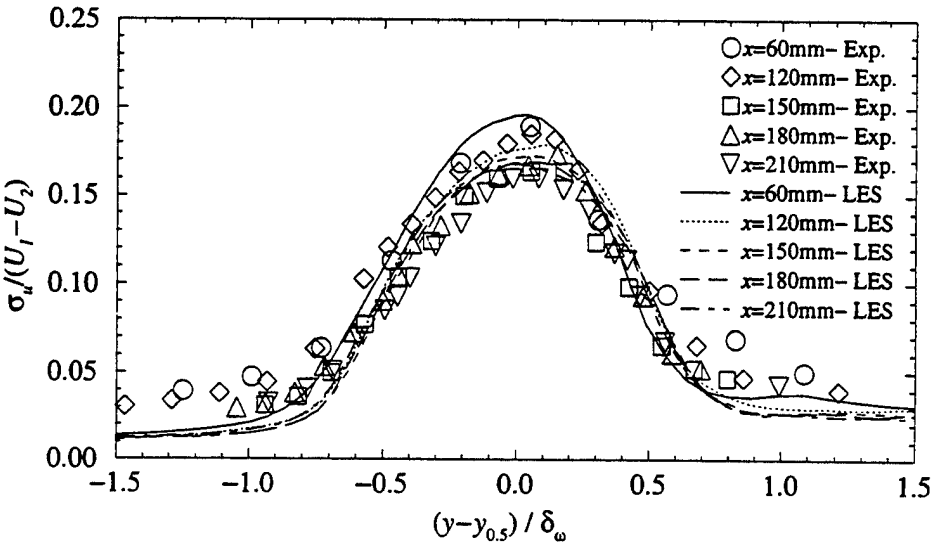


Figure 7.55: Streamwise turbulence intensity profiles in the Case 1 spatial mixing layer

and self-similar nature of the profiles. Note, however, that the freestream values are underpredicted (probably due to lack of resolution in these areas). As with the experiment, the U^* profiles showed self-similarity earlier than the turbulent quantities, which are not fully similar until $150mm$ downstream of the splitter plate. For the succeeding plots of turbulent quantities, data is shown only for those measuring stations which are downstream of the onset of self-similar behavior.

The lateral turbulence intensity, shown in figure 7.56, is also in excellent agreement with experiment. Not only are the shape and the width of the profiles in the self-similar region correct, but the magnitude is also correct. Again, the freestream values are less than those observed in the experiment

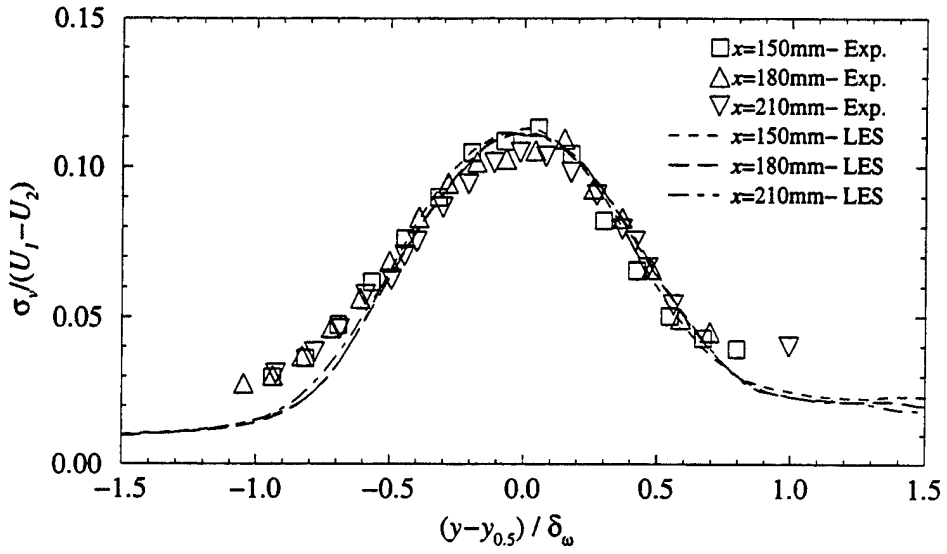


Figure 7.56: Lateral turbulence intensity profiles in the Case 1 spatial mixing layer

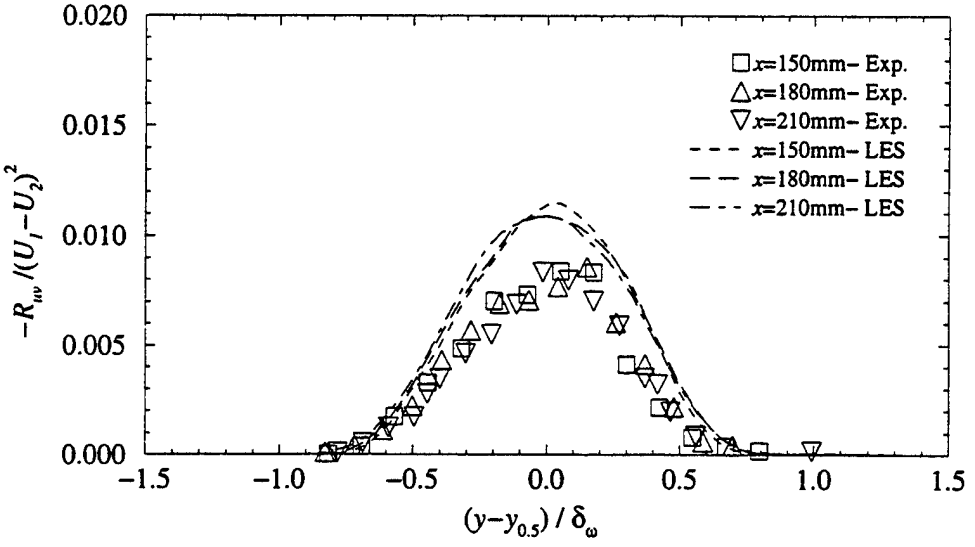


Figure 7.57: Reynolds stress profiles in the Case 1 spatial mixing layer

The Reynolds stress profiles ($\overline{u'v'}$) shown in figure 7.57, are not so well resolved. Although the width of the profiles is correct, and self-similar behavior is predicted, the magnitudes are significantly higher in the simulation. This is possibly a result of deficiencies in the current model, or it could also be a side-effect of errors (primarily dispersion) in the numerical scheme.

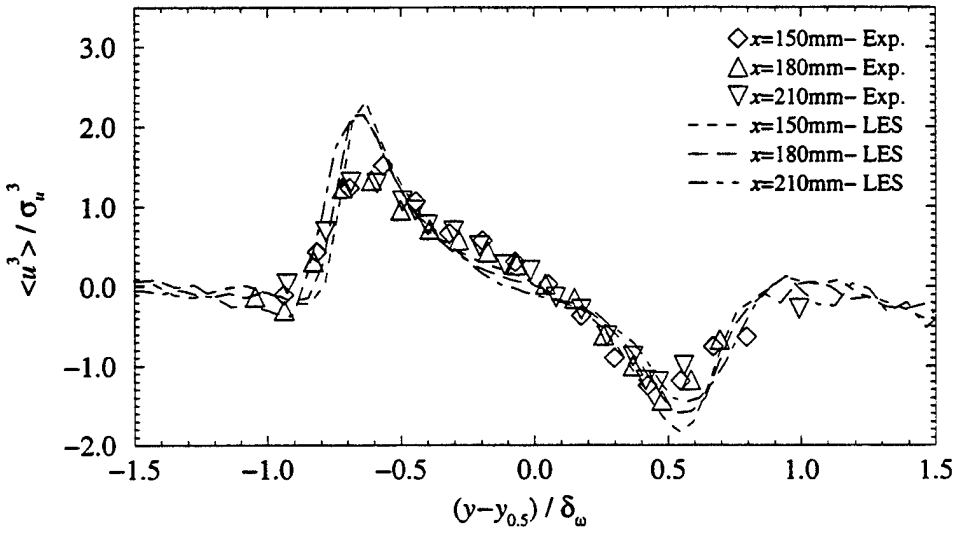


Figure 7.58: Streamwise velocity skewness profiles in the Case 1 spatial mixing layer

Somewhat surprisingly, the streamwise velocity skewness is well resolved for this case (see figure 7.58). Self-similarity is achieved, and the profiles show the correct shape and magnitude within the core region. The peak values, however, are slightly overpredicted. Lack of adequate grid resolution outside the core of the mixing layer is probably the major cause for this behavior. Error in the numerical scheme is a related factor which would be expected to play a role here. A third possibility is

that the inflow pseudo-turbulence, which was shown above to have some effect on higher moments of turbulence, may be adversely influencing the skewness at the fringes of the mixing layer.

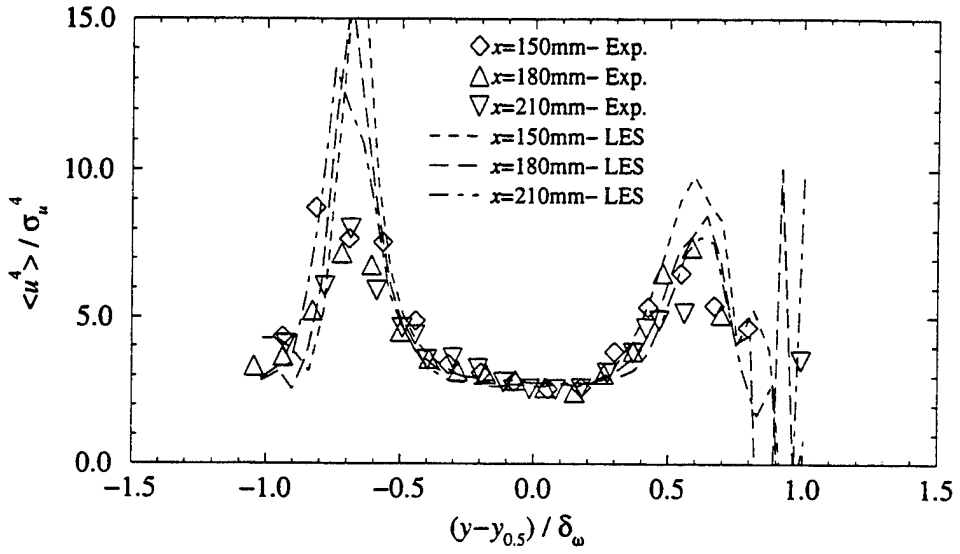


Figure 7.59: Streamwise velocity flatness profiles in the Case 1 spatial mixing layer

The velocity flatness (figure 7.59) shows excellent agreement with experiment in the majority of the mixing layer. On the high speed side, however, the results become unstable above a non-dimensional coordinate of 0.5. Similar, though not as dramatic, instability is observed on the low-speed side for $(y - y_{0.5})/\delta_\omega$ less than 1.0. The reasons for this behavior are likely the same as those cited above for the skewness.

In general, the results from simulations of Case 2 show more divergence from the experimental results than for Case 1. The normalized streamwise velocity profiles

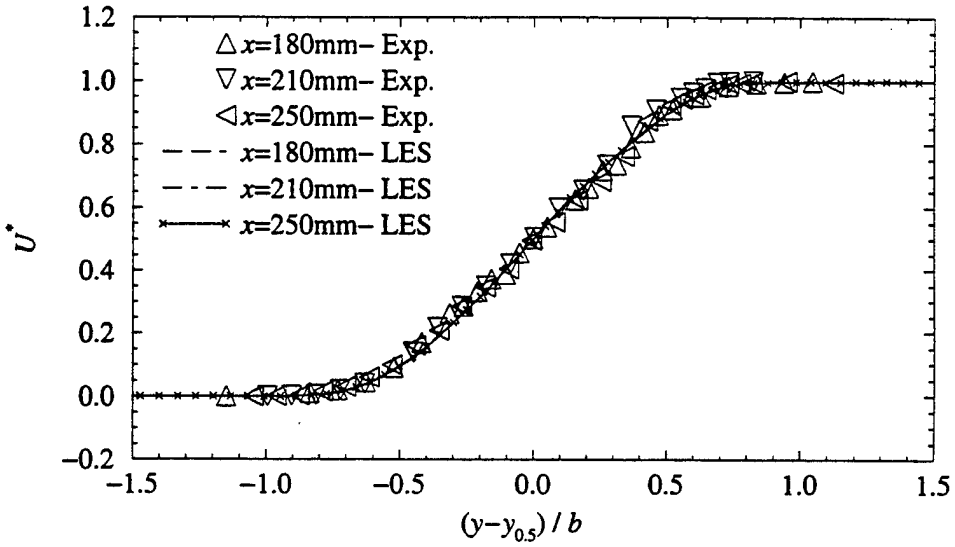


Figure 7.60: Normalized mean velocity profiles in the Case 2 spatial mixing layer

on Grid 3 (averaged over four flow-through times) are shown in figure 7.60. Good agreement is obtained both in the shape and self-similar nature of the curves. Note that the horizontal coordinate for this case has been non-dimensionalized using the shear thickness rather than the vorticity thickness. This is because, as shown above, the vorticity thickness is not as well predicted for this case. Thus, when the vorticity thickness is used as the normalizing factor, an artificial scattering is introduced. The shear thickness does not, in general, exhibit the same problem.

The discrepancies between experiment and simulation become more apparent when turbulent quantities are examined. While the low-speed side of the curve is reasonably well predicted, the streamwise turbulence intensity profiles are significantly overpredicted on the high-speed side. In general, the magnitude is also

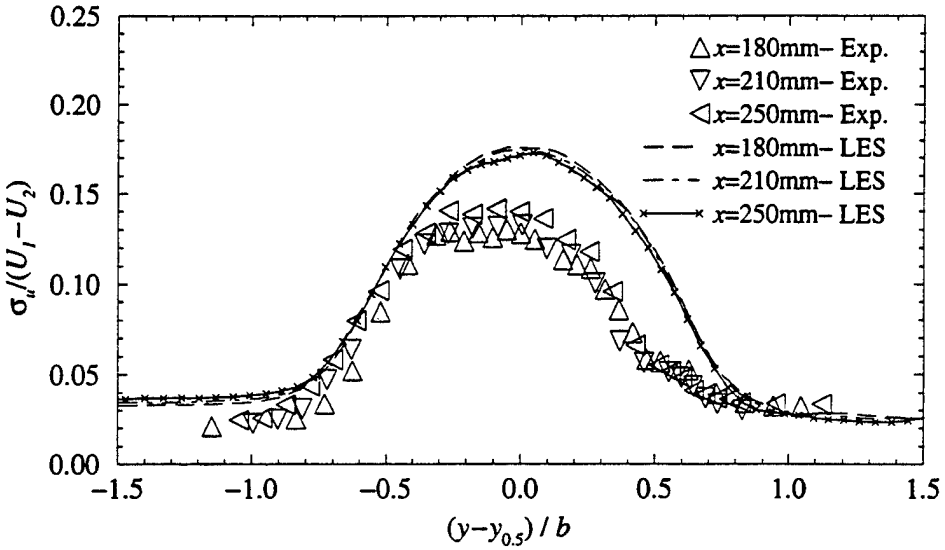


Figure 7.61: Streamwise turbulent intensity profiles in the Case 2 spatial mixing layer

somewhat overpredicted. Also the width of the profile appears to be greater than in the experiments. The results are, however, self-similar.

This trend of reasonable predictions on the low-speed side and overprediction on the high speed side is seen on all of the turbulent quantities. The lateral turbulence intensity profiles, for example, are shown in figure 7.62. As before, they are somewhat skewed toward the high speed side of the flow, and the peak magnitude is somewhat overpredicted, though not as much as is the streamwise intensity. Again, the profiles are strongly self-similar.

The Reynolds stress profiles, shown in figure 7.63, are similarly skewed, but the magnitude is overpredicted to a greater degree than in the previous two plots. This is similar to the behavior that is observed in the Case 1 simulations, as shown above.

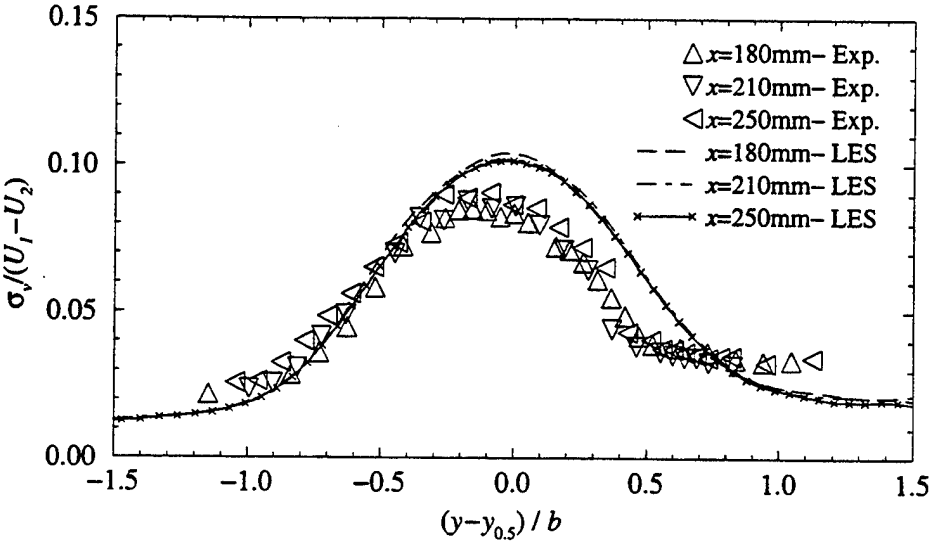


Figure 7.62: Lateral turbulent intensity profiles in the Case 2 spatial mixing layer

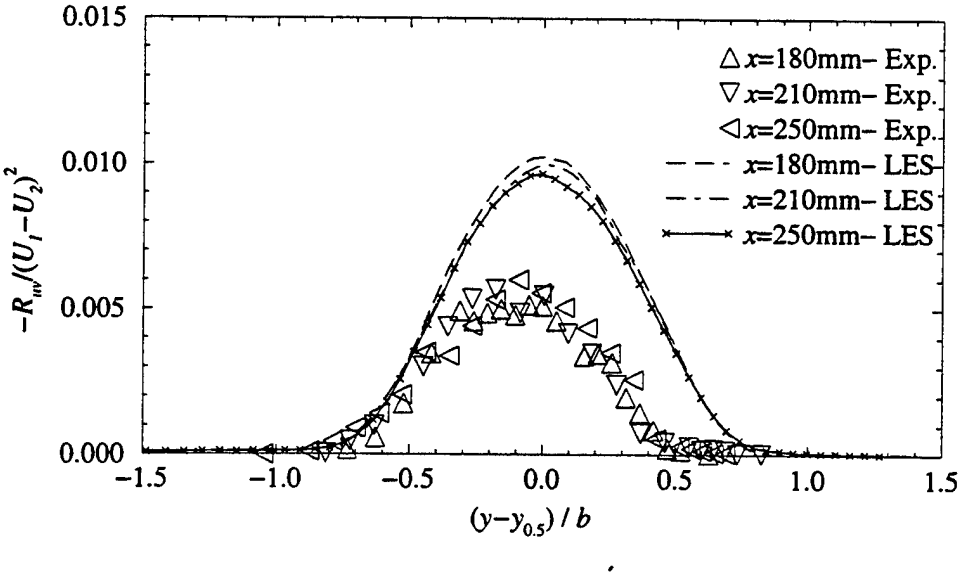


Figure 7.63: Reynolds stress profiles in the Case 2 spatial mixing layer

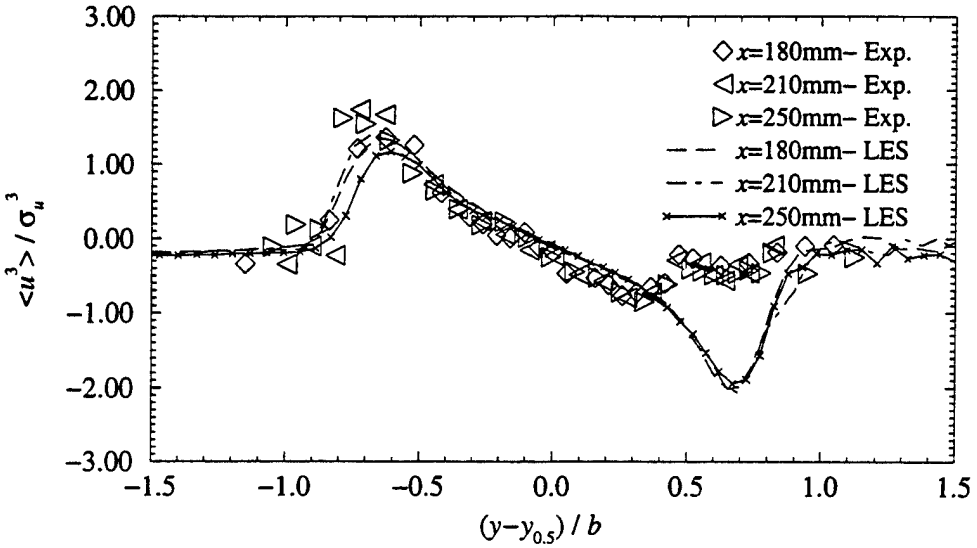


Figure 7.64: Streamwise velocity skewness profiles in the Case 2 spatial mixing layer

The streamwise velocity skewness (figure 7.64) shows excellent agreement on the low-speed side of the mixing layer. Again, however, the high speed side of the mixing layer is not correctly predicted. Instead of the flattened character found in this region in the experiment, the profiles take the same general shape as was observed in the Case 1 mixing layer.

The same behavior is observed in the flatness profiles. Again, the high-speed side is incorrectly predicted in much the same shape as for Case 1, while the low-speed side is in reasonably good agreement with experiment. As with Case 1, the profiles become extremely unstable on the high-speed side beyond the edge of the mixing layer (non-dimensional coordinates greater than about 0.6).

It appears from these plots, that the model is not properly predicting a fundamental feature of highly compressible turbulence. Specifically, it is not capturing

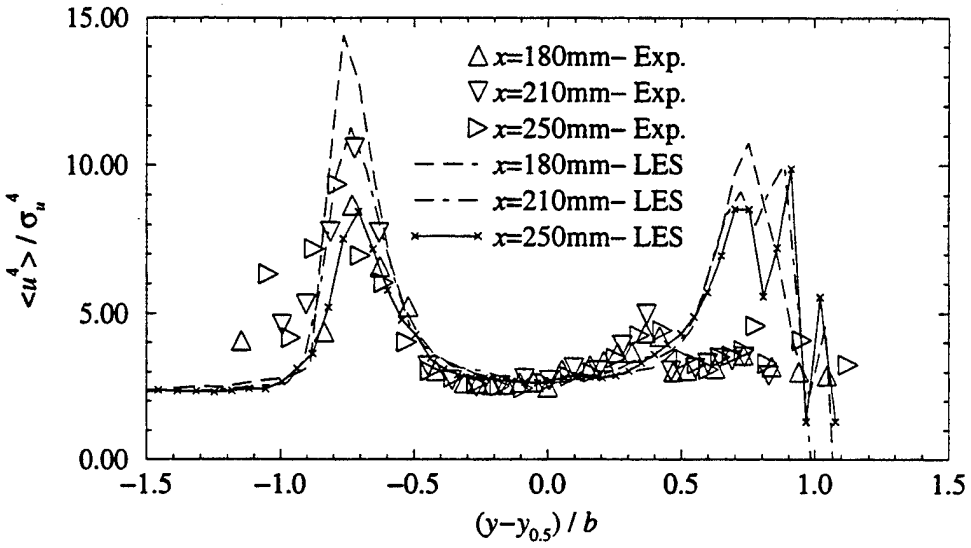


Figure 7.65: Streamwise velocity flatness profiles in the Case 2 spatial mixing layer

the full extent of the suppression of turbulence with increasing compressibility. This is illustrated in figure 7.66 which shows that the peak magnitudes of the streamwise and lateral turbulent intensities, as well as the Reynolds stress. While Elliott observed decreases in all three quantities, the current work predicts a slight rise in the streamwise intensity. A similar trend was observed by Goebel and Dutton [126] (also see Gruber *et al.* [138]), who found that streamwise intensity remained roughly constant as Mach number increased. The behavior of the lateral intensity and Reynolds stress, however, does not agree with either set of experiments. While these values do decrease with increasing convective Mach number, they do not do so to the extent predicted by experiment. Based on the previous plots, it would seem that the majority of the error is from the high speed side of the mixing layer, rather than uniformly distributed throughout. From the experimental results, it appears

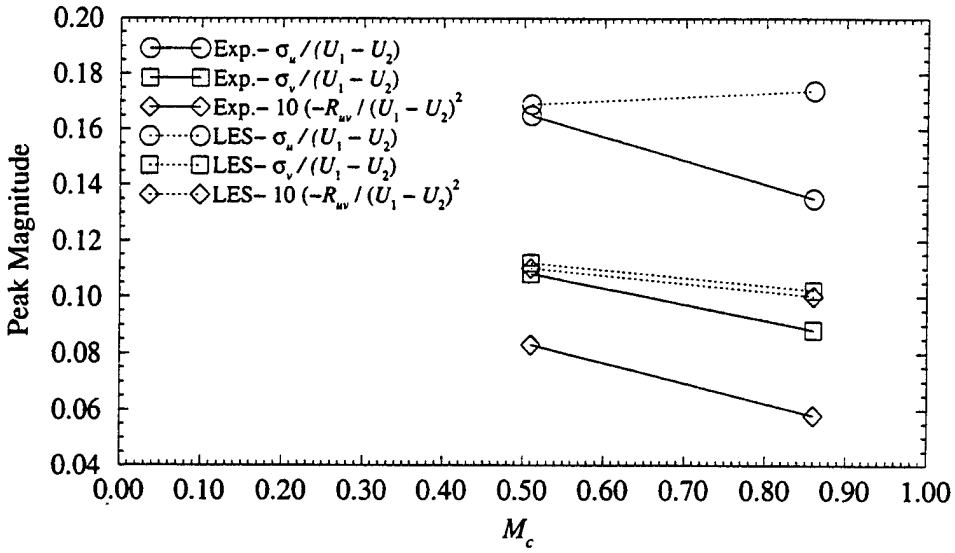


Figure 7.66: Maximum turbulence intensities and Reynolds stress versus convective Mach number

that the effects of strong compressibility are felt more strongly on the high speed side of the mixing layer, and these effects are not being correctly captured by the model. Thus, while the method appears to be adequate for low to moderate compressibility, more work needs to be done to enhance the accuracy for highly compressible, high Reynolds number flows.

CHAPTER VIII

CONCLUSIONS AND RECOMMENDATIONS

The primary accomplishment of this work has been to demonstrate that large eddy simulation of compressible, spatially developing flows at high Reynolds numbers is feasible- even on relatively coarse grids. There are two major requirements in order to accomplish this. First, the numerical scheme must have very low inherent dissipation in order not to artificially destroy the unsteady fluctuations. Secondly, a subgrid model is required in order to correctly transfer energy from the resolved scales to the subgrid and thus prevent the build-up of energy in the smallest resolvable scales.

The current scheme, in combination with the compressible local dynamic subgrid model, has been shown to work reasonably well for turbulent flows with low to moderate compressibility. In the decaying isotropic turbulence cases, the scheme closely matched the mean quantities and turbulent fluctuations computed using a comparable filtered DNS field. In forced isotropic turbulence, the model correctly reached an equilibrium state, and the observed trends were similar to those found by Kim [67]. In the spatial mixing layer cases, the results, considering the coarseness of the grids, compared well with experiment for the lower convective Mach number case. The higher convective Mach number case also captured the growth of the shear layer, as well as the expected self-similarity. Many of the expected qualitative features of the flow were also resolved.

The turbulent profiles, however, reveal that, for the $M_c = 0.86$ mixing layer, the simulations are not capturing some of the fundamental properties of compressible

turbulence. Specifically, they are not predicting the suppression of turbulence on the high-speed side of the mixing layer. It is believed that several factors are involved.

First, it is likely that the results could be significantly improved simply by improving the base numerical scheme. The MacCormack schemes (using the standard predictor-corrector time marching) are known to require many points per wavelength in order to properly capture wave propagation. Because of the coarseness of the grids, the current results are likely to have a great deal of dispersion error in them. This property of MacCormack schemes can be improved in several ways. For example, recent work by Hixon [139] [140] [141] has shown that by using dispersion-relation-preserving (DRP) methods, MacCormack-type schemes can be derived which require far fewer points per wavelength for the same level of accuracy.

Another area that needs investigation is the dynamic model itself. In the spatial mixing layer cases, the average of the dynamically computed model coefficients are only half (roughly speaking) of the commonly used constant coefficient values. There are several indications that this is not correct. Historically, similarity models have been faulted for underpredicted quantities such as dissipation. Since the dynamic model uses assumptions of similarity for various quantities, it is not surprising that it should underpredict as well. Also, the results from the current simulations indicate that the subgrid kinetic energy is being significantly overpredicted (even when using the alternate form of the dissipation model coefficient- equation 3.33). This shows that the dissipation model coefficient should be higher. In addition, this increased subgrid kinetic energy is not resulting in excessive turbulent viscosity, as indicated by the high levels of turbulent intensity shown in the spatial mixing layer cases. This could mean that the dynamic procedure is underpredicting the value of the subgrid stress tensor model coefficient as well. One possible combination which has

not been tried in this work is to use the alternate forms for both c_ϵ (equation 3.33) and c_ν (see Appendix D). Since the latter was found to predict higher values than the "standard" approach taken here, it might, in conjunction with the alternate c_ϵ, yield better results than the current combination of models.

The "compressibility" viscosity terms should also be investigated further. For instance, the pressure switch used in the current work is essentially an *ad hoc* use of a technique employed in artificial dissipation for a similar purpose. It can be argued, however, that a switch based on density would make more sense in the current context. Also, the characteristic velocity should perhaps be reconsidered. The current practice is reasonable for a stationary or slowly moving shock, but not otherwise. What is desired is a velocity which represents the relative speed between the fluid in the grid cell and the nearest compression region in its path. Unfortunately, an efficient means of computing such a quantity is not at all apparent. An additional possibility might be to add a Mach number scaling to increase this term in regions of high Mach number flow.

Recently, Smith [142] has developed several improvements and/or alternate approaches to the boundary conditions and inflow pseudo-turbulence techniques that have been used for the current work. Future research would benefit from incorporating these features. In particular, the inflow boundary could be distanced somewhat from the tip of the splitter plate without requiring an overwhelming number of additional grid points. This would reduce any spurious effects on the mixing layer from artificially truncating the domain in this direction. In addition, future work would benefit from the development of approximate wall boundary conditions for LES. For configurations where near-wall information is not required, such a boundary condition offers the possibility of greatly reducing the resolution needed

near walls (and thus easing memory and CPU requirements) without sacrificing the accuracy of the solution in the core flow regions.

Finally, when considering the limitations of the current methodology, it must be kept in mind that this work represents a very early stage in the development of LES (and dynamic models) for compressible flow- particularly at high Reynolds numbers. With further refinement, many of the current drawbacks and limitations can be overcome. This work has shown, however, that the concept is feasible, and that significant features of the flow (*e.g.*, time traces, instantaneous snapshots, and higher moments or turbulence) can be resolved which are not possible with the RANS approach. This has important implications for the CFD community. For example, the current work opens the possibility of improving simulations of combustion (at realistic Reynolds numbers) by making use of the unsteady flow field information and using the subgrid kinetic energy field to estimate the magnitude of the unresolved turbulent velocity fluctuations. Computational aeroacoustics is another area which could benefit from this added capability in computing unsteady flows, since turbulence is known to be a significant source of jet engine noise. Therefore, it is believed that the current effort brings large eddy simulation one step further away from the realm of the purely academic and closer to being a practical (if expensive) tool which can be used to address real engineering problems.

APPENDIX A

THE FILTERING OPERATION AND LARGE EDDY SIMULATION

It is unfortunate that most reports of LES-related work gloss over filtering, because it is fundamental to the art, and there are some unexpected twists. To begin with, consider a filtering operation with a uniform characteristic filter width Δ. Leonard [49] defined such a filter (in one dimension) in physical space as:

$$\bar{\phi}(x) = \int_{-\infty}^{\infty} G(x-\xi)\,\phi(\xi)\,d\xi \tag{A.1}$$

It is important to note that, although the notation is similar to that used in formulating the Reynolds-averaged Navier-Stokes equations, this and all other filtering discussed in this work is a spatial operation, not temporal (unless otherwise noted). The original field (ϕ) can therefore be defined as the filtered field plus a "subgrid" term:

$$\phi = \overline{\phi} + \phi' \tag{A.2}$$

The function G in equation A.1 is the "filter function," a spatial analog of the spectral transfer function. According to Ghosal [68], filter functions may be any function defined on an infinite domain which satisfies the following requirements:

1. $G(-\xi) = G(\xi)$

2. $\int_{-\infty}^{\infty} G(\xi)\, d\xi = 1$

3. $G(\xi) \to 0$ as $|\xi| \to \infty$ such that all moments $\int_{-\infty}^{\infty} G(\xi)\, \xi^n d\xi$ $(n \geq 0)$ exist

4. $G(\xi)$ is "small" outside $\left(-\frac{\Delta}{2}, \frac{\Delta}{2}\right)$.

One important result of choosing such a function is that:

$$\overline{\frac{\partial \phi}{\partial x}} = \frac{\partial \bar{\phi}}{\partial x} \tag{A.3}$$

Three common filters are the spectral cutoff, Gaussian, and top hat (or box) filters, whose filter functions are as follows (for one dimension):

$$\text{Spectral cutoff: } G(\xi) = \frac{\sin\left(\frac{\pi\xi}{\Delta}\right)}{\frac{\pi\xi}{\Delta}} \tag{A.4}$$

$$\text{Gaussian: } G(\xi) = \frac{1}{\Delta}\sqrt{\frac{C}{\pi}} \exp\left(-\frac{C\xi^2}{\Delta^2}\right) \tag{A.5}$$

$$\text{Box: } G(\xi) = \begin{cases} \frac{1}{\Delta}, \text{ if } |\xi| < \frac{\Delta}{2} \\ 0, \text{ otherwise} \end{cases} \tag{A.6}$$

Note that the spectral cutoff filter is normally applied in spectral space as:

$$\overline{\widehat{\phi}}(k) = \widehat{G}(k)\widehat{\phi}(k) \tag{A.7a}$$

$$\widehat{G}(\xi) = \begin{cases} 1, \text{ if } |k| < \frac{2\pi}{\Delta} \\ 0, \text{ otherwise} \end{cases} \tag{A.7b}$$

Note that the constant, C, in equation A.5 above is set somewhat arbitrarily. Meneveau [143] used a value of 6.0, while Ghosal [68] suggested a value of 2.0. Also of interest, despite Ghosal's assertion that filter functions must be defined on an infinite domain, there is nothing in the definition of the box filter (A.6) which requires an infinite domain, particularly if one considers the discrete form of the filter. For this reason, among others, many people use box filters to relate DNS to LES for physical space numerical schemes (*e.g.*, Meneveau [143] and Kim and Menon [?]).

There are advantages to using spectral and pseudo-spectral fluids codes for LES. First, the approximate field, which is discrete in spectral space, is a finite sum of continuous functions in physical space. Therefore, it is, in principle, a continuous function in physical space. In practice, of course, one uses a finite number of points to represent this field in physical space, but, given the approximations made in spectral space, the values obtained for any given point in physical space are exact. Furthermore, spectral filters and derivatives are also, in principle, continuous in physical space. In this situation, spectral filters (A.7) have some additional useful properties:

$$\overline{\overline{\phi}} = \overline{\phi} \tag{A.8}$$

$$\overline{\phi'} = 0 \tag{A.9}$$

Another advantage which the spectral approach has is that derivatives yield an exact value for the approximate field. In other words, if one is approximating a function using N Fourier modes, then as long as one has at least $2(N+1)$ points *in physical space*, it does not matter if one has 20 or 20 million points: the value of a derivative at any given point is the same. Therefore, one can take a flow field from a spectral DNS run, filter it, and coarsen it, with the result being a flow field which satisfies the governing equations for LES.

There are, however, drawbacks to spectral filters. First, they have limited applicability in realistic flow situations because of boundary constraints. Also, spectral filters are non-positive (i.e. the filter function is negative at some points in space). The latter condition results, as shown by Vreman, Geurts, and Kuerten [88], in a subgrid stress tensor (see equation 2.21) which does not satisfy the realizability conditions (see equation 3.44).

On the other hand, both the Gaussian and box filter functions (A.5 and A.6) are positive, and thus the Reynolds stress realizability conditions will apply to the resulting subgrid stress tensor. Unfortunately, equations A.8 and A.9 no longer hold [56] for these filters. Furthermore, if a spatial numerical solver is to be used, one must discretize the filter as well. Therefore, as suggested by Perot [144] it is necessary to examine the discretized system as it is solved in the actual code because discrete systems sometimes have different properties than the original continuous system from which they were derived.

If one filters the DNS data but leaves it on the original grid, the resulting field will satisfy equation A.3, and there is no problem. Unfortunately, as LES is not usually computed on the same grid as a DNS, the exact data must be discretized/coarsened somehow to match the LES grid. This causes a problem, because the coarsened field will no longer satisfy equation A.3. This is because the derivative algorithm employed in a spatial code is a function of grid resolution. The DNS field satisfies the (numerically approximated) governing equations using a derivative stencil on a fine grid, but the derivative algorithm to be used in the LES is defined on a different, much coarser, grid. In general, these two derivative approximations will not yield the same result.

This was confirmed in numerical experiments conducted using a box filter on a solenoidal DNS field. In fact, the error was of the same magnitude as the velocity derivatives themselves. Obviously, in an incompressible flow this would mean that the LES field would no longer satisfy continuity. If coarsened DNS fields do not satisfy the LES equations of motion (in the form that they are to be solved numerically in an LES code) then a potentially serious problem exists, because most LES subgrid model validation begins with *a priori* analysis from DNS fields. Also, coarsened DNS fields are frequently used as initial conditions for LES. The above analysis suggests that such applications have additional limitations that are not normally discussed. This is not to say that a spatially filtered DNS field is completely uncorrelated with a proper LES field. Many people, among them Kim and Menon [44] and Spyropoulos and Blaisdell [15], have shown a strong correlation between filtered DNS solutions and LES solutions for a variety of flow fields.

A box filter and coarsening combination seems to be compatible with second order central schemes [45], but at the present time, the author knows of no algo-

rithm which is capable of transforming a DNS field on a fine grid into an LES field on a coarser grid which satisfies the LES equations as solved using higher order schemes. Other researchers, among them Meneveau [143] and Veeravalli and Saddoughi [145], have also noted this difficulty, but present no solutions. A cursory comparison of the number of constraints on such a filter (all the derivatives which must commute) versus the number of variables which can be manipulated (the flow variables) indicates that such a filter might not be possible. If this is true, then one possible response is to assert that the current generation of spatial LES schemes are ill-posed from the beginning, and the equations should be re-derived to include commutation error terms. Another possibility is to assert that the LES equations are valid, but that there is no exact means to transfer data from a higher resolution grid to a coarser grid; some error is always introduced. This latter approach is currently the most common.

There are additional errors which occur when filtering is performed on a nonuniform grid. Other researchers have investigated these effects [68] [146]. They report that nonuniform filtering does not commute with derivatives; thus equation A.3 no longer holds. This arises because, in a nonuniform mesh, neighboring cells have different capabilities to resolve small scale motion. Thus a single derivative calculation might use cells which include scales not resolvable at the point of interest or cells that do not cover all the scales which are captured at the location of the derivative. Thus, one side may have information that "should be" in the subgrid, and the other side has information in the subgrid that "should be" resolved. It has been shown that this error is of second order [146]. This problem can, of course, be reduced by using meshes with minimal stretching in the regions of interest.

Despite these problems, LES appears to give physically meaningful answers. Therefore, as mentioned above, while these issues need to be investigated further, one need not reject the idea of spatial LES algorithms out of hand.

Appendix B

Formulation of the Problem using Favre Filtering

B.1 Derivation of the LES Equations

The method that is used in this work to numerically predict fluid motion is known as large eddy simulation (LES). As discussed in Chapters I and II, the idea behind LES is to capture all the scales of motion which the grid is capable of resolving and introducing models to account for the effects of the scales which are unresolved. The approach taken in the main body of this work was to use only "straight" filters to derive the LES equations. The more common approach for compressible flow is to use Favre filtering. This technique will now be described.

As discussed in Appendix A, the exact form of the filter function that yields the LES equations (in the discrete form in which they are actually solved numerically) is not generally known. It is assumed that such a filter exists. Given this, a corresponding Favre filter (in space) can be defined for any variable (designated here as ϕ) as:

$$\widetilde{\phi} = \frac{\overline{\rho\phi}}{\overline{\rho}} \tag{B.1}$$

Thus, for the purposes of LES, the Favre filter may be thought of as a density weighted filter in space.

By filtering equation 2.1, assuming that filtering commutes with the derivative operation, and using the above equation, the continuity equation for LES can be derived:

$$\frac{\partial \bar{\rho}}{\partial t} = -\frac{\partial \overline{\rho}\widetilde{u}_i}{\partial x_i} \tag{B.2}$$

Similarly, the momentum equation becomes:

$$\frac{\partial \overline{\rho}\widetilde{u}_i}{\partial t} = -\frac{\partial}{\partial x_j}\left(\bar{\rho}\widetilde{u}_i\widetilde{u}_j\right) - \frac{\partial \bar{p}}{\partial x_i} + \frac{\partial \widetilde{\tau}_{ij}}{\partial x_j} + \frac{\partial}{\partial x_j}\left(\overline{\tau}_{ij} - \widetilde{\tau}_{ij}\right) - \frac{\partial}{\partial x_j}\overline{\rho}\left(\widetilde{u_i u_j} - \widetilde{u}_i\widetilde{u}_j\right) \tag{B.3}$$

The resolved viscous stress tensor in the above equation takes the following form:

$$\widetilde{\tau}_{ij} = 2\widetilde{\mu}\left[\frac{1}{2}\left(\frac{\partial \widetilde{u}_i}{\partial x_j} + \frac{\partial \widetilde{u}_j}{\partial x_i}\right) - \frac{1}{3}\frac{\partial \widetilde{u}_k}{\partial x_k}\delta_{ij}\right] \tag{B.4}$$

The viscosity in the above expression is assumed to follow equation 2.4 (using the Favre filtered temperature, $\widetilde{T}$, as the argument). The other viscous term in equation B.3, $\overline{\tau}_{ij}$, is simply the filter of the exact viscous stress tensor (from equation 2.3). Next, the energy equation may be written as:

$$\begin{aligned}\frac{\partial \bar{\rho}\widetilde{E}}{\partial t} &= -\frac{\partial}{\partial x_i}\left(\bar{\rho}\widetilde{E}+\bar{p}\right)\widetilde{u}_i - \frac{\partial}{\partial x_i}\bar{\rho}\left(\widetilde{Eu_i}-\widetilde{E}\widetilde{u}_i\right) - \frac{\partial}{\partial x_i}\left(\overline{pu_i}-\bar{p}\widetilde{u}_i\right) \\ &+\frac{\partial}{\partial x_i}\left(\widetilde{u}_j\widetilde{\tau}_{ij}\right) + \frac{\partial}{\partial x_i}\left(\overline{u_j\tau_{ij}}-\widetilde{u}_j\widetilde{\tau}_{ij}\right) + \\ &\frac{\partial}{\partial x_i}\left(\widetilde{\kappa}\frac{\partial\widetilde{T}}{\partial x_i}\right) + \frac{\partial}{\partial x_i}\left(\overline{\kappa\frac{\partial T}{\partial x_i}}-\widetilde{\kappa}\frac{\partial\widetilde{T}}{\partial x_i}\right)\end{aligned} \tag{B.5}$$

The total energy is here defined as:

$$\widetilde{E} = \widetilde{e} + \frac{1}{2}\widetilde{u}_i\widetilde{u}_i + k^{sgs} \tag{B.6}$$

The subgrid kinetic energy, k^{sgs}, is defined as the effect of the subgrid scales on the kinetic energy of the resolved field:

$$k^{sgs} = \frac{1}{2}\left(\widetilde{u_iu_i}-\widetilde{u}_i\widetilde{u}_i\right) \tag{B.7}$$

The LES thermal conductivity ($\widetilde{\kappa}$) and internal energy ($\widetilde{e}$) are, like viscosity, assumed to be functions (see equations 2.6 and 2.8) of the Favre filtered temperature. Finally, the LES equation of state is written as:

$$\bar{p} = \bar{\rho}R\widetilde{T} \tag{B.8}$$

B.1.1 Identification of Subgrid Terms

As with the "straight" filtering approach, there are several terms which are not directly computable in the above set of equations. These terms must either be modeled or neglected in order to close the system of equations. Such terms will now be briefly identified, and the next section will discuss a suggested method of closure.

There are two subgrid terms in the LES momentum equation (B.3) which require closure. One ($\frac{\partial}{\partial x_j}\left(\overline{\tau}_{ij} - \widetilde{\tau}_{ij}\right)$) arises from the viscous terms due to the differences between Favre filtering and "straight" filtering. The other ($\frac{\partial}{\partial x_j}\overline{\rho}\left(\widetilde{u_i u_j} - \widetilde{u}_i\widetilde{u}_j\right)$) arises from the convection terms. Like the Reynolds stress term of the Reynolds-averaged Navier-Stokes equations, this term has been observed to behave much like a viscous stress. Thus, it is frequently written in terms of the so-called subgrid stress tensor, which is defined here as:

$$\tau_{ij}^{sgs} = \overline{\rho}\left(\widetilde{u_i u_j} - \widetilde{u}_i\widetilde{u}_j\right) \tag{B.9}$$

The LES energy equation contains four subgrid terms. The first of these ($\frac{\partial}{\partial x_i}\overline{\rho}\left(\widetilde{Eu_i} - \widetilde{E}\widetilde{u}_i\right)$) arises from the convection term. The second term is a pressure-velocity correlation term ($\frac{\partial}{\partial x_i}\left(\overline{pu_i} - \overline{p}\widetilde{u}_i\right)$) which is also related to convection. The third is a viscous subgrid term which is reminiscent of that in the LES momentum equation ($\frac{\partial}{\partial x_i}\left(\overline{u_j\tau_{ij}} - \widetilde{u}_j\widetilde{\tau}_{ij}\right)$). This represents the transfer of energy due to subgrid viscous forces. The fourth term ($\frac{\partial}{\partial x_i}\left(\overline{\kappa\frac{\partial T}{\partial x_i}} - \widetilde{\kappa}\frac{\partial\widetilde{T}}{\partial x_i}\right)$) is a heat flux subgrid term. In addition, the subgrid kinetic energy (k^{sgs}) used in the definition of total energy (equation B.6) is not directly available.

B.2 Closure of the Subgrid Terms

B.2.1 Closure of the LES Momentum Equation

For the Favre filtering approach, as applied in this work, the subgrid stress tensor, τ_{ij}^{sgs}, which was defined in equation B.9, is modelled as:

$$\tau_{ij}^{sgs} \approx -2\bar{\rho}\nu_t \left(\widetilde{S}_{ij} - \frac{1}{3}\widetilde{S}_{kk}\delta_{ij} \right) + \frac{2}{3}\bar{\rho}k^{sgs}\delta_{ij} \tag{B.10}$$

In the above equation, $\widetilde{S}_{ij}$ represents the resolved rate of strain tensor:

$$\widetilde{S}_{ij} = \frac{1}{2}\left(\frac{\partial \widetilde{u}_i}{\partial x_j} + \frac{\partial \widetilde{u}_j}{\partial x_i} \right) \tag{B.11}$$

The subgrid kinetic energy is used to compute a turbulent velocity scale. This is used to compute the turbulent viscosity, ν_t, which is approximated as:

$$\nu_t \approx c_\nu \sqrt{k^{sgs}}\Delta \tag{B.12}$$

In the above equation, c_ν is the model coefficient, and Δ is a characteristic length that represents the resolution available on the numerical grid. Δ is usually taken to be the local grid spacing. The subgrid kinetic energy, k^{sgs}, is obtained by solving an equation for its transport in parallel with the LES continuity (B.2), momentum (B.3), and total energy (B.5) equations. Since the viscous terms are generally small

compared to the convection terms, the viscous subgrid term in the LES momentum equation (B.3) is neglected. Thus, the modelled momentum equation may be written as:

$$\frac{\partial \bar{\rho}\widetilde{u}_i}{\partial t} = -\frac{\partial}{\partial x_j}\left(\bar{\rho}\widetilde{u}_i\widetilde{u}_j\right) - \frac{\partial \bar{p}}{\partial x_i} + \frac{\partial \widetilde{\tau}_{ij}}{\partial x_j} - \frac{\partial \tau_{ij}^{sgs}}{\partial x_j} \tag{B.13}$$

B.2.2 The k-Equation Model

The exact subgrid kinetic energy equation may be written as:

$$\begin{aligned}\frac{\partial \bar{\rho}k^{sgs}}{\partial t} &= -\frac{\partial}{\partial x_i}\left(\bar{\rho}k_i^{sgs}\widetilde{u}_i\right) - \left(\overline{u_i\frac{\partial p}{\partial x_i}} - \widetilde{u}_i\frac{\partial \bar{p}}{\partial x_i}\right) + \left(\overline{u_i\frac{\partial \tau_{ij}}{\partial x_j}} - \widetilde{u}_i\frac{\partial \bar{\tau}_{ij}}{\partial x_j}\right) \\ &\quad -\frac{\partial}{\partial x_i}\left(\overline{\rho k u_i} - \bar{\rho}\tilde{k}\widetilde{u}_i\right) - \frac{\partial \widetilde{u}_j\tau_{ij}^{sgs}}{\partial x_i} + \tau_{ij}^{sgs}\frac{\partial \widetilde{u}_j}{\partial x_i}\end{aligned} \tag{B.14}$$

This equation contains numerous subgrid terms. Therefore a simplified model equation is used to predict the evolution of subgrid kinetic energy. This model equation is a compressible extension of the incompressible subgrid k-equation model developed by Kim [67]. It is formed by a combination of four terms which represent different physical phenomena: resolved convective transport, subgrid transport, production, and dissipation.

The convection by the resolved field is computed as:

$$\text{Resolved Convection} = -\frac{\partial}{\partial x_i}\left(\bar{\rho}k_i^{sgs}\widetilde{u}_i\right) \tag{B.15}$$

The transport of subgrid kinetic energy by subgrid scales is modelled as:

$$\text{Subgrid Transport} \approx \frac{\partial}{\partial x_i}\left(\overline{\rho}\nu_t \frac{\partial k^{sgs}}{\partial x_i}\right) \tag{B.16}$$

The production of subgrid kinetic energy is:

$$\text{Production} = -\tau_{ij}^{sgs}\frac{\partial \widetilde{u}_j}{\partial x_i} \tag{B.17}$$

This is computed using the modelled subgrid stress tensor (equation B.10) to compute τ_{ij}^{sgs}. Finally, the dissipation is modelled, using simple scaling arguments, as:

$$\text{Dissipation} \approx -\overline{\rho}c_\epsilon \frac{(k^{sgs})^{\frac{3}{2}}}{\Delta} \tag{B.18}$$

Combining these terms, the modelled subgrid kinetic energy equation may now be written as:

$$\frac{\partial \overline{\rho}k^{sgs}}{\partial t} = -\frac{\partial}{\partial x_i}\left(\bar{\rho}k_i^{sgs}\widetilde{u}_i\right) + \frac{\partial}{\partial x_i}\left(\overline{\rho}\nu_t\frac{\partial k^{sgs}}{\partial x_i}\right) - \tau_{ij}^{sgs}\frac{\partial \widetilde{u}_j}{\partial x_i} - \overline{\rho}c_\epsilon\frac{(k^{sgs})^{\frac{3}{2}}}{\Delta} \tag{B.19}$$

where, as before, the turbulent viscosity is given by equation B.12.

B.2.3 Dynamic Calculation of Model Coefficients

The modelled subgrid kinetic energy equation, as derived above, contains two model coefficients (c_ν and c_ε). Rather than specifying these coefficients, they will be computed dynamically as discussed in the following sections. As before, a "test" filter is defined and similarity is assumed between the smallest resolved scales, which are accessed using the "test" filter, and the subgrid scales. As before, the "test" filter (denoted by a circumflex- *e.g.*, $\widehat{\phi}$) must have a characteristic length, $\widehat{\Delta}$, larger than the grid resolution. Usually $\widehat{\Delta}$ is take to be twice the size of the local grid spacing (Δ), but this is somewhat arbitrary. Coefficients may then be computed by comparing quantities that are resolved in the LES flow field but not by a corresponding "test" filtered field.

The Dissipation Model Coefficient In order to compute the dissipation model coefficient, it is necessary to obtain an expression for the subgrid kinetic energy dissipation rate. In the incompressible subgrid kinetic energy equation, the viscous term is easily split into transport and dissipation components:

$$\overline{u_i \frac{\partial \tau_{ij}}{\partial x_j}} - \bar{u}_i \frac{\partial \bar{\tau}_{ij}}{\partial x_j} = \nu \frac{\partial}{\partial x_j}\left(\frac{\partial k^{sgs}}{\partial x_j}\right) - \nu\left(\overline{\frac{\partial u_i}{\partial x_j}\frac{\partial u_i}{\partial x_j}} - \frac{\partial \bar{u}_i}{\partial x_j}\frac{\partial \bar{u}_i}{\partial x_j}\right) \tag{B.20}$$

The first term on the right hand side is the incompressible subgrid viscous transport, and the second term is the subgrid kinetic energy dissipation rate. Unfortunately, the situation is not so straightforward for the compressible equations. The viscous

subgrid terms from equation B.14 may be rewritten as:

$$\overline{u_j \frac{\partial \tau_{ij}}{\partial x_i}} - \tilde{u}_j \frac{\partial \overline{\tau}_{ij}}{\partial x_i} = \overline{u_j \frac{\partial}{\partial x_i}\left(\mu\left[\frac{\partial u_i}{\partial x_j} + \frac{\partial u_j}{\partial x_i}\right] - \frac{2}{3}\mu\frac{\partial u_k}{\partial x_k}\delta_{ij}\right)} - \overline{\tilde{u}_j \frac{\partial}{\partial x_i}\left(\mu\left[\frac{\partial u_i}{\partial x_j} + \frac{\partial u_j}{\partial x_i}\right] - \frac{2}{3}\mu\frac{\partial u_k}{\partial x_k}\delta_{ij}\right)} \quad \text{(B.21)}$$

In the incompressible form of the subgrid kinetic energy equation, the viscosity is a constant, and can be taken outside both derivative and filtering operations. In the compressible case, the viscosity is not constant. Not only that, but two different types of filtering are involved (Favre and "straight"). For the purposes of modelling, however, the two filtering methods are assumed to be equivalent, and the viscosity is assumed to be locally invariant. These are reasonable assumptions except in the presence of extreme density and temperature gradients (respectively). Note that this is assumed only for the purposes of computing the dissipation model coefficient; the resolved viscous stress terms are computed normally (i.e. viscosity varies with temperature). In any case, the viscous terms are usually (but not always) small relative to the convection terms and the subgrid viscous terms smaller still. Given the above conditions, the viscous term may be written as follows:

$$\overline{u_j \frac{\partial \tau_{ij}}{\partial x_i}} - \tilde{u}_j \frac{\partial \overline{\tau}_{ij}}{\partial x_i} \approx$$

$$-\widetilde{\mu}\left(\overline{\frac{\partial u_j}{\partial x_i}\frac{\partial u_j}{\partial x_i}} - \frac{\partial \widetilde{u}_j}{\partial x_i}\frac{\partial \widetilde{u}_j}{\partial x_i}\right)$$

$$-\widetilde{\mu}\left[\left(\overline{\frac{\partial u_j}{\partial x_i}\frac{\partial u_i}{\partial x_j}} - \frac{\partial \widetilde{u}_j}{\partial x_i}\frac{\partial \widetilde{u}_i}{\partial x_j}\right) - \frac{2}{3}\left(\overline{\frac{\partial u_j}{\partial x_j}\frac{\partial u_i}{\partial x_i}} - \frac{\partial \widetilde{u}_j}{\partial x_j}\frac{\partial \widetilde{u}_i}{\partial x_i}\right)\right]$$

$$+\widetilde{\mu}\frac{\partial^2}{\partial x_i \partial x_i}\left(\frac{\overline{u_j u_j}}{2} - \frac{\widetilde{u}_j \widetilde{u}_j}{2}\right)$$

$$+\widetilde{\mu}\left[\frac{\partial}{\partial x_i}\left(\overline{u_j \frac{\partial u_i}{\partial x_j}} - \widetilde{u}_j \frac{\partial \widetilde{u}_i}{\partial x_j}\right) - \frac{2}{3}\frac{\partial}{\partial x_i}\left(\overline{u_i \frac{\partial u_j}{\partial x_j}} - \widetilde{u}_i \frac{\partial \widetilde{u}_j}{\partial x_j}\right)\right] \tag{B.22}$$

Two of the terms in the above equation are recognizable analogs of incompressible terms (in equation B.20): the first term on the right hand side is a dissipation term and the third term is a viscous transport term. The second and fourth right hand terms in equation B.22 have no direct analog in the incompressible equation. It can be shown, however, that term two is dissipative while the fourth term is an additional dispersion term. As a starting point for the purposes of determining the dissipation model coefficient, only the first term will be used. Thus, the subgrid kinetic energy dissipation rate is taken to be:

$$\varepsilon \approx \widetilde{\mu}\left(\overline{\frac{\partial u_j}{\partial x_i}\frac{\partial u_j}{\partial x_i}} - \frac{\partial \widetilde{u}_j}{\partial x_i}\frac{\partial \widetilde{u}_j}{\partial x_i}\right) \approx \overline{\rho} c_\varepsilon \frac{(k^{sgs})^{\frac{3}{2}}}{\Delta} \tag{B.23}$$

By use of the "test" filter on the resolved field and assuming similarity as discussed above, one can construct a "test-field" dissipation as follows:

$$e = \widehat{\mu}\left[\widehat{\frac{\partial\tilde{u}_j}{\partial x_i}\frac{\partial\tilde{u}_j}{\partial x_i}} - \frac{\partial}{\partial x_i}\left(\frac{\widehat{\bar{\rho}\tilde{u}_j}}{\widehat{\bar{\rho}}}\right)\frac{\partial}{\partial x_i}\left(\frac{\widehat{\bar{\rho}\tilde{u}_j}}{\widehat{\bar{\rho}}}\right)\right] \approx \frac{c_\epsilon\widehat{\bar{\rho}}}{\widehat{\Delta}}\left(\frac{\widehat{\bar{\rho}\tilde{u}_k\tilde{u}_k}}{2\widehat{\bar{\rho}}} - \frac{\widehat{\bar{\rho}\tilde{u}_k}}{2\widehat{\bar{\rho}}}\frac{\widehat{\bar{\rho}\tilde{u}_k}}{\widehat{\bar{\rho}}}\right)^{\frac{3}{2}} \tag{B.24}$$

Note that all of the terms, except the model coefficient, in the above equation can be determined from the resolved field. Therefore, equation B.24 can be solved for the model coefficient:

$$c_\epsilon = \frac{\widehat{\mu}\widehat{\Delta}\left[\widehat{\frac{\partial\tilde{u}_j}{\partial x_i}\frac{\partial\tilde{u}_j}{\partial x_i}} - \frac{\partial}{\partial x_i}\left(\frac{\widehat{\bar{\rho}\tilde{u}_j}}{\widehat{\bar{\rho}}}\right)\frac{\partial}{\partial x_i}\left(\frac{\widehat{\bar{\rho}\tilde{u}_j}}{\widehat{\bar{\rho}}}\right)\right]}{\widehat{\bar{\rho}}\left(\frac{\widehat{\bar{\rho}\tilde{u}_k\tilde{u}_k}}{2\widehat{\bar{\rho}}} - \frac{\widehat{\bar{\rho}\tilde{u}_k}}{2\widehat{\bar{\rho}}}\frac{\widehat{\bar{\rho}\tilde{u}_k}}{\widehat{\bar{\rho}}}\right)^{\frac{3}{2}}} \tag{B.25}$$

If desired, the additional dissipation terms from equation B.22 are easily accounted for by adding their "test" level analogs to the numerator of the above equation.

The Subgrid Stress Tensor Model Coefficient The process for determining the coefficient (c_ν) in the subgrid stress tensor model is similar to that shown above. First, equations B.9 and B.10 are combined as follows:

$$\tau_{ij}^{sgs} = \bar{\rho}\left(\widetilde{u_iu_j} - \tilde{u}_i\tilde{u}_j\right) \approx -2\bar{\rho}\nu_t\left(\widetilde{S}_{ij} - \frac{1}{3}\widetilde{S}_{kk}\delta_{ij}\right) + \frac{2}{3}\bar{\rho}k^{sgs}\delta_{ij} \tag{B.26}$$

Next, using the "test" filter and assuming similarity as in section B.2.3, the "test-field" subgrid stress tensor may be written as:

$$t_{ij}^{sgs} = \widehat{\bar{\rho}\tilde{u}_i\tilde{u}_j} - \frac{\widehat{\bar{\rho}\tilde{u}_i}\widehat{\bar{\rho}\tilde{u}_j}}{\widehat{\bar{\rho}}} \approx -2c_\nu\widehat{\Delta}\widehat{\bar{\rho}}\left(\frac{\widehat{\bar{\rho}\tilde{u}_i\tilde{u}_l}}{2\widehat{\bar{\rho}}} - \frac{\widehat{\bar{\rho}\tilde{u}_l}}{2\widehat{\bar{\rho}}}\frac{\widehat{\bar{\rho}\tilde{u}_l}}{\widehat{\bar{\rho}}}\right)^{\frac{1}{2}}\left(\widehat{\bar{\tilde{S}}}_{ij} - \frac{\widehat{\bar{\tilde{S}}}_{kk}}{3}\delta_{ij}\right) + \frac{1}{3}\left(\widehat{\bar{\rho}\tilde{u}_k\tilde{u}_k} - \frac{\widehat{\bar{\rho}\tilde{u}_k}\widehat{\bar{\rho}\tilde{u}_k}}{\widehat{\bar{\rho}}}\right)\delta_{ij} \tag{B.27}$$

The "test" field resolved rate of strain tensor in equation B.27 is defined as:

$$\widehat{\bar{\tilde{S}}}_{ij} = \frac{1}{2}\left[\frac{\partial}{\partial x_j}\left(\frac{\widehat{\bar{\rho}\tilde{u}_i}}{\widehat{\bar{\rho}}}\right) + \frac{\partial}{\partial x_i}\left(\frac{\widehat{\bar{\rho}\tilde{u}_j}}{\widehat{\bar{\rho}}}\right)\right] \tag{B.28}$$

Equation B.27 is actually overspecified since there are six independent tensor components, but only one unknown (c_ν). Thus, it must be contracted in some fashion. The current work follows the approach of Lilly [87], who used a least squares approach to obtain an expression for the dynamic coefficient of a Germano [42] algebraic model. The first step is to write an expression for the model error:

$$\mathrm{E}_{ij} = \widehat{\bar{\rho}\tilde{u}_i\tilde{u}_j} - \frac{\widehat{\bar{\rho}\tilde{u}_i}\widehat{\bar{\rho}\tilde{u}_j}}{\widehat{\bar{\rho}}} - \frac{1}{3}\left(\widehat{\bar{\rho}\tilde{u}_k\tilde{u}_k} - \frac{\widehat{\bar{\rho}\tilde{u}_k}\widehat{\bar{\rho}\tilde{u}_k}}{\widehat{\bar{\rho}}}\right)\delta_{ij} + 2c_\nu\widehat{\Delta}\widehat{\bar{\rho}}\left(\frac{\widehat{\bar{\rho}\tilde{u}_i\tilde{u}_l}}{2\widehat{\bar{\rho}}} - \frac{\widehat{\bar{\rho}\tilde{u}_l}}{2\widehat{\bar{\rho}}}\frac{\widehat{\bar{\rho}\tilde{u}_l}}{\widehat{\bar{\rho}}}\right)^{\frac{1}{2}}\left(\widehat{\bar{\tilde{S}}}_{ij} - \frac{\widehat{\bar{\tilde{S}}}_{kk}}{3}\delta_{ij}\right) \tag{B.29}$$

This can be written in simplified form as:

$$\mathrm{E}_{ij} = L_{ij} + 2c_\nu D_{ij} \tag{B.30}$$

$$\text{where } L_{ij} = \widehat{\overline{\rho}\widetilde{u}_i\widetilde{u}_j} - \frac{\widehat{\overline{\rho}\widetilde{u}_i}\widehat{\overline{\rho}\widetilde{u}_j}}{\widehat{\overline{\rho}}} - \frac{1}{3}\left(\widehat{\overline{\rho}\widetilde{u}_k\widetilde{u}_k} - \frac{\widehat{\overline{\rho}\widetilde{u}_k}\widehat{\overline{\rho}\widetilde{u}_k}}{\widehat{\overline{\rho}}}\right)\delta_{ij} \tag{B.31}$$

$$\text{and } D_{ij} = \widehat{\Delta}\widehat{\overline{\rho}}\left(\frac{\widehat{\overline{\rho}\widetilde{u}_l\widetilde{u}_l}}{2\widehat{\overline{\rho}}} - \frac{\widehat{\overline{\rho}\widetilde{u}_l}}{2\widehat{\overline{\rho}}}\frac{\widehat{\overline{\rho}\widetilde{u}_l}}{\widehat{\overline{\rho}}}\right)^{\frac{1}{2}}\left(\widehat{\widetilde{S}}_{ij} - \frac{\widehat{\widetilde{S}}_{kk}}{3}\delta_{ij}\right) \tag{B.32}$$

Next, the error is contracted with itself to form:

$$\mathrm{E}_{ij}\mathrm{E}_{ij} = L_{ij}L_{ij} + 4c_\nu D_{ij}L_{ij} + 4c_\nu^2 D_{ij}D_{ij} \tag{B.33}$$

In order for the RMS of the error to be a minimum, the derivative of equation B.33 with respect to the model coefficient must be zero:

$$\frac{\partial \mathrm{E}_{ij}\mathrm{E}_{ij}}{\partial c_\nu} = 0 = 4D_{ij}L_{ij} + 8c_\nu D_{ij}D_{ij} \tag{B.34}$$

Using the above expression, the model coefficient can now be computed:

$$c_\nu = \frac{-L_{ij}D_{ij}}{2D_{ij}D_{ij}} \tag{B.35}$$

Because the filters considered here are positive, the resulting subgrid stress tensor must be positive semidefinite. Therefore, using the realizability conditions (similar to equation 3.44), c_ν is constrained such that the resulting modelled subgrid stress tensor, τ_{ij}^{sgs} behaves in this fashion. In addition, the subgrid stress tensor model coefficient is constrained so that the effective viscosity is positive.

B.2.4 Derivation of the LES Energy Equation Model

The LES energy equation (B.5) has several terms that require closure. Using the definition of total enthalpy,

$$H = E + \frac{p}{\rho} \tag{B.36}$$

two of these subgrid terms can be combined to form:

$$-\frac{\partial}{\partial x_i}\left(\overline{\rho E u_i} - \bar{\rho}\widetilde{E}\widetilde{u}_i\right) - \frac{\partial}{\partial x_i}\left(\overline{p u_i} - \bar{p}\widetilde{u}_i\right) = -\frac{\partial}{\partial x_i}\left(\overline{\rho H u_i} - \bar{\rho}\widetilde{H}\widetilde{u}_i\right) \tag{B.37}$$

This term is then modelled with an eddy diffusion model as:

$$\frac{\partial}{\partial x_i}\left(\overline{\rho H u_i} - \bar{\rho}\widetilde{H}\widetilde{u}_i\right) \approx \frac{\partial}{\partial x_i}\left(-c_e \bar{\rho}\sqrt{k^{sgs}}\Delta\frac{\partial \widetilde{H}}{\partial x_i}\right) \tag{B.38}$$

In this model, the coefficient, c_e, combines the subgrid stress tensor model coefficient and the turbulent Prandtl number that were present in the other models

mentioned above. This greatly reduces the numerical instability of the model when c_e is computed dynamically.

The next term to be dealt with is the thermal conduction subgrid term $(\frac{\partial}{\partial x_i}\left(\overline{\kappa\frac{\partial T}{\partial x_i}} - \tilde{\kappa}\frac{\partial \tilde{T}}{\partial x_i}\right))$. Similar to the assumptions made in section B.2.3, the thermal conductivity is assumed to be locally constant, and Favre filtering is taken to be equivalent to "straight" filtering. Under these conditions, the conduction subgrid term vanishes. Therefore, it is neglected.

The final subgrid term in the energy equation is the viscous transport term. It is modelled as follows:

$$\frac{\partial}{\partial x_i}\left(\overline{u_j\tau_{ij}} - \widetilde{u}_j\widetilde{\tau}_{ij}\right) \approx \frac{\partial}{\partial x_i}\left(\widetilde{\mu}\frac{\partial k^{sgs}}{\partial x_i}\right) \tag{B.39}$$

This latter term is usually small compared to the others, so that it may be neglected without introducing significant error.

Thus the modelled LES energy equation may now be written as:

$$\begin{aligned}\frac{\partial \bar{\rho}\widetilde{E}}{\partial t} &= -\frac{\partial}{\partial x_i}\left(\bar{\rho}\widetilde{E} + \bar{p}\right)\widetilde{u}_i + \frac{\partial}{\partial x_i}\left(c_e\bar{\rho}\sqrt{k^{sgs}}\Delta\frac{\partial \widetilde{H}}{\partial x_i}\right) + \frac{\partial}{\partial x_i}\left(\widetilde{u}_j\widetilde{\tau}_{ij}\right) \\ &\quad + \frac{\partial}{\partial x_i}\left(\widetilde{\mu}\frac{\partial k^{sgs}}{\partial x_i}\right) + \frac{\partial}{\partial x_i}\left(\widetilde{\kappa}\frac{\partial \widetilde{T}}{\partial x_i}\right)\end{aligned} \tag{B.40}$$

B.2.5 Dynamic Computation of the Energy Equation Subgrid Model Coefficient

The method for dynamically computing c_e is similar to that described in section B.2.3. First, the exact term and its model are written:

$$\widetilde{\overline{\rho}Hu_i} - \overline{\rho}\widetilde{H}\widetilde{u}_i \approx -c_e\overline{\rho}\sqrt{k^{sgs}}\Delta\frac{\partial\widetilde{H}}{\partial x_i} \tag{B.41}$$

Next, assuming similarity between the subgrid and the highest resolved wavenumbers, the following expression may be written:

$$\widehat{\overline{\rho}\widetilde{H}\widetilde{u}_i} - \frac{\widehat{\overline{\rho}\widetilde{H}}\,\widehat{\overline{\rho}\widetilde{u}_i}}{\widehat{\overline{\rho}}} \approx -c_e\widehat{\overline{\rho}}\left(\frac{\widehat{\overline{\rho}\widetilde{u}_l\widetilde{u}_l}}{2\widehat{\overline{\rho}}} - \frac{\widehat{\overline{\rho}\widetilde{u}_l}}{2\widehat{\overline{\rho}}}\frac{\widehat{\overline{\rho}\widetilde{u}_l}}{\widehat{\overline{\rho}}}\right)^{\frac{1}{2}}\widehat{\Delta}\frac{\partial}{\partial x_i}\left(\frac{\widehat{\overline{\rho}\widetilde{H}}}{\widehat{\overline{\rho}}}\right) \tag{B.42}$$

As with the derivation of the dynamic subgrid stress tensor model coefficient (equation B.27), the above equation is overspecified. Thus, as before, a least squares method is used to contract it so that a single equation for the model coefficient, c_e, may be obtained. First, the error in equation B.42 is written as:

$$E_i = n_i + c_e d_i \tag{B.43}$$

$$\text{where } n_i = \widehat{\overline{\rho}\widetilde{H}\widetilde{u}_i} - \frac{\widehat{\overline{\rho}\widetilde{H}}\,\widehat{\overline{\rho}\widetilde{u}_i}}{\widehat{\overline{\rho}}} \tag{B.44}$$

$$d_i = \widehat{\overline{\rho}}\left(\frac{\widehat{\overline{\rho}\widetilde{u}_l\widetilde{u}_l}}{2\widehat{\overline{\rho}}} - \frac{\widehat{\overline{\rho}\widetilde{u}_l}}{2\widehat{\overline{\rho}}}\frac{\widehat{\overline{\rho}\widetilde{u}_l}}{\widehat{\overline{\rho}}}\right)^{\frac{1}{2}}\widehat{\Delta}\frac{\partial}{\partial x_i}\left(\frac{\widehat{\overline{\rho}\widetilde{H}}}{\widehat{\overline{\rho}}}\right) \tag{B.45}$$

Next, the error, E_i, is contracted with itself to yield:

$$E_i E_i = n_i n_i + 2c_e n_i d_i + c_e^2 d_i d_i \tag{B.46}$$

As before, to minimize the error, the derivative of this equation with respect to the model coefficient must be zero:

$$\frac{\partial E_i E_i}{\partial c_e} = 0 = 2n_i d_i + 2c_e d_i d_i \tag{B.47}$$

Solving this equation for c_e yields:

$$c_e = \frac{n_i d_i}{d_i d_i} \tag{B.48}$$

B.2.6 Additional Subgrid Terms

Because the modelled equation must be solved in discrete form, additional subgrid effects must be taken into account. These effects are not necessarily turbulent in nature; they arise because the physics (specifically, the convection terms) of the flow, which could involve turbulent or laminar phenomena, can be such that the actual solution passes beyond the capability of the numerical scheme to resolve on the available grid. One example of such a situation is a shock in high Reynolds number flow. With most higher order numerical schemes (*sans* limiters *etc.*), the physics of a shock will try to force the scheme to accept curvature which it is not

capable of resolving. To compensate, the scheme introduces spurious oscillations in the vicinity of the perceived discontinuity. It must be noted that such oscillations are in no way a "mistake" on the scheme's part; they are the correct solution of the discrete equations for that particular grid. This solution is, however, unphysical. Shocks are not the only instances where such problems may occur; vortices, pressure waves, and even boundary layers can induce oscillations if grid resolution is inadequate. This situation is very similar to attempting to simulate high Reynolds number turbulence without a subgrid model; in that case, the turbulent energy cascade is interrupted at the limit of grid resolution and energy builds up in the highest resolvable wavenumbers, leading to oscillations.

Numerous approaches have been taken in the past to deal with this problem, but in general, most fall into three classes: artificial viscosity, flux limiters, and essentially non-oscillatory (ENO) algorithms. The artificial viscosity approach adds additional *ad hoc* dissipation terms, which are applied in the computational domain rather than the physical domain (in order to have a maximum damping effect on odd-even oscillations). The limiter approach takes a "high-resolution" scheme, such as a Roe [147] scheme, uses higher order extrapolation for the fluxes, but then adds a flux limiter which progressively reduces the scheme to first order in the vicinity of a discontinuity. The ENO approach uses a numerical "sensor" to detect the presence of large curvature and then selects an appropriately forward or backward biased flux interpolation/extrapolation algorithm of the same order as the core scheme in order to avoid the "dangerous" area.

Each of these approaches has advantages and disadvantages, but all of them require some sort of "tuning." In the case of limiters, this tuning is inherent in the choice of the limiter algorithm. The artificial dissipation methods require choosing

dissipation coefficients and/or an algorithm for computing said coefficients. The ENO schemes require a switching algorithm to tell them when to use the different available stencils. Most, if not all, of the schemes which utilize the above approaches have been designed for steady-state flows, or, if they allow for time dependance, it is in a Reynolds averaged Navier-Stokes sense. In other words, unsteady turbulent phenomena, particularly at small scales (relative to the grid) are generally not considered in the design of these schemes. Consequently, small wavelength oscillations are regarded very negatively, and most schemes attempt to eliminate them entirely. As a result, such algorithms are overly dissipative (in an LES sense) by design. This is not to imply that they are therefore "wrong" or "useless," but it does limit their applicability to LES. This is because LES is based on the idea that all turbulent scales of motion which are larger than the grid size are to be resolved. Thus, in an LES, some of the odd-even oscillations which occur are likely to be due to genuine physics. As a result, most existing algorithms will have numerical dissipation (either implicit to the scheme or explicitly added) which overwhelms the turbulent phenomena, especially at the smallest resolvable scales. This does not mean that LES is impossible to perform with such schemes. As many researchers have demonstrated, good results can be obtained with almost any scheme if the grid is fine enough. Unfortunately, as the Reynolds number increases, these requirements eventually become so severe as to make LES impractical with the current generation of computers. Also, it is not always readily apparent from the solution whether or not the grid is "fine enough," which makes it difficult to use LES for predictive purposes.

Despite these problems, if LES is to be performed, something must be done in order to alleviate the numerical instability due to unresolvable curvature in the flow field. The approach taken here is to treat this as a subgrid phenomenon;

therefore, the appropriate method of dealing with it is a subgrid model. Eddy diffusion turbulence models already do much the same thing with turbulent eddies at the resolution limit, as was noted above. The difference is that the original subgrid terms arose directly from the filtering of the Navier-Stokes equations, whereas these unresolvable curvature terms spring from the interaction between the numerical scheme, the computational grid, and the physics of the flow. Put another way, the unresolvable curvature terms may be thought of as springing from "large" scale structure that is not adequately resolved on the given grid.

The original subgrid terms could be easily expressed in a precise mathematical form (though not one with an analytic solution), but the unresolvable curvature correction terms are not quite so readily identifiable. They would appear to be closely related to the truncation error of the convection terms as implemented by the numerical scheme. Unfortunately, with multistage time marching algorithms, such as the predictor-corrector scheme used here (see Chapter IV), the error becomes highly nonlinear and extremely complicated to analyze. Still, some characteristics of these correction terms can be deduced. It is known that the corrective terms are generally dissipative in nature. This can be seen by noting that the standard means of coping with spurious oscillations are all (effectively) dissipative (*e.g.*, artificial viscosity). Also, the magnitude of these terms is related to the cell Reynolds number. This is seen in that, as the Reynolds number decreases, the natural viscosity is increasingly able to prevent the convective forces from creating excessive curvature in the solution field, thus negating any need for additional terms. Since pressure is generally observed to be the variable that is most sensitive to instability in the solution, it seems reasonable to use it as a trigger to scale the curvature correction terms. Jameson and Baker [148] introduced this idea for their artificial dissipation

algorithm. In addition, since the oscillations arise due to the convection terms, the model should vanish when convection vanishes. Further, a model to account for unresolvable curvature must therefore appear in every equation with convection terms.

A set of models has been developed which meets all of the above criteria. Similar to the "turbulent" viscosity, ν_t, an "unresolvable curvature" viscosity is defined (at a cell face) as:

$$\nu_{uc} = a_{uc} S_p \left|\widetilde{u}_k n_k\right| \Delta \tag{B.49}$$

$$\text{where } a_{uc} = \begin{cases} a_0 \exp\left[\frac{-1}{K_1\left(R_{e_\Delta} - R_{e_{\min}}\right)}\right] & R_{e_\Delta} > R_{e_{\min}} \\ 0 & R_{e_\Delta} \leq R_{e_{\min}} \end{cases} \tag{B.50}$$

$$R_{e_\Delta} = \frac{\left|\widetilde{u}_k n_k\right| \Delta}{\nu + \nu_t} \tag{B.51}$$

In the above equations, n_k represents the unit normal vector of the cell face for which ν_{uc} is being calculated. The pressure switch, S_p, in equation B.49 is defined in a discrete sense in a manner similar to that used by MacCormack and Baldwin [86]. On the i-faces, for example, it may be written:

$$S_{p_{i+\frac{1}{2},j,k}} = \max\left(S_{p_{i,j,k}}, S_{p_{i+1,j,k}}\right) \tag{B.52a}$$

$$\text{where } S_{p_{i,j,k}} = \frac{\left|\bar{p}_{i+1,j,k} - 2\bar{p}_{i,j,k} + \bar{p}_{i-1,j,k}\right|}{\bar{p}_{i+1,j,k} + 2\bar{p}_{i,j,k} + \bar{p}_{i-1,j,k}} \tag{B.52b}$$

The form for equation B.50 (including values for K_1, and $R_{e_{\min}}$) has been determined from numerical experiments on the one-dimensional non-linear Burger's equation. The value used for K_1 is 0.245, and the minimum cell Reynolds number is 1.62. The scaling coefficient, a_0, was determined by a trial-and-error method using decaying isotropic turbulence. A value of 0.35 has been used for this work.

The above unresolvable curvature viscosity is incorporated into the modelled LES equations in the following manner. The LES continuity equation is rewritten with an additional term, as follows:

$$\frac{\partial \bar{\rho}}{\partial t} = -\frac{\partial \bar{\rho}\widetilde{u}_i}{\partial x_i} + \frac{\partial}{\partial x_i}\left(\nu_{uc}\frac{\partial \bar{\rho}}{\partial x_i}\right) \tag{B.53}$$

The LES momentum equation is written in much the same form as before (B.13):

$$\frac{\partial \bar{\rho}\widetilde{u}_i}{\partial t} = -\frac{\partial}{\partial x_j}\left(\bar{\rho}\widetilde{u}_i\widetilde{u}_j\right) - \frac{\partial \bar{p}}{\partial x_i} + \frac{\partial \widetilde{\tau}_{ij}}{\partial x_j} - \frac{\partial \tau'_{ij}}{\partial x_j} \tag{B.54}$$

$$\text{where } \tau'_{ij} = -2\bar{\rho}\left(\nu_t + \nu_{uc}\right)\left(\widetilde{S}_{ij} - \frac{1}{3}\widetilde{S}_{kk}\delta_{ij}\right) + \frac{2}{3}\bar{\rho}k^{sgs}\delta_{ij} \tag{B.55}$$

A model term is added to the LES energy equation:

$$\begin{aligned}\frac{\partial \bar{\rho}\widetilde{E}}{\partial t} = & -\frac{\partial}{\partial x_i}\left(\bar{\rho}\widetilde{E} + \bar{p}\right)\widetilde{u}_i + \frac{\partial}{\partial x_i}\left(c_e\bar{\rho}\sqrt{k^{sgs}}\Delta\frac{\partial \widetilde{H}}{\partial x_i}\right) + \frac{\partial}{\partial x_i}\left(\widetilde{u}_j\widetilde{\tau}_{ij}\right) \\ & + \frac{\partial}{\partial x_i}\left(\widetilde{\mu}\frac{\partial k^{sgs}}{\partial x_i}\right) + \frac{\partial}{\partial x_i}\left[\left(\widetilde{\kappa} + \frac{\overline{p}\gamma c_v \nu_{uc}}{\Pr}\right)\frac{\partial \widetilde{T}}{\partial x_i}\right]\end{aligned} \tag{B.56}$$

Finally, an unresolved curvature term is added to the modelled subgrid kinetic energy equation:

$$\frac{\partial \overline{\rho} k^{sgs}}{\partial t} = -\frac{\partial}{\partial x_i}\left(\bar{\rho} k_i^{sgs} \widetilde{u}_i\right) + \frac{\partial}{\partial x_i}\left(\overline{\rho}\left(\nu_t + \nu_{uc}\right)\frac{\partial k^{sgs}}{\partial x_i}\right) + \tau_{ij}^{sgs}\frac{\partial \widetilde{u}_j}{\partial x_i} - \overline{\rho} c_\varepsilon \frac{\left(k^{sgs}\right)^{\frac{3}{2}}}{\Delta} \quad \text{(B.57)}$$

Because pressure is being used as a trigger for these additional model terms, it is possible that the new terms may capture, at least in part, the effects of the previously neglected pressure-related subgrid terms. The unresolved curvature terms, however, are designed to be strictly transport terms. Therefore, any additional subgrid kinetic energy dissipation will not be directly captured by them.

APPENDIX C

INFLOW TURBULENCE

When simulating spatial flows, especially those which attempt to duplicate experimental results, one must confront the fact that most "real-life" fluid flows are more or less turbulent throughout the entire domain. Thus, a "complete" simulation must account for the turbulence which is entering the domain at the inflow boundary. Whether or not this is done can make a significant difference in the results of the computation. For instance, Soteriou and Ghoniem [149] show the development of an incompressible spatial mixing layer with and without perturbation at the inflow boundary. Compared to the perturbed case, the development of the mixing layer without perturbation is delayed significantly while the Kelvin-Helmholtz instability, activated by minute numerical errors, builds until the layer finally rolls up.

Researchers have taken several approaches to this problem. Sometimes, as in Soteriou and Ghoniem's unperturbed case, nothing is done to emulate turbulence at the inflow. For those who wish to account for inflow turbulence, perhaps the simplest approach is to add random "white noise" to the mean flow profiles at the inflow boundary. Comte *et al.* [150] did this for a plane mixing layer and again [101] for a plane wake. This approach has significant drawbacks, however, because this incoming "turbulence" has no correlation in space or time, which is unphysical.

Another approach is to perturb the velocity at one or more discreet frequencies. These frequencies are usually based on the most unstable frequency (and its subharmonics) as predicted by linear stability analysis. Examples of this approach, in addition to the previously mentioned incompressible work by Soteriou and Ghoniem[149], are compressible mixing layer computations by Sekar and Mukunda [151] and Lele [152]. This approach is quite effective, especially if one specifically desires to simulate a genuinely forced flow, such as in the experimental work by LeBoeuf [153]. Real turbulence, however, does not generally confine itself to a few discrete frequencies; therefore, if a more realistic inflow is desired, something more sophisticated must be done.

The third method (or family of methods) for adding turbulence at the inflow boundary attempts to emulate the full spectrum of turbulence up to the resolution of the grid. In this method, measured or approximated turbulent intensities at the inflow are combined with information on the turbulence energy spectrum (usually an assumed functional form) to derive time varying velocity perturbations. Such an approach has been used by Oh and Loth [154] for supersonic shear layers; Schwer, Tsuei, and Merkle [155] for low speed reacting mixing layers; and Lee, Lele, and Moin [156] for spatially developing isotropic turbulence. The present work will use a variation of this method.

Recently, some researchers have published work in which a separate temporal LES, running in parallel to the spatial case, was used to generate the inflow turbulence [157]. Where it is possible to use such an approach, it would seem to be an ideal solution. Unfortunately, it is computationally very expensive. Furthermore, if one is trying to match experimental data regarding boundary layer thicknesses or turbulence intensities, a temporal simulation may not work at all.

Conceptually, the present approach to inflow turbulence may be described as computing a "box" of frozen turbulence which is convected by the mean flow into the computational domain (see figure C.1).The first step in this process is to calculate a pseudo-random divergence-free isotropic velocity field which conforms to a prescribed energy spectrum. This field is computed initially in a cubic domain that is assumed periodic in all directions. It is computed on a uniform Cartesian grid (here both 32^3 and 48^3 grids have been used). Given the assumed spectrum, which is discussed below, this level of resolution is sufficient to capture the majority of the energy-containing wavenumbers, but it does mean that in regions where grid points are highly concentrated, the computational domain is able to resolve much higher wavenumbers than are calculated in the inflow turbulence.

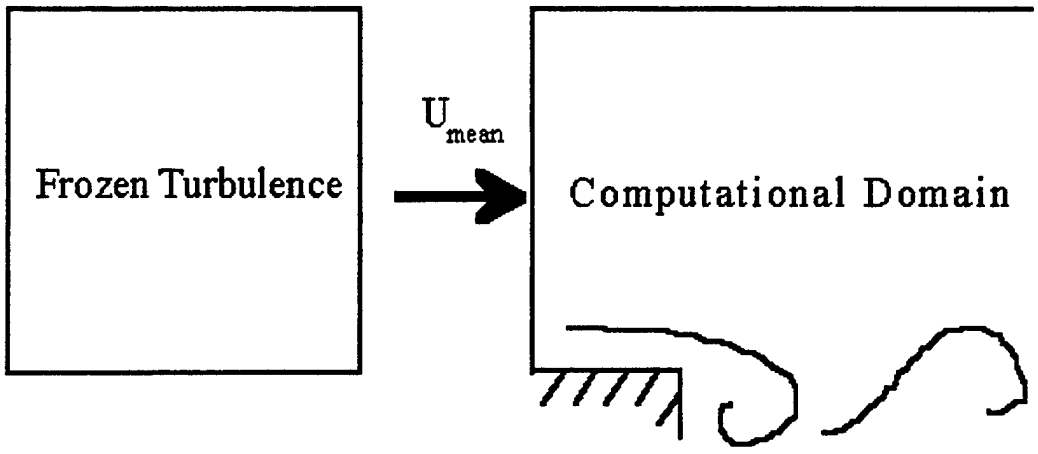


Figure C.1: Conceptualization of the inflow turbulence approximation technique

The method for computing this solenoidal isotropic field is as follows. One first computes a stream function energy distribution in spectral space:

$$E_{\Psi}\left(\vec{k}\right) = \frac{E\left(\vec{k}\right)}{\left|\vec{k}\right|^2} \tag{C.1}$$

In the above equation, $E(\vec{k})$ is the desired energy distribution of the velocity field. The use of the above expression results in a velocity field that approximately matches the desired spectrum. It is assumed that the turbulent energy is distributed evenly throughout each wavenumber shell. Thus $E(\vec{k})$ can be expressed as a function of the magnitude of the wavenumber vector ($k \equiv \left|\vec{k}\right|$). The assumed form of the energy spectrum is the same as that which has been used previously for similar purposes by, among others, Lee, Lele, and Moin [19] [156]:

$$E\left(k\right) = k^4 \exp\left(-2\left(\frac{k}{k_p}\right)^2\right) \tag{C.2}$$

For convenience, the spectrum is normalized such that:

$$\int_0^{\infty} E_{norm}\left(k\right) dk \equiv 1 \tag{C.3}$$

Thus, for the functional form given in equation C.2 above,

$$E_{norm}(k) = \frac{k^4 \exp\left(-2\left(\frac{k}{k_p}\right)^2\right)}{\frac{3}{64}\sqrt{2\pi}k_p^5} \tag{C.4}$$

The wavenumber at which this function reaches its peak, k_p, has been specified as 8.0 for the present work.

Next, the phase angles are chosen randomly (between -π and π). Using this information, a stream function, $\hat{\Psi}_i\left(\vec{k}\right)$, may be computed in spectral space. Using fast Fourier transforms, this leads to a physical stream function, $\Psi_i(\vec{x})$, from which velocities can be computed.

$$u \equiv \frac{\partial \Psi_z}{\partial y} - \frac{\partial \Psi_y}{\partial z} \tag{C.5}$$

$$v \equiv \frac{\partial \Psi_x}{\partial z} - \frac{\partial \Psi_z}{\partial x} \tag{C.6}$$

$$w \equiv \frac{\partial \Psi_y}{\partial x} - \frac{\partial \Psi_x}{\partial y} \tag{C.7}$$

If the field is to be divergence free, it is necessary to perform this calculation using the same algorithm for taking derivatives as the Navier-Stokes solver will use. The velocity field thus calculated will be divergence-free only with respect to the derivative algorithm that was used to compute it. For example, a field that is divergence-free with respect to spectral derivatives is not solenoidal with respect

to a fourth-order central difference derivative algorithm or any other non-spectral derivative scheme.

Because the energy spectrum of the stream function was only approximate (for non-spectral derivatives), the velocity field must be re-scaled in order for its energy spectrum to match the target spectrum. This is done by converting the physical velocity field back into spectral space, where its energy spectrum is calculated. The spectral velocity field is then scaled so that the energy in each wavenumber shell will match the value predicted by the desired energy spectrum. The scaled field is then transformed back into physical space. As long as the derivative algorithm that is used is either spectral or a uniform operator in space (in this instance, a fourth-order central difference scheme), the scaled field will retain the solenoidal properties of the original.

At this stage, a solenoidal velocity perturbation field is available for use, but only on an unstretched Cartesian grid. For curvilinear grids, the velocity field must now be interpolated to a grid whose j-k planes (taking i to be aligned with the mean flow) match the actual inflow boundary and are uniformly spaced in the i direction. For the spatial mixing layer cases reported in this work, the inflow boundary is vertical and is uniformly spaced in the k direction, so that a simple cubic spline along vertical grid lines is sufficient, but in other, more general, cases a two- or three-dimensional interpolating technique would be necessary.

One now has a nearly solenoidal (interpolation will introduce some errors) isotropic velocity field which has been computed on a grid which can be allowed to "convect" into the computational domain. This field, however, does not take into account the experimentally determined distribution of turbulent intensity, nor does it take into account the variation of resolved and unresolved turbulence due to

differences in grid cell sizes. Thus, one must modify the velocity field and compute a subgrid kinetic energy field that satisfies the following relationship:

$$\left\langle \widetilde{u'}^2 \right\rangle_i + \frac{2}{3} \left\langle k^{sgs} \right\rangle_i = \sigma_u^2(y,z) \tag{C.8}$$

In the above equation, the angle brackets, $\langle\rangle_i$, represent averaging along an i line. Note that if additional homogeneous directions are available, then planewise averaging can be performed. The other terms in the above equation are defined as follows: $\widetilde{u'}$ is the resolved inflow turbulence u-velocity field; k^{sgs} is the (yet to be determined) subgrid kinetic energy relative to the grid at the inflow boundary; and σ_u is the experimentally determined streamwise turbulent intensity (from Elliott [117] for the current spatial mixing layer work). Note that, in the absence of more complete information, the v and w components of velocity are assumed to behave in the same manner as u. Obviously, if more information were available, it might be possible to develop a more realistic relationship, although the solenoidal nature of the incoming turbulence would be lost.

In order to use equation C.8, the first thing which must be done is, at each point along the inflow boundary, to estimate, given the assumed form of the energy spectrum (equation C.4) and the grid resolution, what portion of the turbulent energy is resolved and how much energy is in the subgrid . If L is used to denote the length of each side of the "box" of frozen turbulence, and Δ represents the approximate grid filter size at a given point on the inflow boundary ($\Delta = (\Delta_x \Delta_y \Delta_z)^{\frac{1}{3}}$), then the maximum resolvable wavenumber, k_{max}, at that point is $\frac{L}{2\Delta}$. A box filter with a characteristic width of Δ has a corresponding spectral admittance function, which

is given by:

$$g(k) = \frac{k_{\max} \sin\left(\frac{\pi k}{k_{\max}}\right)}{\pi k} \tag{C.9}$$

Thus, if a velocity field is filtered, the corresponding admittance function for its energy spectrum is:

$$g_E(k) = \frac{k_{\max}^2 \sin^2\left(\frac{\pi k}{k_{\max}}\right)}{\pi^2 k^2} \tag{C.10}$$

With the above expression, it is now possible to write an equation for the fraction of turbulent energy which, on average, will be unresolved at any given point on the inflow boundary:

$$E_{sgs} = 1 - \int_0^{k_{\max}} E_{norm}(k)\, g_E(k)\, dk \tag{C.11}$$

For the current work, E_{norm} is as given in equation C.4. In general, E_{sgs} varies in both the j and k directions. If a homogeneous direction is present, then it may be constructed so as to only vary in one direction. In any case, there is, unfortunately, no analytic solution for the above integral; therefore, it must be computed numerically. Fortunately, as long as the grid remains unchanged, it only needs to be computed once (for each point on the inflow boundary). Note that if

$k_{\max}$ is greater than $\frac{N}{2}$ (where N is the number of points in each direction on the original uniform grid) then the latter is used as the limit of the integral in equation C.11. This is simply a recognition that the original solenoidal field only contained information from a finite number of wavenumbers.

Once the subgrid portion of the energy is known, the resolved turbulent velocity field which is entering the computational domain through the location in question can be scaled as follows:

$$\left(\widetilde{u_i'}\right)_{final} = \widetilde{u_i'} \sqrt{\frac{3\left(1 - E_{sgs}\right)\sigma_u^2}{\left\langle \widetilde{u_j'}\widetilde{u_j'} \right\rangle_i}} \tag{C.12}$$

Where $\left\langle \widetilde{u_j'}\widetilde{u_j'} \right\rangle_i$ is the average (in the i direction) of the unscaled inflow velocity perturbation field. Again, if another homogeneous direction is present, then planewise averaging can be performed. One can also compute the average value of k_{sgs} which will enter the computational domain at this point:

$$k_{avg}^{sgs} = \frac{3E_{sgs}\sigma_u^2}{2} \tag{C.13}$$

Note that, once again, v and w are assumed to behave like u.

This provides an estimate for the average amount subgrid kinetic energy entering at any given point, but it does not provide any information as its spatial distribution. Several researchers (such as Liu, Meneveau, and Katz [40] and Meneveau [143])

suggest that similarity subgrid-scale models are an effective way of predicting subgrid stresses- *i.e.* it is assumed that the actual subgrid terms are similar to the highest wavenumber components of the resolved field. In keeping with this idea a subgrid kinetic energy field is computed, using the resolved field and a test field which is created by filtering the resolved field using a filter with a characteristic width of twice the grid cell size. This field is then scaled to match the predicted value of average subgrid kinetic energy from equation C.13:

$$k^{sgs} = \left(\widehat{\widetilde{u}_i'\widetilde{u}_i'} - \widehat{\widetilde{u}}_i'\widehat{\widetilde{u}}_i' \right) \frac{k_{avg}^{sgs}}{\left\langle \widehat{\widetilde{u}_j'\widetilde{u}_j'} - \widehat{\widetilde{u}}_j'\widehat{\widetilde{u}}_j' \right\rangle_i} \tag{C.14}$$

At this point, a velocity perturbation field (and corresponding subgrid kinetic energy) is available which, to a degree, satisfies the experimentally observed properties. There are, however, some limitations. First, the final velocity field is not divergence-free. This might be a significant problem for an incompressible code, but since, in this instance, compressible flow is to be simulated, the density is allowed to fluctuate to compensate for this. Furthermore, in the case of the compressible spatial mixing layer, the region where this will be most apparent is in the boundary layer, where the flow is not expected to be solenoidal in any event.

This, however, leads directly to another drawback; namely that nothing has been said about the behavior of temperature, density, and pressure fluctuations at the inflow. For the spatial mixing layers in the current work, since Elliott presents no

experimental information about these variables, they must be handled somewhat arbitrarily, as described in Chapter VII.

Another limitation, as previously mentioned, is that the actual grid can, in places, resolve higher wavenumbers than are calculated (on the uniform grid). This results in a distorted energy spectrum at such points. Fortunately, the particular shape that has been chosen for the energy spectrum (equation C.4) is such that the contribution of these higher wavenumbers is small. Therefore, this error is comparatively minor.

This leads to the question of the assumed form of the energy spectrum. As discussed above, this particular form has been used by several other researchers, but this author is unaware of any experimental justification for it. Also, it is not expected that the turbulence in the core flow would have the same spectrum as that of the boundary layer. Still, there is no obviously better alternative available at this time. Also, this is not so much a weakness in the method for handling inflow turbulence as it is a lack of data to use in its implementation.

An additional problem, which was briefly mentioned above, is that all three components of velocity are assumed to behave in the same manner. This might be a reasonable approximation in the core flow, but is unlikely to be the case near walls. Again, this is not so much a weakness in the method as a lack of experimental data to use.

Finally, a uniform filter width was assumed in the computation of E_{sgs} when in fact, the grid spacing can be different in every direction. Unfortunately, no general method is currently available for dealing with grid anisotropy, particularly in the context of dynamic modeling. As discussed in Appendix A, the exact amount of inaccuracy that this introduces is unknown, but it is unlikely that it is significantly

greater than other sources of error. This entire method is at best a fairly crude approximation of real inflow turbulence; nevertheless, it is believed that it is as good or better than the available alternatives.

APPENDIX D

ALTERNATE SUBGRID STRESS TENSOR MODEL COEFFICIENT

The approach toward modelling the subgrid stress tensor that was taken in Chapter III is not the only one possible. One obvious alternative is, instead of splitting up the subgrid stress tensor into "incompressible" and "compressible" portions, simply apply the same model to the entire tensor:

$$\tau_{ij}^{sgs} = (\overline{\rho u_i u_j} - \overline{\rho}\bar{u}_i\bar{u}_j) \approx -2\bar{\rho}\nu_t\left(\bar{S}_{ij} - \frac{1}{3}\bar{S}_{kk}\delta_{ij}\right) + \frac{2}{3}\bar{\rho}k^{sgs}\delta_{ij} \tag{D.1}$$

In the above equation, $\bar{S}_{ij}$ again represents the resolved rate of strain tensor:

$$\bar{S}_{ij} = \frac{1}{2}\left(\frac{\partial\bar{u}_i}{\partial x_j} + \frac{\partial\bar{u}_j}{\partial x_i}\right) \tag{D.2}$$

Following the reasoning of Schumann [37], the turbulent viscosity, ν_t, is approximated, as before, as:

$$\nu_t \approx c_\nu\sqrt{k^{sgs}}\Delta \tag{D.3}$$

As before, c_ν is the model coefficient, and Δ is a characteristic length that represents the resolution available on the numerical grid. The subgrid kinetic energy, k^{sgs}, is obtained by solving an equation for its transport in parallel with the other LES equations.

The process for determining the coefficient (c_ν) in the subgrid stress tensor model is similar to that shown in Chapter . First, the trace-free portion of the subgrid stress tensor and its model are written:

$$\left(\overline{\rho u_i u_j} - \overline{\rho}\bar{u}_i\bar{u}_j\right) - \frac{1}{3}\left(\overline{\rho u_k u_k} - \overline{\rho}\bar{u}_k\bar{u}_k\right)\delta_{ij} \approx -2c_\nu\bar{\rho}\nu_t\left(\bar{S}_{ij} - \frac{1}{3}\bar{S}_{kk}\delta_{ij}\right) \tag{D.4}$$

Next, using the "test" filter and assuming similarity as in section 3.4.3, an analogous "test-field" expression may be written:

$$\begin{aligned}
&\left(\widehat{\bar{\rho}\bar{u}_i\bar{u}_j} - \widehat{\bar{\rho}}\widehat{\bar{u}}_i\widehat{\bar{u}}_j\right) - \frac{1}{3}\left(\widehat{\bar{\rho}\bar{u}_k\bar{u}_k} - \widehat{\bar{\rho}}\widehat{\bar{u}}_k\widehat{\bar{u}}_k\right)\delta_{ij} \\
\approx\ & -2c_\nu\widehat{\Delta}\widehat{\bar{\rho}}\left(\frac{\widehat{\bar{u}_k\bar{u}_k}}{2} - \frac{\widehat{\bar{u}}_k\widehat{\bar{u}}_k}{2}\right)^{\frac{1}{2}}\left(\widehat{\bar{S}}_{ij} - \frac{\widehat{\bar{S}}_{kk}}{3}\delta_{ij}\right)
\end{aligned} \tag{D.5}$$

The "test" field resolved rate of strain tensor in equation D.5 is defined as:

$$\widehat{\bar{S}}_{ij} = \frac{1}{2}\left[\frac{\partial\widehat{\bar{u}}_i}{\partial x_j} + \frac{\partial\widehat{\bar{u}}_j}{\partial x_i}\right] \tag{D.6}$$

Equation D.5 is actually overspecified since there are six independent tensor components, but only one unknown (c_ν). Thus, it must be contracted. The least squares approach of Lilly [87] is again employed. The first step is to write an expression for the model error:

$$\begin{aligned} \mathrm{E}_{ij} &= \left(\widehat{\bar{\rho}\bar{u}_i\bar{u}_j} - \widehat{\bar{\rho}}\widehat{\bar{u}}_i\widehat{\bar{u}}_j\right) - \frac{1}{3}\left(\widehat{\bar{\rho}\bar{u}_k\bar{u}_k} - \widehat{\bar{\rho}}\widehat{\bar{u}}_k\widehat{\bar{u}}_k\right)\delta_{ij} \\ &\quad + 2c_\nu\widehat{\Delta}\widehat{\bar{\rho}}\left(\frac{\widehat{\bar{u}_k\bar{u}_k}}{2} - \frac{\widehat{\bar{u}}_k\widehat{\bar{u}}_k}{2}\right)^{\frac{1}{2}}\left(\widehat{\bar{S}}_{ij} - \frac{\widehat{\bar{S}}_{kk}}{3}\delta_{ij}\right) \end{aligned} \tag{D.7}$$

This can be written in simplified form as:

$$\mathrm{E}_{ij} = L_{ij} + 2c_\nu D_{ij} \tag{D.8}$$

$$\text{where } L_{ij} = \left(\widehat{\bar{\rho}\bar{u}_i\bar{u}_j} - \widehat{\bar{\rho}}\widehat{\bar{u}}_i\widehat{\bar{u}}_j\right) - \frac{1}{3}\left(\widehat{\bar{\rho}\bar{u}_k\bar{u}_k} - \widehat{\bar{\rho}}\widehat{\bar{u}}_k\widehat{\bar{u}}_k\right)\delta_{ij} \tag{D.9}$$

$$\text{and } D_{ij} = \widehat{\Delta}\widehat{\bar{\rho}}\left(\frac{\widehat{\bar{u}_k\bar{u}_k}}{2} - \frac{\widehat{\bar{u}}_k\widehat{\bar{u}}_k}{2}\right)^{\frac{1}{2}}\left(\widehat{\bar{S}}_{ij} - \frac{\widehat{\bar{S}}_{kk}}{3}\delta_{ij}\right) \tag{D.10}$$

Next, the error is contracted with itself to form:

$$\mathrm{E}_{ij}\mathrm{E}_{ij} = L_{ij}L_{ij} + 4c_\nu D_{ij}L_{ij} + 4c_\nu^2 D_{ij}D_{ij} \tag{D.11}$$

In order for the RMS of the error to be a minimum, the derivative of equation 3.41 with respect to the model coefficient must be zero:

$$\frac{\partial \mathrm{E}_{ij}\mathrm{E}_{ij}}{\partial c_\nu} = 0 = 4D_{ij}L_{ij} + 8c_\nu D_{ij}D_{ij} \tag{D.12}$$

Using the above expression, the model coefficient can now be computed as:

$$c_\nu = \frac{-L_{ij}D_{ij}}{2D_{ij}D_{ij}} \tag{D.13}$$

REFERENCES

[1] H. Tennekes and J. L. Lumley. *A First Course in Turbulence.* The MIT Press, 1972.

[2] W. D. McComb. *The Physics of Fluid Turbulence.* Oxford University Press, 1990.

[3] M. T. Landahl and E. Mollo-Christensen. *Turbulence and Random Processes in Fluid Mechanics.* Cambridge University Press, 2nd edition, 1992.

[4] S. K. Lele. Compressibility effects on turbulence. *Annual Review of Fluid Mechanics*, 26:211–254, 1994.

[5] S. F. Birch and J. M. Eggers. A critical review of the experimental data for developed free turbulent shear layers. In *Free Turbulent Shear Flows*, pages 11–37. NASA SP-321, 1972.

[6] G. L. Brown and A. Roshko. On density effects and large structure in turbulent mixing layers. *Journal of Fluid Mechanics*, 64(4):775–816, 1974.

[7] D. Papamoschou and A. Roshko. The compressible turbulent shear layer: an experimental study. *Journal of Fluid Mechanics*, 197:453–477, 1988.

[8] D. W. Bogdanoff. Compressibility effects in turbulent shear layers. *AIAA Journal*, 21(6):926–927, 1983.

[9] D. Papamoschou. Structure of the compressible turbulent shear layer. *AIAA Journal*, 29(5):680–681, 1991.

[10] O. Zeman. Dilatation dissipation: The concept and application in modeling compressible mixing layers. *Physics of Fluids A*, 2(2):178–188, 1990.

[11] S. Sarkar, G. Erlebacher, M. Y. Hussaini, and H. O. Kreiss. The analysis and modelling of dilatational terms in compressible turbulence. *Journal of Fluid Mechanics*, 227:473–493, 1991.

[12] A. Brankovic and O. Zeman. Effects of turbulence compressibility and unsteadiness in compression corner flow. In *Center for Turbulence Research-Proceedings of the Summer Program 1994*, pages 301–311, 1994.

[13] D. C. Wilcox. Dilatation-dissipation corrections for advanced turbulence models. *AIAA Journal*, 30(11):2639–2646, 1992.

[14] D. Choi, J. S. Sabnis, and T. J. Barber. Application of an rnd k-ϵ model to compressible turbulent shear layers. *AIAA 94-0188*, 1994.

[15] E. T. Spyropoulos and G. A. Blaisdell. Evaluation of the dynamic subgrid-scale model for large eddy simulations of compressible turbulence flows. *AIAA-95-0355*, 1995.

[16] N. D. Sandham and W. C. Reynolds. Three-dimensional simulations of large eddies in the compressible mixing layer. *Journal of Fluid Mechanics*, 224:133–158, 1991.

[17] N. D. Sandham and W. C. Reynolds. Compressible mixing layer: Linear theory and direct simulations. *AIAA Journal*, 28(4):618–624, 1990.

[18] B. Vreman, H. Kuerten, and B. Geurts. Shocks in direct numerical simulation of the confined three-dimensional mixing layer. *Physics of Fluids*, 7(9):2105–2107, 1995.

[19] S. Lee, S. K. Lele, and P. Moin. Eddy shocklets in decaying compressible turbulence. *Physics of Fluids A*, 3(4):657–664, 1991.

[20] D. Papamoschou. Evidence of shocklets in a counterflow supersonic shear layer. *Physics of Fluids*, 7(2):233–235, 1995.

[21] F. S. Alvi, A. Krothapalli, and D. Washington. Experimental study of a compressible countercurrent turbulent shear layer. *AIAA Journal*, 34(4):728–735, 1996.

[22] P. J. Strykowski, A. Krothapalli, and S. Jendoubi. The effect of counterflow on the development of compressible shear layers. *Journal of Fluid Mechanics*, 308:63–96, 1996.

[23] C. G. Speziale, S. Sarkar, and T. B. Gatski. Modelling the pressure-strain correlation of turbulence: an invariant dynamical systems approach. *Journal of Fluid Mechanics*, 227:245–272, 1991.

[24] P. Koutmos, C. Mavridis, and D. Papailiou. A study of turbulent diffusion flames formed by planar fuel injection into the wake formation region of a slender square cylinder. In *Submitted to 26th International Symposium on Combustion*, 1996.

[25] J. R. Ristorcelli. A pseudo-sound constitutive relationship for the dilatational covariances in compressible turbulence: an analytical theory. Technical Report ICASE 95-22, Institute for Computer Applications in Science and Engineering, 1995.

[26] S. Sarkar, G. Erlebacher, and M. Y. Hussaini. Compressible homogeneous shear: Simulation and modeling. Technical Report ICASE 92-6, Institute for Computer Applications in Science and Engineering, 1992.

[27] S. Sarkar. The stabilizing influence of compressibility on turbulence in high-speed shear flows. *AIAA-94-2243*, 1994.

[28] S. Sarkar. The stabilizing effect of compressibility in turbulent shear flow. *Journal of Fluid Mechanics*, 282:163–186, 1995.

[29] T. J. Barber, Chiappetta L. M., J. R. DeBonis, N. J. Geordiadis, and D. A. Yoder. An assessment of parameters influencing prediction of shear layer mixing. *AIAA-97-2639*, 1997.

[30] J. Ferziger. Higher-level simulations for turbulent flows. In *Computational Methods of Turbulent, Transonic, and Viscous Flows*, page 93ff. Hemisphere, 1983.

[31] R. S. Rogallo and P. Moin. Numerical simulation of turbulent flows. *Annual Review of Fluid Mechanics*, 16:99–137, 1984.

[32] A. Yoshizawa. Large-eddy simulation of turbulent flows. In *Encyclopedia of Fluid Mechanics*, page 1277ff. Gulf Publishing, 1987.

[33] W. C. Reynolds. The potential and limitations of direct and large eddy simulations. In *Whither Turbulence? Turbulence at the Crossroads*, page 313ff. Springer-Verlag, 1990.

[34] U. Piomelli. Applications of large eddy simulations in engineering: an overview. In *Large Eddy Simulation of Complex Engineering and Geophysical Flows*, page 119ff. Cambridge University Press, 1993.

[35] M. Lesieur and O. Métais. New trends in large-eddy simulations of turbulence. *Annual Review of Fluid Mechanics*, 28:45–82, 1996.

[36] J. S. Smagorinsky. General circulation experiments with the primitive equations. I: The basic experiment. *Monthly Weather Review*, 91:99–164, 1963.

[37] U. Schumann. Subgrid scale model for finite difference simulations of turbulent flows in plane channels and annuli. *Journal of Computational Physics*, 18:376–404, 1975.

[38] R. H. Kraichnan. Eddy viscosity in two and three dimensions. *Journal of the Atmospheric Sciences*, 33:1521–1536, 1976.

[39] J. Bardina, J. H. Ferziger, and W. C. Reynolds. Improved subgrid scale models for large eddy simulation. *AIAA-80-1357*, 1980.

[40] S. Liu, C. Meneveau, and J. Katz. On the properties of similarity subgrid-scale models as deduced from measurements in a turbulent jet. *Journal of Fuid Mechanics*, 275:85–, 1994.

[41] A. W. Vreman, B. J. Geurts, and J. G. M. Kuerten. Subgrid-modelling in LES of compressible flow. In *Direct and Large-Eddy Simulation I.* Kluwer Academic Publishers, 1994.

[42] M. Germano, U. Piomelli, P. Moin, and W. H. Cabot. A dynamic subgrid-scale eddy viscosity model. In *Center for Turbulence Research- Proceedings of the Summer Program 1990*, pages 5–17, 1990.

[43] S. Ghosal, T. S. Lund, and P. Moin. A local dynamic model for large eddy simulation. In *Center for Turbulence Research- Annual Research Briefs 1992*, pages 3–25, 1992.

[44] W.-W. Kim and S. Menon. A new dynamic one-equation subgrid-scale model for large eddy simulations. *AIAA-95-0356*, 1995.

[45] D. C. Leslie and G. L. Quarini. The application of turbulence theory to the formulation of subgrid modelling procedures. *Journal of Fluid Mechanics*, 91:65–91, 1979.

[46] U. Schumann. Stochastic backscatter of turbulence energy and scalar variance by random subgrid-scale fluxes. *Proceedings of the Royal Society of London A*, 451:293–318, 1995.

[47] D. Carati, S. Ghosal, and P. Moin. On the representation of backscatter in dynamic localization models. *Physics of Fluids*, 7(3):606–616, 1995.

[48] J. W. Deardorff. A numerical study of three-dimensional turbulent channel flow at large reynolds number. *Journal of Fluid Mechanics*, 41:453–480, 1970.

[49] A. Leonard. Energy cascade in large-eddy simulations of turbulent fluid flows. *Advances in Geophysics*, 18A:237–348, 1974.

[50] W. C. Reynolds. Computation of turbulent flows. *Annual Review of Fluid Mechanics*, 8:183–208, 1976.

[51] S. Biringen and W. C. Reynolds. Large-eddy simulation of the shear-free turbulent boundary layer. *Journal of Fluid Mechanics*, 103:53–63, 1981.

[52] C. G. Speziale. Galilean invariance of subgrid-scale stress models in the large-eddy simulation of turbulence. *Journal of Fluid Mechanics*, 156:55–62, 1985.

[53] W. Cabot. Local dynamic subgrid-scale models in channel flow. In *Center for Turbulence Research- Annual Research Briefs 1994*, pages 143–159. 1994.

[54] K. Squires and O. Zeman. On the subgrid-scale modeling of compressible turbulence. In *Center for Turbulence Research- Proceedings of the Summer Program 1990*, pages 47–59, 1990.

[55] A. Yoshizawa. Statistical theory for compressible turbulent shear flows, with the application to subgrid modelling. *Physics of Fluids*, 29(7):2152–2164, 1986.

[56] G. Erlebacher, M. Y. Hussaini, C. G. Speziale, and T. A. Zang. Toward the large-eddy simulation of compressible turbulent flows. Technical Report ICASE 90-76, Institute for Computer Applications in Science and Engineering, 1990.

[57] P. Moin, K. Squires, W. Cabot, and S. Lee. A dynamic subgrid-scale model for compressible turbulence and scalar transport. *Physics of Fluids A*, 3(11):2746–2757, 1991.

[58] M. Germano. Averaging invariance of the turbulent equations and similar subgrid modeling. Technical Report CTR Manuscript 116, Center for Turbulence Research, 1990.

[59] K. D. Squires. Dynamic subgrid-scale modeling of compressible turbulence. In *Center for Turbulence Research- Annual Research Briefs 1991*, pages 207–223, 1991.

[60] D. Carati and S. Ghosal. A dynamic localization model with stochastic backscatter. In *Center for Turbulence Research- Annual Research Briefs 1994*, pages 115–125. 1994.

[61] S. Ghosal, T. S. Lund, P. Moin, and K. Akselvoll. A dynamic localization model for large-eddy simulation of turbulent flows. *Journal of Fluid Mechanics*, 286:229–255, 1995.

[62] S. A. Ragab, S.-C. Sheen, and M. Sreedhar. An investigation of finite-difference methods for large-eddy simulation of a mixing layer. *AIAA-92-0554*, 1992.

[63] E. T. Spyropoulos and G. A. Blaisdell. Large-eddy simulation of a spatially evolving compressible boundary layer flow. *AIAA 97-0429*, 1997.

[64] D. Vandromme and H. Haminh. The compressible mixing layer. In *Turbulence and Coherent Structures*, pages 507–523. Kluwer Academic Publishers, 1991.

[65] M. P. Martin and G. V. Candler. Evaluation of a subgrid-scale model for temperature fluctuations in reacting turbulence. *AIAA 97-0751*, 1997.

[66] T.-M. Liou, W.-Y. Lien, and P.-W. Hwang. Compressibility effects and mixing enhancement in turbulent free shear flows. *AIAA Journal*, 33(12):2332–2338, 1995.

[67] W.-W. Kim. *A New Dynamic Subgrid-Scale Model for Large-Eddy Simulation of Turbulent Flows.* PhD thesis, Georgia Institute of Technology, 1996.

[68] S. Ghosal. On the large eddy simulation of turbulent flows in complex geometry. In *Center for Turbulence Research- Annual Research Briefs 1993*, pages 111–128, 1993.

[69] C. Chen, J. J. Riley, and P. A. McMurtry. A study of favre averaging in turbulent flows with chemical reaction. *Combustion and Flame*, 87:257–277, 1991.

[70] H. Ha Minh, B. E. Launder, and J. MacInnes. The turbulence modelling of variable density flows- a mixed-weighted decomposition. In *Turbulent Shear Flows 3*, pages 291–308. Springer-Verlag, 1981.

[71] C. G. Speziale, G. Erlebacher, T. A. Zang, and M. Y. Hussaini. The subgrid-scale modeling of compressible turbulence. *Physics of Fluids*, 31(4):940–942, 1988.

[72] S. A. Ragab and S. Sheen. Large-eddy simulation of a mixing layer. *AIAA-91-0233*, 1991.

[73] T. A. Zang, R. B. Dahlburg, and J. P. Dahlburg. Direct and large-eddy simulations of three-dimensional compressible Navier-Stokes turbulence. *Physics of Fluids A*, 4(1):127–140, 1992.

[74] A. W. Vreman, B. J. Geurts, J. G. M. Kuerten, and P. J. Zandbergen. A finite volume approach to large eddy simulation of compressible, homogeneous, isotropic, decaying turbulence. *International Journal For Numerical Methods in Fluids*, 15:799–816, 1992.

[75] N. M. El-Hady, T. A. Zang, and U. Piomelli. Application of the dynamic subgrid-scale model to axisymmetric transitional boundary layer at high speed. *Physics of Fluids*, 6(3):1299–1309, 1994.

[76] B. Geurts, B. Vreman, and H. Kuerten. Comparison of DNS and LES of transitional and turbulent compressible flow: Flat plate and mixing layer. In *Proceedings of the 74th AGARD Fluid Dynamics Symposium on "Application of Direct and Large Eddy Simulation to Transition and Turbulence"*, pages 5–1 – 5–14, 1994.

[77] M. V. Salvetti and S. Banerjee. A priori tests of a new dynamic subgrid-scale model for finite-difference large-eddy simulations. *Physics of Fluids*, 7(11):2831–2847, 1995.

[78] F. F. Grinstein and R. H. Guirguis. Effective viscosity in the simulation of spatial evolving shear flows with monotonic FCT models. *Journal of Computational Physics*, 101:165–175, 1992.

[79] F. F. Grinstein and K. Kailasanath. Chemical energy release and dynamics of transitional, reactive shear flows. *Physics of Fluids A*, 4(10):2207–2221, 1992.

[80] J. P. Boris, F. F. Grinstein, E. S. Oran, and R. L. Kolbe. New insights into large eddy simulation. *Fluid Dynamics Research*, 10:199–228, 1992.

[81] A. Silveira-Neto, D. Grand, O. Métais, and M. Lesieur. A numerical investigation of the coherent vortices in turbulence behind a backward-facing step. *Journal of Fluid Mechanics*, 256:1–25, 1993.

[82] C. Hirsch. *Numerical Computation of Internal and External Flows*, volume 2: Computational Methods for Inviscid and Viscous Flows. John Wiley and Sons, 1990.

[83] A. Yoshizawa and K. Horiuti. A statistically-derived subgrid-scale kinetic energy model for the large-eddy simulation of turbulent flows. *Journal of the Physical Society of Japan*, 54:2834ff, 1985.

[84] S. Weeratunga and S. Menon. Parallel computations of unsteady combustion in a ramjet engine. *AIAA-93-1914*, 1993.

[85] S. Menon and P. K. Yeung. Analysis of subgrid models using direct and large eddy simulations of isotropic turbulence. In *Proceedings of the 74th AGARD Fluid Dynamics Symposium on "Application of Direct and Large Eddy Simulation to Transition and Turbulence"*, pages 10–1 – 10–12, 1994.

[86] R. W. MacCormack and B. S. Baldwin. A numerical method for solving the navier-stokes equations with application to shock-boundary layer interactions. *AIAA-75-1*, 1975.

[87] D. K. Lilly. A proposed modification of the Germano subgrid-scale closure method. *Physics of Fluids A*, 4(3):633–635, 1992.

[88] B. Vreman, B. Geurts, and H. Kuerten. Realizibility conditions for the tubulent stress tensor in large-eddy simulation. *Journal of Fluid Mechanics*, 276:351–362, 1994.

[89] R. W. MacCormack. The effect of viscosity in hypervelocity impact cratering. *AIAA-69-0354*, 1969.

[90] D. Gottlieb and E. Turkel. Dissipative two-four methods for time-dependant problems. *Mathematics of Computation*, 30(136):703–723, 1976.

[91] J. L. Steger and R. F. Warming. Flux vector splitting of the inviscid gas-dynamic equations with application to finite difference methods. Technical Report NASA TM 75605?, NASA Ames Research Center, 1979?

[92] M.-S. Liou and Jr. Steffen, C. J. A new flux splitting scheme. *Journal of Computational Physics*, 107:23–39, 1993.

[93] W. H. Calhoon Jr. *On Subgrid Combustion Modeling for Large-Eddy Simulations.* PhD thesis, Georgia Institute of Technology, 1996.

[94] B. E. Wake and D. Choi. Investigation of high-ordered upwinded differencing for vortex convection. *AIAA-95-1719-CP*, 1995.

[95] R. Hixon, S.-H. Shih, and R. R. Mankbadi. Effect of coannular flow on linearized euler equation predictions of jet noise. *AIAA 97-0284*, 1997.

[96] E. Turkel. On the practical use of high-order methods for hyperbolic systems. *Journal of Computational Physics*, 35:319–340, 1980.

[97] A. Bayliss, P. Parikh, L. Maestrello, and E. Turkel. A fourth-order scheme for the unsteady compressible Navier-Stokes equations. Technical Report ICASE 85-44, Institute for Computer Applications in Science and Engineering, 1985.

[98] S. I. Hariharan and H. C. Lester. Acoustic shocks in a variable area duct containing near sonic flows. *Journal of Computational Physics*, 58:134–145, 1985.

[99] W. Tang, N. M. Komerath, and L. N. Sankar. Numerical simulation of the growth of instabilities in supersonic free shear layers. *Journal of Propulsion and Power*, 6(4):455–460, 1990.

[100] I. H. Tuncer and L. N. Sankar. Numerical simulation of three-dimensional supersonic free shear layers. *AIAA Journal*, 30(4):871–872, 1992.

[101] P. Comte, Y. Fouillet, M.-A. Gonze, M. Lesieur, O. Metais, and X. Normand. Generation of coherent structures in free shear layers. In *Turbulence and Coherent Structures*, pages 45–73. Kluwer Academic Publishers, 1991.

[102] S. Sheen, M. Sreedhar, and S. A. Ragab. Structures and transition to small scales in a mixing layer. In *Engineering Applications of Large Eddy Simulations*, pages 53–64. ASME, 1993.

[103] J. E. Martin. Aeroacoustic computation of a gust-plate interaction via maccormack schemes. In *ICASE/LaRC Workshop on Benchmark Problems in Computational Aeroacoustics (CAA)*, pages 297–301, 1995.

[104] J. N. Scott, S. I. Hariharan, and R. Mankbadi. Evaluation of numerical schemes for the analysis of sound generation by blade-gust interaction. In *Proceedings of ICASE/LaRC Workshop on Benchmark Problems in Computational Aeroacoustics (CAA)*, pages 303–312, 1995.

[105] K. Viswanathan and L. N. Sankar. A comparative study of upwind and MacCormack schemes for CAA benchmark problems. In *ICASE/LaRC Workshop on Benchmark Problems in Computational Aeroacoustics (CAA)*, pages 185–195, 1995.

[106] D. A. Hudson and L. N. Long. Time accurate application of the MacCormack 2-4 scheme on massively parallel computers. In *ICASE/LaRC Workshop on Benchmark Problems in Computational Aeroacoustics (CAA)*, pages 209–215, 1995.

[107] L. Gamet and J. L. Estivalezes. Non-reflexive boundary conditions applied to jet aeroacoustics. *AIAA-95-0159*, 1995.

[108] A. Arnone, M.-S. Liou, and L. A. Povinelli. Integration of Navier-Stokes equations using dual time stepping and a multigrid method. *AIAA Journal*, 33(6):985–990, 1995.

[109] J. R. Herring, S. A. Orszag, R. H. Kraichnan, and D. G. Fox. Decay of two-dimensional homogeneous turbulence. *Journal of Fluid Mechanics*, 66(3):417–444, 1974.

[110] G. Comte-Bellot and S. Corrsin. Simple Eulerian time correlation of full- and narrow-band velocity signals in grid-generated, 'isotropic' turbulence. *Journal of Fluid Mechanics*, 48(2):273–337, 1971.

[111] L. P. Bernal and A. Roshko. Streamwise vortex structure in plane mixing layers. *Journal of Fluid Mechanics*, 170:499–525, 1986.

[112] C. D. Winant and F. K. Browand. Vortex pairing: the mechanism of turbulent mixing layer growth at moderate Reynolds number. *Journal of Fluid Mechanics*, 63:237–255, 1974.

[113] A. K. M. F. Hussain. Coherent structures and turbulence. *Journal of Fluid Mechanics*, 173:303–356, 1986.

[114] M. A. Hernan and J. Jimenez. Computer analysis of a high-speed film of the plane turbulent mixing layer. *Journal of Fluid Mechanics*, 119:323–345, 1982.

[115] A. K. M. F. Hussain and A. R. Clark. On the coherent structure of the axisymmetric mixing layer: A flow-visualization study. *Journal of Fluid Mechanics*, 104:263–294, 1981.

[116] R. D. Moser and M. M. Rogers. Mixing transition and the cascade to smale scales in a plane mixing layer. *Physics of Fluids A*, 3(5):1128–1134, 1991.

[117] G. Elliott. *A Study of Compressible Mixing Layers Using Laser Based Diagnostic Techniques.* PhD thesis, The Ohio State University, 1993.

[118] D. Papamoschou and A. Roshko. Observations of supersonic free shear layers. *AIAA-86-0162*, 1986.

[119] N. T. Clemens and M. G. Mungal. Two- and three-dimensional effects in the supersonic mixing layer. *AIAA Journal*, 30(4):973–981, 1992.

[120] N. L. Messersmith, S. G. Goebel, J. P. Renie, J. C. Dutton, and H. Krier. Investigation of supersonic mixing layers. *Journal of Propulsion and Power*, 6(4):353–354, 1990.

[121] G. S Elliott, M. Samimy, and S. A. Arnette. Study of compressible mixing layers using filtered Rayleigh scattering based visualizations. *AIAA Journal*, 30(10):2567–2569, 1992.

[122] N. T. Clemens and M. G. Mungal. Large-scale structure and entrainment in the supersonic mixing layer. *Journal of Fluid Mechanics*, 284:171–216, 1995.

[123] Y. R. Shau and D. S. Dolling. The detection of large scale structure in undisturbed and disturbed compressible turbulent free shear layers. *AIAA-90-0711*, 1990.

[124] G. Elliott and M. Samimy. Compressibility effects in free shear layers. *AIAA-90-0705*, 1990.

[125] M. Samimy and G. S. Elliott. Effects of compressibility on the characteristics of free shear layers. *AIAA Journal*, 28(3):439–445, 1990.

[126] S. G. Goebel and J. C. Dutton. Experimental study of compressible turbulent mixing layers. *AIAA Journal*, 29(4):538–546, 1991.

[127] C. K. W. Tam and Q. F. Hu. The instability and acoustic wave modes of supersonic mixing layers inside a rectangular channel. *Journal of Fluid Mechanics*, 203:51–76, 1989.

[128] M. Soetrisno, J. A. Greenough, D. S. Eberhardt, and J. J. Riley. Confined compressible mixing layers: Part I. three dimensional instabilities. *AIAA-89-1810*, 1989.

[129] P. J. Lu and K. C. Wu. Numerical investigation on the structure of a confined supersonic mixing layer. *Physics of Fluids A*, 3(12):3063–3079, 1991.

[130] G. S. Elliott, M. Samimy, and S. A. Arnette. The evolution of large scale structures in compressible mixing layers. In *Proceedings of the Ninth Symposium on "Turbulent Shear Flows"*, pages 19–4–1 – 19–4–6, 1993.

[131] G. S. Elliott, M. Samimy, and S. A. Arnette. The characteristics and evolution of large-scale structures in compressible mixing layers. *Physics of Fluids*, 7(4):864–876, 1995.

[132] M. Samimy and G. S. Elliott. Effects of compressibility on the structure of free shear layers. *AIAA-88-3054A*, 1988.

[133] M. Samimy, D. E. Erwin, and G. S. Elliott. Compressibility and shock wave interaction effects on free shear layers. *AIAA-89-2460*, 1989.

[134] M. Samimy, M. F. Reeder, and G. S. Elliott. Compressibility effects on large structures in free shear flows. *Physics of Fluids A*, 4(6):1251–1258, 1992.

[135] M. Ameur Si and J. P. Chollet. Large eddy simulations of shear flows: Mixing layers. In *Advances in Turbulence V*. Kluwer Academic Publishers, 1995.

[136] K. W. Thompson. Time-dependant boundary conditions for hyperbolic systems, II. *Journal of Computational Physics*, 89:439–461, 1990.

[137] T. J. Poinsot and S. K. Lele. Boundary conditions for direct simulations of compressible viscous flows. *Journal of Computational Fluids*, 101:104–129, 1992.

[138] M. R. Gruber, N. L. Messersmith, and J. C. Dutton. Three-dimensional velocity field in a compressible mixing layer. *AIAA Journal*, 31(11):2061–2067, 1993.

[139] R. Hixon, S.-H. Shih, and R. R. Mankbadi. Application of an optimized maccormack-type scheme to acoustic scattering problems. In *2nd ICASE/LaRC Workshop on Benchmark Problems in Computational Aeroacoustics*, 1996.

[140] R. Hixon. On increasing the accuracy of maccormack schemes for aeroacoustic applications. Technical Report ICOMP-96-11, Institute for Computational Mechanics in Propulsion, 1996.

[141] R. Hixon. On increasing the accuracy of maccormack schemes for aeroacoustic applications. *AIAA 97-1586*, 1997.

[142] T. M. Smith, 1997. Private communication.

[143] C. Meneveau. Statistics of turbulence subgrid-scale stresses: Necessary conditions and experimental tests. *Physics of Fluids*, 6(2):815–833, 1994.

[144] J. B. Perot. Comments on the fractional step method. *Letter to Journal of Computational Physics*, 121:190–191, 1995.

[145] S. V. Veeravalli and S. G. Saddoughi. A preliminary experimental investigation of local isotropy in high-Reynolds-number turbulence. In *Center for Turbulence Research- Annual Research Briefs 1991*, pages 3–20, 1991.

[146] S. Ghosal and P. Moin. The basic equations for the large eddy simulation of turbulent flows in complex geometry. *Journal of Computational Physics*, 118:24–37, 1995.

[147] P. L. Roe. Approximate Riemann solvers, parameter vectors, and difference schemes. *Journal of Computational Physics*, 43:357–372, 1981.

[148] A. Jameson and T. J. Baker. Solution of the Euler equations for complex configurations. *AIAA-83-1929*, 1983.

[149] M. C. Soteriou and A. F. Ghoniem. Effects of the free-stream density ratio on free and forced spatially developing shear layers. *Physics of Fluids*, 7(8):2036–2051, 1995.

[150] P. Comte, M. Lesieur, H. Laroche, and X. Normand. Numerical simulations of turbulent plane shear layers. In *Turbulent Shear Flows 6*, pages 360–380. Springer-Verlag, 1989.

[151] B. Sekar and H. S. Mukunda. A computational study of direct simulation of high speed mixing layers without and with chemical heat release. In *Proceedings of the 23rd International Symposium on Combustion*, pages 707–713, 1990.

[152] S. K. Lele. Direct numerical simulation of compressible free shear flows. *AIAA-89-0374*, 1989.

[153] R. L. LeBoeuf. Forced free-shear layer measurements. In *Center for Turbulence Research- Annual Research Briefs 1994*, pages 313–338, 1994.

[154] C. K. Oh and E. Loth. Unstructured grid simulations of spatially evolving supersonic shear layers. *AIAA Journal*, 33(7):1229–1238, 1995.

[155] D. A. Schwer, H.-H. Tsuei, and C. L. Merkle. Computation and validation of spatially reacting mixing layers. *AIAA-95-0261*, 1995.

[156] S. Lee, S. K. Lele, and P. Moin. Simulation of spatially evolving turbulence and the applicability of Taylor's hypothesis in compressible flow. *Physics of Fluids A*, 4(7):1521–1530, 1992.

[157] K. Akselvoll and P. Moin. Large-eddy simulation of turbulent confined coannular jets. *Journal of Fluid Mechanics*, 315:387–411, 1996.

VITA

Christopher C. Nelson was born in Malmö, Sweden on February 15, 1965. He is the son of Noel and Cary Nelson. After graduating from Clarkston High School, Clarkston, Georgia in 1983, he enrolled at the Georgia Institute of Technology in Atlanta, Georgia. He received a Bachelor of Science degree in Aerospace Engineering from Georgia Tech in 1988. He also received a Master of Science degree in Aerospace Engineering from Georgia Tech in 1989. In 1992, he began working with Dr. Suresh Menon toward a Ph.D. in Aerospace Engineering. He has been happily married to Connie Nelson since 1993. Their first child, Deborah, was born on August 17, 1997.